Open Research Online

Acoustical Exploitation of Rough, Mixed Impedance and Porous Surfaces Outdoors

Thesis

oro.open.ac.uk

Acoustical Exploitation of Rough, Mixed Impedance and Porous Surfaces Outdoors

Thesis Submitted by

Imran Bashir, BEng. (Hons.), MSc.

For the Degree of

Doctor of Philosophy

October 2013

In the

Department of Engineering and Innovation,

Faculty of Mathematics, Computing and Technology,

The Open University,

Milton Keynes, United Kingdom.

Date of Submission: 30 September 2013
Date of Award: 29 January 2014

ProQuest Number: 13835811

ProQuest 13835811

Certificate of Originality

This is to certify that I am responsible for the work submitted in this thesis, that the original work is my own except as specified in acknowledgements, in text or in bibliography, and that neither the thesis nor the original work contained therein has been submitted to this or any other institution for a degree.

_____ (Signature)

(Imran Bashir)

_____ (Date)

Supervisors
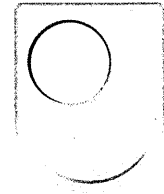
Prof. Keith Attenborough

Research Professor in Acoustics,

Acoustics Research Group,

Department of Engineering and Innovation,

The Open University,

Milton Keynes, United Kingdom.

Dr. Shahram Taherzadeh

Lecturer in Acoustics,

Acoustics Research Group,

Department of Engineering and Innovation,

The Open University,

Milton Keynes, United Kingdom.

The Open University

Abstract

This thesis is a contribution towards developing cost-effective ways for reducing outdoor traffic noise in outdoor environments by exploiting the interaction between sound travelling directly to a listener from the source and sound reflected by the intervening ground.

Sound propagation over different kinds of porous, rough and mixed impedance ground surfaces have been studied experimentally and numerically. Measurements of short-range acoustic level difference spectra over outdoor ground surfaces and artificially-created surfaces outdoors and in the laboratory have been compared with predictions to establish suitable impedance models. Sound propagation over mixed impedance ground having single or multiple impedance discontinuities has also been studied. Acoustic transmission loss through vegetation, crops and hedges has been investigated.

The phenomenon of sound diffraction and periodicity due to rough periodic ground surfaces has been explored through artificially created rough surfaces in the laboratory and outdoors. The phenomenon of surface wave propagation over rough hard surfaces and porous surfaces has been explored through laboratory experiments.

Measured data indoors and outdoors have been used to validate numerical (BEM and FEM), empirical and analytical (MST) prediction techniques. The validated numerical methods have been used to make predictions at scales suitable for attenuating traffic noise by means of carefully designed ground treatments. The work has also been extended to railway and tramway noise.

It has been found that replacing hard ground with porous ground, introducing single or multiple impedance discontinuities, growing vegetation and introducing low height roughness can all contribute between 3 and 15 dB additional attenuation of traffic noise. In respect of replacing hard ground by porous ground, it is concluded that the ground with lowest flow resistivity i.e. grassland left untouched and allowed to grow wild gives the best attenuation performance. However, dividing a single width of soft ground into alternating strips of hard and soft surfaces does not improve the insertion loss. The overall width of the soft surface is the main factor. Cultivating crops over porous ground can enhance the attenuation but the effect is not very significant for A-weighted levels as most of additional attenuation occurs at higher frequencies above 3 kHz.

A 0.3 m high and at least 3 m wide lattice structure design is found to be very useful for traffic noise attenuation since it offers greater insertion loss than the same width and height of parallel low walls and the resulting attenuation is azimuthal angle independent. It has been shown also that the potentially negative effect on insertion loss due to propagation of roughness-induced surface waves over rough surfaces can be reduced by introducing sound absorbing material in between the walls.

Acknowledgements

This dissertation would not have been a real fulfilment without the backing and cooperation from various individuals through various means.

First of all, I would like to express my deepest gratitude and respect to my supervisors Prof. Keith Attenborough and Dr. Shahram Taherzadeh, for their guidance, support and patience during the years I worked on the research reported in my thesis at The Open University, United Kingdom. This work would not have been possible without their guidance, support and encouragement. I would like to express my thanks for all I have learned from them and for their continuous help and support in all stages of this thesis. It has been great pleasure and inspiration to work with them. A special thanks to Keith, for converting my thesis into English. Also, I would like to take this opportunity to thank Dr. Toby Hill for valuable and helpful discussions while he worked with me in the HOSANNA project.

Secondly, the assistance given by the staff and fellow research student in the Acoustics Research Group throughout my research are acknowledged and appreciated. I am indebted to Dr. Ho-chul Shin for his constructive advice on my research and for accompanying me during outdoor measurements over crops. Moreover, special thanks to Peter Seabrook (Project Officer) who contributed much time and effort to source and helps to fabricate materials for experiments. As well as, I should mention with gratitude to Roger Frith and Mikki Thomas (Project Officers) for their help rendered during the laboratory measurements.

Additionally, I would like to express many thanks to Alvin Chong and Paulina Kowal (PhD students) for their insightful suggestions, discussions and help.

Last, but not least, I am truly grateful to my dearest family, whose care and supports have been the important factors for me to seek this higher degree without worries. This thesis is dedicated to my mother and my father (late).

Table of Contents

List of Figures

XII

XIII

XVII

XX

XXIII

XXVI

XXVIII

XXX

List of Tables

XXXII

XXXIII

List of Symbols

∇^2	Laplacian constant
c_0	Speed of sound in air
∂	Partial derivative
$\partial/\partial n$	Normal derivative
$\int_s$	Surface integral
$\sum$	Summation
P	Acoustic wave
p	Acoustic pressure
ϕ	Acoustic potential
$\Re$	Real-valued function
k_0	Wave-number or propagation constant in air
k_c	Propagation constant in air
f	Frequency
λ	Wavelength
i, j	Unit imaginary number
ω	Angular frequency
ρ_0	Density of air
$\rho(\omega)$	Complex density

$C(\omega)$	Complex Compressibility
β	Surface admittance
z	Characteristic impedance
z_c	Surface impedance
$H_0^{(1)}$	Hankel function of first kind
$J_n(\ )$	Bessel function of the first kind and order n
$G(\ )$	Green's function
Ω	Porosity
R_s	Flow resistivity
R_e	Effective flow resistivity
T	Tortuosity
v	Velocity
K	Compressional modulus
k	Structure factor
γ	Adiabatic constant
N_{pr}	Prandtl number
s_p	Pore shape factor ratio
r_h	Hydraulic radius
λ_c	Dimensionless parameter for complex density
μ	Viscosity of air
η	Coefficient of dynamic viscosity

Λ	Characteristic viscous length
α_e	Porosity rate
R_p	Plane wave reflection coefficient
Q	Spherical wave reflection coefficient
R_1	Source-receiver direct distance
R_2	Source-receiver distance through speculary reflected path
R_p	Plane wave reflection coefficient
$F(\ )$	Boundary loss factor
θ	Angle of incidence
d	Layer thickness
n	Refractive index
EA	Excess attenuation
LD	Level difference
P_{total}	Total sound pressure level
P_{direct}	Sound pressure level in free field
δ	Mutual coupling between the semi-cylinders
b	Centre-to-centre spacing
$O()$	Order of error
V	Cross sectional area per unit length
ε	Scattering coefficient
s_2	Shape factor for arbitrary shaped scatterer

K	Hydrodynamic shape factor or Virtual mass
f_{br}	Bragg diffraction frequency
F_2	Fresnel integral function
H_r	Receiver height
H_s	Source height
c_p	Surface wave speed
FL	Foliage area per unit volume
L	Length of the propagation path
ff	Filling fraction
EA	Excess Attenuation
IL	Insertion Loss
r	Scatterer radius
L_{WRN}	Rolling noise sound power
L_{WTN}	Traction noise sound power

Chapter 1

1. Introduction

1.1 Introduction

Traffic noise is a major and increasing problem. A traditional way of reducing traffic noise is to build a noise barrier along the edge of the road. This creates an acoustical shadow zone which benefits receivers close to the barrier but, the effects of noise barriers reduce with increasing distance. Moreover there may be cases where the erection of a noise barrier is undesirable for social, aesthetic or practical reasons.

An alternative to a noise barrier that has not received much attention previously is to reduce the traffic noise by exploiting ground effect. Ground effect is the result of interference between sound travelling directly from source to receiver and that arriving at the receiver after being reflected from the ground. If the ground is hard and smooth then, for typical source-receiver locations near surface transport noise sources and frequencies of interest in traffic noise control, the incident sound pressure is doubled. The first destructive interference is at too high a frequency to make a useful contribution to noise reduction. However the first

destructive interference over soft ground (often incorrectly called ground effect or ground absorption) is a well known source of attenuation of outdoor sound in addition to that due to wave front spreading and air absorption. So far there has been little investigation of the possibilities for exploiting and designing ground effect for traffic noise reduction.

It should be noted that another consequence of erecting a noise barrier is that any pre-existing 'soft' ground effect is reduced. However this may not be the case if there is a vegetation barrier in the form of plants, crops, bushes, hedges or trees on the ground. The extent to which the contributions of the ground beneath vegetation and the vegetation itself to overall sound propagation can be distinguished has not been studied to any great extent.

In this thesis the potential designs of (hard) rough, mixed-impedance, porous and vegetated ground surfaces for traffic noise attenuation are studied. The study has been carried out as part of a European project (EU FP7 HOSANNA) the aim of which was to develop cost-effective ways for reducing traffic noise in outdoor environments by the optimal use of vegetation, soil or ground and both 'natural' and recycled materials in combination with artificial elements.

To establish the range of 'natural' ground effects that are available for potential exploitation, Chapter 4 reviews relevant parameters, impedance models and data. This enables selection of impedance models and parameter ranges for use when assessing the potential of mixed impedance (alternating 'hard' and 'soft') ground for noise reduction in Chapter 7 which considers sound propagation over single and multiple impedance discontinuities and Chapter 11 which considers potential of various ground surface designs for surface transport noise reduction.

A method for altering the ground effect due to hard smooth ground, that has received relatively little previous attention, is to add roughness. This method is investigated in Chapter 5. The phenomena associated with sound diffraction by rough ground with periodic and random roughness distributions of various shapes and packing densities has been explored through measurements over artificially-created rough surfaces in the laboratory and outdoors. Numerical and analytical modelling of sound propagation is used to understand the contributing physical phenomena. Also it is shown possible to describe periodic rough surfaces in terms of an effective impedance in Chapter 6. The effective impedance descriptions are shown to be useful for modelling propagation from surface transport surfaces over various potential ground surface designs in Chapter 11.

One of the important mechanisms for noise reduction through surface roughness is found to be the conversion of incident sound into surface waves. Surface waves can be created also over ground surfaces corresponding to thin porous layers. Without attenuation surface waves could lead to noise enhancement rather than decrease. In Chapter 8 surface wave generation over rough and porous surfaces and methods for their attenuation are explored experimentally and numerically.

The separate contributions of ground effect and scattering by stems and foliage in crops and hedges are considered in Chapter 10 after a laboratory investigation of these effects for sparse arrays of vertical cylinders separately and in combination in Chapter 9. The latter investigation is relevant also to tree planting schemes alongside roads.

Since it would be rather expensive and impractical as part of a PhD thesis to develop these ideas at full scale much of the reported investigations are of laboratory scale measurements, outdoor measurements on treatments of limited extent, predictions and numerical simulations. The numerical and analytical methods that have been used are outlined in Chapter 2. Data acquisition systems have been developed to carry out laboratory and outdoor field experiments and these are described in Chapter 3.

A diagram of the thesis plan and the connections between chapters is shown in Figure 1.1. More detail of each chapter's contents follows in next section. Since the chapters present work on different topics each chapter includes its own literature review. The general structure of each chapter is,

- Introduction
- Literature review
- Measurements
- Predictions
- Analysis and discussion
- Conclusion

```
                    ┌─────────────────────────────────────┐
                    │  Acoustical exploitation of Porous,  │
                    │   Mixed Impedance and Rough surfaces │
                    └─────────────────────────────────────┘
                    ┌─────────────────────────────────────┐
          ┌─────────┤       Chapter # 1: Introduction      ├─────────┐
          │         └──────────────────┬──────────────────┘         │
          │                            │                            │
  ┌───────────────┐          ┌───────────────────┐          ┌───────────────┐
  │    Methods    │          │  Porous surfaces  │          │ Rough surfaces│
  └───────┬───────┘          └─────────┬─────────┘          └───────┬───────┘
```

Methods

- **Chapter # 2** Numerical methods used in simulations: BEM, MST & FEM
- **Chapter # 3** Measurements: data acquisition, processing & materials

Porous surfaces

- **Chapter # 4** Outdoor Ground Impedance models
- **Chapter # 7** Propagation over Impedance discontinuities

Vegetation

- **Chapter # 9** Sound transmission through low filling fraction arrays of identical rigid cylinders perpendicular to the ground
- **Chapter # 10** Sound propagation through crops and hedges

Rough surfaces

- **Chapter # 5** Diffraction assisted rough ground effect: Models & Measurement data
- **Chapter # 6** Effective impedance models
- **Chapter # 8** Surface waves over periodically-rough and porous boundaries

Chapter # 11 Insertion loss calculations for surface transport noise

Chapter # 12 Conclusions & Future work

Figure 1.1 Flow-Chart for overall thesis structure.

1.2 Overview: Thesis chapters

1.2.1 Chapter 1: Introduction

This chapter presents an overview of work carried out for this PhD thesis. It summarizes the major original contributions in the thesis and lists the resulting journal publications.

1.2.2 Chapter 2: Numerical Methods used in Simulations: BEM, MST and FEM

This chapter reviews the three methods used to carry out predictions throughout the thesis i.e. the Boundary Element Method (BEM), Multiple Scattering Theory (MST) and the Finite Element Method (FEM). The chapter outlines the mathematical equations used to formulate these methods. Pros and cons for each of these methods together with their limitations and applicability are discussed. The chapter concludes with comparisons between the three prediction techniques. Existing MST and BEM codes have been exploited in preparing the thesis and the FEM modelling was carried out using commercially available COMSOL® software package.

1.2.3 Chapter 3: Measurements: data acquisition, processing and materials

Chapter 3 provides a detailed overview of the systems used to carry out measurements in laboratory and outdoor environments. It describes the development and implementation of the acoustic measuring systems and explains some basic principles of signal processing. It presents the data acquisition

procedure and describes the pre-processing and post-processing of the data. The experimental arrangements for indoor and outdoor measurements are given. Some example measurements and analyses are given also.

1.2.4 Chapter 4: Outdoor Ground Impedance Models

In Chapter 4 outdoor measurements of short range sound propagation are compared with predictions to investigate the applicability of various ground impedance models to naturally occurring ground surfaces. The mathematical formulations for seven impedance models are given including the Delany and Bazley model, the Miki model, the Taraldsen model, the Zwikker and Kosten model, the Attenborough four parameter model, Identical pore models (Cylindrical pore, Slit pore, Triangular pore, Rectangular pore), the Variable porosity model and the Johnson Allard Umnova model. The procedure of predicting level difference spectra using impedance models and a point source sound propagation model is described in detail. Predictions using these models are compared with data over 47 different naturally occurring outdoor sites. Data over some artificially created surfaces in the laboratory is also compared with predictions. The applicability of each of these impedance models is discussed.

1.2.5 Chapter 5: Diffraction Assisted Rough Ground Effect: Models and Data

In Chapter 5 the study is extended to artificially-created rough surfaces. The phenomenon of sound diffraction by rough ground is explored through measurements on artificially-created rough surfaces in the laboratory and outdoors

and through predictions. Numerical and analytical modelling of sound propagation is used to understand the physical phenomenon

1.2.6 Chapter 6: Effective impedance models

In Chapter 6 it is shown possible to describe propagation over periodic rough surfaces in terms of an effective surface impedance. As well as reviewing possible analytical models for effective surface impedance, empirical models for various forms of rough surface have been deduced from laboratory and outdoor data. The validity of the various models for different roughness configurations has been investigated.

1.2.7 Chapter 7: Propagation over Impedance discontinuities

This chapter reports laboratory studies of sound propagation over ground surfaces containing a single impedance discontinuity or multiple impedance discontinuities. The resulting data have been compared with predictions using the Boundary Element, De Jong, modified De Jong and Fresnel zone methods.

1.2.8 Chapter 8: Surface waves over periodically-rough and porous boundaries

In Chapter 8 the phenomenon of surface wave generation and propagation over rough and porous surfaces is explored experimentally and numerically. The laboratory rough surfaces include a (lighting) lattice surface, randomly and periodically spaced triangular strips, rectangular strips and larger-scale parallel walls. Porous surfaces include polyurethane foam layers having different thickness and felt layers. The conversion of incident sound into surface waves is an

important mechanism in sound attenuation by rough surfaces. However the surface waves generated by rough surfaces can themselves result in negative insertion loss at some frequencies. The noise energy from the environment is taken away by converting it into surface waves which then need to be absorbed. In this chapter, different methods of attenuating surface waves have been investigated. The study of surface wave propagation has been carried also using numerical prediction techniques.

1.2.9 Chapter 9: Sound transmission through low filling fraction arrays of identical rigid cylinders perpendicular to the ground

This chapter reports measurements of sound transmission through regular arrangements of PVC pipes (sonic crystals) placed on a hard ground and a soft ground respectively. The pipe arrays had low filling fractions and large centre-to-centre spacings. The purpose of this study was to investigate the potential insertion loss of regular tree planting schemes at a laboratory scale. The investigations include the effects of perturbing the regular spacing in the arrays and the feasibility of predicting sound propagation through low filling fraction arrays of vertical cylinders on soft ground by simply adding ground and sonic crystal effects.

1.2.10 Chapter 10: Sound propagation through crops and hedges

Chapter 10 reports investigations of acoustic transmission loss through vegetation, crops and hedges and a semi- empirical model for attenuation by vegetation is introduced that enables predictions of total transmission loss over

vegetation-covered ground by adding vegetation attenuation to ground effect predictions.

1.2.11 *Chapter 11: Insertion loss calculations for surface transport*

noise

This chapter investigates the application of the different ground treatments studied and developed in the thesis. Insertion losses near sources of road traffic noise, railway noise and tramway noise have been calculated by subtracting the SPLs predicted in the presence of ground treatments from those predicted without any treatments. The insertion losses have been calculated for several receiver locations and heights for the appropriate given source spectrum. The ground treatments that have been considered include,

- Replacing hard ground with soft ground.
- Introducing low height roughness (Parallel walls, Lattice and Triangles).
- Single or multiple impedance discontinuities.
- Growing dense crops.

1.2.12 *Chapter 12: Summary of conclusions and suggestions for*

further work

Chapter 12 provides an overall summary and suggestions for further work.

1.3 List of thesis contributions

This section details the new work carried out by the candidate in generating this thesis.

1.3.1 Author's contributions

1.3.1.1 Porous and Mixed impedance surfaces

- A detailed comparative study of the application of acoustic impedance models to porous surfaces.

- Extension of knowledge regarding the applicability of semi-analytical models in the study of impedance discontinuities (2D Strips & 3D patches).

1.3.1.2 Rough surfaces

- A comprehensive study of sound propagation over rough surfaces through laboratory experiments, outdoor measurements and numerical predictions.

- Development of effective impedance models to predict sound propagation over a laboratory 3D lattice and outdoor rough surfaces.

- A proposal for a new quicker way of measuring surface wave dispersion by using impedance spectra deduced from complex excess attenuation data.

1.3.1.3 Plantation over porous ground

- Experimental support for a prediction method for sparse 3D vertical sonic crystal arrangements on an impedance ground.

- Further studies of sound propagation through crops and hedges outdoors.

1.3.2 *Journal publications*

1) **I. Bashir**, T. Hill, S. Taherzadeh, K. Attenborough and M. Hornikx, "Reduction of surface transport noise by ground roughness," Submitted to *App. Acoust.* (2013).

2) T. V. Renterghem, K. Attenborough, M. Mannael, J. Defrance, K. Horoshenkov, J. Kang, **I. Bashir**, S. Taherzadeh, B. Altreuther, A, Khan and J. Smyrnowa, "In-situ measurements of road traffic noise reduction by hedges," Submitted to *J. Acoust. Soc. Am.* (2013).

3) **I. Bashir**, S. Taherzadeh and K. Attenborough, "Surface waves over porous and periodically-rough boundaries," Accepted for publication in *J. Acoust. Soc. Am.* (2013)

4) **I. Bashir**, S. Taherzadeh and K. Attenborough, "Diffraction assisted rough ground effect: Models and data," *J. Acoust. Soc. Am.* 133 (3), (2013).

5) S. Taherzadeh, **I. Bashir** and K. Attenborough, "Aperiodicity effects on sound transmission through arrays of identical cylinders perpendicular to the ground," *J. Acoust. Soc. Am.* 132 (4), pp. 323-328 (2012).

6) K. Attenborough, **I. Bashir** and S. Taherzadeh, "Outdoor ground impedance models," *J. Acoust. Soc. Am.* 129 (5), pp. 2806-2819 (2011).

1.3.3 Conference publications and Posters presentations

1) K. Attenborough, **I. Bashir** and S. Taherzadeh, "Surface waves over strips and slits," 165th meeting of the Acoustical Society of America, Montreal, Canada (2013).

2) K. Attenborough, **I. Bashir** and S. Taherzadeh, "Exploiting ground effects for noise control," Internoise, Austria (2013).

3) K. Attenborough, **I. Bashir** and S. Taherzadeh, "Surface waves over rigid-porous and rough surfaces," ASA, 133 (2013).

4) **I. Bashir**, S. Taherzadeh and K. Attenborough, "New mitigation methods for traffic noise," Poster presented at The Open University, Milton Keynes, UK (2012).

5) S. Taherzadeh, **I. Bashir**, and K. Attenborough, "Roughness-based traffic noise barriers," IOA, London, UK (2012).

6) **I. Bashir**, S. Taherzadeh, and K. Attenborough, "Diffraction effects and surface waves," Acoustics, Nantes, France (2012).

7) K. Attenborough, **I. Bashir**, H. Shin and S. Taherzadeh, "Slow waves and surface waves," Acoustics, Nantes, France (2012).

8) S. Taherzadeh, **I. Bashir**, and K. Attenborough, "Sound attenuation by crops and hedges," Acoustics, Nantes, France (2012).

9) K. Attenborough, **I. Bashir** and S. Taherzadeh, "Excess attenuation & effective impedance associated with rough hard ground," 164th meeting of Acoustical Society of America, Kansas, USA (2012).

10) I. **Bashir**, S. Taherzadeh, T. Hill and K. Attenborough, "Sound propagation over vegetated strips," Forum Acusticum, European Acoustics Association, Aalborg, Denmark (2011).

11) K. Attenborough, I. **Bashir**, and T. Hill, "Models for Acoustical properties of green roof materials," Forum Acusticum, European Acoustics Association, Aalborg, Denmark (2011).

12) S. Taherzadeh, T. Hill, I. **Bashir** and K. Attenborough, "Multiple scattering models for the acoustical properties of vegetation," Forum Acusticum, European Acoustics Association, Aalborg, Denmark (2011).

13) T. Hill, S. Taherzadeh, I. **Bashir** and K. Attenborough, "Effects of source side roughness on the acoustical performance of a traffic noise berm," Forum Acusticum, Aalborg, Denmark (2011).

14) I. **Bashir**, S. Taherzadeh and K. Attenborough, "Noise reduction using surface treatments, trees and vegetation," Poster presented at The Open University and at The Midlands Hub competition, Nottingham University, won two prizes (2011).

15) K. Attenborough, I. **Bashir**, S. Taherzadeh and T. Hill, "A review of ground impedance models," 14th International Symposium on Long Range Sound Propagation, Annapolis, MD, USA (2011).

16) T. Hill, I. **Bashir**, S. Taherzadeh and K. Attenborough, "Propagation over periodic and random roughness," 14th International Symposium on Long Range Sound Propagation, Annapolis, USA (2011).

17) **I. Bashir**, K. Attenborough and S. Taherzadeh, "Traffic noise control by surface roughness," 43rd Universities' Transport Study Group, The Open University, Milton Keynes, UK (2011).

18) **I. Bashir**, K. Attenborough, T. Hill and S. Taherzadeh, "Diffraction assisted rough ground effect," 160th meeting of the Acoustical Society of America, Cancun, Mexico (2010).

19) K. Attenborough, **I. Bashir**, and S. Taherzadeh, "Review of ground impedance models for propagation modelling," Internoise, Lisbon, Portugal (2010).

Chapter 2

2. Numerical Methods used in Simulations: BEM, MST and FEM

2.1 Introduction

Sound propagation over different kinds of artificially created and naturally occurring ground surfaces has been studied. The study has been carried out experimentally and theoretically. Experiments help to understand the physics of sound propagation and verify the theoretical predictions. Laboratory experimental arrangements are usually scaled models of real life scenarios. Sometimes, it is very difficult and time consuming to set up an experiment at real life scale. On the other hand, once a prediction method has been shown to agree with the experimental results at model scale, it can be use to predict for real scale cases.

In this chapter, three prediction methods are discussed. These methods are used to carry out predictions in a variety of scenarios and cases throughout the thesis. These methods are,

- Boundary Element Method (BEM)

- Multiple Scattering Theory (MST)

- Finite Element Method (FEM)

MST is an analytical technique which is capable of predicting the sound propagation in arrays of scatterers only with certain geometrical shapes, for example in an array of cylinders or semi-cylinders embedded on a hard ground. For more complicated shapes of scatterers it is not possible to use this analytical method. Alternatives for predicting sound propagation through and over non-ideally-shaped scatterers are provided by numerical methods such as BEM and FEM.

2.2 Boundary conditions for Numerical techniques

The numerical predictions obtained using MST/BEM/FEM are based on the solution to the Helmholtz wave equation. In a homogenous compressible medium, the cylindrically spreading acoustic wave is given as [1], [2],

$$\nabla^2 P - \frac{1}{c_0^2}\frac{\partial^2 P}{\partial t^2} = 0, \tag{2.1}$$

where $\nabla^2 = \dfrac{\partial^2}{\partial x_1^2} + \dfrac{\partial^2}{\partial x_2^2}$ is the Laplacian, c_0 is the constant speed of sound, t is time and P, the wave travelling in the medium, can be written as,

$$P(r,t) = \Re\{p(r)e^{-i\omega t}\}, \tag{2.2}$$

where $\omega = 2\pi f$ is the angular frequency. Similarly, the velocity potential is given by,

$$\phi(r,t) = \Re\{\phi(r)e^{-i\omega t}\}, \tag{2.3}$$

where p and ϕ are acoustic pressure and acoustic potential respectively. These two quantities are related by [2],

$$p = i\omega\rho_0\phi. \tag{2.4}$$

Substituting Eq. (2.2) and Eq. (2.3) into Eq. 2.1 satisfies the Helmholtz equation as shown,

$$\nabla^2 p + k_0^2 p = 0, \quad \text{in } D \subset R^d \tag{2.5}$$

where $d = 1, 2$ or 3 is the dimension of the problem and D is the region above the ground in which the wave propagates and $k_0 = \dfrac{2\pi f}{c_0}$, is the wave number in air.

The impedance boundary conditions on p and ϕ are the locally reacting boundary conditions given by [1],

$$\frac{\partial \phi(r)}{\partial n} = ik_0 \beta(r)\phi(r),$$ (2.6)

$$\frac{\partial p(r)}{\partial n} = ik_0 \beta(r)p(r),$$ (2.7)

where $\partial/\partial n$ is the normal derivative on the boundary i.e. the rate of change in the direction normal to the boundary, and β is the surface admittance. The simplest form of β is when the boundary is acoustically rigid, i.e. $\beta = 0$. For acoustically soft ground, $\Re(\beta) > 0$ and β is the inverse of the surface impedance of ground (see Chapter 4).

The domain D in which the sound propagation is being studied assumes that the region is unbounded. Sommerfeld boundary conditions for an unbounded region imply that there are no incoming reflections from the boundaries. In other words, the Sommerfeld radiation condition says that the acoustic field is travelling outwards towards infinity and there is no incoming wave. Mathematically Sommerfeld radiation condition can be expressed as,

$$\lim_{\substack{r \to \infty \\ r \in D}}, \quad r^{(d-1)/2}\left[\frac{\partial \phi}{\partial r} - ik_0\phi\right] = 0 ,$$ (2.8)

$$\lim_{\substack{r \to \infty \\ r \in D}}, \quad \phi\left(r^{(d-1)/2}\right) = 0 ,$$ (2.9)

where $d = 1, 2$ or 3 is the dimension of the problem. Eq. (2.8) implies that $\frac{\partial \phi}{\partial r} - ik\phi$

should be much smaller, when $r^{(d-1)/2}$ is large. The second equation (Eq. (2.9)) means that sound field attenuates like r^{-1} in 2D and r^{-2} in 3D.

2.3 Boundary Element Method (BEM)

2.3.1 Introduction

The Boundary Element Method (BEM) is a numerical computational method of solving linear Partial Differential Equations (PDE) that have been formulated as boundary integrals. The main idea behind BEM is that the solution to the PDEs can be obtained on the boundary and then that solution can be used to find the field at any point inside the domain by applying boundary conditions. BEM reformulates the PDE for an acoustic problem as a Boundary Integral Equation (BIE).

2.3.2 Literature review

The history of BEM goes back to 1903 when Fredholm [3] introduced the use of integral equations. However, they were not used until the development of modern computers which enables numerical calculations. Daumas [4] was one of the first authors who used BEM to model the sound propagation over vertical screens on a flat ground in outdoor environment. Seznec [5] used BEM to study the diffraction of sound by noise barriers. Originally, BEM was used only to study the sound propagation over a rigid ground surface. Chandler-Wilde and Hothersall [6] made an important modification to the BEM, so that it can be used to predict the sound propagation over a ground surface with acoustic impedance. They used

the BEM to study the sound propagation over mixed impedance ground surface and found that the resulting predictions show good agreement with data. They [7] extended their work to study the noise attenuation by a single noise barrier using BEM. Subsequently Chandler-Wilde and Hothersall [8], [9] studied the propagation from a coherent line source above a homogenous impedance plane of normalized surface admittance. The BEM model presented here is mainly based on the model developed by Chandler-Wilde and Hothersall [6]–[9]. Taherzadeh *et al.* [10] modified the boundary element method to allow for predicting the sound propagation thorough a refracting atmosphere and with a non-uniform boundary. The Green's function has been evaluated using the Fast Field Program (FFP). The resulting method which allows for sound refraction through a medium is named as BIE-FFP. It provides considerable improvements on previous applications of BEM to barriers with a refracting atmosphere. Many applications of the Boundary Element Method (BEM) have been reported [11]–[13].

2.3.3 Numerical derivation

The idea behind BEM is to transform a PDE problem into a BIE and obtain the solution to the problem by using a suitable Green's function. Green's functions first developed in 1830s, have the property that if an arbitrary function *f(x)* is convolved with the Green's function, it gives the solution to the differential equation for *f(x)*. To solve a given problem using this method, it is important to find the Green's function for that problem. To solve the acoustic problem for the propagation of sound above a half plane, the required Green's function has to satisfy the Helmholtz equation. Consider a two dimensional problem in which an

infinitely long line source is radiating cylindrical waves into a fluid medium. The Green's function for a flat surface is given by [6], [10].

$$G_2(\mathbf{r}, \mathbf{r}_0) = -\tfrac{i}{4}\left\{ H_0^{(1)}\left(k|\mathbf{r}_0 - \mathbf{r}|\right) + H_0^{(1)}\left(k|\mathbf{r}_0' - \mathbf{r}|\right)\right\} + P_\beta(\mathbf{r}, \mathbf{r}_0), \qquad \textbf{(2.10)}$$

where

$$P_\beta(\mathbf{r}, \mathbf{r}_0) = \frac{i\beta}{2\pi} \int_{-\infty}^{+\infty} \frac{e^{ik\left[(z+z_0)\sqrt{1-s^2} - (x-x_0)s\right]}}{\sqrt{1-s}\left(\sqrt{1-s^2} - \beta\right)} ds, \quad \textit{Re(β)>0} \qquad \textbf{(2.11)}$$

In the above expressions $H_0^{(1)}(\ )$ is the Hankel function of the first kind, $\mathbf{r}$, $\mathbf{r}_0$ and $\mathbf{r}_0'$ are the receiver, source and image source positions respectively. The wave number, k, and the complex admittance, β, are dependent on the frequency. The function P_β represents the ground wave term. When the source and the receiver positions coincide, (i.e. when $n=m$), the integral $A(\ )$ has a removable singularity. The integral can be evaluated analytically by replacing the Hankel functions by their small argument approximations and then performing the integration numerically. In above case, the boundary integral is a line integral and the Green's function represents the sound field in the medium in the absence of the scattering surfaces.

Assume a 2D problem of sound propagation above a ground surface. Now, consider a line source producing sound field above an impedance plane in a bounded region D. The sound field at any receiver point inside the domain D, with a distance r and height z above the impedance plane given by means of Green's theorem in boundary integral form [6], [10], is

$$\varepsilon\phi(r,z) = G(\mathbf{r},\mathbf{r}_0) - \int_S \left\{ G(\mathbf{r},\mathbf{r}_s)\frac{\partial\phi(r_s,z_s)}{\partial \mathbf{n}(\mathbf{r}_s)} - \phi(r_s,z_s)\frac{\partial G(\mathbf{r},\mathbf{r}_s)}{\partial \mathbf{n}(\mathbf{r}_s)} \right\} ds, \qquad (2.12)$$

where $G(\mathbf{r},\mathbf{r}_0)$, is the solution of the wave equation in the domain in the absence of scatterer elements, $\mathbf{r}_s$ is the position vector of the boundary element ds, and $\mathbf{n}$ is the unit normal vector out of ds. The parameter, ε, is dependent on the position of the receiver. It is equal to 1 for r in the medium, ½ for r on the flat boundary and equal to the $\Omega/2\pi$ at edges where Ω is the solid angle. The integral is then the contribution of the scatterer elements to the total sound field at a receiver position. This Boundary Integral Equation is a Fredholm [3] integral equation of the second kind. Once solved, the contributions of the scatterers can be determined by evaluating the integral and calculating the total field for any point in the entire domain, D. This is the main Boundary Integral Equation (BIE) for the acoustic field potential in the presence of a non-uniform boundary. The Boundary Element Method (BEM) represents the acoustic propagation in a medium by the boundary integral equation and solves the set of integral equations numerically.

Applying the impedance boundary condition given by Eq. (2.6) on Eq. (2.12) gives,

$$\varepsilon\phi(r,z) = G(\mathbf{r},\mathbf{r}_0) - \int_S \phi(r_s,z_s)\left\{ ik_0\beta G(\mathbf{r},\mathbf{r}_s) - \frac{\partial G(\mathbf{r},\mathbf{r}_s)}{\partial \mathbf{n}(\mathbf{r}_s)} \right\} ds, \qquad \mathbf{r},\mathbf{r}_s \in S \qquad (2.13)$$

The above equation is a very useful due to its capability of incorporating the admittance. This allows BEM to have the capability of predicting the propagation of sound over a ground surface or in the presence of scatterers with finite acoustic

impedance. Due to this, the BEM is capable of predicting the propagation of sound above ground surface having multiple impedance discontinuities.

Eq. (2.13) can be used to predict the sound at any point inside the domain D. The integral given by Eq. (2.13) is very complex and cannot be solved analytically. The solution to Eq. (2.13) can be obtained numerically. The method involves using a quadrature technique to discretize the integral and transform it into a set of linear equations [10].
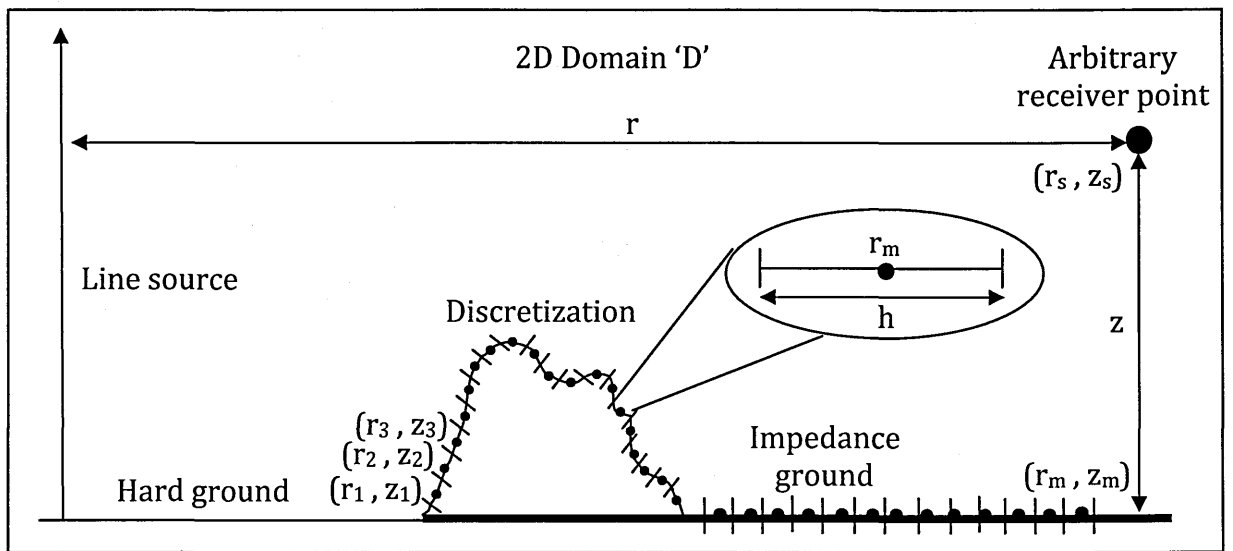
Figure 2.1 A schematic for discretization of a scatterer and impedance ground to solve boundary integral given by Eq. (2.13).

Figure 2.1 shows a hypothetical example which can be used to explain the numerical integration in 2D. Consider a cylindrical line source in a region D placed over a ground surface. The ground surface is a combination of acoustically hard and soft ground with a scatterer of arbitrary cross-sectional shape. The Boundary Integral Equation given by Eq. (2.13) is used to predict the sound field at an arbitrary receiver location with a distance r from the line source and at height h above the ground surface. To solve BIE, the scatterer and impedance ground are

discretized into M elements as shown in Figure 2.1. In other words, the integral given by Eq. (2.13) is discretized and a set of M linear equations is obtained. It is assumed that the unknown potential ϕ is constant within each sub-domain or element. The length of each element is assumed to be h_m with a central point at r_m. The integration is carried out on each element with a limit of $-h_m/2$ and $+h_m/2$. After discretizing the BIE, the integral given by Eq. (2.13) can be rewritten as,

$$\int_S \phi(r_s,z_s)\left\{ik_0\beta G(\mathbf{r},\mathbf{r}_s)-\frac{\partial G(\mathbf{r},\mathbf{r}_s)}{\partial \mathbf{n}(\mathbf{r}_s)}\right\}ds = \sum_{m=1}^{M}\phi(r_m,z_m)\int_{t_m-h/2}^{t_m+h/2}\left\{ik_0\beta G(\mathbf{r},\mathbf{r}_s)-\frac{\partial G(\mathbf{r},\mathbf{r}_s)}{\partial \mathbf{n}(\mathbf{r}_s)}\right\}ds \quad \textbf{(2.14)}$$

Assuming,

$$\Lambda(\mathbf{r},\mathbf{r}_s) = \int_{t_m-h/2}^{t_m+h/2}\left\{ik_0\beta G(\mathbf{r},\mathbf{r}_s)-\frac{\partial G(\mathbf{r},\mathbf{r}_s)}{\partial \mathbf{n}(\mathbf{r}_s)}\right\}ds . \quad \textbf{(2.15)}$$

Putting Eq. (2.14) and Eq. (2.15) into Eq. (2.13) gives,

$$\varepsilon\phi(\mathbf{r}) = G(\mathbf{r},\mathbf{r}_0)-\sum_{m=1}^{M}\phi(\mathbf{r_m})\Lambda(\mathbf{r},\mathbf{r_m}) . \quad \textbf{(2.16)}$$

Eq. (2.16) represents the integration which can be evaluated numerically. The normal acoustic field on each element is obtained by assuming the central point of each element as a receiver. The acoustic field contributions from all other elements and the ground are calculated at the central point of each element. In other words, the acoustic field due to each element represents a linear equation. The solution to the set of M linear equations gives the acoustic field at an arbitrary receiver position. Now, consider $r = r_n$, $n=1...M$, produces a set of M linear equations.

$$\varepsilon\phi(\mathbf{r}_n)+\sum_{m=1}^{M}\phi(\mathbf{r}_\mathbf{m})\Lambda(\mathbf{r}_n,\mathbf{r}_\mathbf{m})=G(\mathbf{r}_n,\mathbf{r}_0). \quad n=1...M \tag{2.17}$$

The unknown potential $\phi(r_n)$ can be obtained by using a known Green's function which satisfies the Helmholtz equation for a cylindrical line source in 2D as given by Eq. 2.10 and Eq. 2.11.

2.3.4 BEM application to traffic noise

BEM is a very useful tool to predict traffic noise propagation. The reason for this can be explained by using Figure 2.1. Figure 2.1 shows a scatterer placed on a ground surface on the left hand side of which there is hard ground and right hand side is a ground surface defined by an acoustic impedance. This is a common traffic noise problem in which the source is on a hard ground (i.e. cars on road), then there may be a noise barrier beyond which that may be any type of naturally occurring ground surface. In the problems considered in this thesis, usually the listener is at a distance of 50 m or 100 m from the road. For receivers at distances of 50 m or larger from the road, it is almost impossible to obtain the prediction of sound propagation using the Finite Element Method (see Section 2.5). To use FEM it is necessary to discretize the whole ground up to the receiver to obtain the solution which implies a tremendous amount of time and computing resources. However, in BEM, by applying the impedance boundary condition to the Green's function; the reflection due to ground can be included inside the Green's function. This means that there is no need to discretize the ground surface. For the example in Figure 2.1, on the left hand side of the scatterer the ground is hard and on right hand side the ground is acoustically soft.

Of these two ground surfaces, only one has to be discretized whereas the other can be included in the Green's function. In case of a two impedance ground, the ground covering the shorter area should be discretized to speed up the BEM predictions. However, in the Figure 2.1 example, the ground surface on the right hand side is discretized. In the case of a single ground type, only the scatterers need to be discretized. In BEM the element size must be atleast 1/5th of the wavelength of the highest frequency of interest to obtain good predictions.

2.4 Multiple Scattering Theory (MST)

2.4.1 Introduction

MST is an analytical prediction technique and only applicable to objects with shapes for which the wave equation is separable, for example cylindrically-shaped or elliptically-shaped objects. Consider a wave travelling in a medium e.g. air. If the wave comes across an obstacle it will be diffracted, and thereby interfere with the incident wave or be scattered depending on the size of the scatterer relative to the incident wavelength. For a single obstacle or scatterer, the total sound field at the receiver is calculated by summing up the incident field and the scattered field. However, if several scatterers are present in close proximity, the incident wave undergoes multiple scattering before it reaches the receiver. Suppose a number of cylindrical scatterers are placed at a centre-to-centre spacing of d on a surface as shown in Figure 2.2. A sound wave is incident on these scatterers. Now consider that the incident wave is scattered by the scatterer 'D'. The scattered wave travels in all directions. The wave scattered by scatterer 'D' interacts with neighbouring scatterers i.e. 'C' and 'E' and is again scattered by

them. The scattered wave can also reach scatterers beyond the nearest neighbouring scatterers i.e. 'B' and 'F' and so on. It depends on the magnitude of the distance between the scatterers relative to their incident field wavelength. If the incident field wavelength is much smaller than the distance between the scatterers, then the field scattered by one scatterer will have no effect on a nearby scatterer. It is concluded that whether the field scattered by scatterer 'D' will reach the scatterer 'E' , 'F' or 'G', depends on the ratio between the incident field wavelength and the distance between them. Scatterer 'D' acts as a secondary source for the neighbouring scatterers. Similarly, the scattered sound field is also scattered by these scatterers and they can act as a source as well. As a result, the field scattered by one scatterer interferes with the scattered field of other scatterers and this process goes on until the energy in the field has decayed. This phenomenon is called multiple scattering.
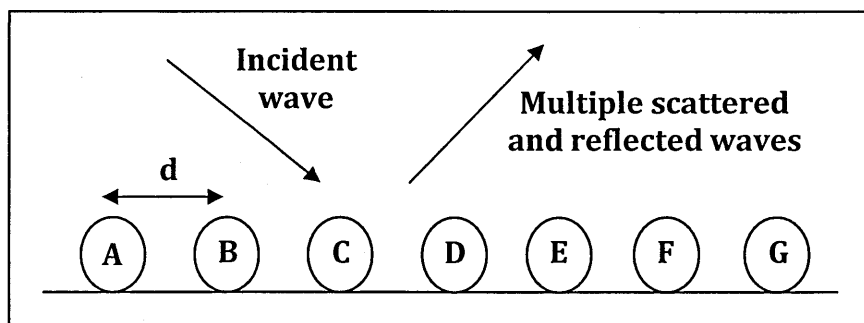
Figure 2.2 A schematic for scattering of wave from cylindrical scatterers.

2.4.2 Literature review

Multiple scattering by random and periodic arrangements of scatterers is a topic with an extensive literature. Twersky [14] presented a solution for multiple scattering of radiation by an arbitrary configuration of parallel cylinders. Twersky's work was based on earlier work by Rayleigh [15] on scattering. Twersky's [14]

method is an iterative method, which becomes unmanageable as the number of scatterers increases. Linton and Evans [16] have presented the solution for the problem of plane wave scattering by finite arrays of hard cylinders in water based on earlier work by Zaviska [17]. Linton and Martin [18] extended their work to multiple scattering by random configurations of circular cylinders having finite impedance. Boulanger *et al.* [19] presented a new analytical theory for multiple scattering of cylindrical acoustic waves by an array of finite impedance semi-cylinders embedded in a smooth acoustically hard surface. The theory is derived by extending previous work by Linton and Martin [18]. The agreement between measured data and analytical multiple scattering theory predictions is found to be good for both periodic and random distributions of semi-cylinders embedded in a smooth hard ground surface [19]. Umnova *et al.* [20] modified the multiple scattering theory to predict the sound propagation through a vertical array of cylinders with porous covering. The agreement between data for transmission through porous covered vertical cylinders is found good with the predictions using extended multiple scattering theory [20].

The next two subsections outline the analytical theory for plane and cylindrical acoustic waves scattering by a finite array of finite impedance semi-cylinders embedded in a smooth hard surface [19]. The derivation is based on earlier work by Linton and Evans [16] and Linton and Martin [18].

2.4.3 Plane wave incidence

Consider an array of N non-identical semi-cylinders embedded on a smooth hard ground surface. The polar coordinates of the field point in the Cartesian reference frame (Ox, Oy) are represented by (r, θ), and the polar coordinates of the

field point in the reference frame (O_{jx}, O_{jy}) centred at the jth semi-cylinder centre O_j

(x_j, y_j) are represented by (r_j, θ_j) (see Figure 2.3). The semi-cylinders are fixed

along the z-axis and it is assumed that waves propagate in the plane

perpendicular to the main axis of the semi-cylinders. Since the boundary

conditions and the geometry are independent of z, the problem can be reduced to

a 2-dimensional one and each scatterer can be represented by its circular cross-

section as shown in Figure 2.3.

For semi-cylinder j and the pressure field, P_j, Eq. (2.5) can be rewritten as,

$$\nabla^2 P_j + k_j^2 P_j = 0.$$ (2.18)

Thus, solution can be obtained by solving for equation 2.18 and satisfying some

boundary conditions on the scatterers and a radiation condition at infinity.
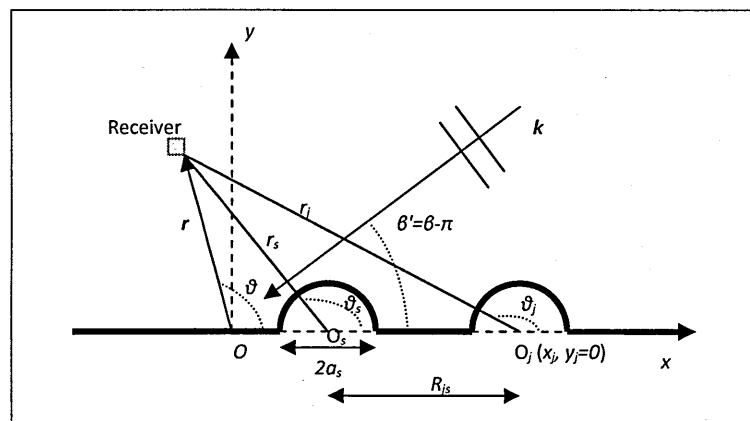
Figure 2.3 Cross-sections of two semi-cylinders and the geometry used in
developing the theory for plane waves.

Consider an incident plane wave at angle β with respect to the +x-axis on

an array of N infinitely long semi-cylinders embedded in a smooth surface (see

Figure 2.3).

$$P_{in} = e^{i\vec{k}\cdot\vec{r}} = e^{ikr\cos(\theta-\beta)}. \qquad\qquad (2.19)$$

The propagation vector $\vec{k}$ is considered to be perpendicular to the cylinder axes. When applying the boundary conditions, it is useful to express the incident wave in terms of the radial position, r_j, of the jth semi-cylinder and the polar angle θ_j. Writing $\vec{r} = \overrightarrow{OO_j} + \vec{r_j}$, the dot product $\vec{k}\cdot\vec{r}$ enables expression of the incident plane wave equation (2.19) as,

$$P_{in} = I_j e^{ikr_j\cos(\theta_j-\beta)}, \qquad\qquad (2.20)$$

where I_j is a phase factor associated with semi-cylinder j defined as $I_j = e^{ikx_j\cos\beta}$. The incident field is reflected and scattered by the array of semi-cylinders embedded on a smooth hard surface. The total field can be written as a sum of,

$$P = P_{in} + P_{ref} + P_{scat}. \qquad\qquad (2.21)$$

The reflected wave takes into account of the effect of hard embedding plane and is given as,

$$P_{ref} = e^{ikr\cos(\theta+\beta)}. \qquad\qquad (2.22)$$

This is the mirror reflection of the incident wave in the plane containing the semi-cylinder axes. In terms of r_j and θ_j, the reflected wave (2.20) is,

$$P_{ref} = I_j e^{ikr_j\cos(\theta_j+\beta)}, \qquad\qquad (2.23)$$

where $I_j = e^{ik(x_j\cos\beta+y_j\sin\beta)}$ is a phase factor associated with the j_{th} cylinder. The sum of the incident and reflected waves can be expanded as series of Bessel functions [21],

$$P_{in} + P_{ref} = 2I_j \sum_{n=-\infty}^{+\infty} J_n(kr_j) e^{in(\pi/2+\theta_j)} \cos(n\beta).$$ (2.24)

The incident field is scattered by the scatterers. For a given scatterer, the total scattered field is the sum of the field scattered by itself and rest of the neighbouring scatterers. The scattered term P_{scat} can be decomposed into a sum of the contributions from the N semi-cylinders. The scattering contribution from the jth semi-cylinder is sought in the form of a cylindrical wave which can be expanded using the basis function set $e^{in\theta_j}$ for the polar angle contribution and Hankel functions of the first kind and order n, $H_n(kr_j)$, for the radial coordinates. The total scattered wave is written as,

$$P_{scat} = \sum_{j=1}^{N} \sum_{n=-\infty}^{\infty} A_n^j Z_n^j H_n(kr_j) e^{in\theta_j} .$$ (2.25)

The solution to Eq. (2.18) is sought in the form,

$$P_j = \sum_{n=-\infty}^{\infty} B_n^j J_n(k_j r_j) e^{in\theta_j} ,$$ (2.26)

where $J_n(k_j r_j)$ is the Bessel function of the first kind and order n. The coefficients A_n^j and B_n^j needed for the solution of Eqs. (2.18) are determined from the boundary conditions. Graf's addition theorem [21] for Bessel functions is used to express $H_n(kr_j)$ in terms of coordinates (r_s, θ_s) needed for the boundary conditions at the surface of cylinder s, and Eq. (2.25) becomes,

$$P_{scat} = \sum_{n=-\infty}^{\infty} A_n^s Z_n^s H_n(kr_s) e^{in\theta_s} + \sum_{j=1,j\neq s}^{N} \sum_{n=-\infty}^{\infty} A_n^j Z_n^j \sum_{m=-\infty}^{m=\infty} J_m(kr_s) H_{n-m}(kR_{js}) e^{im\theta_s} e^{i(n-m)\alpha_{js}} ,$$ (2.27)

where α_{js} is 0 or π depending on the respective positions of the jth and s^{th} semi-cylinders. This equation is valid provided $r_s < R_{js}$ where R_{js} is the distance between the centres of cylinders j and s.

Putting Eqs. (2.24) and (2.27) into Eq. (2.21) gives the total field at receiver by a finite array of semi-cylinders embedded into a smooth hard ground.

$$P = 2I_j \sum_{n=-\infty}^{+\infty} J_n(kr_j) e^{in(\pi/2+\theta_j)} \cos(n\beta) + \sum_{n=-\infty}^{\infty} A_n^s Z_n^s H_n(kr_s) e^{in\theta_s} \qquad (2.28)$$

$$+ \sum_{j=1, j\neq s}^{N} \sum_{n=-\infty}^{\infty} A_n^j Z_n^j \sum_{m=-\infty}^{m=\infty} J_m(kr_s) H_{n-m}(kR_{js}) e^{im\theta_s} e^{i(n-m)\alpha_{js}}.$$

2.4.4 Cylindrical wave incidence

Consider a cylindrical wave incident from a single source on an array of N different finite impedance semi-cylinders embedded in a flat hard surface. The Helmholtz Eq. (2.18) is solved using the same coordinate system as used for plane waves. The incident pressure amplitude can be written as,

$$P_{in} = H_0(k\rho_1). \qquad (2.29)$$

where ρ_1 is the source receiver distance (see Figure 2.4). It is useful for subsequent development to express $H_0(k\rho_1)$ in terms of the coordinates (r_s, θ_s) by using Graf's addition theorem [21],

$$P_{in} = \sum_{n=-\infty}^{+\infty} J_n(kr_s) H_n(kS_{s1}) e^{-in\sigma_{s1}} e^{in\theta_s}, \qquad (2.30)$$

with the restriction $r_s < S_{s1}$, where S_{s1} is the radial distance between the cylinder center s and the source 1. To develop an expression for the wave scattered by a

finite array of non-identical finite impedance semi-cylinders embedded in a smooth hard surface, the effect of the hard surface embedding the semi-cylinders is taken into account by assuming an image source and hence a reflected wave,

$$P_{ref} = H_0(k\rho_2),$$

(2.31)

where ρ_2 is the image source to receiver distance (see Figure 2.4).
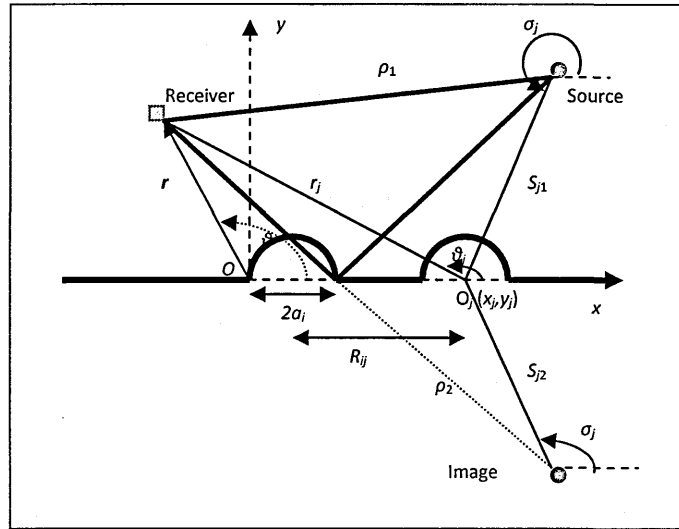
Figure 2.4 Cross-sections of two semi-cylinders and geometry used in the theory developed for a line source.

If the reflected wave (Eq. 2.31) is expressed in terms of r_s and θ_s as in (2.30), the total field outside the semi-cylinders becomes,

$$P = \sum_{n=-\infty}^{+\infty} J_n(kr_s)e^{in\theta_s}\left[H_n(kS_{s1})e^{-in\sigma_{s1}} + H_n(kS_{s2})e^{-in\sigma_{s2}}\right] + \sum_{n=-\infty}^{\infty} A_n^s Z_n^s H_n(kr_s)e^{in\theta_s}$$

(2.32)

$$+ \sum_{j=1, j\neq s}^{N} \sum_{n=-\infty}^{\infty} A_n^j Z_n^j \sum_{m=-\infty}^{m=\infty} J_m(kr_s)H_{n-m}(kR_{js})e^{im\theta_s}e^{i(n-m)\alpha_{js}},$$

provided that $r_s < S_{s1}$ and $r_s < S_{s2}$.

2.5 Finite Element Method (FEM)

2.5.1 Introduction

The Finite Element Method (FEM) is a numerical method for solving a differential or integral equation. It is a numerical technique for finding approximate solutions to boundary value problems. A solution for a complex geometrical problem involves dividing the problem into numbers of subdomains. The subdomains are further divided by a set of elements. These elements are represented by equations according to the given problem. The sets of element equations are combined into a global system of equations for final calculations. These equations are solved numerically to obtain the solution to the problem.

FEM is based on the numerical solutions of Partial Differential Equations (PDE). For some of the problems, the PDE reaches an exact solution i.e. to a steady state. However, sometimes a steady state solution is not possible. In these cases, the solution is approximated by ordinary differential equations, which are then solved numerically by integration using standard techniques such as Euler's method or the Runge-Kutta method.

2.5.2 Literature review

FEM was originally developed by Clough [22], to study the stresses in complex air-frame structures. Later on, it was extended by Zienkiewicz and Cheung [23] to study the general field of continuum mechanics. FEM is receiving considerable attention and becoming increasingly popular. FEM is being used in various fields such as thermodynamics, acoustics, aeronautics and fluid mechanics.

FEM began to be used in the field of acoustics in the 1990s. In 1995, Kang and Bolton [24] used FEM to model isotropic porous materials coupled with acoustical elements. Later on, Kang and Bolton [25] studied sound transmission through foam-lined double-panel structures. In 1995, for the first time, Johansen *et al.* [26] used FEM to predict the acoustical properties of porous materials. Panneton and Atalla [27], [28] used FEM to study the sound propagation through poroelastic materials. They [27], [28] carried out FEM prediction of sound propagation through multilayer systems with isotropic poroelastic materials.

2.5.3 *FEM modelling using COMSOL® Multiphysics*

The FEM acoustic modeling for different arrangements reported in this thesis has been carried out using a software package called COMSOL® Multiphysics. COMSOL® multi-physics provides interactive environment for modelling and solving acoustical problems based on the solution of partial differential equations (PDE) using a finite element method (FEM) and assuming a cylindrical (line) source. The geometrical structure i.e. 1D, 2D and 3D are modelled in COMSOL using a set of CAD tools. The acoustic module has a capability to analyze pressure acoustics such as the propagation of total and scattered waves.

The Finite Element Method is based on the concept of dividing the complex geometries into small areas called as subdomains. These subdomains consist of a finite number of elements arranged in a geometrical pattern. The solution for each subdomain is obtained by solving Partial Deferential Equations. The process of discretization into subdomains is called meshing. Figure 2.5 shows an example of triangular meshing of a circle. A single triangle is called a domain, the sides are

called elements and the points where the different elements interconnect with each other are called nodes. Meshing is one of the most important parts of the solution. The finer the mesh is, the more accurate the predictions are. However, as the meshing gets finer, it will increase the need for computational resources and time. There will always be a compromise between the meshing and computational resources. Experience shows that the agreement between data and predictions is largely dependent on meshing. COMSOL® provides various useful options and controls for meshing. Adaptive meshing in COMSOL® is a very useful tool. It automatically adapts finer meshing at edges and corners of the model. COMSOL® has a capability to analyze and plot results in various formats.
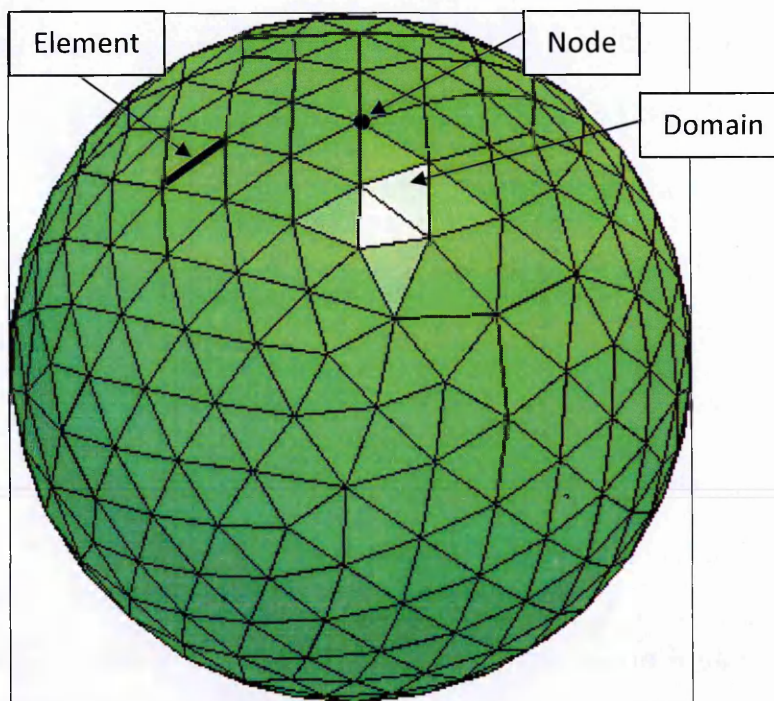
Figure 2.5 An example of triangular meshing using FEM.

2.5.4 A modelling example

Due to limited computational resources, only 2D acoustic modelling has been carried out. Usually the 2D structure is modelled inside a rectangular box as shown in Figure 2.6. In this example, FEM predictions have been carried out for an array of rigid cylinders placed periodically over a hard ground with a centre-to-centre spacing of 0.1 m. The material properties inside the box such as fluid density, speed of sound and PDE coefficients are specified through sub-domain settings. In this case the medium inside the box is air. Predictions of the sound field at each frequency are obtained in a domain (box) with the boundary locations determined according to the geometry of interest. To obtain accurate predictions, it is important to minimize reflection from the rectangular box boundaries. The rectangular box is a 2D representation of an anechoic chamber in which the walls are insulated with sound absorbing materials to minimize the reflection of sound during experiments. Initially, the boundaries were defined by a radiation condition. However, the use of radiation boundary conditions needs a larger rectangular box to obtain satisfactory predictions. The width and height of the box need to be large enough to reduce the spurious reflections. To carry out FEM computation, the whole box needs to be meshed and discretized. This increases the requirements for computational resources and time significantly. An alternative to using a larger box is to implement Perfectly Matched Layers (PML) at these boundaries. A PML is an artificial absorbing layer in which the wave equation has been modified with an anisotropic damping. The key property of a PML that distinguishes it from an ordinary absorbing material is that it is designed so that waves incident upon the PML from a non-PML medium do not reflect at the interface. This property allows

the PML to strongly absorb outgoing waves from the interior of a computational region without reflecting them back into the interior. Thus, it reduces the computational resources and simulation time required. Perfectly Matched Layers are defined at the top and right side of rectangular box shown in Figure 2.6. No PML is present on the left hand side or the bottom of the box. The left hand side of the box is defined by a radiation condition for line source and the bottom is defined as an acoustically hard surface.

The frequency range, 'linear system solver' and solution type is specified in the solver parameters. A fine triangular mesh is generated for a 2D model as shown in Figure 2.6. A finite element mesh is generated automatically for the specified geometry and starts the solver for the COMSOL® simulation. Initially, the excess attenuation predictions were carried out by running two simulations, i.e. for total field and free field. It is found that, in COMSOL® the excess attenuation can be obtained by only running one simulation for total field and by using the following equation in post-processing before plotting the results.

$$EA = 20 \log \left(\frac{P\_acpr\_total}{P\_acpr\_in} \right). \tag{2.33}$$

Figure 2.7 compares the measured excess attenuation spectra and predictions using FEM (COMSOL) with source and receiver height at 0.15 m from an MDF board and separated by 2.0 m over a surface composed of PVC pipes placed over the MDF board with centre-to-centre spacing of 0.1 m. The agreement between the measured excess attenuation spectra and FEM COMSOL® predictions is very good.
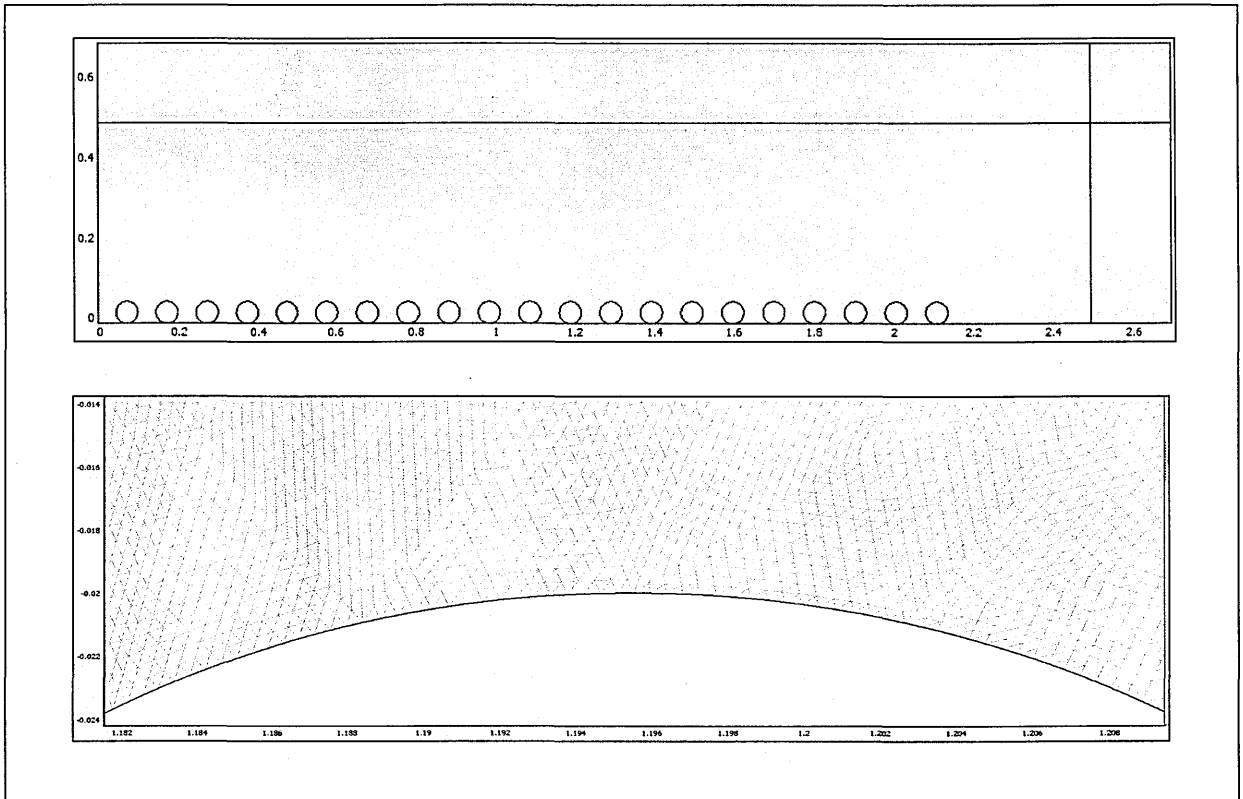
Figure 2.6 An example of meshing in FEM COMSOL.
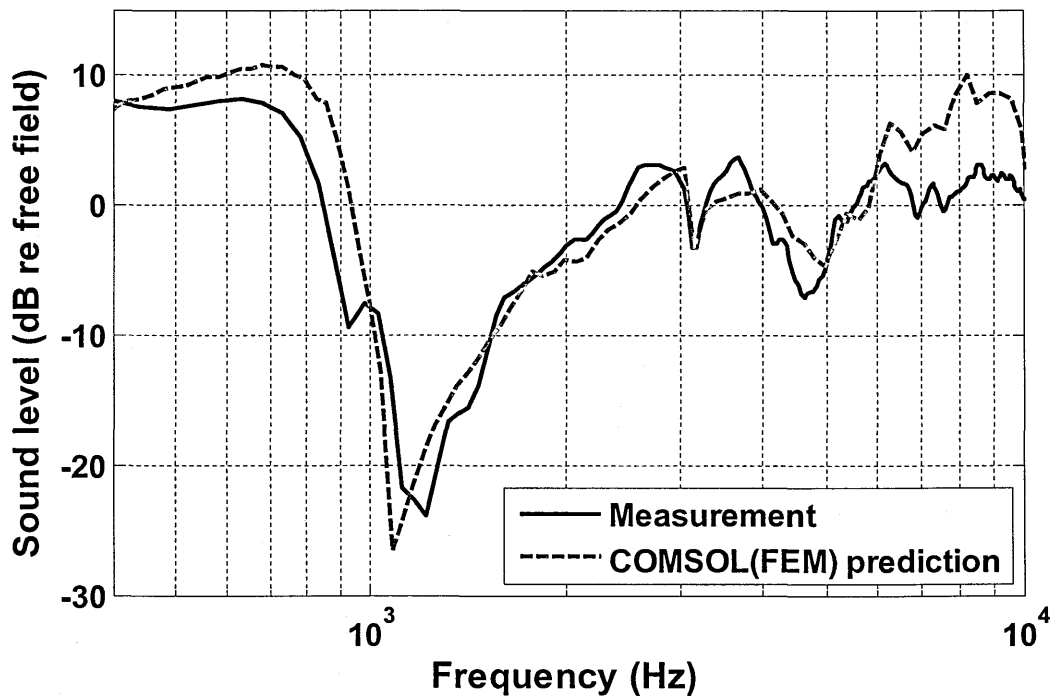
Figure 2.7 Comparisons between measured EA spectra and predictions using FEM (COMSOL) with source and receiver height at 0.15 m from MDF board and separated by 2.0 m over a surface composed PVC pipes placed over MDF board with centre-to-centre spacing of 0.1 m.

Figures 2.8 (a) – (h) shows sound pressure level reference to free field surface plot (excess attenuation in dB inside the box) computed at various frequency points using FEM COMSOL® over rigid circular cylinders with centre-to-centre spacing of 0.1 m placed on a smooth hard ground. The source is placed at height of 0.07 m and excess attenuation is computed at multiple points inside the box by using Eq. 2.17. Figure 2.9 shows the excess attenuation spectra which corresponds to surface plot in Figure 2.8 by selecting a single receiver point inside the box at a distance of 2.0 m from the source and at height of 0.07 m above ground. The source and receiver was placed very close to rough surface to measure the surface wave as well as the rough ground effect. Excess attenuation values in dB at various frequency points are also given in Figure 2.9. Different patterns of sound propagation, reflection and scattering at different frequencies corresponding to different wavelengths can be seen in Figure 2.8. At 200 Hz, the excess attenuation spectra shows a constant value of 3.9 dB (see Figure 2.8) which can also be seen by corresponding surface plot (see Figure 2.9 (a)). FEM COMSOL® computational results shown by Figure 2.8 (b), (c), (d) and (g) present a very interesting phenomenon. As shown by the excess attenuation spectra in Figure 2.9, that the surface wave exists between 600 Hz and 1 kHz. The surface plot at 700 Hz (see Figure 2.8 (b)) and 1 kHz (see Figure 2.8 (c)) shows the propagation of strong surface wave. Similarly, the first excess attenuation maximum occurs at 1.1 kHz (see Figure 2.9). This excess attenuation maximum occurs due to diffraction grating effects caused by the periodically spaced scatterers on a hard ground (see Chapter 5). The diffraction grating effect means that the sound propagation pattern at 1.1 kHz is different from the pattern at other frequencies. The sound attenuation due to cylinders can also be seen by low

magnitude excess attenuation blue surface plot in Figure 2.8 (d). The second excess attenuation maximum due to periodicity effect at 3 kHz can be seen Figure 2.9. The diffraction effect due to periodicity can be visualize by Figure 2.8 (g).FEM COMSOL® is a useful tool to visualize the various kinds of phenomena such as the sound propagation, reflection scattering and diffraction.
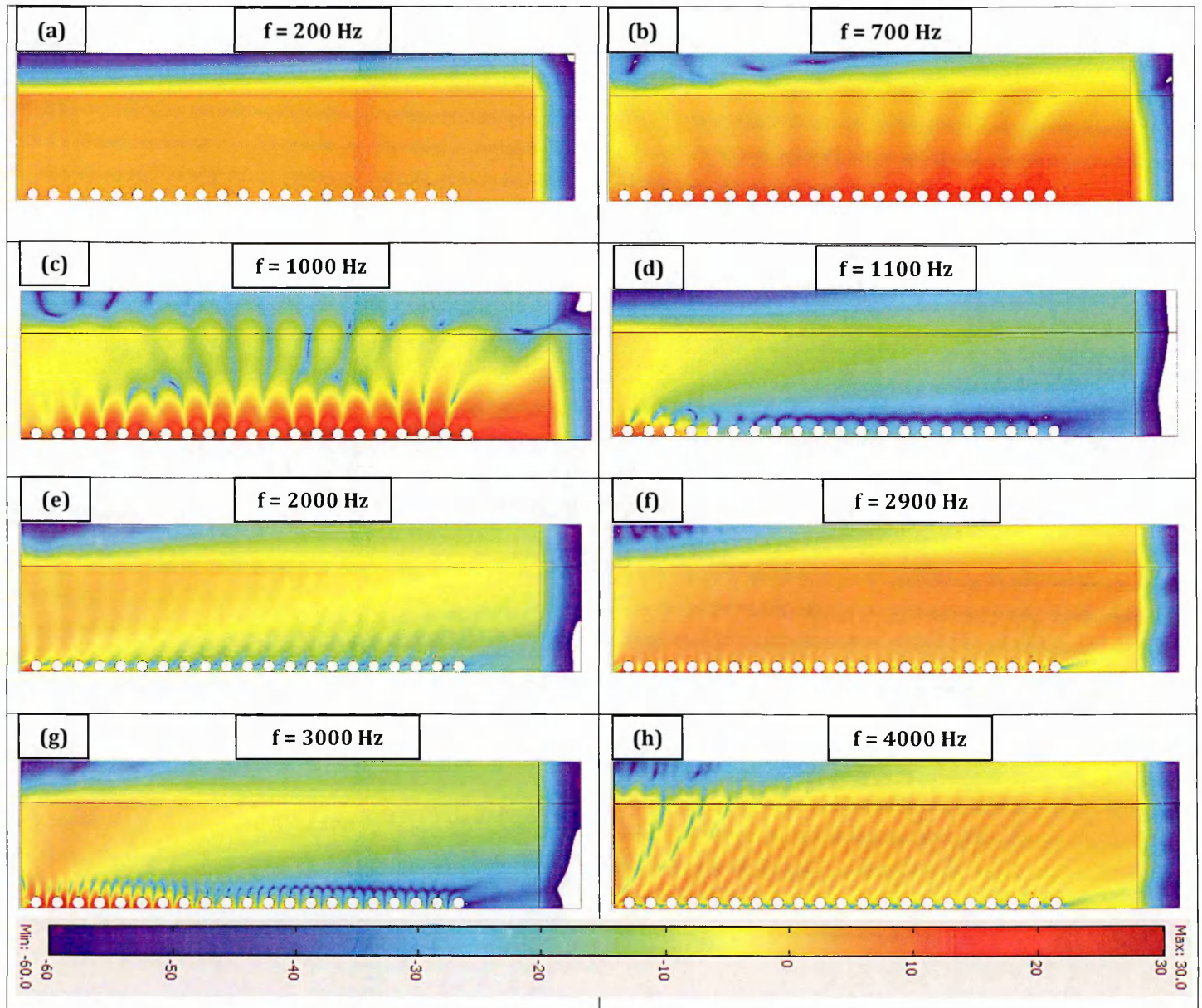
Figure 2.8 Sound level reference to free field in dB computed using FEM COMSOL® inside the whole box (surface plot) with source placed at height of 0.07 m above hard ground over rigid circular cylinders placed on a smooth hard ground for frequency (a) 200 Hz (b) 700 Hz (c) 1000 Hz (d) 1100 Hz (e) 2000 Hz (f) 2900 Hz (g) 3000 Hz (h) 4000 Hz.
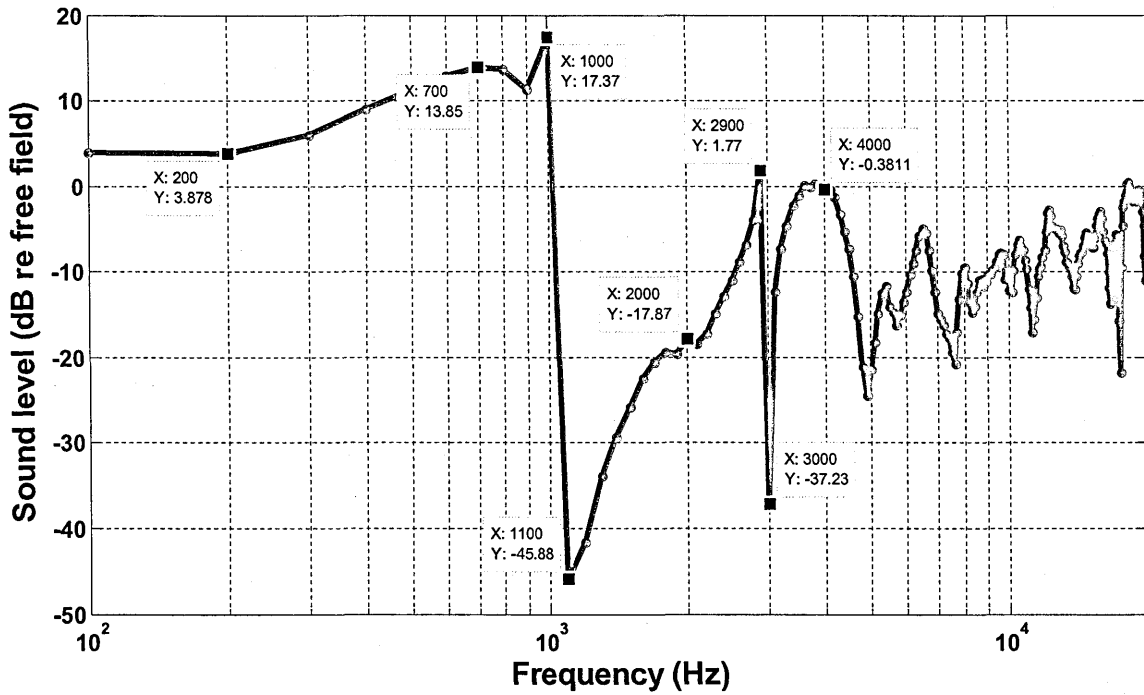
Figure 2.9 Sound level reference to free field spectra(excess attenuation) using FEM (COMSOL®) with source placed at height of 0.07 m and receiver is placed at a single point inside the box at a distance of 2.0 m and height of 0.07 m above hard ground over a surface composed of rigid circular cylinders placed on a smooth hard ground. The excess attenuation values at several frequencies are also shown which corresponds to surface plot in Figure 2.8.

2.6 Conclusions: Comparison between MST, FEM and BEM

MST is an efficient analytical prediction technique, needs less time and computational resources than BEM or FEM but is only valid for particular shapes of scatterers. BEM and FEM are numerical techniques based on the solution of Partial Differential Equations. FEM requires discretization of the whole domain to obtain a solution. However, BEM only requires discretization of the boundary. Therefore, for a given problem, BEM is more efficient than FEM in terms of required time and computational resources.

MST and BEM are the more suitable methods for carrying out predictions for traffic noise because FEM requires discretization of the entire domain to obtain a solution. Moreover, for traffic noise prediction, the receiver may be placed at some distance from the source which makes it extremely difficult to carry out predictions using FEM. However, FEM may be more suitable than BEM for predicting propagation over complex structures i.e. slit-cylinder-roughness (see Chapter 5, Section 5.8.1).

Chapter 3

3. Measurements: data acquisition, processing and materials

3.1 Introduction

Measurements have been carried out to investigate sound propagation over different kinds of artificially created surfaces in the laboratory and over artificial and naturally occurring ground surfaces. This chapter gives the details of measurement systems data processing and materials used in the laboratory and outdoors.

The choice of measurement system must be made according to the nature of experiment and surrounding environment. Most contemporary analysis is carried out through computers and with digital machines. However, the physical world is analogue. So, there must be an interface which connects the digital world with the analogue physical world. The bridge which connects the digital world with analogue world is a digital to analogue convertor which can be used also to

convert analogue signals to digital information. A measurement system captures the instantaneous (analogue) physical reality and stores it in digital form for further analysis. A simple measurement system is shown in Figure 3.1. A simplified measurement system consists of a control system to generate a digital signal, which is passed to a digital to analogue convertor. This signal is transmitted through the physical medium of interest, the transmission-modified signal is received, sampled and back converted from analogue to digital form and finally stored for the purpose of further analysis.
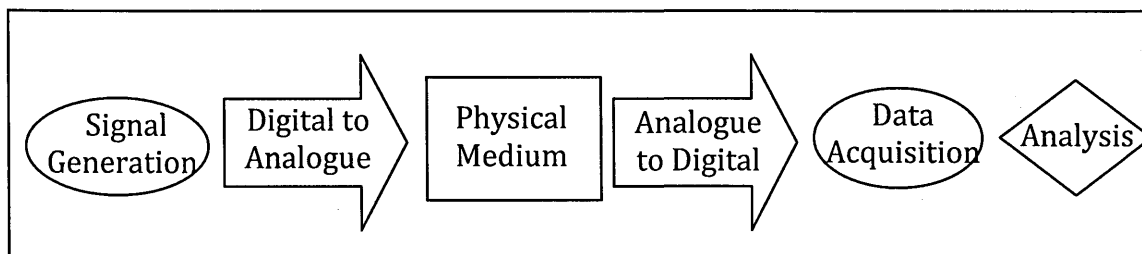
Figure 3.1 A schematic of a simple measurement system.

For acoustic measurements, a digital signal is generated which is passed to a speaker through digital to analogue convertor. The speaker generates acoustic pressure waves that propagate through the medium and the configuration of objects and surfaces used for the acoustic test. The signal is recorded by a microphone which is connected to an analogue to digital convertor to store the data in digital form. Measurements have been divided into two major categories.

1) Laboratory measurements.

2) Outdoor measurements.

The details for arrangements for each type of measurement are given in the following subsections.

3.2 Laboratory measurement arrangements

3.2.1 Anechoic chamber

An anechoic chamber is a room in which the walls, ceiling and floor are lined with a sound absorbent material to minimise reflections. The room is usually constructed in isolation with thick walls to prevent any noise from outside interfering with the experimental work inside it. The OU anechoic chamber has dimensions of 4.3 m × 4.3 m × 4.3 m and is designed to completely absorb reflections of sound waves above a frequency of 125 Hz by lining the walls roof and floor with polyurethane foam wedges. The lowest absorption frequency is calculated using the formula given below $f_{lowest} = {c_o}/{4h}$

$$f_{lowest} = {c_o}/{4h},$$ (3.1)

where c_o is the speed of sound and h is the length of each foam wedge. Above the foam wedges on the floor of the chamber is an aluminium grid which supports moveable mesh floor sections with mesh size 3.4 m x 3.4 m. Although the chamber floor is anechoic, there are always some reflections from the grid and mesh floor which can be minimized by covering them with absorbing material and removing some mesh sections. These reflections are further reduced by windowing during post processing. Two heavy acoustic doors with rubber seals are used to minimise the sound entering the room from outside. The backs of the doors are fitted with conical foam wedges similar to those used on the walls. An anechoic chamber provides a controlled environment to carry out experimental work. The temperature inside the chamber is kept constant and acoustic measurements are not affected by wind or turbulence.

3.2.2 MLSSA measurement system

A data acquisition system, Maximum Length Sequence System Analyzer (MLSSA) was used for signal generation and signal processing. This system is based on Maximum Length Sequences (MLS). The MLS technique was first proposed by Schroeder [30] and has been in use for many years. The MLS technique generates a pseudo-random sequence of +1 and -1. The number of samples in one period of a MLS sequence depends on its order m, given by,

$$L = 2^m - 1. \tag{3.2}$$

MLS is generated using linear feedback shift registers. The mathematical form of MLS coefficients is given by,

$$a_k[n+1] = \begin{cases} a_0[n] + a_1[n], & k = N \\ a_{k+1}[n], & otherwise \end{cases} \tag{3.3}$$

The mathematical formulation is implemented by a feedback system as shown in Figure 3.2.
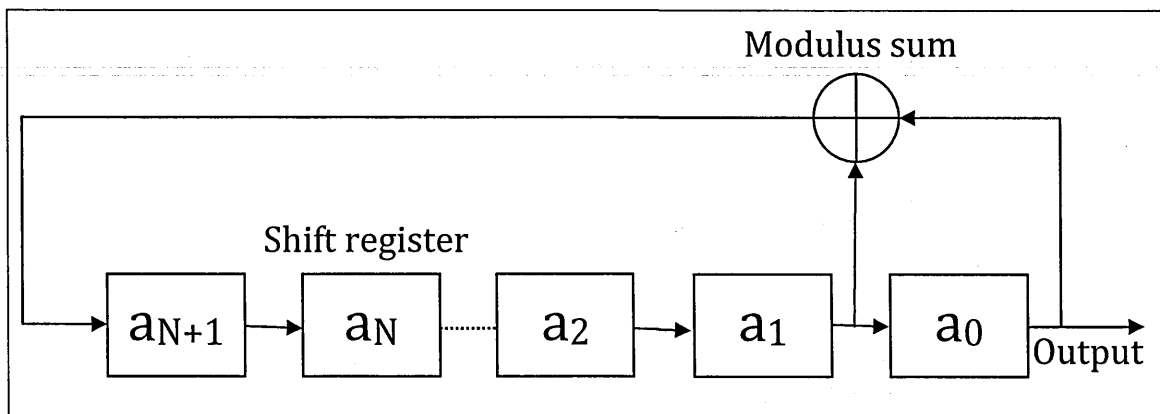
Figure 3.2 Schematic for generating MLS signal using shift register.

An MLS is deterministic and periodic with a period of L. An MLS signal leads to a flat frequency response over a broad frequency range and gives a high signal to noise ratio. The quality of an MLS signal is dependent on its order m. The higher the order, the higher is the signal to noise ratio. However, it will increase the length of the output signal and measurement time. As, inside the anechoic chamber the level of ambient noise is very low, we have found that a MLS sequence of order 16 offers a reasonable compromise between measurement time and good signal to noise ratio.

A schematic of a typical measurement arrangement in the laboratory is shown in Figure 3.3.
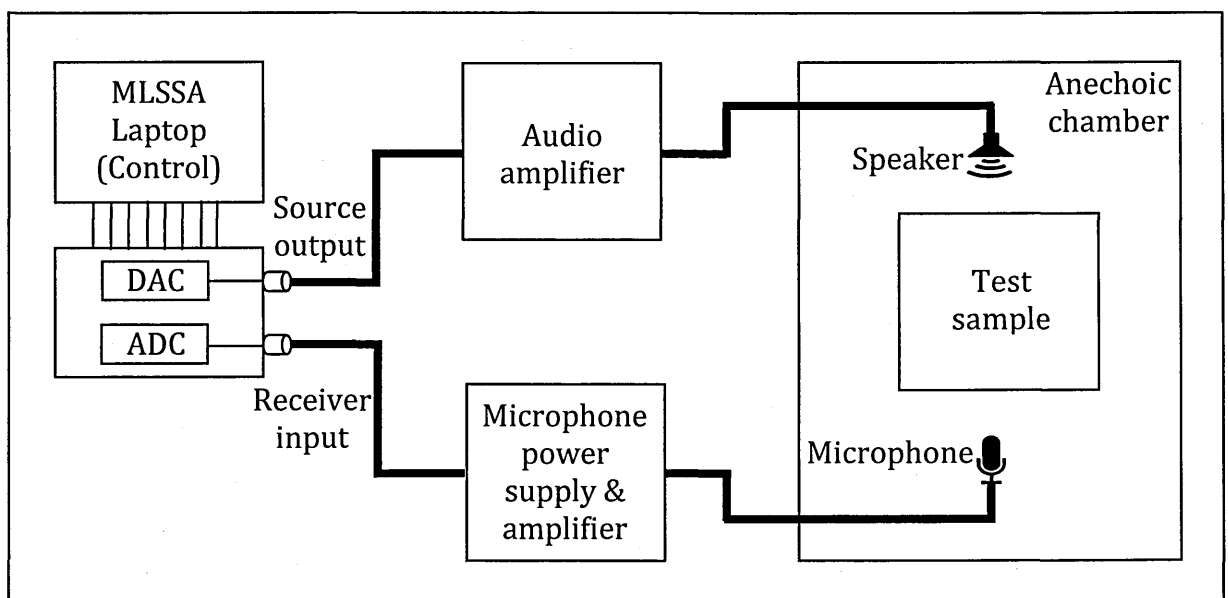
Figure 3.3 A schematic diagram for laboratory measurement system using MLSSA.

The MLSSA that has been used consists of a single input and single output channel system. The MLSSA acquisition system consists of two major parts, a control system and an acquisition box. The control system is to generate the desired digital MLS pulse according to a user defined bandwidth. The MLS order

and sampling frequency are defined by the user. The pulse is passed to the data acquisition box which converts it from digital to analogue. The analogue output of MLSSA is connected to a Cambridge audio stereo amplifier. The amplitude of the signal can be adjusted by the amplifier gain. Care must be taken in adjusting the amplifier gain. It should not be so high that the speaker source starts operating in the non-linear region and not so low that the microphone cannot pick up sufficient signal. The audio amplifier is connected to a speaker source. The MLSSA system and audio amplifier are placed outside the anechoic chamber to minimize reflections. A Bayonet Neill–Concelman (BNC) cable connects the source inside the anechoic chamber to the amplifier outside. A hole is drilled carefully into the laboratory walls for the passage of BNC cables. The hole is sealed around the cables to reduce noise entering the chamber. Similarly, the microphone is connected to a microphone power supply and pre-amplifier which is connected to MLSSA analogue input through a BNC cable. The material whose acoustical properties have to be measured is placed between source and receiver as shown in Figure 3.3. The MLSSA system impulse response can be tested through loop back connection. The source output is directly connected with the receiver input through a cable. The measured time pulse and frequency response through loop back is shown in Figure 3.4. The FFT of the MLS signal shows a broadband flat frequency response.
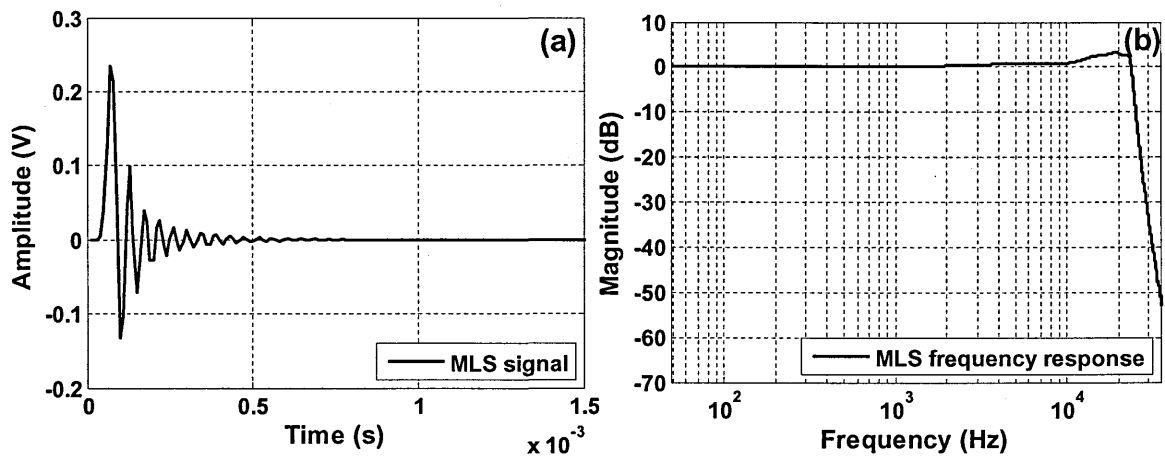
Figure 3.4 (a) MLS impulse response (b) FFT of MLS signal.

3.2.3 Source and receiver

In the OU laboratory two types of point sources i.e. a Tannoy driver plus tube source and a Bruel & Kjaer (B&K) source are available. Due to the limited size of the laboratory, usually scaled model measurements are carried out. The scaled modelling measurements involve a relatively high frequency range. The Tannoy driver generates good signals between 300 Hz and 20 kHz. The B&K type 4295 point source is specially designed as a point source for audio-frequency measurements between 80 Hz and 10 kHz. Due to high frequency requirements we used the Tannoy point source as our primary source for laboratory measurements. A B&K type 4189-B-001-½ inch microphone was used in laboratory. However, at later stage some measurements were also carried out with a quarter-inch ACO-pacific type microphone.

The Tannoy driver was fitted with a 1.0 m long brass tube, of 0.02 m internal diameter. Some of the experimental work was also carried out by connecting the Tannoy source to a 2.0 m long and 0.026 m internal diameter non-flexible Perspex tube. Two different tube lengths were used according to the

nature of the experiment. Due to the impedance discontinuity between the air inside the tube and the air in the anechoic chamber, sound reflection occurs at the end of the tube which reflects the sound back and forth into the tube. This introduces a second arrival in the measured time signal. The second arrival depends on the length of the tube. The shorter the tube, the earlier is the arrival. Figure 3.5 shows the measured free field at a range of 1.0 m with Tannoy source connected to a 1.0 m long tube and 2.0 m long tube respectively. With the 1.0 m long tube and sound travelling at speed of 340 m/s, the reflection due to impedance discontinuity arrives 5.88 ms later than the main pulse. With the 2.0 m long tube it arrives 11.765 ms later than the main pulse. As an example from Figure 3.5, the main pulse arrival for the 1.0 m long tube is at 5.95 ms and reflection at 11.83 ms. Similarly, for the 2.0 m long tube the first arrival is at 8.71 ms and second arrival is at 20.41 ms. The reflection introduces unwanted noise to the measured signal. This reflection must be windowed out as explained later. Most of the laboratory measurements were carried out using the 1.0 m long tube. However, a 2.0 m long tube was used for surface wave measurements. Surface waves travel slower and arrive later than the main direct air arrival pulse. Surface waves also exhibit longer duration tails in the time signal. With a 1.0 m long tube, it was not possible to separate out the surface wave and the tube end reflection, which means that measured signal, is noisier. Although this problem was solved by replacing the 1.0 long tube by the 2.0 m long tube it is more difficult to handle and position the 2 m long tube given the limited dimensions of the anechoic chamber. The tubes were connected, so that the end of the tube behaves like a point source.
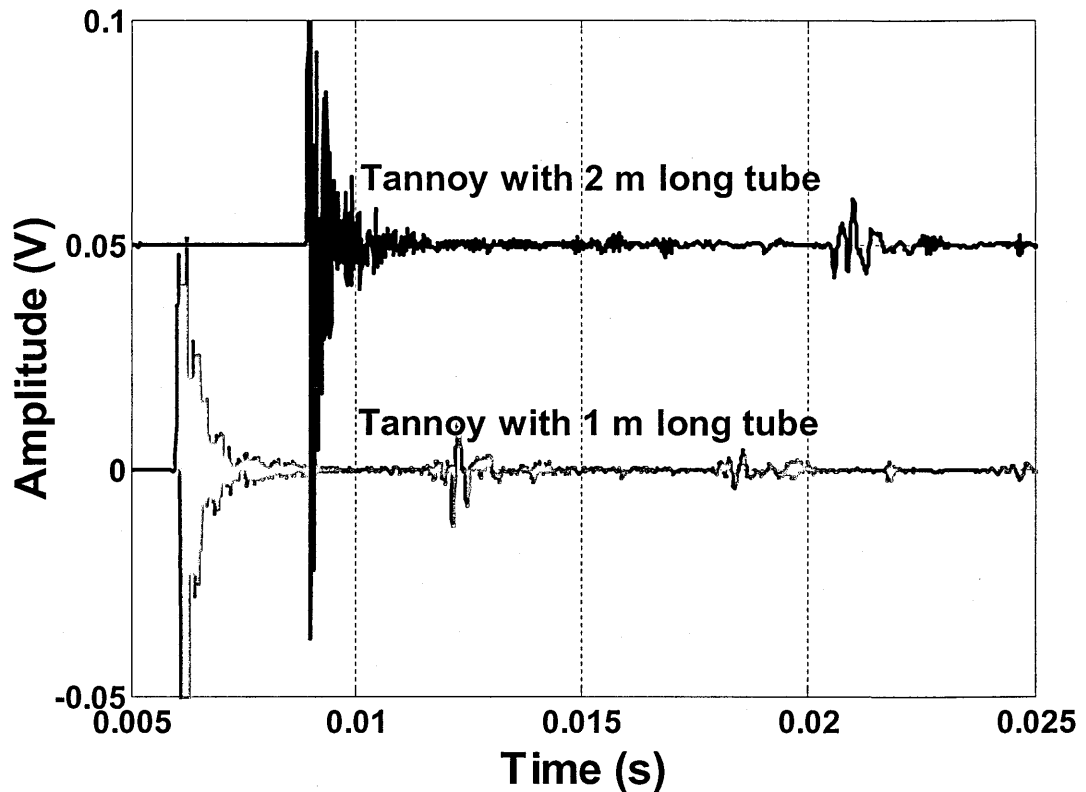
Figure 3.5 Comparison between measured free field at a range of 1.0 m using 1.0 m and 2.0 m long tubes connected to the Tannoy source respectively.

3.2.4 Excess attenuation measurements

Excess attenuation (EA) measurements have been carried using above described MLSSA system. EA needs two separate measurements i.e. a free field measurement and a total field measurement (for definitions and details see Chapter 4, Sec. 4.4.3.1). Figure 3.6 (a) shows the free field measurement arrangements. The Tannoy source and microphone were raised 2 m above the mesh floor to minimize reflection from the floor. The mesh was removed during the free field measurement and the underlying unmovable support grid was covered with acoustically soft absorbing material. The tripod stand for the source and the microphone stand used in the measurements were covered with soft materials to minimize reflections. The control system was placed outside the chamber. After

the free field measurements, the material or surface of interest was prepared and moved inside the chamber. The total acoustic field was measured in the presence of that material or surface and divided by the previously-measured free field to obtain the excess attenuation spectrum. Figure 3.6 (b) shows the measurement of the total acoustic field over an artificially created mixed impedance ground surface. The surface was composed of lead shot and wooden strips on an MDF board and then moved inside the anechoic chamber for the acoustic measurements.

Another important factor for acoustic measurements is averaging. Repeating the measurement several times and taking the average improves the signal to noise ratio and the measured signal is made more reliable. Test measurements have been carried out using different number of averages. By trial and error I have concluded that the 16 averages is the best choice because further increase in averaging doesn't improve the signal to noise ratio. For the data presented in this thesis, 16 averages were used for each measurement.
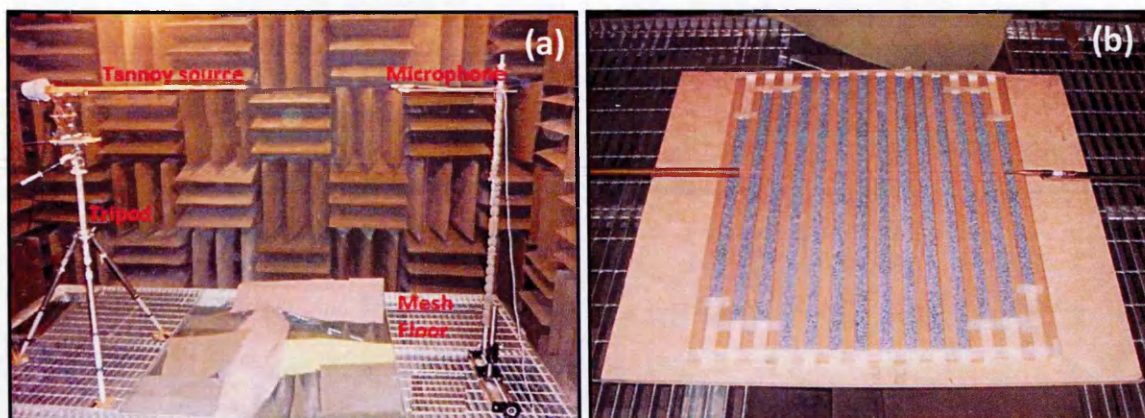
Figure 3.6 Laboratory Measurements of (a) free field (b) total field above a mixed impedance surface composed from lead shot and felt strips on an MDF board.

3.2.5 Data processing

3.2.5.1 Pre-processing

After switching on system components such as the MLSSA system, microphone, amplifier and pre-amp, the system was allowed to settle down for few minutes before making a test measurement and checking that everything was working properly. A check was made inside the chamber to see that the source was producing a good enough signal and that the BNC connectors were covered properly with soft material and not in direct contact with the mesh-aluminium floor. The mesh floor is capable of inducing impulse noise, which can introduce spurious noise in measured data. In a test measurement the amplitude of the received signal was checked and the amplifier gains (audio amplifier gain and microphone pre-amplifier gain) adjusted if necessary while making sure that the source was not operating in a non-linear region and that the operating channel was not overloaded. Overload is indicated by blinking red LEDs on the microphone pre-amplifier. The MLSSA system has a built in algorithm to adjust its gain. Once everything was checked properly, a few test measurements were made to let MLSSA adjust its gain. The system was then ready to take a free field measurement and store it to a disk. After that the measurement system was not adjusted before the total field measurement. Although another free field measurement is advisable as a check at the end of each total field measurement, it was found that the very stable environment inside the chamber meant that there was no difference between morning and evening free field data. So, during any one day a single free field measurement could be made to speed up the measurement process.

3.2.5.2 Post-processing

Once a time signal was acquired and stored, it was analyzed using MLSSA. Figure 3.7 (a) shows the waveform of the free field impulse response obtained by MLSSA using a Tannoy driver attached to the 1 m long tube with its open end at a distance of 0.7 m from the B & K microphone. The measured time signal shows a second arrival at approximately at 11 ms due to internal tube reflections. The second arrival introduces unwanted noise into the measured data. It can be filtered out from time domain signal through windowing before converting into the frequency domain. Figure 3.7 (a) shows envelopes corresponding to two types of windowing i.e. half-Blackman Harris window and rectangular window. Figure 3.7 (a) shows that through windowing the desired signal can be kept and the part of signal corresponding to unwanted reflection is discarded. There are many different kinds of window designs [31]. Each of these windowing techniques has its own pros and cons. In time-domain the window is selected based on ripples in pass-band and the width of the transition band e.g. flat pass band and smaller the transition band is desirable. However, the window cannot be selected only based on time domain, the frequency response plays an important role. In frequency domain the width of main lobe and magnitude of side lobe with respect to main lobe become important. A well-known signal processing principle states that the limited signal is time domain become unlimited signal in frequency domain and vice versa. A abrupt change in time domain results in spectral leakage and high side lobes magnitude. Based on these principles, an appropriate windowing has been selected which is explained later in the section by help of an example. It becomes more important to select appropriate windowing when multiple channels

are being operated in a given bandwidth and signal to noise ratio is very low. However, for laboratory measurements under controlled and stable environment where the signal to noise ratio is high, we do not need to look extensively at different kinds of windowing. Here we will only consider two types of windowing, which fulfil our purpose. The major purpose of the windowing is to reject unwanted reflections from measured data. It is clear from Figure 3.7 (a) that both windows fulfil our purpose and at first glance we think that the rectangular window is ideal. However, this is not true. According to the Fourier transform principle, a signal limited in the time domain gives an unlimited frequency domain signal and vice versa. The abrupt change in the time domain associated with the rectangular window, gives rise to the Gibbs phenomenon [31] in the frequency domain. This produces very high side-lobes in the frequency domain as well as spectral leakage i.e. the energy of signal shows up as a different frequency due to the abrupt change in windowing. Using a rectangular window gives noisier frequency spectra. The side lobes magnitude and spectral leakage can be reduced by tapering the window smoothly to zero as in case of the Blackman Harris window. When using a rectangular window, for a given main lobe magnitude of 0 dB, the side lobes have a magnitude of -13 dB but the side lobe magnitude is only -57 dB when using a Blackman Harris window [31]. Figure 3.7 (b) shows the frequency domain spectra of the MLSSA-generated measured free field impulse using a half-Blackman Harris and a rectangular window. The half-Blackman Harris gives a smoother spectrum due to the reduced Gibbs phenomenon as compared to a rectangular window. So, we have selected a half-Blackman Harris window for analysing data measured in laboratory using MLSSA. Other factors affected by windowing are the frequency resolution and the lowest valid measured frequency. The longer the

window, the better is the frequency resolution and the lower the valid frequency resolution. This means that there is another potential advantage in using the longer tube on the Tannoy source i.e. a lower valid frequency. So the question arises of why use a 1.0 m long tube for most of measurements instead of a 2.0 m long tube? However, since we are not interested in lower frequencies in laboratory, there is no real advantage from using the longer tube except to measure surface waves. Once a signal window is selected, the frequency spectrum is obtained using built in algorithm in MLSSA for FFT.
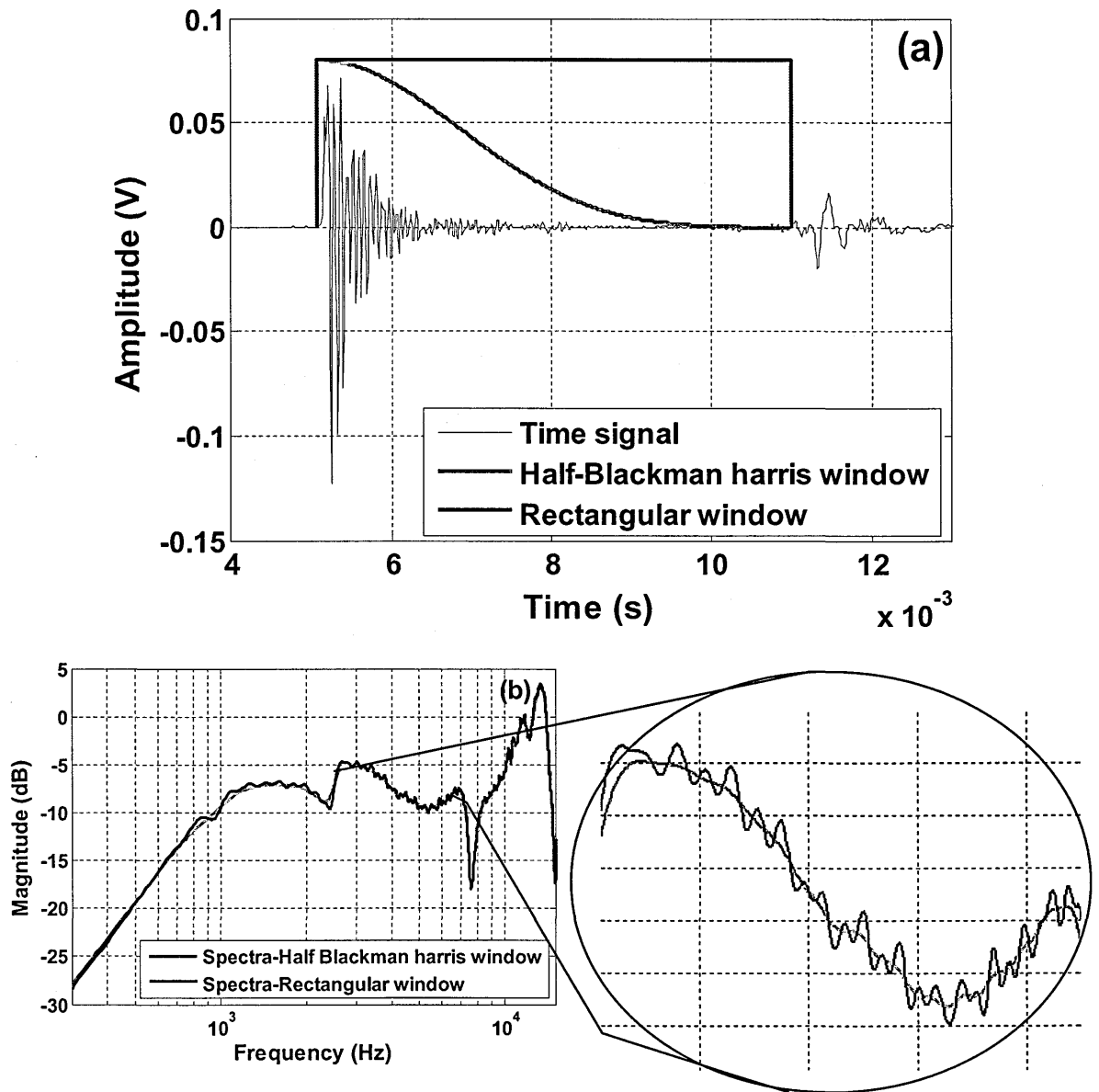
Figure 3.7 (a) Waveform of the free field impulse response obtained by MLSSA using a Tannoy driver and a 1 m long tube with its open end at a distance of 0.7 m from the B & K microphone and envelopes corresponding to a half-Blackman harris window and a rectangular window (b) Comparison between the spectra obtained using a half-Blackman Harris window and a rectangular window.

3.2.6 Laboratory Materials

Much of the laboratory work presented in this thesis concerns sound propagation over artificially created ground surfaces. These surfaces have been created by placing roughness elements on a surface, which should be acoustically hard. For example, artificial rough surfaces have been created by placing strips with different cross-sectional shapes on a glass sheet or on an MDF board. The acoustical properties of these supporting materials have been tested in the laboratory.

3.2.6.1 Glass sheet

An excess attenuation measured over hard surface can be compared with that predicted by well established theory (see Chapter 4, Section 4.4). Figure 3.8 shows the excess attenuation spectra measured over a smooth glass sheet. The glass sheet used for measurement was 0.008 m thick, 1.5 m long and 1.2 m wide. The source and receiver were placed at height of 0.07 m above the glass sheet and source-receiver separation was 0.7 m. The destructive interference between the sound travelling directly from a source to a receiver and that reflected from the acoustically-hard smooth ground takes place over relatively narrow ranges of frequencies determined entirely by the source-receiver geometry. The lowest frequency at which destructive interference will occur can be estimated from,

$$f = \frac{c_0}{2(R_2 - R_1)},$$
(3.4)

where c_0 is the speed of sound in air and R_2 and R_1 are the reflected and direct path lengths respectively. For example, with a source and receiver at 0.07m height

and separated by 0.7 m, the lowest destructive interference frequency is at 12.4 kHz as shown by Figure 3.8. The excess attenuation prediction shown in Figure 3.8 was carried out using a point source propagation model (see Chapter 4, Section 4.4.1) with infinite impedance i.e. the admittance value equals to zero. The agreement between measured data and theoretical predictions is very good. Nevertheless, there is small difference between the measured and predicted depth of the excess attenuation maximum. This is because the prediction was carried out by assuming a hard ground with infinite impedance corresponding to an admittance value of zero.
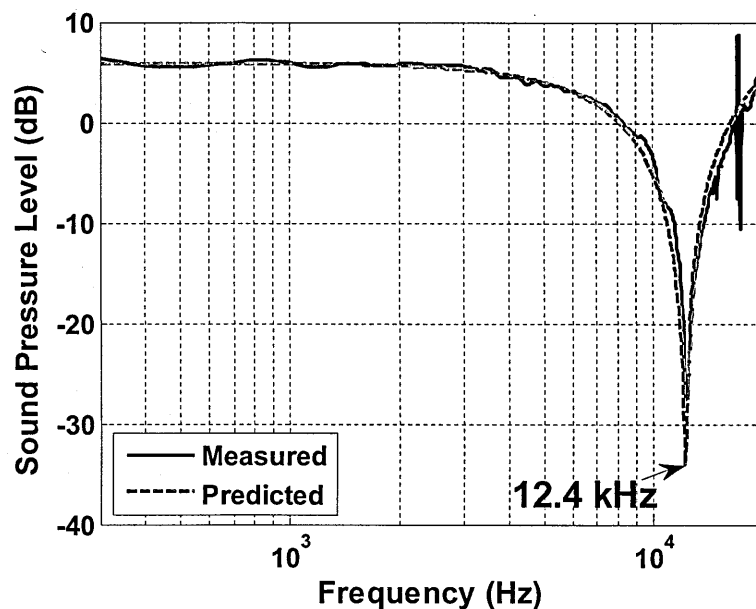
Figure 3.8 Comparison between a measured excess attenuation spectrum and that predicted assuming an admittance value of zero over a smooth glass sheet with source and receiver at a height of 0.07m and source-receiver separation of 0.7m.

However, in reality every surface exhibits finite impedance. The impedance of a ground surface can be predicted using an impedance model along with a propagation model. The best fit impedance parameters are obtained by fitting the measured EA data with the prediction using appropriate impedance models (see Chapter 4, Section 4.4). The impedance parameters for a glass sheet have been

obtained by fitting the measured EA data over a glass sheet using a two-parameter slit pore surface impedance model. The best fitted slit pore impedance parameters are a flow resistivity of 1500 MPa s m^{-2} and a porosity of 0.1. Figure 3.9 shows that improved agreement is obtained between data and prediction by assuming that the glass sheet has a very high but nevertheless finite impedance.
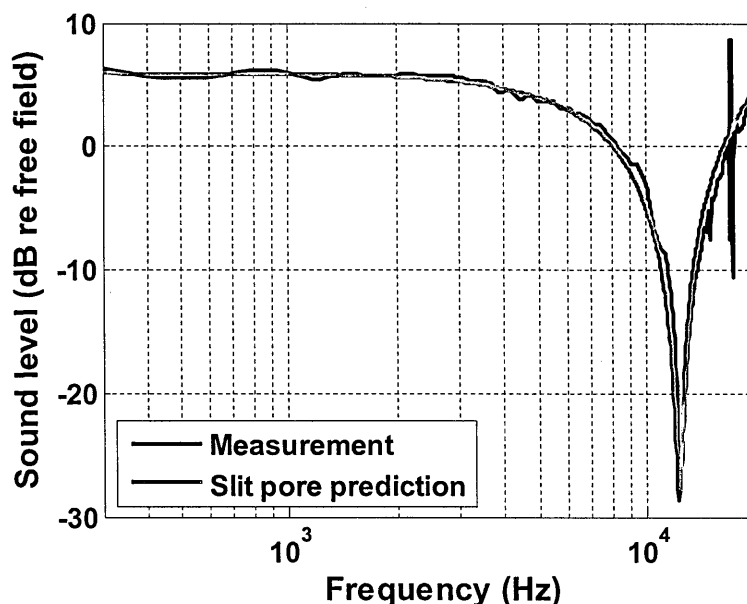
Figure 3.9 Comparison between measured EA spectra with prediction using slit pore model with best fitted flow resistivity of 1500 MPa s m^{-2} and porosity of 0.1 over a glass sheet with source and receiver at height of 0.07 m and source-receiver separation of 0.7 m.

3.2.6.2 Medium Density Board (MDF board)

A 12 mm thick, 2.2 m long and 1.2 m wide (0.012 m × 2.2 m × 1.2 m) MDF board has been used extensively in laboratory experiments as an acoustically-hard supporting ground when creating different kinds of rough and mixed impedance ground surfaces. Impedance model parameters for MDF board have been obtained by fitting EA spectra Measured over the MDF sheet using the two-parameter slit pore impedance model (see Chapter 4, Section 4.4). The best fit

impedance model parameters for MDF board are a flow resistivity of 150 MPa s m^{-2} and porosity of 0.1. Figure 3.10 compares a measured EA spectrum over a MDF board with source and receiver at height of 0.07 m and source-receiver separation of 0.7 m with that predicted using the slit pore model. The agreement between measured predicted EA spectra is very good.
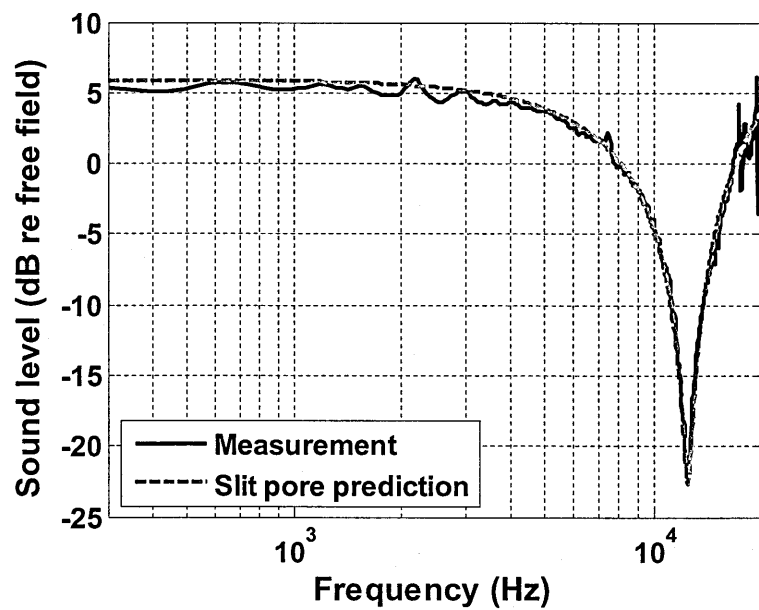
Figure 3.10 Comparison between measured EA spectra with prediction using slit pore model with best fitted flow resistivity of 150 MPa s m^{-2} and porosity of 0.1 over a glass sheet with source and receiver at height of 0.07 m and source-receiver separation of 0.7 m.

The glass sheet and MDF board are near acoustically hard ground surfaces. However, the measured EA spectra and the best fit impedance parameters obtained are different from each other. For the previously-stated source-receiver geometry, the magnitude of the EA maxima over glass sheet and MDF board are -29.0 dB and -22.0 dB respectively. Figures 3.9 and 3.10 show that the measured EA spectrum over glass sheet is smoother than that measured over a MDF board using the same source-receiver geometry. The best fit flow

resistivity for a glass sheet is 10 times higher than the best fitted flow resistivity for a MDF board. The smooth glass sheet is acoustically harder than the MDF board.

3.2.6.3 Layer of bricks

Commercially available bricks have been used extensively in our outdoor measurements. The bricks were used to construct low parallel walls and lattice structures as part of traffic noise measurements and drive by tests (for details see chapter 5) carried out to investigate the attenuation due to the brick structures. There was a need to know the acoustical properties of bricks for predictions using Boundary Element Method (BEM) and for other data analysis. A layer of bricks was created in the anechoic chamber by placing them together on an MDF board (see Figure 3.11).
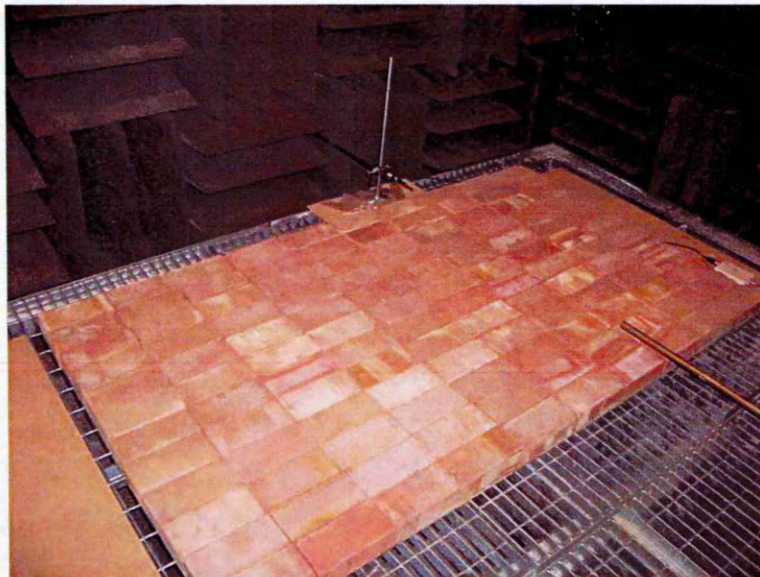
Figure 3.11 Photograph of a layer of bricks placed together (frogs down) over a MDF board.

Excess attenuation spectra due to the layer of bricks were measured using different geometries. The measured EA spectra have been fitted using the 2-parameter slit pore impedance model and the point source propagation models to

obtain impedance model parameters (see Chapter 4, Section 4.4.1). The best fit impedance parameters using the 2-parameter slit pore model are a flow resistivity of 20 MPa s m^{-2} and a porosity of 0.1. Figure 3.12 compares measured and predicted EA spectra due to a layer of bricks.
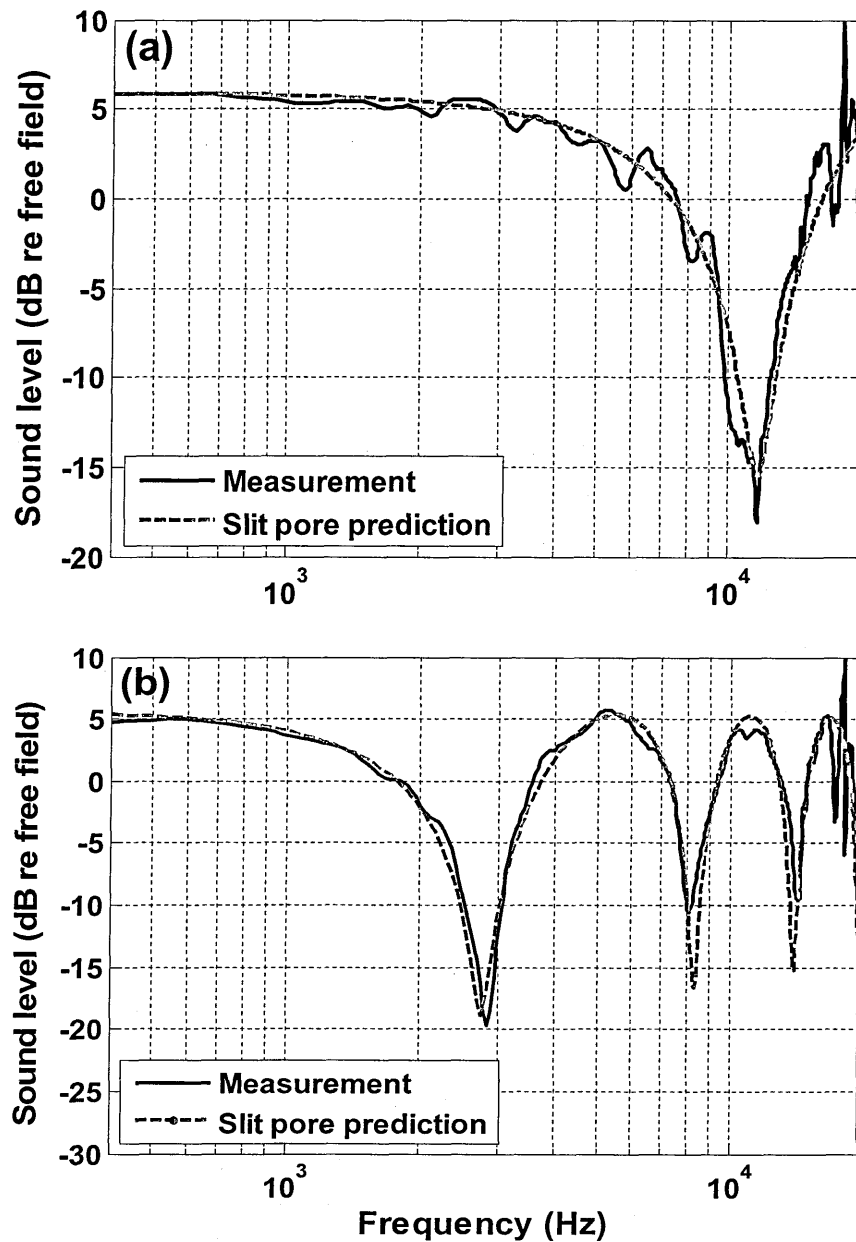
Figure 3.12 Comparison between measured excess attenuation over a layer of bricks placed next to each other on a MDF board and predictions using slit pore model with flow resistivity of 20 MPa s m^{-2} and porosity of 0.1 (a) with source and receiver at height of 0.07 m and source receiver separation of 0.7 m (b) with source and receiver at height of 0.15 m and source receiver separation of 0.7 m.

A layer of bricks is not as acoustcally-hard as the MDF board and glass sheet. The best fit flow resistivity for a layer of bricks is almost 10 times lower than that for the MDF and 100 times lower than that for a glass sheet. The top surface of the brick layer is not very smooth, due to the small irregular gaps between adjacent bricks which means that the brick surface is not as smooth as a glass sheet or the MDF board.

Another type of 6 mm thick MDF board and 10 mm thick, hard and smooth sheet made of Poly Vinyl Chloride (PVC) plastic was also used in laboratory. Table 3.1 summarizes the best fitted impedance parameters obtained using semi-infinite slit pore model for different ground surfaces used in laboratory. Different kind of hard surfaces can be differentiated and characterized using a semi-infinite impedance model. The characterization of hard surfaces improves the agreement between the data and numerical predictions for artificially designed surfaces where these hard surfaces were either used as a hard backed layer or as a supporting surface except bricks which were used to create parallel walls (see Chapter 4).

Table 3.1 Best fitted impedance fitting for ground surface using slit pore model.

Ground type	Thickness (m)	Slit pore best fitted impedance parameters	
		Flow resistivity (MPa s m^{-2})	Porosity
Glass sheet	0.008	1500	0.1
MDF board	0.012	150	0.1
MDF board	0.006	150	0.1
PVC sheet	0.010	300	0.1
Layers of bricks	0.10	20	0.1

3.3 Outdoor measurement arrangements

Larger scale measurements have been carried out outdoors. Most of the outdoor measurements have been carried out at two sites, i.e. a car park at The Open University and an experimental crops site at Woburn Sands operated by Rothamsted Research. A few other outdoor measurements have been carried out near the tennis court and a second car park at The Open University. Also some measurements on a green roof were carried out in Sheffield. The details of each measurement are given at different placed in the thesis e.g. See Chapter 5, Section 5.10.3; Chapter 10, Sections 10.4 & 10.5. However, a similar measurement system was used for all these field exercises with some modifications as required by each specific field test.

Outdoor measurements are carried out in an uncontrolled open-environment. Sound travels as a pressure waves through air. These longitudinal pressure waves are strongly affected by wind speed gradients and turbulence either wind-driven or due to uneven heating of the ground. Wind and turbulent eddies induce unwanted noise into the measured data. The extreme weather conditions were avoided and most of the outdoor measurements were carried out under lower wind speed and in cloudy weather conditions. To reduce wind noise, windshields were always used with the microphones and broadband noise source signal was used instead of impulse noise. Measurements were repeated several times as it improves the signal to noise by averaging. Wind is a low frequency noise source; it was avoided by filtering the measured data during post-processing. Similarly, since sound speed is directly proportional to temperature, temperature gradients also affect outdoor measurements. The temperature was

noted down regularly i.e. every half an hour during the measurements; this information was used while predicting the sound propagation using an impedance model (see Chapter 4).

3.3.1 Outdoor measurement system

Essentially the outdoor measurement system has a similar architecture to that shown in Figure 3.1. The schematic for the outdoor measurement system is shown in Figure 3.13. A laptop installed with Matlab and data acquisition tool box is connected to 16 bit National Instruments-USB 6259 data acquisition box (NI-DAQ). The NI-DAQ box provides interface between digital and analogue world. It consists of four output channels and 16 input channels. A Matlab code written by Dr. Shin was modified for controling the outdoor measurement system. The code is capable of generating a digital signal, communicating and controlling the NI-DAQ, acquiring the measured input and storing it in a digital form. The code also has the capability to do a quick on-site analysis. At end of each measurement, it plots the acquired time signal, its frequency spectrum, transfer function and microphone coherence. The coherence between the microphones helps to identify any possible bias between the signals acquire by two microphones connected with same data acquisition system. Coherence is a function of frequency with values ranges between 0 and 1 that indicate how well the one microphone signal corresponds to the second microphone signal at each frequency. If the coherence between the microphones is poor i.e. close to zero, it means that extra noise is being introduced into measurement system. By looking at these plots, the user can easily identify if there is any problem in the measurement system or any adjustment needed. On-site data analysis proved very useful, since it helped to

verify each and every outdoor measurement carried out. The Matlab code developed is automated to perform the task on one click. The data acquisition board is connected to the speaker through an audio amplifier. Since the outdoor measurements are at larger scales than those used for laboratory measurements we are interested in lower frequencies, which means using a different source. For outdoor measurement we used two types of speaker, the B&K type 4295 point source and a Mordaunt-Short MS 902 speaker. For most of the outdoor measurements, the B&K point source was used. It produces a very good signal between 80 Hz to 10 kHz with uniform power spectral density. However, for some long range measurements we have used the Mordaunt-Short speaker. This is because at longer ranges i.e. > 10 m B&K source was not capable of producing loud enough signal. White noise is used as an input signal for outdoor measurements. In contrast to lab measurements, the outdoor measurements were carried out with multiple microphones. Between 2 to 4 microphones were used for data collection depending on the specific scenario. The microphones were connected to NI-DAQ through a microphone amplifier as shown in Figure 3.13. The source and receiver were placed on the ground surface of interest and everything was connected as shown in Figure 3.13 prior to measurements.
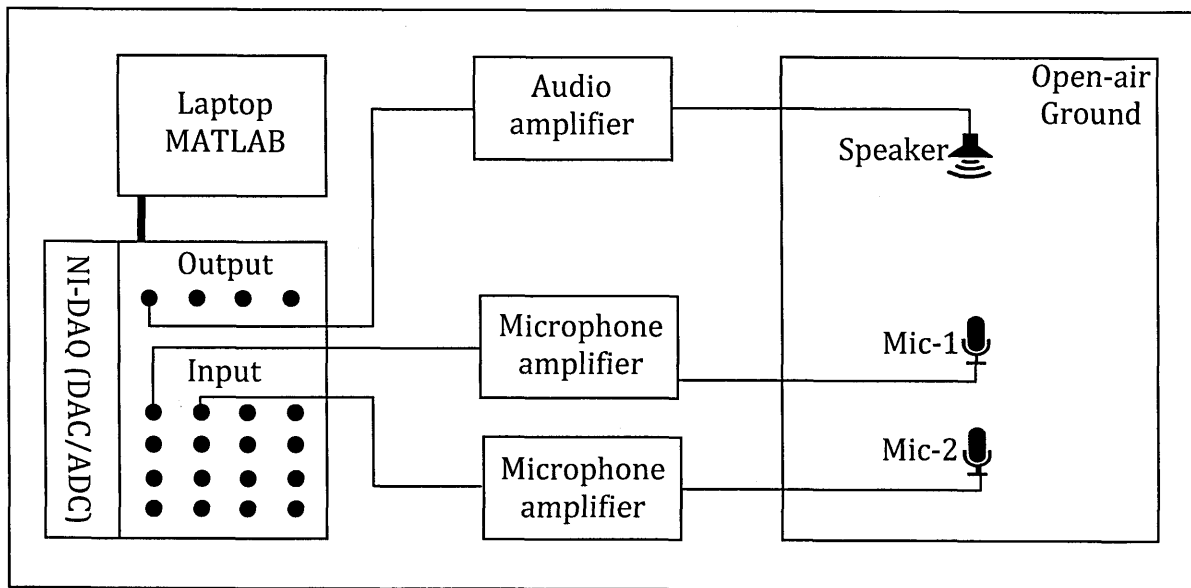
Figure 3.13 A schematic diagram for outdoor measurement system.

3.3.2 Microphone calibration and level difference measurement

Each microphone must be calibrated before the start and after the end of the measurements. The calibration was accomplished using a B&K 4231 calibrator. The microphone is inserted into the calibrator which generates sound pressure of 94 dB at a single frequency of 1 kHz. A recording of a few seconds' duration is carried out of the sound pressure generated by calibrator to obtain the root mean square value of recorded signal. The microphone sensitivity value is calculated by dividing the root mean square value of recorded signal with standard reference sound pressure level. An example of calibration data acquired by the B&K microphone using the B&K calibrator is shown in Figure 3.14 (a). There are two ways to calibrate the microphone once a calibration value is obtained. The first method is complicated and time consuming which should be done once in a year and the second one should be carried out during every measurement. For the first method, the microphone power supply has to be calibrated to achieve the

reference microphone sensitivity value given in microphone reference manual. A small knob on microphone power supply needs to be adjusted slowly and then the above procedure of obtaining calibration value is repeated. This process is repeated until the calibration value matches with the value given in the manual. ..
The second calibration method is implemented during post-processing of acquired data. The calibration value for each microphone is obtained in similar method as described above. These values are used to normalize the data acquired with the corresponding microphones.

The vertical level difference is the transfer function between upper and lower microphones. An example of measurement arrangement for vertical level difference is shown in Figure 3.14 (b). The outdoor measurements are carried out in an uncontrolled environment. The temperature gradient, humidity and wind speed affects the measurements and measurement system. For outdoor, the microphone must be covered with wind shield.
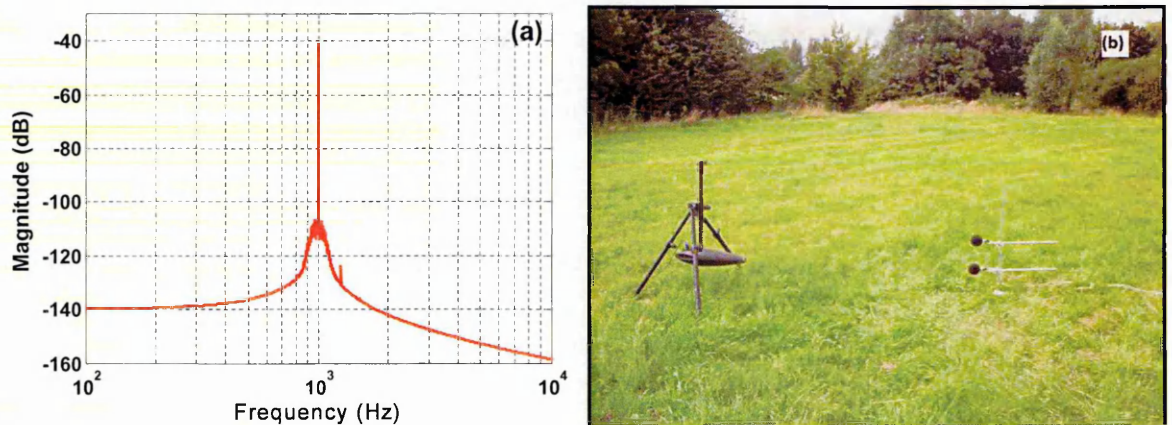
Figure 3.14 (a) An example of acquired data for microphone calibration (b) an example of outdoor level difference measurement over grass.

3.3.3 Data processing analysis

3.3.3.1 Pre-processing

Once everything is connected as shown Figure 3.13 it is important to check that the source signal level is sufficiently greater than the background noise by adjusting the audio amplifier gain and microphone gain if needed. All connections and BNC connectors were covered with a water proof tape. Also it was ensured that there were no reflecting objects near the measurement system and the wind speed and temperature were measured and recorded.

3.3.3.2 Post-processing

Outdoor environments are usually noisy and windy, so measured data needs some filtering to achieve high signal to noise ratio. Usually wind noise introduces low frequency noise which can be avoided through proper filtering. Figure 3.15 (a) shows time domain data measured in very windy conditions at the outdoor site in Woburn Sands. The wind noise introduces fluctuations into the data. These low frequency fluctuations can be removed from the data by passing it through a Butterworth filter with bandwidth of [50 - 10000] Hz. The filtering improves the data quality without the loss of any useful information as shown in Figure 3.15 (b).

For spectral and transfer function analysis, the measured time series data is converted into the frequency domain. For outdoor data, usually lots of averaging is required to obtained good signal to noise ratio. Most of the time, each measurement recording was carried out for a span of 10 sec and each

measurement was repeated 3 times. Figure 3.16 shows a schematic of analysis and conversion of time domain to frequency domain through a method called Periodogram.
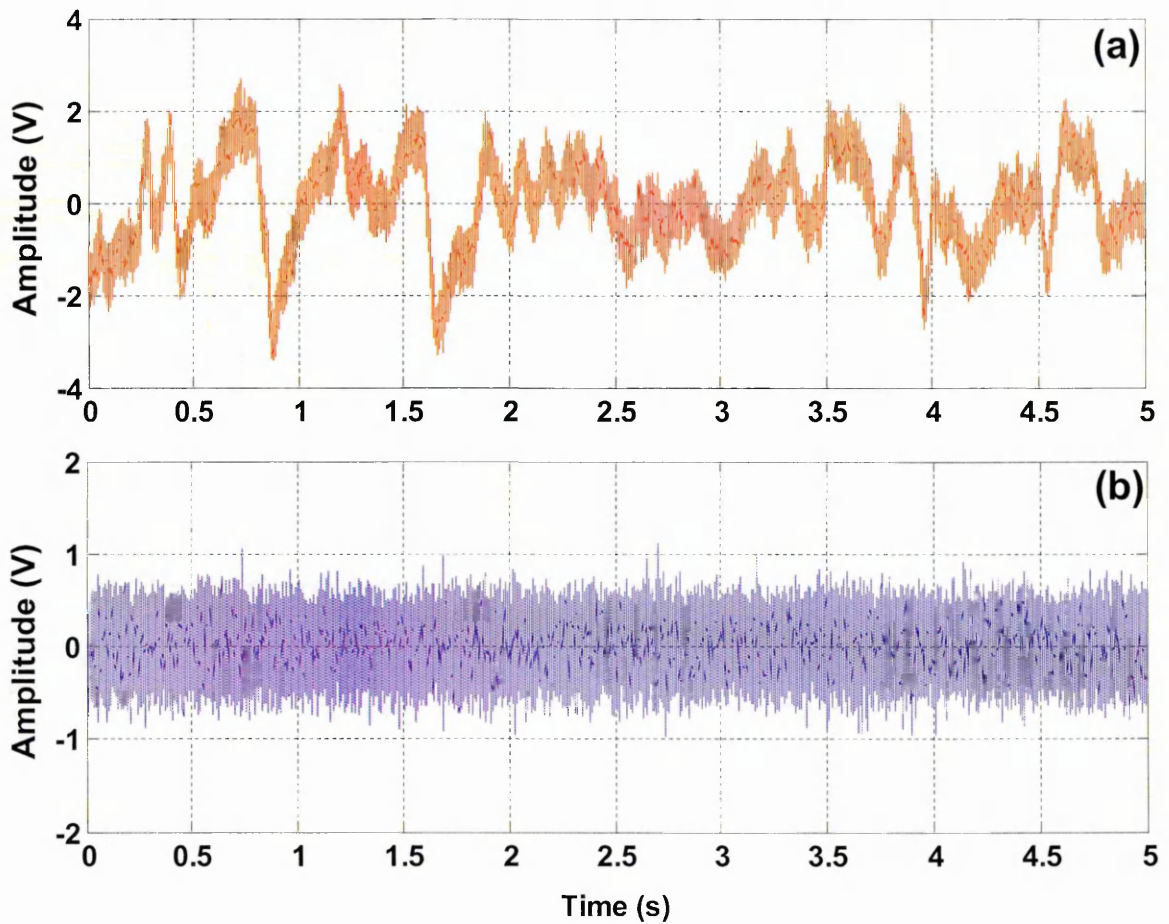
Figure 3.15 The time domain signal measured in windy conditions at the outdoor site in Woburn sands (a) raw time domain data (b) filtered data using Butterworth filter with bandwidth of [50 – 10000] Hz.

We will use an example to explain the averaging and frequency domain conversion of measured data using the Periodogram method. A measurement recording is carried out for 10 seconds with a sampling frequency of 40 kHz. The total number of samples stored is therefore 400,000. The measured data is windowed using a Hamming window which divides the data into sets of small chunks; say 4000 samples in each chunk. The total number of data chunks is 100.

However, we have used 50 % window overlap as shown in Figure 3.17. The total numbers of windowed data chunks becomes 200. The windowed data is passed through FFT block to convert it into frequency domain. After that the resulting data is averaged to obtain the final frequency domain spectrum for input data. A 10 sec long recording gives averaging of 200 times and repeating same measurement three times gives the total averaging number of 600 times. Figure 3.18 (a) shows the FFT for single data chunk of 4000 samples with no averaging and Figure 3.18 (b) shows the FFT for 10 sec long recording obtain by averaging it for 200 times. There is a clear difference between the measured data with and without averaging. The averaged data is smooth and is much less noisy than un-averaged data.
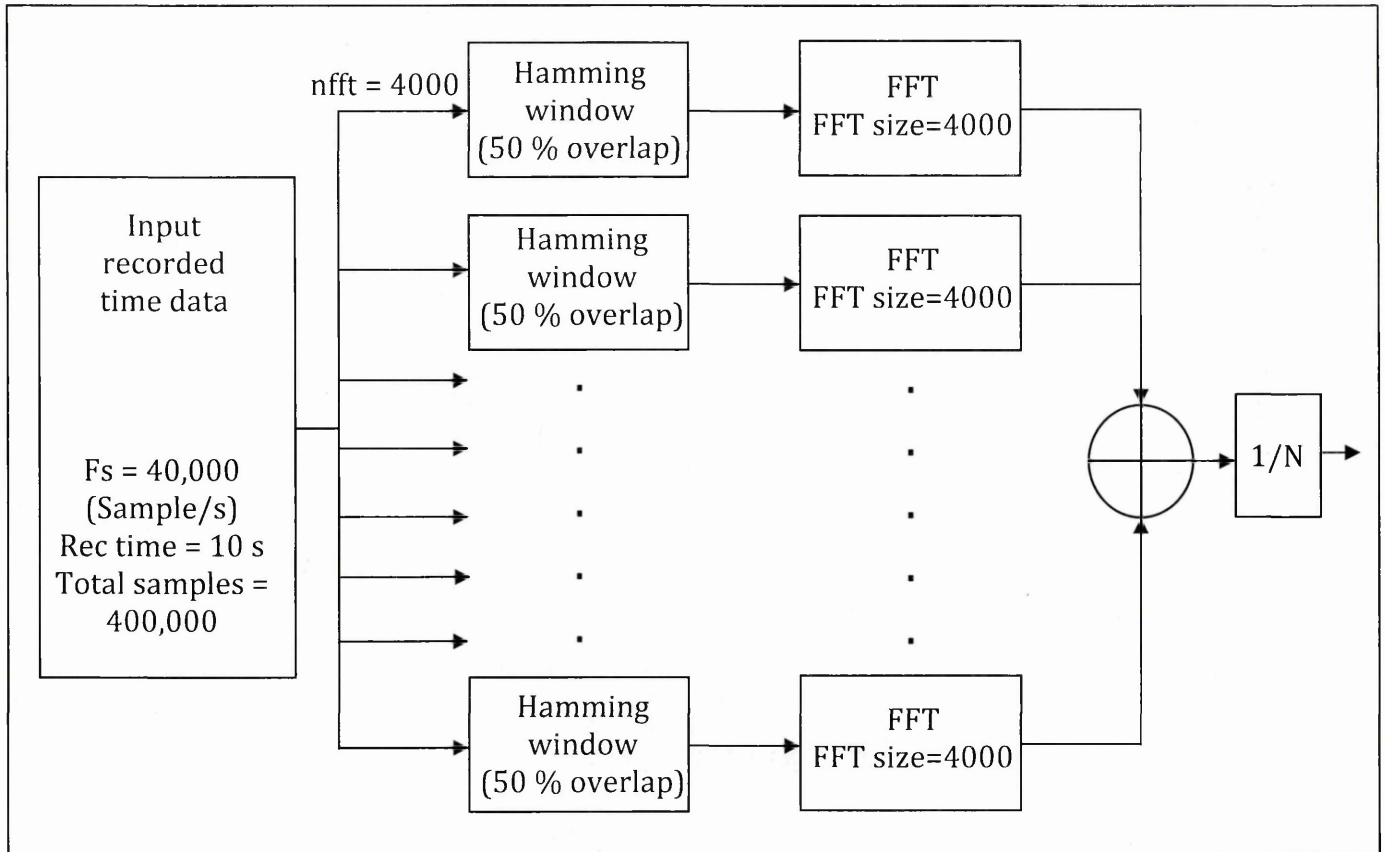
Figure 3.16 Schematic for data analysis and its conversion to frequency domain.
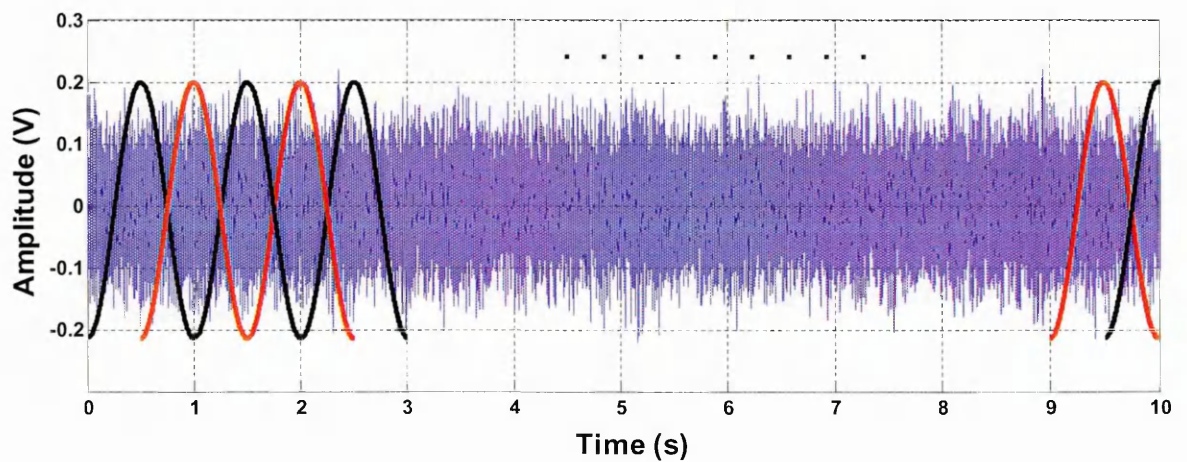
Figure 3.17 Windowing of time domain data
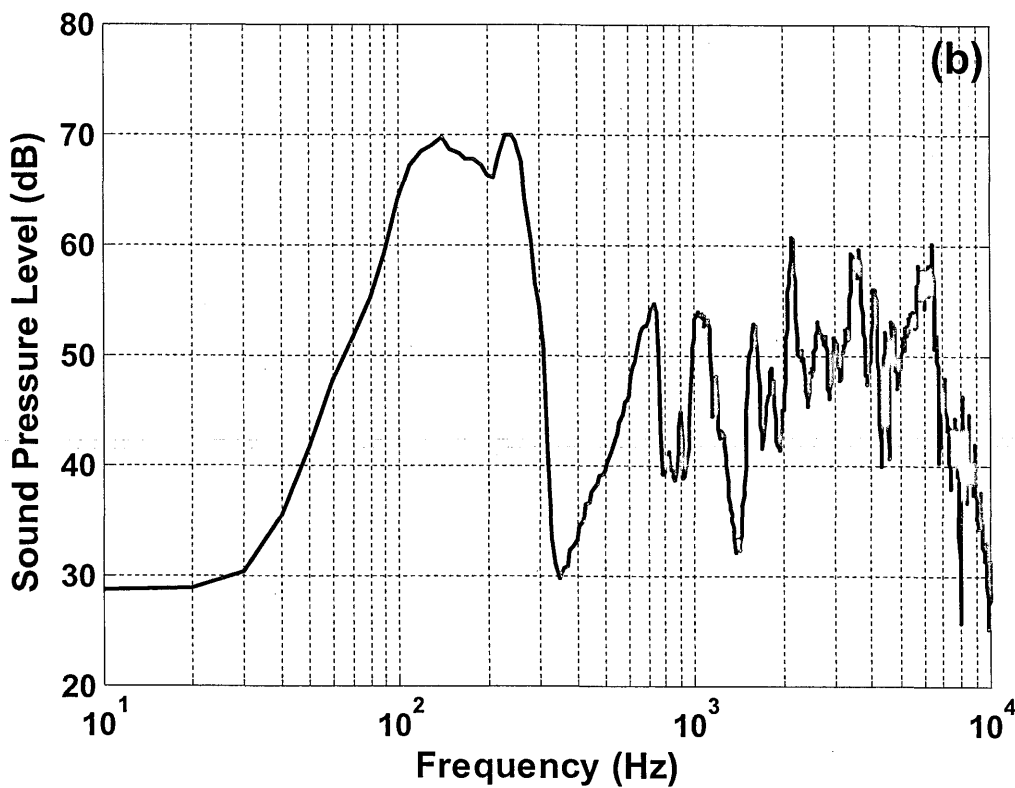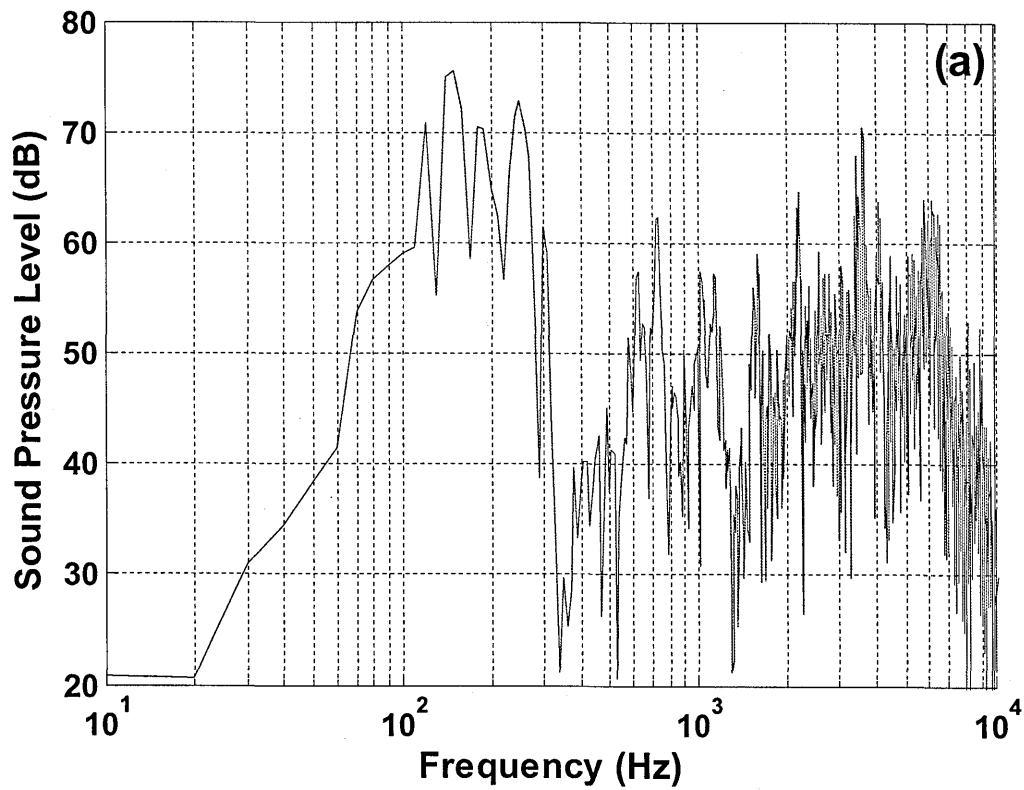
Figure 3.18 Measured sound pressure level over an outdoor site (a) No averaging – FFT for a single chuck of 4000 samples (b) Averaging 200 times for 10 second long recording.

3.3.4 A Test case (hard asphalt)

The measurement system was tested outdoor by carrying out measurement over a hard asphalt ground surface (car park) as shown in Figure 3.19. This hard asphalt ground was later used when constructing parallel walls and lattice structures. Figure 3.20 shows the comparison between measured and predicted level difference spectra over asphalt. The level difference spectrum shown in Figure 3.20 (a) was obtained by placing the source at a height of 0.3 m, the upper and lower microphones at heights of 0.3 m and 0.15 m respectively and with a source-receiver separation of 1.0 m. The level difference spectrum shown in Figure 3.20 (b) was obtained by placing source at height of 0.325 m, upper and lower microphone at height of 0.46 m and 0.23 m respectively and with source-receiver separation of 1.75 m. The spectra have been predicted also using a point source propagation model (see Chapter 4, Section 4.4) and by assuming zero ground admittance. The agreement between measured data and predictions of the well established theoretical model is very good and it helps to validate the developed outdoor measurement system.

Figure 3.19 Level difference measurement over a hard asphalt ground car park.
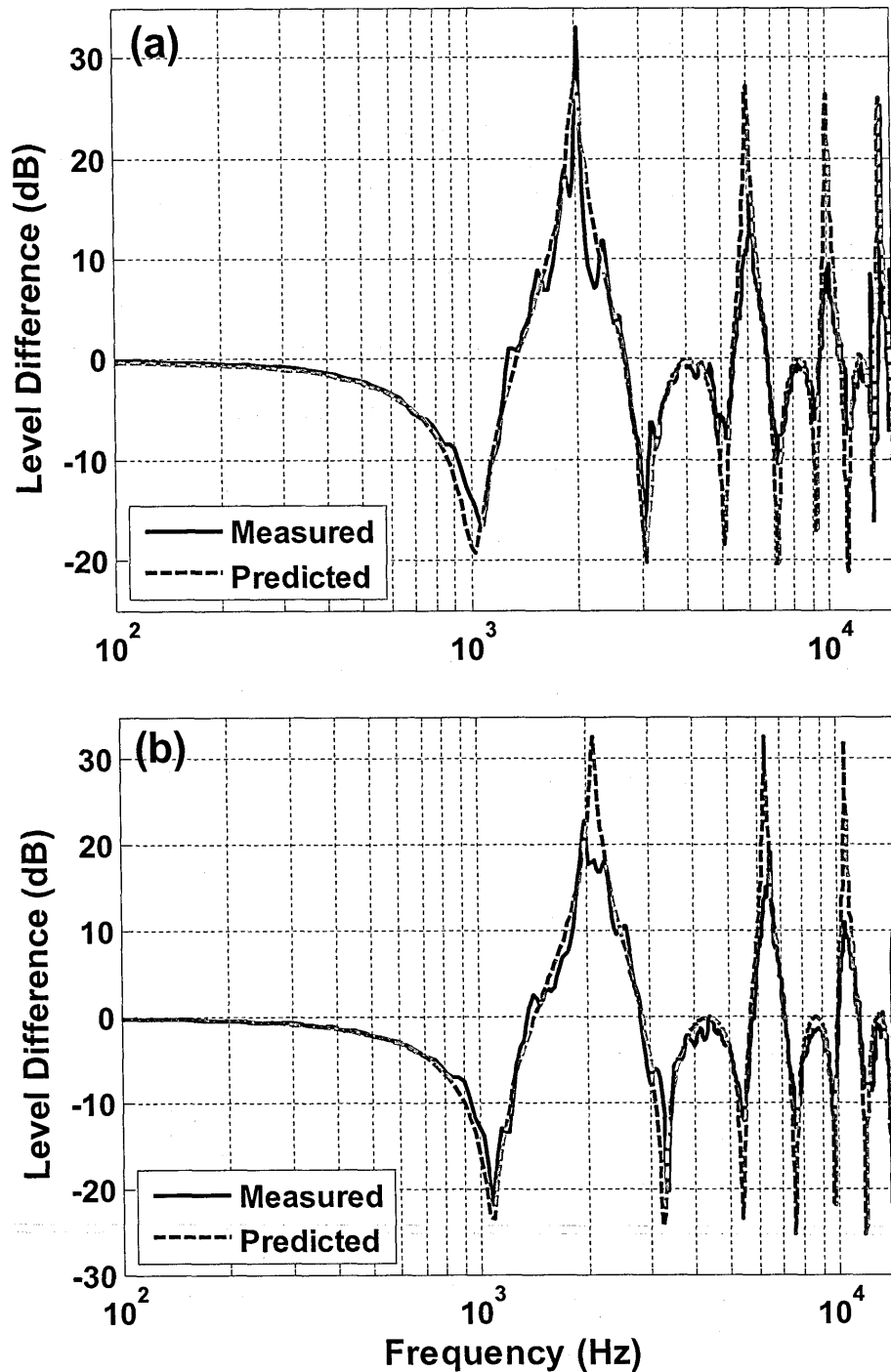
Figure 3.20 Comparison between measured level difference spectra over an asphalt car park and predictions using a point source propagation model with zero surface admittance (a) The source is placed at height of 0.3 m, upper and lower microphones at heights of 0.3 m and 0.15 m respectively and with source-receiver separation of 1.0 m (b) The source is placed at height of 0.325 m, upper and lower microphones at heights of 0.46 m and 0.23 m respectively and with source-receiver separation of 1.75 m.

3.4 Conclusions

The acoustical properties of materials used either to support the structures of interest i.e. glass sheet, MDF board or to make the structures i.e. bricks have been tested in laboratory. These materials have been found to exhibit finite impedance, since the depths of measured excess attenuation maxima are less than those predicted for an infinite impedance surface. Moreover, the depths of excess attenuation maxima depend on the material properties, hardness and smoothness of the surface. A glass sheet provides the deepest EA maximum with a magnitude of 29 dB. MDF provides an EA maximum with a magnitude of 23 dB and a layer of bricks provides an EA maximum with a magnitude of 18 dB. Although the materials (except brick) are not porous it has been found possible and convenient to fit the measured EA maxima using a two parameter slit pore model (see Chapter 4). The maxima in EA spectra obtained over glass sheet, MDF board and layer of bricks were fitted respectively with a flow resistivity of 1500 MPa s m^{-2}, 150 MPa s m^{-2} and 20 MPa s m^{-2}.

Chapter 4

4. Review of Outdoor Ground Impedance Models and their applicability

4.1 Introduction

In this chapter, outdoor sound propagation over different types of ground surfaces has been studied. A large part of this chapter is based on a published paper by Attenborough *et al.* [32]. The signal from a source near the ground to a receiver near the ground is modified by the ground surface in a way that depends on the ground's acoustical properties and the source-receiver geometry. The ground effect is the result of destructive and constructive interference between direct sound from source to receiver and sound arriving at the receiver after being reflected from the ground surface. The resulting interference patterns appear as dips and peaks in the excess attenuation (ground effect) spectrum. The magnitude

and frequency at which these dips occur in ground effect depends on the acoustical ground impedance. These ground effects depend also on the source-receiver geometry. The lower the source and receiver height, the higher the frequencies of the dips and vice versa.

Several impedance models are available to predict the sound propagation over a ground surface. However, this chapter offers a review of 15 models and the basis for selected three of them for the research reported elsewhere in the thesis. The applicability of each model has been tested against 47 different outdoor ground sites and several materials in laboratory. On this basis it is found possible to decide which impedance models are appropriate to be used for characterization of the various ground sites and materials of interest.

Short range propagation spectra predicted by using the impedance models listed in Table 4.1 along with a propagation model described later are compared with data measured over different types of ground surfaces. . Sound propagation from a point source near an impedance surface has been studied extensively [35] and the well established Weyl-Van der Pol approximation [36] is used in the predictions. It calculates the spherical wave reflection coefficient, assuming [36] the ground surface to be locally reacting (for details, see Section 4.4.1). It [36] assumes the ground surface to be locally reacting to calculate spherical wave reflection coefficient (for details, see Section 4.4.1). Table 4.1 summarizes 13 impedance models and the parameters on which they depend. Flow resistivity is an important parameter and is needed in the impedance models listed in Table 4.1. However, the best fit flow resistivity values for a particular ground surface obtained by using each impedance model are different, so, typically, the flow

resistivity value must be regarded as an 'effective flow resistivity'. The second most important parameter for ground impedance is porosity which is present in all models having more than one parameter. Three parameter impedance models such as those for identical tortuous pores and phenomenological models can be transformed into two parameter models by expressing tortuosity or structure factor in terms of porosity. In addition to the parameters listed in Table 4.1, layer thickness may be required as an additional parameter to characterize sites where a hard-backed uniform layer representation of surface impedance is more appropriate. The variable porosity model does not include layer thickness explicitly since it assumes an 'exponential rate of change of porosity with depth' which essentially takes into account of near surface layering.

Table 4.1 Impedance Models and parameters

Model	No. of parameters	Parameters
Delany and Bazley	1	Effective flow resistivity
Miki	1	Effective flow resistivity
Taraldsen	1	Effective flow resistivity
Variable porosity	2	Effective flow resistivity, rate of porosity variation with depth
Kelders-Allard	2	Porosity, effective layer depth
Zwikker and Kosten (Phenomenological)	3	Porosity, effective flow resistivity, structure factor
Hamet Phenomenological	3	Porosity, effective flow resistivity, structure factor
identical tortuous pores	3	Porosity, effective flow resistivity, tortuosity
Attenborough	4	Porosity, flow resistivity, tortuosity, pore shape factor
Pore size distribution	4	Porosity, effective flow resistivity, tortuosity, distribution parameter
Kelders-Allard	2	Porosity, effective layer depth
Wilson Relaxation	4 (or 2)	porosity, flow resistivity, tortuosity shape factor (Viscous and thermal relaxation times)
Johnson/Allard/Umnova	4	Porosity, effective flow resistivity, tortuosity, viscous characteristic length
Johnson/Allard	5	Porosity, effective flow resistivity, tortuosity, viscous and thermal characteristic lengths

Knowledge of the source-receiver geometry along with the acoustical properties of a surface and a sound propagation model can make it possible to predict the propagation of sound over that surface. Several models are available to predict the acoustical properties of ground surfaces. A short review of the sound propagation model and impedance models along with associated literature will be given later in this chapter. The impedance models can be divided into three major categories.

1. **Empirical (or semi-empirical)**

   (a) Delany and Bazley model

   (b) Miki model

   (c) Taraldsen model

2. **Phenomenological**

   (a) Zwikker and Kosten model

   (b) Morse and Ingard

   (c) Hamet model

   (d) Wilson model

3. **Micro-structural**

   (a) Attenborough four parameter model

   (b) Identical pore models (Cylindrical pore, Slit pore, Triangular pore, Rectangular pore)

(c) Variable porosity model

(d) Johnson Allard Umnova model

(e) Kelders-Allard Model

It is important here to define some of the parameters used later in impedance models for ground surfaces. Porous materials have empty spaces filled with a fluid such as air. Porosity is defined as the ratio between the total-volume of (connected) empty spaces in the material which can be occupied by a fluid to the total volume of the material. Porosity is represented by Ω having values between 0 and 1. Typically acoustically soft and hard materials have high and low porosity values respectively. The fluid flow inside pores encounters resistance due to viscosity. Flow resistivity is defined as the ratio of the pressure difference to the flow velocity, divided by thickness of the material [33] and represented by R_s. If the pores are not straight or uniform i.e. change in cross section along their lengths, the fluid flow inside porous material follows an irregular pattern. The deviation of the steady-flow path from a straight line is called tortuosity, defined as square of increase in path length per unit thickness of material and represented by T. The acoustical behaviour of a medium is usually expressed as acoustic impedance which is defined as the ratio of acoustic pressure to the associated particle speed in that medium [34]. For a hard-backed porous ground surface, the layer depth d is also an important parameter to define the surface impedance of the surface.

Section 2 of this Chapter reviews the impedance models used subsequently for fitting data. The third section presents analytical and numerical comparisons between different impedance models. Section 4 summarizes the prediction and

measurement of outdoor sound propagation. Section 5 details comparisons between already available measured data over a number of outdoor ground sites with predictions using the above listed impedance models. This section also discusses the validity of different impedance models with respect to ground type. Comparisons between laboratory propagation data and predictions are given in section 6. Section 7 presents the conclusions.

4.2 Review of impedance models

When sound propagates over a surface, it interacts with the surface which modifies it. The modification depends on the ground properties which give rise to an interesting phenomenon, particularly if the ground is porous or rough. Sound propagation over rigid porous materials has been studied since the 18th century [37]. A number of theories have been presented for interaction of sound with different kind of ground surfaces and for the acoustical properties of porous materials. Typically the acoustical properties of ground surfaces are represented by their surface impedance. It is not possible to review all of the work that has been carried out in this area. However, a very good review of impedance models before 1981 was published by Attenborough [38]. The impedance models reported here will be restricted to those used for data-fitting and analysis purposes. Broadly, porous materials may be divided into two major categories; rigid porous materials and elastic porous materials. The latter category is not included in this study, because most ground surfaces can be regarded as rigid-framed when predicting their influence on sound propagation over them. Theories of acoustic propagation in rigid porous materials assume that the solid parts of the porous materials are perfectly rigid and the pores are filled with a fluid such as air or water. When sound is incident on a rigid porous material, it propagates through the fluid inside the pores and is subject to viscous and thermal losses. These losses depend on the pore size, shape and the extent to which pores are open or closed (connectivity) and pore size distributions. Sound reflection from and propagation in porous materials can be modelled by taking into account the pore structure and fluid losses.

Zwikker and Kosten [39] developed models for the acoustical properties of rigid porous materials by deriving expressions for the effective or dynamic density and effective compression modulus of fluid inside porous material. They assumed a matrix of straight circular tubes filled with a fluid having density ρ_0 and derived expressions for effective density and complex modulus in a single pore. This theory was extended to allow for many cylindrical circular tubes with equal diameter. However, typical porous materials do not have cylindrical pores neither do the pores have identical cross-sections and diameters. Therefore they generalised the identical cylindrical pore approach and divided the compressional modulus by porosity Ω and multiplied the effective density by the ratio of a (phenomenological) structure factor k and porosity. The full mathematical derivation is given elsewhere [39], whereas a simplified version of the Zwikker and Kosten model will be presented here. According to Newton's second law of motion,

$$-\frac{\partial p}{\partial x} = \rho_o \frac{\partial v}{\partial t},$$

(4.1)

The equation of continuity in open air is given by,

$$-\frac{\partial v}{\partial x} = \frac{1}{\rho_o} \frac{\partial \rho}{\partial t},$$

(4.2)

where v is the velocity and ρ_o is the density of the medium. In rigid porous materials the velocity of air increases by a factor of $1/\Omega$ due to materials properties and irregularities. In similar way the equation of continuity for porous material is given by,

$$-\frac{\partial v}{\partial x} = \frac{\Omega}{\rho_o} \frac{\partial \rho}{\partial p} \frac{\partial p}{\partial t}.$$ (4.3)

However, there will be some heat conduction and density changes between compressions and expansions associated with sound propagation. In a compression the air is warmer and its density is higher than in an expansion. The resulting heat conduction, changes in density and viscous effects cause the modulus of air and its density to be complex quantities. According to Kirchhoff's theory [39], the compressional modulus K depends only on thermal effects whereas, dynamic density ρ depends only on viscous losses. Zwikker and Kosten [39] derived an expression for the compressional modulus K while ignoring the viscous losses and an expression for effective density ρ by not taking thermal effects into account. The compressional modulus K which accounts only for thermal effects can be derived from Eq. (4.3).

$$K = \frac{\rho_o}{\Omega} \frac{dp}{d\rho},$$ (4.4)

$$K = \frac{K_o}{\Omega},$$ (4.5)

Where $K_o = \rho_o \dfrac{dp}{d\rho}$ and $K_o = \rho_o c_o^2$ is the modulus of air in free space.

The equation of motion for the enclosed air in porous material is given by,

$$-\frac{\partial p}{\partial x} = \frac{k\rho_o}{\Omega} \frac{\partial v}{\partial t} + R_s v.$$ (4.6)

A plane sound wave travelling in the direction of the positive x-axis is $p = A\exp(-j\omega t + \tau x)$ such that $\dfrac{\partial}{\partial x} = \tau$ and $\dfrac{\partial}{\partial t} = -j\omega$. It is important to note here that time-convention used here differs from that in the original text [39]. The complex density ρ in porous materials which accounts for viscous effects from Eq. (4.6) is given by,

$$\rho = \frac{k\rho_o}{\Omega}\left(1 + \frac{jR_s\Omega}{\omega k\rho_o}\right),$$ (4.7)

where k is the structure factor and R_s is the flow resistivity of the material. It is not possible to calculate the structure factor except in idealised cases. However, experiments shows that its value is always greater than 1, lies between 3 and 7 for granular materials and near to 1 for fibreglass and polyurethane foam. The characteristic impedance of a surface is given by,

$$z = \sqrt{K\rho}.$$ (4.8)

Putting Eq. (4.5) and (4.7) into Eq. (4.8) gives the normalized impedance of a porous material.

$$\frac{z}{\rho_o c_o} = \frac{\sqrt{k}}{\Omega}\sqrt{1 + \frac{jR_s\Omega}{\omega k\rho_o}}.$$ (4.9)

The propagation constant inside porous materials is given by,

$$k_c = j\omega\sqrt{\rho/K}.$$ (4.10)

Putting Eq. (4.5) and (4.7) into Eq. (4.10) gives the complex propagation constant in porous materials.

$$k_c = \frac{j\omega\sqrt{k}}{c_o}\sqrt{1 + \frac{jR_s\Omega}{\omega k\rho_o}} \, , \tag{4.11}$$

which can be written,

$$k_c = j\Omega k_o z \, , \tag{4.12}$$

where k_o is the propagation constant in free space. It is important to differentiate between k, k_o and k_c which are notations for structure factor, propagation constant in free space and propagation constant in a porous material respectively. The Zwikker and Kosten model has also been called a phenomenological model [2], [39].

Morse and Ingard [2] modelled the sound propagation in pores by assuming that the fluid inside pores has complex effective density and complex effective sound speed which leads to a complex propagation constant. The fluid flow inside pores undergoes some frictional forces which results an increase in the free-field fluid density ρ to an effective fluid density ρ_p in the pores. Similarly the sound wave velocity changes from the free field value c to c_p in the pores due to friction between the walls and enclosed fluid. Morse and Ingard [2] gave a frequency dependent formulation for complex fluid density and complex sound speed in terms of flow resistivity R_s and porosity Ω,

$$\rho_e = \rho_p\left(1 + \frac{iR_s}{\rho_p\omega}\right), \tag{4.13 a}$$

$$\kappa_e = \Omega\kappa_p \, , \tag{4.13 b}$$

$$c_e = c_p \left(1 + \frac{iR_s}{\rho_p \omega} \right)^{-\frac{1}{2}} ,$$

(4.14)

where $K_p = \rho_o c_o^2$ and $c_p = \sqrt{1 \Big/ \rho_p K_p \Omega}$. It is not clear in Morse and Ingard [2] about

the expression for ρ_p. In fact if $\rho_p = k \rho_o / \omega$, then the Morse and Ingard [2]

formulation is identical to that of Zwikker and Kosten [39].

The phenomenological model given by Eq. (4.9) assumes adiabatic

conditions in the pores [32]. To predict the acoustical properties of porous asphalt,

Berengier *et al.* [40], [32] have proposed a modified form of this model

(subsequently called the Hamet model), which allows for frequency dependent

thermal effects. The Hamet model may be written as,

$$Z_c = \left(\frac{1}{\Omega} \right) \left(\frac{T}{\gamma} \right)^{\frac{1}{2}} \left\{ 1 + \frac{\gamma - 1}{\gamma} \left(\frac{1}{F_0} \right)^{\frac{1}{2}} \right\} F_\mu^{\frac{1}{2}} , \quad k = \gamma \Omega k_0 Z_c$$

(4.15)

where $F_\mu = 1 + i \omega_\mu / \omega$, $F_0 = 1 + i \omega_0 / \omega$, $\omega_\mu = (R_s / \rho_0)(h/T)$, $\omega_0 = \omega_\mu (T / N_{PR})$ and N_{PR}

is the Prandtl number for air.

Delany and Bazley [41] derived a single parameter model for predicting the

acoustical properties of porous materials. Their model is based on many

impedance tube measurements on highly porous materials. The resulting

experimental data was fitted using power-law relationships. Most of the

measurements were performed over fibrous materials having porosities close to 1.

According to the Delany and Bazley [41] model the surface impedance z and

propagation constant k for a locally reacting semi-infinite surface can be written as,

$$z = 1 + 9.08\left(\frac{1000f}{R_s}\right)^{-0.75} + i11.9\left(\frac{1000f}{R_s}\right)^{-0.73}, \qquad (4.16)$$

$$k_c = \left(\frac{\omega}{c_o}\right)\left[1 + 0.0978\left(\frac{\rho_o f}{R_s}\right)^{-0.70} + i0.087\left(\frac{\rho_o f}{R_s}\right)^{-0.595}\right], \qquad (4.17)$$

where ω being the angular frequency, ρ_o the density of air, c_o the speed of sound, f the frequency and R_s is the flow resistivity. Surface impedance, z and the propagation constant, k_c are characterized by a single adjustable parameter known as the effective flow resistivity, which has units of $Pa\,s\,m^{-2}$. To characterize an outdoor ground surface, an 'effective' flow resistivity value is used instead of the actual flow resistivity value. When fitting data for propagation over a ground surface it rarely takes a value equal to the actual flow resistivity value.

Dunn and Davern [42] studied the surface impedance and propagation constant for four different types of reticulated polyurethane foam materials using a similar method to that used by Delany and Bazley [41]. They measured the impedance for polyurethane foam by the impedance tube method and modified the Delany and Bazley regression constants to fit their data. Their best fit equations for foam materials are,

$$z = 1 + 0.114\left(\frac{\rho_o f}{R_s}\right)^{-0.369} + i0.0985\left(\frac{\rho_o f}{R_s}\right)^{-0.758}, \qquad (4.18)$$

$$k_c = \left(\frac{\omega}{c_o}\right)\left[1 + 0.168\left(\frac{\rho_o f}{R_s}\right)^{-0.715} + i0.136\left(\frac{\rho_o f}{R_s}\right)^{-0.491}\right], \qquad (4.19)$$

They found that Delany and Bazley [41] predicts an incorrect value of surface impedance at low frequencies even for materials with high porosity. This is due to the fact that the real component of complex impedance must always be positive for a finite thickness layer of material but sometimes, according to the Delany and Bazley model, it becomes negative at low frequencies. Miki [43] derived new regression constants for the Delany and Bazley model based on experimental data. Later on, Miki [44] derived effective flow resistivity (R_e) from an empirical relationship between porosity, flow resistivity and tortuosity and accordingly modified the regression constants. According to Miki a three parameter model is given by [44],

$$R_e = \frac{\Omega R_s}{T}, \qquad (4.20)$$

$$z = 1 + 0.070\left(\frac{f}{R_e}\right)^{-0.632} + i0.107\left(\frac{f}{R_e}\right)^{-0.632}, \qquad (4.21)$$

$$k_c = \left(\frac{\omega}{c_o}\right)\left[1 + 0.160\left(\frac{f}{R_e}\right)^{-0.618} + i0.109\left(\frac{f}{R_e}\right)^{-0.618}\right]. \qquad (4.22)$$

Taraldsen [45], [46] presented a one parameter model of sound propagation through rigid porous materials based on Darcy's law. According to Taraldsen the three parameter model derived from Darcy's law is given as,

$$\frac{z}{\rho_o c_o} = \frac{\sqrt{T}}{\sqrt{\gamma}\,\Omega} \sqrt{1 + \frac{jR_s\Omega}{\omega T \rho_o}} \;.$$

(4.23)

Eq. (4.23) is similar to Eq. (4.9) for the phenomenological model except it is divided by square root of the adiabatic constant (γ) and the structure factor is interpreted as tortuosity. Taraldsen has transformed the three parameters Darcy model into a two parameter model, by introducing effective porosity, and effective flow resistivity as given below.

$$\Omega_e = \frac{\Omega}{\sqrt{T}} \quad , \quad R_e = \frac{R_s}{\sqrt{T}}\;.$$

(4.24 a, b)

Putting Eq. (4.24) into Eq. (4.23) gives,

$$\frac{z}{\rho_o c_o} = \frac{1}{\sqrt{\gamma}\,\Omega_e} \sqrt{1 + \frac{jR_e\Omega_e}{\omega \rho_o}}\;.$$

(4.25)

Eq. (4.25) can be simplified further by deriving effective porosity Ω_e as a function of effective flow resistivity R_e. According to Taraldsen [45], [46], the relationship between R_e and Ω_e is given by,

$$\Omega_e = 10^{(0.1x-2)}\;,$$

(4.26)

$$x = \left[\frac{-y + A + 2\emptyset B - \sqrt{4BC + (-y + A - 2\emptyset B)^2}}{2B}\right],$$

(4.27)

$$y = 10\log\!\left(\frac{R_e}{R_o}\right).$$

(4.28)

The values of coefficients are $A = 206.95$, $B = 9.88$, $C = 13.82$ and $R_o = 1000 Ns/m^4$.

The complex propagation constant is given as,

$$k_c = jk_o \gamma \sqrt{T}\Omega_e z.$$
(4.29)

Eq. (4.29) shows that the propagation constant depends on two parameters: tortuosity and flow resistivity. For a hard-backed porous ground surface with a layer depth of L, Taraldsen's model needs three parameters i.e. flow resistivity, tortuosity and layer depth (see Eq. 4.29). However, Taraldsen [45], [46] combined the tortuosity, the effective flow resistivity and the layer depth into an effective layer depth L_e to obtain a two parameter model. The resulting model for a hard-backed layer ground depends on only two parameters, effective flow resistivity and effective layer depth. This is similar to the corresponding Delany-Bazley model which depends on flow resistivity and layer thickness. Tortuosity and effective flow resistivity can be combined together into an effective layer depth.

$$L_e = \gamma \sqrt{T}\Omega_e L.$$
(4.30)

The Taraldsen, Delany and Bazley and Miki one parameter models predict similar results as shown later in this chapter.

Many theories of sound propagation in porous materials are based on micro-structural pore models in which, for example, wave propagation normal to the surface in a single cylindrical pore is modelled [37] and then this formulation is extended to the bulk medium. The models that will be presented later are based on the initial work by Rayleigh [37] and later on by Zwikker and Kosten [39]. In particular, the detailed formulations for micro-structural models by Attenborough

[38], [47], [48] derived from Rayleigh [37], Zwikker and Kosten [39] and Biot theory [49] will be presented here.

Attenborough [38], [47], [48] modelled sound propagation through a single pore based on fluid flow into two extreme pore shapes such as cylindrical cross-section and parallel walled slits respectively. According to Kirchhoff's theory [39], the compressional modulus K contains only thermal effects, whereas the density ρ accounts only for viscous losses. Zwikker and Kosten [39] have shown that the viscous and thermal loses for fluid flowing perpendicularly in a cylindrical tube can be treated independently. Consider a straight cylindrical pore of radius a filled with a fluid having density ρ_o, the expression for the complex density while ignoring the thermal effects derived by Zwikker and Kosten [39] may be written as,

$$\rho_c(\omega) = \frac{\rho_o}{1 - 2(\lambda_c \sqrt{i})^{-1} T(\lambda_c \sqrt{i})}, \tag{4.31}$$

where

$$T(\lambda_c \sqrt{i}) = \frac{J_1(\lambda_c \sqrt{i})}{J_0(\lambda_c \sqrt{i})}, \tag{4.32}$$

where $J_0()$ and $J_1()$ are the zeroth and first order Bessel functions respectively. The frictional losses between fluid flowing through pore and pore wall are due to viscous layer of depth $\sqrt{v/\omega}$. The dimensionless factor λ_c is the ratio between pore radius to the viscous layer along the pore wall, given by,

$$\lambda_c = a\sqrt{\omega/v}, \tag{4.33}$$

where v is the kinematic viscosity of air.

In a similar way the complex density function for parallel sided slits having width 2b is given by [48],

$$\rho_s(\omega) = \frac{\rho_o}{1 - (\lambda_s\sqrt{-i})^{-1}\tanh(\lambda_s\sqrt{-i})},$$ (4.34)

where

$$\lambda_s = b\sqrt{\omega/v}.$$ (4.35)

Consider a non-viscous fluid in a cylindrical pore. When the fluid inside pore undergoes compression, it generates heat energy which flows inside the pore. These thermal effects inside the pore, while ignoring the viscous effects, can be taken into account through the complex compressibility. If the pressure inside the pore is assumed to be uniform, the complex compressibility of air within the cylindrical pore is given by [39],

$$C_c(\omega) = (\gamma P_o)^{-1}\left(1 + 2(\gamma - 1)T(\sqrt{iN_{pr}}\lambda_c)\right),$$ (4.36)

where N_{pr} is the Prandtl number.

In a similar way the complex compressibility function for parallel sided slits having width 2b is given by [48],

$$C_s(\omega) = (\gamma P_o)^{-1}\left(1 + \frac{(\gamma - 1)}{\sqrt{-iN_{pr}}\lambda_s}\tanh(\sqrt{-iN_{pr}}\lambda_s)\right).$$ (4.37)

Biot [49] studied the fluid flow between parallel walls and in a circular tube. The fluid flow has viscous effects due to frictional losses and pore shape which can be taken into account by introducing a structural factor. Attenborough [14, 15]

redefined the dimensionless parameter λ_p for arbitrary shaped pores by following the work of Biot [49].

$$\lambda_p = (l/n)\sqrt{\omega/v}, \tag{4.38}$$

where n is the dynamic shape factor and l is the characteristic dimension of the pore. The dynamic shape factor ranges between $0.5 \leq n \leq 1$, for which the lower and upper bounds corresponds to the extremes of parallel sided slit and cylindrical shaped pore respectively. Thus, the complex density and complex compressibility for arbitrary shaped pore is given as,

$$\rho_p(\omega) = \frac{\rho_o}{1 - 2(\lambda_p\sqrt{i})^{-1}T(\lambda_p\sqrt{i})}, \tag{4.39}$$

$$C_p(\omega) = (\gamma P_o)^{-1}\left(1 + \frac{2(\gamma-1)}{\sqrt{iN_{pr}}\lambda_p}T(\sqrt{-iN_{pr}}\lambda_p)\right), \tag{4.40}$$

The fluid flow inside pores encounters resistance which is measured as flow-resistance. The flow resistance R_{so} per unit length in a single pore is given as [48], [50],

$$R_{so} = 8\mu s/l^2, \tag{4.41}$$

where μ, s and l are dynamic viscosity, static shape factor and characteristic length respectively.

Assuming that the all pores in porous materials are identical, the derivation for a single pore can be extended for a bulk material by multiplying and dividing by

tortuosity and porosity respectively. Thus, the complex density and flow resistivity for a bulk porous material from Eq. (4.39) and Eq. (4.41) respectively, is given as,

$$\rho_b(\omega) = (T/\Omega)\rho_p(\omega),$$
(4.42)

$$R_s = 8\mu s T / l^2 \Omega,$$
(4.43)

$$l = \sqrt{8\mu s T / \Omega R_s}.$$
(4.44)

Putting Eq. (4.44) into Eq. (4.38) gives dimensionless parameter λ_p for bulk medium.

$$\lambda_p = (1/n)\sqrt{8\rho_o T s \omega / \Omega R_s}.$$
(4.45)

There is an empirical relationship between dynamic shape factor and static shape factor.

$$n = 2 - s. \qquad 1 \leq s \leq 1.5, \ 0.5 \leq n \leq 1.0$$
(4.46)

If $s_f = {}^{n}\!/\!{\sqrt{s}}$ being the pore shape factor ratio, the dimensionless parameter λ_p becomes [47], [48],

$$\lambda_p = (1/s_f)\sqrt{8\rho_o T \omega / \Omega R_s},$$
(4.47)

Attenborough [51] modified the pore shape factor ratio to $s_p = {}^{nA}\!/\!{\sqrt{s}}$, where A is the ratio between hydraulic radius r_h and the characteristic dimension l for any given geometry. The modified λ_p is given by,

$$\lambda_p = (1/2s_p)\sqrt{8\rho_o T\omega/\Omega R_s} \; . \tag{4.48}$$

Stinson and Champoux [52]–[54] studied the Attenborough model [47], [48], [51] considered its predictions for hypothetical idealised porous materials and suggested that the pore shape factor ratio s_p must be frequency dependent. Measurements were carried out over two types of porous ceramic materials. A comparison with Attenborough theory [47], [48], [51] shows that pore shape factor ratio has to be frequency dependent to have good agreement with data. Stinson and Champoux [53] also derived expressions for acoustical behaviour of porous materials for other pore shapes such as rectangular and triangular cross-section. However, Attenborough [55] showed that the complex density and complex compressibility are sensitive to the frequency dependent shape factor. Whereas for a given bulk flow resistivity, porosity and tortuosity, the frequency dependent shape factor has relatively little effect on the characteristic impedance and absorption coefficient for a rigid bulk porous medium. Moreover, the Attenborough [55] four parameter model can be transformed into a three parameter identical pore model for particular pore shapes. Attenborough's [38], [47], [48], [51], [55] three parameter identical pore models for different pore shapes are summarized in Table 4.2 and 4.3.

Table 4.2 Complex density and complex compressibility functions for various pore shapes

Pore shape	Complex density $\rho(\omega)$	Complex Compressibility $C(\omega)$
Cylinder (radius 'a')	$\rho_o\left(1-\dfrac{2}{\lambda_c\sqrt{i}}\dfrac{J_1(\lambda_c\sqrt{i})}{J_0(\lambda_c\sqrt{i})}\right)^{-1}$	$(\gamma P_o)^{-1}\left[1+\dfrac{2(\gamma-1)}{\lambda_c\sqrt{iN_{Pr}}}\dfrac{J_1(\lambda_c\sqrt{iN_{Pr}})}{J_0(\lambda_c\sqrt{iN_{Pr}})}\right]^{-1}$
Slit (width '2b')	$\rho_o\left(1-\dfrac{\tanh(\lambda_s\sqrt{-i})}{(\lambda_s\sqrt{-i})}\right)^{-1}$	$(\gamma P_o)^{-1}\left[1+\dfrac{(\gamma-1)\tanh(\lambda_s\sqrt{-iN_{Pr}})}{\lambda_s\sqrt{-iN_{Pr}}}\right]^{-1}$
Triangle (side 'd')	$\rho_o\left(1-\dfrac{3\coth(\lambda_t\sqrt{-i})}{(\lambda_t\sqrt{-i})}+\dfrac{3i}{\lambda_t^2}\right)^{-1}$	$(\gamma P_o)^{-1}\left\{\gamma-\dfrac{\gamma-1}{N_{Pr}\lambda_t^2}\left(\dfrac{N_{Pr}\lambda_t^2-3\lambda_t\sqrt{-iN_{Pr}}}{\coth(\lambda_t\sqrt{-iN_{Pr}})}+3\right)\right\}$
Rectangle (sides '2a', '2b')	$\rho_o\left(\dfrac{\pi^4}{4}\right)\left(\displaystyle\sum_{m=0}^{\infty}\sum_{n=0}^{\infty}m^-n^-\left(1+\dfrac{2i(m^-+n^-)}{\lambda_r^2}\right)\right)$	$(\gamma P_o)^{-1}\left(\gamma-(\gamma-1)\rho_r\left(\lambda_r\sqrt{N_{Pr}}\right)\right)$

$^*m^- = (m+0.5)^2$, $n^- = (n+0.5)^2$

Table 4.3 Hydraulic radius, Steady flow shape factor and dimensionless parameter λ for various pore shapes.

Pore shape	Hydraulic radius (r_h)	Shape factor (s_o)	Single pore (λ_{single})	Bulk medium (λ_{bulk})
Cylinder (radius 'a')	$\dfrac{a}{2}$	1	$a\sqrt{\dfrac{\omega\rho_o}{\mu}}$	$\sqrt{\dfrac{8\omega\rho_o T}{\Omega R_s}}$
Slit (width '2b')	b	1.5	$b\sqrt{\dfrac{\omega\rho_o}{\mu}}$	$\sqrt{\dfrac{3\omega\rho_o T}{\Omega R_s}}$
Triangle (side 'd')	$\dfrac{d}{4\sqrt{3}}$	$\dfrac{5}{6}$	$\dfrac{d\sqrt{3}}{4}\sqrt{\dfrac{\omega\rho_o}{\mu}}$	$\sqrt{\dfrac{15\omega\rho_o T}{\Omega R_s}}$
Rectangle (sides '2a', '2b')	$\dfrac{2ab}{a+b}$	0.89	$\dfrac{2ab}{\sqrt{a^2+b^2}}\sqrt{\dfrac{\omega\rho_o}{\mu}}$	$\sqrt{\dfrac{14.24\omega\rho_o T}{\Omega R_s}}$

The hydraulic radius r_h is defined as the ratio of wetted area to perimeter for uniform pores. From Eq. (4.41), the flow resistivity in a single as a function of hydraulic radius r_h can be rewritten as [48], [50],

$$R_{so} = 2\mu s_o / r_h^2 . \qquad \text{(4.49 a)}$$

In similar way the flow resistivity for bulk medium can be rewritten as,

$$R_s = 2\mu s_o T / \Omega r_h^{\,2}.$$

(4.49 b)

Rearranging Eq. (4.50) for μ gives,

$$\mu = 2s_o T / R_s \Omega r_h^{\,2}.$$

(4.50)

Eq. (4.51) can be placed into λ_{single} given in Table 4.2 (column # 4) to obtained λ_{bulk} (column # 5) for different pore shapes also given in Table 4.2.

The acoustical characteristics of interest for a bulk porous material such as characteristic impedance and complex propagation constant can be calculated by using the complex density and complex compressibility expressions listed in Table 4.1 in the formulae given below,

$$k_c = \omega \sqrt{T \rho(\omega) C(\omega)},$$

(4.51 a)

$$z = \frac{1}{\rho_o c_o} \sqrt{\frac{T}{\Omega^2} \frac{\rho(\omega)}{C(\omega)}}.$$

(4.51 b)

The three parameter identical pore model for a semi-infinite porous medium can be converted into two parameter model by assuming a relationship between tortuosity and porosity [33].

$$T = \frac{1}{\Omega^{n'}}$$

(4.52)

where $n' = 0.5$, gives reasonable results. However, a range of tortuosity values for different materials are given elsewhere [33].

By viewing the viscous and thermal diffusion in porous materials as relaxation processes, Wilson [56], [57] has obtained models for the acoustical

properties of porous materials in simple forms that, nevertheless, enable accurate predictions over wide frequency ranges. His results may be expressed as,

$$Z = \frac{\sqrt{T}}{\Omega}\left[\left(1+\frac{\gamma-1}{\sqrt{1-i\omega\tau_e}}\right)\left(1-\frac{1}{\sqrt{1-i\omega\tau_v}}\right)\right]^{-\frac{1}{2}},$$ (4.53 a)

$$k = \frac{\omega\sqrt{T}}{c_0}\left[\left(1+\frac{\gamma-1}{\sqrt{1-i\omega\tau_e}}\right)\Big/\left(1-\frac{1}{\sqrt{1-i\omega\tau_v}}\right)\right]^{\frac{1}{2}}.$$ (4.53 b)

where, for identical uniform pores, τ_e and τ_v, the thermodynamic and aerodynamic characteristic times respectively, are given by,

$$\tau_v = 2\rho_0 T/\Omega R_s , \ \tau_e = N_{PR}s_B^2\tau_v$$ (4.54)

Donato [58] proposed an impedance model in which the porosity varies exponentially with depth and found that it enables good agreement with measured data over a grass covered surface. Attenborough [47] used Donato's approach to derive a two parameter variable porosity model by applying approximations of the four parameter model [38], [48]. Attenborough [47] pointed out that porosity decreasing exponentially with depth is more likely than the variation assumed in the Donato model in which ground become more porous with depth. Later on, Raspet and Sabatier [59] suggested some modifications to Attenborough's [47] variable porosity model. The surface impedance of a ground in which the porosity varies exponentially with depth is given as [33], [59],

$$z = \frac{1+i}{\sqrt{\pi \gamma \rho_o}} \sqrt{\frac{R_e}{f}} + \frac{ic_o \alpha_e}{8\pi \gamma f},$$ (4.55)

where $\alpha_e = (n'+2)\alpha / \Omega$ is the effective rate of change of porosity and n' is the grain shape factor. The positive value of porosity rate means that the porosity is decreasing with depth, whereas the negative values represent that the porosity increases with depth.

Umnova *et al.* [60] developed a cell model for the acoustical properties of granular materials. The predicted impedance of the cell model depends strongly on the inner structure of the material. According to the Johnson-Allard-Umnova model [60] the dynamic complex tortuosty is,

$$\alpha(\omega) = T + \frac{R_s \Omega}{-i\omega \rho_o} \sqrt{1 + (-i\omega)\frac{4T^2 \rho_o \eta}{R_s^2 \Omega^2 \Lambda^2}},$$ (4.56)

where Λ is the characteristic viscous length, η is the coefficient of dynamic viscosity and ρ_o is the density of air. The dynamic compressibility for stacked spheres is derived from the relationship between thermal and viscous effects,

$$C(\omega) = \gamma - \frac{\gamma - 1}{\left(\frac{2}{3}(1-\Theta)(\alpha(\omega N_{\mathrm{Pr}}) - T) + 1\right)},$$ (4.57)

where $\Theta = 0.675(1 - \Omega)$.

4.3 Analytical and Numerical comparisons of impedance models

4.3.1 Comparisons between the slit pore, Hamet and Wilson models

By assuming $n' = 0.5$ in Eq. (4.52), the slit pore model (see Tables 4.2 and 4.3) and Hamet model (see Eq. 4.2) can be reduced into a two parameter model. Also by assuming a constant value of the pore shape factor ($s_B = 1.4$), the number of free parameters in the Wilson model (see Eq. 4.53 and Eq. 4.54) is reduced to two as well [32]. Figure 4.1 compares the predictions for surface impedance of a hard-backed porous layer and corresponding level difference spectra (source height 0.5 m, receiver heights at 0.5 m and 0.2 m, separation 1.75 m) using three impedance models (slit pore (continuous lines) , Hamet (broken lines) and Wilson (dotted lines)) with parameter values (a) Ω = 0.4, R_s = 100 kPa s m^{-2}, n' = 0.5, d = 0.05 m and (b) Ω = 0.6, R_s = 10 kPa s m^{-2}, n' = 0.5, d = 0.05 m. Figure 4.1 is taken from the paper by Attenborough *et al.* [32] (Figure 2 in ref). Figure 4.1 shows that, for typical parameter values, the two parameter versions of the Hamet, Wilson and slit pore models give rise to practically identical predictions for the impedance of a porous layer and short range level difference spectra. Since the Hamet and Wilson model give similar results to the slit pore model the latter only is chosen for data fitting in the remainder of the chapter.
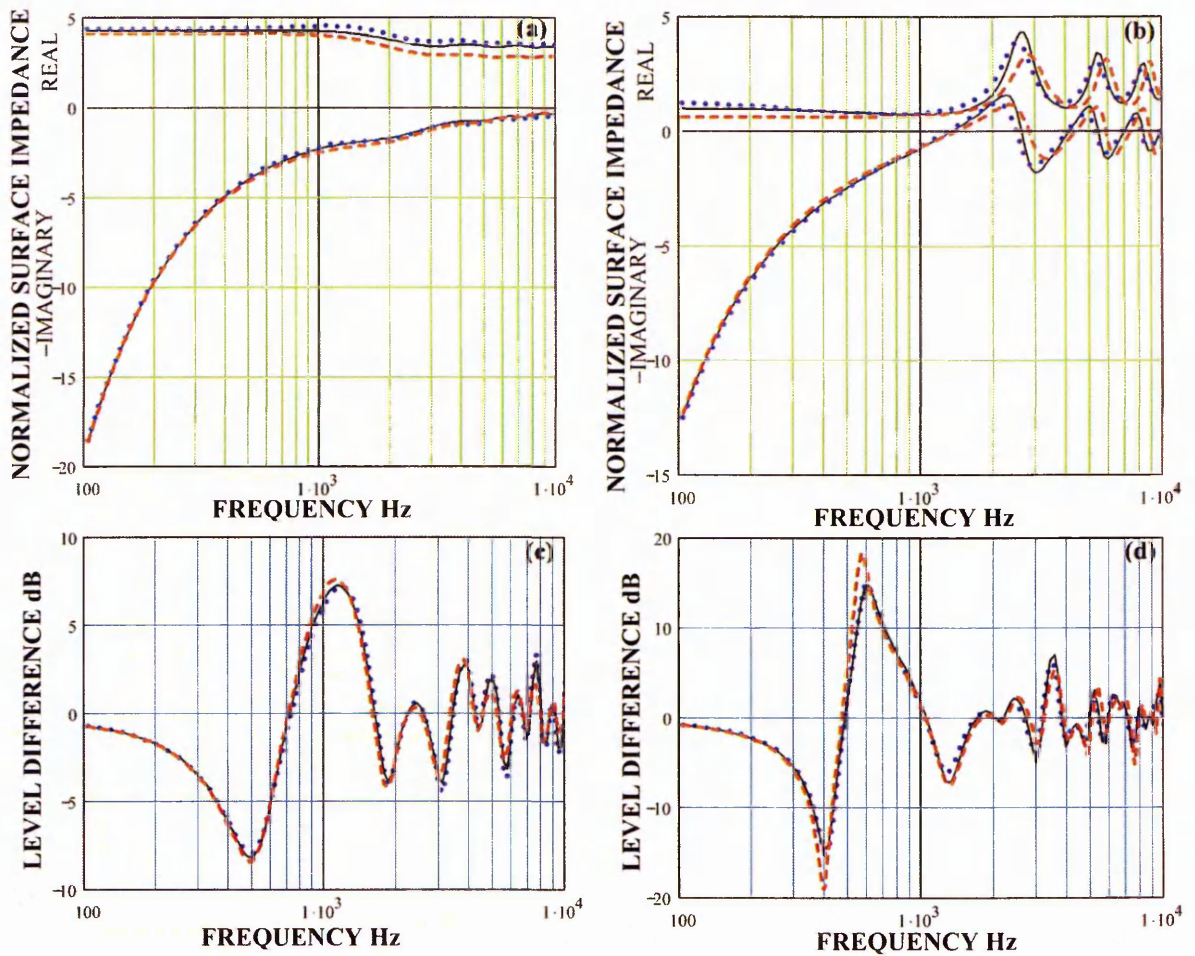
Figure 4.1 Comparison of predictions for surface impedance of a hard-backed porous layer and corresponding level difference spectra (source height 0.5m, receiver heights at 0.5m and 0.2m, separation 1.75m) using three impedance models (slit pore (continuous lines) , Hamet (broken lines) and Wilson with $s_B = 1.4$ (dotted lines)) with parameter values (a) $\Omega = 0.4$, $R_s = 100$ kPa s m^{-2}, $n' = 0.5$, $d = 0.05$ m and (b) $\Omega = 0.6$, $R_s = 10$ kPa s m^{-2}, $n' = 0.5$, $d = 0.05$ m (Figure taken from ref [32]-Fig. 2).

4.3.2 Comparisons between the slit pore and Zwikker and Kosten models

The Zwikker and Kosten model given by Eq. (4.1) – (4.12) represents a low frequency and/or high flow-resistivity approximation of identical pore models (see Tables 4.2 and 4.3). In this section the relationship between the Zwikker and Kosten model and a low frequency/high flow resistivity approximation of the slit pore model will be explored. The complex density function and λ_s for a slit pore model from Table 4.2 are given by,

$$\rho_c(\omega) = \rho_o\left(1 - \frac{\tanh(\lambda_s\sqrt{-i})}{(\lambda_s\sqrt{-i})}\right)^{-1}, \tag{4.58}$$

$$\lambda_s = \sqrt{\frac{3\omega\rho_o T}{\Omega R_s}}. \tag{4.59}$$

For low frequency limit, λ_s approaches to zero and the $tanh()$ can be approximated by [33], [48],

$$\frac{\tanh(z)}{z} \approx 1 - \frac{z^2}{3}. \tag{4.60}$$

Putting Eq. (4.60) into Eq. (4.58) and some simplification through Eq. (4.59) gives complex density.

$$\rho_c(\omega) = \frac{i\Omega R_s}{\omega T}. \tag{4.61}$$

If $R_{eff} = \dfrac{\Omega R_s}{\omega T}$, then complex density becomes,

$$\rho_c(\omega) = iR_{eff} .$$

(4.62)

In similar way using the slit pore model expression for complex compressibility for given in Table 4.2 and simplifying it through Eqs. (4.59) and 4.60 gives,

$$C_c(\omega) = \left(\frac{1}{\rho_o c_o^2}\right)\left(\gamma - (\gamma - 1)\frac{N_{PR}\rho_o}{iR_{eff}}\right),$$

(4.63)

$$C_c(\omega) = \left(\frac{1}{\rho_o c_o^2}\right)\left(\frac{i\gamma R_{eff} - (\gamma - 1)N_{PR}\rho_o}{iR_{eff}}\right).$$

(4.64)

Applying high flow-resistivity and low frequency limit $R_{eff} \gg N_{PR}\rho_o(\gamma - 1)$, ignoring the term $N_{PR}\rho_o(\gamma - 1)$, then the complex compressibility becomes,

$$C_c(\omega) = \left(\frac{\gamma}{\rho_o c_o^2}\right).$$

(4.65)

By putting Eq. (4.62) and Eq. (4.65) into Eq. (4.53) gives the approximate impedance of a slit pore medium,

$$z = \frac{1}{\sqrt{\gamma}}\sqrt{\frac{iR_s}{\omega \rho_o \Omega}} .$$

(4.66)

If the structure factor is interpreted as tortuosity, i.e. $k = T$, then the Zwikker and Kosten model from Eq. (4.9) is,

$$z = \sqrt{\frac{T}{\Omega^2} + \frac{iR_s}{\omega \rho_o \Omega}} .$$

(4.67)

Applying a high flow-resistivity and low frequency approximation to Eq. (4.67) whereby the first term inside the square root is small compared with the second

gives a similar impedance expression to that obtained by approximating the slit

pore model except a factor of $\frac{1}{\sqrt{\gamma}}$ is present in Eq. 4.66.

$$z = \sqrt{\frac{iR_s}{\omega \rho_o \Omega}}.$$ (4.68)

The reason for the presence of this factor in slit pore model is that it assumes the

thermal effects in pores are isothermal in the limit of low frequency and high flow

resistivity, whereas the Zwikker and Kosten model assumes an adiabatic

condition.

Figure 4.2 compares predictions of characteristic impedance by the Zwikker

and Kosten model (red dash line) and the slit pore model (blue continuous line)

multiplied with a factor of $\sqrt{\gamma}$. The purpose of multiplying the slit model with a factor

of $\sqrt{\gamma}$ is to obtain numerical equality as it has been shown analytically (Eqs. 4.58 –

4.68) that the Zwikker and Kosten model is a low frequency and high flow

resistivity approximation of the slit pore model if the latter is multiplied by $\sqrt{\gamma}$.

Figures 4.2 (a) and (b) compare the predicted characteristic impedance spectra

with flow resistivity of 100 Pa s m^{-2} and porosity of 0.3 and Figures 4.2 (c) and (d)

with flow resistivity of 500 kPa s m^{-2} and porosity of 0.3. Figures 4.2 (a) and (c)

shows the corresponding predictions of the real part of the impedance and Figures

4.2 (b) and (d) show the corresponding predictions of the imaginary part of the

impedance. It is clear from these Figures that the slit pore model and adjusted

Zwikker and Kosten model give significantly different impedance predictions for

low flow resistivity whereas they gives identical impedance for high flow resistivity.
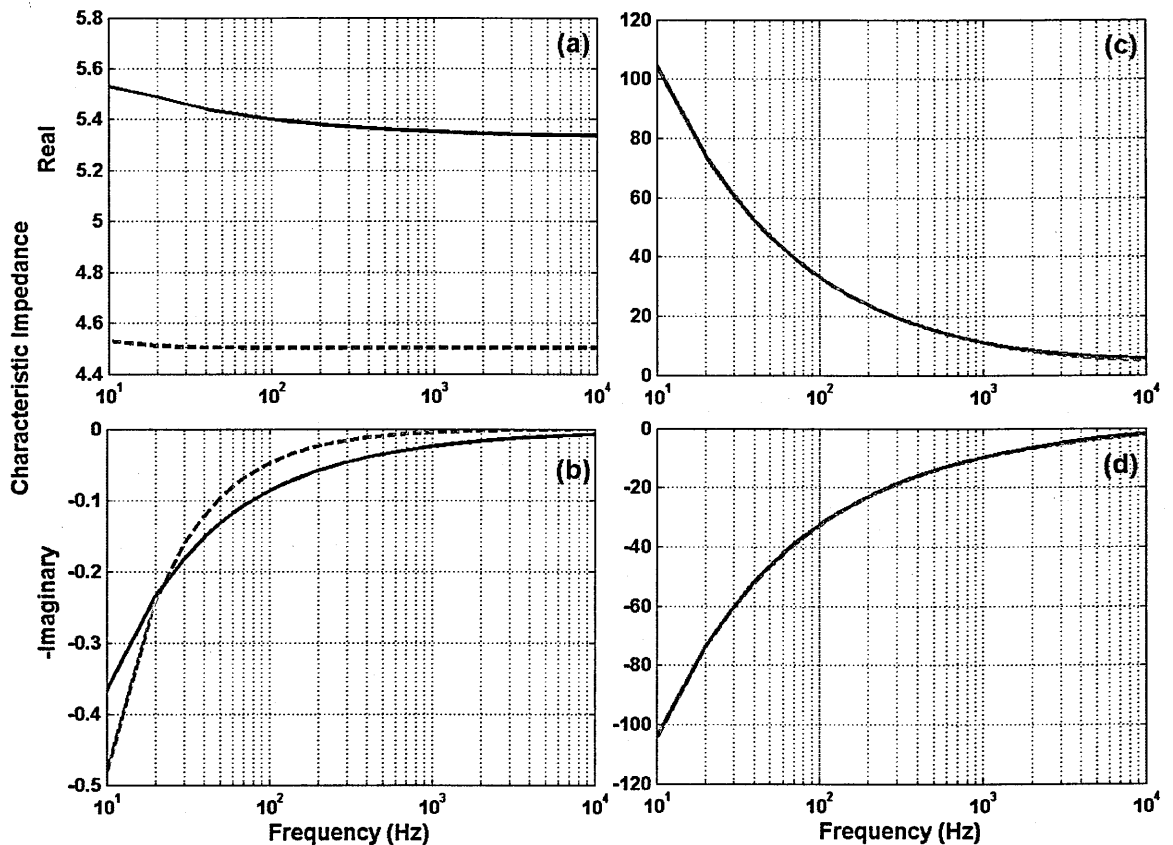
Figure 4.2 Comparison between characteristic impedance predicted by the slit pore model multiplied with a factor of $\sqrt{\gamma}$ (blue continuous line) and the Zwikker and Kosten model (red dash line) with parameters (a, b) Flow resistivity of 100 Pa s m^{-2} and porosity of 0.3 (c, d) Flow resistivity of 500 kPa s m^{-2} and porosity of 0.3 (a) real (b) –imaginary (c) real (d) – imaginary.

4.3.3 Comparisons between the Delany and Bazley, Taraldsen and Miki models

The Delany and Bazley [41], Taraldsen [45], [46] and Miki [43], [44] models were obtained empirically by fitting measured data and applying some approximations. These one parameter models depend only on the effective flow resistivity of the material. The characteristic impedances corresponding to Delany and Bazley, Taraldsen and Miki models are given by Eq. (4.16), Eq. (4.21) and Eq. (4.25) respectively. Figure 4.3 compares characteristic impedance spectra predicted by the Delany and Bazley (black continuous line), Taraldsen (blue dash

line) and Miki (red dash-dotted line) models for a flow resistivity of 10 kPa s m^{-2}. It is clear from the Figure 4.3, that these three models give similar impedance predictions for effective flow resistivities of 10 kPa s m^{-2} and 200 kPa s m^{-2}. However, the magnitude of differences between the impedance spectra predicted by these three models increases with increase in flow resistivity.
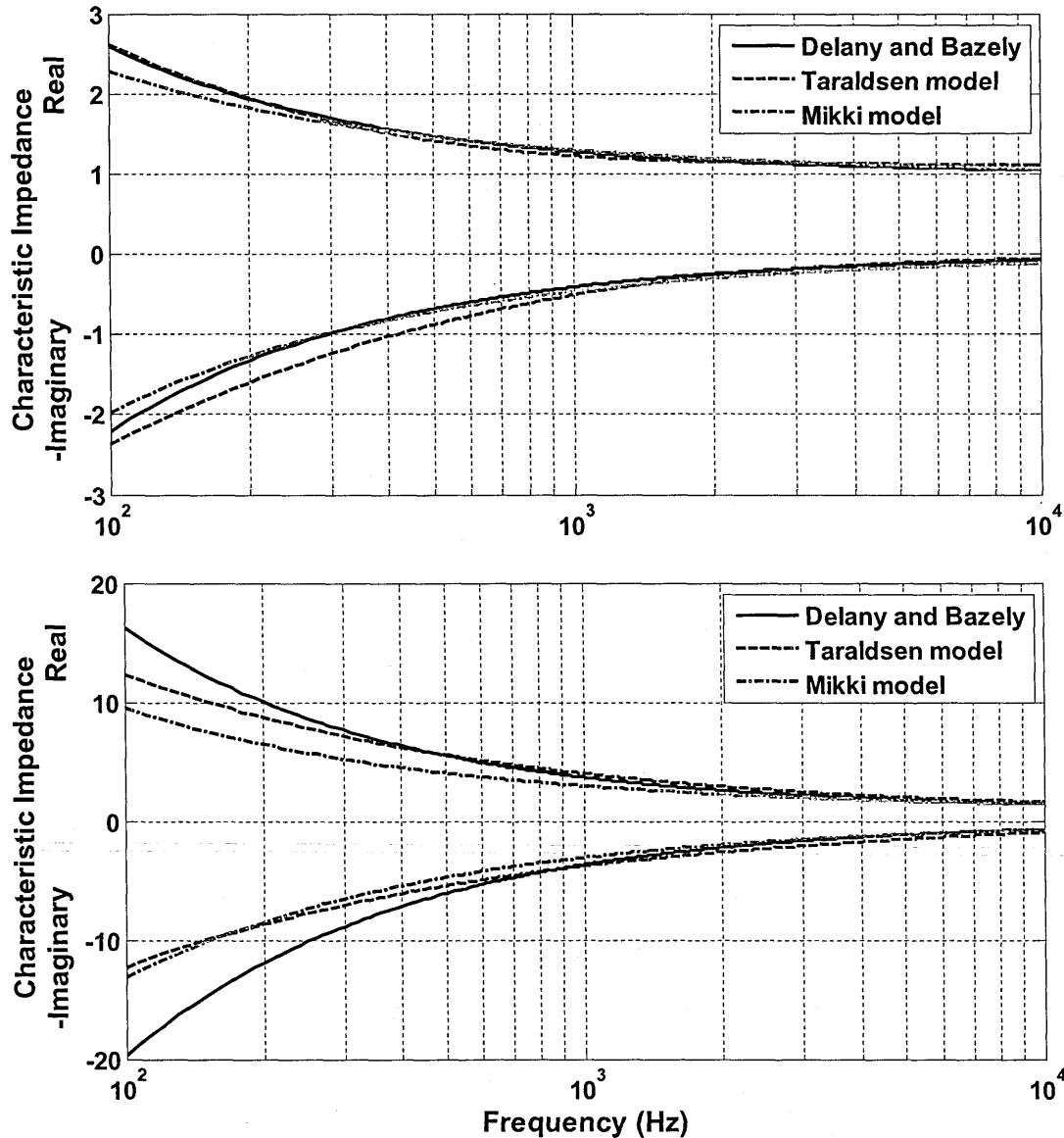
Figure 4.3 Comparison between characteristic impedance spectra predicted by the Delany and Bazley (black continuous line), Taraldsen (blue dash line) and Miki (red dash-dotted line) models for flow resistivities of (a) 10 kPa s m^{-2} (b) 200 kPa s m^{-2}.

4.4 Outdoor sound propagation

4.4.1 Sound propagation from a point source above an impedance plane

So far, in this chapter we have only discussed and concentrated on modeling the acoustic impedance of ground surfaces. However, sound propagation models are essential part of predicting the sound level produced by a source. Moreover they can be used in indirect methods for deducing ground impedance. Consider a point source placed at a height of 'Hs' and a receiver at height of 'Hr' above a plane ground surface as shown in Figure 4.4. The point source generates spherical waves which exhibits spherical spreading while propagating through the medium. The total signal received by the microphone consists of a direct wave and a reflected wave from the ground surface. The direct wave follows a direct path through R_1 and the reflected wave follows path through R_2. The total sound pressure level at the receiver due to a point source above a locally reacting ground surface is given by [61],

$$P_{total} = \frac{Pe^{ikR_1}}{R_1} + \frac{QPe^{ikR_2}}{R_2},$$

(4.69)

where Q is the spherical wave reflection coefficient.

Sommerfeld [62] presented the most sophisticated solution for the reflection coefficient of a spherical wave from a plane surface. Weyl [63] and Van der pol [64] extended Sommerfeld's work to give approximate solutions to the problem. Since then, this problem has been studied extensively by many authors, including Ingard [35], Chein and Soroka [65], Donato [66] and Attenborough *et al.* [67].

Nowadays, the most commonly used solution for spherical wave reflection coefficient is given by the Weyl-Van der Pol approximation [68],

$$Q = R_p + (1 - R_p)F(w),$$

(4.70)

where R_p is the plane wave reflection coefficient and $F(w)$ is the boundary loss factor. A spherical wave produced by a point source is modelled as a summation of plane waves at each angle of a hemisphere. These plane waves get reflected by the ground and integrated at the receiver to obtain spherical wave. The numerical formulation for this problem is given by Eq. 4.70, in which the spherical wave reflection coefficient is written in terms of plane wave reflection coefficient plus a 'correction' involving the boundary loss factor. The boundary loss factor accounts for spherical spreading and corrects for the sphericity of the wave front. The plane wave reflection coefficient and boundary loss factor are given by,

$$R_p = \frac{\cos\theta - \beta}{\cos\theta + \beta},$$

(4.71)

$$F(w) = 1 + i\sqrt{\pi}we^{-w^2}erfc(-iw),$$

(4.72)

$$w = \sqrt{\frac{ikR_2}{2}}(\cos\theta + \beta),$$

(4.73)

where β the admittance is the inverse of acoustic impedance of ground surface, and θ is the angle of incidence.
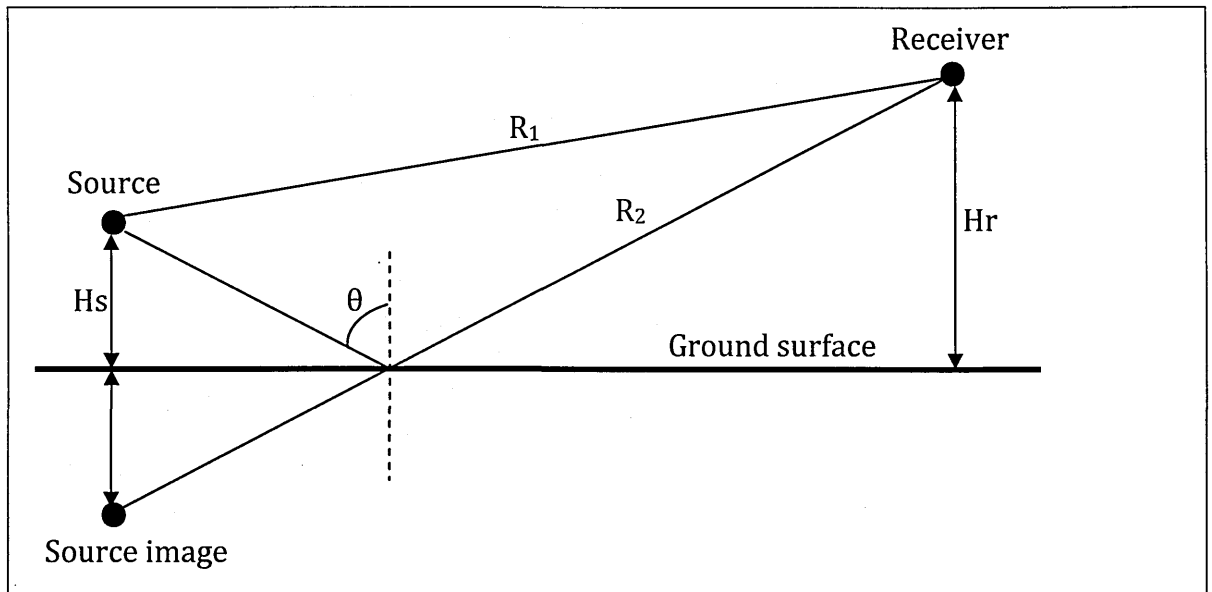
Figure 4.4 Reflection of sound from a ground surface.

4.4.2 Local and Extended reaction and layered ground

When sound is incident on a surface, it reflects, diffracts and is absorbed depending on ground surface properties and wavelength. If the surface is porous, then the acoustic pressure tends to move the fluid inside pores normal to surface. If the fluid motion inside pores is dependent only on incident acoustic pressure at that part of surface and independent of fluid motion in other parts of surface, then this kind of surface behaviour is known as locally reacting. On the other hand, if the fluid motion inside pores at one part of surface is affected by fluid motion at other parts, then this is an externally reacting surface. Ground surfaces having low flow resistivity values usually behave as externally reacting.

In some cases a naturally occurring ground surface consists of multiple layers. Consider ground with a porous surface layer with thickness d over a hard (non-porous) ground surface as shown in Figure 4.5. When a sound wave is incident on such a porous hard backed layer surface, some of it gets reflected and

some of it travels though porous layer. At depth d sound will be reflected from the hard substrate boundary and travel back into free space after passing through the porous layer. The received signal at the microphone is a combination of sound travelling through the free space, reflection and absorption by the porous layer, and sound travelling through the porous layer being reflected by the hard backing. The propagation constant for a wave travelling in free space is different from that of the wave travelling in porous materials. Consider a porous surface with a layer thickness d. The characteristic impedance z and propagation constant k_c for a porous material is given by impedance models described above. The surface impedance for a locally reacting hard backed porous layer is given by [33], [39],

$$z_c = z(\omega)\coth(-ik_c d),$$
(4.74)

The surface impedance of an externally reacting surface depends on the angle of incident wave. If the incident sound wave makes an angle θ with the normal of the porous surface as shown in Figure 4.5, then the surface impedance for an externally reacting hard backed porous layer is given by [33],

$$z_c = \frac{z(\omega)}{\alpha}\coth(-ik_c \alpha d),$$
(4.75)

where

$$\alpha = \sqrt{1 - \frac{\sin^2\theta}{n^2}}, \quad n = \frac{k_c}{k_o}.$$
(4.76 a, b)
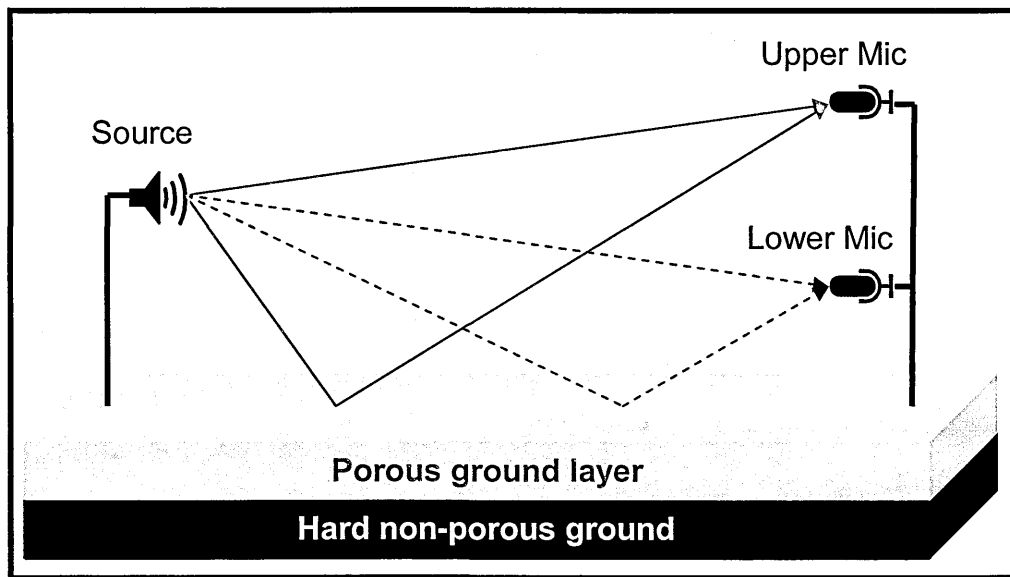
Figure 4.5 Level difference measurement arrangements over a hard-backed porous ground surface.

4.4.3 Ground characterization

Ground characterization involves short range measurements of either level difference or excess attenuation. The measured data is fitted using a propagation model along with impedance models to obtain the impedance parameters. The complete ground characterization procedure is described in the following subsections.

4.4.3.1 Excess attenuation

Excess Attenuation (EA) is obtained from a single microphone measurement technique. The total sound field is measured by placing source and microphone at a certain height above the ground surface. The Free field measurement must be carried out under anechoic conditions i.e. in the absence of contributions from ground reflection. Measurement arrangements with and without ground are shown in Figure 4.6. An example measured excess attenuation spectrum over a smooth hard ground at source and receiver height of 0.07 m and

separated by 0.7 m is shown in Figure 4.7. Excess Attenuation (EA) is the attenuation that occurs in excess of that due only to wave front spreading defined by,

$$EA = 20\log\left(\frac{P_{total}}{P_{direct}}\right).$$
(4.77)

where P_{total} and P_{direct} is the measured sound pressure level at the receiver with and without ground present respectively. It is easy to carry out EA measurements inside a laboratory due to the availability of a controlled environment and removable ground surfaces. However, for outdoor ground surfaces, where it is not possible to remove the ground surface; EA measurements are not easy due to the difficulty in obtaining accurate measurements of the free field. The free field can be measured in an anechoic chamber and then the same equipment should be moved outdoors to measure the ground surface. By doing this, there is a possibly of adding some error in measured data due to the difference in conditions, i.e. temperature, wind and turbulence between the two measurements. The other possibility for free field measurement is to raise the source and receiver high enough to remove the ground effect. Neither method is ideal for measuring the free field and there is always a possibility of adding some error to excess attenuation measurements for outdoor ground surfaces.
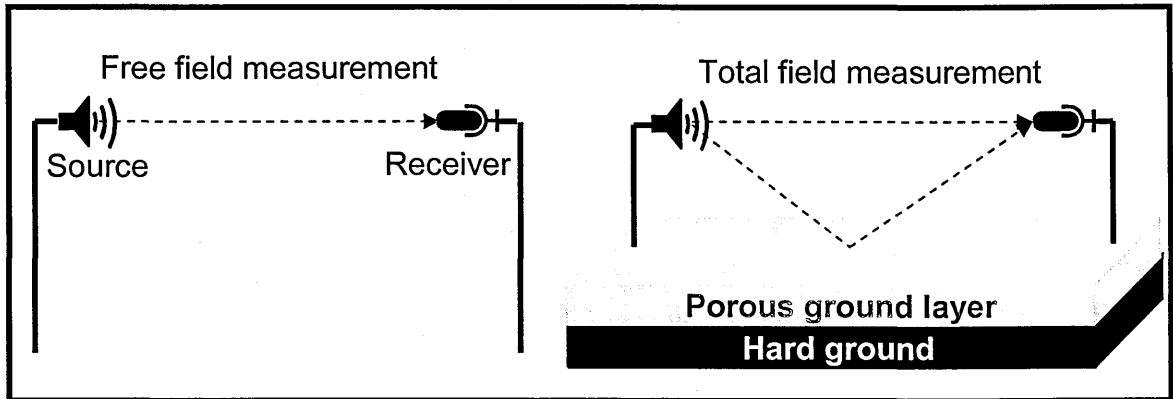
Figure 4.6 Excess attenuation measurement arrangements.
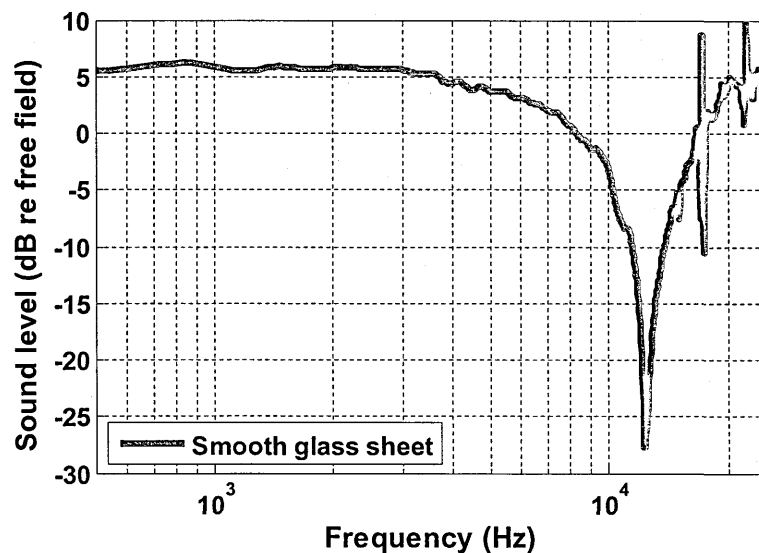
Figure 4.7 EA spectrum measured over smooth glass sheet at source and receiver height of 0.07 m separated by 0.7 m.

4.4.3.2 Level difference

The previous section concluded that a single microphone measurement technique is not ideal for outdoor measurements of ground impedance A two microphone measurement system [69]–[71] named as 'level difference (LD)' has been developed to be used for outdoor ground measurement. Level difference measurements are carried out by placing two vertically or horizontally (horizontal level difference measurements are described in Chapter 10) separated microphones at a certain height above the ground surface. Figure 4.5 shows a

schematic of vertical level difference arrangements. The level difference is calculated by subtracting the measured sound pressure level spectrum at the upper microphone to that measured at the lower microphone. It is basically a transfer function between two microphones, which make it independent of the free field measurement.

$$LD = 20\log\left(\frac{P_{UpperMic}}{P_{LowerMic}}\right).$$ (4.78)

It is also recommended to exchange the microphones and repeat the measurement. The resultant data will be the average of both measurements. In this way, the phase, calibration and manufacturing differences between the two microphones will be cancelled out. It is also essential to measure the source-receiver geometry as accurately as possible. If the ground surface to be characterized is uneven, then measurements should be carried out at a few locations to average out the uneven ground effect. Figure 4.8 shows level difference spectra measured over hard asphalt with source at height of 0.325 m, upper and lower microphone at heights of 0.46 m and 0.23 m respectively and source-receiver separation of 1.75 m. If the two microphones are accurately calibrated, then the level difference spectra should be 0 dB at low frequency as shown by Figure 4.8.

The complex measured level difference or excess attenuation spectra can be used to deduce impedance spectra [68] or the magnitudes fitted using impedance models to obtain best-fit impedance parameters [32]. The best fit impedance parameters may be used to represent the acoustical characteristics of

a ground surface. The data fitting and impedance deduction procedures are described in following subsections.
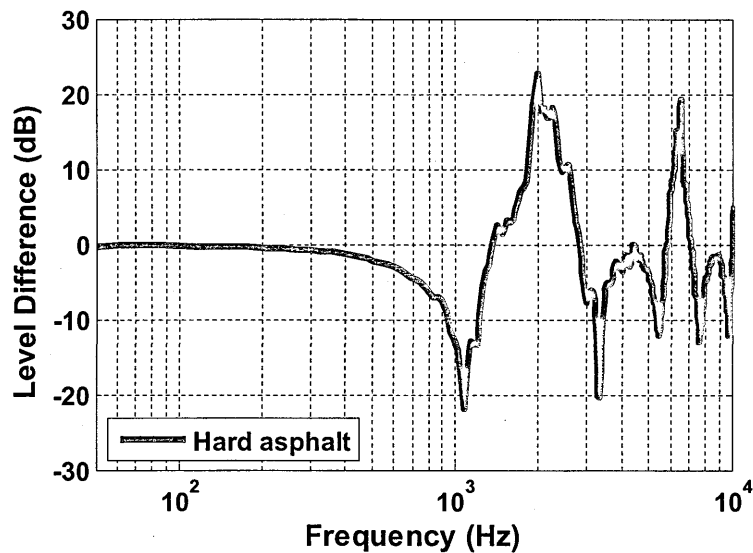
Figure 4.8 Level difference spectrum measured over hard asphalt by placing source at height of 0.325 m, upper and lower microphone at heights of 0.46 m and 0.23 m respectively and horizontal separation between source and receiver is 1.75 m.

4.4.3.3 Deduced impedance

Impedance spectra may be deduced indirectly from measurements without the need of any impedance model [68], [72]. The complex effective impedance of a ground surface for a given geometry can be deduced from measured complex excess attenuation or level difference data. This method deduces the impedance by minimizing the difference between measured data and the theoretical predictions at each frequency point. Nocke *et al.* [72] developed the direct impedance deduction method based on two-dimensional minimization technique. This method is very expensive in terms of the computational resources and time required to obtained a desirable solution. Taherzadeh and Attenborough [68] developed an alternative numerical method for this minimization problem. It calculates the spherical reflection coefficient from measured complex excess

attenuation/level difference spectra at each frequency point. The measured spherical reflection coefficient is used to obtain the theoretical value of impedance. The difference between measured and theoretical reflection coefficient is minimized to obtain the complex impedance [68].

$$\Gamma(\beta, f) = Q(\beta, f) - Q_{measured} \quad ,$$

(4.79)

where β is the admittance and Q is the spherical reflection coefficient given by Eq. 4.70 – 4.73. The spherical reflection coefficient Q can be rewritten by putting Eq. 4.71 and Eq. 4.72 into Eq. 4.70.

$$Q = \frac{\cos\theta - \beta}{\cos\theta + \beta} + \frac{2\beta}{\cos\theta + \beta} \left[1 + i\sqrt{\pi} w e^{-w^2} erfc(-iw) \right] ,$$

(4.80)

$$W(w) = e^{-w^2} erfc(-iw) ,$$

(4.81)

$$Q = 1 + \frac{2i\sqrt{\pi}\beta w W(w)}{\cos\theta + \beta} .$$

(4.82)

From Eq. 4.73, w may be rewritten as,

$$w = \tau(\cos\theta + \beta), \quad \because \tau = \sqrt{0.5ikR_2} .$$

(4.83 a, b)

Using Eq. 4.83 into Eq. 4.82 and simplifying it gives,

$$Q = 1 + 2(w - \tau\cos\theta)\left[i\sqrt{\pi} W(w) \right].$$

(4.84)

Since Q is an analytical function, the solution for Eq. 4.79 can be obtained using Newton-Raphson method [68]. For a given function Γ, its derivative Γ' and with an initial guess x_0 the approximated value for x_1 is given as,

$$x_1 - x_0 = \delta x_0 = -\frac{\Gamma(x_0)}{\Gamma'(x_0)}. \tag{4.85}$$

This process is repeated 'n' times until a desired accuracy is achieved.

$$x_{n+1} - x_n = \delta x_n = -\frac{\Gamma(x_n)}{\Gamma'(x_n)}. \tag{4.86}$$

For admittance the x is replaced by β,

$$\beta_{n+1} - \beta_n = \delta\beta = -\frac{\Gamma(\beta_n)}{\Gamma'(\beta_n)}. \tag{4.87}$$

The derivative may be obtained as,

$$\frac{d\Gamma}{d\beta} = \frac{dQ}{dw}\frac{dw}{d\beta}. \tag{4.88}$$

The derivative of function, $W(w)$ given by Eq. 4.81 is [73],

$$W'(w) = -2wW(w) + \frac{2i}{\sqrt{\pi}}. \tag{4.89}$$

Eq. (4.89) can be used to calculate the derivative of Eq. 4.84 with respect to w. This result and the derivative of Eq. 4.83 with respect to β are given by,

$$\frac{dQ}{dw} = 2\left[i\sqrt{\pi}W(w) - 2(w - \tau\cos\theta)\left(1 + i\sqrt{\pi}wW(w)\right)\right] \text{ and } \frac{dw}{d\beta} = \tau. \tag{4.90}$$

This alternative impedance deduction technique is very efficient and requires very little time to obtain a desirable solution. However, sometimes more than one value of impedance exists for a given measured value of spherical reflection coefficient at that frequency. There is the possibility of choosing a wrong

value of impedance rather than actual value. This is a common minimization problem when a solution converges to local minima, instead of a global minimum. This error can be avoided by taking several measurements with different geometries. The impedance value which appears more times as a result of measurement taken with different geometries is more likely to be the true value of impedance at that frequency. If level difference data are used for deducing impedance spectra, it is advisable to exchange the microphones and average the results. Figure 4.9 shows the complex impedance deduced from a level difference spectra measured over bare-cultivated ground by placing source at height of 0.2 m, upper and lower microphone at heights of 0.2 m and 0.05 m respectively and horizontal separation between source and receiver is 1.0 m. The fact that impedance spectra become zero after 5 kHz means that it was not possible to converge to a valid solution.
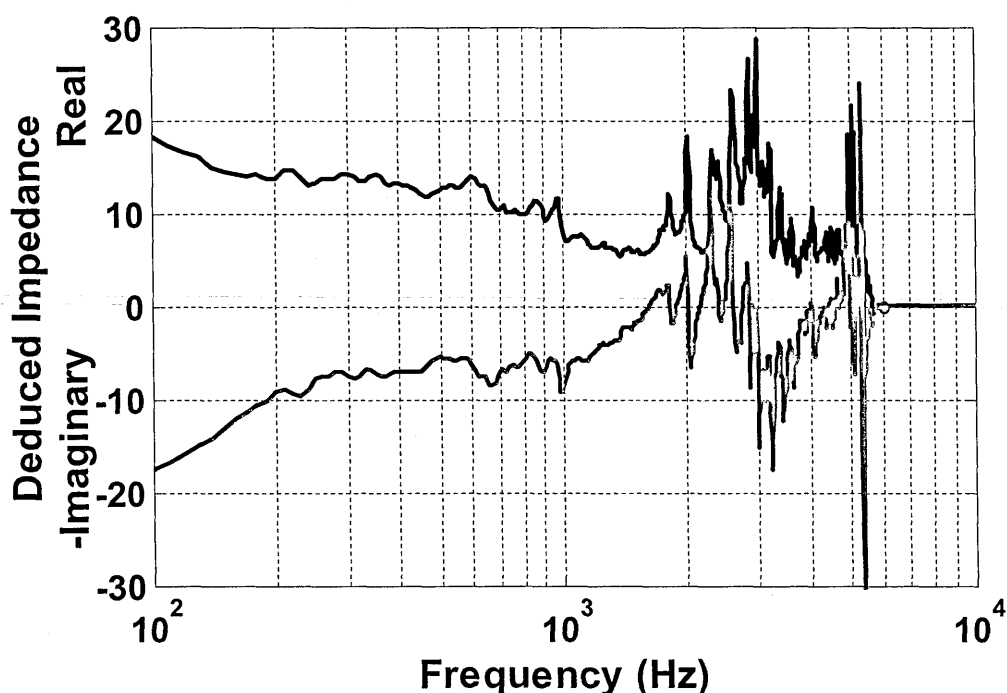
Figure 4.9 Complex impedance deduced from (complex) level difference spectra measured over bare-cultivated ground by placing source at height of 0.2 m, upper and lower microphone at heights of 0.2 m and 0.05 m respectively and horizontal separation between source and receiver is 1.0 m.

4.4.3.4 Data fitting

The magnitudes of measured level difference or excess attenuation spectra over a ground surface can be used to obtain the acoustic impedance of that ground. It is an indirect method of predicting acoustic impedance in which propagation model is used with any suitable impedance model to obtain best-fit impedance model parameter values [74]. Measured data are fitted through a minimization algorithm to obtain impedance parameters. The numerical minimization technique minimizes the error value between measured and predicted level difference or excess attenuation spectra at each frequency point. It takes initial guesses for impedance parameters and tries to minimize the error value with different sets of impedance parameters.

$$Error = \sum_f \left| LD_M(f) - LD_P(f) \right|,$$

(4.91)

where LD_M and LD_P is the measured and predicted level difference spectra respectively at a given geometry. For excess attenuation LD is replaced by EA. The list of impedance models given in Table 4.1 shows that the number of impedance parameters ranges between 1 and 5, depending on the choice of impedance model. As the number of impedance parameters increases, it is more difficult to find a unique solution. The minimization algorithm may converge to local minima instead of actual global minima. This problem of uniqueness of solution can be addressed by taking measurements with different geometries.

There are several aspects that require care to be taken when obtaining impedance parameters by fitting measured data with a minimization algorithm. Sometimes, it is difficult to obtain a good fit to data over the whole frequency

range. However, the lower frequency end of the level difference spectrum is more sensitive to impedance of the surface whereas the high frequency spectrum is more sensitive to the geometry. So it is more likely that the impedance parameters which give best-fit to the lower frequency level difference spectra represent the acoustic impedance of that surface. Although, in principle, the porosity value ranges between 0 and 1, the minimization technique must be restricted to converge to a practical value of porosity representative of a ground surfaces. Sometimes it is possible to measure the actual layer depth for hard-backed layer of porous ground. Moreover, the flow resistivity value can be restricted to a certain range, if the measured ground type is known.
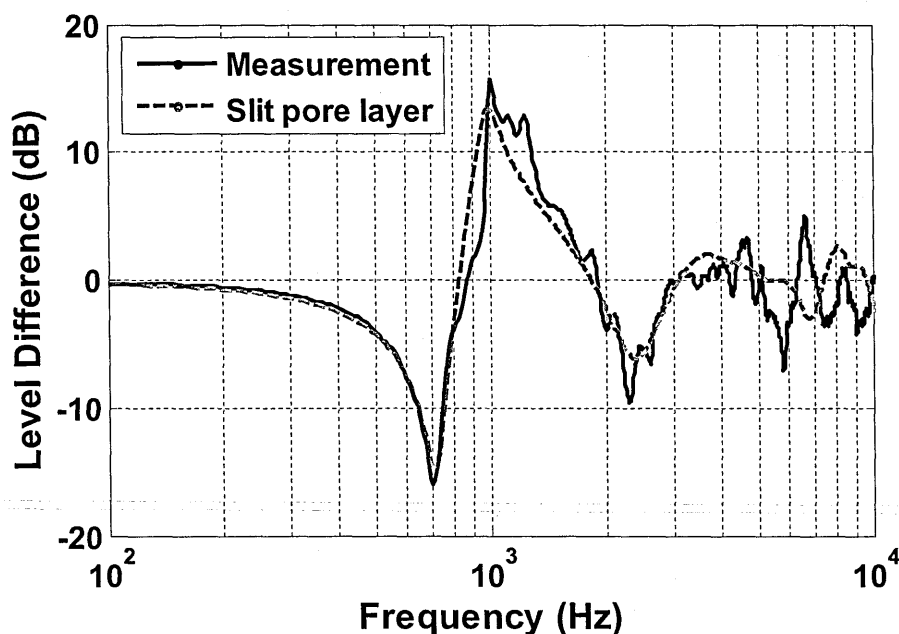
Figure 4.10 Numerically-obtained best fits to level difference data (continuous black line) over grassland at Open University – Noise Barrier site with source height 0.325 m, distance between source and microphones 1.75 m, and microphone heights 0.46 m and 0.23 m (red broken line) using slit pore layer with flow resistivity of 70 kPasm^{-2}, porosity of 0.6 and layer depth of 0.02 m.

Figure 4.10 shows an example level difference spectrum measured over grassland at the Open University with source at height of 0.325 m, distance

between source and microphones 1.75 m, and microphone heights of 0.46 m and 0.23 m. The measured data is numerically fitted with slit pore layer prediction using a minimization algorithm. The best fit impedance parameters are flow resistivity = 70 kPa s m^{-2}, porosity =0.6 and layer depth = 0.02 m. The agreement between data and prediction is very good.

4.4.3.5 Standard methods for ground characterisation

International standard methods have been developed to describe the procedure and strategies for outdoor ground effect measurements and for characterizing the acoustical properties of outdoor ground surfaces. NT ACOU 104 'Ground surfaces: Determination of the acoustic impedance' [69] recommends procedures for carrying out outdoor measurements and data fitting. The geometry recommended in this method is source height 0.5 m, horizontally separated by 1.75 m from two vertically separated microphones at heights of 0.5 m and 0.2 m respectively. The frequency band of interest is between 200 Hz to 2500 Hz. The Delany and Bazley one parameter impedance model is suggested for impedance fitting to third-octave level difference spectra. This method has been successful to some extent but it is unable to characterize all types of ground surfaces. The method has been revised [70] to include a modified geometry and a three parameter impedance model. In the revised geometry, the horizontal distance between source and microphones is increased to 8.75 m, and the 3rd octave frequency range is modified to between 800 Hz and 6300 Hz. In the revised Nordtest report [70], Hamet [40] three parameter impedance model was introduced for porous road surfaces and layered ground.

The second standard method, ASA/ANSI S1.18-2010: *Determining the Acoustic Impedance of Ground Surfaces* [71] also describes procedures for carrying out outdoor measurements of level difference spectra and associated impedance fitting. This method recommends two short-range level difference measurement geometries identified as A and B (see Table 4.4). The frequency range is between 250 and 4000 Hz. The acoustic impedance of the ground surface varies with location. Therefore, It is advised to take at least four measurements at adjacent locations for each geometry. The Delany and Bazley one parameter and variable porosity two parameter models are recommended to predict the acoustical impedance of ground surfaces. Table 4.4 summarises these standard methods for ground characterization.

Table 4.4 Standard methods for ground characterization

Standard method	Recomme-nded Models	Frequency Range (Hz)	Source Height (m)	Upper Mic (m)	Lower Mic (m)	Separation (m)
NT ACOU 104 (1999)	Delany and Bazley & Hamet models	200 - 2500	0.50	0.50	0.20	1.75
NT ACOU 104 (2006)		800 - 6300	0.50	0.50	0.20	8.75
ANSI S1.18 (2010)	Delany and Bazley & Variable Porosity	250 - 4000	0.325	0.46	0.23	1.75
			0.20	0.20	0.05	1.00

4.5 Comparison of available data with predictions

In this section, already available measured level difference data over different types of ground surfaces are compared with predictions using different impedance models. Many level difference measurements have been carried out in connection with the validation and revision of the Nord Test NT ACOU 104 [69], [70] for ground characterization procedures. The geometry used for these measurements is with the source of height 0.5 m, horizontally separated by 1.75 m from two vertically separated microphones at heights of 0.5 m and 0.2 m respectively. The available data is for 3rd octave frequencies between 200 Hz and 2500 Hz. To characterize each ground surface, level difference data were obtained at four different locations. If the mean standard deviation for measurements at four different locations exceeded 4 dB, then the measured data was considered to be invalid. Measured data are available for 44 different sites which include 26 grass land sites, 13 forest floors (pine forest and beech forest) and 5 gravel and sand pit sites. In addition to this, some data is also available in connection with ANSI. S1. 18-2010 [71] over three different ground types, i.e. sports ground, newly laid porous asphalt and railway ballast.

Impedance fittings have been carried out using available level difference data for 47 different sites. Five impedance models namely, the Delany and Bazley model, slit pore model, the variable porosity model, the phenomenological (Zwikker and Kosten) model and the Taraldsen model along with Weyl-Van der Pol propagation model have been used for predictions. In the slit pore model and phenomenological model predictions, unless stated otherwise, it is assumed that

$T = \dfrac{1}{\sqrt{\Omega}}$, so that these models need only two parameters, i.e. flow resistivity and

porosity. Measured data have been used to obtain best fit impedance parameters

for each model. Consequently, these best fit impedance parameters along with

impedance models can be used to predict level difference spectra for any given

geometry. Best fit impedance parameters are obtained through an automated

numerical minimization technique in Matlab. The numerical technique minimizes

the error value between measured and predicted level difference spectra at each

frequency point as given by Eq. 4.91. The minimization program takes starting

initial guesses for the impedance parameters as an input and applies the

fminsearch algorithm to minimize error in order to obtained best fitted impedance

parameters. A minimum of up to 100 different initial guesses were used to obtain a

stable and unique solution. Once a solution has been established, it was

rechecked against a range of initial values to confirm its validity and uniqueness.

The minimization algorithm works very well for one dimensional (1-D) and two

dimensional (2-D) searches. However, it shows some instability to obtain unique

solutions for three dimensional (3-D) and four dimensional (4-D) searches. A 3-D

search is needed when considering hard-backed layer ground along with two

parameter impedance models. A 4-D search is needed when tortuosity is also

considered as an independent fitting parameter. The uniqueness problems for 3-D

and 4-D searches are solved by transforming them into 2-D searches. However, it

becomes computationally more expensive. Consider a 3-D search on three

impedance parameters such as flow resistivity, porosity and layer thickness. The

value of porosity ranges between 0 and 1. A matrix has been created for all

possible values of porosity between 0 and 1 with an increment of 0.01. For each

input constant value of porosity, the minimization program searches for best fitted values of flow resistivity and layer thickness and stores all solutions into another matrix. Another search routine finds the best solution out of all solutions stored for each input value of porosity. In similar way, 4-D search is converted into 2-D by generating two input constant values matrixes. Although, in the searches for best fit impedance the parameters were varied independently, in fact, as described earlier in the chapter, the impedance parameters are related and interdependent.

The available data is sub grouped into sections depending on their ground type. In the following sub-sections, level difference spectra predicted by using the two-parameter slit pore, variable porosity and phenomenological models, and the one parameter Delany and Bazley and Taraldsen models are compared with data.

4.5.1 Grassland

44 different ground types, for which level difference data were obtained in connection with Nord Test NT ACOU 104 [69], [70], for have been categorized as grassland sites, forest floors and gravel and sand pit sites. Out of 44 sites, 26 are grouped together as grassland sites. The level difference data for these 26 grasslands have been fitted using the Delany and Bazley and Taraldsen single parameter models and the variable porosity model, phenomenological model and slit-pore two parameter models to obtained best fit parameter values. Table 4.6 summarizes the best fit parameter values and the corresponding errors between measured data and predictions using the above described impedance models. It is found that, the variable porosity model gives the best fits, i.e. smaller fitting errors and better spectral shape agreement, to the third octave frequency band data for these 26 'grassland' sites. The average error value using the variable porosity

model is 6.7 dB, with maximum and minimum error values of 13.4 dB and 3.3 dB respectively. There are only four sites for which error values resulting from use of the variable porosity model are greater than 10 dB. The corresponding average error value using either the slit pore model or the phenomenological model is 8.7 dB with the maximum and minimum values of 20.6 dB and 3.7 dB respectively. The Delany and Bazley one parameter impedance model gives the largest error values for most of the grassland sites. It gives an average error value of 9.3 dB. For eight grassland sites (#1, 12, 16, 17, 22, 26, 31 and 40), the errors from using all of the four models to fit data are comparable. With the exception of only two (#27 and 41) out of twenty six grassland sites, use of the variable porosity model provides better fits than other (semi-infinite) models.

The porosity value ranges between 0 and nearly 1 for acoustically hard and soft ground respectively. The porosity value for different ground types are summarized in Table 4.5. For some of ground types given in Table 4.6, the best fit porosity value obtained, when fitting data using the slit pore and phenomenological models, is near to 1.0. These values are outside the porosity range given by Table 4.5 for naturally occurring ground types and must be regarded as effective porosities. On the other hand it is found that the error values are not very sensitive to the porosity for ground types with higher flow resistivity. The best fit flow resistivity values obtained using the Delany and Bazley, slit pore or phenomenological (semi-infinite) models for most of grassland sites lie outside of range given in Table 4.5. The flow resistivity values obtained by fitting these models must be regarded as effective values. The best fit effective flow resistivity values obtained using the phenomenological model are a factor of γ less than

those obtained by use of the slit pore model as a consequence of the differences between equations 4.66 and 4.68, in the low frequency/high flow resistivity approximation.

Table 4.5 Non-acoustically measured values of air-filled porosity and flow resistivity [32].

Ground type	Air-filled Porosity	Flow resistivity (kPa s m^{-2})
snow	0.5 – 0.9	5 – 16
Uncompacted gravel	0.3 – 0.4	1.5 – 59
Newly-laid porous asphalt	0.15 – 0.3	2 – 15
Forest floor	0.4 – 0.8	9 – 200
Grassland	0.3 – 0.7	100 – 240
Cultivated soils	0.4 – 0.6	100 – 2000

For 12 of 26 grasslands sites, use of either slit pore or phenomenological models results in error values close to or higher than 10 dB with an average value of 11.4 dB . Moreover, 4 of these sites lead to very high error values close to or higher than 15 dB. The Delany and Bazley model results in higher error values than the other two. On the other hand, use of the variable porosity model gives very good fits for these twelve grassland sites with an average value of 7.6 dB. This suggests that these twelve grassland sites might be treated as hard-backed-layers. It is found that the fitting results are improved by using hard-backed-layer versions of these three impedance models. The mean error value when using the Delany and Bazley model to fit data for these twelve sites is reduced from 11.8 dB to 7.5 dB by implementing the hard-backed-layer version. Similarly, the mean error values for slit pore model and phenomenological model are reduced from 11.4 dB

to 7.0 dB and 7.3 dB respectively when using the hard-backed-layer versions for fitting. The best fit porosity values obtained when using the slit pore layer model (see Table 4.7) are more realistic (see Table 4.5). The Taraldsen two parameter layer model derived from the phenomenological model has been used also to fit data for these twelve sites. The results from using the Taraldsen layer model (mean error value 7.3 dB) are not much different to those obtained by using the Delany and Bazley layer model. Moreover, use of the Taraldsen model fails to give good fits for other non-hard-backed-layer sites, specifically for sites where use of the Delany and Bazley (semi-infinite) model fails to give good fitting. Hard-backed-layer versions of all four impedance models give good fits and smaller error values when used to fit level difference spectra for these twelve grasslands sites (see Table 4.7). Figure 4.12 compares level difference data with those predicted by using impedance models for some six selected sites.

Narrow-band level difference data measured over three different grassland sites are also available obtained in connection with ANSI. S1. 18 - 2010 [71]. These measurements, at the Open University (OU), UK over grass covered sport fields and over institutional grass at National Research Council (NRC), Canada, have been carried out using standard geometry-B [71] with source at a height of 0.2 m, upper and lower microphone at heights of 0.2 m and 0.05 m respectively and with a source-receiver separation of 1.0 m. A numerical fitting procedure, similar to that employed for the Nordtest data has been used to obtain the best-fitted impedance parameters. The four impedance models i.e. Delany and Bazley, slit pore, phenomenological and variable porosity models are used to fit these data to obtain impedance parameters and error values. The narrow band error values

obtained using Eq. (4.91) are converted into third octave band error values to make it comparable with calculation given above. The impedance parameters obtained using these four models and their corresponding errors values are summarized in Table 4.8. Similar conclusions are obtained from fitting ANSI. S1. 18 data, as were obtained from fitting Nordtest data. The variable porosity model gives the best fits with minimum error values for grassland ground surfaces. Slit pore and phenomenological models gives similar fitting results but the resulting error values are greater than those obtained using the variable porosity model and less than those obtained using the Delany and Bazley model over grass land sites.

Figure 4.11 Photos of 26 grassland sites [69], [70].
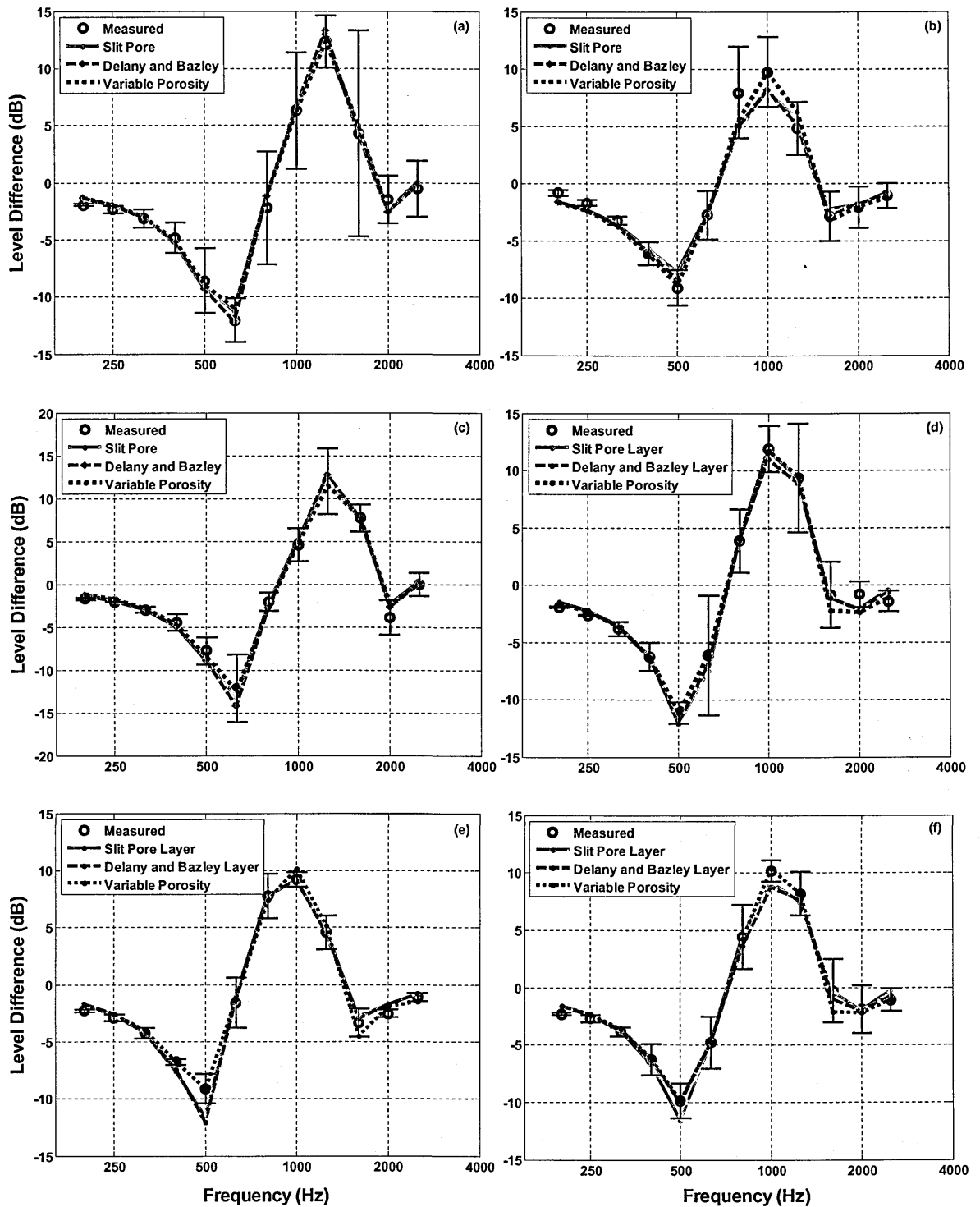
Figure 4.12 Example level difference predictions using the best slit-pore model (continuous red lines), variable porosity model (black dotted lines) and the Delany and Bazley model (blue broken lines) to Nordtest data [69], [70] (open circles; error bars indicate 90% confidence limits (±1.65 S.D.)) with the parameter values listed in Tables 4.6 (a) site 12 'bare' (b) site 16 'lawn' (c) site 28 'sports field' and in Table 4.7 for (d) site 17 'arable' (e) site 39 'pasture' and (f) site 44 'heath'.

Table 4.6 Comparative best fit model parameter values and fitting errors (Eq. 4.91) for level difference data from twenty-six grassland sites [69], [70].

Model		Delany and Bazley		Slit pore			Phenomenological			Variable porosity		
Site #	Ground type	Effective flow resistivity kPa s m⁻²	Error (Eq. 4.91) dB	Effective flow resistivity kPa s m⁻²	Effective porosity	Error (Eq. 4.91) dB	Effective flow resistivity kPa s m⁻²	Effective porosity	Error (Eq. 4.91) dB	Effective flow resistivity kPa s m⁻²	Effective porosity change rate	Error (Eq. 4.91) dB
1	Lawn	245	6.6	294.0	1.00	7.8	210.2	0.71	7.9	75.3	46.8	6.3
7	Arable	93	14.2	106.0	1.00	14.3	75.3	1.00	14.3	21.7	17.2	12.6
8	Urban	41	22.8	48.9	1.00	20.6	34.7	1.00	20.6	67.2	25.0	10.2
9	Urban	67	9.6	44.6	0.56	8.2	34.6	0.61	8.3	20.9	0.2	13.4
12	bare	665	5.9	514.8	0.38	6.1	388.6	0.40	6.1	366.55	-48.8	6.1
16	Lawn	124	8.3	175.7	1.00	9.2	124.5	1.00	9.2	39.4	17.2	6.8
17	Arable	208	10.7	351.0	1.00	11.4	248.9	1.00	11.2	44.5	81.2	4.5
18	Arable	358	5.4	397.0	0.50	5.1	284.1	0.71	5.1	138.55	27.9	4.0
19	Pasture	114	14.0	152.8	1.00	13.2	108.4	1.00	13.2	383.4	42.6	7.0
20	Long grass	102	15.4	119.4	1.00	14.2	84.6	1.00	14.2	167.2	47.6	7.0
21	Pasture	645	5.3	1134.4	0.50	5.1	804.5	1.00	5.1	277.9	12.4	5.0

22	Pasture	595	7.6	1344.2	0.50	9.4	953.1	1.00	9.4	227.4	68.0	7.9
23	Pasture	1145	9.3	288.3	0.18	5.3	223.0	0.20	5.3	814.8	-403.8	5.3
24	Arable	1744	5.2	2250.7	0.50	4.8	1604.9	0.50	4.8	1296.9	-199.7	4.3
25	Arable	1932	7.0	428.3	0.13	3.7	336.2	0.15	3.7	1720	-490.4	3.3
26	Pasture	266	7.2	420.9	1.00	8.2	298.4	1.00	8.2	824.6	60.8	4.9
27	Long grass	47	9.1	52.0	0.93	8.5	36.7	0.92	8.6	140.1	1.0	10.7
28	Sports field	1371	7.4	663.8	0.22	6.0	513.9	0.24	6.0	987.6	-266.2	5.4
30	Lawn	746	10.4	413.0	0.32	7.7	313.1	0.34	7.7	366.5	-75.9	6.9
31	Lawn	202	7.1	302.7	1.00	8.0	214.6	1.00	8.0	60.1	14.5	7.1
39	Pasture	111	9.7	145.4	1.00	9.5	103.1	1.00	9.5	25.5	34.1	5.5
40	Pasture	141	8.7	178.3	1.00	9.9	126.3	0.80	9.9	338.4	46.4	4.7
41	Long grass	178	8.5	104.4	0.36	5.3	78.0	0.38	5.3	799.3	-9.2	9.1
42	Pasture	187	12.4	279.1	1.00	11.7	197.7	1.00	11.6	357.5	80.2	6.2
43	Heath	323	6.5	368.6	0.70	5.2	263.7	0.71	5.2	114.2	17.4	4.9
44	Heath	169	7.8	265.5	1.00	7.4	188.3	1.00	7.4	51.9	32.7	4.2

Table 4.7 Layer model fits to third octave band data for twelve grassland sites [69], [70].

Site #	Delany and Bazley			Slit pore				Phenomenological				Taraldsen		
	Effective flow resistivity y kPa s m⁻²	Effective layer depth m	Error (Eq. 4.91) dB	Effective flow resistivity y kPa s m⁻²	Effective porosity y	Effective layer depth m	Error (Eq. 4.91) dB	Effective flow resistivity y kPa s m⁻²	Effective porosity y	Effective layer depth m	Error (Eq. 4.91) dB	Effective flow resistivity y kPa s m⁻²	Effective layer depth m	Error (Eq. 4.91) dB
7	117.0	0.025	10.7	85.3	0.56	0.034	10.5	67.6	0.60	0.044	10.5	105.7	0.028	11.2
8	50.1	0.033	8.1	50.9	0.88	0.033	5.7	36.6	0.86	0.047	6.3	41.4	0.040	6.3
9	75.4	0.042	7.5	59.0	0.52	0.050	4.6	46.5	0.55	0.064	5.4	65.8	0.048	9.5
17	276.5	0.012	6.3	215.4	0.52	0.016	6.1	156.1	0.5	0.023	6.4	256.9	0.013	5.7
19	151.0	0.022	9.6	153.2	0.70	0.024	9.2	111.7	0.71	0.033	9.5	139.6	0.024	8.9
20	120.8	0.019	11.5	107.3	0.70	0.022	10.9	79.6	0.71	0.030	11.3	102.1	0.022	10.3
26	371.8	0.010	6.1	338.9	0.57	0.012	5.6	259.5	0.60	0.016	5.5	356.6	0.010	5.8
27	63.2	0.038	6.5	51.0	0.65	0.046	6.0	45.1	0.81	0.056	6.4	52.3	0.047	6.6
39	142.7	0.019	6.4	129.9	0.70	0.022	6.7	96.3	0.71	0.030	7.0	119.0	0.022	6.5
40	185.9	0.017	5.1	127.1	0.50	0.023	6.5	98.6	0.50	0.031	7.2	167.2	0.018	5.8
42	255.6	0.012	6.8	265.1	0.70	0.015	6.2	193.1	0.71	0.020	6.3	229.0	0.015	6.1
44	210.6	0.021	5.2	175.6	0.50	0.024	5.6	137.1	0.50	0.029	6.0	218.7	0.018	4.6

Table 4.8 Best fit impedance model parameters and errors based on fitting on narrow band level difference data for three grass-covered sites at the Open University (OU) UK and institutional grass at NRC Canada [71]. The errors are computed by normalizing the error summed over the narrow band center frequencies (197 for OU, 1024 for NRC) to the error over the 12 third octave band center frequencies as used for the Nordtest data [69], [70].

Model	Parameter or error (Eq. 4.91)	OU 1	OU 2	NRC
Delany and Bazley	effective flow resistivity (kPa s m^{-2})	277	246	228
	Error (dB)	15.0	15.4	14
Slit pore	Effective flow resistivity (kPa s m^{-2})	265	228	159
	Effective porosity	0.70	0.70	0.45
	Error (dB)	16.7	16.7	9.7
Phenomenological	Effective flow resistivity (kPa s m^{-2})	205	160	135
	Effective porosity	0.71	0.71	0.53
	Error (dB)	18.8	18.5	9.4
Variable porosity	Effective flow resistivity (kPa s m^{-2})	65.8	57.9	101
	Effective rate of change of porosity (m^{-1})	77.7	157.6	-53.1
	Error (dB)	10.6	12.3	10.2

4.5.2 Forest floors

Out of the 44 Nord Test NT ACOU 104 [69], [70] sites, 13 are categorized as forest floors. These 13 sites are divided into three sub groups: 5 mixed forest floors, 5 pine forest floors and 3 beech wood forest floors respectively. Sites 2, 3, 4, 5 and 6 are mixed forest floors; 10, 11, 13, 14 and 15 are pine forest floors and 34-36 are beech wood floors [69], [70]. Table 4.9 and Figure 4.13 (a) & (b) compare best-fit parameters and errors using the single parameter Delany and Bazley model (blue broken line), the two parameter variable porosity model (black dotted line), the slit pore model (red continuous line) and phenomenological model (brown dash dotted line) for mixed forest sites. Use of the Delany and Bazley model failed to give good agreement between predictions and data for these five forest sites. The mean error value is 13.8 dB for the Delany and Bazley model. Use of the Taraldsen layer model is also unable to give good fit for these data sites with a mean error value of 13.8 dB. Use of the variable porosity model also gives a relatively high mean error value of 10.5 dB. However, use of the slit pore and phenomenological models gives very good agreement between predictions and data for these forest sites with mean error value of 5.0 dB. This is confirmed by the example spectra in Figure 4.13 (a) and (b).

All impedance models give similar best fit spectral shapes and error values for the five pine forest sites (#10, 11, 13, 14 & 15), as summarized in Table 4.10. Out of five pine forest sites, three sites (#10, 11 & 15) cannot be classified according to the Nordtest ACOU 104 [69], [70] procedure for any of the impedance models due to the fact that the error values are more than 20 dB. Using layer models gives no or very little insignificant improvement. Two pine forest sites (# 13

& 14) give very good fitting output for all impedance models (see Table 4.10). Figure 4.13 (c) and (d) present example plots for two out of five sites listed in Table 4.10. Figures 4.13 (c) shows that all models give very good agreement between data and predictions for pine forest # 13, whereas all models failed to characterize pine forest # 15. It also should be noted that the error bars are very high for these pine forest sites. Three beech wood sites cannot be classified according to Nordtest ACOU 104 [69], [70] using the Delany and Bazley model. Hard-backed Layer versions of the Delany and Bazley and Taraldsen models also fail to improve fitting results. Use of the Variable porosity and Taraldsen layer models yields very high mean error values of 24.4 dB and 27.8 respectively. However, using both the slit-pore and phenomenological (semi-infinite) models leads to smaller fitting errors. Fitting results are improved by using hard backed layer versions. Considerable improvement is achieved for sites 35 and 36 by using the slit pore layer model compared to other models. More specifically, for these sites with relatively low fitted flow resistivities, use of the slit pore layer model results in smaller fitting errors than resulting from use of the phenomenological layer model. Figures 4.13 (e) and (f) compare Nordtest beech wood sites 34 and 35 data and predictions using the different impedance models given in Table 4.11. It also should be noted that the predictions using the slit pore and phenomenological models reproduce the detailed frequency dependence shown by the data. The slit pore model failed to characterize beech wood site 34 according to Nordtest criteria. However, the agreement for spectral shape is very good as shown in Figure 4.13 (e).
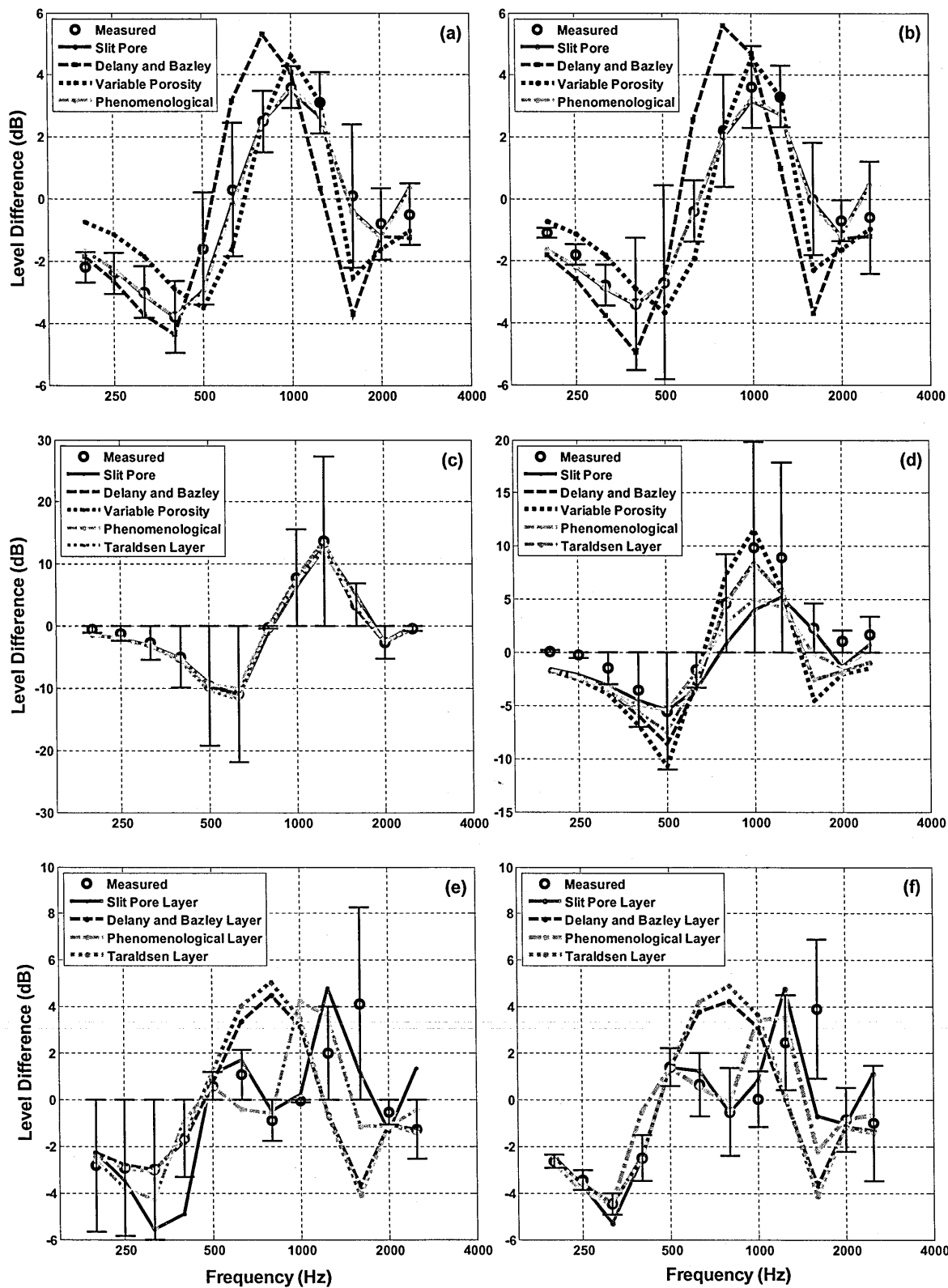
Figure 4.13 Comparisons between best-fit predictions using slit-pore, Delany and Bazley, variable porosity, phenomenological and Taraldsen models and Nordtest data [69], [70] (open circles; error bars indicate 90% confidence limits (±1.65 S.D.)) using the parameters listed in Table 4.9 for (a) site 2 'lichen' (b) site 5 'forest' and in Table 4.10 for (c) site 13 'pine' (d) site 15 'pine' and in Table 4.11 for (e) site 34 'beech wood' and (f) site 35 'beech wood'.

Table 4.9 Best fit impedance model parameters and fitting errors based on third octave band data for five sites in mixed forest floors [69], [70].

Site #	Delany and Bazley		Slit pore			Zwikker and Kosten			Variable porosity		
	Effective flow resistivity (kPa s m^{-2})	Error (Eq. 4.91) dB	Effective flow resistivity (kPa s m^{-2})	Effective porosity	Error (Eq. 4.91) dB	Effective flow resistivity (kPa s m^{-2})	Effective porosity	Error (Eq. 4.91) dB	Effective flow resistivity (kPa s m^{-2})	Effective rate of change of porosity (m^{-1})	Error (Eq. 4.91) dB
2	43	15.8	26.7	0.44	4.9	19.5	0.46	4.9	44.1	-80.9	13.5
3	38	11.3	33.03	0.56	7.1	23.9	0.57	6.9	23.9	-27.3	12.5
4	133	14.6	62.38	0.38	3.4	46.0	0.40	3.4	66.7	-75.1	6.9
5	51	18.7	22.75	0.43	3.8	16.4	0.44	3.7	47.9	-88.1	9.5
6	74	8.8	52.65	0.63	5.9	38.2	0.56	6.0	28.5	-18.3	10.3

Table 4.10 Best fit impedance model parameters and fitting errors based on third octave band data for five pine forests [69], [70].

Model	Parameter or error (Eq. 4.91)	#10	#11	#13	#14	#15
Delany and Bazley	effective flow resistivity (kPa s m^{-2})	106	50	497	662	136
	Error (Eq. 4.91) dB	20.5	26.3	4.7	7.3	28.1
Delany and Bazley layer	effective flow resistivity (kPa s m^{-2})	116.5	73.4	494.5	648.7	124.7
	Effective layer depth m	0.03	0.03	0.03	0.01	0.04
	Error (Eq. 4.91) dB	19.7	18.0	4.7	6.8	27.6
Slit pore	Effective flow resistivity (kPa s m^{-2})	102.5	42.0	648.6	593.5	35.3
	Effective porosity	0.58	0.99	0.70	0.44	0.31
	Error (Eq. 4.91) dB)	21.5	25.1	6.2	6.2	24.7
Slit pore layer	Effective flow resistivity (kPa s m^{-2})	60.5	61.6	531.0	583.0	6.9
	Effective porosity	0.30	0.7	0.38	0.43	0.3
	Effective layer depth m	0.06	0.03	0.01	0.04	0.27
	Error (Eq. 4.91) dB	20.3	19.0	5.4	6.1	20.7
Phenome-nological	Effective flow resistivity (kPa s m^{-2})	75.4	32.8	464.5	454.0	25.3
	Effective porosity	0.60	0.85	0.71	0.47	0.32
	Error (Eq. 4.91)dB	21.5	26.3	6.2	6.2	24.6
Phenome-nological layer	Effective flow resistivity (kPa s m^{-2})	57.9	62.3	476.4	439.8	36.4
	Effective porosity	0.39	0.99	0.48	0.46	0.47
	Effective layer depth m	0.07	0.03	0.01	0.05	0.17
	Error (Eq. 4.91) dB	20.2	18.8	5.3	6.1	24.5
Variable porosity	Effective flow resistivity (kPa s m^{-2})	30.6	9.84	192.6	35.9	56.6
	Effective rate of change of porosity (m^{-1})	10.6	31.0	91.6	-35.4	-59.1
	Error (Eq. 4.91)dB	21.7	24.2	3.3	6.0	23.8

Table 4.11 Best fit impedance model parameters and fitting errors based on third octave band data for three beech wood sites [69], [70].

	Parameter and Error values	Site 34	Site 35	Site 36
Delany and Bazley (semi-infinite)	Effective flow resistivity (kPa s m^{-2})	26	29	74
	Error (Eq. 4.91) dB	24.5	26.3	28.1
Delany and Bazley layer	Effective flow resistivity (kPa s m^{-2})	31	36.8	61.4
	Effective depth (m)	0.09	0.06	0.04
	Error (Eq. 4.91) dB	22.5	21.9	23.4
Variable porosity	Effective flow resistivity (kPa s m^{-2})	26.2	55.6	75.6
	Effective rate of change of porosity	-117	-147	-129
	Error (Eq. 4.91) dB	22.4	25.0	27.1
slit pore (semi-infinite)	Effective flow resistivity (kPa s m^{-2})	14.1	17.5	22.4
	Effective porosity	0.51	0.47	0.35
	Error (Eq. 4.91) dB	17.0	19.0	20.5
Slit pore layer	Effective flow resistivity (kPa s m^{-2})	21.8	19.6	31.9
	Effective porosity	0.37	0.41	0.35
	Effective layer thickness (m)	0.08	0.09	0.07
	Error (Eq. 4.91) dB	17.0	11.8	6.0
Phenomenological (semi-infinite)	Effective flow resistivity (kPa s m^{-2})	10.0	13.2	16.6
	Effective porosity	0.52	0.51	0.36
	Error (Eq. 4.91) dB	17.4	20.0	20.9
Phenomenological layer	Effective flow resistivity (kPa s m^{-2})	16.5	15.7	29.0
	Effective porosity	0.47	0.50	0.41
	Effective layer thickness (m)	0.1	0.1	0.08
	Error (Eq. 4.91) dB	17.5	14.0	10.0
Taraldsen layer	Effective flow resistivity (kPa s m^{-2})	24.6	30.1	79.5
	Effective layer thickness (m)	0.1	0.08	0.04
	Error (Eq. 4.91) dB	25.1	23.9	24.1

4.5.3 Gravel in a pit

Five of the 44 Nord Test NT ACOU 104 [69], [70] ground types, are gravel and sand pit sites. Sites (# 29, 32, 33, 37 and 38) are described as in an area covered with a layer of stone chippings (gravel) with sizes between 5 and 50 mm and with an unknown layer depth. Table 4.12 compares best-fit parameters and errors using the Delany and Bazley model, Delany and Bazley layer model, Taraldsen layer model, the slit pore model, the slit pore layer model and the variable porosity model for gravel and sand pit data sites. Analysis shows that numerical fitting using Delany and Bazley fails to give good predictions to gravel-in-a-pit data with a high mean error value of 17.4 dB. Use of the Delany and Bazley layer model does not give any improvement in fitting data. The Taraldsen layer model gives more or less identical results to those obtained by the Delany and Bazley layer model with the similar mean error value of 16.7 dB. The variable porosity model gives good fitting results for site 32 and 33 sites, but fails for the other three. Moreover, the best fitted porosity rate value obtained for site 32 and 33 is very high and as well as negative. The high porosity value means that a very thin layer exists and the negative sign means the porosity is increasing exponentially with layer depth. These parameter values are not very realistic for a ground surface. The mean error value using the variable porosity model is 13.2 dB. Using the slit pore model and the phenomenological model gives better fitting to data and smaller error values compared to other models listed in Table 4.12. In contrast to the Delany and Bazley layer model, the slit pore layer model improves the data fitting by a remarkable amount in terms of reducing error value and reproducing the detailed frequency dependence shown by the data. The mean

error value using the (semi-infinite) slit pore model is 13.6 dB, which is reduced to 8.2 dB for the slit pore layer model. Although not listed in Table 4.12 the phenomenological model gives similar fitting results to those obtained by using the slit pore model. Figure 4.15 compares the level difference data over gravel and sand pit site 38 (black open circles) with predictions using the slit pore layer model (red continuous line), the Delany and Bazley model (blue broken lines), the Delany and Bazley layer model (black dotted lines), the phenomenological layer model (brown dashed line) and the Taraldsen layer model (magenta broken lines joined dots). The Delany and Bazley, Delany and Bazley layer and Taraldsen layer models give poor agreement between predictions and data over site 38 with very high error values of 26.5 dB, 22.3 dB and 22.9 dB respectively. The variable porosity model also gives a high error value of 26.8 dB. However, the slit pore layer model enables a very good agreement between data and predictions with an error value of just 3.7 dB. Moreover it should be noted that, only the slit pore and phenomenological model predictions reproduce the detailed frequency dependence of the measured level difference spectra shown by Figure 4.15.
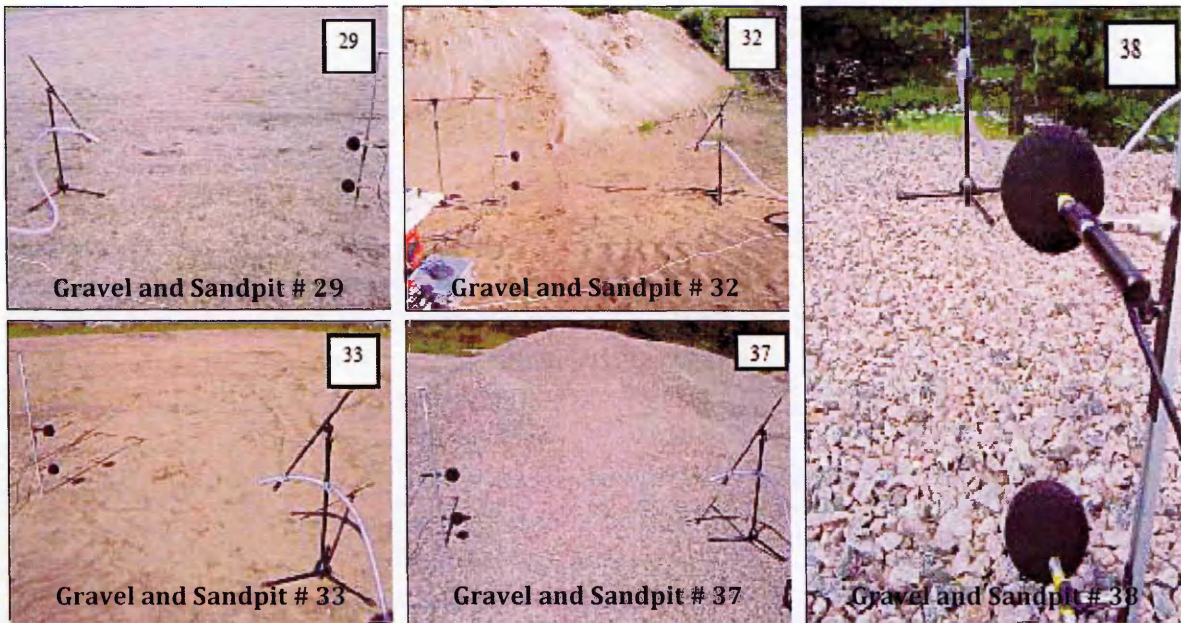
Figure 4.14 Photos of five gravel and sand pit sites [27, 28]
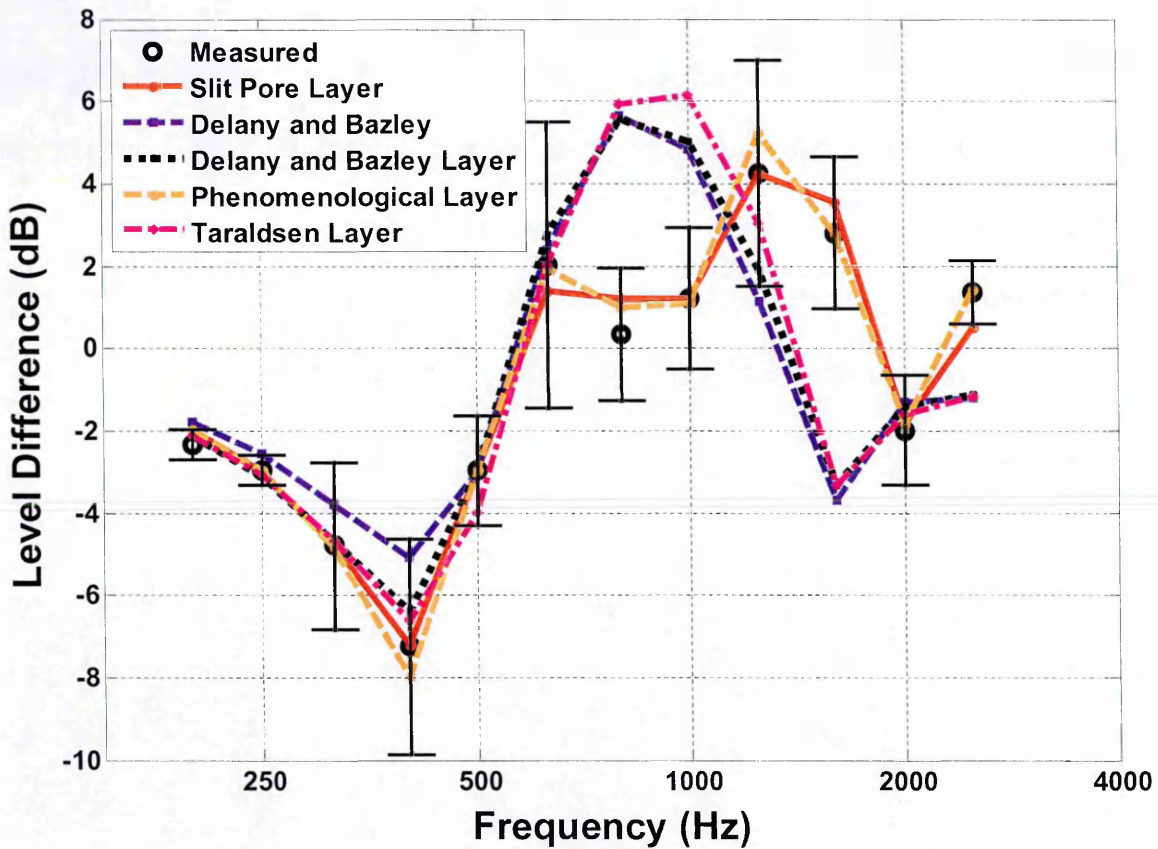
Figure 4.15 Best fit predictions using the slit-pore (red continuous line), the Delany and Bazley (blue broken lines), the Delany and Bazley layer (black dotted lines), phenomenological (brown broken line) and Taraldsen layer (magenta broken lines joined dots) models and Nordtest data (black open circles; error bars indicate 90% confidence limits (±1.65 S.D.)) obtained at a gravel pit [69], [70] (site #38) (parameter values are given in Table 4.12).

Table 4.12 Best fit impedance model parameters and fitting errors based on third octave band data for five pine forests [69], [70].

Model	Parameter or error (Eq. 4.91)	#29	#32	#33	#37	#38
Delany and Bazley	effective flow resistivity (kPa s m^{-2})	10943	10000	10000	158	53
	Error (Eq. 4.91) dB	20.1	9.3	18.1	13.2	26.5
Delany and Bazley layer	effective flow resistivity (kPa s m^{-2})	10000	10000	10000	170	68
	Effective layer depth m	0.10	0.10	0.10	0.02	0.04
	Error (Eq. 4.91) dB	20.3	9.3	18.2	13.1	22.3
Slit pore	Effective flow resistivity (kPa s m^{-2})	100	100	10	129	19
	Effective porosity	0.05	0.04	0.11	0.70	0.34
	Error (Eq. 4.91) dB)	17.3	7.6	9.8	15.4	17.8
Slit pore layer	Effective flow resistivity (kPa s m^{-2})	9.5	15.7	84.8	42.8	33.6
	Effective porosity	0.04	0.05	0.05	0.22	0.33
	Effective layer depth m	0.05	0.22	0.07	0.04	0.07
	Error (Eq. 4.91) dB	11.8	5.5	8.6	11.4	3.7
Taraldsen layer	Effective flow resistivity (kPa s m^{-2})	26065	78567	3583	140	67
	Effective porosity	0.06	0.15	0.05	0.02	0.04
	Error (Eq. 4.91)dB	20.0	9.1	17.8	13.7	22.9
Variable porosity	Effective flow resistivity (kPa s m^{-2})	1224	3455	1950	55	76
	Effective rate of change of porosity (m^{-1})	-2466	-2490	-1404	8	-142
	Error (Eq. 4.91)dB	13.7	3.2	7.5	14.7	26.8

Table 4.13 Mean fitting errors (Eq. (4.91)) dB to third-octave band data [69], [70] corresponding to use of eight impedance models.

Model	Delany and Bazley	Delany and Bazley layer	Slit pore	Slit pore layer	Phenomen-ological	Phenomen-ological layer	Variable porosity	Taraldsen layer
Grassland (Table 4.6)	9.3	-	8.7	-	8.7	-	6.7	-
Grassland (Table 4.7)	11.8	7.5	11.4	7.0	11.4	7.3	7.6	7.3
Forest floor (pine, Table 4.9)	13.8	-	5.0	-	5.0	-	10.5	13.8
Forest floor (beech, Table 4.11)	26.3	22.6	18.8	11.6	19.4	13.8	24.8	24.4
Gravel and sand (Table 4.11))	15.2	15.2	12.5	9.4	12.5	9.9	9.8	15.2

4.5.4 Porous asphalt

As part of the study related to potential revision of Nordtest NT ACOU 104 [69], [70], measurements have been made above newly laid single layer drainage asphalt. A different geometry to standard Nordtest geometry is used with a source at height of 0.42 m, distance between source and microphones of 4.0 m, and microphone heights of 0.28 m and 0.075 m. The measured flow resistivity value for a typical porous asphalt lies between 2 and 15 kPa s m^{-2}, measured porosity values are between 0.15 and 0.3 [32]. Numerical fitting using the Delany and Bazley layer model gives poor agreement between predictions and level difference data over porous asphalt with a large error value of 34.0 dB. The best fitted effective flow resistivity is 2687 kPa s m^{-2} and layer thickness of 0.097 m. The Taraldsen layer model also gives very high error of 28.9 dB with best-fit effective flow resistivity of 1948 kPa s m^{-2} and layer thickness of 0.14 m. The best fit flow

resistivity values obtained using Delany and Bazley layer model and Taraldsen layer model are much larger than measured flow resistivity values for typical porous asphalt which lie between 2 and 15 kPa s m^{-2} [32]. However, the slit pore layer model gives a very good numerical fit to the data with an error of just 3.7 dB. Figure 4.16 (a) compares the level difference data with predictions using Delany and Bazley layer, Taraldsen layer and slit pore layer models. Fittings obtained with Delany and Bazley layer and Taraldsen layer models are nowhere close to data. Whereas, use of the slit pore model gives a spectral shape close to that of the data. Numerically obtained best fitted parameters which give an error of 4.9 dB by using the slit pore layer model are with flow resistivity of 67.5 kPa s m^{-2}, porosity of 0.18 and layer thickness of 0.036 m. The tortuosity value is obtained by using the relationship ($T = \frac{1}{\Omega^{n'}}$) between the tortuosity and the porosity. The best fitted value of n' is 0.5 which gives the tortuosity value of 2.36. Figure 4.16 (a) gives another spectral fitting using slit pore layer model shown by black dotted line with a slightly higher error value of 5.6 dB and it is visually better for all but the 3 kHz data point. The overall error value obtained for later fitting is made higher due to last data point; otherwise the error value obtained by ignoring last data point is only 1.8 dB. The latter fitting is obtained by using effective flow resistivity of 61.2 kPa s m^{-2}, porosity of 0.22 and with a layer thickness of 0.036 m. A value of $n' = 0.64$ is used, which gives a tortuosity value of 2.64. Figure 4.16 (b) compares the level difference data over porous asphalt with predictions obtained using the slit pore layer and phenomenological layer models. The phenomenological model gives comparable fits with similar parameters values to those obtained with the slit pore layer but fitting errors are somewhat larger, 7.4 dB & 11.7 dB respectively.
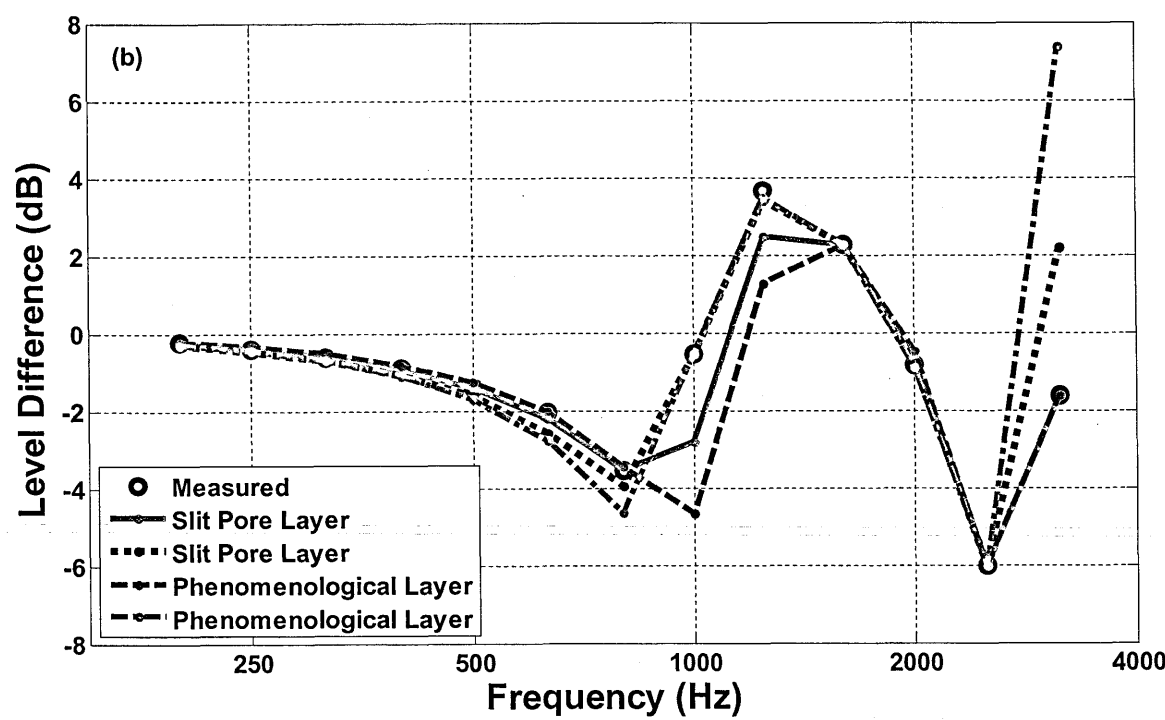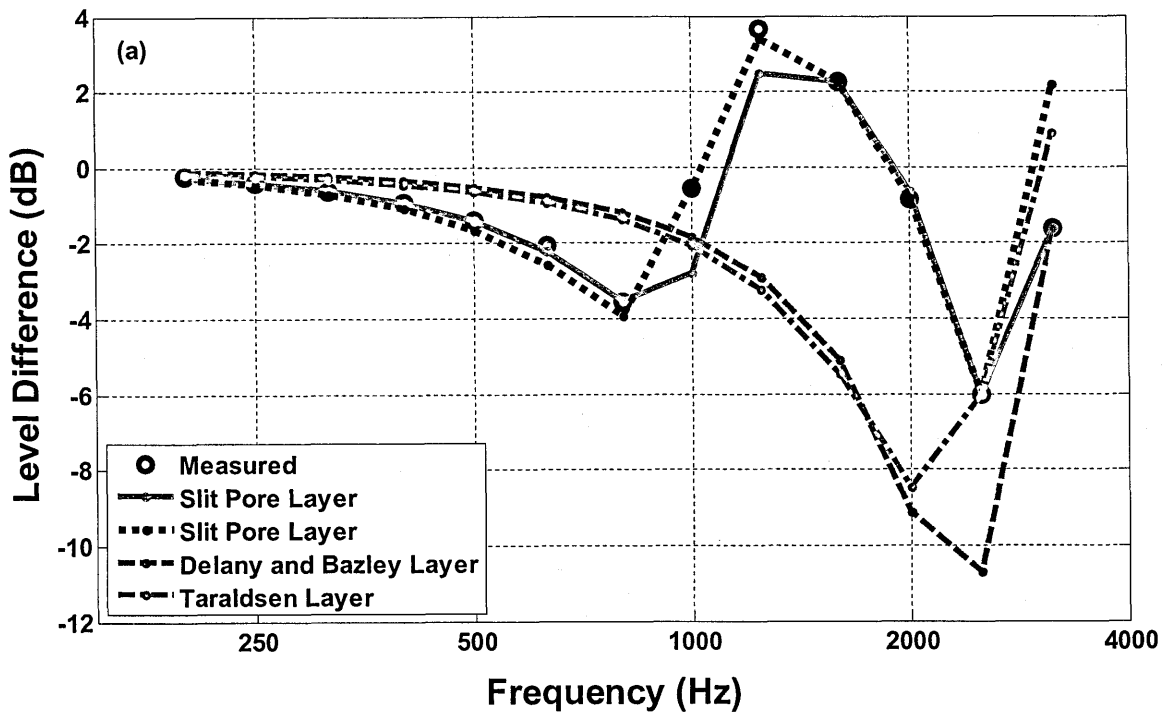
Figure 4.16 Numerically-obtained best fits to level difference data (open circles) over newly laid porous asphalt [69], [70] source height 0.42 m, distance between source and microphones 4 m, and microphone heights 0.28 m and 0.075 m (red continuous line – slit pore layer R_s = 67.5 kPa s m^{-2}, h = 0.18, n' = 0.5, d = 0.036 m; black dotted line - R_s = 61.2 kPa s m^{-2}, h = 0.22, n' = 0.64, d = 0.036 m); (a) blue broken line – Delany and Bazley layer, effective flow resistivity 2687 kPa s m^{-2}, d = 0.097 m; magenta dash-dot line – Taraldsen layer, flow resistivity 1948 kPa s m^{-2}, d = 0.14 m; and (b) blue broken line – Phenomenological layer, R_s = 86.9 kPa s m^{-2}, h = 0.18, n' = 0.5, d = 0.040 m; magenta dash-dot line – Phenomenological layer, R_s = 71.6 kPa s m^{-2}, h = 0.26, n'=0.8, d = 0.040 .

4.5.5 Railway ballast

Excess attenuation measurements over railway ballast made by Heutschi [75] have been compared with predictions using the Delany and Bazley layer, Taraldsen layer, slit pore layer and the phenomenological layer models. Figure 4.17 shows the measurement arrangements over railway ballast with source at height of 0.5 m, receiver at height of 1.2 m and with horizontal separation of 7.5 m. Heutschi [75] has shown that railway ballast with layer depth of 0.3 m must be treated as having extended reaction. Figure 4.18 (a) compares the data with predictions using the local reaction assumption and the hard-backed-layer versions of the Delany and Bazley, slit-pore and phenomenological models. The Delany and Bazley layer model significantly over-predicts the first ground effect dip magnitude and width. The locally reacting ballast assumption gives a reasonable fit to excess attenuation spectra albeit with a best fit layer depth of 0.2 m compared with the actual measured layer depth of railway ballast of 0.3 m [75]. The use of measured layer depth of 0.3 m and assuming locally reacting ballast reduced the agreement by a significant amount between data and predictions. Figure 4.18 (b) compares the data with predictions using the extended reaction assumption and hard-backed-layer versions of the Delany and Bazley, slit-pore and phenomenological models. The agreement between data and predictions assuming extended reaction is very good. The externally reacting slit pore layer model predictions gives more realistic parameters with flow resistivity of 100 Pa s m^{-2} and layer depth of 0.3 m which is equal to the measured value. However, the Delany and Bazley layer model fails to predict the measured layer depth since the best fit layer depth for externally reacting ballast is 0.7 m. The impedance models

and corresponding best-fit parameter values are listed in Table 4.14. The phenomenological model also fails to predict the measured layer depth since the best fit layer depth for externally reacting ballast is 1.5 m and measured layer depth is 0.3 m. The fitting results for the Taraldsen layer model (not given here) are similar to those obtained using the Delany and Bazley layer model.

Table 4.14 Fitted parameter values for railway ballast corresponding to Figure 4.12 [75].

Impedance Model	Local Reaction			Extended Reaction		
	Delany and Bazley Layer	Slit pore layer	Phenomen-ological Layer	Delany and Bazley Layer	Slit pore layer	Phenomen-ological Layer
Effective flow resistivity (Pa s m^{-2})	15	5409	161	10	100	66
Effective porosity	-	0.2	0.28	-	0.2	0.67
Effective layer depth (m)	0.274	0.2	0.23	0.7	0.3	1.445

Figure 4.17 Excess attenuation measurement over railway ballast [75].
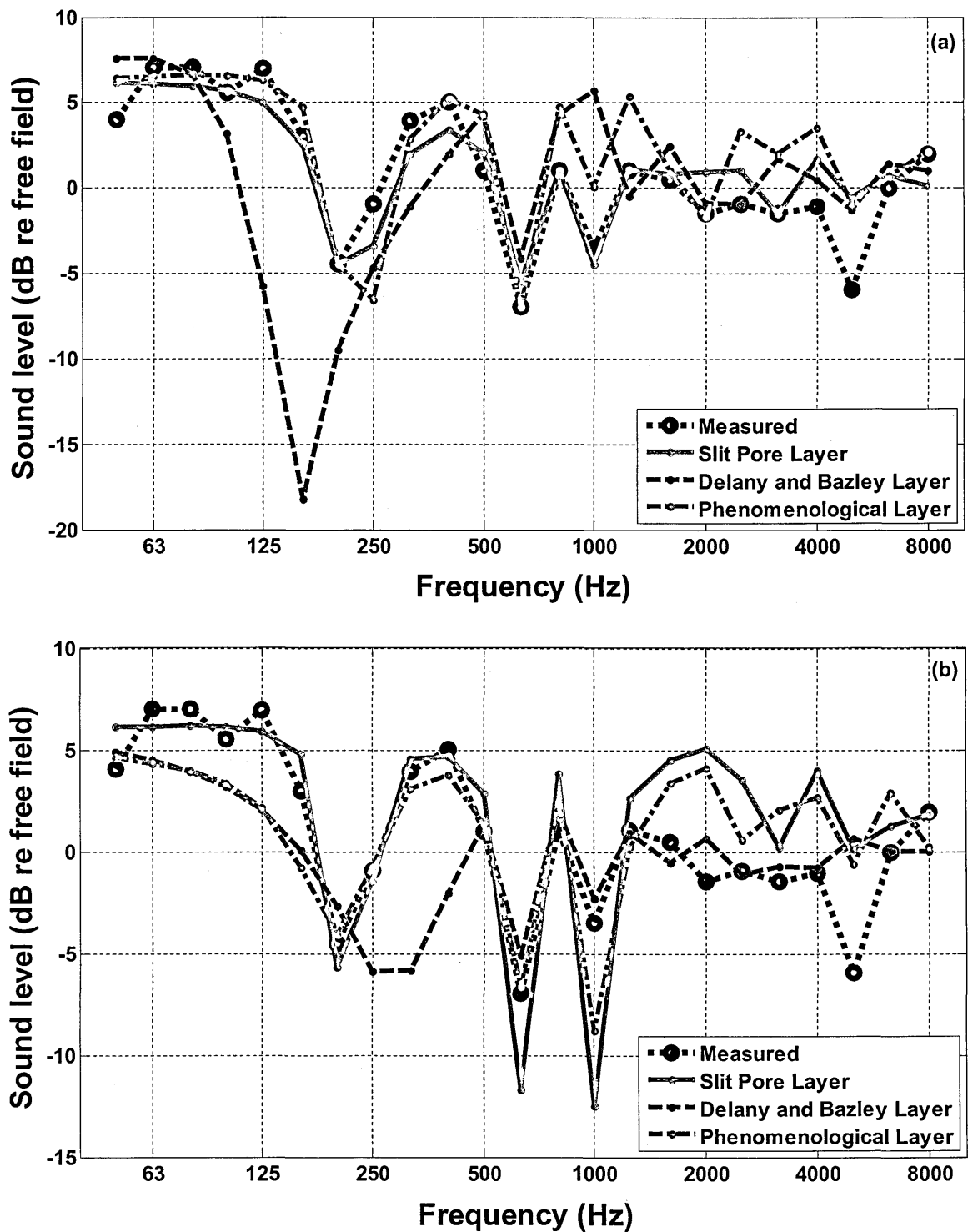
Figure 4.18 Comparison of data (black dotted line and circles) for excess attenuation spectra over railway ballast [ref. [75], Figure 6] and predictions (a) assuming local reaction and (b) assuming extended reaction using hard-backed-layer versions of the Delany and Bazley model (blue broken lines), the slit pore model (red continuous lines) and the phenomenological model (magenta dot-dash lines) with the parameter values given in Table 4.14.

4.6 Comparisons between laboratory data and predictions

The laboratory provides a controlled environment and compared with naturally-occurring surfaces, the materials used as ground surfaces in the laboratory are fairly uniform. In this section, laboratory data obtained over different types of ground surfaces are compared with predictions using different impedance models. This serves also to characterise the acoustical properties of materials that have been used in the laboratory for different purposes (see Chapter 5, 7, 8 and 9). Section 4.5 compared predictions using five different impedance models with data over a variety of ground types. It was concluded that the variable porosity model is best for grassland sites whereas, the slit pore or slit pore layer models give very good predictions for other ground types.

Layers of felt and open-cell foam have been used to create acoustically-soft surfaces in the laboratory. The acoustical characterization of felt and foam has been achieved using variable porosity and slit pore models. These two models have been found to give minimum mean error value (see Table 4.13) for most of ground types in which data is compared with prediction. Moreover the slit pore and layered slit pore models have been found to give very good agreement with data using measured values of porosity and flow resistivity (see Chapter 3, section 3.26; Chapter 4, section 4.6.1 and 4.6.2; Chapter 6, section 6.2.2; Chapter 7).

Some laboratory measurements have been made also using granular materials. The Johnson-Allard-Umnova [60] model for granular material has been used to predict the acoustical characteristics of lead shot and gravel. Predictions of the Miki [44] have been compared also with some laboratory data.
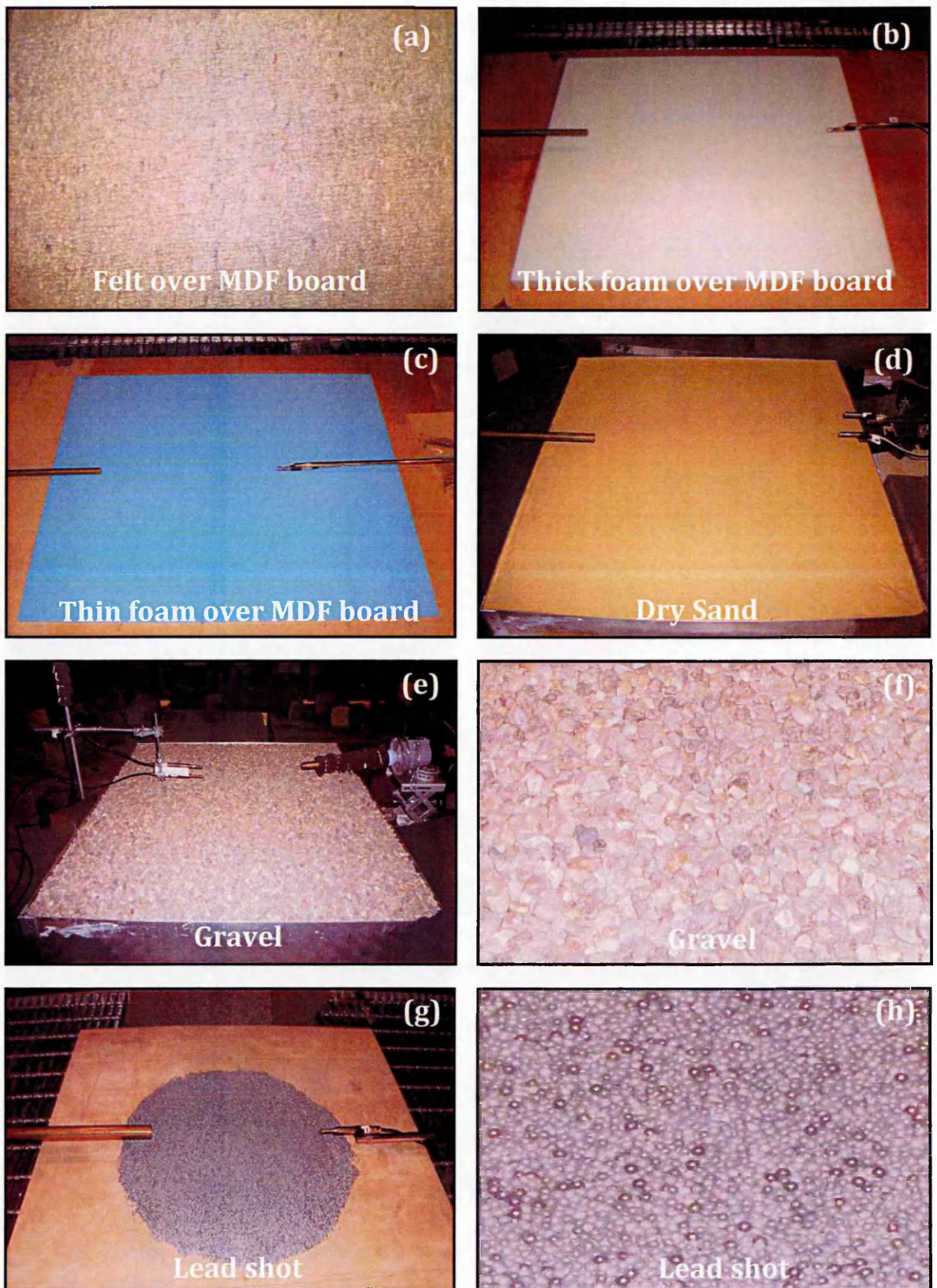
Figure 4.19 Photos for different materials measured in laboratory (a) felt over MDF (b) thick foam over MDF (c) thin foam over MDF (d) dry sand (e) gravel (f) gravel - enlarged view (g) lead shot over MDF (h) lead shot = enlarged view.

Excess attenuation spectra have been measured over felt and different types of foam placed on a MDF board and over granular materials such as lead shot, gravel and sand. A Maximum Length Sequence System Analyzer (MLSSA) is used for these measurements the details of which are given in chapter 3. The measured data obtained with different geometries are numerically fitted using the specified impedance models. The impedance parameters which give good fit to most of geometries are used for characterization. The impedance deduction technique described above also is used for laboratory data and compared with the impedance spectra predicted by impedance models.

4.6.1 Artificially created ground surfaces

4.6.1.1 Felt on MDF board

Figures 4.19 (a), (b) and (c) show three artificially created acoustically-soft grounds used in the laboratory. A set of measurements using between 5 and 10 source-receiver geometries were used to characterize these materials. The accuracy of impedance predictions is improved by numerically fitting data over same ground, with more than one geometry. However, the data given in Figure 4.20 (a) – (f) was measured with source and receiver at height 0.07 m and horizontally- separated by 0.7 m. Figure 4.20 (a) shows numerically obtained best fits to excess attenuation data over felt placed on MDF board with source and receiver at height 0.07 m and horizontally- separated by 0.7 m using the slit pore layer model with flow resistivity, porosity and layer thickness of 118.5 kPasm^{-2}, 0.7 and 0.012 m respectively, and Figure 4.20 (b) compares the corresponding impedance spectra deduced directly from data with the impedance spectra

predicted by the slit pore layer model. The agreement between data and slit pore layer predictions is very good. Figure 4.20 (c) compares the numerically obtained best fits to excess attenuation data using the slit pore layer model with flow resistivity of 85 kPa s m^{-2}, and a porosity value of 0.5 and layer thickness of 0.014 m and Figure 4.20 (d) compare the corresponding impedance deduced directly from data and impedance predicted by slit pore layer model. In the latter case, the agreement between predicted and deduced impedance in Figure 4.20 (d) is better than that in Figure 4.20 (b). However, the best fits are obtained with an incorrect layer depth of 0.014 m (the measured thickness of felt is 0.012 m). Moreover, the EA predictions in Figure 4.20 (a) are better than those in Figure 4.20 (b). It is concluded that given the better agreement between measured and predicted EA using measured layer depth, the impedance parameters given by the fitting the data in Figures 4.20 (a) & (b) are to be preferred to those used in Figures 4.20 (b) & (c). Figure 4.20 (e) shows the numerically obtained best fits to excess attenuation data using the variable porosity model with flow resistivity of 23 kPa s m^{-2} and a porosity rate of 60 m^{-1} and figure 4.20 (f) compares the corresponding impedance deduced directly from data and impedance predicted by the variable porosity model. The variable porosity model gives good agreement between excess attenuation data and predictions but the agreement between deduced and predicted impedance is not good.
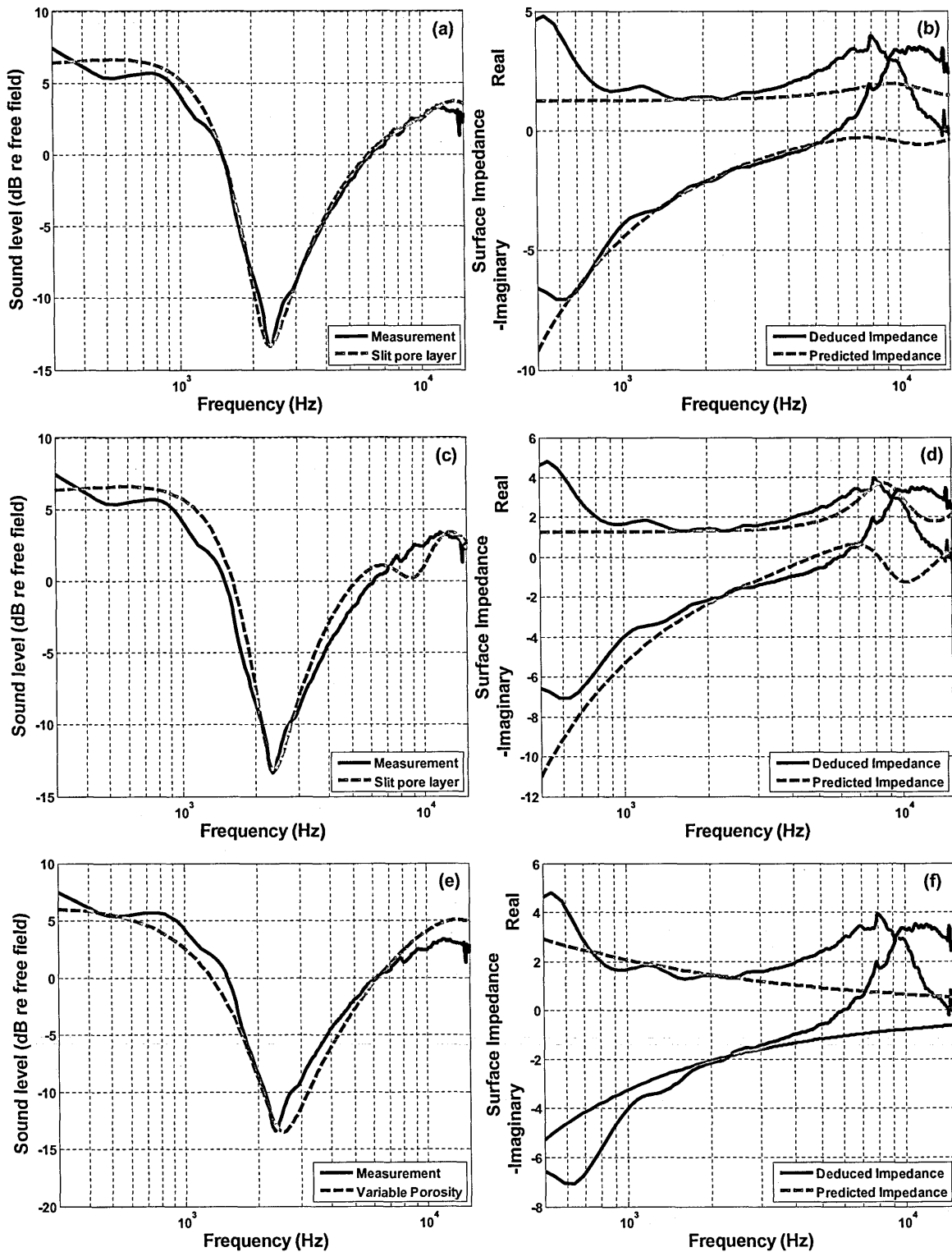
Figure 4.20 Excess attenuation data (black continuous line) compared with fittings and deduced impedance (real – blue continuous line, -imaginary – black continuous line) for felt placed over MDF with source and receiver at height of 0.07 m, distance between source and receiver 0.7 m (a)&(b) broken line – slit pore layer R_s = 118.5 kPasm⁻², Ω = 0.7, d = 0.012 m (a) excess attenuation (b) Impedance; (c)&(d) broken line – slit pore layer R_s = 85 kPasm⁻², Ω = 0.5, d = 0.014 m (c) excess attenuation (d) Impedance; (e)&(f) broken line – variable porosity model R_s = 23 kPasm⁻², Porosity rate = 60 m⁻¹ (e) excess attenuation (f) Impedance.

4.6.1.2 Foam layers of different thickness on MDF board

The acoustical properties of five commercially available foam layers having different thicknesses have been studied in the laboratory. Excess attenuation measurements over these foam layers have been carried out by placing them on an MDF board. Various geometries have been used for these measurements and resulting data are compared with predictions using the slit pore layer, the variable porosity, the Miki one parameter and the Miki layer two parameter models. Typically open cell foams are acoustically-soft with very high porosity values and low flow resistivity. Figure 4.21 (a) compares excess attenuation data obtained over 0.03 m thick foam with source and receiver at height of 0.015 m and horizontally-separated by 0.7 m with predictions obtained using the slit pore layer model and assuming either external reaction or local reaction. The comparisons show that these foams must be treated as externally reacting since the predictions assuming external reaction are in very good agreement with the data when using the measured foam layer thickness. The agreement between data and predictions assuming local reaction is not as good, when using the measured foam thickness. However, a reasonably good fit can be achieved by using an unrealistically high flow resistivity value and a significantly smaller layer depth than the actual measured foam thickness. Moreover, the agreement between impedance spectra deduced from complex excess attenuation data over different foam layers and the impedance predicted by the slit pore layer model when assuming external reaction is very good. An example comparison between deduced impedance from complex EA data over 0.03 m thick foam and predicted surface impedance using externally reacting slit pore layer model is shown in Figure 4.21.
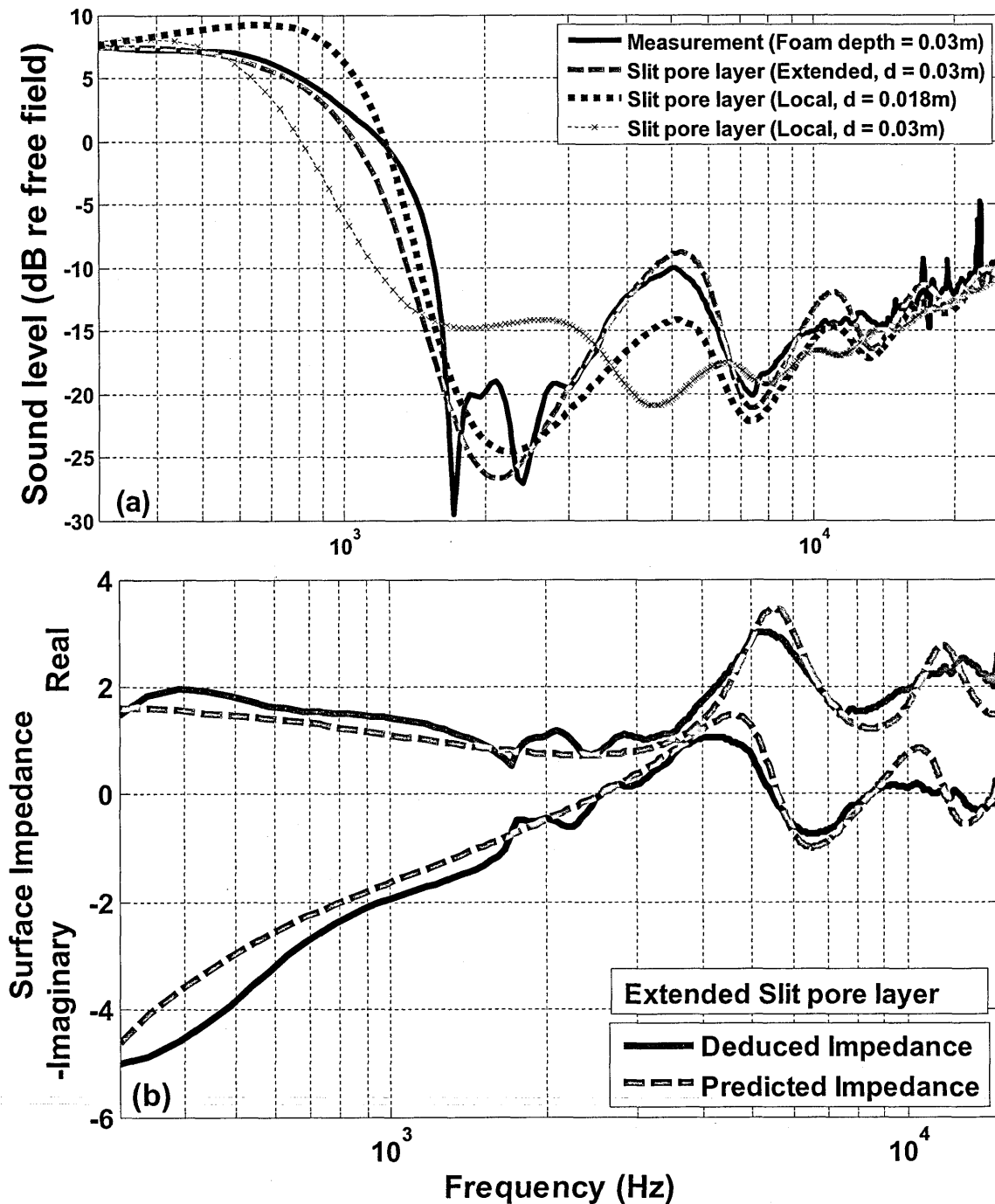
Figure 4.21 Example comparison between measured excess attenuation (black continuous line) over foam with thickness of 0.03 m placed over MDF with source and receiver at height of 0.015 m, distance between source and receiver 0.7 m with numerically obtained best fits using (a) externally-reacting slit pore layer (red broken line) - R_s = 7.0 kPasm^{-2}, Ω = 0.98, d = 0.03 m; locally-reacting slit pore layer (blue dotted line) - R_s = 40.0 kPasm^{-2}, Ω = 0.98, d = 0.018 m; local slit pore layer (brown dotted-cross line) - R_s = 40.0 kPasm^{-2}, Ω = 0.98, d = 0.03 m; (b) Comparison between deduced impedance (broken line) from complex EA data and predicted impedance (solid line) using externally reacting slit pore layer using parameters as given in (a).

Figure 4.22 compares data with predictions using the variable porosity, Miki one parameter and Miki two parameter models. The detailed mathematical expressions for these models are given above (see Eq. 4.55 and Eq. 4.21). The agreement between data over foams and predictions is not very good when using the variable porosity model. Even when allowing for external reaction, the one parameter Miki layer model fails to give adequate predictions of excess attenuation spectra over foam placed on a MDF board. The two parameter Miki model uses effective flow resistivity and effective porosity as input parameters. The two-parameter Miki model with numerically obtained best-fit flow resistivity of 10 kPa s m^{-2} and measured porosity of 0.98 gives poor agreement with data (see figure 4.22). However, a better fit to data can be achieved by using unrealistically low porosity value of 0.6 (the measured porosity is 0.98).

Best predictions of excess attenuation spectra measured over different types of foam layers using measured parameters is achieved by assuming external reaction and using the two parameter slit pore layer model. On the other hand use of the, variable porosity, Miki one parameter model and Miki two parameter models fails to reproduce the detailed frequency dependence shown by the data. Nevertheless, with adjusted parameter values, all models give comparably good fits to measured excess attenuation data on felt placed over MDF board.
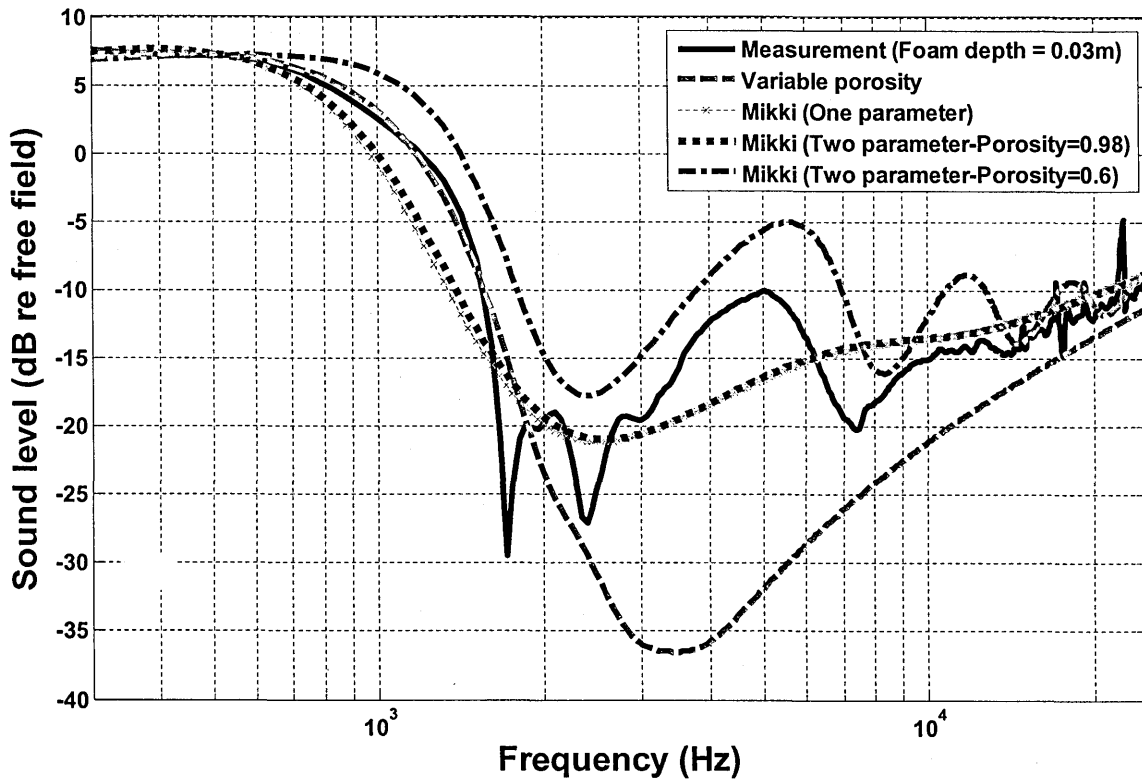
Figure 4.22 Example comparison between measured excess attenuation (black continuous line) over foam with thickness of 0.03 m placed over MDF with source and receiver at height of 0.015 m, distance between source and receiver 0.7 m with numerically obtained best fits using variable porosity model (red dash line) - R_s = 5.0 kPasm⁻², porosity rate = 40 m⁻¹; extended Miki layer one parameter (brown dotted-cross line) - R_s = 10.0 kPasm⁻², d = 0.03 m; extended Miki layer two parameter (blue dotted line) - R_s = 10.0 kPasm⁻², measured porosity = 0.98, d = 0.03 m; extended Miki layer two parameter (magenta dash-dotted line) - R_s = 10.0 kPasm⁻², unrealistic lower porosity = 0.6, d = 0.03 m.

4.6.2 Granular materials

Laboratory measurements have been made of short range propagation over lead shot and gravel. Such granular materials are interesting because their acoustical properties can be deduced from their particle size, particle shape and packing density. The measured impedance parameters along with a suitable impedance model are useful to predict excess attenuation spectrum for a given geometry. Umnova *et al.* [60] presented a cell model to predict acoustical properties of granular materials. It is a four parameter model, identified in this thesis as the Johnson-Allard-Umnova model, and is given above (see Eq. 4.56 and Eq. 4.57). The four parameters are flow resistivity, porosity, viscous characteristic length and thermal characteristic length. This four parameter model can be converted into a three parameter model by using a relationship between the viscous and thermal characteristic lengths for granular materials.

$$\Lambda = \frac{2\Lambda'T(1-\Theta)}{3}, \qquad (4.92)$$

where Λ' and Λ are the thermal and viscous characteristic lengths respectively. T is the tortuosity and Θ is a parameter which can be determined from a known porosity value,

$$\Theta = 0.675(1-\Omega). \qquad (4.93)$$

For granular materials, the thermal characteristic length Λ' can be determined from porosity and particle radius [60],

$$\Lambda' = \frac{2\Omega R}{3(1 - \Omega)},$$

(4.94)

where R is the mean particle radius of the granular material and Ω is the porosity.

The tortuosity and flow resistivity of granular materials can be calculated from the following empirical formulas,

$$T = \frac{1}{\sqrt{\Omega}},$$

(4.95)

$$R_s = \frac{108\eta(1 - \Omega)^2}{(2R)^2 \Omega^{3.5}}.$$

(4.96)

Hence only values of volume porosity and particle radius of a granular material are needed to calculate the acoustic impedance.

4.6.2.1 Lead shot on MDF board

Figure 4.19 (g) and (h) shows the lead shot used in laboratory measurements. The measured distribution of the lead shot diameters with mean value of 3.1 mm is given in Figure 4.23.
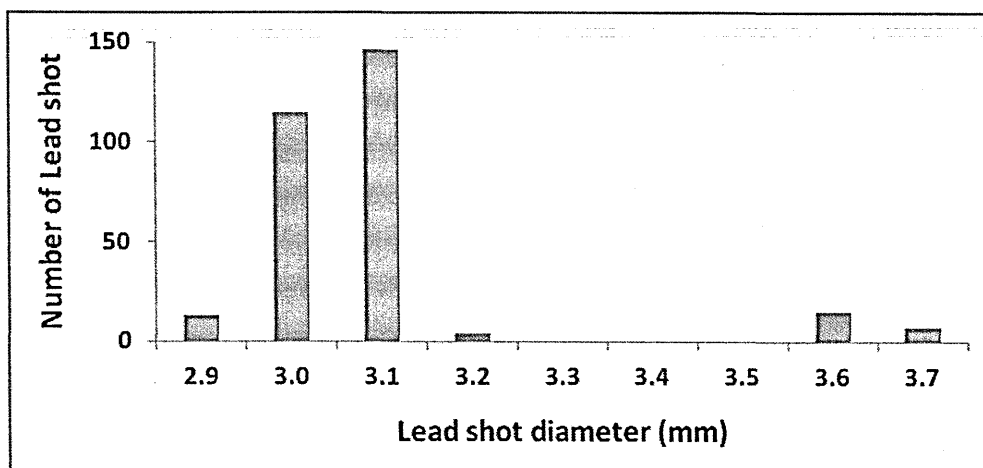
Figure 4.23 Measured distributions of the diameter in 300 Lead shot with mean diameter of 3.1 mm.

The porosity of the lead shot has been determined by weighing a known volume and using a reference value of the density of lead [11.3 kg m^{-3}]. The measured porosity value for lead shot is 0.4. The calculated flow resistivity of lead shot using Eq. (4.96) is 1.8 kPa s m^{-2}. The measured layer depth of lead shot is 0.012 m. The predicted viscous characteristic length using the relationship between viscous and thermal characteristic lengths given by Eq. (4.92) to Eq. (4.94) is 4.326e-4. Figure 4.24 compare the EA predictions using the slit pore layer, Johnson-Allard-Umnova layer, Miki one parameter layer and Miki two parameter layer models with measured excess attenuation over lead shot with source-receiver separation of 0.5 m and (a) source and receiver at a height of 0.038 m (b) source and receiver at a height of 0.058 m. The agreement between data and predictions using the slit pore layer and Johnson-Allard-Umnova layer models is very good. The slit pore layer model uses the measured porosity value of 0.4 and measured layer depth of 0.012 m. However, it uses numerically obtained best fit effective flow resistivity of 5.0 kPa s m^{-2} instead of the flow resistivity of 1.8 kPa s m^{-2} calculated from Eq. (4.96). The Johnson-Allard-Umnova layer model gives equally good fit using the calculated flow resistivity value of 1.8 kPa s m^{-2}, measured porosity value of 0.4, measured layer depth of 0.012 m and viscous characteristic length of 3.5 ×10^{-4} m. The value of viscous characteristic length calculated using Eq. (4.92) is 4.3 ×10^{-4} m. However this value is adjusted to obtained better fits [60]. In contrast to the slit pore layer model which uses an effective flow resistivity value, it seems that Johnson-Allard-Umnova (JAU) model gives good predictions using the calculated flow resistivity value of 1.8 kPa s m^{-2}. Changing the flow resistivity value up to 5 kPa s m^{-2} has almost no effect on the predicted excess attenuation spectrum when using the JAU model. However,

changing viscous characteristic length affects the excess attenuation spectrum in a similar manner to the effect of changing the flow resistivity value in the slit pore layer model. It is concluded that reasonably good fits with excess attenuation data can be obtained over lead shot by using either the slit pore layer model or the Johnson-Allard-Umnova layer model with a combination of measured and fitted parameters. However, the fits can be improved either by adjusting flow resistivity in the slit pore layer model or the viscous characteristic length in the Johnson-Allard-Umnova layer model. There remains a discrepancy near the second excess attenuation minimum (see Figure 4.24). This discrepancy can be reduced, if the porosity value is adjusted from 0.4 to 0.3. Figure 4.24 compares excess attenuation data with predictions using the one and two parameter Miki layer models. The one parameter Miki model fails to give good fit to measured excess attenuation data. Use of the two parameter Miki model predicts a shifted excess attenuation spectrum with measured layer depth and numerically best fitted flow resistivity value. However, a better fit to data can be achieved by using an effective layer depth of 0.008 m which is significantly lower than the measured layer depth of 0.012 m.
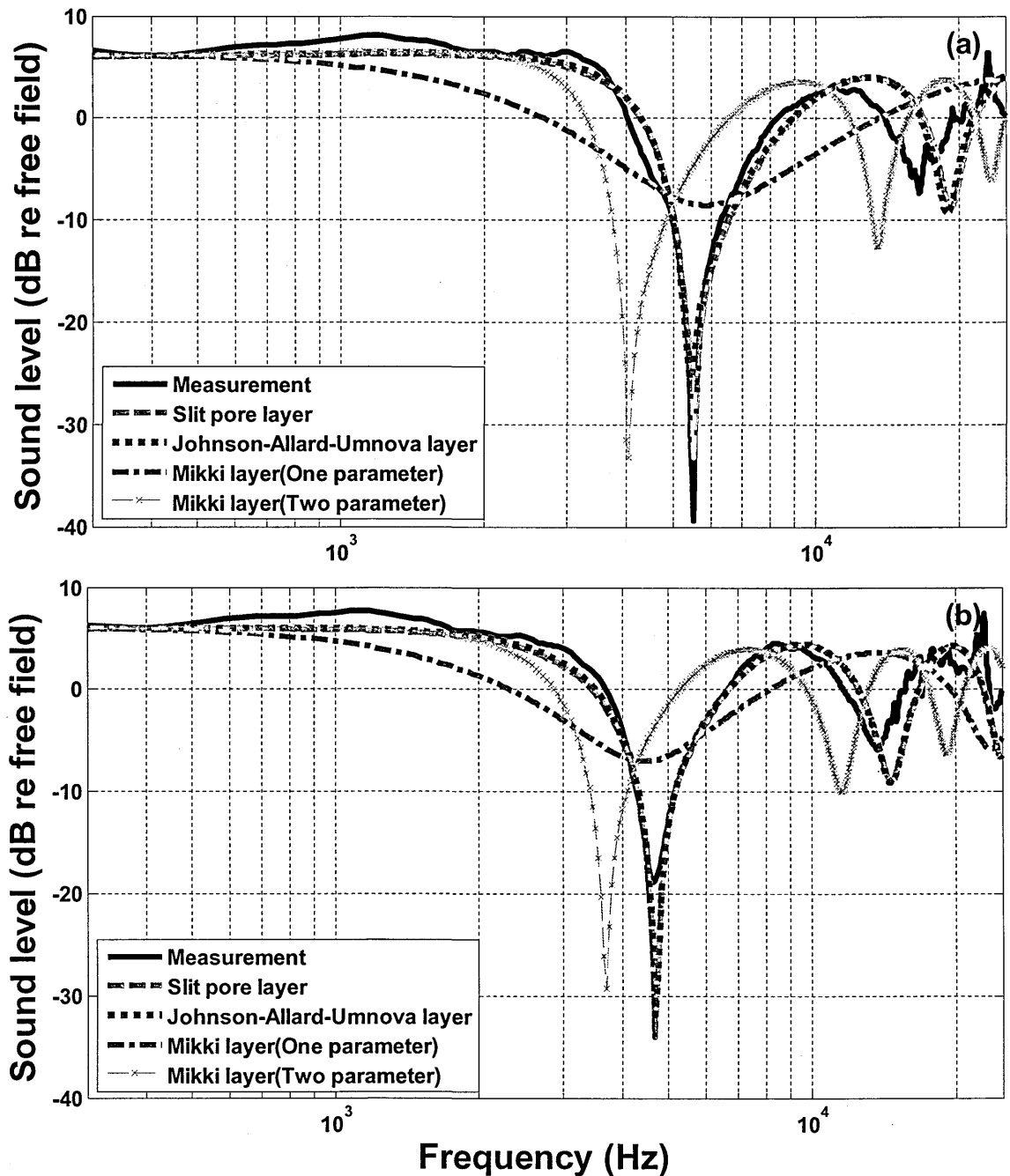
Figure 4.24 Comparison between measured excess attenuation spectra (black continuous lines) over a 0.012 m thick layer of lead shot on MDF board and numerically obtained best fit predictions using externally reacting slit pore layer (red broken line) - R_s = 5.0 kPasm^{-2}, Ω = 0.4, d = 0.012 m; Johnson-Allard-Umnova (blue dotted line) - R_s = 1.8 kPasm^{-2}, Ω = 0.4, Λ = 3.5e-4, d = 0.012 m; Miki layer one parameter (magenta dash-dotted line) - R_s = 3.0 kPasm^{-2}, d = 0.012 m; Miki layer two parameter (brown dotted-cross line) - R_s = 10.0 kPasm^{-2}, Ω = 0.4, d = 0.012 m (a) with source and receiver at height of 0.038 m, distance between source and receiver 0.5 m (b) with source and receiver at height of 0.058 m, distance between source and receiver 0.5 m.

4.6.2.2 Gravel

Figures 4.19 (e) and (f) show results of laboratory level difference measurements over gravel. The gravel is placed inside a rigid aluminium box with dimensions 1.2 m x 1.2 m x 0.12 m. The gravel is 0.12 m deep with a mean grain size of 4 mm. The porosity of the gravel has been determined by weighing the gravel and the volume occupied by it in the box. The measured porosity value for gravel is 0.374. The calculated flow resistivity of gravel with mean size of 3.79 mm using Eq. (4.96) is 1.6 kPa s m^{-2}. The formula given by Eq. (4.96) is for stackings of identical spherical grains. However gravel grains are not perfectly spherical, neither are the grains of equal size. Level difference spectra have been measured over gravel with the source at a height of 0.097 m, upper and lower microphones at heights of 0.066 m and 0.053 m respectively and with a horizontal source-receiver separation of 0.353 m. Another geometry has been used but since it gives similar results these are not given here. Figure 4.25 (a) compares predictions using the slit pore layer, the Johnson-Allard-Umnova layer, phenomenological layer and variable porosity models. The agreement between data and predictions assuming external reaction and either the slit pore layer or Johnson-Allard-Umnova layer models is very good. The slit pore layer model uses the measured porosity value of 0.374 and measured layer depth of 0.12m. However, it uses an adjusted flow resistivity of 2.5 kPa s m^{-2} instead of the flow resistivity of 1.6 kPa s m^{-2} calculated from Eq. (4.96). The Johnson-Allard-Umnova layer model gives an equally good fit with flow resistivity of 1.6 kPa s m^{-2}, measured porosity value of 0.374, measured layer depth of 0.12 m and viscous characteristic length of 4.3×10^{-4} m. However, the viscous characteristic length is adjusted numerically to

obtained best fit to data [60]. It is concluded that reasonably good fits to excess attenuation data over gravel can be obtained using either the slit pore layer model or the Johnson-Allard-Umnova layer model with measured and calculated parameters. The agreement between data and phenomenological layer model predictions (see Fig. 4.23(a)) is not very good. It over-predicts the magnitudes of the level difference peaks and their frequency locations. Also the variable porosity model gives poor agreement with data thereby emphasizing the previous conclusion that while it gives very good predictions for grassland sites it fails for granular materials. Figure 4.25 (b) compares the predictions using as the Delany and Bazley layer, Taraldsen layer, Miki one parameter layer, and Miki two parameter layer models. For the first three models, the measured layer depth of 0.12 m is used. However for the Miki two parameter layer model a numerically obtained best fit layer depth of 0.09 m is used. The agreement between data and predictions using any of these empirical models is not good. These empirical models have been used also to fit the excess attenuation data using numerically obtained best fit impedance parameter values instead of measured values. It was found that numerically obtained best fit impedance parameters also failed to give good agreement with data except the Miki two parameter layer model which gives very good predictions by using effective layer depth of 0.09m instead of measured layer depth of 0.12m. The impedance parameter values used for different model predictions are detailed in the caption for Figure 4.25.
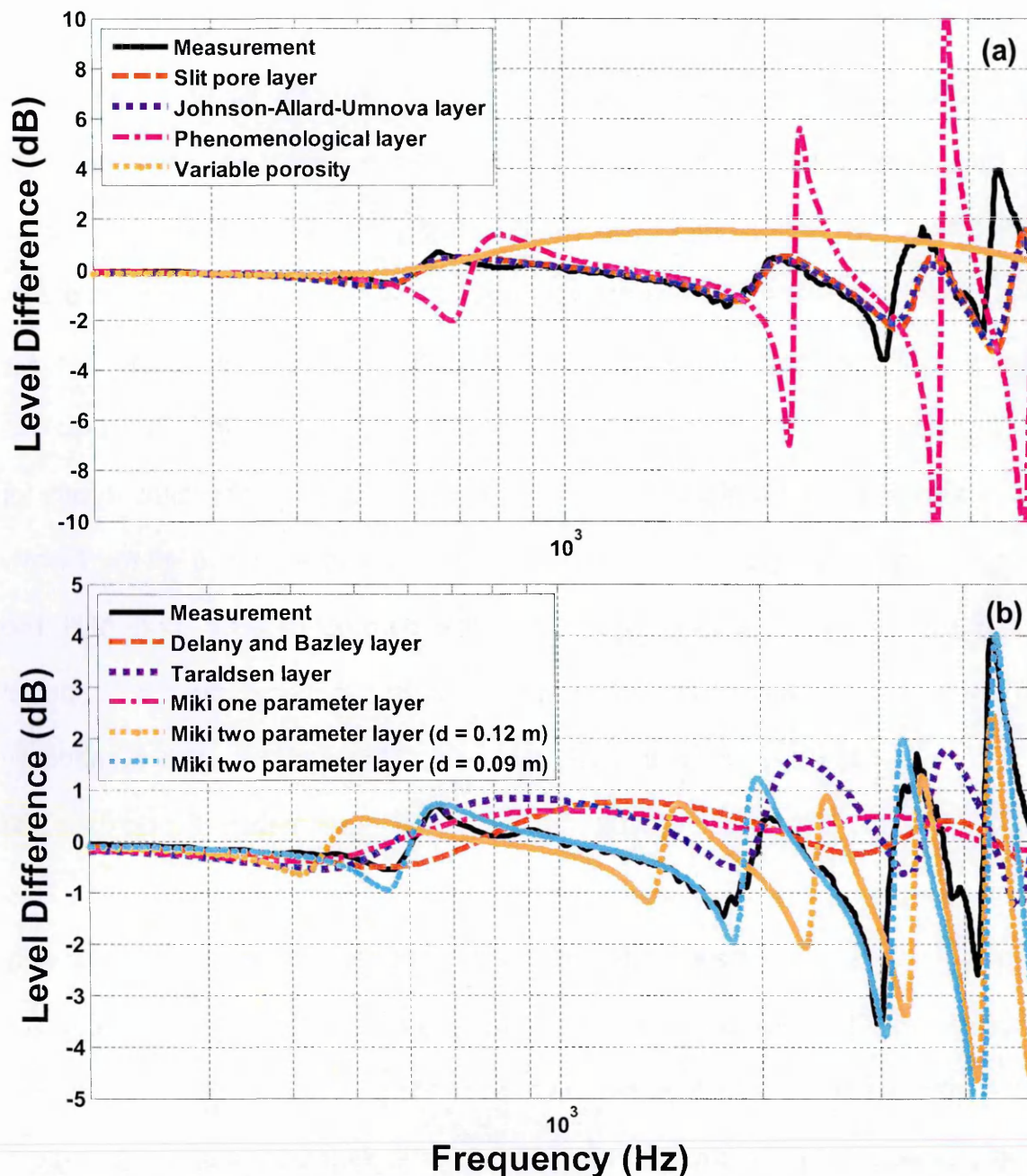
Figure 4.25 Comparison between measured level difference spectra (black continuous lines) over gravel having mean grain size of 4 mm, filling an 0.12 m deep rectangular box with source at height of 0.097 m, upper and lower microphone at height of 0.066 m and 0.053 m respectively and horizontal separation of 0.353 m with numerically obtained best fits using externally reacting (a) slit pore layer (red broken line) - R_s = 2.5 kPasm^{-2}, Ω = 0.374, d = 0.12 m; Johnson-Allard-Umnova layer (blue dotted line) - R_s = 1.6 kPasm^{-2}, Ω = 0.374, Λ = 4.3e-4, d = 0.12 m; phenomenological layer (magenta dash-dotted line) - R_s = 2.5 kPasm^{-2}, Ω = 0.374, d = 0.12 m; variable porosity (brown dotted-cross line) - R_s = 3.0 kPasm^{-2}, Porosity rate = 10 m^{-1}; (b) Delany and Bazley layer (red broken line) - R_s = 1.0 kPasm^{-2}, d = 0.12 m; Taraldsen layer (blue dotted line) - R_s = 3.0 kPasm^{-2}, d = 0.12 m; Miki layer one parameter (magenta dash-dotted line) - R_s = 2.5 kPasm^{-2}, d = 0.12 m; Miki layer two parameter (brown dotted-cross line) - R_s = 1.6 kPasm^{-2}, Ω = 0.374, d = 0.12 m; Miki layer two parameter (cyan dotted-dotted line) - R_s = 1.6 kPasm^{-2}, Ω = 0.374, d = 0.09 m.

4.7 Conclusions

Many impedance models have been reviewed and predictions obtained by using these models have been compared with measured data. The review has included one-parameter models including the Delany and Bazley model, the one-parameter Miki model and the Taraldsen model; two-parameter models including the phenomenological, variable porosity, two-parameter Miki and slit pore models and the four-parameter Johnson-Allard-Umnova model. A three-parameter slit pore model is converted into a two-parameter model by assuming a fixed relationship between porosity and tortuosity. Predictions for hard backed layered ground need the extra parameter of layer depth 'd'.

It is concluded that use of the slit pore model and phenomenological model shows best agreement with measured data and gives minimum error value for most of the ground sites. However, the phenomenological model fails to give good agreement over ground with low flow resistivity value such as railway ballast. Moreover, it also fails to give good agreement for laboratory data over gravel using measured impedance parameters. The Variable porosity model was found to give best agreement with measured data and minimum mean error value over grassland sites. On the basis reported in this Chapter, the slit pore model and variable porosity model are selected to be used to characterize the ground surfaces during the course of further research.

The Delany and Bazley one parameter model has been used successfully for many grassland sites. However, better predictions can be obtained by using either the two parameter slit pore model or the phenomenological model. Moreover, the two parameter variable porosity model enables best agreement to data over 26

grassland sites with mean error value (defined by Eq. (4.91)) of 6.7 dB. The fitting for some grassland sites is improved by using hard-backed-layer versions of the impedance models. The Taraldsen model gives similar error values to those obtained by using the Delany and Bazley model. The variable porosity model, the Delany and Bazley model and the Taraldsen model fail to give good fits, in terms of spectral shape and error values, to Nordtest forest floor data and to data for a newly laid single layer of porous asphalt. However, the slit pore and phenomenological models give equally good fits to level difference data obtained over newly laid porous asphalt and over most of the forest floor data sites. Similar results have been achieved in fitting data over 'Gravel in a pit' sites.

Laboratory measurements of excess attenuation spectra have been carried out over felt and foam surfaces and over surfaces composed from gravel and lead shot. All of the models enable good agreement to data obtained over the layer of felt placed over MDF board. However, only the slit pore layer model and the phenomenological layer model enable good agreement with measured excess attenuation over different types of open cell foam. A four parameter Johnson-Allard-Umnova model for granular materials enables good agreement with data. The slit pore layer and phenomenological layer models enable equally good fits for data over lead shot. However, the phenomenological layer model fails to give good agreement to low flow resistivity data over gravel. Use of empirical impedance models results in poor agreement to data over granular materials except that the Miki two parameter model can give reasonably good fit to data if the layer depth is regarded as an adjustable parameter.

There are some surfaces (e.g. felt) for which impedance model parameters cannot be measured or are very difficult to measure so the parameters are obtained empirically through fitting the data. However, even for materials such as lead shot for which, in principle, impedance parameters can be measured or determined from measurable parameters such as shot diameters and packing density, predictions using the measured parameters do not fit the data. This is due to the fact that the excess attenuation predictions assume propagation over idealised porous surfaces under ideal conditions. They do not include effects due to air absorption and non-ideal noise source and data acquisition characteristics such as directivity and finite bandwidth. Consequently there are always some discrepancies. Some other surfaces such as those of MDF or glass sheets are not porous but it is convenient to predict their acoustical properties by assuming a porous material impedance model. For such cases the impedance model is a surrogate for viscous and thermal boundary layer effects.

Chapter 5

5. Diffraction Assisted Rough

Ground Effect: Measurements

and Predictions

5.1 Introduction

As a result of increasing traffic in residential areas, highway noise is an increasing problem. A common remedy is to use noise barriers but these are visually intrusive and may divide communities so may not always be suitable. An alternative is to exploit the acoustical effects of the ground surfaces along and near the roads. Ground effect results from the interference between sound travelling directly from a source to a receiver and that reflected coherently from the ground. The frequencies associated with first and subsequent order destructive interference in Excess Attenuation (EA) spectra are determined by the source-receiver geometry and the ground impedance. Typically if the ground is hard and

smooth then at grazing incidence, i.e. source at a height of 0.01 m (road-tyre noise) and at a 1.5 m high receiver at least 10 m from a road, the first destructive interference occurs at too high a frequency to be useful in noise control as shown in Figure 5.1 (black line). On the other hand three destructive interference dips in the EA spectrum occur below 3 kHz at a 4 m high receiver which is 10 m from the 0.3 m high (engine) source in road traffic as shown in Figure 5.1 (red line). However, near grazing incidence, the effective impedance of a rough hard surface is finite so destructive interference can occur at much lower frequencies than if the surface is smooth, particularly for a low (0.01 m) source height. This suggests that a potential passive method of noise reduction is to exploit the acoustical properties of roughened hard ground surfaces between the road and listeners. This should be visually less intrusive than, for example, erecting noise barriers. This chapter reports work based on this idea.

To enable design of rough surfaces for reducing traffic noise by exploiting the space between the traffic noise source and the receiver, the sound propagation over different cross-sectional shaped roughness along with the effect of spacing between elements has been studied in the laboratory. The laboratory data have been used validate the prediction methods such as MST, BEM and FEM. BEM is further used to design real scale rough surfaces. The work has been extended to real scale outdoor measurements. Parallel walls and 3D lattice structures have been constructed using bricks on Open University car parks. The use of BEM to predicted the effect of parallel walls has been validated by outdoor measurements. Drive-by tests have been carried out to measure the insertion loss due to parallel walls and lattice structures.

This chapter describes laboratory and outdoor measurements over data over various rough surfaces. After reviewing previous work aimed at understanding and modelling sound scattering by roughness at scales significantly smaller than the smallest wavelength of interest in section 5.2, sections 5.3 – 5.6 report an extensive series of laboratory experiments on propagation over random and periodically-rough surfaces and comparisons of the resulting data with predictions (a) using various analytical models for effective impedance, including a new empirically-derived effective impedance model (section 5.6), and (b) numerical models (section 5.5). Section 5.7 explains a method devised for assessing the comparative overall reductions due to various roughness configurations. Section 5.8 describes how an FEM model has been used to make initial investigations of the novel idea of achieving excess attenuation by using resonant roughness elements. Conclusions from the experiments are drawn in section 5.9.

Section 5.10 describes how some of the conclusions drawn from the reported experimental work have been used for further numerical and experimental (including drive-by tests) exploration of rough surface scattering at a larger scale suitable for traffic noise reduction. Section 5.11 gives the conclusions from the work described in section 5.10.
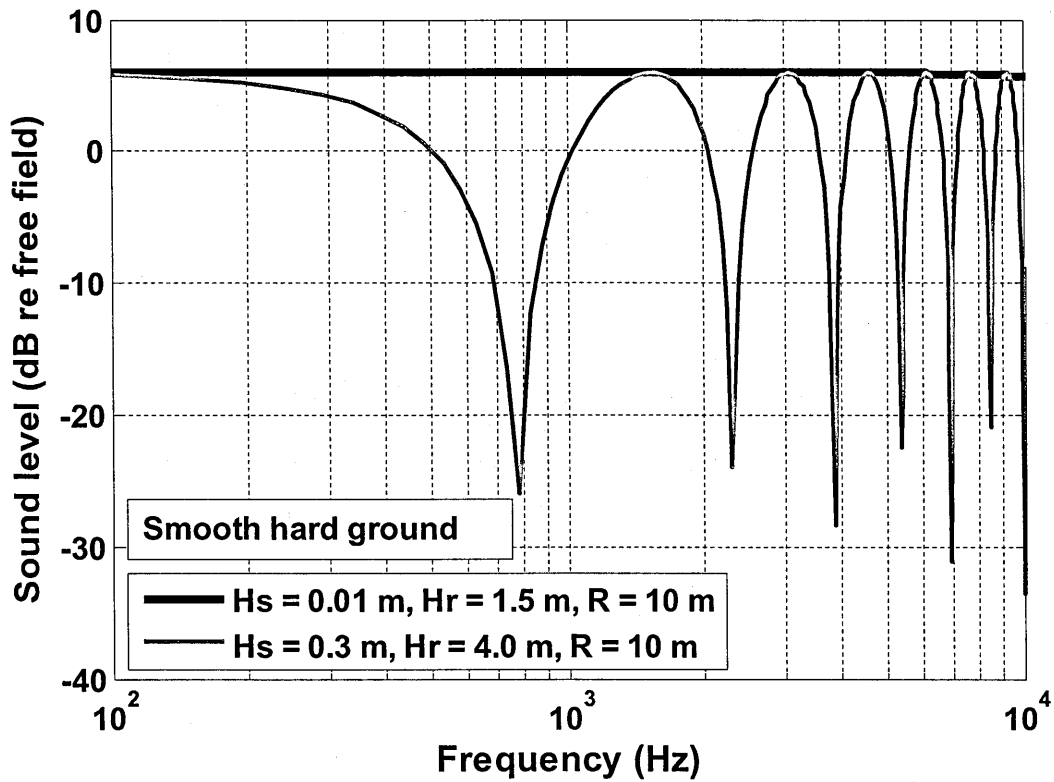
Figure 5.1 Predicted excess attenuation spectra over smooth hard ground for a source and receiver at a height of 0.01 m and 1.5 m respectively compared with predicted excess attenuation spectra over smooth hard ground for a source and receiver at a height of 0.3 m and 4.0 m respectively. The distance between source and receiver assumed to be 10 m.

5.2 Literature review

Consider a sound wave travelling in a medium across an obstruction, some of the wave energy is deflected or scattered from its original course and some may be absorbed i.e. converted into heat within the obstacle. Scattering causes the spreading out of (scattered) waves from the obstacle in all directions. Similarly, when sound waves propagate over a rough hard surface at near grazing angles, they are scattered both coherently and incoherently. The scattered waves may distort and interfere with the original wave and give rise to relatively complicated wave patterns. For a point source above a relatively smooth surface, the coherently scattered waves consist of direct and reflected waves. However, at near grazing angles an additional surface wave may be generated at a rough surface as long as the roughness height is small compared with the incident wavelengths,

$$P_t = P_d + P_r + P_s, \qquad\qquad (5.1)$$

where P_t is total wave, P_d is the direct wave, P_r is the reflected wave and P_s is the surface wave. The direct wave is the wave which travels directly between source and the receiver. The wave which is received at the specular angle after reflection from a rough surface is the coherently reflected wave. The surface wave is an evanescent wave which exists in the close vicinity of ground surface. A similar surface wave associated with propagation over a thin porous layer is associated with an imaginary part (reactance) of the surface impedance that is greater than the real part (resistance).

Seminal work on scattering by rough surfaces has been carried out by Biot, Twersky and Tolstoy. Biot [76], [77] developed a model for scattering of sound by hemi-spherical bosses whose dimensions and associated spacing were assumed to be small compared to the incident wavelength. He treated the roughness embedded in a plane as a continuous distribution of monopole and dipole sources. The resultant field at the receiver is the sum of diffracted fields from a rough surface. Biot [76], [77] derived expressions based on coherent reflection and did not account for incoherent scattering. Biot's generalised theory [77] allows for different scatterer shapes and non-uniform distributions.

In his earlier work, Twersky [78] presented the theory for reflection and scattering of plane waves of sound either from a single or a distribution of rigid semicylindrical or hemispherical bosses over an infinite plane. The multiple scattering effects due to neighbouring elements have been ignored in the formulation of sound scattering from periodic and randomly spaced bosses over an infinite plane. Twersky [79] modified his theory to take into account for acoustically soft roughness. Furthermore, Twersky [80] extended his work on scattering of sound from distributions of semi-cylinders and hemi-spheres to relate coherent specular scattering and incoherent scattering of sound through an energy principle. Twersky [81] approximated his formulation to obtain the solution for different shape roughness elements. However, by assuming that the scatterer sizes are small compared to incident wavelength, the incoherent scattering due to scatterers was treated by inclusion of separate loss terms [82]. In contrast to previous assumption, Burke and Twersky assumed that scattering objects are large as compare to the incident wavelength [82]. They considered the reflection,

refraction and scattering of sound from large objects or scatterers at longer distances.

In a later series of papers [83]–[87] on multiple scattering of sound, Twersky derived a theory for scattering of sound by a planar grating of equally spaced arbitrary semi-cylinders, a line of equally spaced identical obstacles and an uniform distribution of parallel cylinders. Twersky's model for sound propagation over bosses includes contributions due to coherent and incoherent sound scattering. The coherent scattering is modelled by adding the contributions due to each scatterer over a hard plane and incoherent scattering is modelled by adding some real part to the effective impedance. He then shows that periodically spaced roughness elements placed over a hard plane, only contribute to coherent scattering. However, randomly spaced roughness elements contribute to both coherent and incoherent sound scattering. Moreover, multiple scattering effects due to neighbouring elements have been taken into account by a mutual interaction term dependent on their centre-to-centre spacing

Consider a plane wave incident over a surface composed of semi-cylindrical roughness with radius a placed over a hard plane with centre-to-centre spacing of b as shown in Figure 5.2. Representing the angle of incidence with respect to normal by α and the azimuthal angle between the wave vector and the roughness axes by φ, the effective relative admittance β of a rough hard surface containing non–periodically or periodically spaced 2-D circular semi-cylinders may be written as [61], [8] - [12],

$$\beta = \eta - i\xi,$$ (5.2)

where,

$$\xi(\alpha,\varphi) \approx kV\left[-1+\left(\delta\cos^2(\varphi)+\sin^2(\varphi)\right)\sin^2(\alpha)\right]+O(k^3),$$ (5.3)

$$\eta(\alpha,\varphi) \approx \frac{nk^3\pi^2 a^4}{8}(1-W^2)\left\{\left(1-\sin^2\alpha\sin^2\varphi\right)\left[1+\left(\frac{\delta^2}{2}\cos^2\varphi-\sin^2\varphi\right)\sin^2\alpha\right]\right\}+O(k^5).$$ (5.4)

where $O()$ represents the order of error. If the number of semi-cylinders per unit length is n, given by $n = 1/b$ then the total raised cross sectional area per unit length is $V = n\pi a^2 / 2$. Delta (δ) is a measure of the mutual coupling between the semi-cylinders due to multiple scattering effect. The mutual coupling between elements depends on the scatterer size and centre-to-centre spacing. The mutual coupling between elements increases with the increase in scatterer size and decreases with the increase of centre-to-centre spacing. The dipole coupling factor is given as,

$$\delta = \frac{2}{1+I}, \quad I = \frac{a^2}{b^2}I_2,$$ (5.5 a, b)

where,

$$I_2 \cong 2W\left(1+0.307W+0.137W^2\right), \quad for \ W < 0.8,$$ (5.6)

$$I_2 \cong \frac{\pi^2}{3}\left[1-\frac{2(1-W)}{W}\right]+\frac{6(1-W)^2}{W^2}\left[\frac{\pi^2}{6}+1.202\right], \quad for \ W \geq 0.8,$$ (5.7)

$$I_2 \cong \frac{\pi^2}{3}, \quad for \ periodic \ spacing \ W = 1.$$ (5.8)

For randomly spaced semi-cylindrical roughness, W is the minimum centre-to-centre spacing and for periodically spaced elements, it is equal to 1. The

incoherent scattering included by introducing a real part to the admittance (see Eq. 5.2) is strongly dependent on the packing factor given by $(1-W)^2$. For grazing incidence normal to the cylinder axes, $\alpha = \pi/2$ and azimuthal angle $\varphi = 0$, the admittance for randomly-spaced semi-cylindrical roughness is simplified to,

$$\beta = \frac{na^2k}{2}\left((1-W^2)\frac{(1+\delta^2/2)k^2\pi^2a^2}{4} - i\pi(\delta-1)\right). \tag{5.9}$$

For periodically-distributed semi-cylindrical roughness, $W = 1$ the real part equal to zero and (5.9) simplifies to a purely imaginary admittance,

$$\beta = \frac{na^2k}{2}\left(-i\pi(\delta-1)\right), \tag{5.10}$$

For semi-elliptical cylinders with eccentricity K, the raised cross-sectional area per unit length is modified to $V = n\pi a^2 K/2$. The dipole coupling factor given by Eq. 5.5 (a) is modified to,

$$\delta = \frac{1+K}{1+I\frac{K(1+K)}{2}}. \tag{5.11}$$
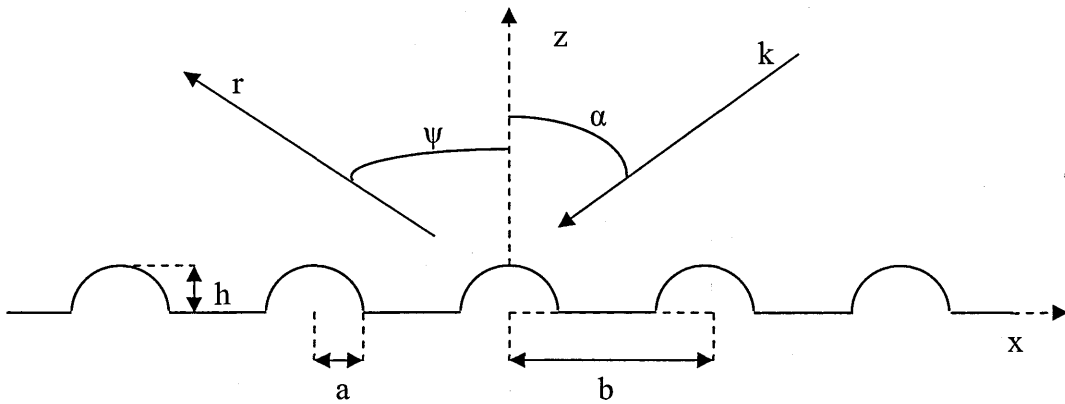
Figure 5.2 The 2-D representation of a plane wave incident on a surface containing a regularly spaced grating of semi-cylindrical roughness.

Tolstoy [88]–[90] formulated stochastic and boss models for predicting scattering of sound from surface roughness which is small compared to the incident wavelength. Tolstoy's models [88]–[90] are derived from Biot [76], [77] and Twersky [78] - [87] theories by using suitable boundary conditions at a smoothed boundary. Tolstoy's formulation [88] includes the addition of two different propagating waves; a body wave and a boundary wave. The body wave consists of the direct and reflected sound waves modified by roughness. The boundary wave is produced by energy trapping between the roughness elements. It only exists in close vicinity to the rough surface, propagates with cylindrical spreading along the roughness and attenuates exponentially with height. It is important to note that this boundary wave is a surface wave. In Chapter 8 we use the term surface wave but for here we will continue to use the term boundary wave as in the papers being reviewed to avoid confusion. Medwin *et al* [91] devised a model experiment to test Tolstoy's theoretical formulation [88]. A rough surface was constructed of close-packed rigid hemispherical bosses. The purpose was to validate the existence of the predicted boundary wave, and to show that it is strongest near grazing. A point source and a receiver were embedded in the rough plane flush with the surface to measure the boundary wave. The agreement between measured data [91] and Tolstoy's theory [88] was found to be reasonably good. Tolstoy [89] extended his formulation for other roughness shapes such as spheroidal and cylindrical cross-sections. Unlike Twersky, Tolstoy [90] ignored the incoherent scattering and his formulation assumes only coherent scattering from a rough surface. Tolstoy explained that the most of the energy scattered from a rough surface has a phase relationship to the incident wave. However this phenomenon holds only for coherent reflection and it valid only when the spacing

and perturbation dimensions are small compared to the wavelength. Tolstoy replaced the scatterers on a plane with a distribution of monopole and dipole sources. Since they do not include incoherent scatter, Tolstoy's models predict that the effective impedance of a rough hard surface is purely imaginary (see Eq. (5.12)). According to Tolstoy, the admittance (inverse of impedance) for arbitrary shaped scatterers is given by [61], [88]–[92],

$$\beta = -ik\varepsilon\left(\cos^2 \varphi - \sigma \cos^2 \alpha\right), \tag{5.12}$$

where k is the wave number, α is the angle of incidence with respect to normal and φ is the azimuthal angle between the wave vector and the roughness. The scattering coefficient ε is the key parameter in determining the rough ground effect, due to the fact that the correction parameter is a very small number at near grazing incidence. The scattering coefficient ε and correction coefficient σ are given by,

$$\varepsilon = V\left(\frac{2s_2}{v_2} - 1\right), \tag{5.13}$$

$$\sigma = \left(\frac{2s_2}{v_2} - 1\right)^{-1}. \tag{5.14}$$

$V = nA$ is the cross-sectional scatterer area above the plane per unit length, n is number of scatterer per unit length and A is the area of a single scatterer. $s_2 = \frac{1}{2}(1+K)$ is the shape factor for arbitrary shaped scatterer in which K is called as hydrodynamic factor or virtual mass. The virtual mass a body is defined as steady potential flow around that scatterer. Well established fluid dynamics theory

enables calculation of the hydrodynamic factor [90]. The values of K for simple smooth shapes whose surface integral can be obtained easily such as sphere, circular cylinder and semi-cylinders are 0.5, 1.0 and 1.0 respectively. For semi-elliptical cylinders, $K = \dfrac{h}{a}$, where h is the height and a is the semi-base. Values of K for more complex shapes will be presented later.

Medwin *et al.* [91] have carried out experimental studies of scattering of sound from a hemispherical boss surface at near grazing angles. They [93] extended their laboratory experiments to other cross-sectional shape roughness elements. Measurements were carried out over a surface composed of close packed rigid spheres on a rigid plane. Measured data was found to give good agreement with Tolstoy theory for short range experiments of up to 50 cm. However, for longer ranges the agreement between data and theory was not very good. Medwin *et al.* [93] argued that this disagreement arises, because Tolstoy's theory overestimates the boundary wave component at longer ranges. According to Tolstoy, the boundary wave continues to grow as it propagates over a rough surface. However, Medwin's model experiments show that it grows up to a certain range and then it stays the same. This is due to incoherent energy loss and other attenuation mechanisms such as boundary wave dispersion at ranges greater than 50 cm. To improve agreement with their experimental data at longer ranges, Medwin *et al.* [93], [94] heuristically modified Tolstoy theory to include a loss term. Also Medwin *et al.* [93], [94] carried out experiments over closed packed and regularly-spaced full-cylindrical and semi-cylindrical roughness on a hard ground plane. It was concluded that measured propagation over closed packed roughness elements show good agreement with the theory. However, the agreement between

data and spaced cylindrical roughness was poor. Medwin *et al.* [93] also investigated the propagation of sound over wedge-shaped corrugations with different wedge angles and heights. Tolstoy's theory predicts that the coherent reflection from rough surface depends mostly on the cross-sectional area of the scatterer. However, Medwin *et al.* [93], [94] concluded that for same volume/area ratio wedges, having different wedge slopes give significantly different spectra. Moreover, they showed that the scattering coefficient is a function of roughness slope. Based on experimental data over various closed packed wedges Medwin *et al.* [93], [94] proposed hydrodynamic shape factors for wedges, given by,

$$K = 1.05(h/u) + 0.14(h/u)^2,$$ (5.15)

where h is the height of the triangular wedges and u is the side of the wedge. Medwin's shows that using Eq. (5.15) along with Tolstoy theory gives good agreement between prediction and measured data over closed packed wedges. In summary, the important conclusions from Medwin *et al.* [91], [93], [94] measurements, most of which were carried out over closed packed hemi-spherical, spheres, cylinders, semi-cylinders and triangular bosses embedded in a hard plane, are (i) that Tolstoy's theory with some empirical corrections to the scattering coefficient gives predictions in good agreement with data obtained over close packed rough surfaces and (ii) that the agreement between measured data over *spaced* semi-cylindrical roughness and Tolstoy theory is not so good.

Howe [95] proposed that a rough surface can be modelled as having an effective impedance. Attenborough and Taherzadeh [96] modified Tolstoy and Howe theories and obtained good agreement with laboratory measured data over

rough surfaces. Attenborough and Taherzadeh [96] proposed that the rough surface can be treated as a smooth surface with a modified surface admittance. This is very useful for predicting sound propagation over a rough surface when both source and receiver are elevated above the rough surface. The effective impedance of a rough surface can be used in a standard model for propagation over a finite impedance surface (see Eq. 5.69 - 5.73) to predict excess attenuation spectra over a rough surface for a given geometry. Chambers *et al.* [97] carried out experiments over rough surfaces and compared the resulting data with predictions using Attenborough and Taherzadeh's [96] model. He found that the agreement between measured excess attenuation and predictions is reasonably good. Twersky's boss theory is only valid for cylindrical bosses; however the Tolstoy's boss theory is valid for arbitrarily shaped scatterers. Boulanger *et al.* [61] heuristically generalized Twersky's cylindrical boss theory (see Eq. 5.2 – 5.11) to obtain a formulation for arbitrary shaped scatterers by comparing it with equivalent work by Tolstoy (see Eq. 5.12 – 5.15). Boulanger *et al.* [61] suggested that Twersky's and Tolstoy's expressions for the imaginary part of effective admittance are equivalent for circular semi-cylinders if δ is replaced by $\varepsilon / V + 1 = 2s_2 / v_2$.

According to Boulanger *et al.* [61], the simplified Tolstoy's expressions for scattering coefficient ε and correction coefficient σ for semi-cylindrical bosses are given by,

$$\varepsilon = \frac{\pi a^2}{2b} \left(\frac{2}{1 + \left(\pi^2 / 3 \right) \left(a / b \right)^2} - 1 \right), \tag{5.16}$$

$$\sigma = \left(\frac{2}{1 + \left(\pi^2/3\right)\left(a/b\right)^2} - 1 \right)^{-1}.$$

(5.17)

For oblique incidence at grazing angle α and azimuthal angle φ to the semi-cylindrical roughness axes, the effective admittance using Eq. 5.12 of a surface containing 2-D roughness is given by ,

$$\beta = -ik\varepsilon.$$

(5.18)

Putting Eq. 5.16 into Eq. 5.18 gives the admittance based on Tolstoy theory,

$$\beta = -ik\frac{\pi a^2}{2b}\left(\frac{2}{1 + \left(\pi^2/3\right)\left(a/b\right)^2} - 1 \right).$$

(5.19)

Twersky's semi-cylindrical boss model can be simplified to obtain an equivalent form to Tolstoy's model. Eq. 5.3 can be simplified by using the trigonometric identity, $\sin^2 \theta = 1 - \cos^2 \theta$.

$$\xi(\alpha,\varphi) \approx kV\left[(\delta - 1)\cos^2(\varphi) - \cos^2(\alpha)\left(1 + (\delta - 1)\cos^2(\varphi)\right) \right].$$

(5.20)

The admittance for a periodically spaced roughness from Eq. 5.2 is given by,

$$\beta = -i\xi.$$

(5.21)

Putting Eq. 5.20 into Eq. 5.21 and simplifying it using Eqs. 5.5 through 5.8 gives,

$$\beta = -ik\frac{\pi a^2}{2b}\left(\frac{2}{1 + \left(\pi^2/3\right)\left(a/b\right)^2} - 1 \right).$$

(5.22)

The admittance for semi-cylindrical bosses given by Tolstoy (see Eq. 5.19) is identical to what we obtain from Twersky's semi-cylindrical boss model (see Eq. 5.22). Similarly, Eq. 5.4 can be rewritten as,

$$\eta(\alpha,\varphi) \approx \frac{k^3 b V^2}{2}(1-W^2)\left\{\left(1-\sin^2\alpha\sin^2\varphi\right)\left[1+\left(\frac{\delta^2}{2}\cos^2\varphi-\sin^2\varphi\right)\sin^2\alpha\right]\right\}. \tag{5.23}$$

A heuristic generalization of Twersky theory by making δ dependent on shape factor makes it possible to predict the admittance for arbitrary shaped scatterers. The shape factor is determined by hydrodynamic factor K. As a result δ is dependent on K. The hydrodynamic factor for different cross-sections of scatterers is given in Table 5.1.

Table 5.1 Hydrodynamic shape factor (K).

Roughness shape	Formula
Semi-cylinders	1
Semi-elliptical	height/semi-base
Triangular wedges	1.05(h/u)+0.14(h/u)²
Rectangular strips	2(height/base)
Thin rectangles	1

Measured excess attenuation spectra over periodically spaced different cross-sectional shapes show multiple excess attenuation maxima [61]. However, the modified Tolsty/Twersky theory predicts a single excess attenuation maximum. Boulanger *et al.* [61] explained that these additional maxima observed over periodic rough surfaces are caused by diffraction grating effects. They [61]

incorporated the diffraction grating effect by heuristically modifying the classical analytical approximation for the propagation of sound from a point source over an impedance plan at near grazing incidence (see Eq. 4.69 - 4.73). An additional term was used to include the diffraction grating effect. The total pressure at the receiver due to a point source after propagation over a periodic rough surface is given by [61],

$$P_{total} = P_{direct} + P_{reflected} + P_{diffracted},$$
(5.24)

where P_{direct} is the pressure due to direct wave from the source. If R_1 is the direct path length from source to receiver, then P_{direct} is given by,

$$P_{direct} = \frac{P_o e^{ikR_1}}{R_1},$$
(5.25)

$P_{reflected}$ is the pressure due to reflected wave from the rough surface given by,

$$P_{reflected} = \frac{QP_o e^{ikR_2}}{R_2},$$
(5.26)

R_2 is the reflected path length from source to receiver through specular reflection point and Q is the spherical wave reflection coefficient (see section 4.4.1 for details). $P_{diffracted}$ is the diffracted term from roughness elements given by,

$$P_{diffracted} = \frac{P_o e^{ik(R_2 + \Delta)}}{R_2 + \Delta},$$
(5.27)

where $\Delta = pb\sin\alpha$ is the extra path length due to wave diffraction grating phenomenon and p is an integer depending on the order of the interference. According to the law of conservation of energy, the energy scattered by roughness is divided between reflected and diffracted waves. Eq. 5.28 modified according to law of conservation of energy is given by,

$$P_{total} = P_{direct} + W_a P_{reflected} + W_b P_{diffracted},$$
(5.28)

where W_b is the proportion of the ground between source and receiver that is covered by roughness and $W_a = 1 - W_b$ is the proportion of the ground not covered by roughness. In the original paper [61], there might be a typographical error because P_{direct} is also multiplied by the W_a factor. The measured excess attenuation over periodically spaced roughness shows some good agreement with heuristically modified and extended Twersky/Tolstoy model predictions. Attenborough and Waters-Fuller [98] carried out excess attenuation measurement over a rough porous ground surface. The surface is made with sand and approximately semi-cylindrical soft roughness was created on the surface. The measured data was compared with predictions using the Twersky-Boulanger boss model, which gives reasonable agreement. Twersky [85] also presented the theory of reflection from porous roughness elements over a hard plane. To check validity of this theory, Boulanger *et al.* [99] carried out measurement of surfaces composed of porous roughness such as polystyrene hemispheres, polystyrene pyramids and hemispheroids of sand on a glass sheet. Twersky's theory for the effective admittance of a surface containing porous roughness elements on a hard plane along with slit pore model [33] to define the acoustical characteristics of

porous roughness was used for prediction. The agreement between measured excess attenuation and prediction was found to be satisfactory.

Boulanger *et al.* [19] have developed a model for acoustic scattering by a finite array of semi-cylinders embedded in a smooth hard surface using multiple scattering theory. This semi-analytical theory is more accurate for prediction than the boss theories described earlier. The predictions of this semi-analytical theory were shown to be in good agreement with results of measurements on randomly-spaced roughness but the theory is valid only if the roughness elements are semi-cylindrical. The details of this multiple scattering theory are given in chapter 2.

5.3 Laboratory investigations of scattering by randomly- and periodically-rough boundaries

The laboratory measurement system and measurement procedures used for investigating propagation over rough surfaces are explained in Chapter 3. Figure 5.3 shows a typical experimental arrangement for square strips arranged periodically on a glass sheet. As described in the previous section, in the past, most experimental work has been carried out over randomly spaced or close-packed roughness elements. This section presents a comprehensive experimental study of the sound pressure level spectra relative to free field above periodically and randomly spaced roughness elements. Since relatively little is known about the ground effect spectra that result from periodically-distributed roughness and the effects of roughness element shapes, systematic measurements have been made in an anechoic chamber of EA spectra due to a point source over variously shaped, periodically-spaced identical roughness configurations on an acoustically-hard boundary. Measurements have been made of sound propagation over several small scale roughness formed by placing strips of different cross-sectional shapes (semi cylindrical, triangular, short rectangular, tall rectangular, metal rectangular and (approximately) square) with random or periodic spacing on the glass sheet. The strip locations were centred on the point of specular reflection which was halfway between source and receiver since they were at equal heights. The roughness arrays had centre-to-centre spacing of between 0.03 m to 0.08 m. The cross sectional shapes and dimensions of the strips are given in Table 5.2. The following subsections will provide the details and analysis of data collected in laboratory and their comparison with predictions along with some discussion.
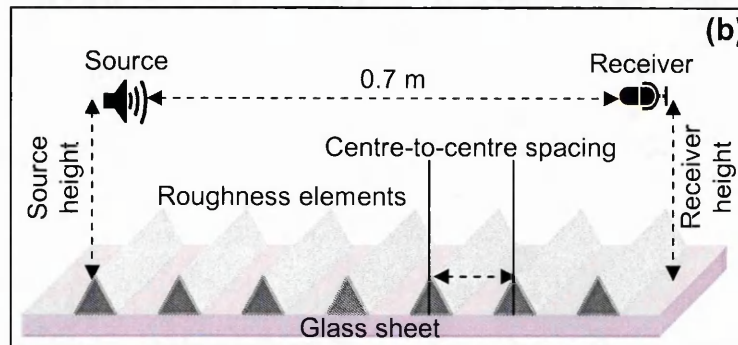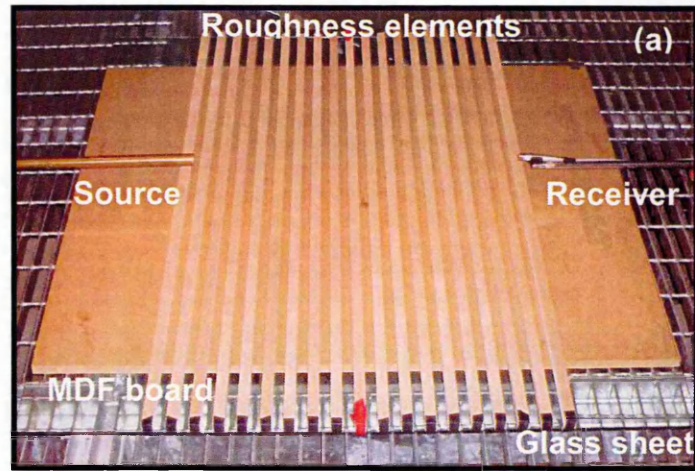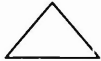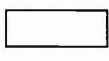
Figure 5.3 (a) photograph of a measurement over periodically arranged square strips (b) a schematic of the laboratory geometry.

Table 5.2 Characteristic of roughness elements.

	Shape	Height (m)	Width (m)	Cross sectional area mm²
Semi-Cylinders		0.008	0.020	117
Triangular Strips		0.015	0.030	218
Short Rectangular Strips		0.012	0.0285	342
Tall Rectangular Strips		0.0285	0.012	342
Tall Rectangular Metal Strips		0.025	0.013	325
'Square' Strips		0.018	0.020	360

5.3.1 Data for random spacing

Identical strips having one of the cross-sections listed in Table 5.2 were located randomly between source and receiver. For comparison with corresponding periodic configurations, the spacings between the strips were normalized such that the sum of the separations divided by the total number of strips was equal to the mean centre-to-centre spacing. To avoid overlapping roughness elements, a set of random numbers were generated with a mean value equal to the edge-to-edge distance (i. e, the centre-to-centre spacing minus the strip width). Five random distributions were tested for each mean centre-to-centre spacing between 0.03 m and 0.08 m. The individual edge-to-edge spacings between roughness elements for each distribution are listed in Table 5.3.
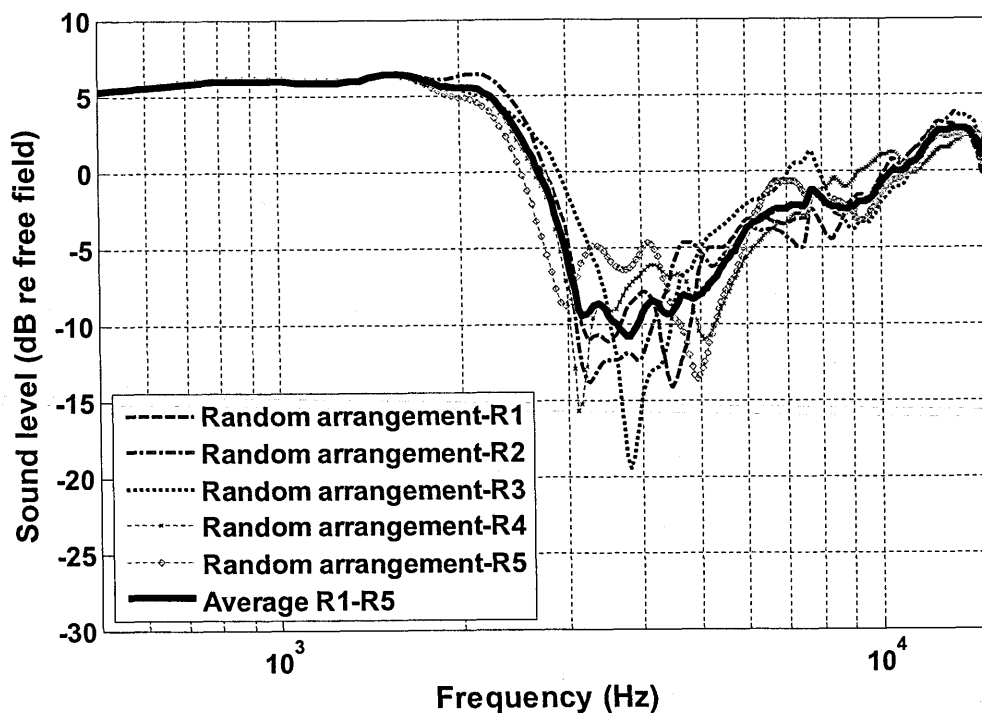
Figure 5.4 EA spectra measured over 15 randomly spaced parallel triangular strips with mean centre-to-centre spacing of 0.05 m with source and receiver at a height of 0.07 m and separated by 0.7 m. The data correspond to five different random distributions (R1-blue dashed line, R2-red dash-dotted line, R3-magenta dotted line, R4-brown dotted-cross line, R5-green dotted-diamond line) and the average spectrum is shown also (black solid line).

Figure 5.4 shows the measured EA spectra for each of five random distributions of 15 triangular strips with mean centre-to-centre spacing of 0.05 m and the arithmetic mean spectrum. As is conventional, the excess attenuation maxima are shown as minima. The averaging of the EA spectra reduces and broadens the ground effect dips due to each deterministic random distribution.

Averages of EA spectra measured over five random distributions of strips with source and receiver height at 0.07 m separated by 0.7 m over surfaces composed of semi-cylinders (black solid line), triangular strips (blue dashed line), square strips (red dotted line), short rectangular strips (magenta dash-dotted line) or tall rectangular strips (brown dash-diamond line) randomly spaced on a glass sheet are shown in Figures 5.5 (a) and (b). For source and receiver heights of 0.07 m and a separation of 0.7 m, the first destructive interference above a smooth hard ground should occur at a frequency of 12.3 kHz. This is confirmed by the EA spectrum measured over the glass plate alone (no roughness). The measured EA maxima in the presence of identical randomly spaced strips with various cross-sectional shapes (semi cylindrical, triangular, square, short rectangular and tall rectangular) are at lower frequencies. Moreover, for a given average spacing, these maxima increase in magnitude and become sharper as the roughness height increases. There is not much difference between the EA spectra measured for average random spacings of 0.05 m and 0.08 m.
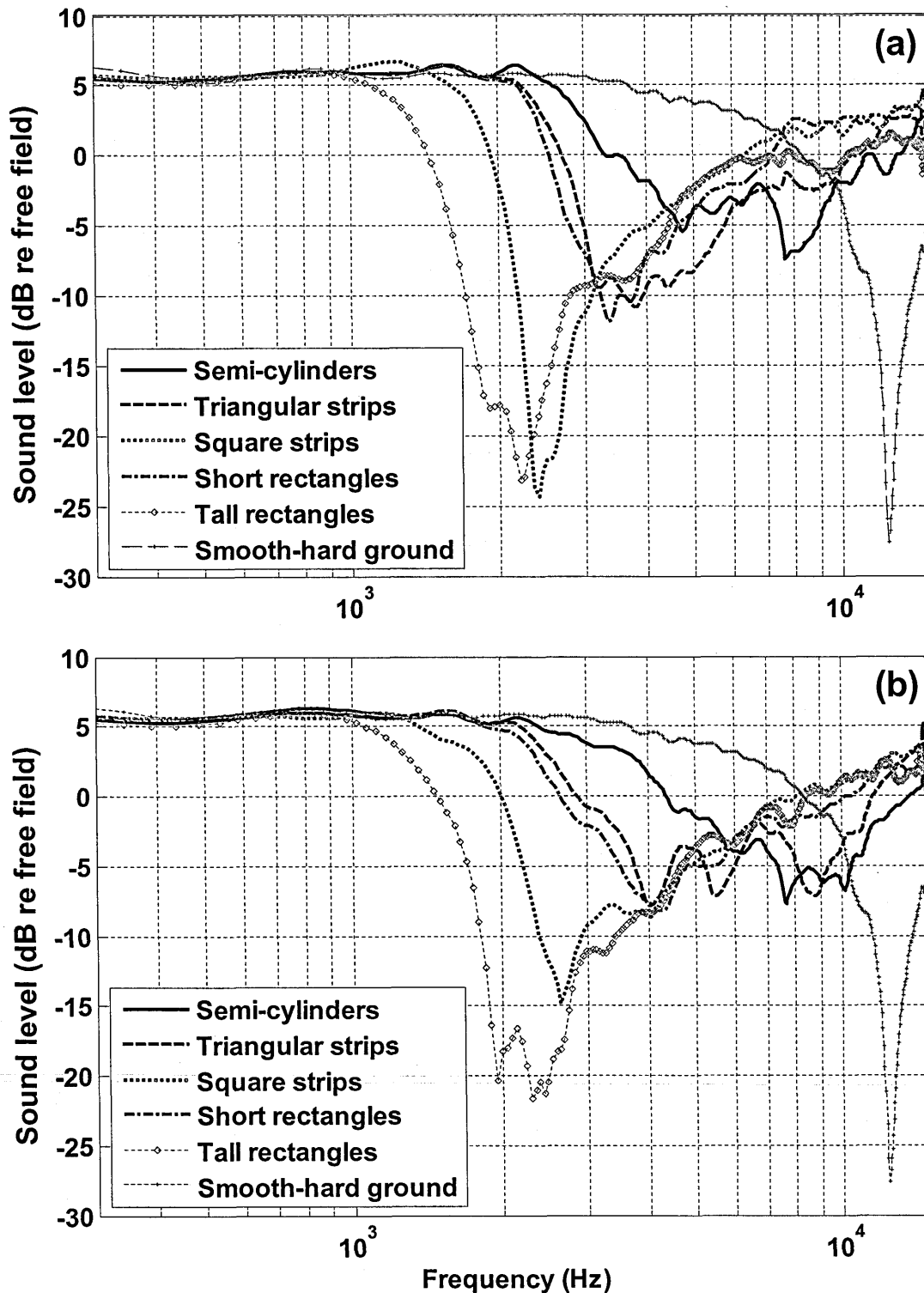
Figure 5.5 Averages of EA spectra measured over five random distributions of strips with source and receiver height at 0.07 m separated by 0.7 m over surfaces composed of semi-cylinders (black solid line), triangular strips (blue dashed line), square strips (red dotted line), short rectangular strips (magenta dash-dotted line) or tall rectangular strips (brown dash-diamond line) randomly spaced on a glass sheet with mean centre-to-centre spacing of (a) 0.05 m and (b) 0.08 m. In both cases the EA spectra measured over the smooth hard glass sheet (no roughness) are shown by the dotted (purple asterisk) curves.

Table 5.3 Randomly-generated, normalized roughness elements edge-to-edge separations.

Average edge-to-edge spacing	#	Edge-to-edge distances (cm) between adjacent strips													
		x1	*x2*	*x3*	*x4*	*x5*	*x6*	*x7*	*x8*	*x9*	*x10*	*x11*	*x12*	*x13*	*x14*
1cm (normalized sum of 14 cm)	R1	1.3	1.4	0.2	1.5	1.0	0.2	0.4	0.9	1.5	1.5	0.3	0.5	2.5	0.8
	R2	2.3	0.7	0.4	1.0	0.9	1.3	1.4	1.5	0.5	1.3	1.3	0.3	0.2	0.9
	R3	1.7	1.8	1.3	1.5	1.5	0.8	1.3	0.3	1.4	0.1	0.5	0.1	0.2	1.5
	R4	1.2	0.2	0.7	1.4	1.2	1.5	1.0	0.1	1.3	1.4	1.0	1.2	1.1	0.7
	R5	1.6	0.4	1.8	0.1	0.7	0.1	0.2	2.0	1.7	0.8	2.4	0.1	1.1	0.9
2cm (normalized sum of 28 cm)	R1	0.8	3.3	0.6	3.0	2.0	3.6	0.3	1.6	0.4	3.5	0.0	2.8	3.0	3.1
	R2	0.4	1.9	1.3	3.9	2.1	4.4	0.9	1.3	0.7	0.7	4.2	2.8	2.7	0.7
	R3	4.0	2.9	1.7	2.4	1.9	0.4	1.1	0.6	0.9	1.1	2.0	0.2	4.3	4.5
	R4	2.6	2.9	0.4	2.9	2.0	0.3	0.9	1.7	3.0	3.1	0.5	3.1	3.0	1.6
	R5	2.9	0.3	1.2	1.8	4.1	0.1	0.2	0.8	3.2	3.7	3.2	2.3	2.7	1.5
3cm (normalized sum of 42 cm)	R1	4.5	4.6	1.1	2.9	2.6	3.8	4.1	4.4	1.6	4.0	3.8	1.0	0.7	2.9
	R2	5.5	2.0	3.4	1.3	4.3	1.5	2.9	4.0	5.2	5.5	3.2	0.8	0.9	1.5
	R3	4.8	1.5	4.7	1.4	5.4	2.0	1.1	1.4	3.6	2.7	2.0	4.8	3.4	3.2
	R4	5.3	1.7	4.4	4.4	2.2	3.3	0.4	0.3	3.1	4.5	5.4	0.8	3.3	2.9
	R5	3.7	0.7	2.0	4.2	3.7	4.4	3.0	0.2	3.9	4.3	3.1	3.5	3.4	1.9
4cm (normalized sum of 48 cm)	R1	5.3	5.9	0.8	6.0	4.1	0.6	1.8	3.6	6.2	6.3	1.0	6.4		
	R2	5.8	2.9	4.8	0.9	2.5	5.5	4.8	5.8	4.0	0.2	5.1	5.7		
	R3	6.1	6.8	6.6	3.5	5.8	1.5	6.3	0.3	2.5	0.4	0.9	7.3		
	R4	5.4	2.5	7.4	0.3	3.4	3.0	6.0	6.2	1.5	3.8	3.5	5.0		
	R5	5.7	6.1	2.2	5.5	5.3	1.3	1.0	4.0	7.7	2.7	4.7	1.8		
5cm (normalized sum of 50 cm)	R1	7.3	2.5	4.9	6.8	8.6	9.3	5.3	1.3	1.4	2.6				
	R2	2.9	6.9	4.9	4.6	7.7	2.4	6.3	6.3	3.2	4.8				
	R3	1.0	0.7	6.8	10	12	1.7	7.3	6.0	0.2	4.3				
	R4	1.6	8.1	3.2	5.4	1.7	6.1	2.7	6.6	7.0	7.6				
	R5	4.8	0.9	2.4	9.7	1.6	8.8	5.7	11	0.8	4.7				
6cm (normalized sum of 48 cm)	R1	1.3	11.5	0.1	9.3	9.8	10.4	1.0	4.6						
	R2	4.0	12.3	6.6	14	2.8	4.0	2.2	2.1						
	R3	9.3	6.2	5.9	1.6	9.1	6.7	3.8	5.4						
	R4	11	2.1	6.6	3.4	5.1	6.7	12	1.4						
	R5	9.5	10	5.2	5.2	3.6	9.5	3.9	1.1						

5.3.2 Data for periodic spacing

Figure 5.6 shows EA spectra obtained over a glass sheet on which were placed odd numbers of semi-cylindrical strips (between one and fifteen) at a regular centre-to-centre spacing of 0.05 m. The first strip was placed at the specular reflection point, i.e. halfway between source and receiver since the source and receiver heights were equal and alone causes a measurable change in the first destructive interference observed for the smooth glass sheet. Subsequently strips were placed symmetrically either side of this location. The frequency of the first (lowest frequency) EA maximum shifts to lower frequencies as the number of strips increases and multiple distinct narrow maxima are created compared with the broader EA maxima observed for random spacing (see Figures 5.4 and 5.5).
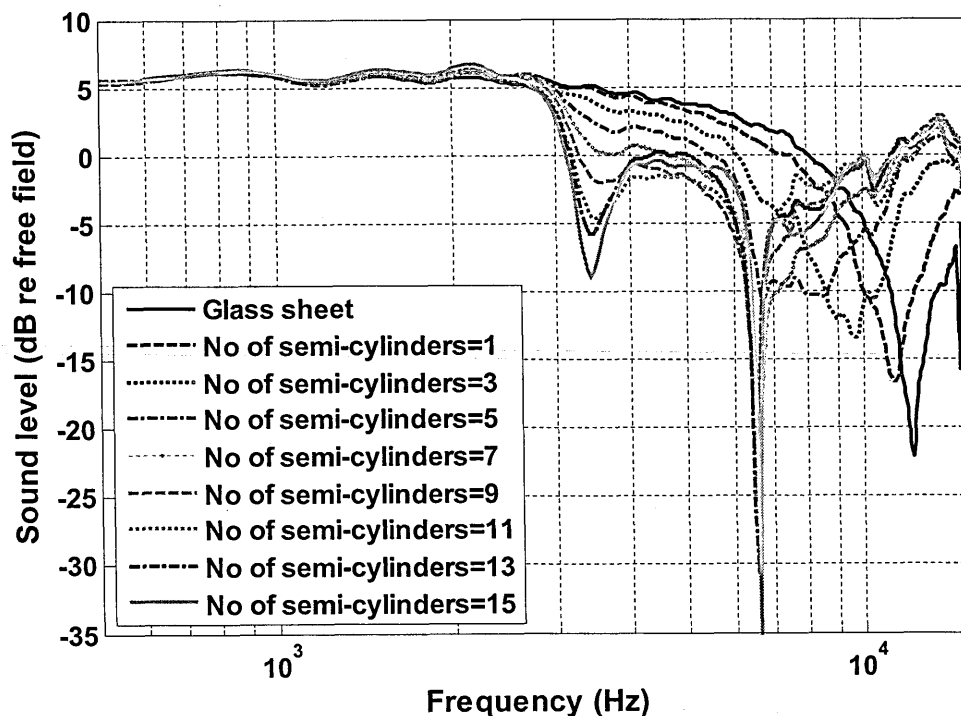
Figure 5.6 Measured EA spectra for source and receiver heights of 0.07 m separated by 0.7 m over surfaces including between 3 and 15 semi-cylindrical strips with regular centre-to-centre spacing of 0.05 m. The measured EA spectrum for the smooth glass sheet (no roughness) is shown by the solid black line.

Note that even with only one semi-cylinder at the specular reflection point; the EA differs from that obtained with the glass sheet alone. Introducing three or more semi-cylinders causes significant departures from the excess attenuation spectrum for smooth surface. In contrast to the spectra measured with randomly spaced roughness elements, which exhibit a single broad EA maximum, those obtained with periodic spacing show the development of up to three distinct EA maxima.

Measured EA spectra for regularly-spaced triangular strips (see Figure 5.7) show that the two distinct EA maxima at 3.7 kHz and 8.4 kHz for a centre-to-centre spacing of 0.04 m (black solid line) shift to lower frequencies if the centre-to-centre spacing is increased to 0.06 m (blue dash line). With a 0.06 m centre-to-centre spacing there is some indication of a third EA maximum near 7 kHz. At a centre-to-centre spacing of 0.07 m (red dotted line) a third EA maximum is clear at 7.3 kHz while the other maxima move to even lower frequencies and that at the lowest frequency (near 2.5 kHz) becomes relatively shallow. Similar behavior has been observed in the EA spectra obtained over strips with other cross-sectional shapes (square, short and tall rectangles). The magnitude, number and frequency of occurrence of the multiple EA maxima vary with shape, cross-sectional area, height and centre-to-centre spacing. Consistently however increase in the centre-to-centre spacing between periodically spaced roughness elements moves the secondary (higher frequency) EA maxima to lower frequencies.
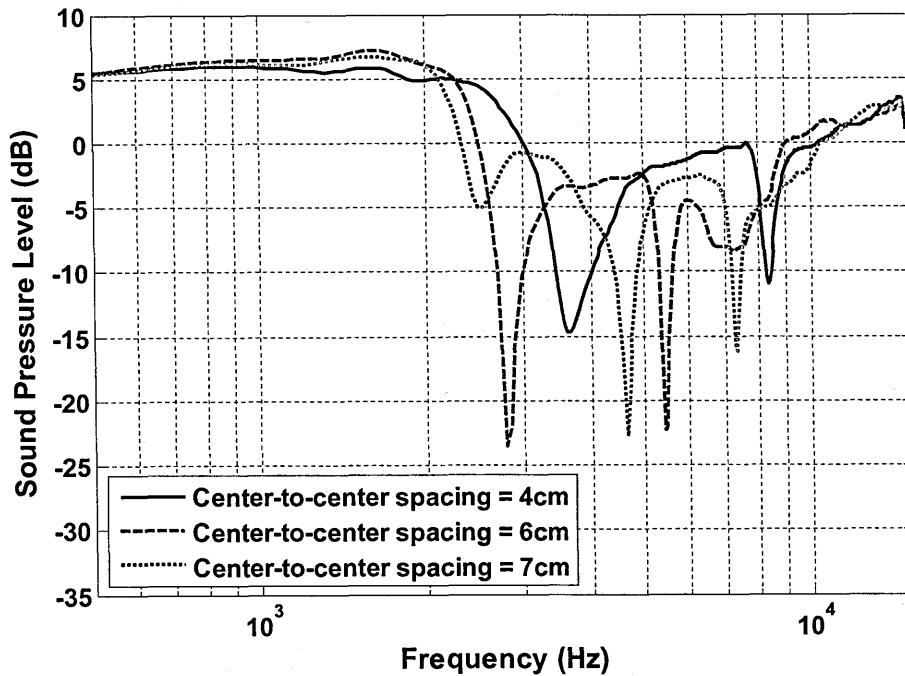
Figure 5.7 Measured EA spectra for source and receiver heights of 0.07 m separated by 0.7 m over surfaces including regularly-spaced triangular strips with mean centre-to-centre spacings of 0.04 m, 0.06 m and 0.07 m.

Figure 5.8 compares measured EA spectra for source and receiver at 0.07 m height and separated by 0.7 m above surfaces containing regularly-spaced identical roughness elements with each of five cross sectional shapes and heights (see Table 5.2). Data in Figure 5.8 (a) are for 15 roughness elements at 0.04 m (centre-to-centre) spacing and those in Figure 5.8 (b) are for 9 elements at 0.08 m spacing. As shown by Figure 5.8, roughness height is the major factor which affects the EA maxima. The higher the roughness, the deeper will be the maximum.

Figure 5.8 EA spectra measured with source and receiver heights of 0.07 m separated by 0.7 m (a) over a surface composed of 15 regularly spaced strips on a glass sheet (centre-to-centre spacing 0.04 m) (b) over a surface composed of 9 regularly spaced strips on a glass sheet (centre-to-centre spacing 0.08 m): semi-cylinders (black solid line), triangular strips (blue dashed line), square strips (red dotted line), short rectangular strips (magenta dash-dotted line) or tall rectangular strips (brown dash-diamond line) (see Table 5.2). In both cases the EA spectra measured over the smooth hard glass sheet (no roughness) are shown by the dotted (purple asterisk) curves.

5.3.3 Comparison between random and periodic spacing

Figure 5.9 compares measured EA spectra for randomly and periodically spaced triangular strips with mean centre-to-centre spacing of 0.05 m. The EA spectrum for randomly spaced elements represents an average over five deterministic random distributions. The spectrum for periodic spacing shows two distinct EA maxima, where as that for random spacing exhibits a single broad, shallower EA maximum. This demonstrates that the secondary (higher frequency) EA maxima are due to the periodicity.
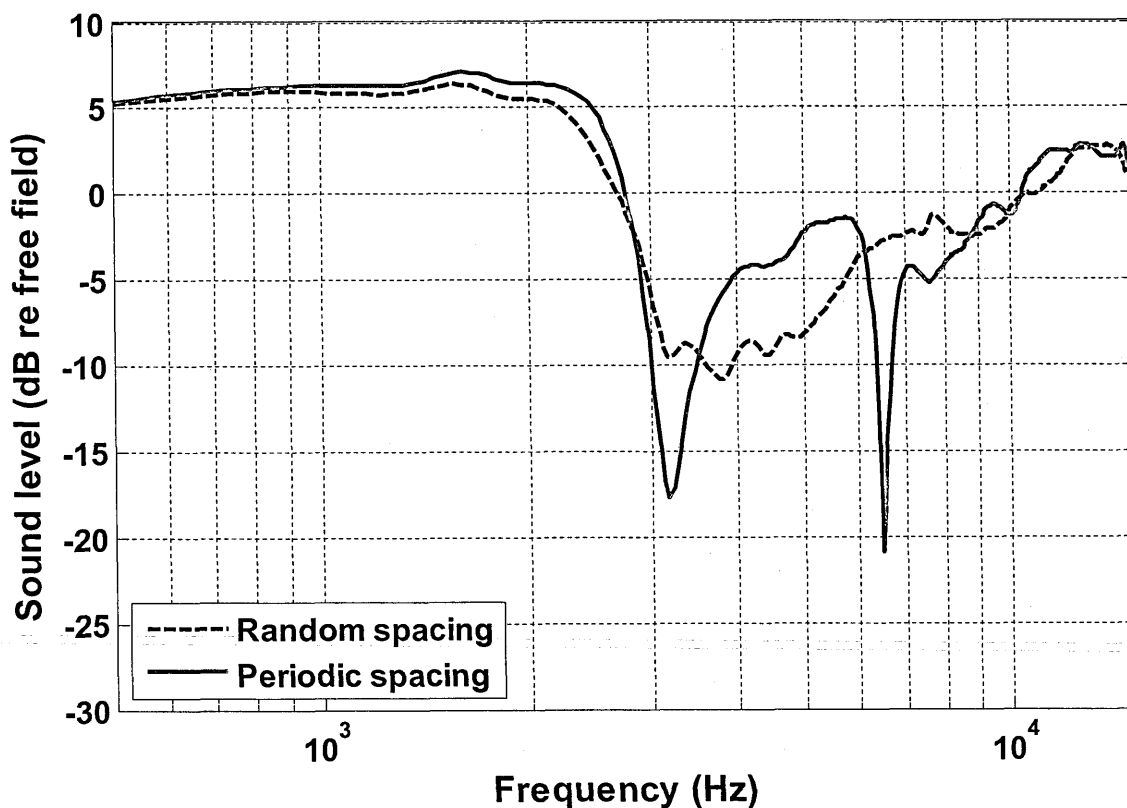
Figure 5.9 Comparison between measured EA spectra for random (broken line) and periodic (red continuous line) spacing with source and receiver heights at 0.07 m separated by 0.7 m over surfaces composed of 15 triangular elements with mean centre-to-centre spacing of 0.05 m on a glass sheet. The random spacing spectrum is the result of averaging measurements over five random distributions (black dash line).

5.4 Discussion

5.4.1 First EA maximum

Figure 5.9 shows that the frequency of the first EA maximum observed over regularly-spaced roughness elements is similar to that of the lowest frequency encompassed by the main ground effect attenuation maximum observed for randomly distributed roughness elements with the same shape and mean spacing. Figure 5.10 shows the result of changing the source-receiver height from 0.06 m to 0.15 m over a surface containing 19 square strips with centre-to-centre spacing of 0.04 m. As would be the case for the EA maxima due to finite impedance ground, the frequencies encompassing the lowest-frequency EA maximum become lower as the source and/or receiver height is increased. Consequently it may be regarded as the first order 'roughness-induced ground effect maximum'.
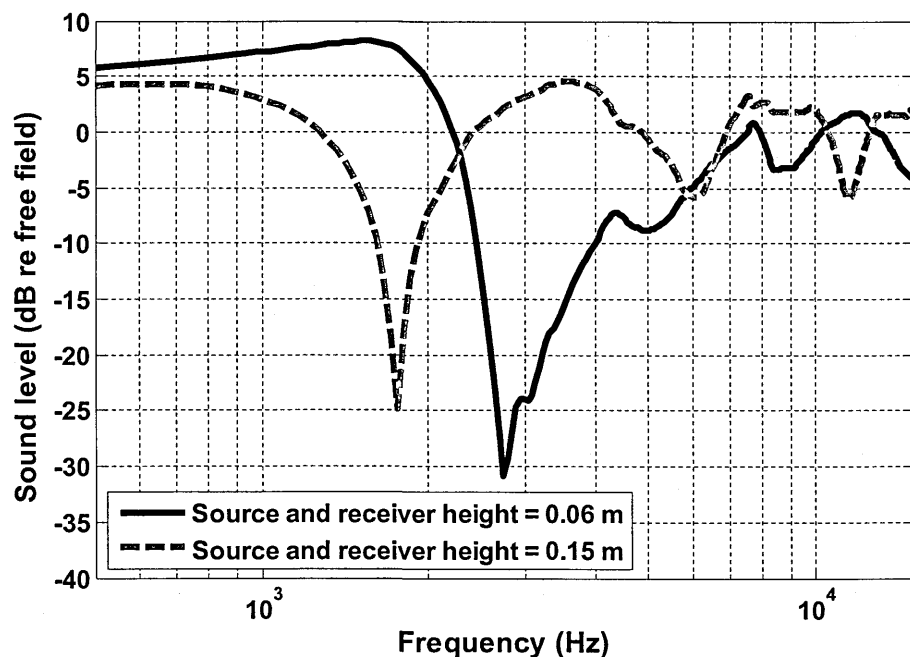
Figure 5.10 EA spectra measured with source and receiver at 0.06 m height (continuous line) and 0.15 m height (dash line) and separated by 0.7 m over rough surfaces consisting of 19 square strips arranged periodically on a glass sheet with centre-to-centre spacing of 0.04 m.

5.4.2 Second EA maximum

The second EA maxima observed over periodically spaced roughness elements are influenced by the centre-to-centre spacing of the roughness elements. As shown in Figure 5.11, except for two square strip arrays, there is approximately a linear relationship between the wavelength at the second EA maximum and the centre-to-centre spacing. The vertical axis in the Figure 5.11 represents the wave length (λ) at the frequency corresponding to the second EA maximum and horizontal axis is the centre-to-centre spacing (b) between roughness elements. The linear relationship between λ and b for different cross-sectional shapes can be represented by the set of linear equations given in table 5.4. The coefficients values vary with cross-sectional shape and height.
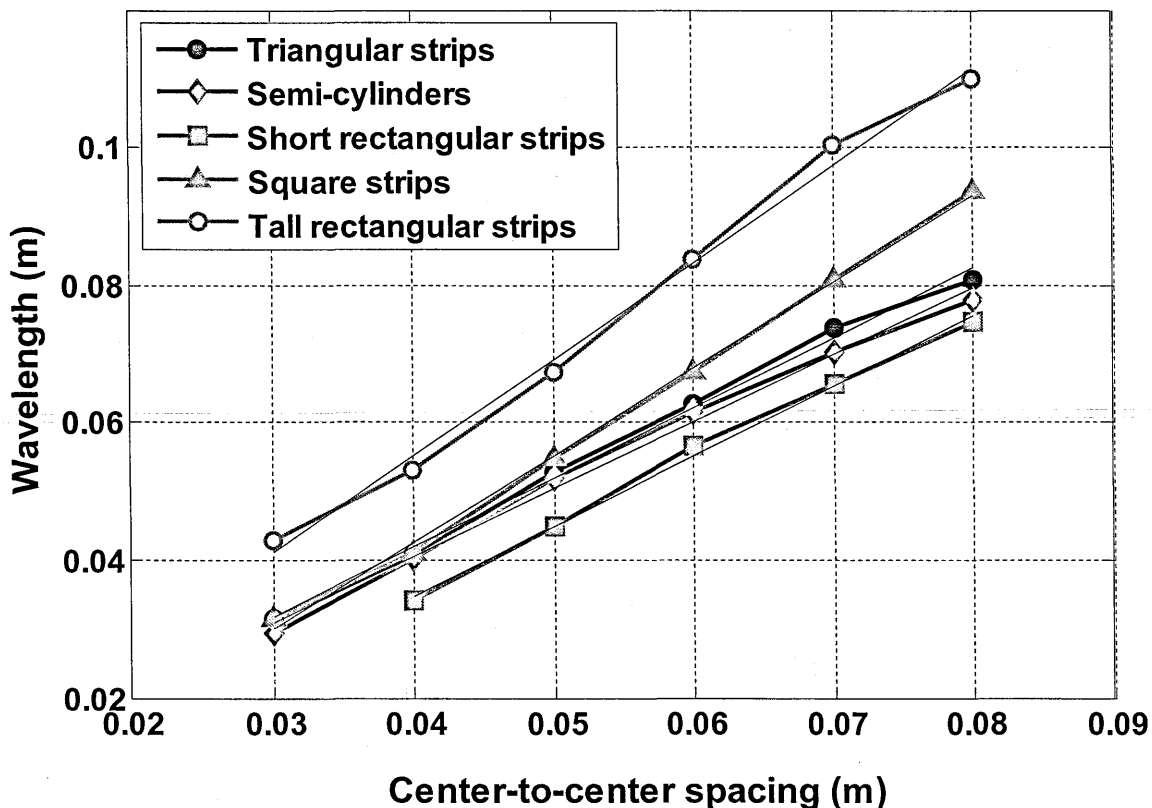
Figure 5.11 Relationships between wavelengths at 2nd EA maxima and centre-to-centre spacing for different cross-sectional shapes.

Table 5.4 Linear relationships between centre-to-centre spacing, b, and wavelengths, λ, at the 2ⁿᵈ EA maxima for different shapes.

Shape	Best fit linear relationship
Semi-Cylinders	$\lambda = 1.013b + 0.001$
Triangular Strips	$\lambda = 0.974b + 0.001$
Short Rectangular Strips	$\lambda = 1.018b - 0.005$
'Square' Strips	$\lambda = 1.262b - 0.007$
Tall Rectangular Strips	$\lambda = 1.405b - 0.001$

The Bragg diffraction phenomenon occurs when two diffracted waves interfere destructively or constructively due to the path length difference between them. The frequencies at which the destructive and constructive interference occur are called Bragg frequencies and denoted by f_{br}. According to the Bragg diffraction formula interferences should occur when,

$$f_{br} = \frac{nc_o}{2b\sin\alpha}, \quad n = 1, 2, 3\ldots\ldots \tag{5.29}$$

where c_o is the speed of sound in air, b is the centre-to-centre spacing between roughness elements and α is the angle of incidence.

Table 5.5 compares the observed second EA maxima frequencies with predicted second order Bragg frequencies corresponding to $n = 2$. The frequencies of the second EA maxima, particularly for semi-cylinders, triangular and square strips are in reasonable agreement with those predicted by 2nd order Bragg diffraction for a given centre-to-centre spacing. However Bragg diffraction

associated destructive interferences should correspond to odd values of n. The data in Figure 5.10 indicate that the frequencies of the second EA maxima become lower as the source height is increased. However the Bragg diffraction interferences should move to higher frequencies as the angle of incidence decreases (see Eq. (5.29)). Nevertheless, since the second EA maximum does not appear to be a frequency-shifted version of the 2nd order smooth ground effect dip, it appears that the second EA maxima observed for periodically-spaced roughness are associated with diffraction grating effects.

Table 5.5 Second EA maxima and 2nd order Bragg frequencies.

centre-to-centre spacing (m)	2nd order Bragg frequencies (kHz)	Observed frequencies for 2nd EA maxima (kHz)				
		Semi-Cylinders	Triangular Strips	Short Rectangular Strips	'Square' Strips	Tall Rectangular Strips
0.03	11.56	11.57	10.84	-	10.84	7.76
0.04	8.67	8.50	8.40	10.06	8.35	6.45
0.05	6.93	6.59	6.49	7.62	6.25	5.08
0.06	5.78	5.57	5.47	6.06	5.08	4.10
0.07	4.95	4.88	4.64	5.23	3.76	3.42
0.08	4.33	4.40	4.25	4.59	3.66	3.13

5.4.3 Third EA maximum

Table 5.6 compares observed third EA maxima frequencies (corresponding to $n = 3$) for different cross-sectional shapes with the third order Bragg frequencies predicted for different centre-to-centre spacings. The agreement between the measured third EA maxima frequencies and those of the predicted 3rd order Bragg diffraction for a given centre-to-centre spacing depends on the spacing, being better for the larger spacings (see Table 5.6). The percentage of exposed surface between the strips plays an important part in determining the appearance of the third EA maxima which are observed when at least 50 % of the ground surface is exposed i.e. the percentage roughness coverage is 50 % or less. Periodic roughness configurations composed respectively of tall rectangular strips, short rectangular strips and square strips cause similar third EA maxima if they have the same edge-to-edge spacing. The 3rd EA maximum moves towards lower frequencies with increasing source and receiver height. For semi-cylindrical strips having centre-to-centre spacing of 0.05 m, the first EA maxima occurs at 3.4 kHz which represents 28 % of first ground effect dip frequency for smooth hard ground which is at 12 kHz. The second EA maximum for a smooth hard ground occurs at 36.6 kHz. 28 % of this frequency is 10.4 kHz which corresponds to the frequency of the third EA maxima for semi-cylindrical roughness with centre-to-centre spacing of 0.05 m. Phenomenologically therefore, it seems to correspond to a frequency-shifted version of 2nd order smooth surface ground effect dip.

Table 5.6 Third EA maxima and 3rd order Bragg frequencies.

centre-to-centre spacing (m)	3rd order Bragg frequencies (kHz)	Observed frequencies for 3rd EA maxima (kHz)				
		Semi-Cylinders	Triangular Strips	Short Rectangular Strips	'Square' Strips	Tall Rectangular Strips
0.03	17.34	-	-	-	-	12.40
0.04	13.00	-	-	14.40	13.23	10.35
0.05	10.40	10.45	-	15.77	11.52	8.69
0.06	8.67	7.67	7.28	11.18	8.79	7.47
0.07	7.43	7.47	7.28	8.79	7.47	6.25
0.08	6.50	7.81	6.06	10.69	6.20	5.47

In summary it appears that the first and third EA maxima observed over a periodically rough hard surfaces are frequency-shifted versions of the 1st and 2nd order smooth surface ground effect dips, whereas the second order EA maxima are diffraction grating related and due to the periodic spacing of the roughness elements.

5.5 Numerical simulations and comparisons with data

The predictions of sound propagation over rough surfaces has been carried out using three numerical techniques such as Multiple Scattering Theory (MST), Boundary Element Method (BEM) and Finite Element Method (FEM). The details for these numerical methods are given in chapter 2. Here measured excess attenuation spectra over different kind of rough surfaces are compared with numerical predictions.

5.5.1 Multiple Scattering Theory (MST)

Boulanger *et al.* [19] have developed a semi-analytical Multiple Scattering theory (MST) for the scattering of cylindrical acoustic waves by a finite array of semi-cylinders on a smooth hard surface based work by Linton *et al.* [16], [18] who studied scattering of plane waves by finite arrays of identical penetrable cylinders. The appropriate system of equations [19] for calculating the pressure field at a receiver has been programmed and implemented in FORTRAN.

Figure 5.12 (a) and (b) compare the measured EA spectra for a surface formed by semi-cylinders with a centre-to-centre spacing of 0.04 m and 0.06 m over a glass sheet with MST predictions. The predictions are in good agreement with the data. MST requires much less computational time and resources than either the Boundary Element Method (BEM) or COMSOL (Finite Element Method (FEM)) but is restricted to semi-cylindrical roughness. For configurations in which predictions are needed for large semi-cylindrical roughness, the MST is very useful due to its efficiency in time and computational resource utilization.
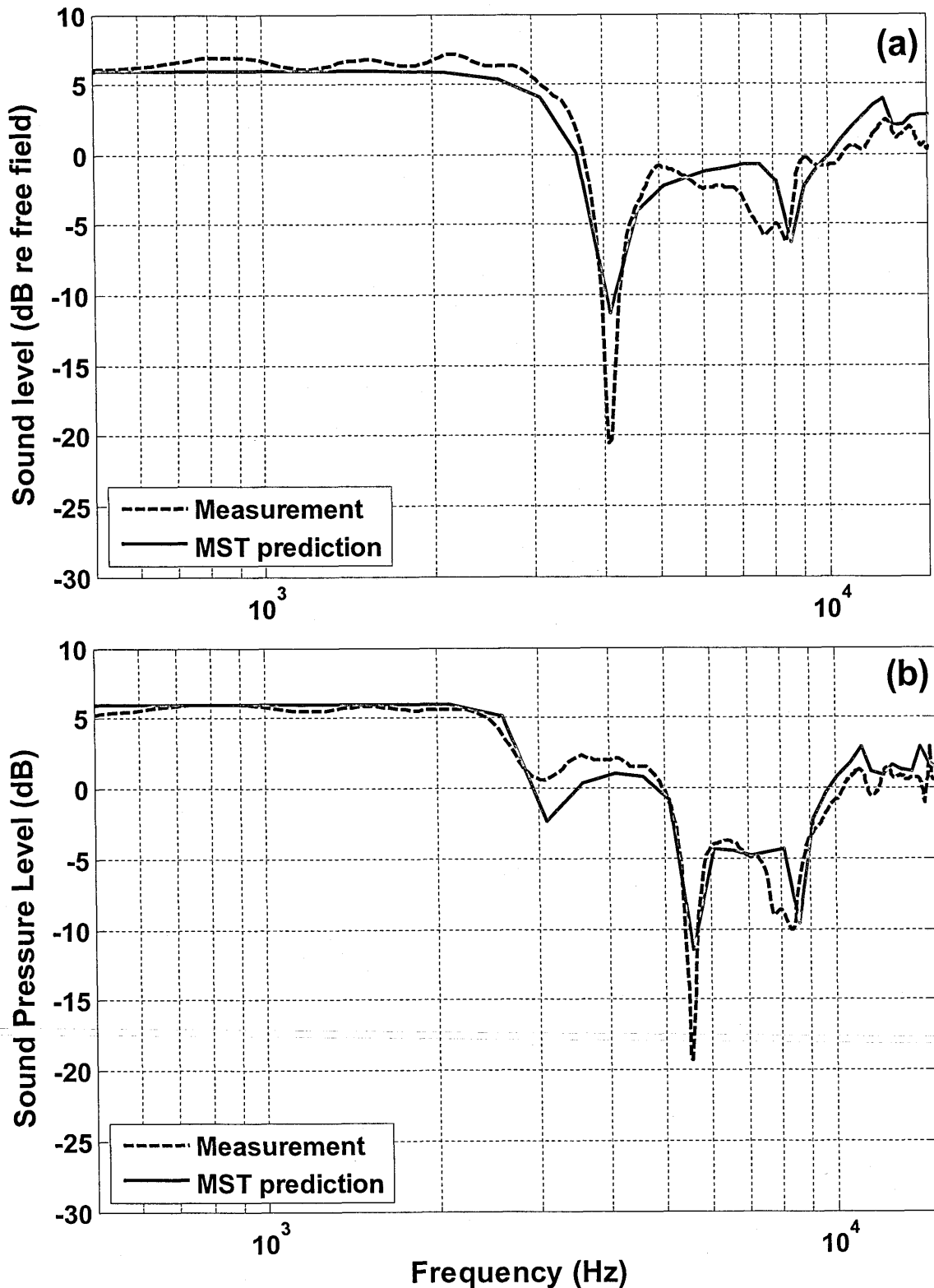
Figure 5.12 Comparisons between multiple scattering theory predictions and measured excess attenuation spectra with source and receiver at 7cm and separated by 70cm over a glass sheet for (a) 15 semi-cylinders with regular centre-to-centre spacing of 4cm (b) 11 semi-cylinders with regular centre-to-centre spacing of 6 cm.

5.5.2 Boundary Element Method (BEM)

A boundary integral equation method was developed by Chandler-Wilde and Hothersall [6]–[9] for solving the Helmholtz equation for sound pressure at the receiver generated by a line source above an impedance ground. The BEM, a numerical method in which only the boundaries are discretized, is used to solve the resulting Helmholtz integral equation. The Green's function is in the form of a Hankel function of zero order. In BEM the element size must be at least five times smaller than the wavelength of interest. As it only meshes the boundaries, the resulting number of unknowns is reduced compared for example with the number required when using Finite Elements, however, the matrix equation is non-sparse.

Figure 5.13 presents comparisons between BEM predictions and measured EA spectra over a glass sheet supporting (a) random distribution of 15 triangular strips with mean centre-to-centre spacing of 0.04 m (b) 15 triangular strips on with regular centre-to-centre spacing of 0.05 m (c) 15 semi cylinders on with regular centre-to-centre spacing of 0.04 m (d) 15 tall rectangles on with regular centre-to-centre spacing of 0.025 m. Although the agreement between data and predictions is good, the predictions tend to overestimate the levels between 1 kHz and 2 kHz. The accuracy of BEM predictions can be improved by decreasing the size of the boundary elements but this increases the computational resources required. The data shown in Figure 5.13 (d) were measured over aluminum metal strips placed on an MDF board instead of a glass sheet. The MDF is acoustically hard but not as smooth as a glass sheet. The surface impedance of the MDF board has been obtained using the method explained in chapter 3. The best fit two-parameter slit pore impedance model parameters for MDF board are a flow resistivity of 20 MPa

s m^{-2} and a porosity of 0.1. The BEM predictions given in Figure 5.13 are obtained by discretizing the ground surface between the roughnesses according to measured impedance.
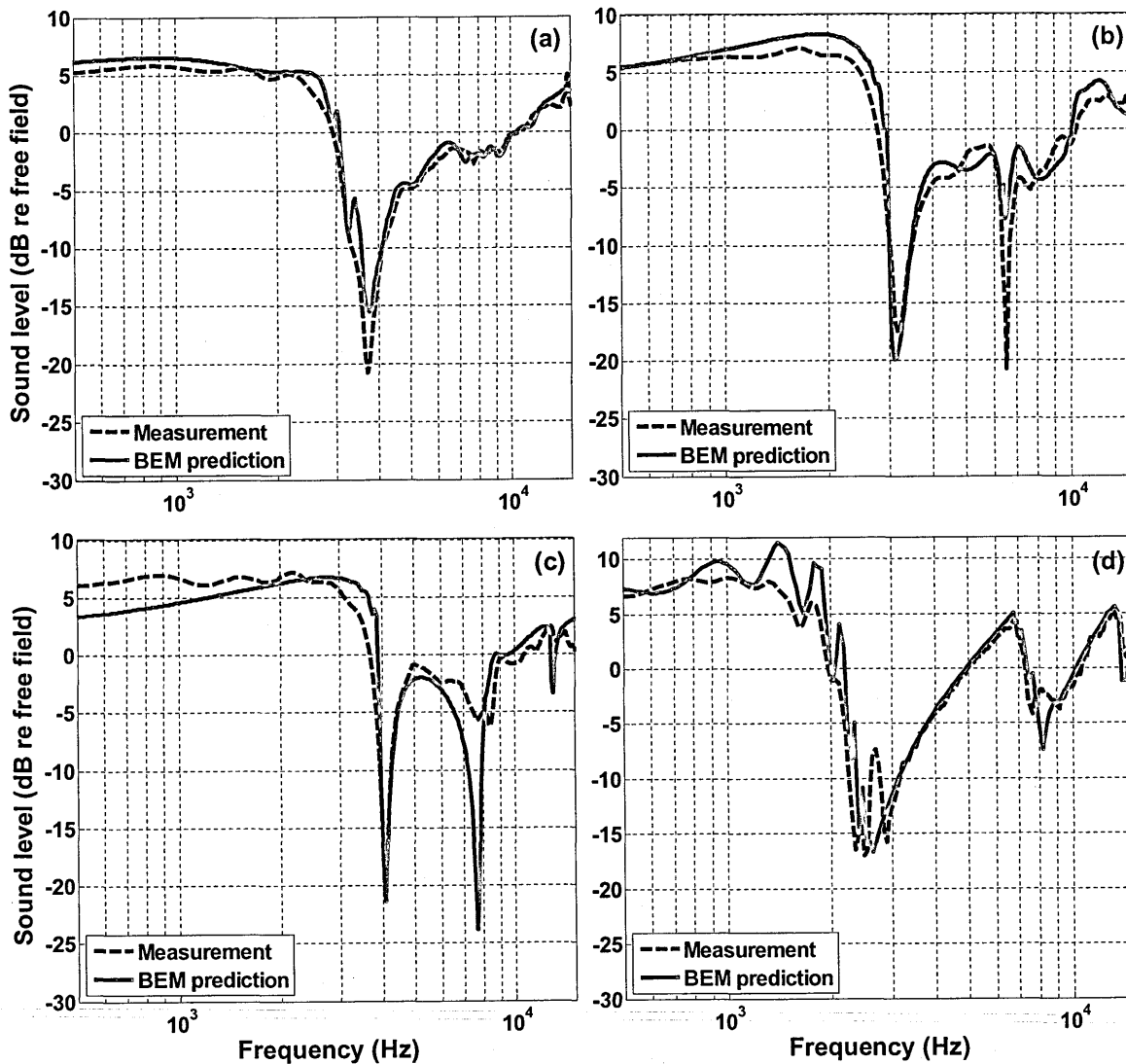
Figure 5.13 Comparisons between Boundary Element Method (BEM) predictions (continuous line) and EA spectra measured (broken line) with source and receiver height of 0.07 m and separated by 0.7 m over a glass sheet supporting (a) random distribution of 15 triangular strips with mean centre-to-centre spacing of 0.04 m (b) 15 triangular strips with regular centre-to-centre spacing of 0.05 m (c) 15 semi cylinders with regular centre-to-centre spacing of 0.04 m (d) 15 tall rectangles (metal strips) with regular centre-to-centre spacing of 0.025 m placed on a MDF board instead of glass sheet. Details of the strip dimensions are given in Table 5.2.

5.5.3 Finite Element Method (FEM - COMSOL®)

COMSOL® multi-physics provides an interactive environment for modeling and solving acoustical problems based on the solution of partial differential equations using the FEM and assuming a cylindrical (line) source. Consequently it is suitable for predictions and investigations of sound propagation over rough surfaces. A two-dimensional finite element triangular mesh is generated to represent the fluid medium while the rough surface is modeled as a rigid boundary with a similar profile. The other boundaries are modeled with a radiation boundary condition. The accuracy of simulation results depend on mesh-element size but very fine meshing increases the cost of simulation in terms of time and computational resources. So calculations involve a compromise between accuracy and the required computational resources.

Figures 5.14 (a) – (d) compare measured EA spectra and FEM (COMSOL®) predictions (a) for random distribution of 15 triangular strips with mean centre-to-centre spacing of 0.05 m (b) for periodic distributions of 13 short rectangular strips with centre-to-centre spacing of 0.06 m(c) a periodic distribution of 13 semi-cylinders with centre-to-centre spacing of 0.06 m (d) a periodic distribution of 13 triangular strips with centre-to-centre spacing of 0.06 m. Although agreement between data and FEM (COMSOL®) predictions is good above 2 kHz the predictions are not valid below 2 kHz as a consequence of 'numerical' reflections.
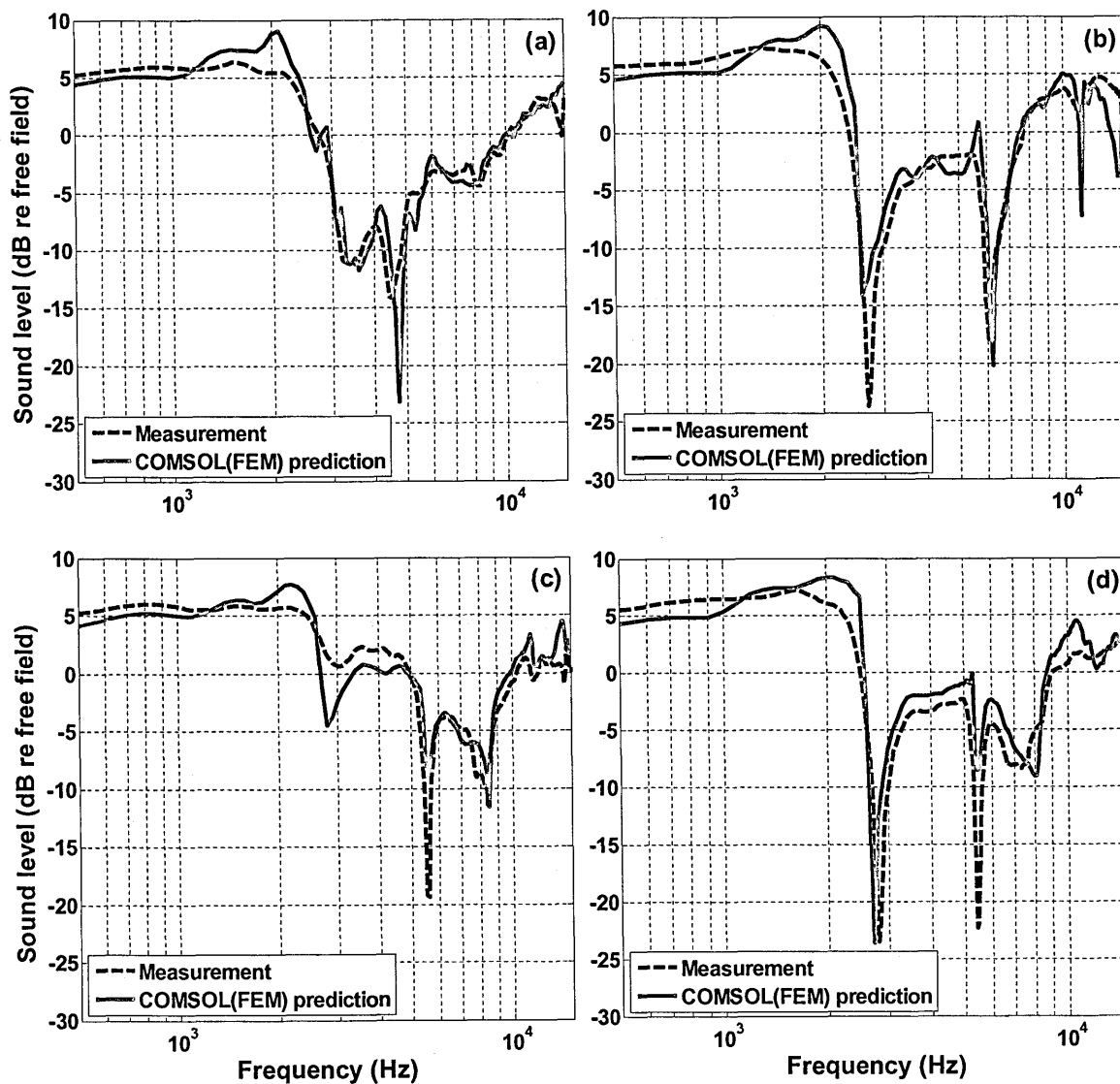
Figure 5.14 Comparisons between FEM (COMSOL®) predictions and measured excess attenuation spectra with source and receiver height at 7cm and separated by 70cm over a glass sheet for (a) average of 5 random distributions of 15 triangular strips with mean centre-to-centre spacing of 5cm (b) a periodic distribution of 13 short rectangular strips with centre-to-centre spacing of 6cm (c) a periodic distribution of 13 semi-cylinders with centre-to-centre spacing of 6 cm (d) a periodic distribution of 13 triangular strips with centre-to-centre spacing of 6 cm.

5.5.4 Comparison between MST, BEM and FEM predictions in respect of laboratory data

Three predictions methods (MST, BEM and FEM) have been used to compare with laboratory data to test their validity and efficiency. Most of the data presented here, were from laboratory scale measurements. Later in this thesis, we investigate some larger scale predictions. It is important to use the most efficient and reliable prediction technique for larger scales.

Figure 5.15 compares the measured EA spectra over surface composed of semi-cylindrical strips with centre-to-centre spacing of 0.06 m with predictions using MST, BEM and FEM. All of prediction methods give reasonably good agreement with data, but the agreement between data and FEM predictions is not very good below 2 kHz. Each of these prediction methods has its own limitations and advantages. MST is an analytical prediction technique, which is only valid for semi-cylinders. However, it is very efficient, fast and requires rather less computational resources. BEM and FEM (COMSOL®) can be used to model any kind of cross-sectional shape. However, these are computationally more expensive and take much longer time than MST. BEM is less expensive in terms of computational resources and time than FEM and gives better agreement with data over the whole frequency range. BEM can be used for large scale prediction. However, FEM (COMSOL®) cannot be used for large scale predictions due to its high resource demand. Moreover a typical desk top computer cannot handle the required meshing due to memory limitations. BEM can be used to model ground surfaces using different acoustical impedance models. However FEM, being a commercial package, cannot be adapted to model a ground surface with different

impedances. Nevertheless FEM is useful to model complex shapes and 3D (hard surface) situations where BEM cannot be used. For example we have used FEM (COMSOL®) to investigate propagation over slitted circular cylinders (see section 5.9). This was not possible using BEM since it has only 2D modeling capability.
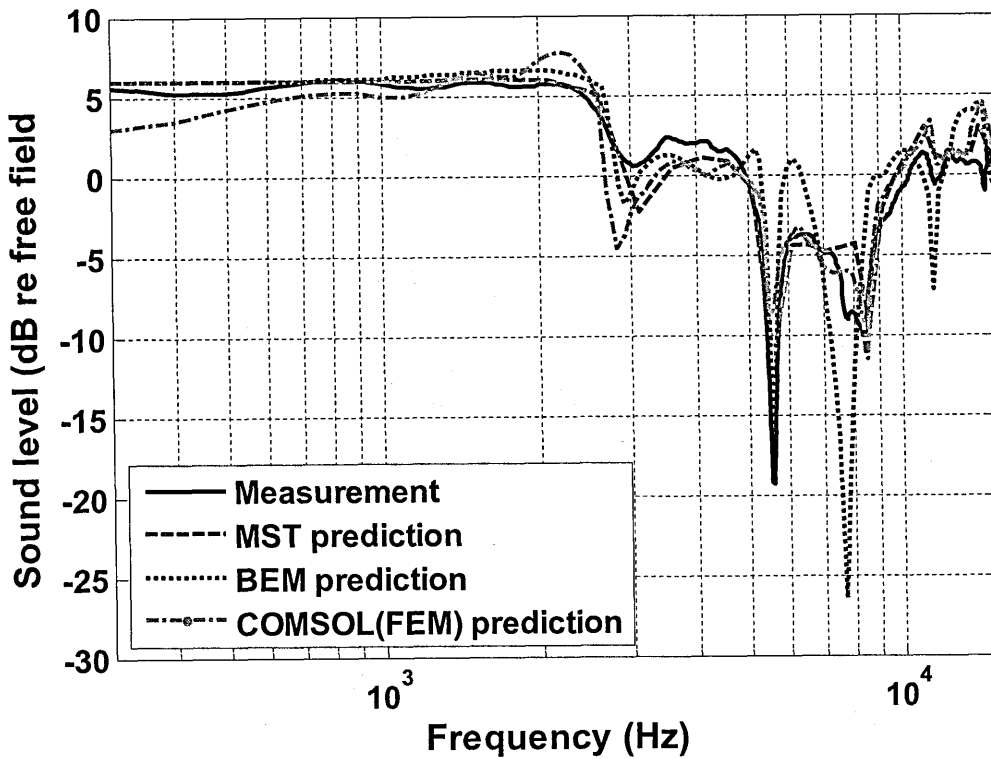
Figure 5.15 Comparisons between measured EA spectra and predictions using MST, BEM and FEM with source and receiver height at 0.07 m and separated by 0.7 m over a glass sheet supporting 13 semi cylinders with regular centre-to-centre spacing of 0.06 m.

5.6 Effective impedance models

5.6.1 Tolstoy's boss model for effective admittance

Details of Tolstoy's boss model are given earlier (see Eq. 5.12 – Eq. 5.15). Predictions using Tolstoy's model [61], [88]–[92] have been compared with measured data obtained over rough surfaces composed of strips with different cross-sectional shapes and spacing. It has been found that agreement between data and predictions using Tolstoy's model is not good. Medwin *et al.* [93], [94] have proposed values of the hydrodynamic shape factor for wedges but using Medwin's modification does not give good agreement with measured data. Boulanger *et al.* [61] heuristically modified the Tolstoy model (see Eq. 5.24 – 5.28) which was used to predict sound propagation over rough surfaces and compared with measured data. Again, the agreement between measured data and predictions using the Boulanger-Tolstoy model was not satisfactory. The original Tolstoy model predicts only one EA maximum, however the data over periodically spaced roughness shows multiple EA maxima. A diffraction-modified Boulanger-Tolstoy model is capable of predicting multiple maxima, but the magnitude and frequency location of these predicted maxima do not coincide with the measured ones.

In Medwin's work, the scattering coefficient (see Eq. 5.12) value was modified numerically to obtained good predictions with the measured data. The work presented here uses a similar approach. By analysing the measured data over rough surfaces, Tolstoy's model is modified heuristically as explained in following subsections.

5.6.2 A heuristic surface impedance model

5.6.2.1 A modified 'Tolstoy' component

The measurements reported in Section 5.3 show that changing the centre-to-centre spacing between roughness elements of a given shape results in different EA spectra. Laboratory data indicate that the lowest frequency EA maxima depend on cross-sectional shape, centre-to-centre spacing between roughness elements and on the angle of incidence so they may be regarded as the 'roughness-induced ground effect maxima'.

The only dependence on spacing in Eq. (5.12) is through v_2. The EA spectra predicted by Eq. (5.12) are not altered significantly if the centre-to-centre spacing is changed according to the values used in the reported experiments. On the other hand, the shape factor, s_2, is assumed to have a constant value for any centre-to-centre spacing. It has been found that agreement between predictions and data can be improved by making the shape factor also dependent on spacing. The empirically-derived spacing-dependent shape factor is given by,

$$s_2 = \frac{1}{2}(39b + 0.07)(1 + K),\qquad\qquad (5.30)$$

where b in meters is the centre-to-centre spacing between roughness elements.

5.6.2.2 Effective layer component

Eq. (5.12) predicts a single EA maximum, whereas the measured EA spectra (see for example Figures 5.6 – 5.9) show multiple distinct maxima. Figure 5.16 (a) shows measured EA spectra obtained with source and receiver at different heights and separated by 0.7 over a surface composed of periodically

spaced triangular strips with centre-to-centre spacing of 0.04 m. The complex effective impedance of a rough surface for a given geometry can be deduced from complex EA data [68]. Figure 5.16 (a) also shows the deduced impedance spectra obtained from complex EA data over triangular strips as dotted lines. Similarly, Figure 5.16 (b) shows measured EA spectra obtained with source and receiver at different heights and separated by 0.7 m over a surface composed of periodically spaced rectangular strips with centre-to-centre spacing of 0.08 m. Figure 5.16 (b) shows the deduced impedance spectra which produced similar 'resonances' to those seen for triangular strips in Figure 5.16 (a). These impedance spectra show resonances in the real and imaginary parts of impedance at the frequencies at which the second EA maxima occur (see Figure 5.16). In this respect, they resemble the impedance spectra expected for a hard-backed layer of porous material. The second EA maximum resonance frequency corresponds to a half-wavelength resonance in the 'effective layer'.

An additional empirically-derived impedance of an equivalent hard backed layer is introduced in the form,

$$Z_l = \coth(-ikd_e(1+0.04i)),$$ (5.31)

where,

$$d_e = (0.5+4h)b,$$ (5.32)

is the effective layer depth, $k(1 + 0.04i)$ represents an effective wave number and h is the measured height of the roughness element.
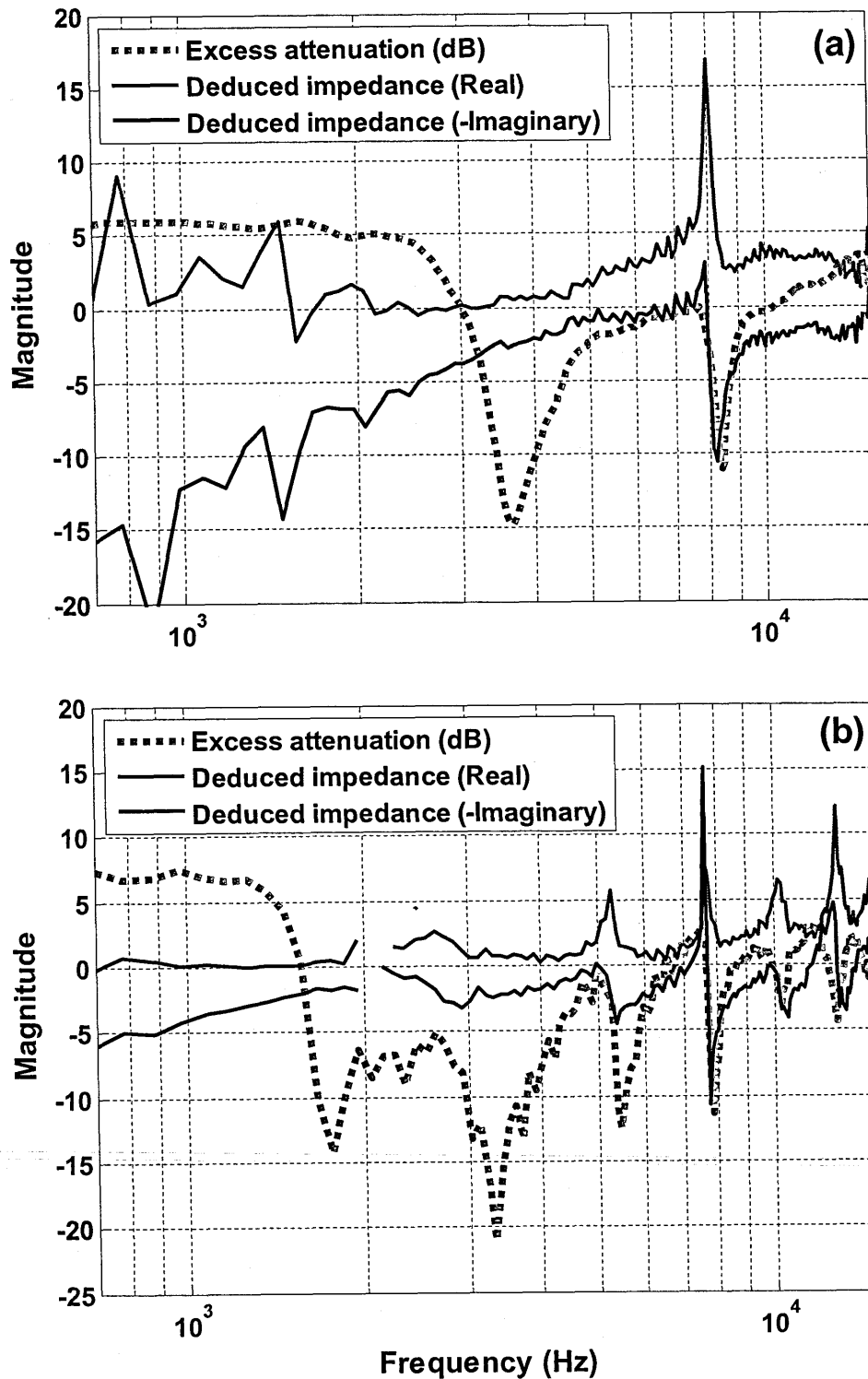
Figure 5.16 Measured EA spectra (red dotted line) with source and receiver heights of 0.07 m separated by 0.7 m, Impedance deduced spectra from complex EA data: blue solid line – real part of deduced impedance, black solid line – imaginary part of deduced impedance (a) 15 Triangular Strips on a glass sheet with centre-to-centre spacing of 0.04m (b) 9 tall rectangular Strips on a glass sheet with centre-to-centre spacing of 0.08m.

The measured 'layer-resonance' frequency at 8 kHz (see Figure 5.16 (a)) corresponds to a half wave-length of 0.022 m. The calculated effective layer depth d_e is also 0.022 m for the given centre-to-centre spacing of 0.04 m. The complex layer impedance in Eq. (5.31) has a real part which takes account of incoherent scattering from the periodic rough surface. Viscous attenuation effects are taken into account through the imaginary part of the effective wavenumber. This represents a heuristic modification of the generalized effective admittance theory [61] which introduces incoherent scattering only for random scattering.

The first EA maximum over a rough surface may be called the *'Roughness-induced ground effect maximum'*. This roughness effect is predicted by Eq. (5.12) through Eq. (5.25) with the modification given by Eq. (5.30). A linear relationship between the secondary EA maxima and periodicity (centre-to-centre spacing) is observed and reported in Section 5.4. This leads to formulation of effective layer resonance effect (Eq. (5.31)). The roughness-induced impedance (Eq. (5.12) – Eq. (5.15), Eq. (5.30)) is combined in series with the effective hard-backed layer resonance effect (Eq. (5.31)). The combined effective impedance for a periodically-rough surface is given by,

$$Z = 1/\beta + Z_l. \tag{5.33}$$

Measured data over rough surface at different angle of incidence implies that the rough surface behaves as an externally-reacting one at the lower frequencies. The heuristic effective impedance given by Eq. (5.33) assumes a locally reacting surface. Modification of this formula to allow for the observed external reaction should be the subject of future work.

5.6.3 Comparison of EA data with predictions based on effective surface impedance models

Figures 5.17 (a) – (d) compare measured EA spectra at source and receiver height of 0.07 m separated by 0.7 m with those predicted using either the original Tolstoy effective admittance model (Eq. (5.12)) or the heuristic modification Eq. (5.33) for (a) periodically spaced triangular strips with centre-to-centre spacing of 0.05 m (b) semi-cylinders with regular centre-to-centre spacing of 0.03 m (c) 'square' strips with regular centre-to-centre spacing of 0.06 m (d) and short rectangular strips with regular centre-to-centre spacing of 0.04 m. The agreement between data and predictions using Eq. (5.33) is significantly better. As long as the centre-to-centre spacing is comparable with the scatterer height, the agreement using Eq. (5.33) is reasonable. However when the scatterer height is substantially less than the centre-to-centre spacing, the agreement between data and predictions using Eq. (5.33) is not as good.
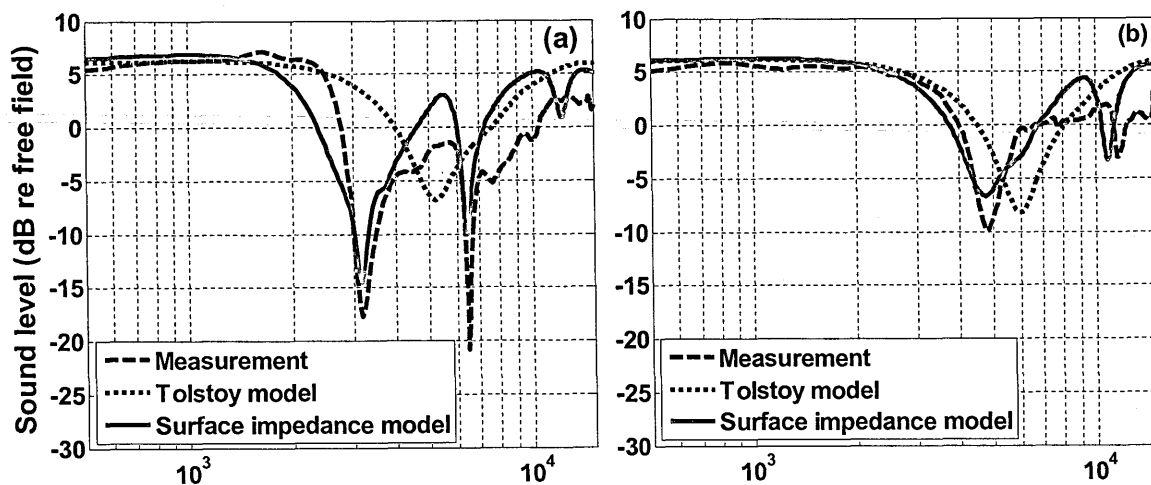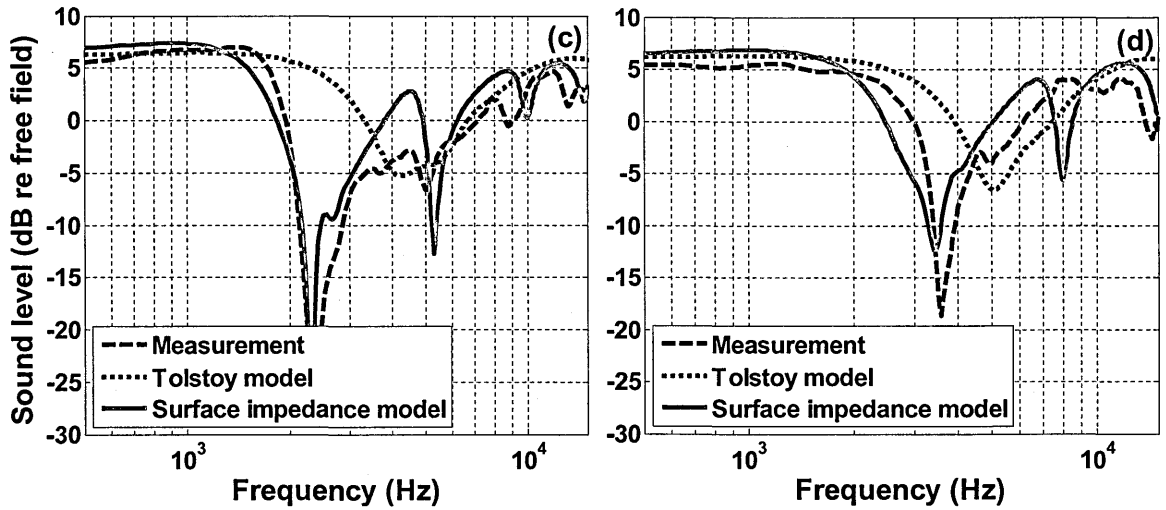
Figure 5.17 Comparison of predictions using the Tolstoy effective admittance model (Eq. (5.12) and the heuristic surface impedance model (Eq. (5.33)) with measured EA spectra with source and receiver at a height of 0.07 m and separated by 0.7 m over a glass sheet on which were placed (a) 15 triangular strips with regular centre-to-centre spacing of 0.05 m (b) 19 semi-cylinders with regular centre-to-centre spacing of 0.03 m (c) 13 'square' strips with regular centre-to-centre spacing of 0.06 m and (d) 15 short rectangular strips with regular centre-to-centre spacing of 0.04 m.

5.7 Comparative attenuation performance

5.7.1 Laboratory data

A single figure rating of excess attenuation performance of different rough surfaces has been determined as illustrated in Figure 5.18. The mean excess attenuation per Hz is computed by dividing the area between the +6 dB SPL line and the EA spectrum level (shaded in Fig. 5.17) by the frequency range. Typically the starting frequency for the area calculation is above 500 Hz. The maximum frequency has been set at 11 kHz since the main excess attenuation spectral contributions of the surfaces studied are below this frequency. Moreover the adopted laboratory source-receiver geometry involves a larger grazing angle (11°) than those that would result from the geometries of practical interest and the corresponding smooth surface excess attenuation spectra for these geometries would have maxima at higher frequencies than 12.3 kHz. The areas between the +6 dB SPL line and the EA spectrum levels have been calculated using the trapezoidal rule. The formulae used to compute the mean EA (dB) are [100],

$$\text{total area} = \delta f \left[\left(\sum_{i=1}^{N} 6 - EA_i \right) - \frac{1}{2} \left(EA_0 + EA_{n+1} \right) \right], \qquad (5.34)$$

$$\text{Mean attenuation(dB)} = \frac{\text{total area}}{N \delta f}. \qquad (5.35)$$

where δf is the frequency increment for the excess attenuation measurements, EA_i = Excess Attenuation in the frequency interval between f_i and $f_i + \delta f$, and N = total number of frequency points. Using this method of calculation, the smooth surface of the glass sheet gives a mean excess attenuation of 3.1 dB.
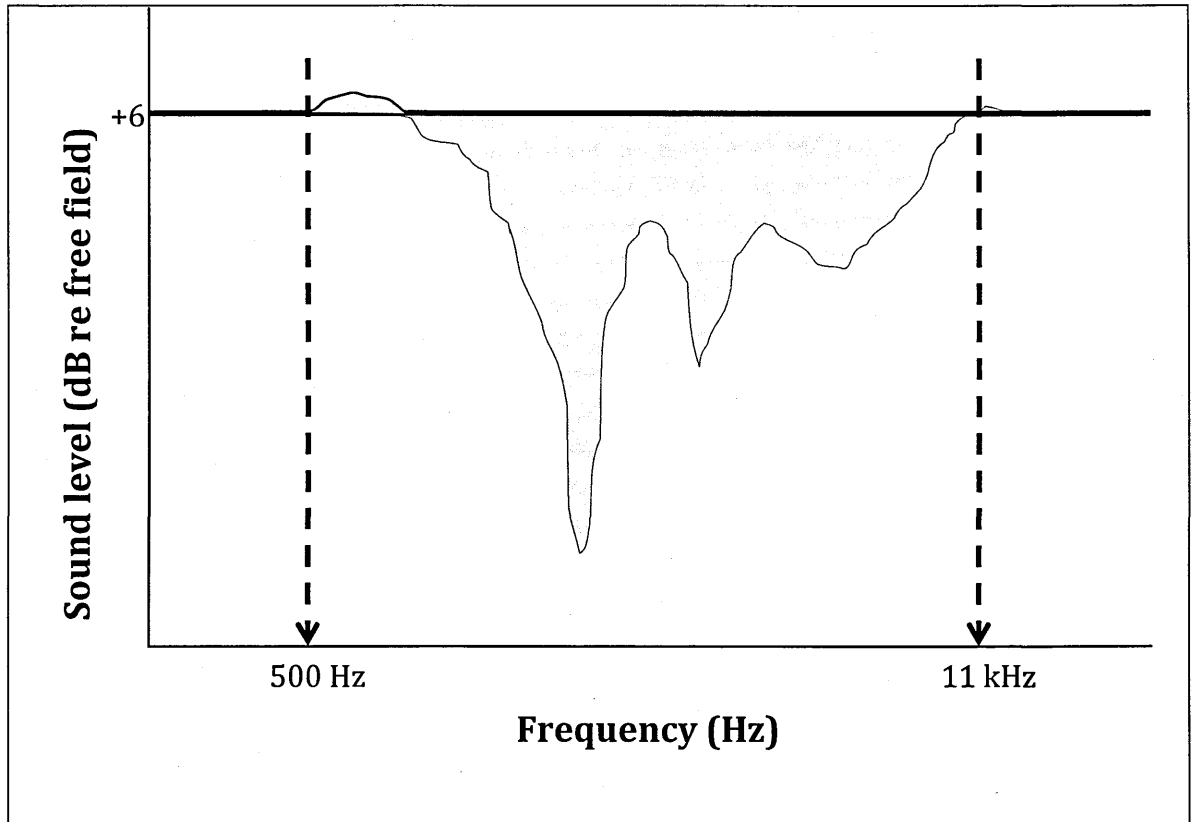
Figure 5.18 Illustration of area used to calculate mean excess attenuation performance in dB.

Table 5.7 Mean attenuations calculated for laboratory roughness configurations (source and receiver heights at 7 cm and separated by 70 cm).

Strip shape	Spacing	Mean Attenuation (dB/Hz)				
		0.04m	0.05m	0.06m	0.07m	0.08m
Equilateral triangles	Periodic	7.1	7.9	8.3	8.5	8.0
	Random	7.7±0.2	8.2±0.2	8.4±0.1	8.3±0.1	8.2±0.2
Semi-cylinders	Periodic	6.5	7.2	7.1	7.5	6.1
	Random	7.2±0.2	7.2±0.2	7.3±0.3	7.1±0.2	7.2±0.2
Short rectangles	Periodic	5.2	6.3	6.9	7.4	7.0
	Random	5.3±0.1	6.2±0.2	6.9±0.1	6.8±0.1	6.9±0.1
Squares	Periodic	6.7	6.9	7.8	8.2	8.4
	Random	6.8±0.2	7.1±0.2	7.5±0.1	7.8±0.1	7.9±0.3

Table 5.7 compares the overall mean attenuations, relative to that over a smooth hard surface, due to periodic and random roughness configurations with variously shaped wooden strips computed from laboratory measurements of excess attenuation spectra. The mean attenuation is calculated using Eq. (4.34) and Eq. 4.35. Also EA values of greater than +6 dB (due to roughness-induced surface waves) have been included as negative attenuations. Each random array leads to a different EA spectrum so the average and range of the mean attenuation values are listed.

On average for all roughness shapes and a mean spacing of between 4 and 8 cm, there is no acoustical advantage in terms of mean attenuation for periodic spacing over random spacing. Other possible benefits of periodic spacing are that they may be easier to manufacture and they may be more 'tunable' to particular frequency bands. Moreover, the triangular strips give best attenuation performance. Similarly, larger scale BEM predictions of insertion loss at a 1.5 m high receiver at 50 m range due to randomly spaced and periodically spaced roughness gives similar conclusions to those obtained through laboratory data [101]. Although periodically spaced roughness produces deeper EA maxima as than randomly spaced roughness, the calculations shows no benefit in terms of insertion loss. There are two reasons for this. One reason is that periodically spaced roughness produces stronger surface waves than does randomly spaced roughness at near grazing angle and the second reason is that the EA maxima for periodically spaced roughness are deep but not broad enough to avoid the effect of periodicity being averaged out when calculating overall A-weighted reductions..

5.7.2 Large scale predictions

Some predictions for large scale semi-cylindrical roughness were carried out before a standard method for insertion loss calculations was agreed and made available in the HOSANNA project, details of which are given in chapter 11. The details for these predictions and calculations can be found in HOSANNA-deliverable 4.2 [100]. Only the major conclusions from these calculations are given here. A conclusion from laboratory data is that edge-to-edge separation of the order of the element base width will give a higher mean attenuation per unit roughness cross sectional area than close-packing. Figure 5.19 compares predicted excess attenuation spectra using MST for close-packed and with 0.3 m edge-to-edge spacing (0.6 m centre-to-centre spacing) of the semi-cylinders. The semi-cylinders have a radius of 0.15 m. The source is assumed to be at height of 0.05 m, receiver at height of 1.2 m with a separation of 80 m between them. It is clear from Figure 5.19 that the spaced roughness gives a broader-in-frequency attenuation performance than closed packed roughness.
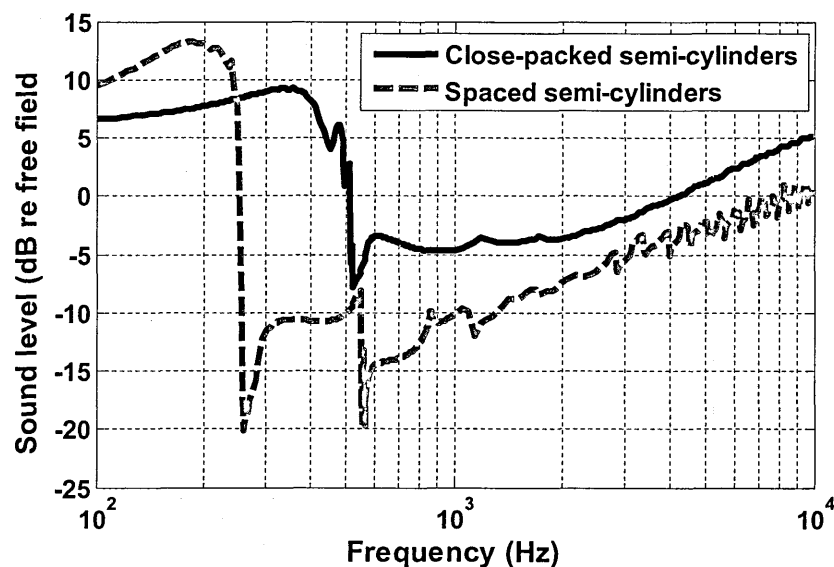
Figure 5.19 Predicted excess attenuation spectra for source height at 0.05 m and receiver height at 1.2 m separated by 80 m for close-packed and spaced semi-cylindrical roughness with radius of 0.15 m.

5.8 Cylindrical roughness with slits

Sound propagation over cylindrical roughness containing slits has been explored through laboratory measurements and predictions. Figure 5.20 (a) shows an array of complete cylindrical PVC pipes placed on an MDF board. These PVC pipes are acoustically hard but hollow. The hollow PVC pipes have external and internal diameters of 0.055 m and 0.0526 m respectively. The creation of discontinuous slits in the pipes as shown in Figure 5.20 (b) is expected to give rise to an additional resonance peak in the excess attenuation spectrum. EA spectra have been measured with different centre-to-centre spacings of 0.1 m, 0.15 m and 0.2 m. The Tannoy driver connected with a 2 m long tube was used as a source. The width of the single slit cut on each PVC pipe is 0.00263 m.
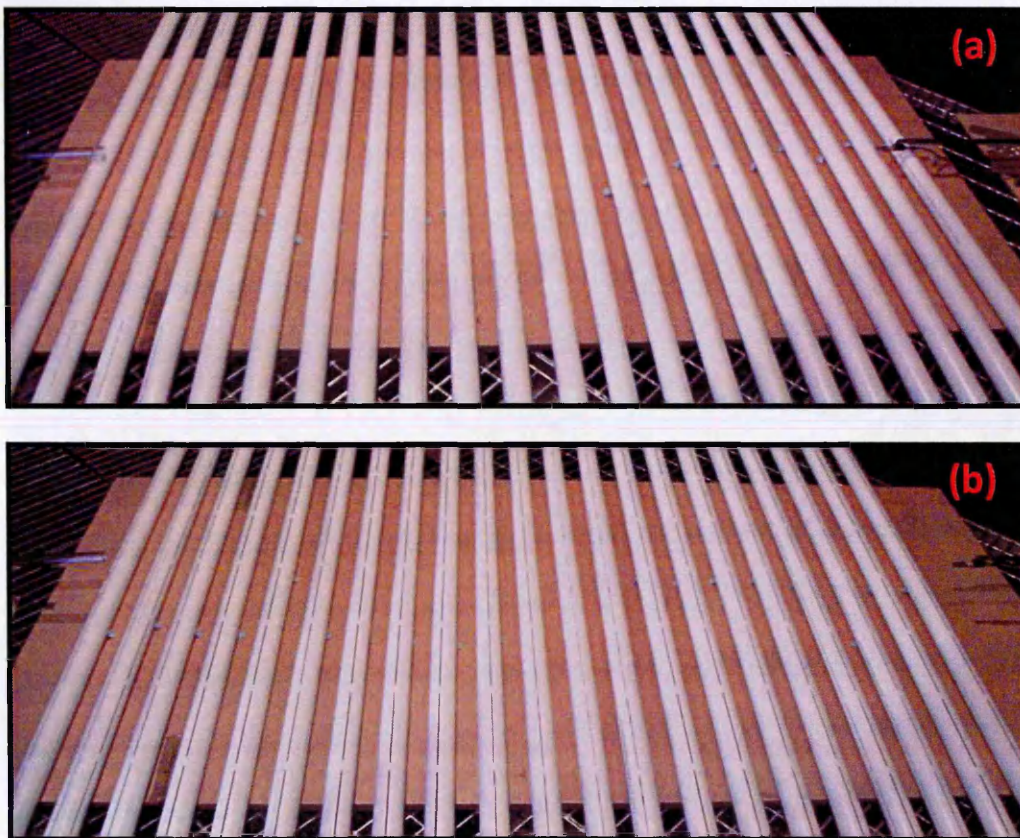
Figure 5.20 (a) Photograph of complete PVC pipes placed on MDF board (b) Photograph of PVC pipes with slits placed on MDF board.
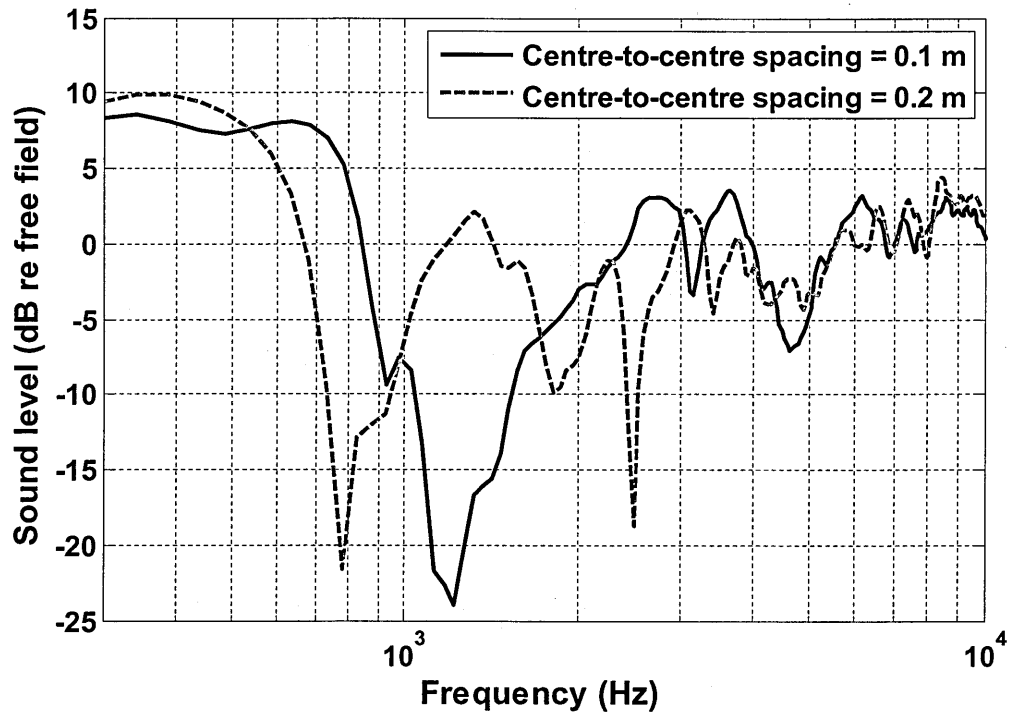
Figure 5.21 Measured EA spectra for source and receiver heights of 0.15 m separated by 2.0 m over surfaces composed from regularly-spaced circular PVC pipes (without slits) placed on an MDF board with mean centre-to-centre spacings of 0.1 m and 0.2 m.

Figure 5.21 shows the measured excess attenuation over a surface composed of periodically spaced circular PVC pipes placed on an MDF board with centre-to-centre spacing of 0.1 m and 0.2 m. The source and receiver are at a height of 0.15 m and a horizontal separation of 2.0 m. The heights are measured from the MDF board surface. Measurements were also carried out with two more geometries and spacings. As discussed previously periodicity introduces an extra EA maximum and by increasing the spacing the EA maxima move to lower frequencies. However, periodicity also induces strong surface waves, which have a negative effect on attenuation performance of a periodically rough surface. A discontinuous line of vertical slits with a width of 0.00263 m have been cut into each PVC pipe as shown in Figure 5.20 (b). Figure 5.22 compares the measured EA spectra over no-slit PVC and with single (discontinuous) slit PVC pipes placed

over MDF board with centre-to-centre spacing of 0.1 m. The EA spectrum over PVC pipes with slits shows an extra EA maximum at 650 Hz without modifying the remaining EA spectra. This new EA maximum is the result of a Helmholtz-type resonance. The hollow PVC provides a cavity and when air is forced into the cavity through the partial slits, the pressure inside it increases. When the external force pushing the air into the cavity is removed, the higher pressure inside the cavity will cause air to flow out. The cavity will then have a pressure slightly lower than the outside, causing air to be drawn back in. This process repeats and the structure starts resonating. The resonance frequency depends on the inside volume of the cavity and the length and width of cavity opening.
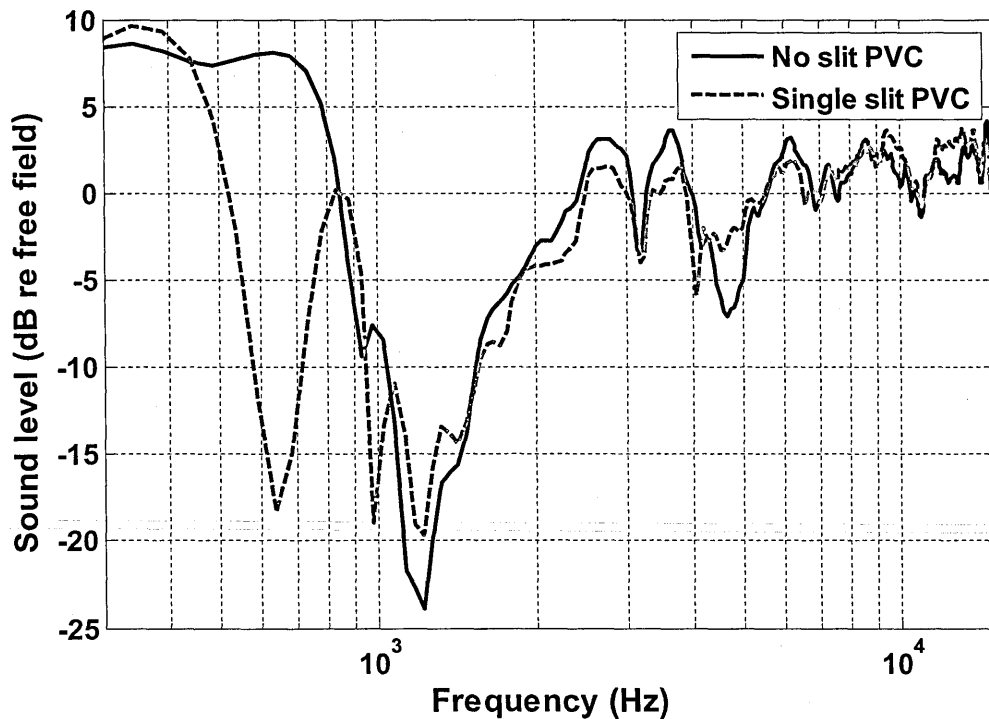
Figure 5.22 Measured EA spectra over surfaces composed of periodically spaced no-slit PVC and single-slit PVC pipes placed with centre-to-centre spacing of 0.1 m on an MDF board. The source and receiver are at heights of 0.15 m above the MDF board surface and horizontal separation between them is 2.0 m.

5.8.1 Comparison between data and predictions

Figure 5.23 (a) compares measured EA spectra with predictions using MST and FEM (COMSOL) over a surface composed of circular PVC pipes arranged periodically over a MDF board with centre-to-centre spacing of 0.1 m. The agreement between data and predictions is very good. Figure 5.23 (b) compares measured EA spectra with predictions using FEM (COMSOL) over a surface composed of single slit PVC pipes arranged periodically over a MDF board with centre-to-centre spacing of 0.1 m. The source and receiver are placed at a height of 0.15 m from MDF board and horizontal separation between them is 2.0 m. The agreement between data and predictions is very good. Although MST is very efficient and quicker than FEM (COMSOL) for predicting EA spectra over complete pipes, it is not possible to model the ground effect using PVC pipes with slits using MST. On the other hand FEM is capable of predicting the resonance-associated EA maxima due to the slits as shown in Figure 5.23 (b).

The comparison between measured EA spectra and FEM (COMSOL) EA predictions over rough surface given in section 5.5.3 do not show any benefit from using COMSOL compared with using BEM or MST. Moreover, FEM is more expensive in terms of simulation time and computing resource requirements. On the other hand, the usefulness of FEM for simulating hollow roughness with slits has been demonstrated.
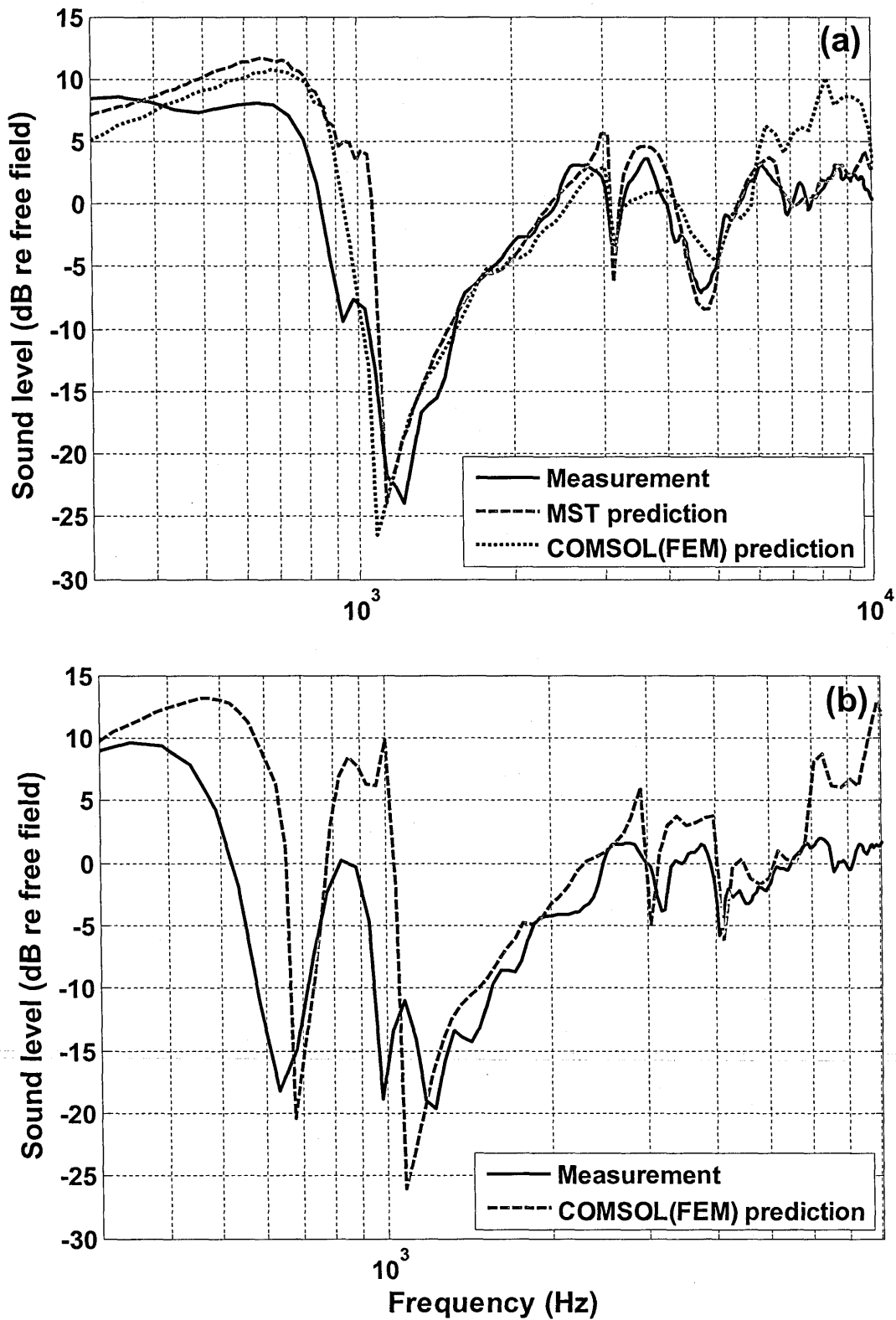
Figure 5.23 Measured EA spectra and predictions using MST and FEM (COMSOL) with source and receiver height at 0.15 m from MDF board and separated by 2.0 m over a surface composed PVC pipes placed over MDF board with centre-to-centre spacing of 0.1 m (a) No slit PVC pipes (b) slit PVC pipes.

5.8.2 Using slit width as a design parameter

Figure 5.22 shows that the making slits in hollow roughness elements introduces an additional low frequency EA maximum, where otherwise the roughness-induced surface wave would have a dominant negative effect on the rough surface attenuation performance. The design of rough surfaces for noise control can be improved by using slit-induced resonance effect. However, the frequency at which this maximum occurs must be controlled to make it tuneable to a specific frequency. Some effort has been made to understand the relationship between the resonance frequency with the slit width, slit height and internal volume of the cavity by making FEM (COMSOL) predictions. Figure 5.24 show the snapshot from COMSOL to show the slit width and its height. Figure 5.25 (a) shows the EA spectra predicted as the slit width is increased while keeping the slit length and internal cavity volume constant. Increasing the slit width is predicted to move the resonance frequency to higher frequencies. Figure 5.25 (b) shows the EA spectra predicted as the slit wall thickness is increased while decreasing the corresponding internal cavity volume and keeping the slit width constant. Increasing the slit wall thickness from 0.1 cm to 1.0 cm is predicted to have almost no effect on resonance frequency, however after that the frequency is predicted to increase with the increase in slit length.
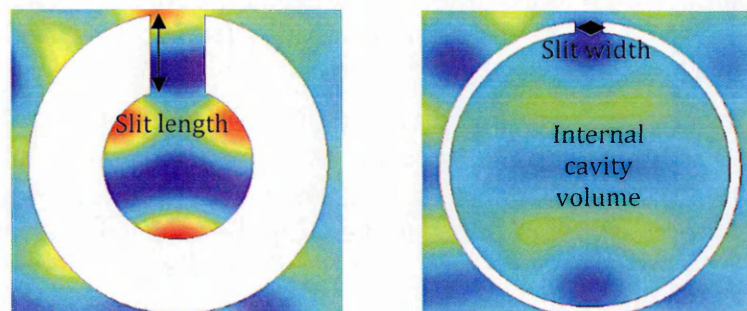
Figure 5.24 Snapshot from FEM (COMSOL) showing the length and width of the slit.
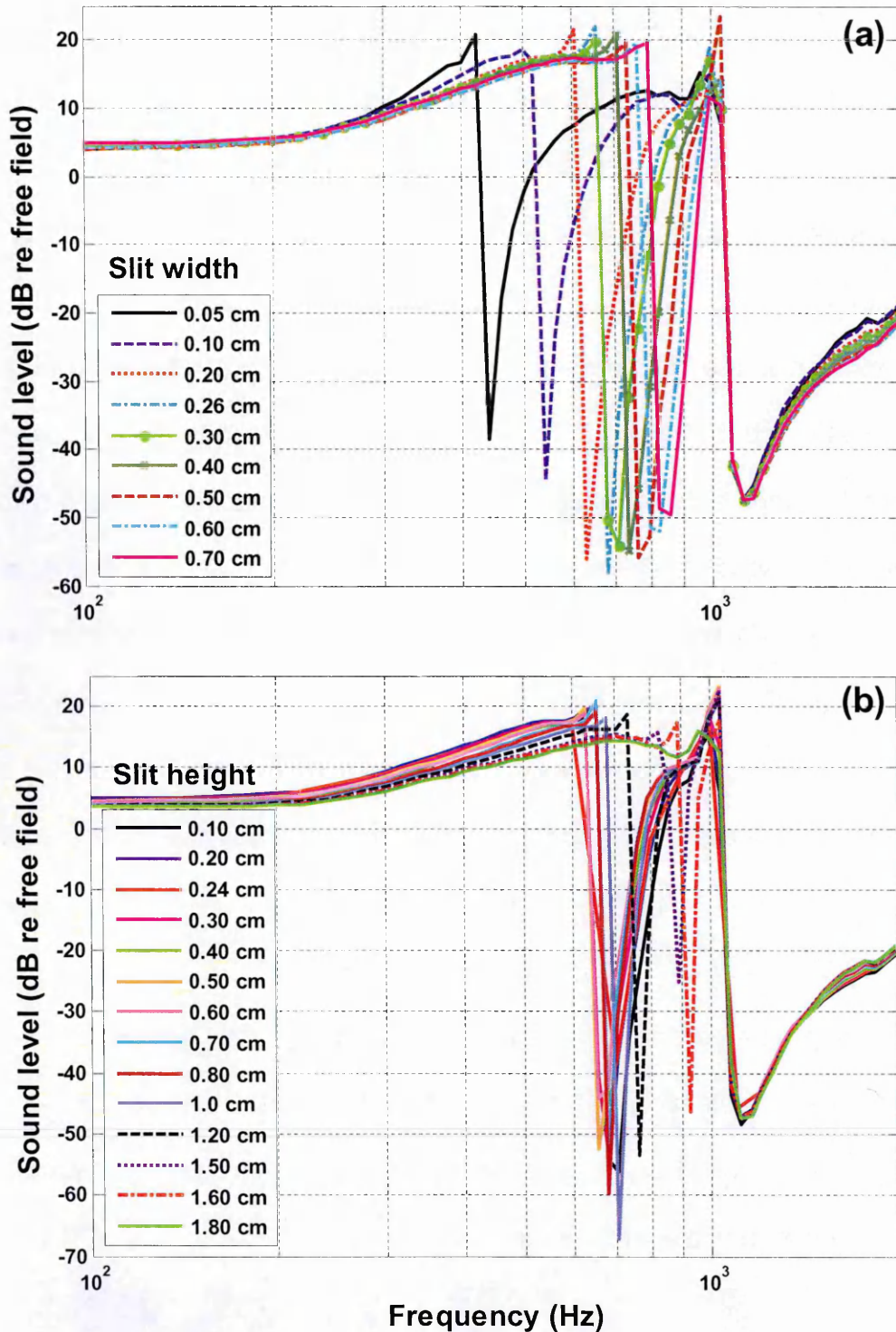
Figure 5.25 EA spectra predicted using FEM (COMSOL) for surface composed of single slitted PVC pipes placed with centre-to-centre spacing of 0.1 m and source and receiver at height of 0.075 m from a hard plane with the horizontal separation of 2.0 m (a) Changing the slit wall thickness keeping the internal cavity volume constant; Wall thickness = 0.24 cm, Slit width = 0.05 cm – 0.7 cm (b) Changing slit depth while also changing the internal cavity volume but keeping the width of slit constant ; Wall thickness = [0.1 cm – 1.8 cm], Slit width = 0.26 cm.

The excess attenuation maximum due to the slits is consistent with a resonance phenomenon. During the compression phase of the pressure cycle associated with an incident sound wave, air is forced into the hollow pipes through the slits and the pressure inside the cavity increases. During the rarefaction phase, the external force pushing the air into the cavity is removed, and, due to the induced higher-pressure, the air inside will flow out. This means that the pipe cavity will be left at a pressure slightly lower than the outside, causing air to be drawn back in. This process repeats during each pressure cycle, as a result of which some energy is lost by viscous action as air movies in and out of the pipe. Moreover the pipes with slits are caused to resonate with a resonance peak that appears at lower frequencies. This resonance is similar to Helmholtz resonance. However the frequency of the peak predicted by the Helmholtz formula differs from the peak predicted using FEM (COMSOL).
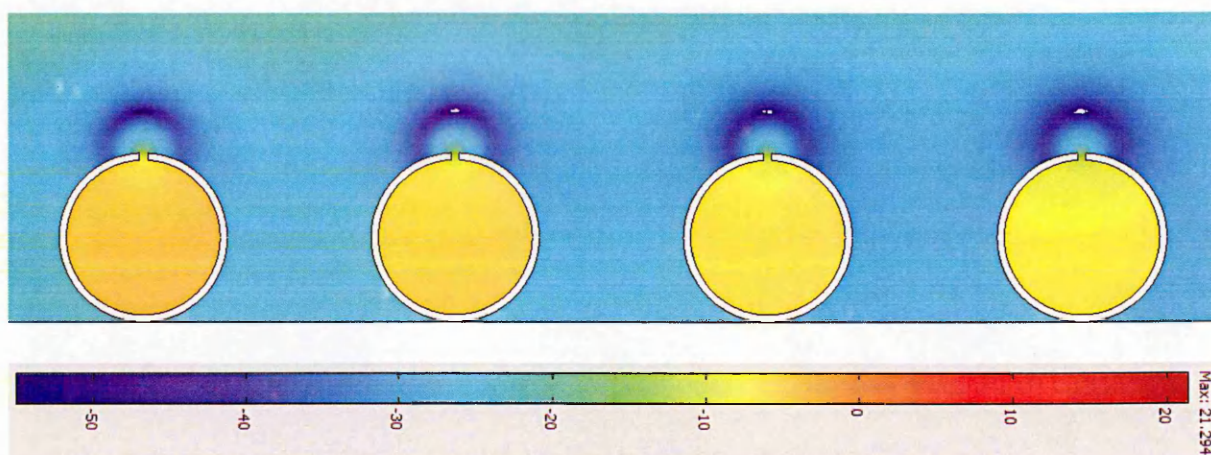
Figure 5.26 Snapshot of surface plot for EA spectra at 700 Hz predicted using FEM (COMSOL) for surface composed of single slitted PVC pipes.

Figure 5.26 shows a snapshot of surface plot for EA at resonance frequency of 700 Hz predicted over slitted cylinders using COMSOL. It shows that the resonance effect exist very close to slits. These are just initial investigations

into the effects of resonant roughness. Further work is needed to understand the resonance phenomenon and enable creation of a resonant rough surface with the resonance peak at a desired frequency.

5.9 Discussions

The work described in sections 5.1 – 5.8 mostly relates to laboratory data. Numerical methods have been validated by comparing the measured data with predictions. Rough surfaces have been studied to understand the physics of surface scattering.

In comparison to that over a smooth hard surface, the ground effect dips, corresponding to the first destructive interference, observed in EA spectra measured over surfaces supporting randomly and periodic spaced roughness elements, which are small compared to the incident wavelengths, are at significantly lower frequencies. Although a single broad EA maximum is observed for random spacing, multiple maxima appear in measured EA spectra over periodically spaced roughness. The first EA maximum may be regarded as roughness-induced ground effect. The frequencies of the second EA maximum depend on the spacing and the appearance of a third EA maximum depends on the percentage of ground surface 'exposed' between the roughness elements. Analysis shows that the first and third EA maxima observed over a periodically rough hard surface are frequency-shifted versions of the 1st and 2nd order smooth surface ground effect dips, whereas the second order EA maxima are diffraction grating related as a result of the periodic spacing of roughness elements.

Predictions using MST (for semi-cylindrical roughness elements), FEM (COMSOL®) and a 2D BEM have been found to provide good agreement with measurements. However the FEM predictions have been found not to be valid below 2 kHz and BEM is computationally expensive. A heuristic effective impedance model for a periodically-rough surface has been obtained by adding a modified Tolstoy imaginary impedance component to the impedance of a lossy hard-backed layer. Predictions of the resulting model show reasonably good agreement with laboratory data.

Measured laboratory data and large scale predictions show that periodically spaced and randomly spaced roughness of the same height and mean spacing give similar attenuation. Spaced roughness gives rise to attenuation over a broader frequency range than close-packed roughness of the same height.

Studies of propagation over -slit-hollow-pipe roughness elements shows that an extra excess attenuation maximum at lower frequencies. This maximum appears due to resonance phenomenon and the modification in roughness doesn't modify the remaining spectra.

Some of the conclusions drawn from experimental work are used for further study and exploration of rough surface scattering at a larger scale in the following sections. In the next few sections the numerical techniques validated by laboratory and outdoor experiments are used to investigate the effects of larger scale roughness arrays suitable for traffic noise reduction.

5.10 Large scale low parallel walls and lattices

5.10.1 Introduction

Previous sections of this chapter concentrated on understanding diffraction assisted rough ground effect due to various cross-sectional shapes. Laboratory experiments were carried out over different cross-shapes roughness with periodic and random spacing. The measured data was used to validate and test the numerical prediction techniques such as MST, BEM and FEM (COMSOL). The major conclusions from the laboratory experiments is that height is a major factor for rough ground effect and that triangular roughness gives best attenuation performance. However, insertion loss calculations for HOSANNA two lane urban road cases (for details see Chapter 10) show that for large (0.15 m - 0.3 m high) roughness the shape effect is minimal. The shape effect is apparent in excess attenuation spectra. However, when overall (A-weighted) insertion loss is calculated for the two lane urban road case using the HOSANNA standard procedure the effect of shape is averaged out. Since there would be practical engineering difficulty in deploying triangular roughness and the shape factor is not very important for large scale implementation, low parallel rectangular walls rather than roughness with any other cross-sectional shapes will be considered further. Low parallel walls are easy to deploy, paths can be made through them (see Section 5.10.3.3.3) and they are more durable than other cross-sections of roughness.

The higher the roughness, the more it is effective for traffic noise attenuation. However, according to agreed HOSANNA project guidelines, we

consider roughness only up to 0.3 m high; a roughness element of height greater than 0.3 m would be considered as a low noise barrier. The effect of low parallel walls is greatest when they are placed as close to the source as possible. However, according to HOSANNA project guidelines, the no abatement may start closer than 2.5 m from the nearest source.

The idea of using regularly-spaced low parallel walls for road traffic noise reduction was suggested by van der Heijden and Martens in 1982 [102]. They reported outdoor experiments using sixteen 21 cm high parallel brick walls with edge-to-edge spacing of about 20 cm during which they measured a broadband (100 Hz and 12,500 Hz) insertion loss of slightly more than 4 dB(A) and an insertion loss of up to 20 dB(A) in the 400 to 1000 Hz 3rd octave bands. Van der Heijden and Martens invoked the creation and subsequent destruction of surface waves as the main mechanism for noise reduction. Although surface wave creation may be an important part of the acoustical effects of a parallel wall structure placed on an acoustically-hard ground, the structure has a significant influence on ground effect over a wider range of frequencies than those affected directly by the surface wave. Bougdah *et al.* [103] have reported laboratory measurements over arrays of up to 17 thin walls with (equal) heights and spacing between 8 cm and 25 cm. They measured a maximum overall insertion loss of 10.3 dB for a 14-wall array with height and spacing of 0.25 m occupying 3.25 m with the first wall from the source at the specular reflection point halfway between source and receiver at 0.4 m height and separated by 10 m. They discussed three physical effects other than surface wave creation and the effective ground impedance that may be involved. One of these is quarter wave resonance. In an

array of identical 0.3 m high walls, this resonance would occur at 283 Hz. They refer also to diffraction-grating effects. The third additional mechanism they suggest is that of interference between direct and multiply-reflected (between adjacent walls) paths. But this mechanism can be considered as part of diffraction assisted ground effect.

5.10.1.1   Designing of parallel walls configurations

Low parallel walls design for noise control has been investigated extensively in HOSANNA, Deliverable 4.3 [101]. The (2D) Boundary Element Method has been used to predict excess attenuation spectra for a grid of receiver locations in the presence of various intervening parallel wall systems. From these spectra, broadband and 1/3rd octave insertion losses have been calculated using source spectra for rolling (tyre) and traction (engine) noise at 70 km/h [104]. The wall array has been assumed to start at 2 m from the single lane of cars. The effect on insertion loss due to parallel walls with different centre-to-centre spacing, wall width and parallel walls array width has been investigated. Quadratic Residue Diffuser (QRD) profiles and fractal profiles have been investigated in Deliverable 4.3 [101]. However, only the major conclusions are presented here.

These conclusions have been verified through measurements. The next few sections will give related laboratory and outdoor measurement results.

The insertion loss due to low parallel walls increases as the receiver moves away from the edge of walls. Put another way, parallel walls become more acoustically-effective with increasing range and closer to grazing angles. This is contrary to the acoustical performance of a conventional noise barrier, which

becomes less effective with increasing range since it depends on the path length difference between the (hypothetical) direct path between source and receiver and the path from source to the receiver via the top of the barrier. For a 1.5 m high receiver and a 6 m wide wall array, the predicted insertion loss at 10 m range is substantially lower than the insertion loss predicted at 20 m range as shown in Figure 5.27 (a). The predicted insertion loss increases marginally when range is increased from 20 m to 50 m.

It is shown in Figure 5.27 (a), that there is negligible change in insertion loss with varying wall centre-to-centre spacing from 0.1 to 0.5 m. Similarly, changing wall width gives more or less similar insertion at different ranges as shown in Figure 5.27 (b). A minimum number of 8 walls is required to see the low parallel walls effect. According to these initial calculations for acoustically-hard walls, increasing the number of walls does not give any improvement in insertion loss. This was justified on the basis that increasing the number of walls results in propagation of stronger surface waves, thereby mitigating the additional attenuation due to increasing the width of the parallel walls array [101]. Subsequent calculations have indicated that the presence if absorption means that this conclusion does not hold anymore. Calculations of insertion loss over lattices using an effective impedance incorporating absorption given later show that increasing the width of array increases the insertion loss since the surface wave propagation is reduced by the presence of absorption.
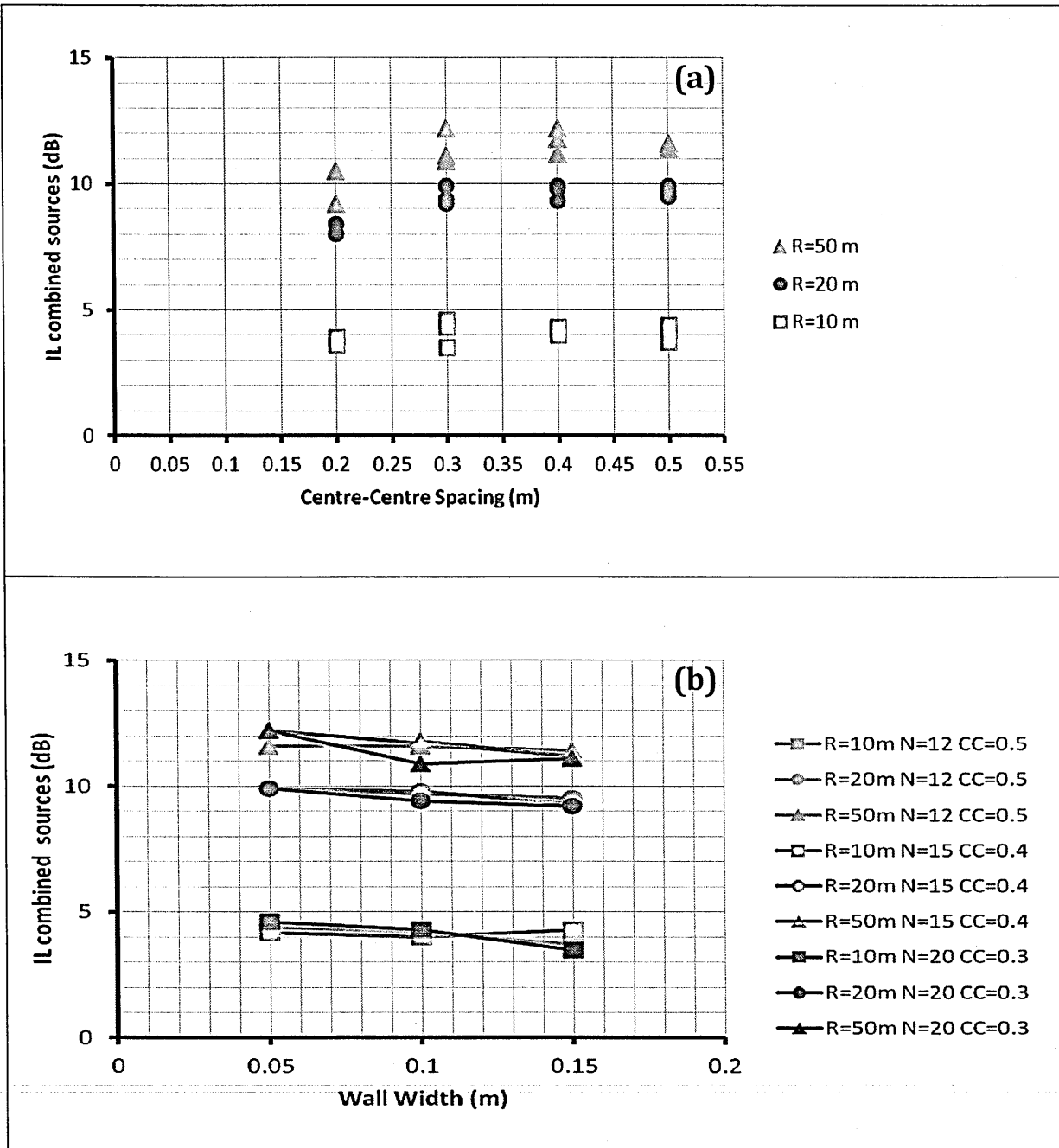
Figure 5.27 Predicted insertion loss at a 1.5 m high receiver at 10, 20 and 50 m from a single lane of combined 70 km/h car road/tyre and engine sources due to a 6 m wide 30 (acoustically-hard) wall array at a 1.5 m high receiver (a) as a function of wall centre-centre spacing and source-receiver range (b) as a function of wall width, source-receiver range (R), number of walls (N) and, centre-to-centre spacing (CC).

5.10.2   Laboratory data over Parallel walls and Lattices

5.10.2.1   Parallel walls

Figure 5.28 shows a laboratory measurement over small parallel walls. These laboratory arrangements are $1/25^{th}$ scale of the geometry used for previous BEM predictions in which the distance between source and first wall was 2.0 m, the 1.5 m high receiver is placed at a distance of 50 m. In the laboratory approximately 1:25 scale geometry, the distance between source and first wall was 0.08 m; receiver was placed at a distance of 2.0 m and at a height of 0.06 m above MDF board. For BEM predictions, the point source was assumed to be at height of 0.01 m above ground. However it was not possible to place the source at $1/25^{th}$ of this height in the laboratory due to the practical limitations. The minimum possible point source height above the MDF sheet in the laboratory was 0.02 m. To achieve this, the lower source tube edge was located only 3 mm above the MDF board surface.
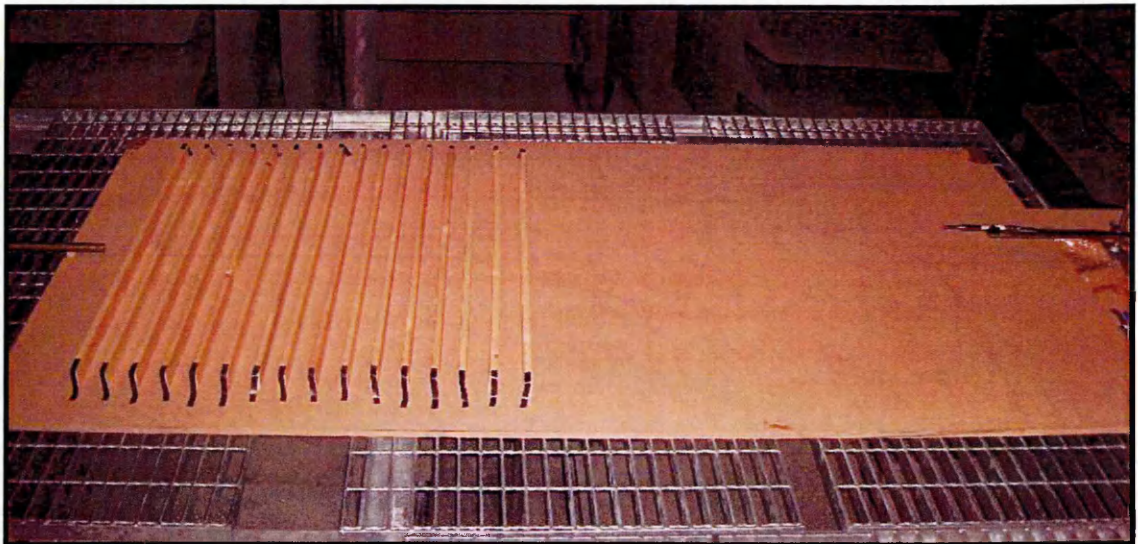
Figure 5.28 Photograph of an array of 16 wooden parallel walls strips spaced regularly on an MDF board.
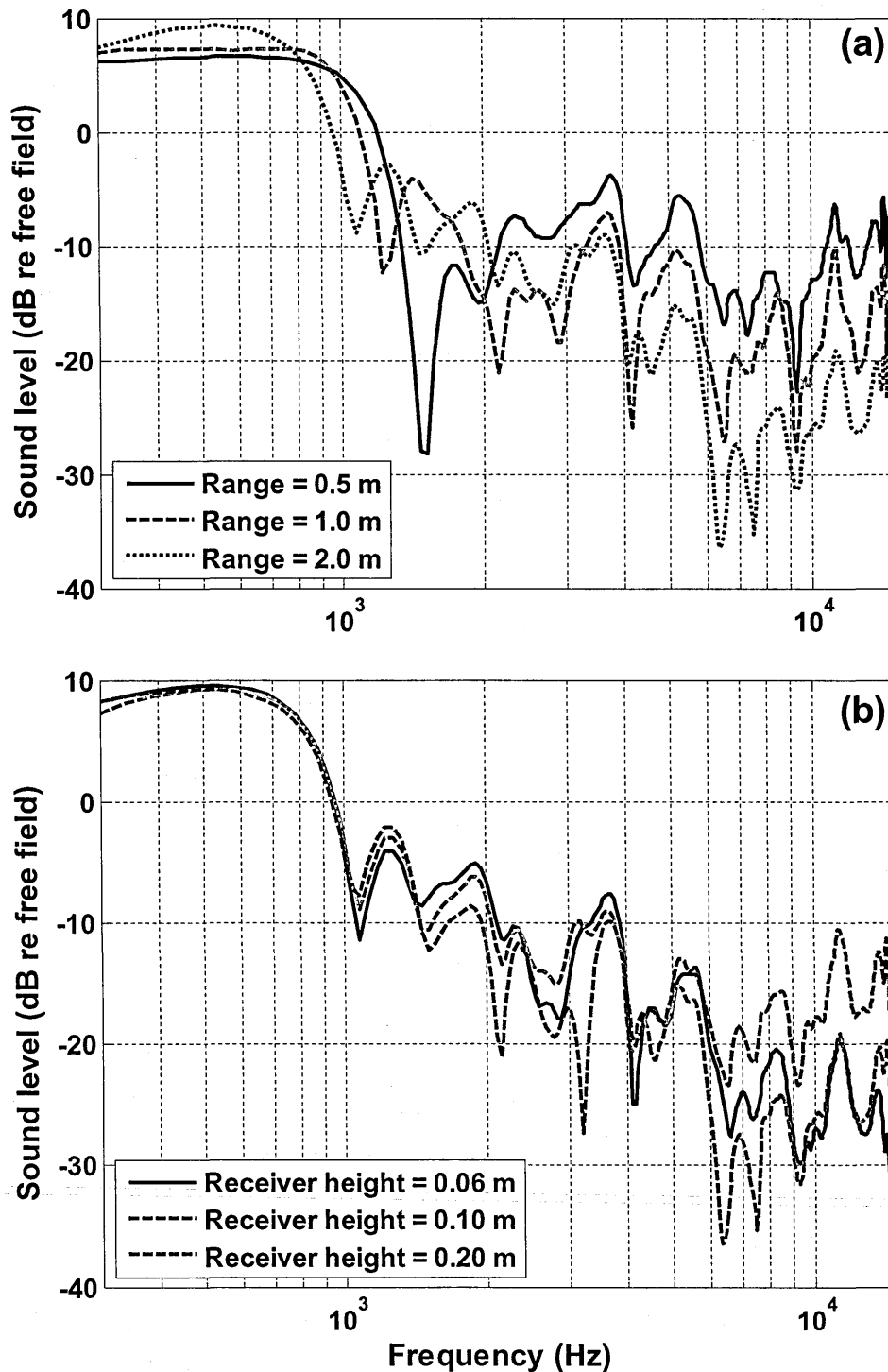
Figure 5.29 Measured excess attenuation spectra over 16 walls (4.0 cm (H) × 1.2 cm (W), 6.0 cm centre-to-centre) starting 8 cm from the source: source height 2 cm (a) for three source-receiver ranges of 0.5 m, 1.0 m and 2.0 m and receiver at height of 10 cm above MDF board (b) for three receiver heights of 0.06 m, 0.10 m and 0.20 m and source-receiver range of 2.0 m.

Figure 5.29 shows the excess attenuation spectra over parallel walls measured outdoors by placing the source at height of 0.02 m and at a distance of 0.08 m from the nearest wall. Three source-receiver ranges of 0.5 m, 1.0 m and 2.0 m have been tested which correspond to full scale dimensions of 12.5 m, 25.0 m and 50.0 m respectively. The results shown in Figure 5.29 (a) supports the conclusion that the effect of low parallel walls increases with increasing range. Figure 5.29 (b) shows the results of laboratory scale measurements for different receiver heights, which also support the conclusion drawn in HOSANNA deliverable 4.3 [101] that the insertion loss due to parallel low walls decreases with the increase in receiver height.

5.10.2.2   A case for using Lattice forms of roughnesss

Figure 5.30 shows the EA spectra measured with source and receiver heights of 0.07 m separated by 0.7 m over a surface composed regularly spaced rectangular strips on a MDF board with different azimuthal angles between the source-receiver axis and 2D rough surface. These indicate that the diffraction assisted rough ground effect is dependent on azimuthal angle between the source receiver axis and rough surface element axes. The maximum rough ground effect is observed, when sound propagates normal to rough surface element axis. The change in angle of up to $30°$ gives rise to more or less similar spectra to that obtained at $0°$. However, when azimuthal angle exceeds $30°$, the roughness effect deteriorates significantly as shown in Figure 5.30. The increase in azimuthal angle causes the EA maxima move to higher frequencies, the magnitude and the numbers of EA maxima are also reduced. As, a result the periodically spaced parallel element rough surface does not remain very effective for traffic noise

attenuation when the noise source impinges the energy at an angle to the

roughness element axes.
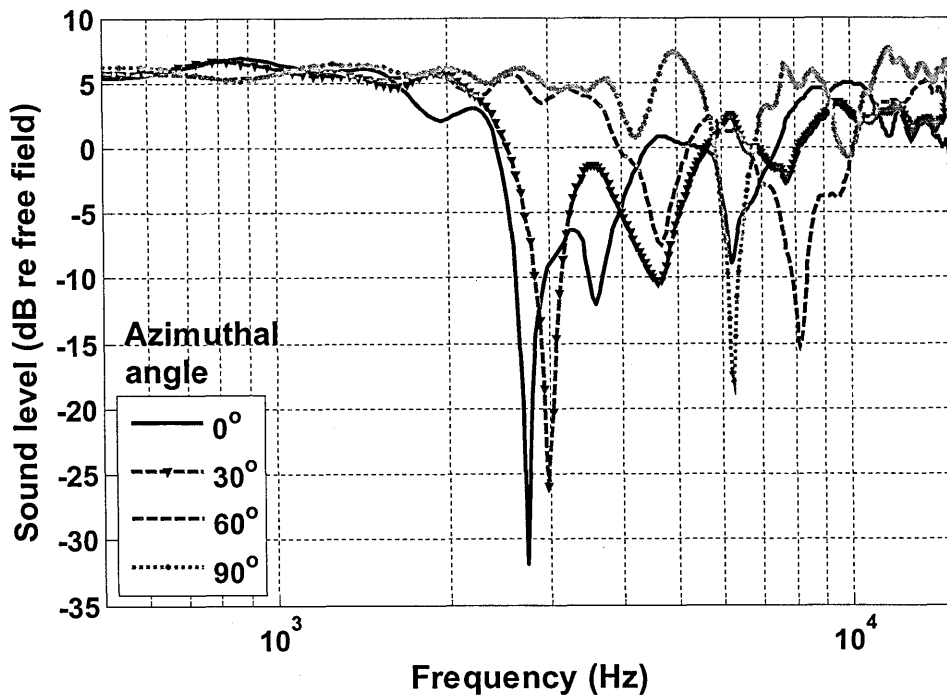
Figure 5.30 EA spectra measured with source and receiver heights of 0.07 m
separated by 0.7 m over a surface composed regularly spaced parallel rectangular
strips on a MDF board with different azimuthal angle between source-receiver axis
and the strip axes.

One way of overcoming the azimuthal angle dependence associated with

2D roughness, is to use roughness consisting of a square cross section lattice.

Another possibility is the 'chequerboard' array discussed in the next section (see

Section 5.10.3.1-B). A square lattice has been tested in the laboratory (see Figure

5.31). A single square pore in the lattice is 1.263 cm deep and 1.404 cm wide. The

lattice walls are 0.185 cm thick with centre-to-centre spacing of 1.589 cm. EA

spectra measured over this laboratory lattice using different geometries shows that

the rough ground effect is not angle dependent (see Chapter 6, Section 6.3.3 &

Figure 6.10). Excess attenuation spectra have been also measured over single,

double and triple layer lattice surfaces showing, as observed previously, that the

rough ground effect is strongly dependent on roughness height as shown in Figure 5.32.
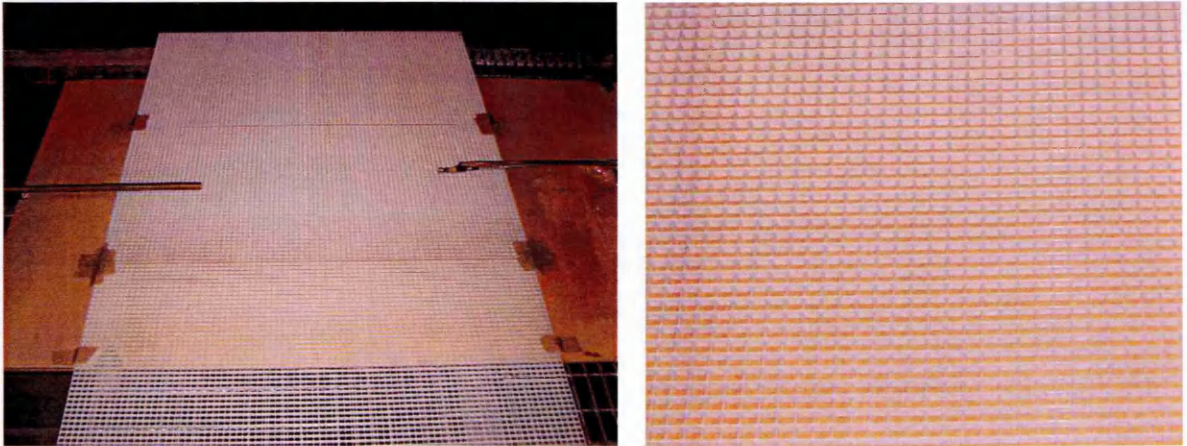
Figure 5.31 Photograph of 3D square lattice used for laboratory measurements.

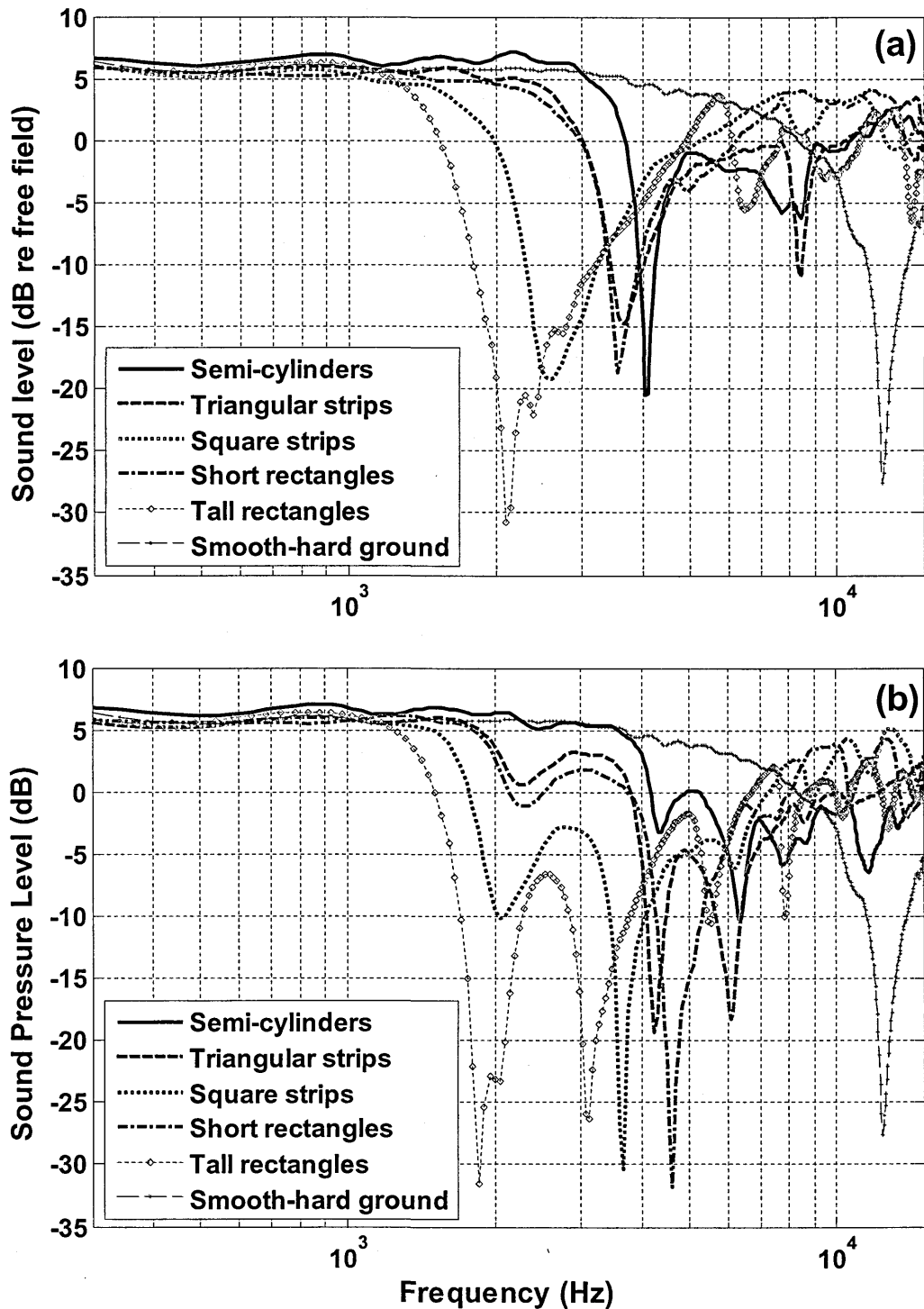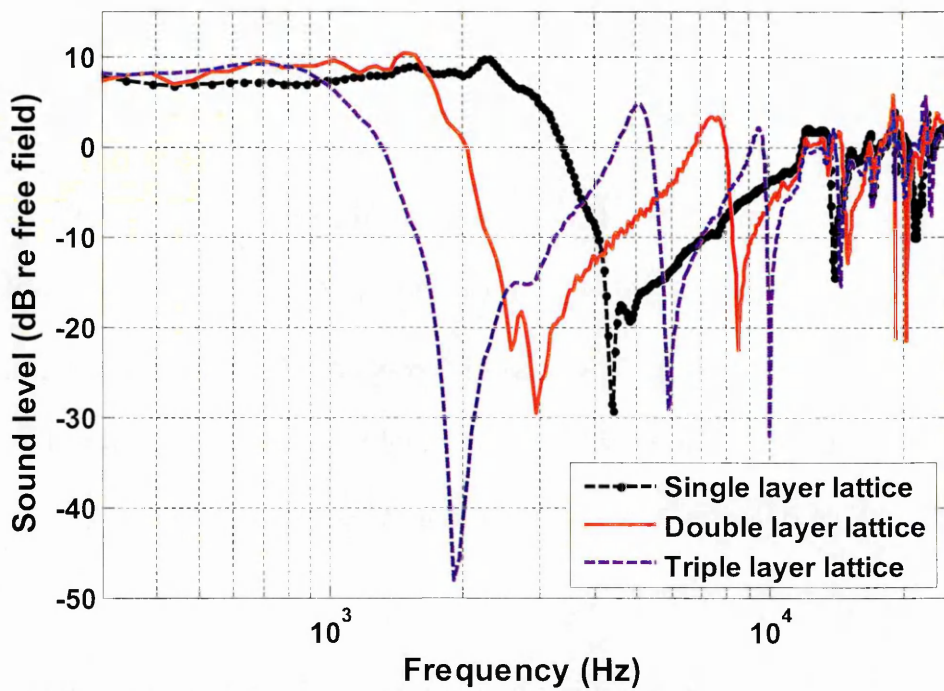**Figure 5.32** EA spectra measured with source and receiver heights of 0.03 m separated by 0.7 m over a surface composed single layer lattice, double layer lattice and triple layer lattice placed over an MDF board.

5.10.3   Outdoor measurements with brick arrays

Outdoor measurements have been carried out over 0.2 m high parallel brick walls at an Open University car park. Different configurations of parallel walls were created using commercially available bricks. The measurement system explained in Chapter (3) has been used for the outdoor measurements.

5.10.3.1   Measurements using noise from distant traffic

5.10.3.1.1   Parallel walls

Outdoor investigations of the acoustical performance of parallel wall arrays have been performed using both a loudspeaker noise source and noise from a nearby road. On a small asphalt-covered car park at the south-west corner of the Open University campus near a busy road in Milton Keynes, an array of nine parallel walls was constructed from 594 standard (UK) house bricks (21.5 cm length × 10 cm height × 6.4 cm largest width) with 'frogs' facing towards the road (away from the loudspeaker). There were 2 rows of 33 bricks in each wall giving walls of length of 7 m. Each wall had a height of 0.20 m (i.e. two lengthwise bricks), a width of 0.064 m and the edge-to-edge spacing between the walls was 0.25 m. The total area occupied by bricks was 18 m^2.

The road (H9 'Groveway') is approximately 135 m from the wall area and elevated by approximately 5 m (see Figure 5.33) with respect to the car park. According to the Principle of Reciprocity the road traffic noise level at a receiver location 0.5 or 1 m from the wall furthest from the road and at a height of 10 cm should correspond to a vehicle source at the microphone position and a receiver at the road. In the first measurement the furthest receiver from the road was located

50 cm from the nearest wall and 10 cm above ground. Figure 5.34 shows the walls and the microphone positions.

Figure 5.33 Location of parallel wall system with respect to nearby road.
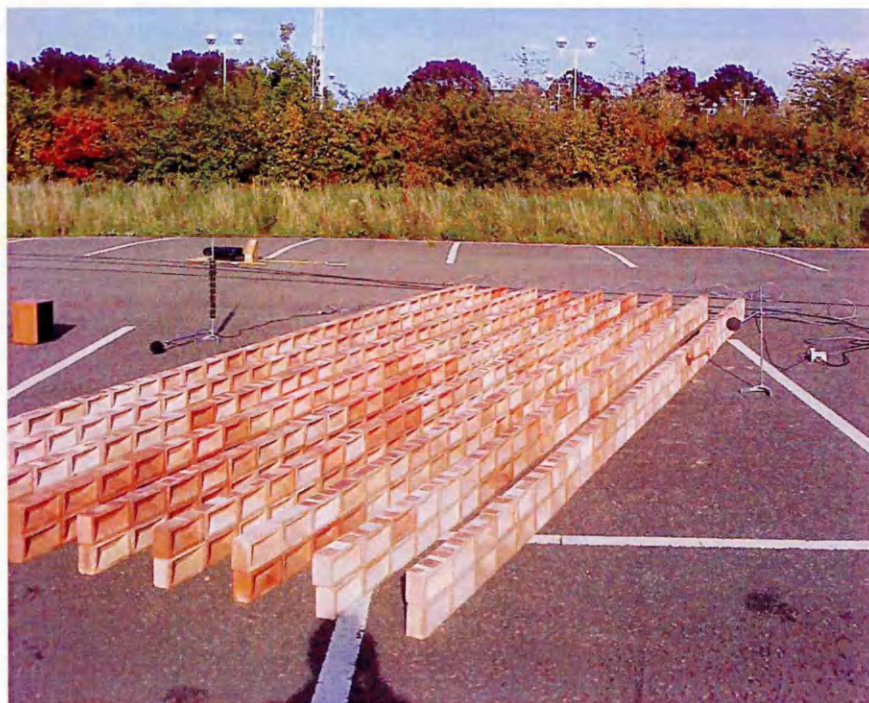
Figure 5.34 The outdoor configuration of nine parallel walls on a car park showing also two microphones and the loudspeaker source.

The experiment was repeated but with the reference microphone at a distance of 100 cm (instead of 50 cm) from the nearest wall. Each experiment was repeated twice (Run #1 and Run #2) and yielded similar insertion losses of between 4 and 4.6 dB. Table 5.8 shows the measured insertion losses. Figure 5.35 (a) shows the A-weighted sound level spectra measured simultaneously at the receiver locations either side of the walls without and with the walls present and Figure 5.35 (b) shows corresponding IL spectra.

The measured negative insertion loss with parallel walls (see Figures 5.35 and 5.39) between 100 and 250 Hz is caused due to the propagation of surface waves. Similarly, the negative insertion loss between 100 and 250 over 'chequerboard' pattern (see Figures 5.37 and 5.40) and brick lattice (see Figure 5.40) is also due to propagation of surface waves. The insertion loss spectra measured without walls i.e. on hard ground (see Figures 5.35 (b) and 5.37 (b), red broken-circle line-IL with no walls) also show negative insertion loss between 1 and 5 kHz. This may be caused by measurement uncertainty. However, it is important to note that the negative insertion loss without walls between 1 and 5 kHz will effectively reduce the insertion loss with walls. Therefore the uncertainty in measurement does not unduly enhance the measured insertion loss values due to walls reported in this chapter.
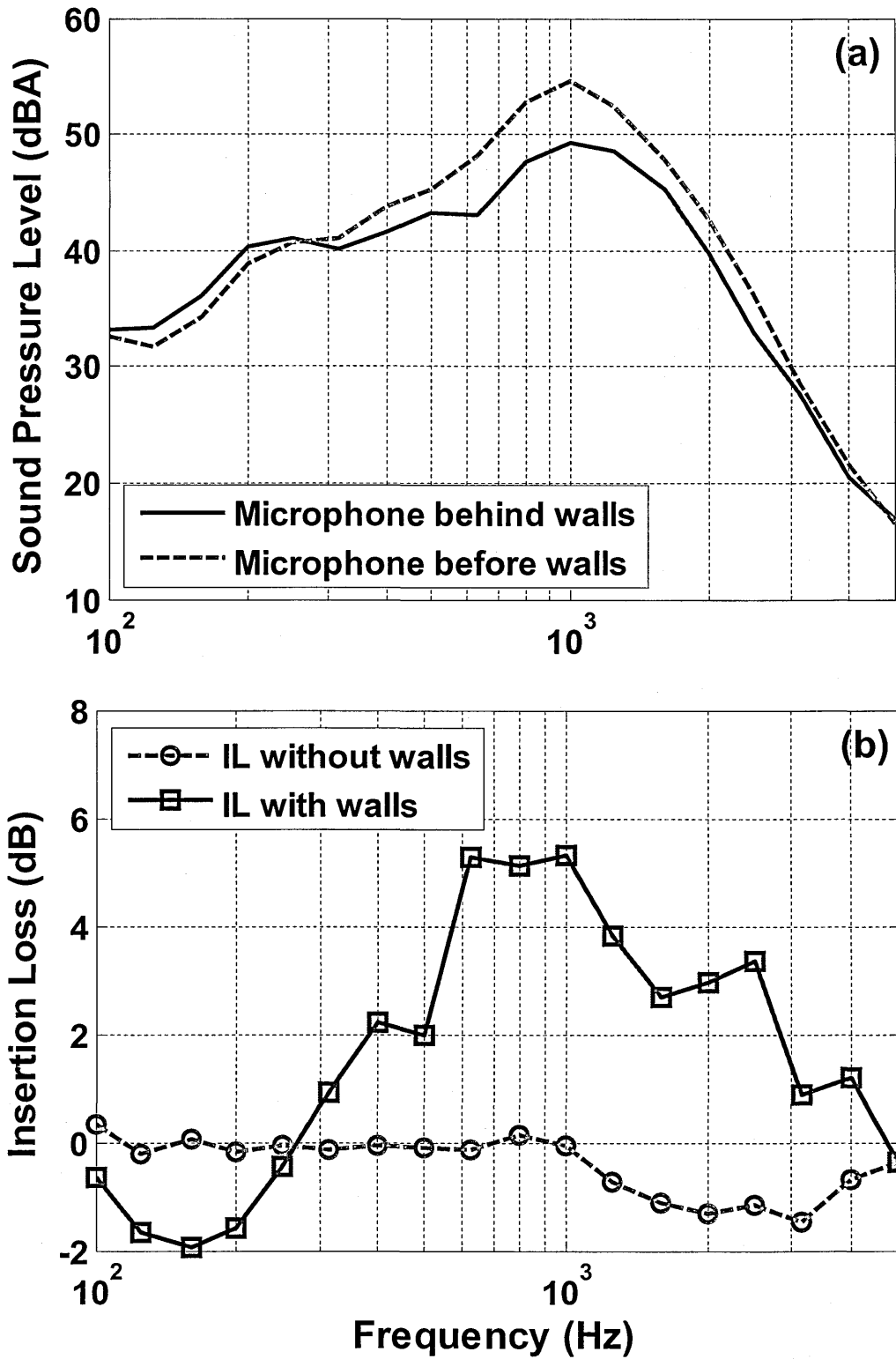
Figure 5.35 (a) Average A-weighted sound pressure levels at microphone locations either side of the walls (see Figure 5.34) and (b) insertion loss spectra before and after the introduction of the walls.

Table 5.8 Measured overall insertion losses for road traffic noise due to parallel walls at two microphone locations.

Centre Frequency (Hz)	Average Insertion Loss (dB)			
	Reference microphone to first wall distance = 50 cm		Reference microphone to first wall distance = 100 cm	
	Run #1	Run #2	Run #1	Run #2
100	-0.4	-0.1	-0.7	-0.9
125	-0.5	-0.4	-1.7	-1.7
160	-0.5	-0.8	-1.9	-1.9
200	-1.4	-1.2	-1.6	-1.3
250	-1.3	-1.1	-0.4	-0.3
315	0.5	0.5	0.9	0.9
400	2.6	2.5	2.2	2.0
500	1.2	1.3	2.0	2.1
630	6.5	6.2	5.3	5.0
800	5.3	5.0	5.1	4.8
1000	5.3	5.3	5.3	5.7
1250	5.4	5.0	3.8	4.0
1600	3.7	3.6	2.7	3.9
2000	3.3	3.6	3.0	4.0
2500	3.0	3.0	3.4	4.8
3150	2.1	1.8	0.9	3.4
4000	0	1.9	1.2	2.0
5000	0.5	0.6	-0.4	0.0
Broadband	**4.6**	**4.2**	**4.0**	**4.1**

5.10.3.1.2 'Chequerboard' configurations

The 594 bricks used in the wall system shown in Figure 5.34 have been rearranged into a 'chequerboard' pattern by displacing alternate pairs of bricks in the parallel walls to the midpoint between the original walls. The resulting array has the same 'roughness' volume per unit area as the parallel wall arrangement. Figure 5.36 shows the 'chequerboard' arrangement, reference and receiver microphone positions. The measurements with road traffic as the noise source show insertion losses between 2.4 and 3.5 dB (Table 5.9 and Figure 5.37).

Table 5.9 gives the summary of measured insertion losses for road traffic noise due to a parallel wall configuration and a chequerboard configuration at three microphone locations. It is concluded that the parallel wall arrangements give better traffic noise attenuation than the 'chequerboard' configurations.
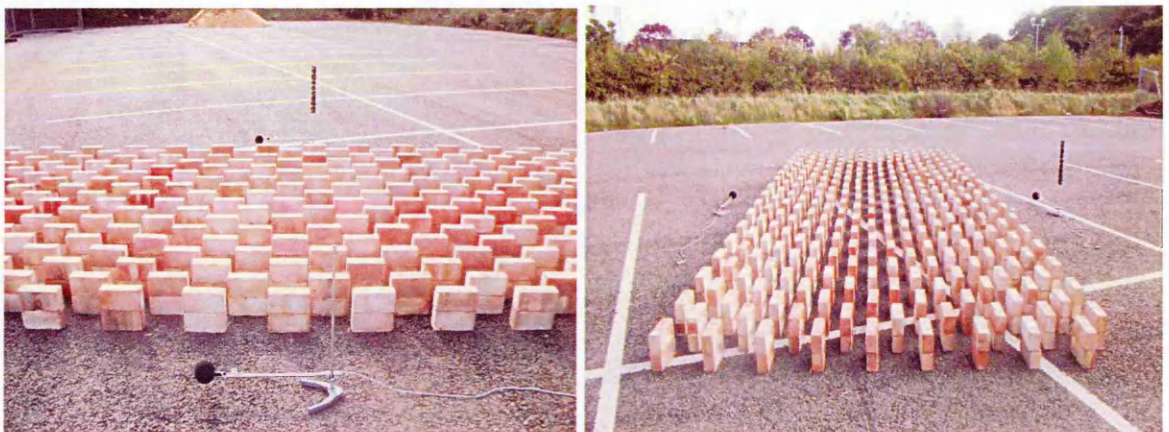
Figure 5.36 Photographs of a brick 'chequerboard' pattern constructed from household bricks on a small car park. Also shown are microphones 1 and 2.
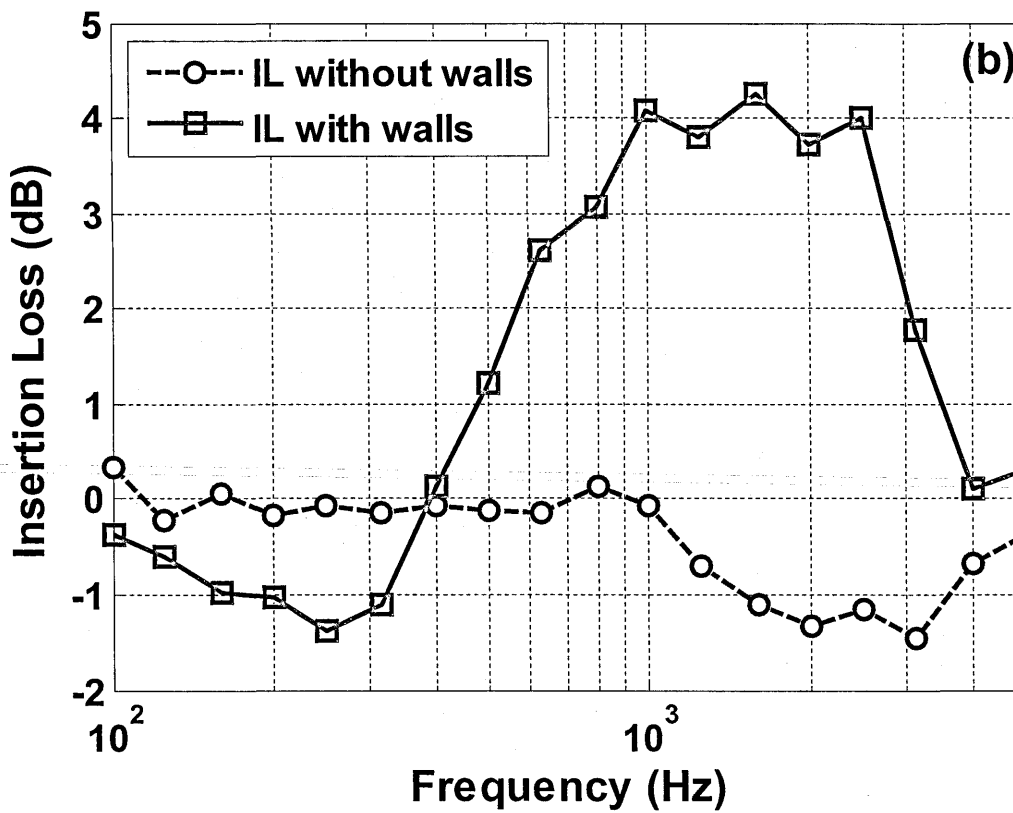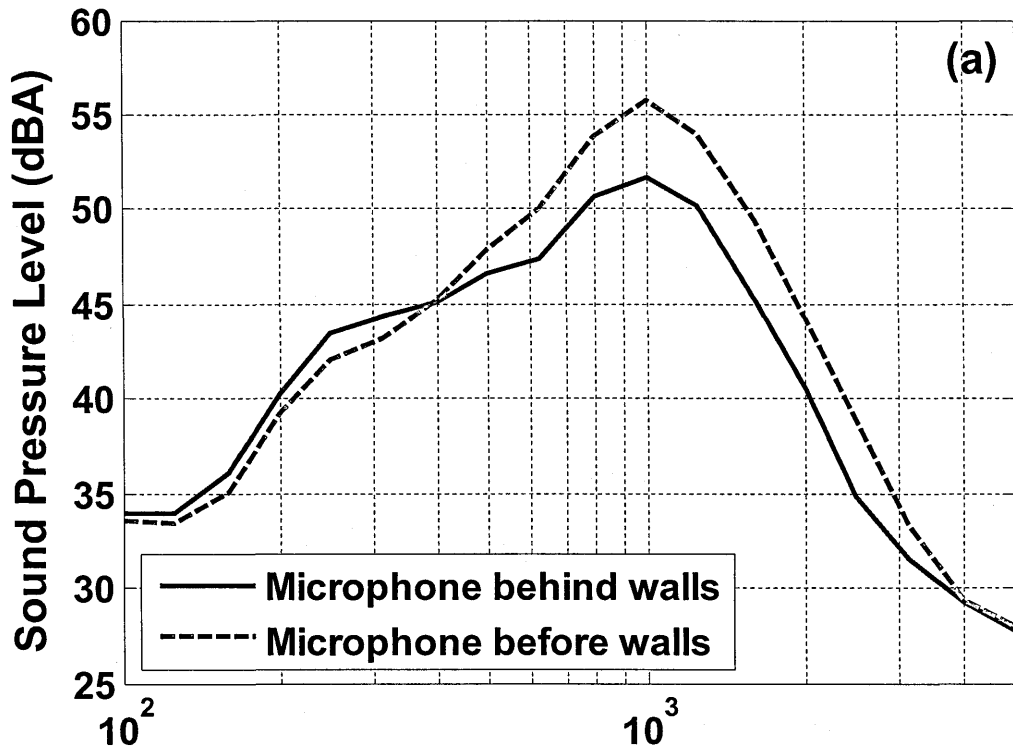
Figure 5.37 Average A-weighted sound pressure levels at microphone locations either side of the brick 'chequerboard' configuration and (b) insertion loss spectra before and after its introduction.

Table 5.9 Overall insertion losses due to a brick 'chequerboard' between two microphone positions obtained with road traffic noise.

Centre Frequency (Hz)	Average Insertion Loss (dB)					
	Ref mic to 1st wall 50 cm		Reference microphone to wall = 100 cm			
	Ref mic height 10 cm 2nd mic height 10 cm		Ref mic height 10 cm 2nd mic height 10 cm		Ref mic height 30 cm 2nd mic height 30 cm	
	Run #1	Run #2	Run #1	Run #2	Run #1	Run #2
100	-0.2	-0.3	-0.4	-0.6	-0.5	-0.4
125	-0.2	-0.5	-0.6	-1.1	-0.8	-0.7
160	-0.8	-0.7	-1.0	-0.5	-0.8	-1.1
200	-1.2	-1.1	-1.0	-0.9	-0.6	-0.7
250	-1.5	-1.4	-1.4	-1.2	-0.1	0.0
315	-1.7	-1.2	-1.1	-1.8	-0.2	-0.2
400	-0.1	0.0	0.1	-0.1	1.0	0.9
500	1.9	1.9	1.2	1.3	2.1	2.5
630	2.7	3.5	2.6	2.9	3.5	3.9
800	3.9	3.4	3.1	3.2	3.5	3.3
1000	4.9	4.7	4.1	4.7	3.5	3.4
1250	4.5	4.1	3.8	4.2	2.6	2.3
1600	4.2	4.2	4.2	4.3	0.5	0.2
2000	4.1	3.9	3.7	4.1	0.2	0.0
2500	4.8	4.2	4.0	4.2	0.5	0.5
3150	2.7	2.1	1.8	2.1	0.3	0.4
4000	0.7	0.1	0.1	0.3	0.1	0.5
5000	0.6	-0.6	0.3	0.6	0.1	0.2
Broadband	**3.5**	**3.4**	**3.0**	**2.8**	**2.6**	**2.4**

Table 5.10 A summary of measured insertion losses for road traffic noise due to a parallel wall configuration and a 'Chequerboard' configuration at three microphone locations.

Array configuration and microphone locations	Average Insertion Loss (dB)	
	Run #1	Run #2
Parallel walls; microphone heights 0.1 m; distance of microphone 1 to nearest wall = 0.5 m	4.6	4.2
Parallel walls; microphone heights 0.1 m; distance of microphone 1 to nearest wall = 1 m	4.0	4.1
'Chequerboard'; microphone heights 0.1 m; distance of microphone 1 to nearest wall = 0.5 m	3.5	3.4
'Chequerboard'; microphone heights 0.1 m; distance of microphone 1 to nearest wall = 1 m	3.0	2.8
'Chequerboard'; microphone heights 0.3 m; distance of microphone 1 to nearest wall = 1 m	2.6	2.4

5.10.3.2   Measurements using a loudspeaker source

Outdoor measurements have been carried out to verify the predicted insertion losses due low parallel walls reported in HOSANNA, Deliverable 4.3 (for details see Section 5.10.1.1). Most of the BEM predictions given in D 4.3, assumed that the source is at a distance of 2.0 m from nearest wall. According to Deliverable 4.3, a minimum number of eight walls is needed to achieve significant insertion loss due to parallel walls. So, an array consisting of 9 parallel walls was constructed. A Mordaunt loudspeaker was placed on the ground at 2m from the nearest wall of the configuration shown in Figure 5.34. The Mordaunt loudspeaker was used for brick walls measurement instead of the B&K point source since the measurements were carried out over longer ranges than at which the B&K source was not loud enough to give good signal to noise ratio. A reference microphone was placed 1.0 m from the source at a height of 0.1 m. A second microphone was placed at 5.0 m and 10.0 m from the source. Most insertion loss calculation results given in Deliverable 4.3 [101] assumed 1.5 high receivers placed at a distance of 20.0 m and 50.0 m from the source. Since the limited extent of the car park used for the outdoor wall experiments does not allow measurements to be made at distances from the wall array greater than 10 m, the effects of larger distances have been simulated by keeping the 'grazing' angle between the top of the wall furthest from the source and the second microphone constant. The corresponding receiver locations lie on a line parallel to the shadow zone boundary caused by the wall array in the absence of meteorological effects (see Figure 5.38). This required placing the microphone at heights of 0.85m and 0.36m to simulate the effects of distances of 20 m and 50 m respectively as shown by schematic in Figure 5.38.
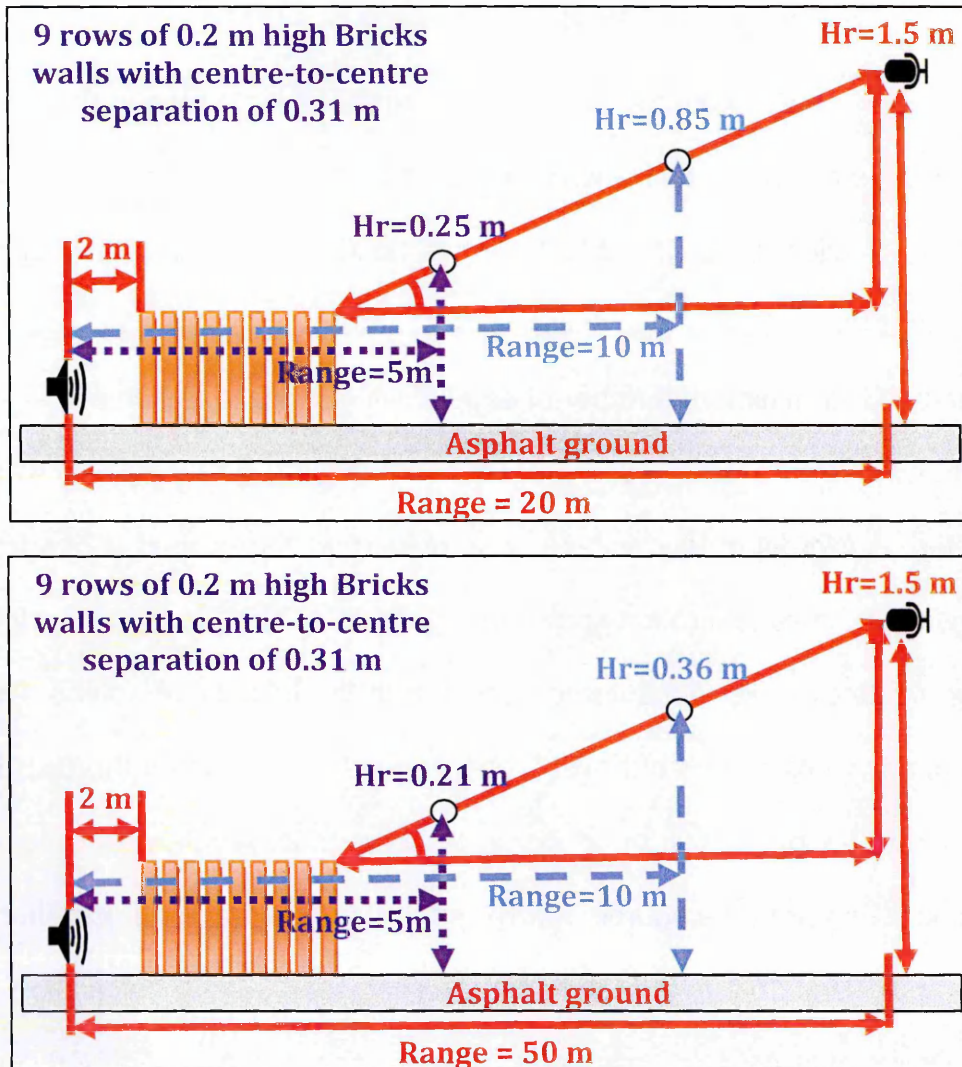
Figure 5.38 Receiver heights at 10 m range corresponding to locations on the edge of the shadow zone due to nine 0.2 m high 0.25 m edge-to-edge parallel walls at ranges of 20 m and 50 m.

5.10.3.2.1 *Parallel walls*

The averaged results of measurements using broadband noise from the loudspeaker source are listed in Table 5.11 and shown in Figure 5.39. Overall insertion losses of between 8.5 and 11.0 dB were measured for 0.2 high and 2.57 m wide parallel walls arrangements. According to the results of BEM calculations given in Deliverable 4.3 [101]; for a 1.5 m high receiver an array of nine walls can give an insertion loss of 10.1 dB and 10.0 dB for the ranges of 20 m and 50 m

respectively. The outdoor measurements, although not for exactly the same geometry as BEM calculations due to practical limitations, nevertheless give similar insertion losses to those calculated at ranges of 20 m and 50 m.
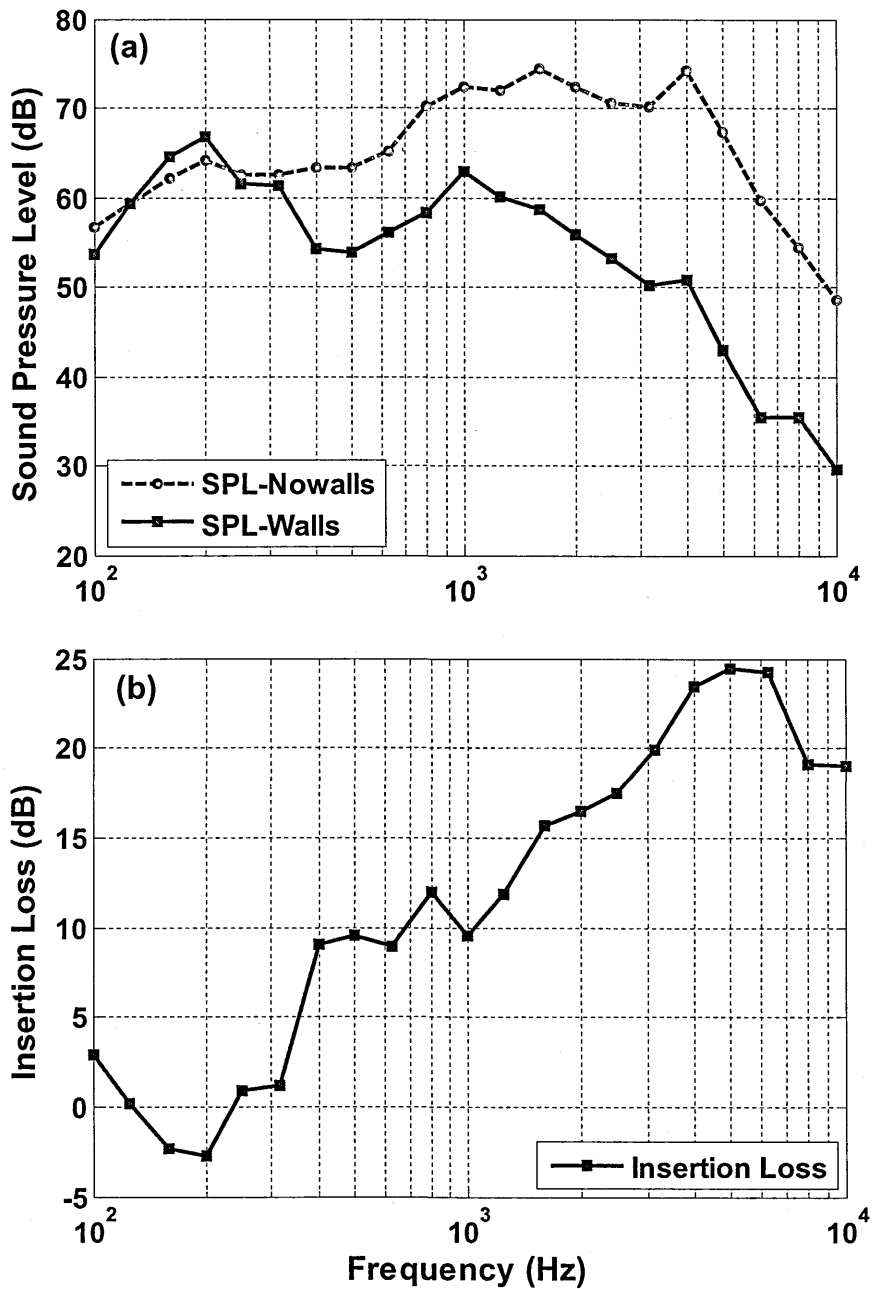
Figure 5.39 Measured sound pressure level with and without brick-based parallel walls configurations and the corresponding insertion loss spectrum for microphone placed at a height of 0.36 m and at a distance10 m from the source. The distance between source and the abatements is 2m and the corresponding overall insertion losses are listed in Table 5.11.

Table 5.11 Overall insertion losses due to nine parallel walls measured at distances of 5 m and 10 m; heights of 0.25 m and 0.85 m (corresponding to a 1.5 m high receiver at 20 m range (see Figure 5.38)); heights of 0.21 m and 0.36 m(corresponding to a 1.5 m high receiver at 50 m range (see Figure 5.38).

Centre Frequency (Hz)	Average Deduced Insertion Loss (dB)			
	Corresponds to a 1.5 m high receiver at 20 m range		Corresponds to a 1.5 m high receiver at 50 m range	
	Hr = 0.25m R = 5m	Hr = 0.85m R = 10m	Hr = 0.21m R = 5m	Hr = 0.36m R = 10m
100	0.5	-1.5	-2.1	-0.3
125	-1.5	-1.0	-1.9	-0.6
160	-2.1	-2.6	-2.3	-2.5
200	-2.9	-2.6	-2.9	-2.7
250	-0.8	1.5	-1.2	0.9
315	5.8	1.6	5.2	1.1
400	8.4	9.5	8.2	8.9
500	15.1	10.1	16.8	9.2
630	15.7	9.3	17.1	8.8
800	18.3	11.8	21.3	11.9
1000	13.1	9.6	16.2	9.7
1250	14.7	12.5	17.1	12.0
1600	18.3	12.9	19.3	15.8
2000	20.0	11.9	21.0	16.6
2500	19.2	11.4	21.5	17.7
3150	19.9	11.2	22.7	20.0
4000	23.5	12.7	25.0	23.5
5000	24.6	12.8	28.4	24.5
6300	24.2	11.0	28.0	24.3
8000	20.3	4.0	24.0	19.4
10000	19.2	2.1	23.7	19.2
Broadband	**10.8**	**8.5**	**11.0**	**9.6**

5.10.3.2.2   'Chequerboard' configurations

BEM is only capable of simulating 2D surfaces such as parallel walls. However, it was not possible to test other configurations using BEM. To test some other configurations, the parallel walls were rearranged as 'Chequerboard' patterns and measured outdoors. The averaged results of measurements using broadband noise from the loudspeaker source are listed in Table 5.12 and shown in Figure 5.40. Overall insertion losses of between 8.5 and 11.0 dB were measured for 0.2 high and 2.57 m wide 'Chequerboard' arrangements.
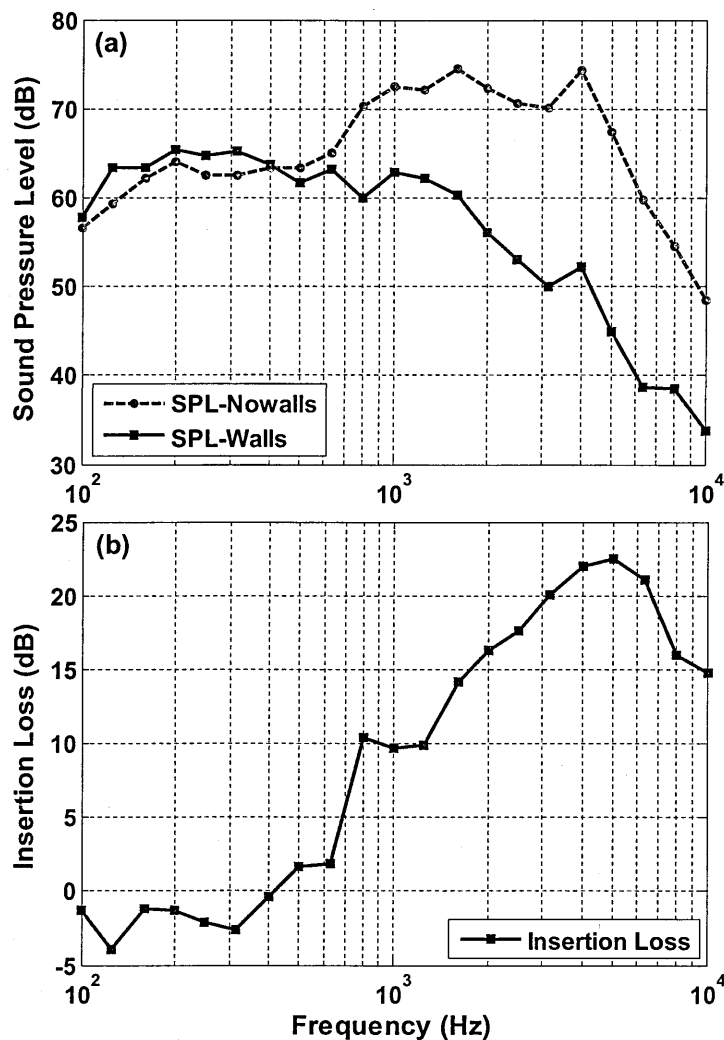
Figure 5.40 Measured sound pressure level with and without brick-based 'Chequerboard' configurations and the corresponding insertion loss spectrum for at a microphone placed at a height of 0.36 m and at a distance10 m from the source. The distance between source and the abatements is 2m and the corresponding insertion losses are listed in Table 5.12.

Table 5.12 Insertion losses due to 'Chequerboard' configurations measured at distances of 5 m and 10 m; heights of 0.25 m and 0.85 m-corresponds to a 1.5 m high receiver at 20 m range (see Figure 5.38); heights of 0.21 m and 0.36 m-corresponds to a 1.5 m high receiver at 50 m range (see Figure 5.38).

Centre Frequency (Hz)	Average Deduced Insertion Loss (dB)			
	Corresponds to a 1.5 m high receiver at 20 m range		Corresponds to a 1.5 m high receiver at 50 m range	
	Hr = 0.25m R = 5m	Hr = 0.85m R = 10m	Hr = 0.21m R = 5m	Hr = 0.36m R = 10m
100	1.2	-2.0	-1.6	-2.2
125	-0.5	-0.9	-0.8	-2.2
160	-0.8	-1.8	-1.0	-1.3
200	-1.5	-1.3	-1.4	-1.2
250	-2.3	-1.7	-2.4	-2.0
315	-2.6	-1.9	-3.1	-2.6
400	-1.9	0.9	-2.7	-0.3
500	-1.0	2.0	-1.9	1.9
630	1.7	2.5	0.7	2.0
800	17.3	10.8	18.2	10.8
1000	13.0	9.6	15.3	10.0
1250	13.6	10.7	14.8	10.2
1600	14.6	11.7	17.0	14.3
2000	17.9	11.6	19.3	16.5
2500	19.3	11.1	21.0	17.9
3150	19.4	11.2	22.2	20.3
4000	21.0	11.1	22.6	22.3
5000	22.4	11.3	26.6	22.8
6300	21.0	8.5	25.1	21.3
8000	17.2	1.7	22.1	16.2
10000	13.7	-1.4	19.7	14.8
Broadband	**8.5**	**7.2**	**8.3**	**7.9**

5.10.3.2.3   Lattice Configurations

To test another potentially azimuthal-angle-independent configuration, the outdoor parallel walls were rearranged into lattice patterns. The details of the lattice arrangements are given in next section. The averaged results of measurements using broadband noise from the loudspeaker source are listed in Table 5.13 and shown in Figure 5.42. Overall insertion losses of between 7.6 and 11.5 dB were measured for 0.2 m high and 2.3 m wide lattice arrangements.
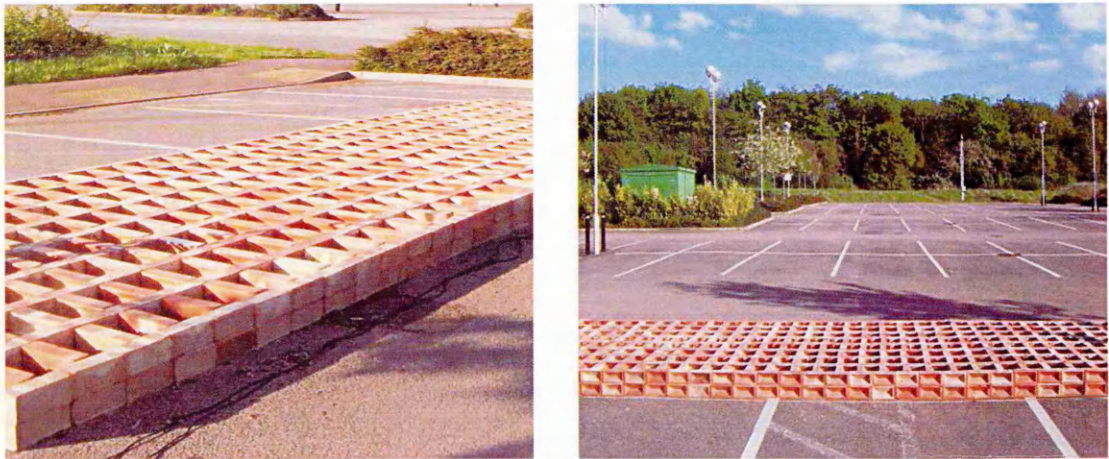
Figure 5.41 Photographs of lattice configurations.
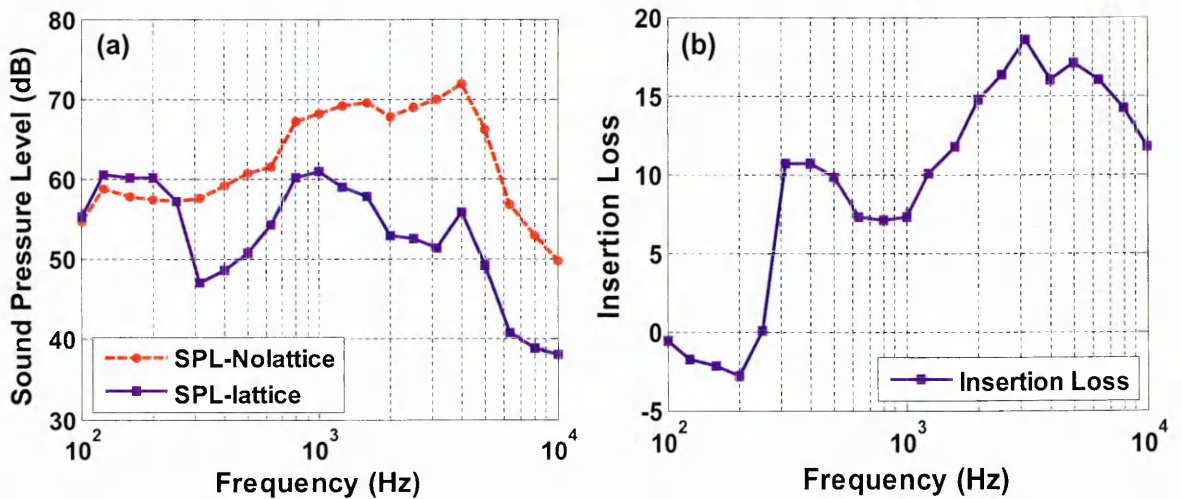
Figure 5.42 Measured sound pressure level with and without a brick-based lattice configuration and the corresponding insertion loss spectrum at a microphone placed at a height of 0.36 m and at a distance10 m from the source. The distance between source and the start of the abatement is 2m and the corresponding insertion losses are listed in Table 5.13.

Table 5.13 Insertion losses due to Lattice configurations measured at distances of 5 m and 10 m; heights of 0.25 m and 0.85 m-corresponds to a 1.5 m high receiver at 20 m range (see Figure 5.38); heights of 0.21 m and 0.36 m-corresponds to a 1.5 m high receiver at 50 m range (see Figure 5.38).

Centre Frequency (Hz)	Average Deduced Insertion Loss (dB)			
	Corresponds to a 1.5 m high receiver at 20 m range		Corresponds to a 1.5 m high receiver at 50 m range	
	Hr = 0.25m R = 5m	Hr = 0.85m R = 10m	Hr = 0.21m R = 5m	Hr = 0.36m R = 10m
100	-0.9	-1.0	-1.4	-0.6
125	-1.8	-1.7	-2.3	-1.8
160	-2.3	-2.1	-2.0	-2.2
200	-2.9	-2.4	-3.4	-2.7
250	-2.2	0.7	-2.8	0.0
315	7.4	10.5	6.9	10.3
400	18.4	9.7	18.0	10.5
500	16.4	9.6	16.5	9.7
630	15.2	9.2	14.8	7.3
800	15.5	10.0	15.4	7.1
1000	14.1	8.8	16.2	7.3
1250	14.4	9.7	17.4	10.0
1600	14.4	8.8	17.2	11.7
2000	14.3	8.5	16.5	14.6
2500	15.8	7.9	17.1	16.1
3150	17.6	8.0	19.3	18.2
4000	18.0	8.0	21.8	15.9
5000	20.4	7.2	23.0	16.3
6300	16.1	4.5	18.1	12.1
8000	12.5	2.9	13.3	9.1
10000	9.0	3.3	10.4	7.2
Broadband	**11.0**	**7.6**	**11.5**	**9.5**

5.10.3.3   Drive by tests

Additional bricks were used to construct longer arrays on a larger car park at the Open University and thereby enable measurements of drive by noise reductions. A schematic of the drive by test arrangements is shown in Figure 5.43. The car was driven at a distance of 2.5 m from the walls along a straight line. Microphone B was set up behind the walls and 10 m distance from the centre line of the car drive-by line. Microphone A was set up on the opposite side of the drive-by line and at the same distance of 10 m from it. Both microphones were 1.5 m above hard ground (asphalt). 10 to 15-second recordings were taken of noise levels at the two receptors as a car drove past with a constant speed. It was very important to determine accurately the period when the car was passing directly in front of the walls to assess the effect of the walls alone. A simple approach was applied by placing two BNC cables on the ground at points A and B. Two microphones were placed on asphalt ground next to BNC cables. When the car tyre passed over the cables, it produced a short impulsive sound. The impulsive spike was picked up by microphones on the ground so that In the recorded data there was a spike for each tyre passing over the cables. At point A when the car passed over the cable, two spikes were picked up by the microphone placed close to the cable. These two spikes helped to calculate the start of the pass by (denoted by 'car exposure time' in Figure 5.43) and also the vehicle speed at point A. Similarly, the end of the pass by and the vehicle speed at point B were measured. The car was drove in both directions. Microphones were calibrated before and after each drive by test.

2.3 m wide and 0.2 m high parallel walls arrangement; 9 × 0.064 m thick rows, 0.28 m centre-to-centre spacing

Microphone 1

Hr1 = 1.5 m

d = 10 m

Point A

Point B

Car type 'A'

Car exposure time

2.5 m

L = 2.2 m

W = 16 m

d = 10 m

Hr2 = 1.5 m

Microphone 2
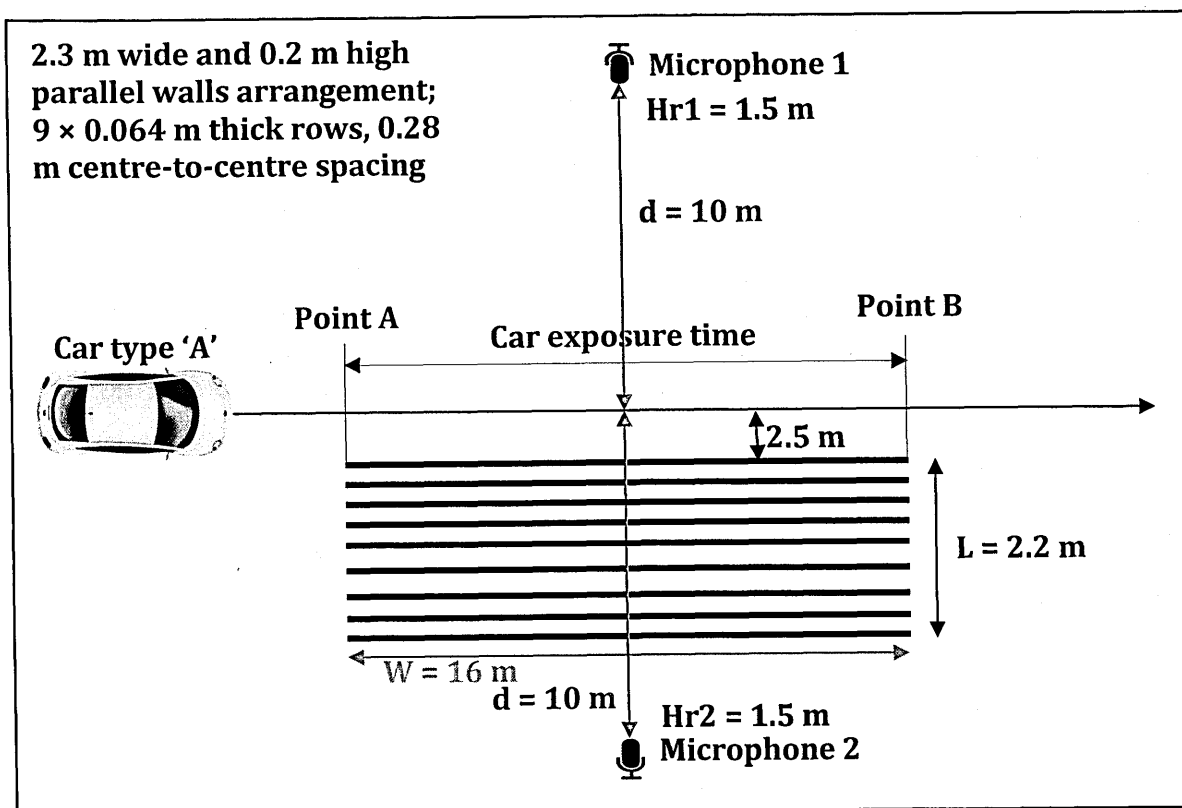
Figure 5.43 A schematic of drive by test near parallel walls.

5.10.3.3.1   *Parallel walls*

A total of 1440 bricks were deployed to create a 2.3 m wide and 16 m long nine parallel walls brick array with centre-to-centre spacing of 0.28 m. A single brick was 0.1 m tall, 0.2 m long and 0.064 m wide. Two stacked bricks were used to obtain a height of 0.2 m. An old sports car (car type 'A') was used for measurement as shown in Figure 5.44. Measured spectra at a 1.5 m high receiver 10 m from the pass-by of the car type 'A' before and after the insertion of the low wall system are shown in Figure 5.45. The measured insertion loss and average speed due to car type 'A' are listed in Table 5.14. The average car pass-by speed was 35.4 km/h and average insertion loss due to low parallel walls at a 1.5 m high

receiver and 10 m during the pass by is 2.7 dB. The old sports car had a spectrum with an SPL peak around 200 Hz (see Figure 5.45).
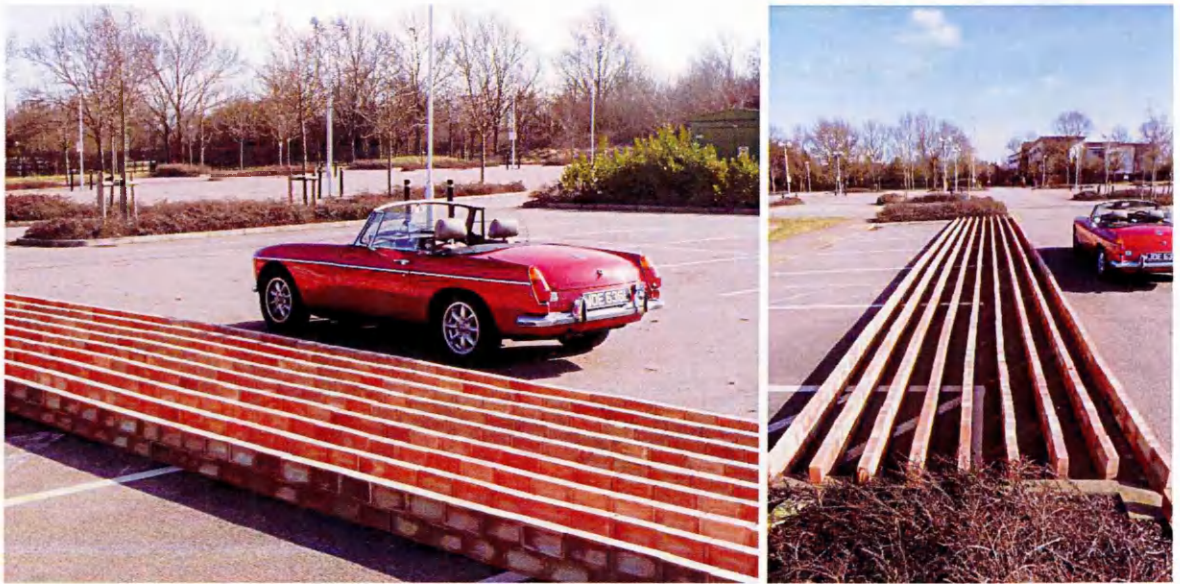
Figure 5.44 Photographs of drive-by tests near parallel walls using car type 'A'.

Table 5.14 Measured Insertion loss for drive by test near parallel walls.

Source – Car type1	A-weighted SPL no walls (dB)	A-weighted SPL with walls (dB)	Insertion loss (dB)	Approximate Car Speed (km/h)
Measurement # 1	70.7	68.2	2.6	39.0
Measurement # 2	71.1	68.5	2.6	38.0
Measurement # 3	70.8	68.0	2.8	35.0
Measurement # 4	62.5	59.9	2.6	33.0
Measurement # 5	64.8	62.1	2.6	36.0
Measurement # 6	62.7	59.9	2.8	32.5
Measurement # 7	74.4	72.0	2.5	35.0
Measurement # 8	63.7	60.9	2.8	35.0
Averaged results	**69.7**	**67.0**	**2.7**	**35.4**
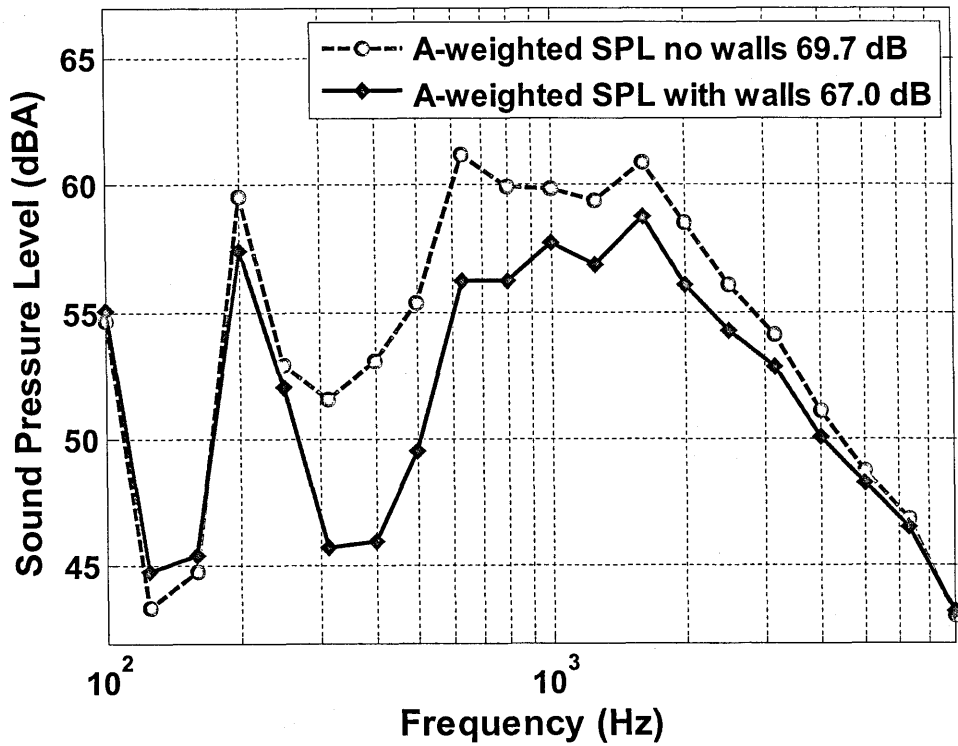
Figure 5.45 Averaged A-weighted sound pressure level with walls and no walls, measured during drive by tests using sports car travelling at a speed of 35.4 km/h.

5.10.3.3.2   Lattice

The rough ground effect due to parallel walls is azimuthal angle dependent (for details see section 5.10.2.1). Consequently the 2D parallel walls were rearranged into a 3D lattice (for details see section 5.10.2.2). When 9 brick walls were rearranged into a lattice structure, only 5 lattice rows could be constructed from the available bricks. The resulting lattice had a rectangular cell with dimensions 0.215 m x 0.151m x 0.2 m (length x width x height). A detailed schematic of the drive by test near the lattice is shown in Figure 5.46 and the corresponding photographs are in Figure 5.47. A different car to that used near the parallel walls was used for the drive-by tests near the lattice (see Figure 5.47). This is a newer type of car with less engine noise (car type 'B'). Similar measurements and analyses were made as near the parallel walls. Measured

spectra at a 1.5 m high receiver 10 m from the pass-by of the car type 'B' before and after the insertion of the lattice structure are shown in Figure 5.48. Each plot represents the average of levels recorded during eight pass-bys. The measured insertion losses and speeds during test with car type 'B' are listed in Table 5.15.
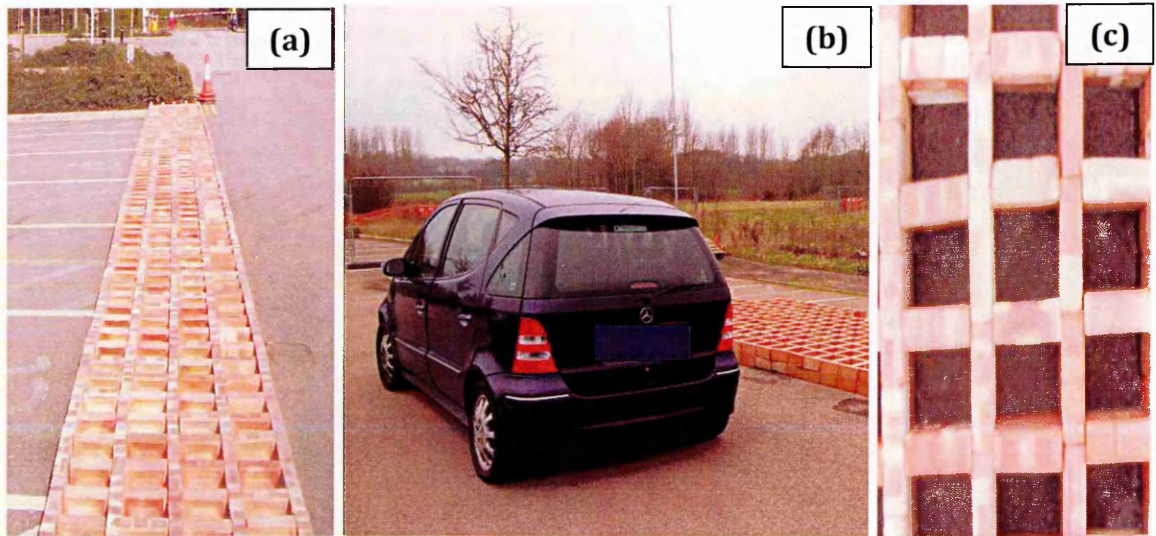
Figure 5.46 (a) brick lattice (b) drive-by test using car type 'B' and (c) plan view of brick lattice.
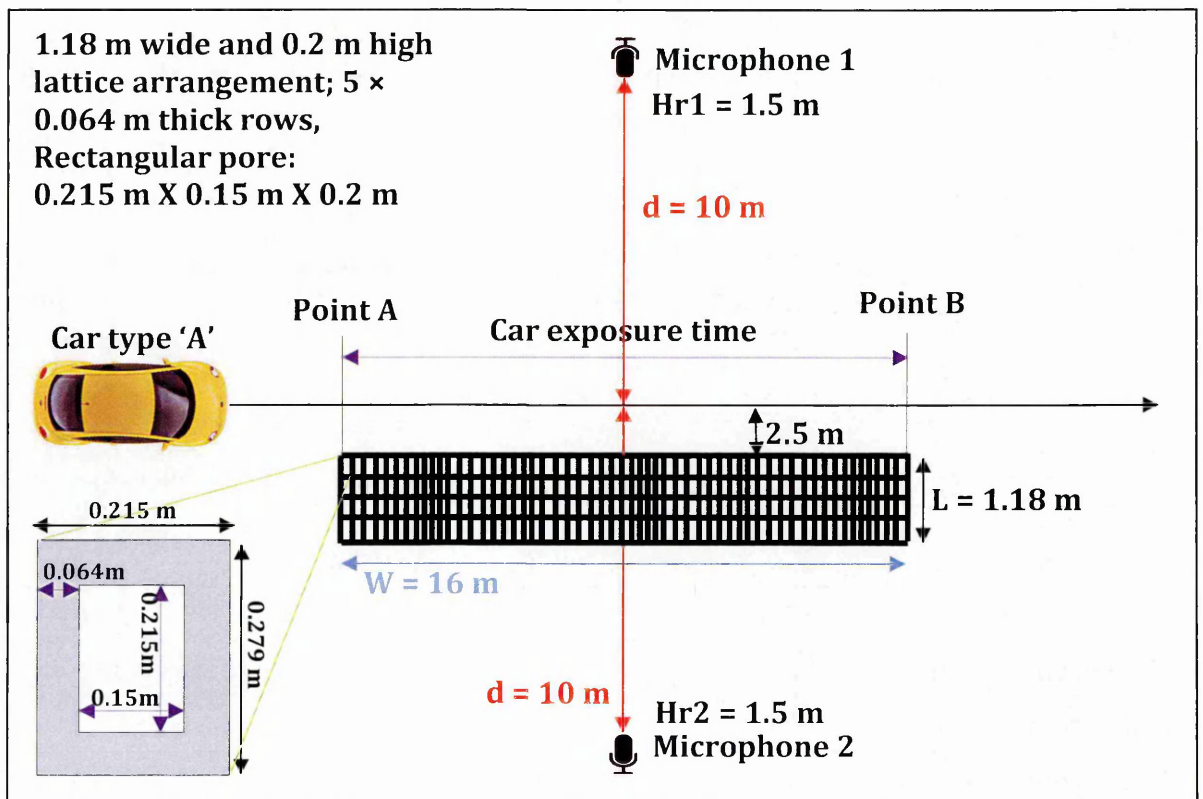
Figure 5.47 A schematic of an drive by test near a brick Lattice arrangement.

The average car pass-by speed was 38.0 km/h and average insertion loss due to lattice at a 1.5 m high receiver and 10 m from pass by drive line was 2.6 dB.
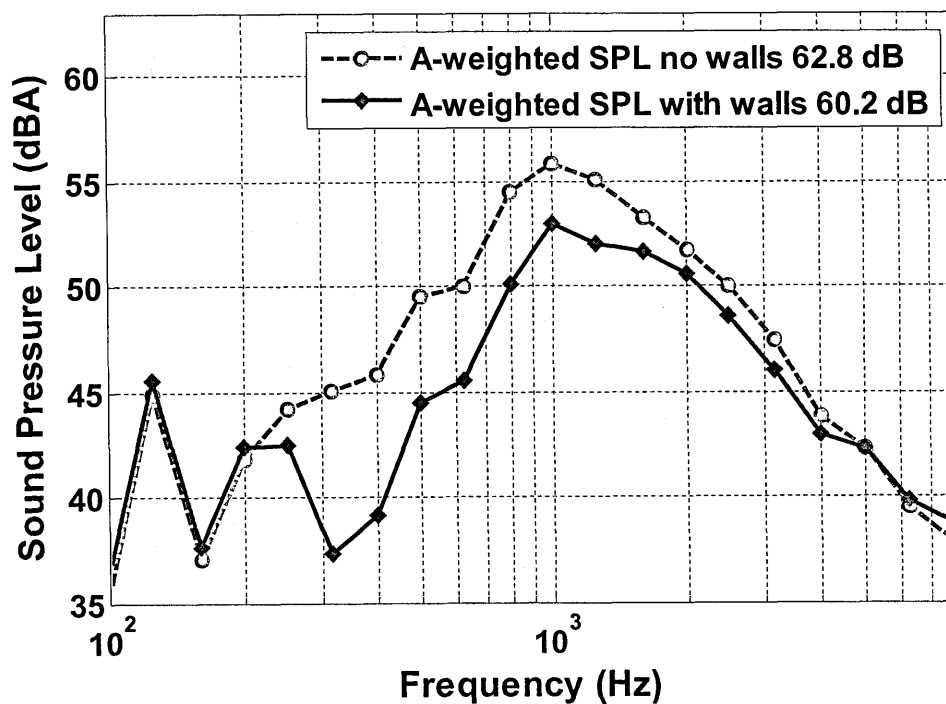
Figure 5.48 Averaged A-weighted sound pressure level spectra with lattice and no lattice, measured during drive by tests using car type 'B' travelling at a speed of 38.0 km/h.

Table 5.15 Measured Insertion loss for drive by test over lattice.

Source – Car type2	A-weighted SPL no walls (dB)	A-weighted SPL with walls (dB)	Insertion loss (dB)	Approximate Car Speed (km/h)
Measurement # 1	63.6	60.6	3.0	40.0
Measurement # 2	62.2	59.4	2.8	37.0
Measurement # 3	63.1	60.5	2.6	37.5
Measurement # 4	63.3	60.8	2.5	38.0
Measurement # 5	62.6	59.6	3.0	39.0
Measurement # 6	62.3	59.9	2.4	36.0
Measurement # 7	63.0	60.7	2.3	36.0
Measurement # 8	61.7	59.6	2.1	40.0
Averaged results	**62.8**	**60.2**	**2.6**	**38.0**

The overall broadband reduction in the noise from car B due to the 1.18 m wide square cell lattice wall configuration was found to be more or less the same as that due to the 2.3 m wide nine parallel walls configuration for car A albeit occupying significantly less land area. As mentioned earlier another major advantage of a lattice configuration over a parallel wall configuration is that the ground effect due to the lattice is azimuthal angle independent.

5.10.3.3.3   *Pathways through lattice structure*

A potential advantage of ground roughness based noise abatement compared with a conventional noise barrier is that it can be walked over or through. In this connection it is interesting to investigate the effects on attenuation of pathways through the lattice structure. Further measurements have been made while car 'B' was driven past an 8.6 m long 2.30 m wide lattice arrangement (located on a different car park) without and with a central 0.4 m wide pathway (see Figure 5.49). The lattice was rearranged to make it 2.30 m wide and to create a pathway through it. Due to the limited availability of bricks, the lattice length was reduced. Similar measurements were made to those described previously. Two kinds of pathways were tested, i.e. a straight-central pathway and a diagonal pathway. Averaged insertion losses (3 passbys at an average speed of 41.0 km/h without a path, 4 passbys at an average speed of 45 km/h with the central path) and 4 passbys at an average speed of 42 km/h with the diagonal path) are detailed in Table 5.16. A consequence of the different lattice array dimensions and faster average speeds is that without a path the measured IL (2.2 dB) is slightly less than that measured (2.6 dB) due to the 16 m long 1.18 m wide array. Nevertheless the creation of the path results only in a small reduction (about 0.5

dB) in insertion loss at a 1.5 m high receiver 10 m from the nearest wheels. The central and diagonal pathway gives overall insertion losses of 1.8 dB and 2.0 dB respectively. The reduction in attenuation due to the diagonal pathway is slightly less than that due to the straight central pathway.
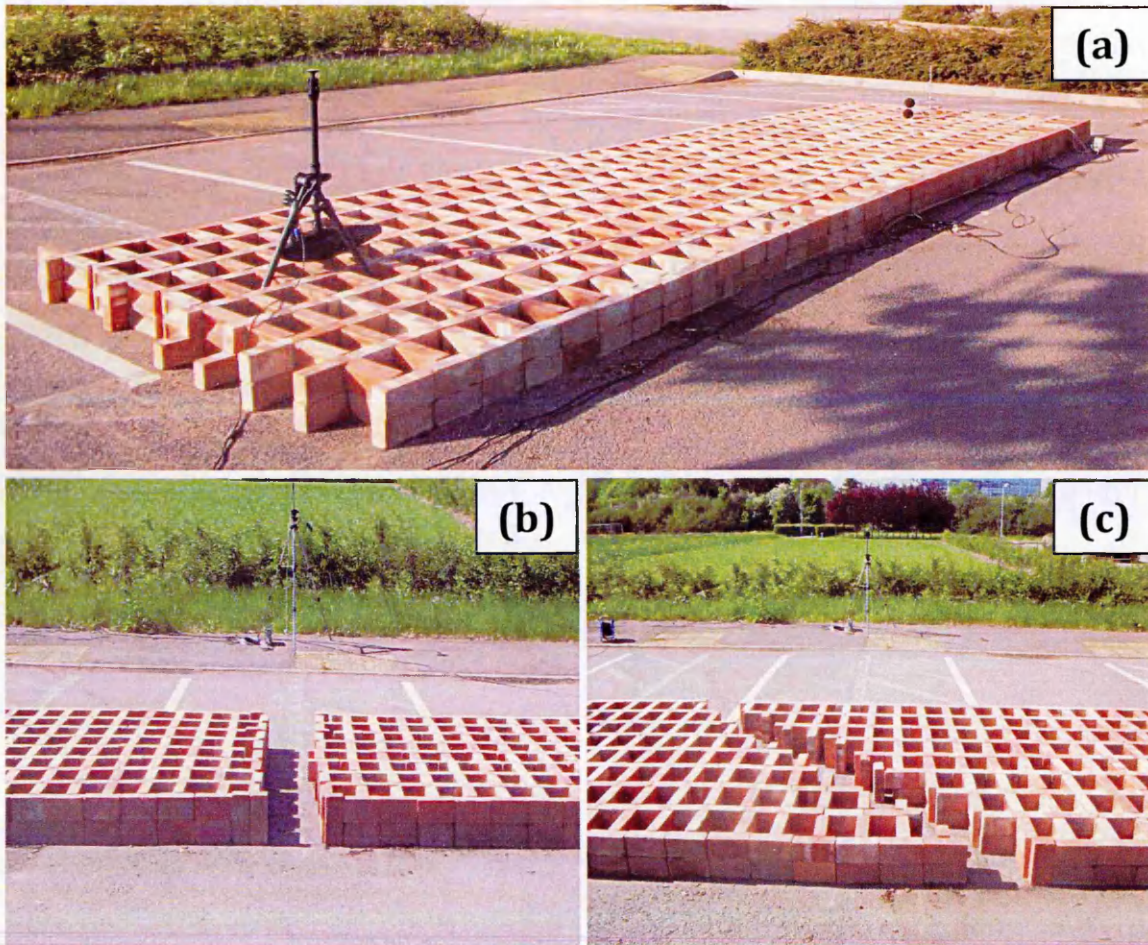
Figure 5.49 Photographs of 8.6 m long 2.30 m wide brick lattice (a) without and (b) with a 0.4 m wide central path (c) with a 0.4 m wide diagonal path.
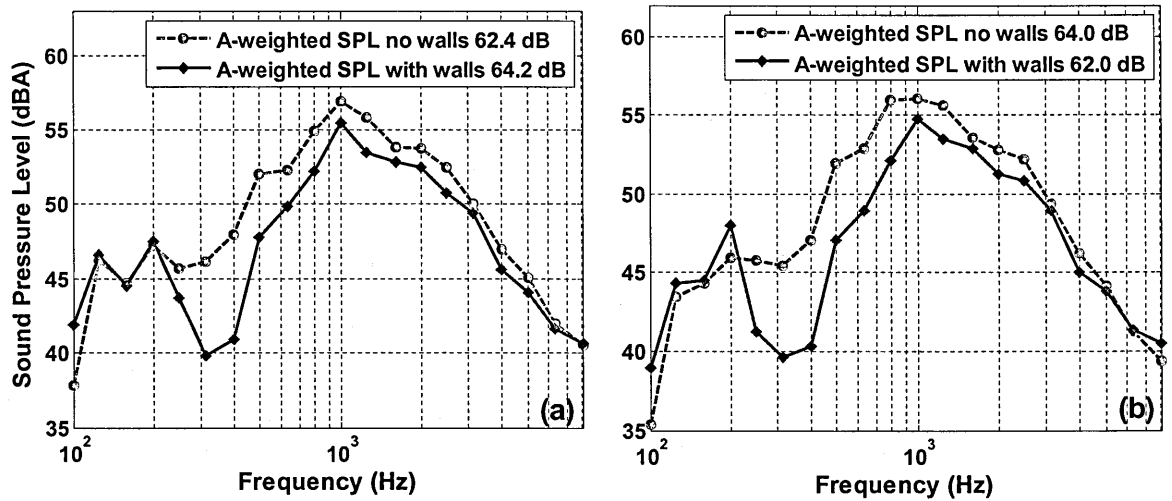
Figure 5.50 Averaged A-weighted sound pressure level with lattice and no lattice, measured through drive by test using car type 'B' (a) with a 0.4 m wide central pathway (b) with a 0.4 m wide diagonal pathway.

Table 5.16 Measured Insertion losses during drive by tests near a lattice without, with a 0.4 m wide central path and with a 0.4 m wide diagonal path.

	Source – Car type2 Measurement	A-weighted SPL no walls (dB)	A-weighted SPL with walls (dB)	Insertion loss (dB)	Approximate Car Speed (km/h)
No pathway	#1	63.2	60.9	2.3	38.7
	# 2	65.4	63.3	2.1	41.2
	# 3	63.9	61.8	2.1	43.0
	Averaged	**64.2**	**62.0**	**2.2**	**41.0**
Central pathway	#1	63.5	61.4	2.1	43.0
	# 2	62.7	61.2	1.5	45.0
	# 3	64.2	62.6	1.6	44.2
	# 4	65.9	63.9	2.0	46.8
	Averaged	**64.2**	**62.4**	**1.8**	**44.8**
Diagonal pathway	#1	64.1	62.1	2.0	36.4
	# 2	63.7	61.7	2.0	44.0
	# 3	63.3	61.3	2.0	45.0
	# 4	64.7	62.8	1.9	44.0
	Averaged	**64.0**	**62.0**	**2.0**	**42.2**

5.11 Conclusions

In this chapter the sound diffraction by rough surfaces is studied through laboratory and outdoor experiments. An extensive study has been carried out over different cross-sectional shaped roughness with different centre-to-centre spacing. It was found that replacing smooth hard ground along the road side with rough ground can attenuate traffic noise. It was also found that the roughness shape and spacing is not an important factor. On the other hand, the roughness height and width of the array are found to be the most important factors in determining insertion loss. Moreover, it is concluded that lattice structures give the best traffic noise attenuation performance for a given height and width and that the ground effect due to lattice is azimuthal angle independent.

The conclusions drawn for first part of the chapter concerned with laboratory studies were given in Section 5.9. These conclusions were taken further, as reported in the second part of the chapter, to design low roughness configurations for carrying out outdoor measurements and drive by tests.

As a consequence of diffraction-assisted rough ground effect, the deliberate introduction of acoustically-hard regular roughness up to 0.3 m high on otherwise acoustically-hard ground can attenuate road traffic noise. A 7 m long, 2.57 m wide nine wall array made from 594 household bricks has been found to give a broadband reduction of about 10 dB at receivers up to 0.85 m high and 10 m from a loudspeaker on the ground. About 4 dB insertion loss has been measured at a receiver close to the ground for traffic noise from a road located 140 m away and elevated by 5 m with respect to the wall array. According to reciprocity similar

reductions should be obtained at 5 m high receiver 140 m from a road traffic source.

Outdoor investigations of the acoustical performance of parallel wall arrays, 'chequerboard' configurations and lattice structures have been performed using a loudspeaker noise source. Measurements have shown that lattice arrangements give better noise reductions than parallel walls or 'chequerboard' configurations of the same width and height.

Drive by test measurements have been carried out over parallel walls and lattice structure. A 0.2 m high, 2.3 m wide and 16 m long nine parallel walls brick array with centre-to-centre spacing of 0.28 m gave an average insertion loss of 2.7 dB for a 1.5 m high receiver and at 10 m distance from a car passing by at an average speed of 35.4 km/h. Similarly, for a 1.2 m wide and 0.2 m high lattice, the measured average insertion loss was 2.6 dB for a car passing by with an average speed of 38.0 km/h. From pass by measurements it is concluded that using lattice structure with half of the width of parallel walls array gives more or less similar insertion loss. Another important advantage of lattice over parallel walls is that attenuation due to a lattice structure is azimuthal angle independent. The creation of a 0.4 m wide pathway through low wall configurations does not have a significantly adverse impact on their acoustical performance against traffic noise.

Future work should explore the influence of meteorological conditions on roughness-based noise reduction and slit-element roughness.

Chapter 6

6. Effective impedance models

6.1 Introduction

A two-dimensional Boundary Element Method (BEM) (see chapter 2) involves dividing the surfaces of interest into a number of small hypothetical elements and adding their contributions to the overall sound field resulting from a line source. Although it is a 2D method, it is able to predict the sound field from a point source over surfaces containing parallel roughness strips along a line normal to the roughness element axes and has been found to give good agreement with laboratory data (see section 5.5.2). However to predict sound propagation over the (3D) lattice configurations using a (2D) BEM an indirect approach is necessary.

An indirect approach to predicting the sound propagation over a lattice structure using 2D BEM requires (i) making level difference measurements over a lattice surface and (ii) fitting the measured data with an impedance model to obtain effective impedance parameters. These best fit impedance parameters can be

used to model the lattice surface as an effective impedance using 2D BEM. Experiments over lattices to obtain effective impedance have been carried out in laboratory and outdoors. The measured data have been fitted using impedance models. Similarly, the effective impedance of parallel wall arrays has been investigated. Laboratory data obtained over aluminium rectangular strips is compared with slit pore layer and Kelders-Allard model predictions.

This first section is an introduction to the chapter. The second section of this chapter describes deduction of the effective impedance of a small scale lattice from laboratory measurements. The third section describes deduction of the effective impedance parameters for an outdoor lattice constructed from bricks. The fourth section compares measured and predicted excess attenuation spectra over periodically spaced aluminium rectangular strips, with different centre-to-centre spacing on a MDF board. The fifth section of this chapter describes deduction of the effective impedance parameters for outdoor large scale parallel walls. All the predictions carried out when deducing effective impedance parameters use either the slit pore layer model or the Kelders-Allard model (which is described in this section). The validity for these models for different roughness configurations has been investigated. Conclusions are drawn in section six.

It is important to distinguish between 'measured impedance parameters' and 'best fit impedance parameters'. Measured impedance parameters are obtained from the structural geometry of the surface and the best fit impedance parameters are those obtained by fitting the data through a numerical minimization technique (for details see Chapter 4).

6.2 Effective impedance of a laboratory lattice

As it was discussed in chapter 5, the rough ground effect due to a square lattice structure is azimuthal angle independent. Consequently the ability to predict sound propagation over a lattice becomes very important. Prediction using a 2D BEM of propagation over a 3D structure needs an indirect technique. Excess attenuation spectra over single, double and triple layers of lighting diffuser lattice have been measured in the laboratory (for details see Section 5.10.2.2). The measured excess attenuation data has been fitted using an impedance model in conjunction with a propagation model (for details see Chapter 4). The impedance parameters obtained through fitting the data are used to characterize the acoustical properties of the lattice. Three impedance models have been used to fit the measured data.

6.2.1 Kelders-Allard model

According to modal analysis [105], if viscous losses are neglected and the squares in the lattice have depth d side a and wall thickness $(b - a)$, then, at wavelengths larger than a, the effective normalised impedance of a hard-backed lattice layer is given by,

$$Z(d)\Big/\rho c_o = \left(1\Big/\Omega\right)\coth\left(-ik_o d'\right),\tag{6.1}$$

$$d' = d - a\log(2)\big/\pi,\tag{6.2}$$

where the porosity $\Omega = (a/d)^2$. A schematic of a rectangular groove grating and a square lattice structure is given in Figure 6.1. This can be used with the classical

formulae for propagation from a point source over a finite impedance boundary (see chapter 4) to predict propagation over an infinitely long lattice.
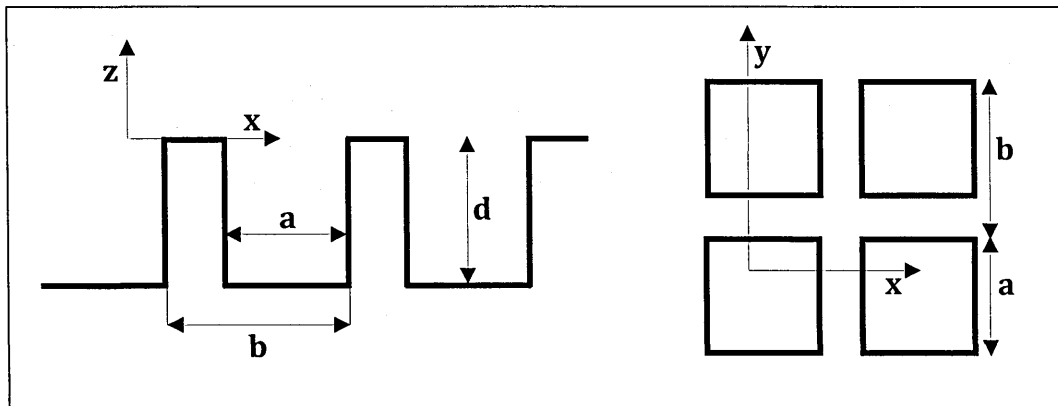
Figure 6.1 A rectangular groove grating and a square lattice structure.

Figure 6.1 compares the measured and predicted excess attenuation spectra over single, double and triple lighting diffuser lattice layers placed over a MDF board. Three different geometries were used for excess attenuation measurement by placing source and receiver at three different heights i.e. 0.015 m, 0.03 m and 0.05 m above the lattice surface. The source-receiver separation was fixed at 0.7 m. The predictions were carried out for a point source over an impedance plane, where the surface is defined using impedance given by Kelders-Allard model (see Eq. 6.1 and Eq. 6.2). A single cell of the laboratory lattice has a depth of 0.01263 m, centre-to-centre spacing between lattice cell of 0.01589 m and lattice wall width of 0.00185 m. The square cell width is 0.01404 m. The porosity of a the lattice according to the cell dimensions is 0.78. The measured single lattice layer depth is 0.01263 m. The effective lattice single layer depth obtained using Eq. (6.2) is 0.0095 m. Similarly, the measured double and triple lattice layer depths are 0.02526 m and 0.03789 m respectively. The corresponding effective double and triple layer depths calculated from Eq. (6.2) are 0.02216 m

and 0.0348 m respectively. The measured porosity and effective layer depth for different lattice layers are used in Eq. (6.1) to obtain the effective normalized impedance of a hard-backed layer lattices. These effective impedances are used along with a point source propagation model (see Chapter 4, Section 4.4.1) to predict excess attenuation spectra such as those shown in Figure 6.1. The lattice layer is assumed to be a locally reacting surface. The overall agreement between measured data and the Kelders-Allard model (identified as the Allard model in the keys of Figure 6.2) predictions are very good. The frequency of occurrence for the first excess attenuation maximum is predicted correctly, however, in some cases the depth of the maximum is under or over predicted by between 1 dB and 10 dB Moreover the Kelders-Allard model is unable to predict the frequencies of the second excess attenuation maxima correctly.
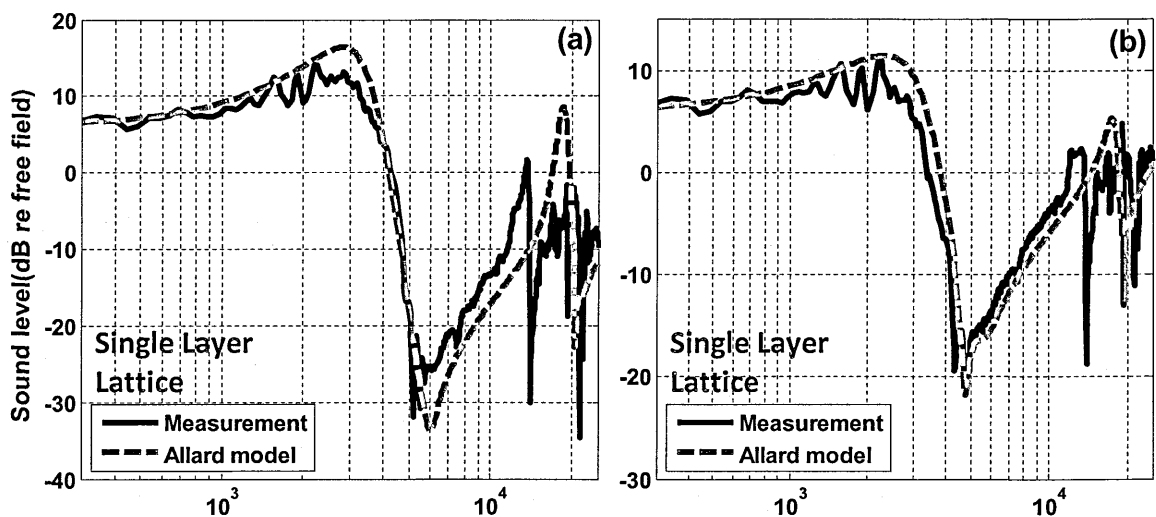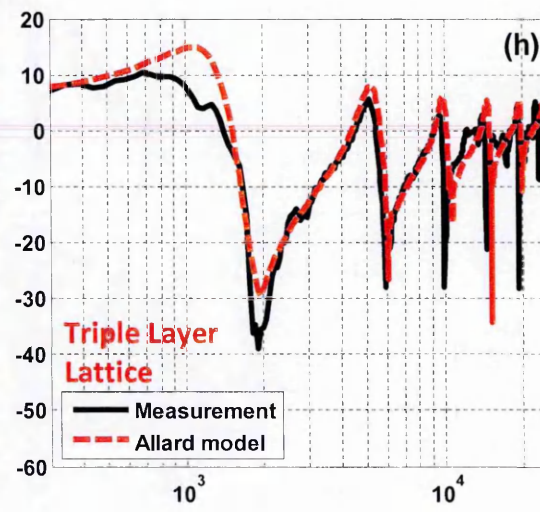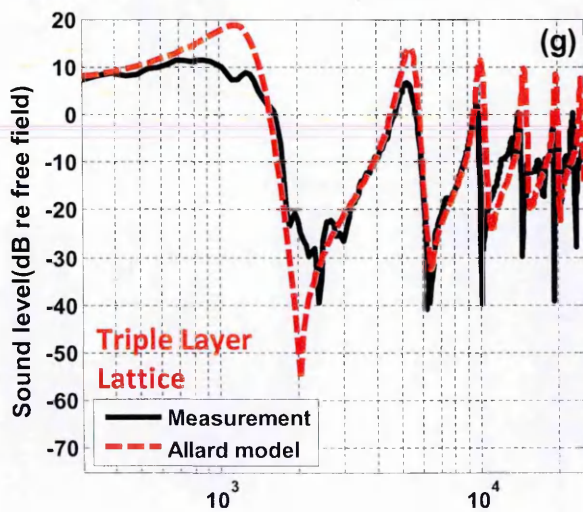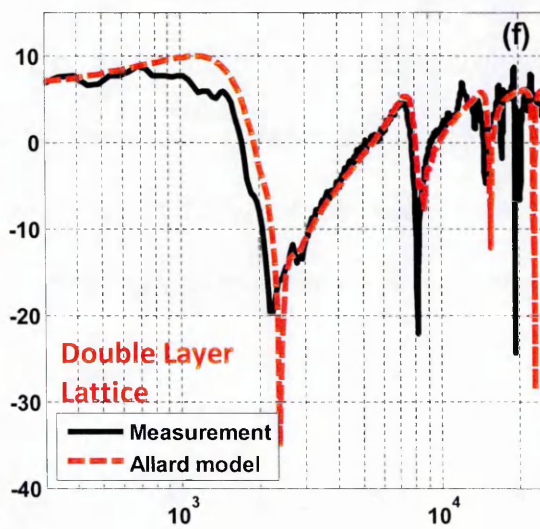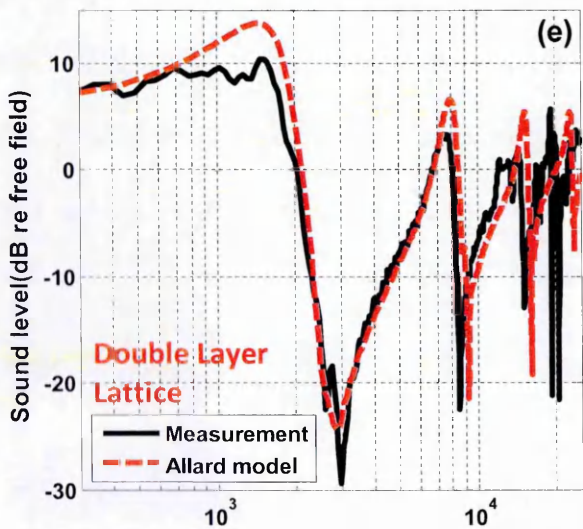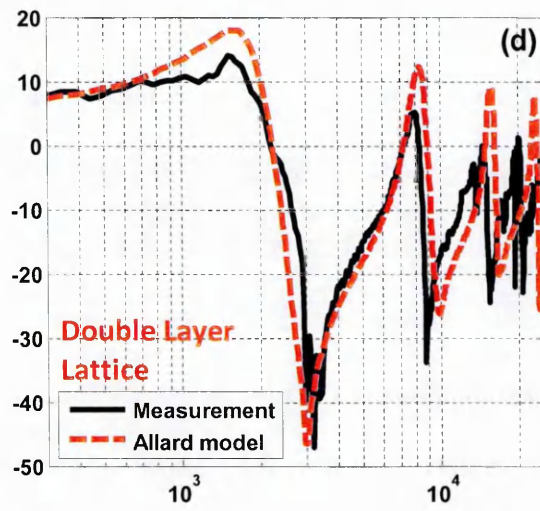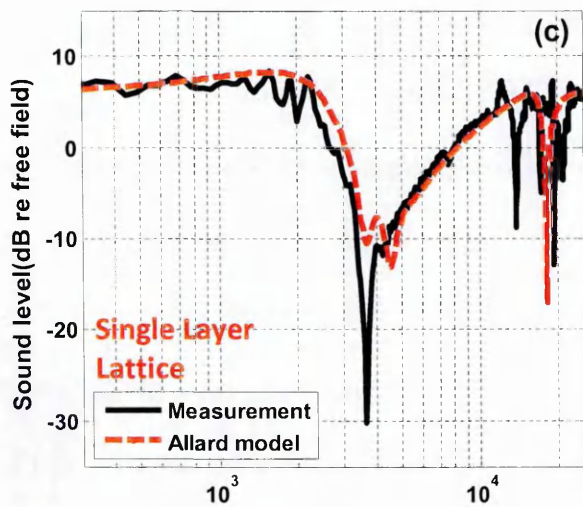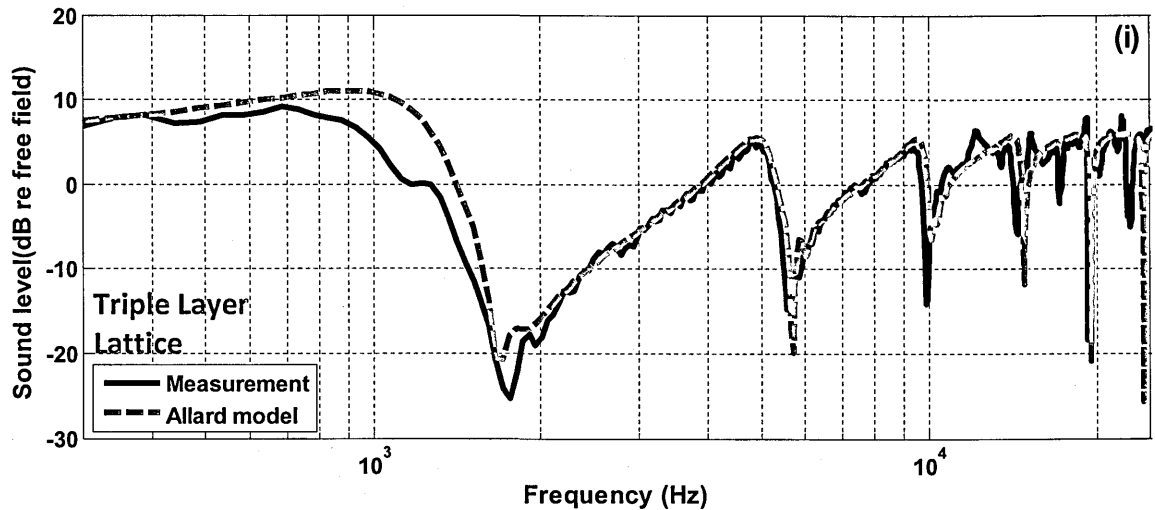
Figure 6.2 Comparison between measured and predicted excess attenuation spectra over single, double and triple lattice layer placed over MDF board with source-receiver separation of 0.7 m and with different geometries as given (a), (d) & (g) source and receiver are placed at height of 0.015 m above lattice surface (b), (e) & (h) source and receiver are placed at height of 0.03 m above lattice surface (c), (f) & (i) source and receiver are placed at height of 0.05 m above lattice surface.

6.2.2 Pore-based models

Predictions of the acoustical properties of the laboratory lattice are possible using impedance models that assume idealised pore shapes e.g. square or slit-like pores. The measured excess attenuation spectra over the lattice placed on MDF board is compared with predictions using slit pore and square pore layer models impedances along with a point source propagation model. The mathematical forms for these models are given in chapter 4 (for details see Eq. (4.52) and Eq. (4.53), Table 4.2 and Table 4.3). The parameters needed to predict impedance using slit pore or square pore models are flow resistivity, porosity and layer depth. The flow resistivity required for the predictions is calculated using the formula [33],

$$R_s = \frac{2\mu q^2 s_o}{\Omega r_h^2}, \qquad (6.3)$$

where μ is the dynamic viscosity coefficient in air, q^2 is tortuosity, s_0 is a shape factor, r_h is the hydraulic radius. The value of dynamic viscosity coefficient in air is

1.811 × 10^{-5}, tortuosity is equal to 1 and the shape factor s_0 is equal to 0.89 for square pores. The hydraulic radius is equal to pore width divided by 4, which is 0.0035 for the laboratory lattice. The porosity value is 0.78. The resultant flow resistivity value obtained by putting the above given parameters into Eq. 6.3 is 3.35 Pa s m^{-2}. The measured layer depth for a single laboratory lattice layer is 0.01263 m. Similarly, the measured layer depths for double and triple lattice layer are 0.0253 m and 0.0379 m respectively. Figure 6.3 compares the measured and predicted excess attenuation spectra over lattice using the slit pore hard-backed layer model. Source and receiver were placed at three different heights of 0.015 m, 0.03 m and 0.05 m above lattice surface. The source-receiver separation was fixed at 0.7 m. Overall the agreement between data and predictions using the slit pore layer model with parameters obtained from the geometry of the lattice structure are very good. The frequency of occurrence for first excess attenuation maximum is reasonably well predicted to within less than 300 Hz. However, sometimes, the depth of the maximum is under or over predicted by between 1 dB and 10 dB. Discrepancies may be due to the fact that the predictions are carried out using an effective impedance model rather than by fully descretizing the boundaries. Nevertheless the good agreement obtained by using an effective impedance is encouraging.
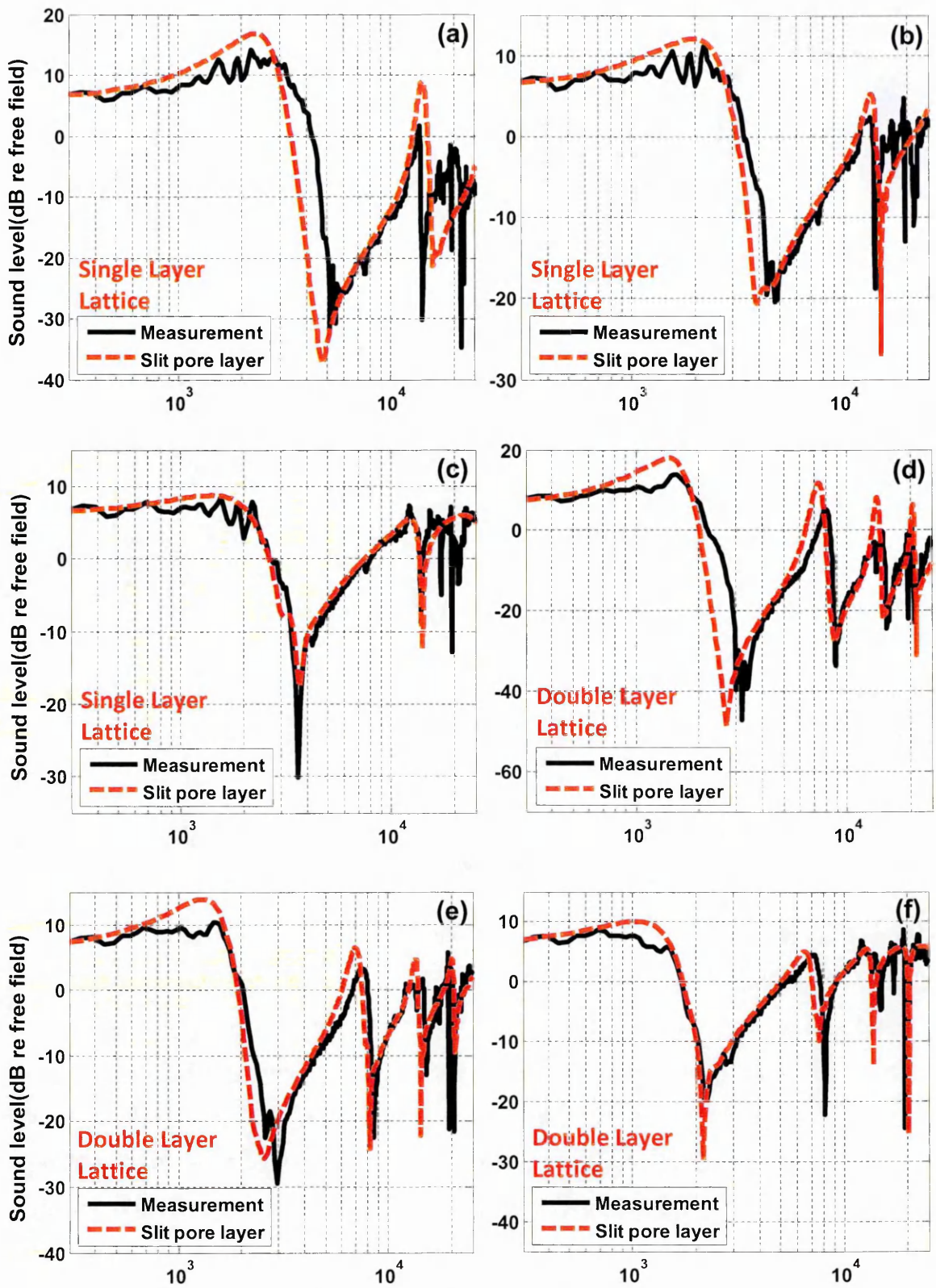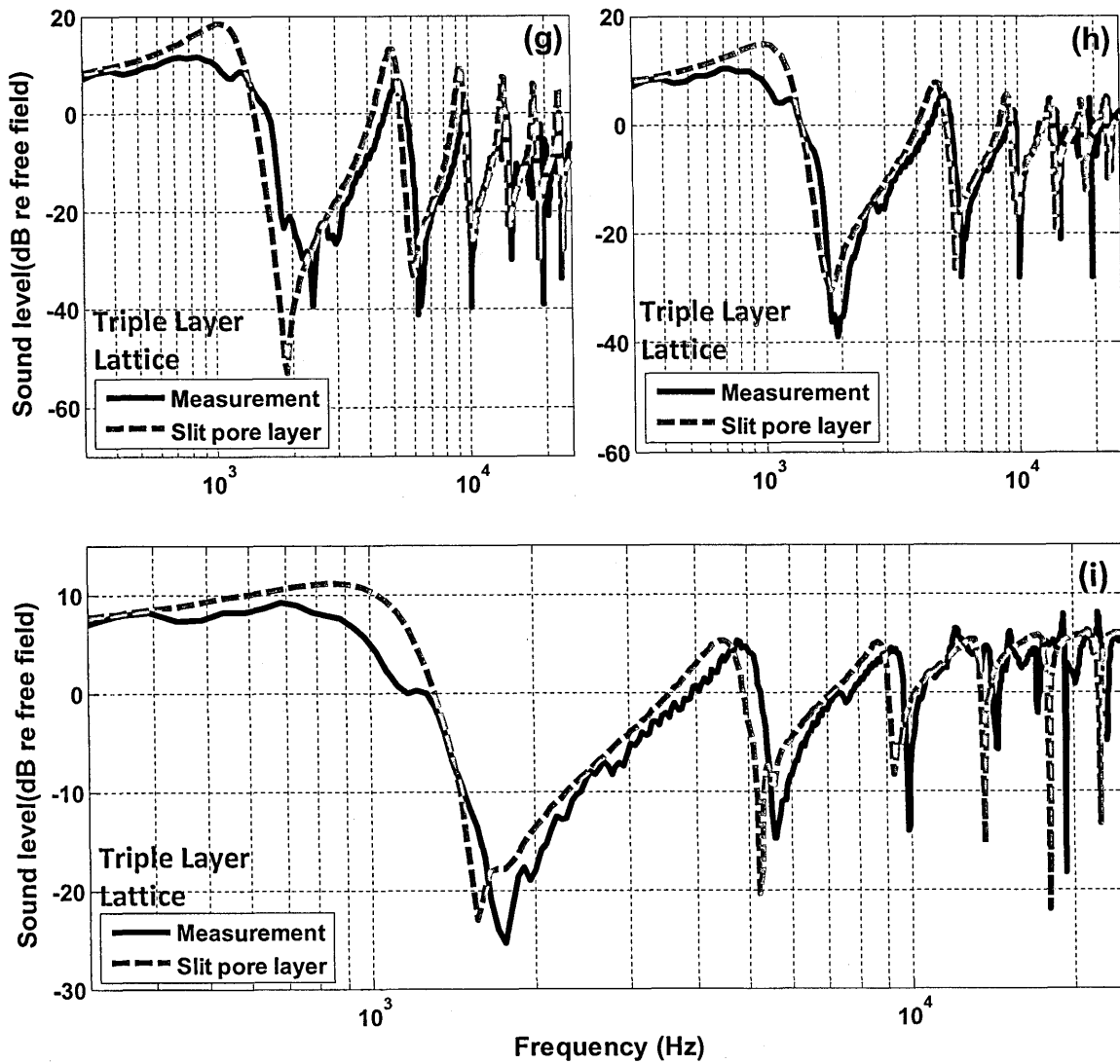
Figure 6.3 Comparison between measured and predicted excess attenuation spectra over single, double and triple lighting lattice layers placed over MDF board with a fixed source-receiver separation of 0.7 m but with different source and receiver heights: (a), (d) & (g) source and receiver are placed at height of 0.015 m above the lattice surface (b), (e) & (h) source and receiver are placed at height of 0.03 m above the lattice surface (c), (f) & (i) source and receiver are placed at height of 0.05 m above the lattice surface. The excess attenuation predictions are carried out using propagation model for a point source above an impedance plane and the slit pore layer impedance model (see Section 6.2.2).

6.2.1 Comparison of Kelders-Allard and pore-based models

Figure 6.4 compares excess attenuation spectra predicted using impedance given by Kelders-Allard, slit pore layer and square pore layer models with data over single lattice layer placed over MDF board with source and receiver at height of 0.015 m, and source-receiver separation of 0.7 m. The EA spectra are predicted for a point source over an impedance plane in which the top surface of the array is modelled as having a slit pore layer or Kelders-Allard model impedance. The parameters used for predictions are calculated from the lattice structure. The Kelders-Allard model uses the porosity of 0.78 and effective layer depth of 0.0095m according to Eq. (6.1). The slit and square pore layer model uses the flow resistivity of 3.35 Pa a m^{-2}, porosity of 0.78 and measured layer depth of 0.01263 m. It can be observed that the predictions obtained using slit pore model are identical to those obtained by using the square pore model. Since the slit pore model calculations are simpler than those for the square pore model the slit pore model can be used to predict the effective impedance of a lattice layer instead of the square pore model. Predictions obtained by using Kelders-Allard model differ from those obtained using the slit pore layer model as shown in Figure 6.4. Nevertheless both models give equally good fits to the measured data.

Compared to the Kelders-Allard model (abbreviated as 'Allard model' in the Figure keys and sometimes in subsequent text), pore-based models require flow resistivity as an additional parameter. There is an advantage of having a flow resistivity value as an adjustable input parameter in describing data obtained over outdoor lattices (see section 6.3). The prediction using above given models with measured parameters gives a good fit to the first excess attenuation maxima.

However, in some cases the agreement between predicted and measured second

EA maxima is not very good. The fit at higher frequencies can be improved using a

smaller effective depth but this worsens the fit to the first peak.
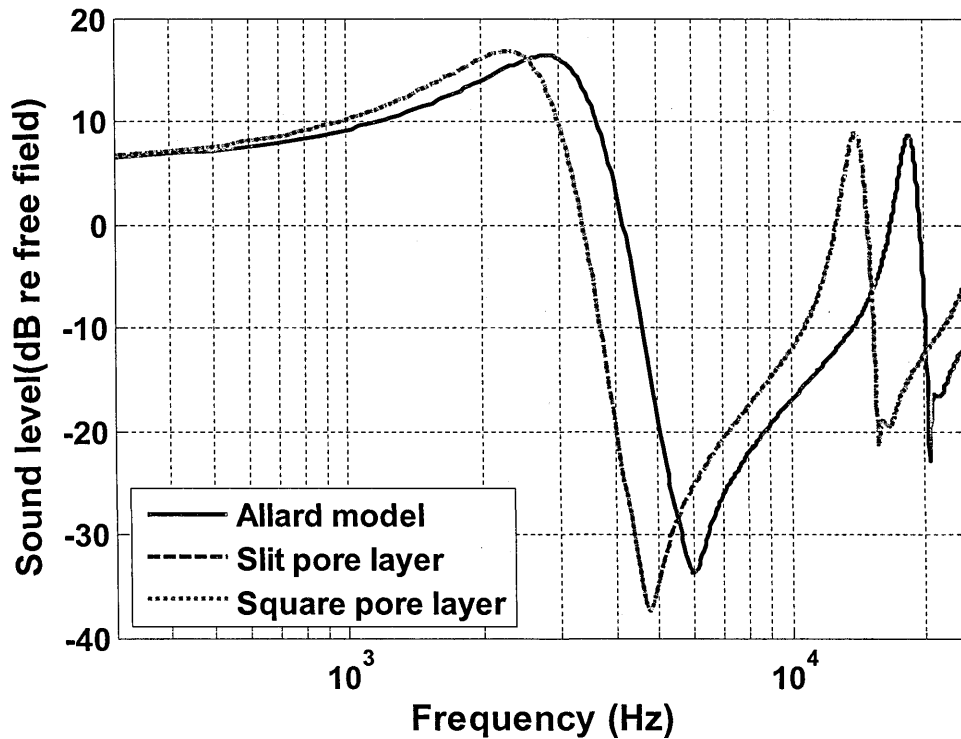
Figure 6.4 Comparison between excess attenuation predictions using impedances
given by Kelders-Allard, slit pore layer and square pore models over single lattice
layer placed on MDF board with source and receiver at height of 0.015 m, and source-
receiver separation of 0.7m. The parameters used to predict impedance are
calculated from lattice structure. The excess attenuation is predicted using
propagation model for a point source above an impedance plane and the impedance
models given above.

6.3 Effective impedance of outdoor (brick) lattices

Large scaled outdoor measurements over brick lattices were carried out at an Open University car park (for details see chapter 5). The bricks are arranged in a lattice structure (see Figure 6.5). A similar procedure to that described previously was used to obtain the effective impedance of the outdoor brick lattice i.e. level difference measurements were carried out with different geometries. The measured data was fitted using both the Kelders-Allard and slit pore models since these models were found to give slightly different results for the laboratory lattices (see Figure 6.3).
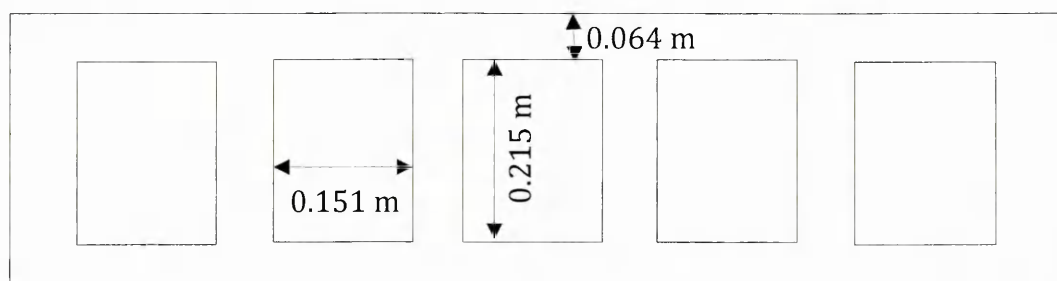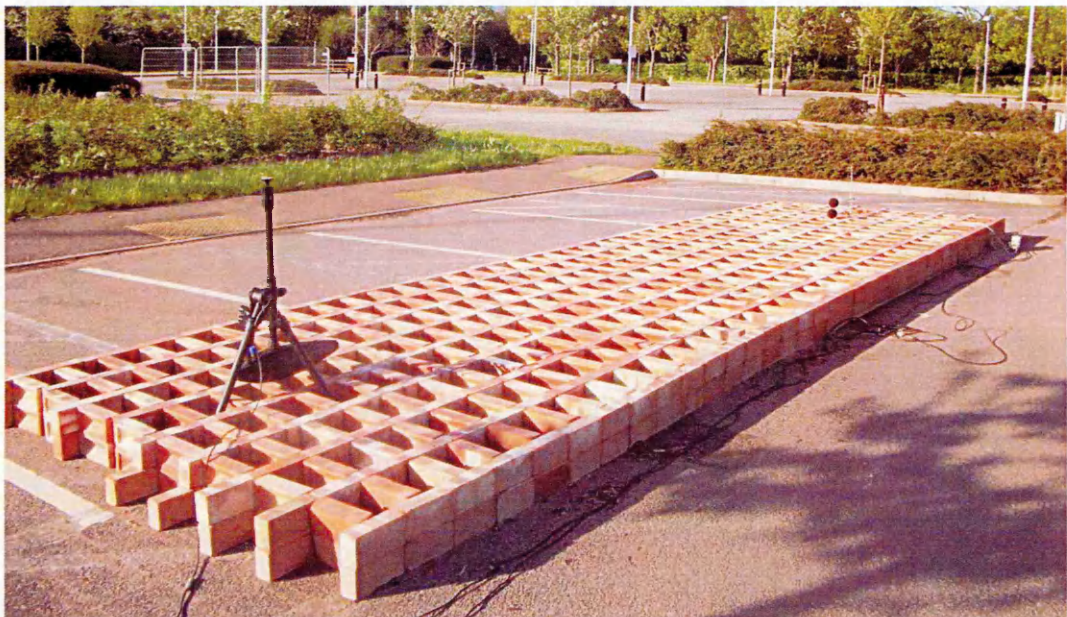
Figure 6.5 Photograph of outdoor brick lattice and schematic of rectangular lattice cell structure.

6.3.1 Comparison between data and predictions using the slit pore model

Figure 6.6 compares the measured level difference data over an outdoor brick lattice and predictions using a propagation model for a point source above an impedance plane with impedance predicted by the slit pore layer model. The source is placed at a height of 0.1 m, the upper microphone at a height of 0.15 m, the lower microphone at a height of 0.05 m and the source-receiver horizontal separation was 2.0 m. The outdoor lattice consists of rectangular pores or cells. A schematic of the rectangular lattice structure is shown in Figure 6.5. The brick lattice is 0.2 m deep. Each rectangular pore has width and length of 0.151 m and 0.215 m respectively. The width of each lattice wall is 0.064 m. The centre-to-centre spacing along one direction is 0.215 m and along the other direction it is 0.279 m. The slit pore layer prediction given in Figure 6.6 uses impedance parameters deduced from the lattice structure. The calculated flow resistivity value for the outdoor lattice using Eq. (6.3) is 0.04 Pa s m^{-2}. The measured porosity is 0.54. The measured layer depth is 0.2 m.

The agreement between measured level difference spectra and those predicted using the slit pore layer model with the measured parameters is reasonable, but not as good as obtained with the laboratory lattice. Also the amplitude peaks and dips in the predicted level difference spectra are much greater and at frequencies that are much higher than those in the measured level difference spectra. Probably the discrepancies can be attributed to the effects of atmospheric turbulence (reducing coherence at high frequencies) and air absorption and the fact that bricks are not acoustically hard (see section 3.2.6.3).

The best fit impedance slit pore model parameters for a surface made with bricks are flow resistivity of 20 MPa s m^{-2} and porosity of 0.1 (see Chapter 3).
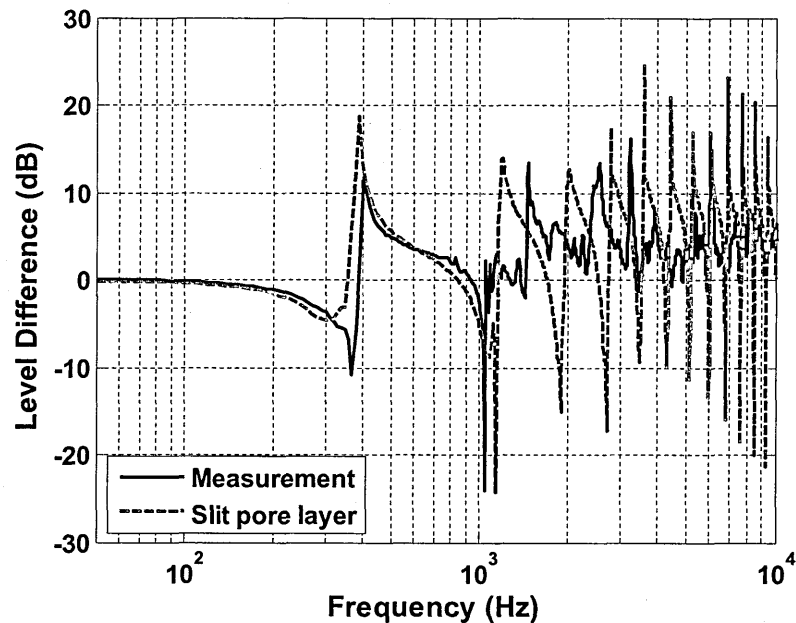
Figure 6.6 Comparison between measured level difference spectra and those predicted using the slit pore layer model for a 0.2 m high lattice with source at height of 0.1 m, upper microphone at height of 0.15 m, lower microphone at height of 0.05 m and horizontal separation between them is of 2.0 m. The level difference predicted spectra uses propagation model along with impedance given by slit pore layer with measured parameters with flow resistivity of 0.04 Pa s m^{-2}, porosity of 0.54 and measured layer depth of 0.2 m.

The agreement between data obtained over the brick lattice and predictions can be improved by adjusting the slit pore layer parameters. Figure 6.7 (b) compares the measured level difference spectra over the brick lattice and predictions using slit pore layer model with parameters (other than porosity) adjusted for best fit i.e. flow resistivity of 400 Pa s m^{-2}, and layer depth of 0.16 m. The amplitude peaks predicted at higher frequencies shown in Fig. 6.6 are reduced by the higher flow resistivity of 400 Pa s m^{-2}. However a consequence of increasing flow resistivity to 400 Pa s m^{-2} is that the level difference spectra shift towards lower frequencies as shown in Figure 6.7 (a). To compensate the

frequency shift spectra due to higher flow resistivity value, the effective layer depth is reduced to 0.16 m. The agreement between measured level difference spectra and slit pore layer predictions using best fit parameters is much improved as shown in Figure 6.7 (b). The difference between measured and predicted peaks is reduced from 20 dB (see Figure 6.6) to a maximum of 5 dB (see Figure 6.7).
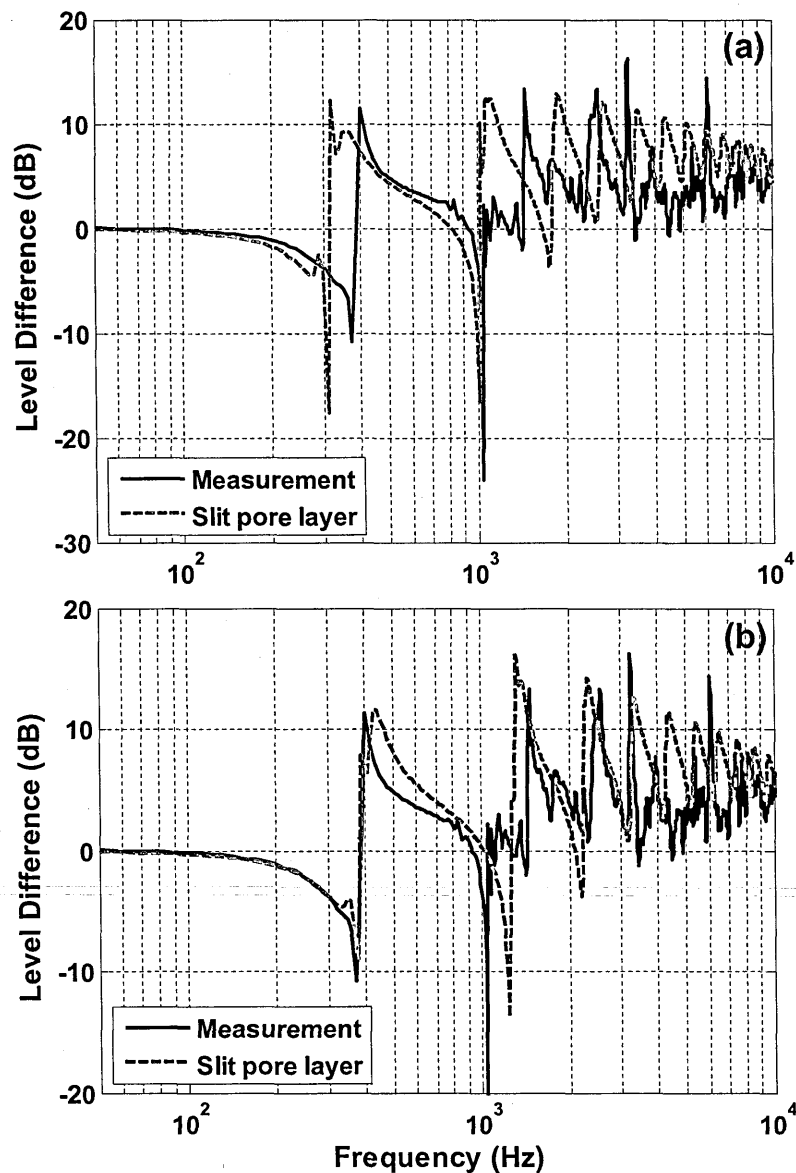
Figure 6.7 Comparison between measured level difference spectra and those predicted using the slit pore layer model for a 0.2 m high brick lattice with source at height of 0.1 m, upper microphone at height of 0.15 m, lower microphone at height of 0.05 m and horizontal separation between them is of 2.0 m. The level difference predicted spectra uses propagation model along with impedance given by slit pore layer with best fit flow resistivity of 400 Pa s m^{-2} and the measured porosity of 0.54 (a) with the measured layer depth of 0.2 m (b) with the best fit layer depth of 0.16 m.

6.3.2 Comparison between data and predictions using the Kelders-Allard model

Figures 6.8 (a) and (b) compare the level difference spectra measured over the outdoor brick lattice structure and those predicted using the impedance given by Kelders-Allard model along with propagation model for a point source above an impedance plane. The measurement arrangements are described in section 6.3.1. Figure 6.8 (a) shows the predictions obtained using the Kelders-Allard model and measured parameters. The measured porosity value is 0.5412 and the effective layer depth using Eq. (6.2) is 0.16 m. The predicted level difference spectra differ from the measured spectra. The first and second level difference dips and peaks are predicted at too high a frequency. Also the predicted spectra show higher amplitude peaks than are present in the measured spectra. The agreement between measured and predicted level difference spectra can be improved by using best fit impedance parameters. The Kelders-Allard model has two parameters. The frequency shift in predicted spectra can be compensated by adjusting the layer depth. However, the amplitudes of peaks and dips at higher frequencies cannot be reduced by modifying either of these parameters. The slit pore model has the advantage that the predicted peak amplitudes can be adjusted by adjusting the flow resistivity. Alternatively, the level difference peak and dip amplitudes predicted by the Kelders-Allard model are reduced by making the propagation constant k_o complex i.e. replacing k_o by $k_o(1+0.03i)$. The best fit using the Kelders-Allard model is obtained with a porosity of 0.54, a layer depth of 0.18 m and by replacing the real propagation constant by a complex propagation constant. Figure 6.8 (b) shows the comparison between measured and predicted

level difference spectra using the best fit Kelders-Allard model. Use of the best fit impedance parameters reduces the difference between measured and predicted peaks from nearly 20 dB to a maximum of 5 dB (see Figure 6.8).
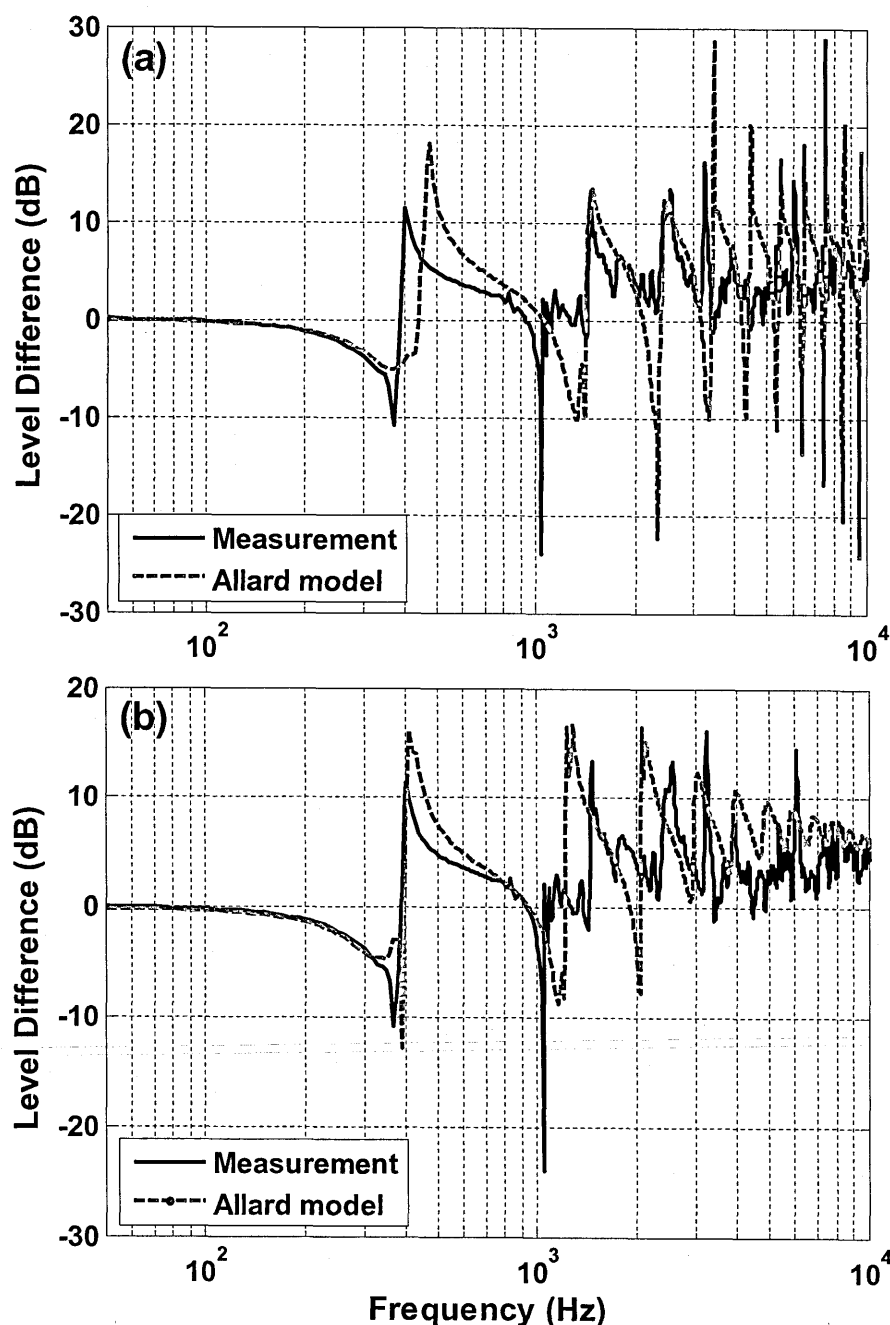
Figure 6.8 Comparison between measured level difference spectra and those predicted using the Kelders-Allard model for a 0.2 m high brick lattice with source at height of 0.1 m, upper microphone at height of 0.15 m, lower microphone at height of 0.05 m and horizontal separation between them is of 2.0 m. (a) The Kelders-Allard predictions using measured impedance parameters with porosity of 0.54 and effective layer depth of 0.16 m (b) The best fit Kelders-Allard predictions with porosity of 0.54, layer depth of 0.18 m and real propagation constant, k_o replaced by a complex one $k_o(1+0.03i)$.

6.3.3 Angle dependence and effects of rectangular cells

The outdoor lattice constructed with bricks is a rectangular lattice. Level difference measurements have been made over the outdoor lattice to test the angle dependence. The reference measurement was carried out along the pore width of 0.151 m which is assumed to be along x-axis (see Figure 6.5). This reference measurement was assumed to correspond to a source-receiver axis angle of $0°$ with the lattice structure. The source-receiver axis was rotated slowly to make an angle ϕ with the reference direction as shown in Figure 6.9. Level difference measurements were carried out with different angles between the source-receiver axis and the lattice. The measured level difference spectra at different azimuthal angles are shown in Figure 6.10. The first level difference dip is found to move to slightly lower frequencies when measured at increasing azimuthal angles. However the level difference peaks and dips at higher frequencies are relatively unaffected.
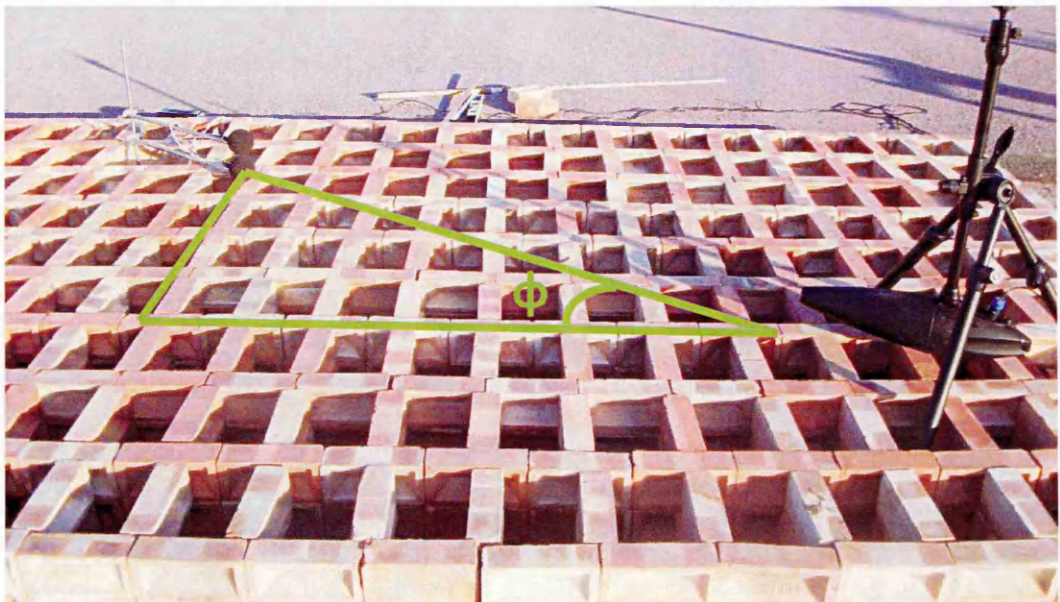
Figure 6.9 Photograph of angle dependence measurements over a brick lattice.
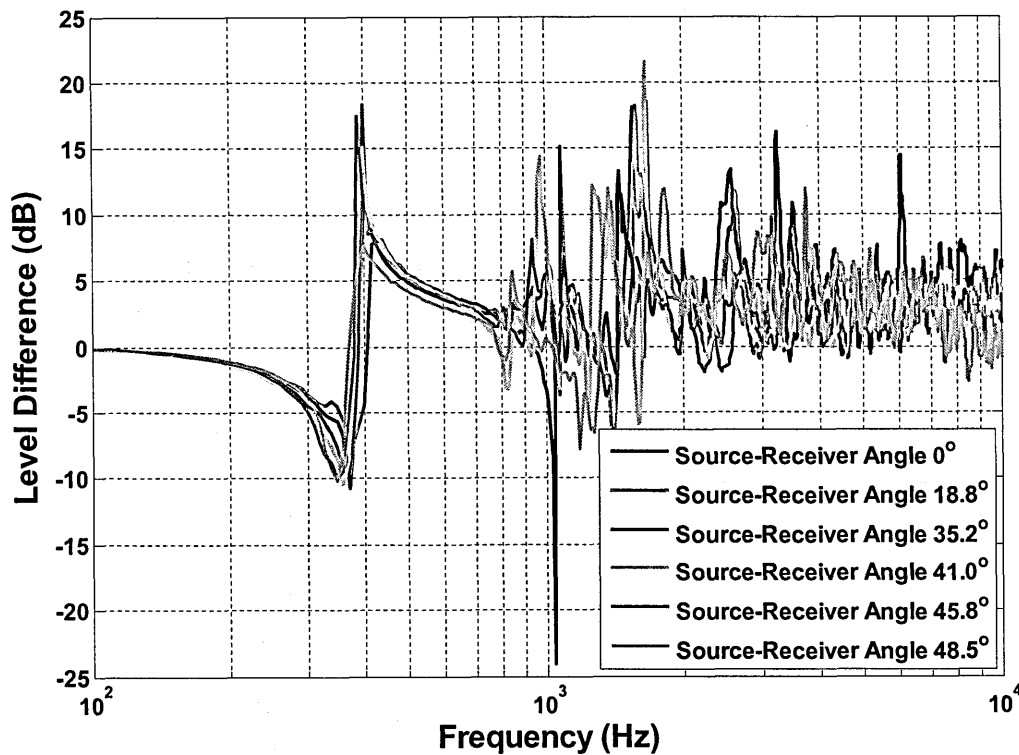
Figure 6.10 Comparison between level difference spectra measured over an outdoor 0.2 m high brick lattice with source at height of 0.1 m, upper microphone at height of 0.15 m, lower microphone at height of 0.05 m and horizontal separation between them is of 2.0 m at different angles between source-receiver axis and the lattice.

Figure 6.11 compares the measured level difference spectra obtained by placing source and microphones along x-axis direction (corresponding to the 0.15 m cell dimension) and along the y-axis direction (corresponding to the 0.215 m cell dimension). These measured level difference spectra show a small shift in the first peak and dip frequencies. Laboratory data and slit pore predictions obtained over idealised slit pore surfaces (section 6.4.1) have shown that excess attenuation maxima move to lower frequencies as the spacing between the strips is increased. But It is shown in sections 6.4 and 6.5 that the slit pore model is only valid for narrow spacing, so this may not be true for large spacing between the strips. However in the brick lattice the cell dimension along the y-axis is larger than that along the x-axis. The first peak frequency in the measured level difference

spectrum corresponding to larger dimension (0.215 m) direction is lower than that in the spectrum measured along the smaller dimension (0.151 m) direction in the lattice. The observed peak shift to lower frequency with the increase in spacing is consistent with conclusions drawn elsewhere (see sections 5.32 and 6.4.1).

The shift shown in Figure 6.11 is not due to measurement error, because laboratory data and BEM predictions over rough surfaces with different element spacing shows that increasing the spacing moves the peaks to lower frequencies, which is consistent with the data shown in Figure 6.11.
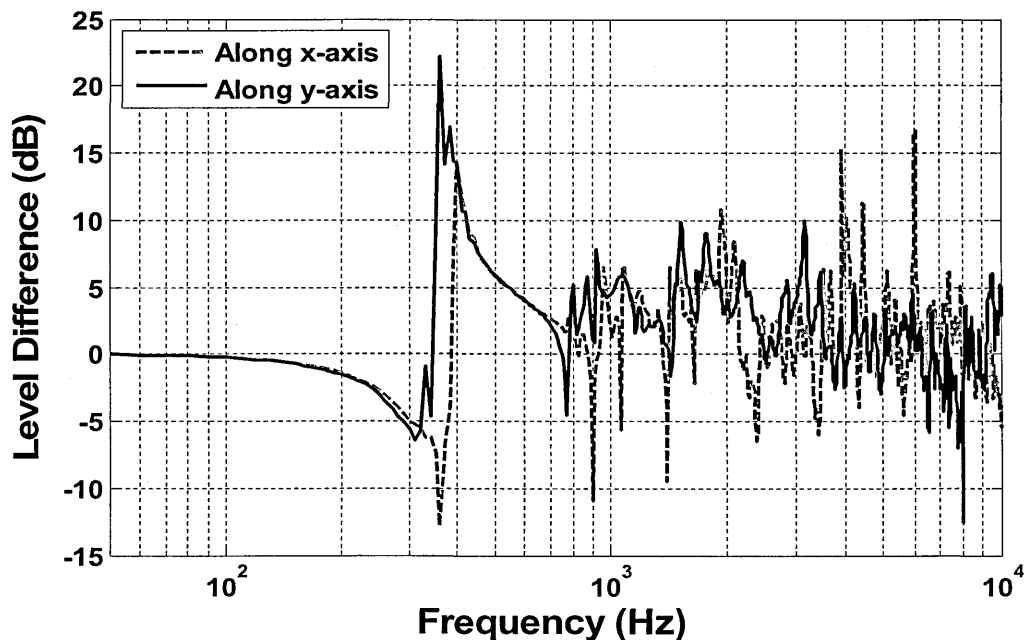
Figure 6.11 Comparison between measured level difference spectra over lattice along x-axis and along y-axis.

It should be noted that this observation is not supported by the Allard model. In level difference predictions using the Allard model the peaks move towards higher frequencies with increase in roughness element spacing. Figure 6.12 compares predictions of level difference spectra using these Kelders-Allard model impedance and a propagation model for a point source over an impedance

for different edge-to-edge spacing. The impedance parameters i.e. the porosity and effective layer depth are calculated to correspond to their different edge-to-edge spacing using Eq. (6.1) and Eq. (6.2). The peaks in the predicted spectra move to higher frequencies as the edge-to-edge spacing is increased in contradiction to the spectrum shift to lower frequencies with the increase in spacing shown by measured data and BEM predictions.
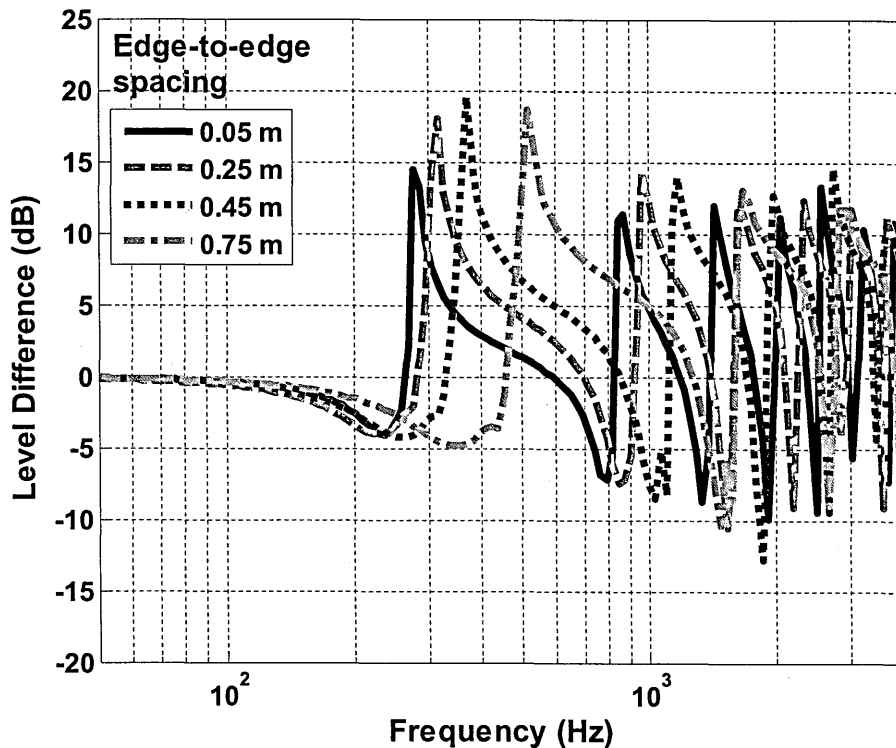
Figure 6.12 Comparison between predicted level difference spectra using the Kelders-Allard model for a 0.3 m high brick lattice with source at height of 0.1 m, upper microphone at height of 0.15 m, lower microphone at height of 0.05 m and horizontal separation between them is of 2.0 m. The edge-to-edge spacing and Kelders-Allard model parameters are (a) edge-to-edge spacing = 0.05 m, porosity = 0.4386 and effective layer depth = 0.289 m (b) edge-to-edge spacing = 0.25 m, porosity = 0.7962 and effective layer depth = 0.2448 m (c) edge-to-edge spacing = 0.45 m, porosity = 0.8755 and effective layer depth = 0.2007 m (d) edge-to-edge spacing = 0.75 m, porosity = 0.9214 and effective layer depth = 0.1345 m.

6.3.4 Comparison between lattice data and BEM predictions

As explained earlier, sound propagation over a 3D lattice cannot be predicted using 2D BEM. However, a 2D BEM can be used if the lattice surface is modelled as an effective impedance surface. The effective impedance of the lattice is obtained by fitting a measured level difference using a slit pore layer impedance model (see Figure 6.8 (b) for an example fitting over a brick lattice)). In the 2D BEM, the brick lattice is modelled as a raised effective impedance surface (see Figure 6.13). The sides of the lattice are assumed to be acoustically hard and the impedance of the lattice top is modelled by using a slit pore layer impedance model.
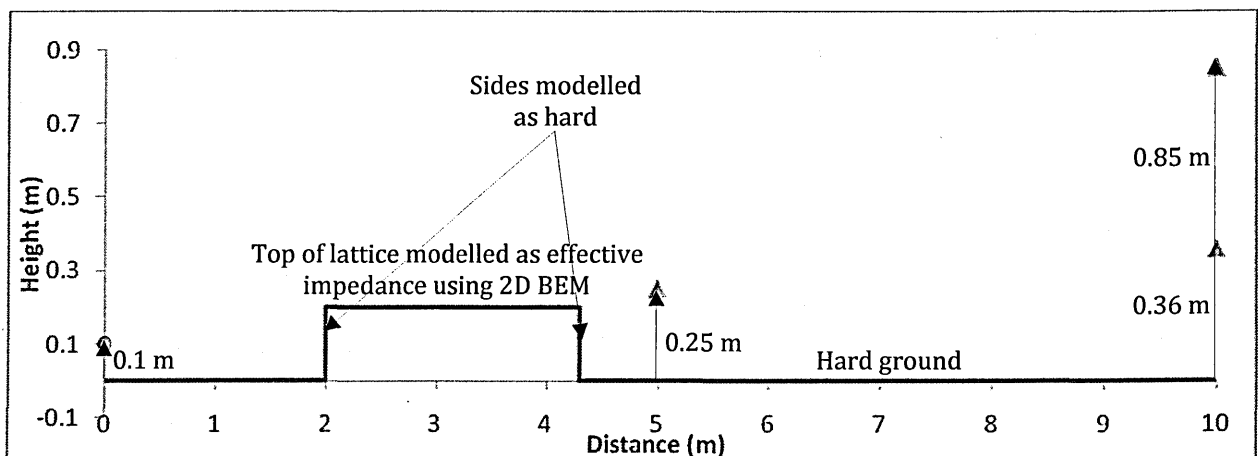
Figure 6.13 Modelling a lattice as a raised effective impedance surface within a 2D BEM calculation.

Results of horizontal level difference measurements over a brick lattice have been compared with 2D BEM predictions. The measurement arrangements are those shown in Figure 6.13. The source is placed at a height of 0.1 m and at a distance of 2.0 m from the lattice. The reference microphone is placed at a distance of 5.0 m from the source and at a height of 0.25 m above acoustically-hard asphalt. The second microphone is placed at a distance of 10 m from the

source and at two different heights i.e. 0.36 m and 0.85 m. The measurement system described in chapter 3 was used to acquire the data. The horizontal level difference spectra were calculated from the difference between the sound pressure levels measured by the reference microphone at a distance of 5.0 m and the second microphone at a distance of 10.0 m from the source. To compare the measured horizontal level difference spectra with BEM predictions, the same arrangements were modelled using BEM. The lattice was 2.3 m wide was modelled as a 0.2 m high raised platform with a surface impedance given by the slit pore model and the best fit impedance parameters deduced from the fitting shown in Figure 6.8 (b) i.e. Flow resistivity of 400 Pa s m^{-2}, porosity of 0.54 and effective layer depth of 0.16 m. Figure 6.14 compares measured and predicted horizontal level difference spectra (a) with reference microphone at a distance of 5.0 m and at a height of 0.25 m and the second microphone at a distance of 10.0 m and at height of 0.36 m and (b) when the second microphone placed at a height of 0.85 m. The agreement between data and predictions is very good thereby supporting the fact that the 3D lattice can be modelled as a raised effective impedance in 2D BEM. Use of a raised effective impedance and BEM to predict lattice attenuation performance and insertion loss for a traffic noise source, will be reported in a later section.
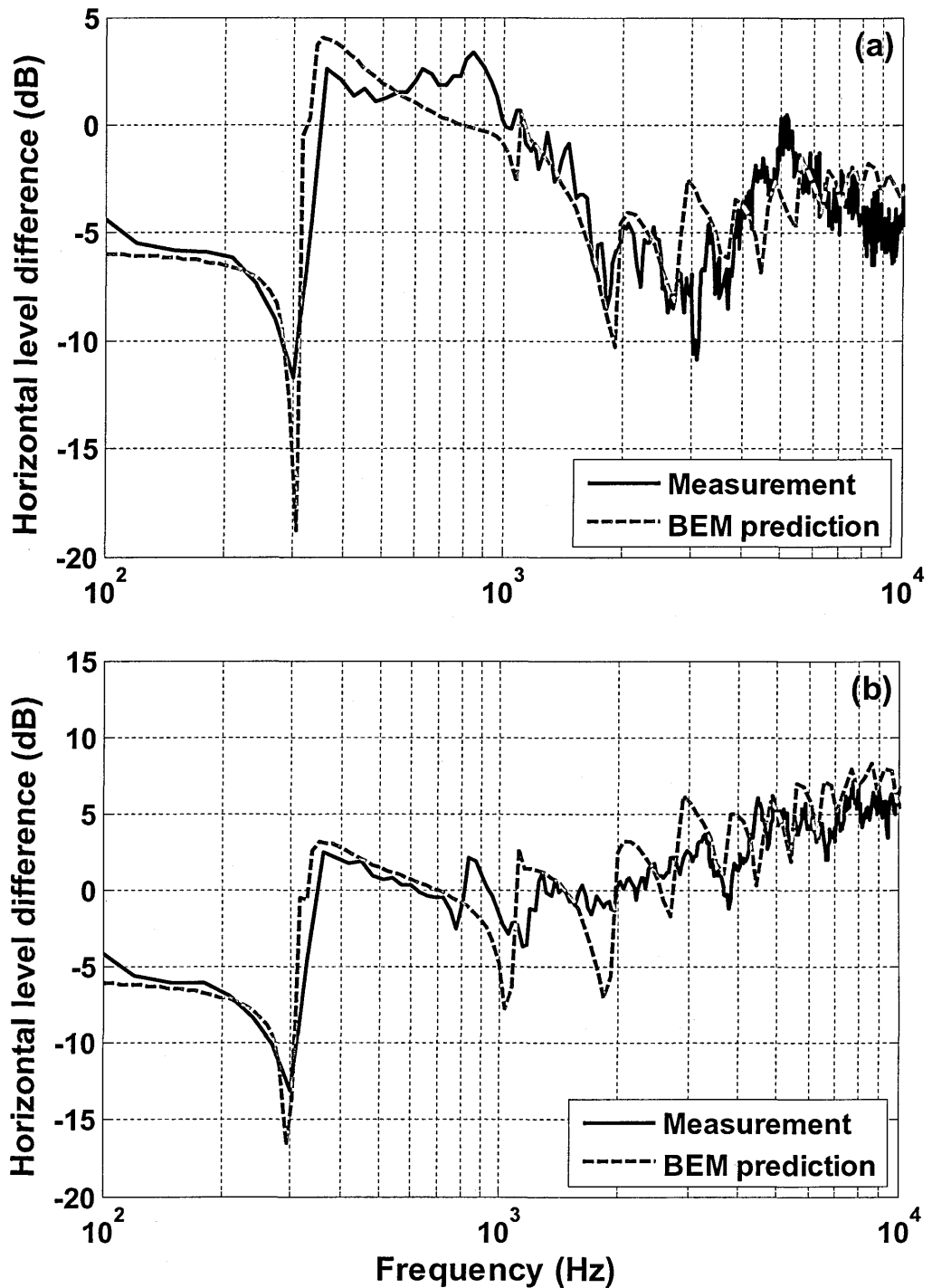
Figure 6.14 Comparison between BEM predictions and measured horizontal level difference spectra over a brick Lattice constructed in a car park with a centre-to-centre spacing of 0.28m, height of 0.2m and total width of 2.3 m. The source was placed at height of 0.1 m above hard ground and at a distance of 2.0 m from lattice edge and the first (reference) microphone was placed at height of 0.25 m and at distance of 5.0 m from the source. (a) the second microphone was at a height of 0.36 m and a distance of 10 m from the source (b) the second microphone was at a height of 0.85 m and at a distance of 10 m from the source. For the BEM predictions the lattice was modelled as a raised impedance using the slit pore layer model with flow-resistivity 400 Pa s m^{-2}, porosity 0.55 and effective layer depth L' = 0.16 m.

6.4 Effective impedance of parallel walls in the laboratory

Although sound propagation over parallel walls can be predicted accurately using 2D BEM (see chapter 5), the fact that it has been found that propagation over a 3D lattice can be predicted as over a raised impedance plane, which needs less resources and time, raises the question of whether the same is true for sound propagation over parallel walls. Here an effective impedance model for laboratory scale parallel walls will be investigated. Excess attenuation has measured over periodically spaced aluminium strips placed over MDF board with different edge-to-edge spacings. The measurement arrangements are shown in Figure 6.15. The source and receiver were placed at a height of 0.02 m above aluminium rectangular strips and 0.045 m above an MDF board. The source and receiver were placed at a horizontal separation of 0.7 m. Each aluminium rectangular strip is 1.0 m long, 0.0253 m tall and 0.0126 m wide (1.0 m X 0.0253 m X 0.0126 m).

6.4.1 Application of the slit pore model

Rectangular aluminium strips were arranged periodically to create very small slit like pores between them as shown in Figure 6.15 (a) and then the edge-to-edge spacing between the strips was increased slowly to create a rough surface. Figure 6.16 compares the measured and predicted excess attenuation spectra for different edge-to-edge spacing. The predictions are carried out using slit pore layer model (see Chapter 4) with parameters deduced from the measured geometry. The slit pore model is appropriate where there are viscous and thermal boundary layers between the slit walls due to sound propagation. As the gap between the strips widens, slit pore model become less applicable. As well as providing a means to investigate the validity of representing the surface composed from

parallel walls by an effective impedance, these laboratory measurements also served to check the applicability of slit pore theory as the slit width is widened. Figures 6.15 (a) and (b) show the laboratory measurement arrangements and Figures 6.16 (a) and (b) show the corresponding EA spectra. Figure 6.15 (a) shows the measured EA spectrum obtained over periodically spaced aluminium strips with the edge-to-edge spacing of 0.003 m. The measured porosity for this arrangement is 0.1923. The value of s_o for slit like pores is 1.5 and r_h is the edge-to-edge spacing/2. The flow resistivity value calculated by putting these values into Eq. 6.3 is 125.6 Pa s m^{-2}. The measured layer depth for the parallel strip surface 0.0253 m. Figure 6.16 (a) compares the measured data with predictions obtained using the slit pore layer model with the impedance parameters given above. The agreement between data and predictions is very good. The impedance parameters for aluminium strip arrangements with different edge-to-edge spacing are given in Table 6.1. Figure 6.16 (a) – (g) compare measured and predicted excess attenuation spectra for different edge-to-edge spacing. The agreement between predictions obtained using the slit pore layer model and measured EA for edge-to-edge spacing of 0.003 m and 0.005 m is very good. In particular the frequency of occurrence for EA maximum is predicted very accurately. It also predicts reasonably well the EA maxima frequencies (to within 50 Hz) as the edge-to-edge spacing is increased to 0.0124 m, 0.0174 m and 0.0274 m (see Figures 6.15 (c), (d) and (e)). However, further increase in edge-to-edge spacing to 0.0474 m and 0.0674 m results in poor agreement between measured EA spectra and those predicted using the slit pore layer model. Moreover the overall shapes of the predicted spectra are significantly different from those measured at higher spacings. It can be concluded that once the edge-to-edge spacing is comparable

to or greater than the layer depth, the surface behaves more like a periodically-rough surface than a slit pore layer.

Table 6.1 The measured flow resistivity, porosity for different edge-to-edge spacings. The layer depth is 0.0253 m.

Edge-to-edge spacing 'a' (m)	Flow resistivity (Pa s m^{-2}) $R_s = \dfrac{2\mu q^2 s_o}{\Omega r_h^2}$ $\mu =1.811e^{-5}, q^2=1.0, s_o=1.5, r_h=a/2$	Porosity 'Ω'
0.003	125.6	0.1923
0.005	30.6	0.2841
0.0124	2.85	0.496
0.0174	1.24	0.58
0.0274	0.423	0.685
0.0474	0.122	0.79
0.0674	0.06	0.8425
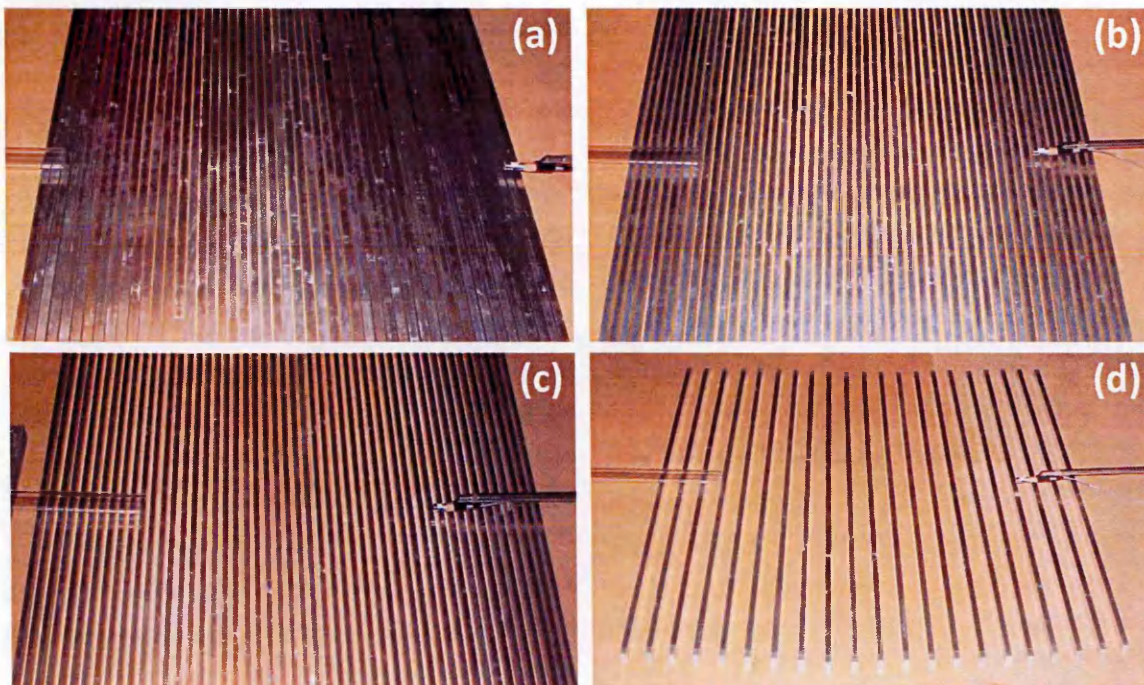
Figure 6.15 Photographs of periodically spaced aluminium strips placed over MDF board with different edge-to-edge spacing (a) 0.003 m (b) 0.005 m (c) 0.0124 m (d) 0.0674 m.
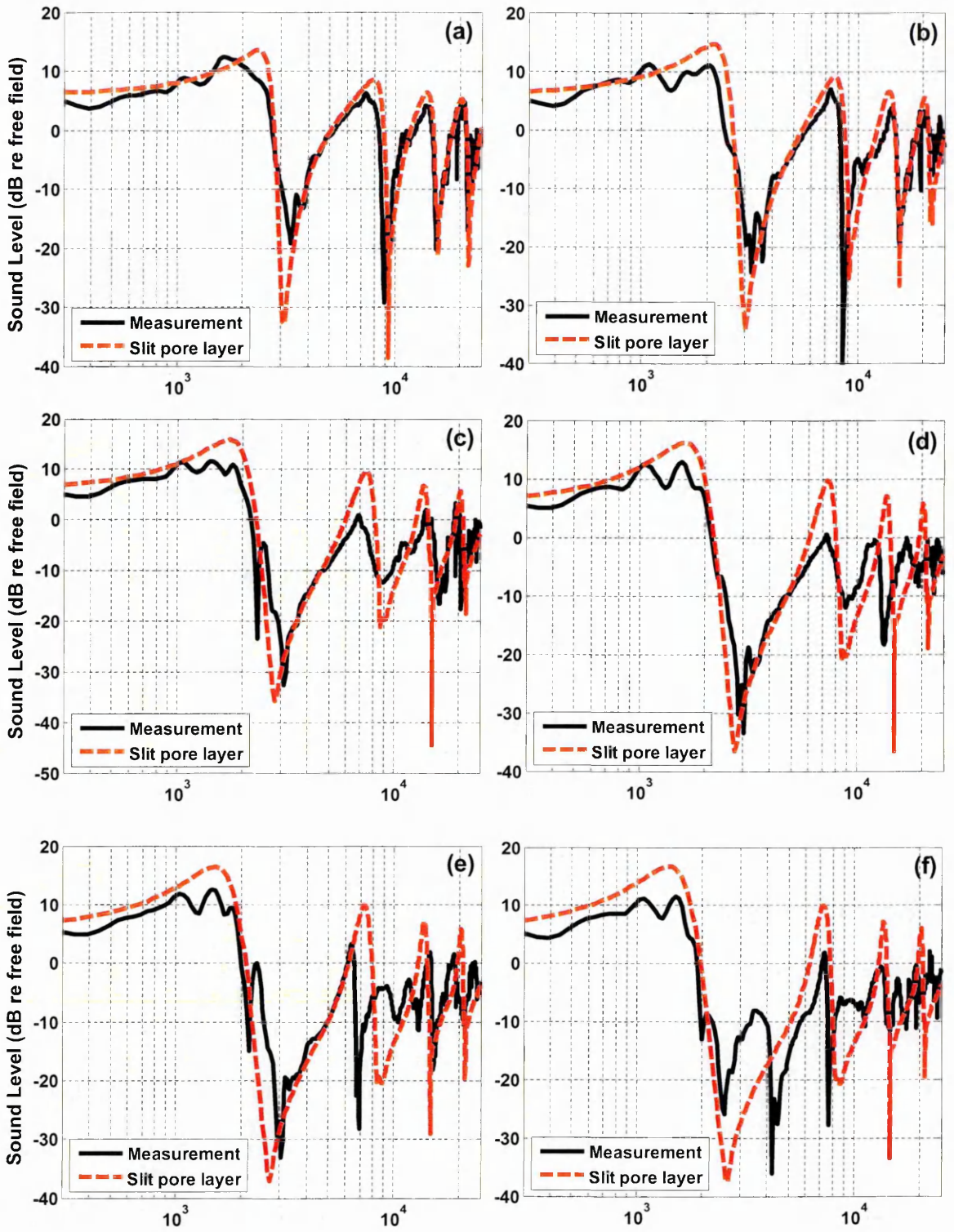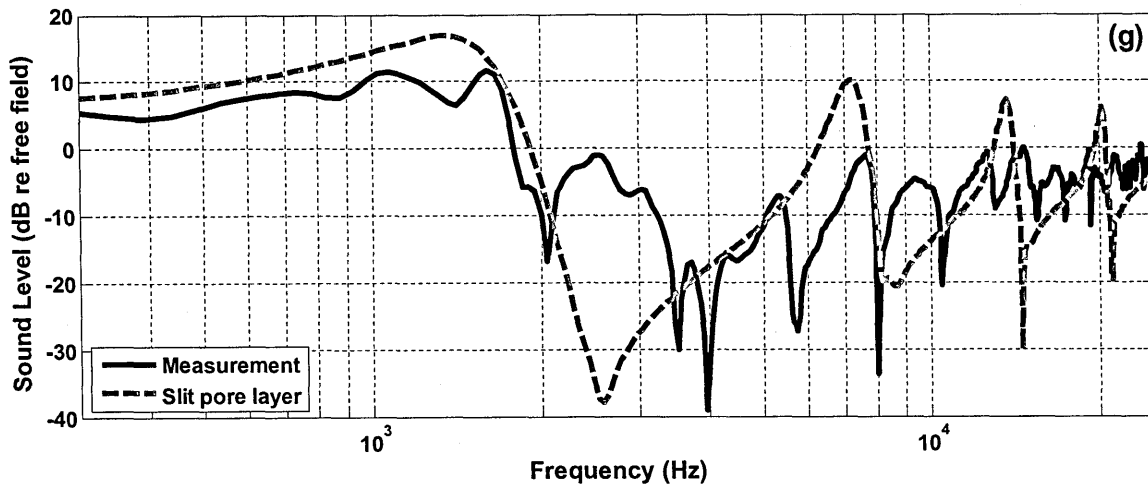
Figure 6.16 Comparison between measured excess attenuation spectra obtained with source and receiver at heights of 0.045 m and separated by 0.7 m over periodically spaced aluminium rectangular strips on MDF board with edge-to-edge spacing of (a) 0.003 m (b) 0.005 m (c) 0.0124 m (d) 0.0174 m (e) 0.0274 m (f) 0.0474 m and (g) 0.0674 m and EA spectra predicted by using a slit pore layer model. The predictions use the measured parameters listed in Table 6.1. The EA is predicted by using impedance given by slit pore layer along with propagation model for a point source above an impedance plane.

Figure 6.17 shows the excess attenuation spectra measured (black continuous line) with source and receiver at 0.045 m height and 0.7 m separation over aluminium strips placed on MDF board with edge-to-edge spacing of (a) 0.0030 m (b) 0.0124 m (c) 0.0274 m and (d) 0.0674 m. Also shown are BEM calculations (dotted lines) and predictions assuming that the effective surface impedance of the parallel strips can be modelled as that of a slit-pore layer (dashed lines). The parameter values used for the slit-pore predictions (broken line) are listed in Table 6.1. BEM predictions (dotted line) assume that the MDF board impedance is given by the 2-parameter variable porosity model (see Chapter 4) with effective flow resistivity 10 MPa s m^{-2} and effective porosity rate 1.0 m^{-1}.The source and receiver heights are measured with respect to the MDF

board base. If we look at the Figure 6.17 (a) with edge-to-edge spacing of 0.0030 m, the predicted excess attenuation spectra using slit pore layer model or 2D BEM are almost identical. Similarly, as shown by Figure 6.16 (b), BEM gives very good agreement with the measured data. However, the slit pore layer model over-predicts the measured amplitudes of the second and third EA maxima by nearly 5 dB. For a larger edge-to-edge spacing of 0.0274 m, BEM give good predictions for the amplitudes and frequencies of EA maxima. On the other hand, the slit pore model enables a reasonable fit to data with some shift in predicted EA maxima. Use of the slit pore layer model over/under-predicts the 2nd EA by nearly 5 dB and the predicted frequency differs from that measured by nearly a 1 kHz. For the even larger edge-to-edge spacing of 0.0674 m, the BEM predictions follow the measured EA spectra very well but the slit pore layer model leads to poor agreement with measured data. The spectral shapes predicted using the slit pore model are quite different from those measured and predicted using BEM (see Figure 6.17 (d)). This supports the previous conclusion that parallel walls can be modelled as having an effective impedance as long as the spacing between the walls is not much larger than their depth.
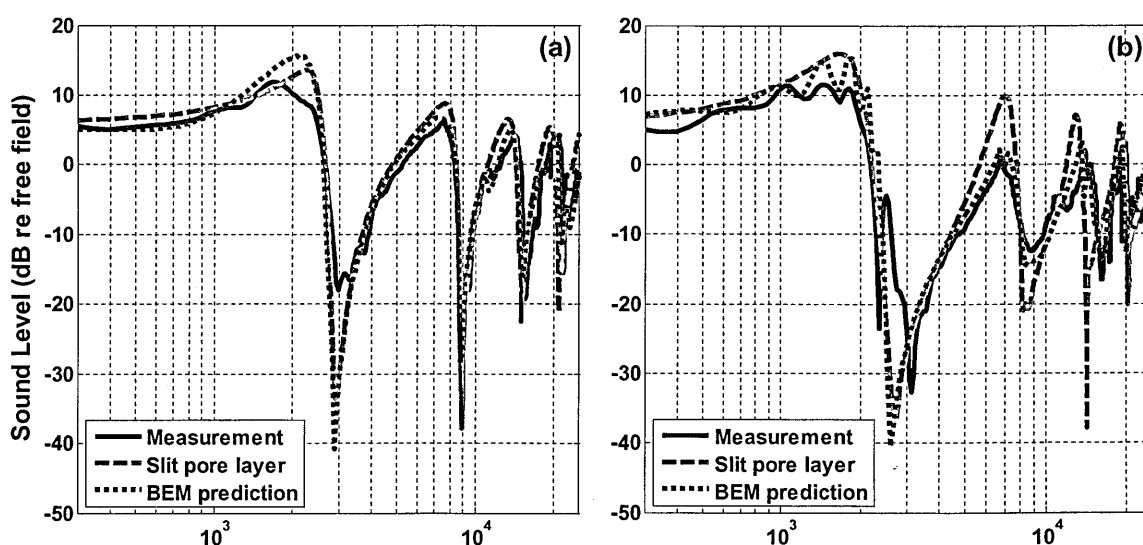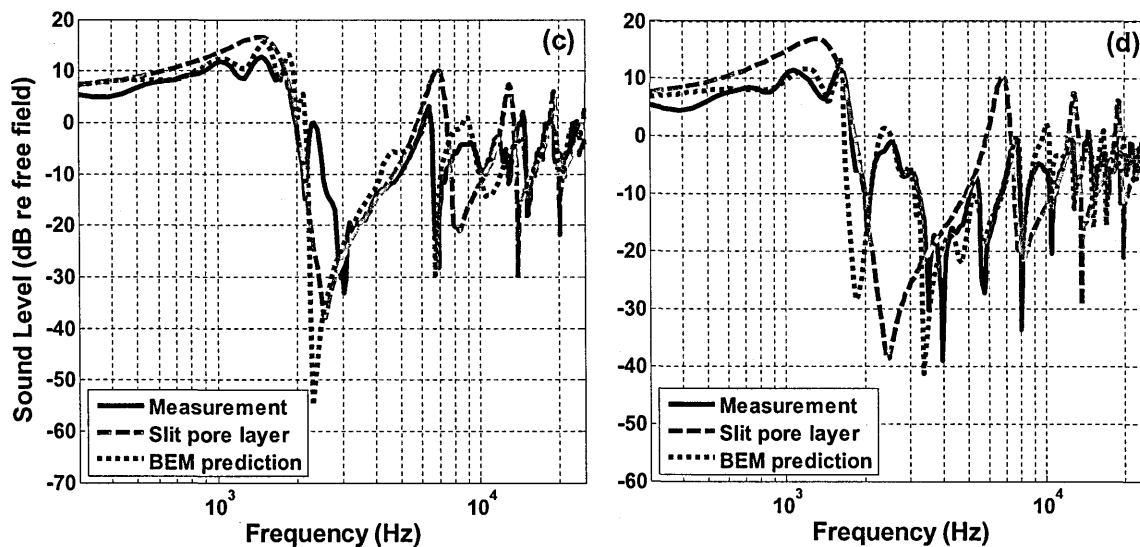
Figure 6.17 Excess attenuation spectra measured (black continuous line) with source and receiver at 0.045 m height and 0.7 m separation over aluminium strips placed on MDF board with edge-to-edge spacing of (a) 0.0030 m (b) 0.0124 m (c) 0.0274 m and (d) 0.0674 m. Also shown are BEM calculations (dotted lines) and predictions assuming a slit-pore layer impedance (dashed lines). The parameter values used for the slit-pore predictions (broken line) are listed in Table 6.1. BEM predictions (dotted line) assume that the MDF board impedance is given by the 2-parameter variable porosity model (see Chapter 4) with effective flow resistivity 10 MPa s m^{-2} and effective porosity rate 1.0 m^{-1}.The source and receiver heights are measured with respect to the MDF board base.

6.4.2 Comparison with predictions using the Kelders-Allard model

Figure 6.18 compares the measured and predicted EA spectra using the Kelders-Allard model over periodically spaced aluminium rectangular strips with different edge-to-edge spacing between them. The measured parameters used for these predictions are given in Table 6.2. The measurement arrangements are explained at the start of section 6.4. For narrow edge-to-edge spacing between aluminium rectangular strips, the agreement between data and predictions is good as shown in Figure 6.18 (a) and (b). As the spacing increases there is still some agreement between data and predictions as shown by Figure 6.18 (c) and (d). However, the predicted frequencies differ from those measured by between 100 Hz and 200 Hz. Further increase in spacing reduces the agreement between data and predictions as expected. For an edge-to-edge spacing of 0.0274 m, the frequency differences between those predicted and measured for first and second EA maxima are 500 Hz and 4 kHz respectively. The agreement between the Kelders-Allard model predictions and data is not as good as that obtained for the same edge-to-edge spacing with the slit pore model. Moreover according to the Kelders-Allard model predictions the EA spectra shift to higher frequencies with the increase in edge-to-edge spacing i.e. with increase in pore width. However, the measurements over aluminium strips and other roughness elements (see chapter 5) with different centre-to-centre spacing between elements shows that the spectra move to lower frequencies with increase in the spacing. It is concluded that, overall, the slit pore model gives better predictions than the Kelders-Allard model for propagation over periodically spaced rectangular strips.

Table 6.2 The measured porosity and effective layer depth for different edge-to-edge spacings.

Edge-to-edge spacing 'a' (m)	Porosity 'Ω'	Effective layer depth (m) $d' = d - a\log(2)/\pi$
0.003	0.1923	0.0246
0.005	0.2841	0.0242
0.0124	0.496	0.0226
0.0174	0.58	0.0215
0.0274	0.685	0.0193
0.0474	0.79	0.0148
0.0674	0.8425	0.0104
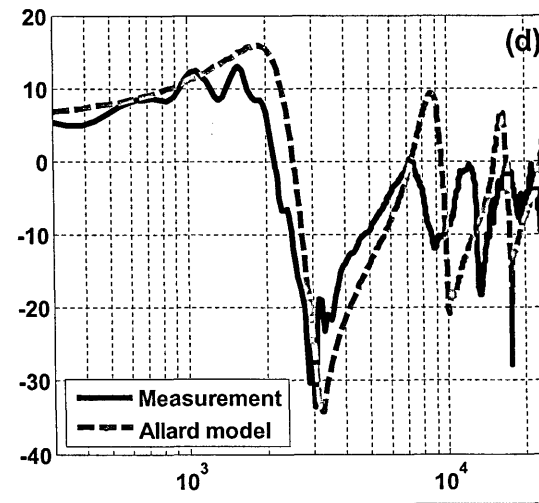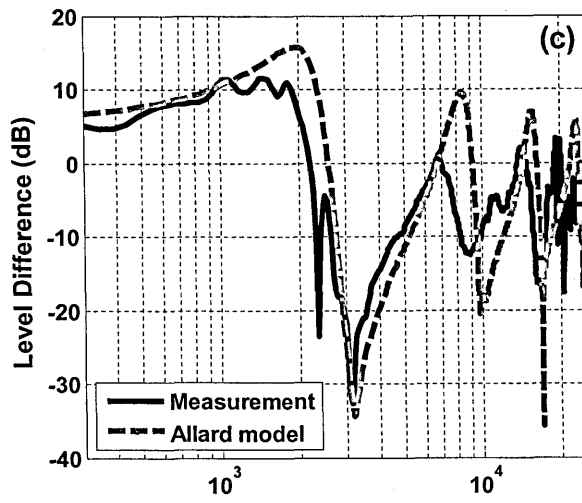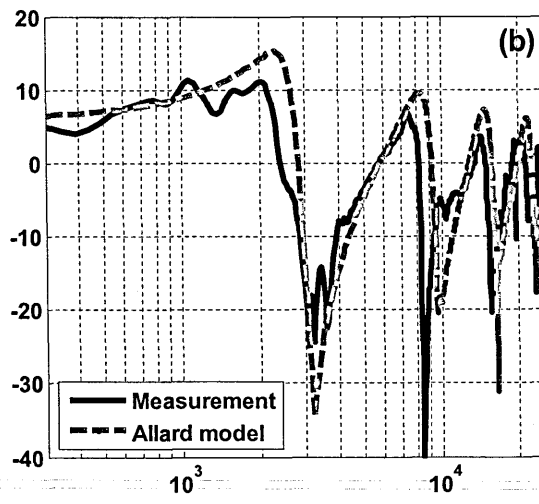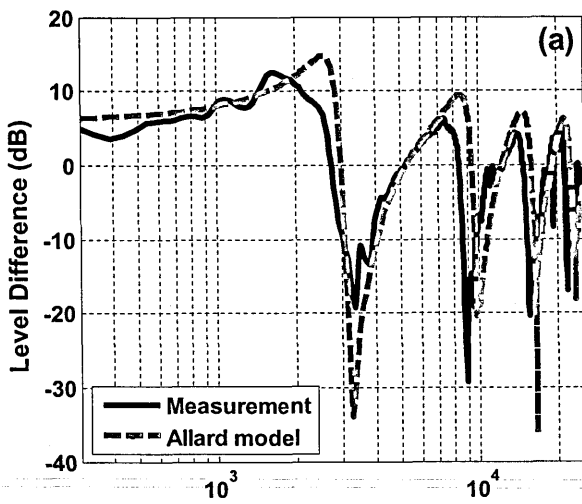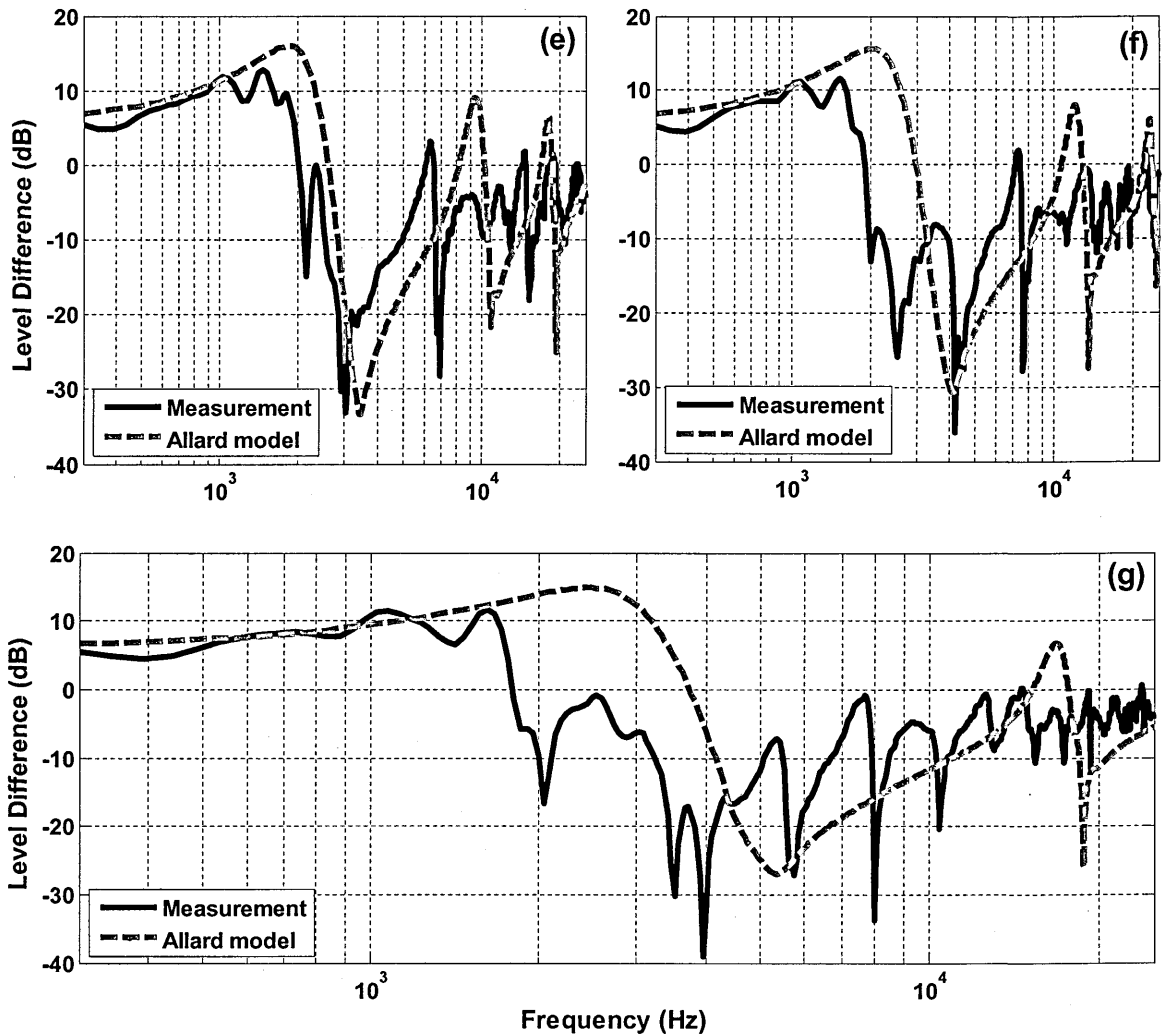
Figure 6.18 Comparison between measured excess attenuation spectra obtained with source and receiver at heights of 0.045 m and separated by 0.7 m over periodically spaced aluminium rectangular strips on MDF board with edge-to-edge spacing of (a) 0.003 m (b) 0.005 m (c) 0.0124 m (d) 0.0174 m (e) 0.0274 m (f) 0.0474 m and (g) 0.0674 m and EA spectra predicted by using a Kelders-Allard model. The predictions use the measured parameters listed in Table 6.2. The EA is predicted by using impedance given by slit pore layer along with propagation model for a point source above an impedance plane.

6.5 Effective impedance of Outdoor Larger scale parallel walls

6.5.1 BEM calculations using an effective impedance

As shown in chapter 5, a 2D BEM gives good agreement with measured data for sound propagation over parallel walls. The aim pursued here is to make the BEM calculations more efficient by replacing a surface composed of parallel walls by an effective impedance. Modelling the parallel walls as a raised platform with an effective impedance in BEM could be a quicker way of calculating the sound field than full discretisation of the boundaries.
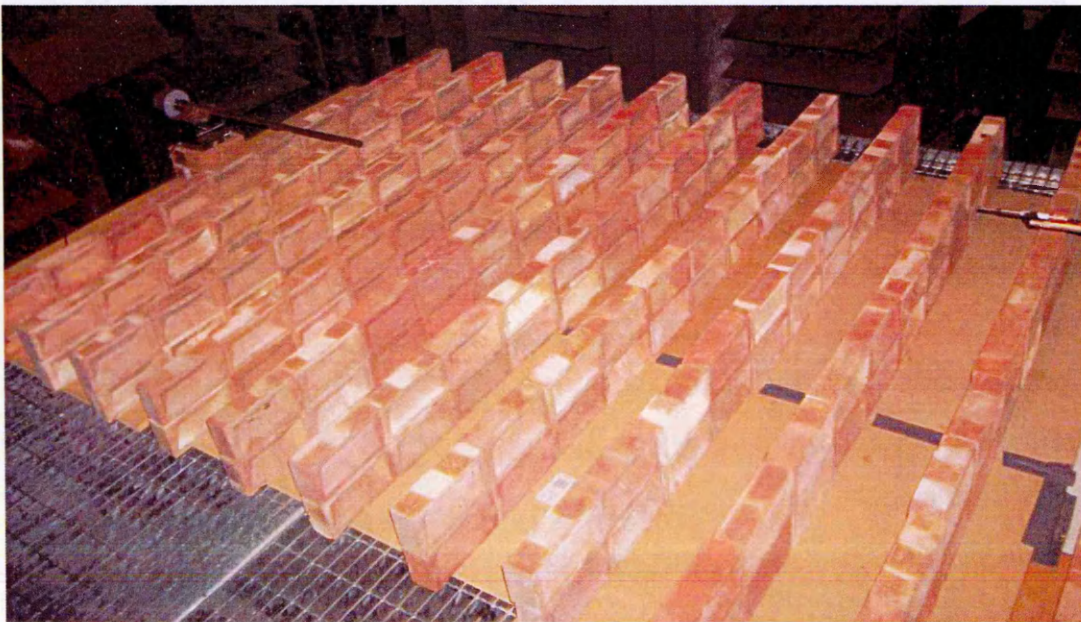
Figure 6.19 Photograph of periodically spaced parallel walls placed over MDF board in the laboratory.

First however it is necessary to obtain the effective impedance representation for two-brick-sized parallel walls. This can be obtained by a much less tedious, time consuming and lengthy procedure than that required to deduce the effective impedance of a lattice which involved many outdoor measurements and extensive data fitting. So far all of the data presented was collected over small

scale parallel walls such as wooden strips and aluminium rectangles in the laboratory. Although BEM calculations were found to fit these data very well, it is necessary also to validate the use of the BEM for predicting propagation over larger scale parallel walls. Excess attenuation spectra have been measured over an array of low brick walls placed on an MDF board in the laboratory as shown in Figure 6.19. The bricks walls were 0.2 m high and periodically spaced with centre-to-centre spacing of 0.28 m. The source and receiver were placed at height of 0.4 m above the MDF board with a horizontal separation of 2.0 m. Figure 6.20 shows the comparison between measured excess attenuation spectra over the brick walls and those predicted using BEM. The agreement between measured data and predictions is very good. To investigate the effective impedance concept for parallel wall arrays with different height and spacing, BEM has been used instead of making many more measurements and constructing other parallel walls using bricks. A range of BEM predictions over two-brick-sized parallel walls have been carried out and comparisons have been made between 2D BEM calculations in which the boundaries in the wall array are fully discretised and simpler calculations for a point source over an impedance plane in which the top surface of the wall array is represented by an effective impedance.

Based on the investigations of the acoustical performance of parallel brick wall configurations reported in Chapter 5, a 0.05 m thick and 0.3 high parallel wall array with centre-to-centre spacing of 0.2 m have been selected as the 'reference profile' for further investigations. First, the effective impedance model for the reference wall profile is obtained and its validity and applicability is tested.
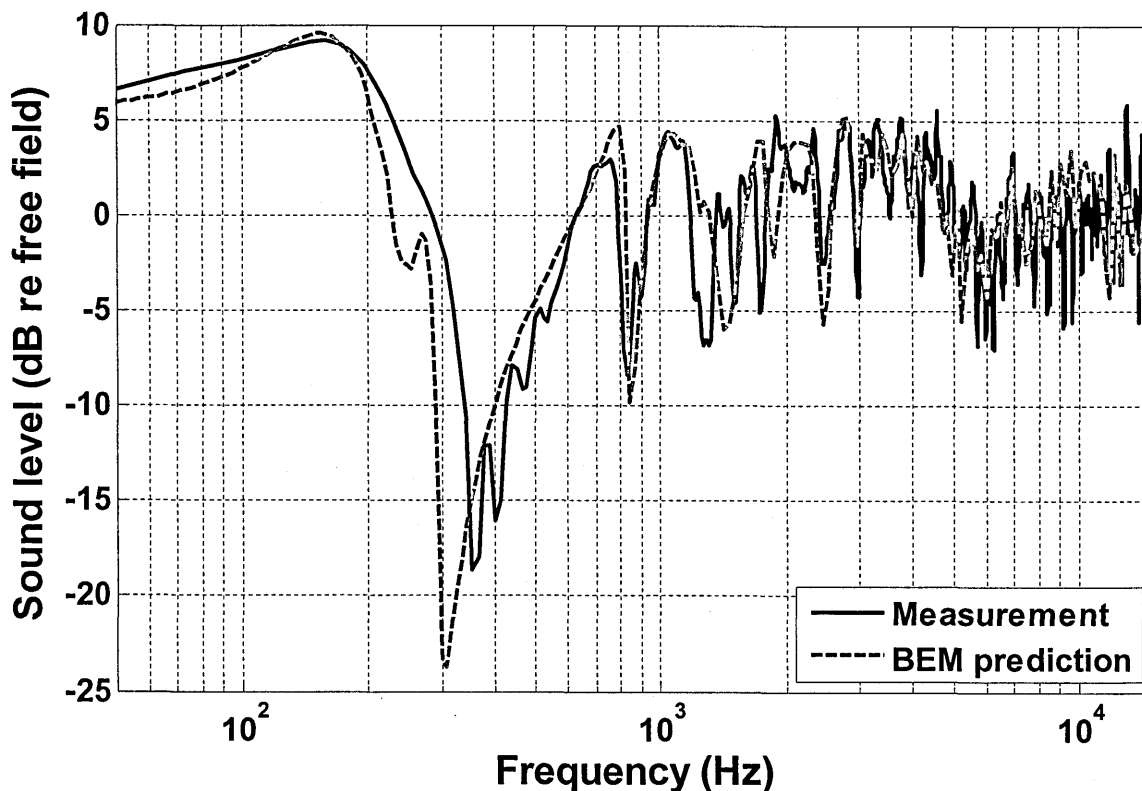
Figure 6.20 Comparison between BEM prediction and measured excess attenuation over periodically spaced parallel walls constructed with bricks over MDF board with the centre-to-centre spacing of 0.28 m and height of 0.2 m. The source & receiver are placed at height of 0.4 m above MDF sheet with a separation of 2.0 m between them.

6.5.2 Influence of Source and Receiver positions

Figure 6.22 show excess attenuation spectra predicted using BEM with a full discretisation of an array of 0.05 m thick and 0.3 m high parallel walls with centre-to-centre spacing of 0.2 m (configurations shown in Figure 6.21).
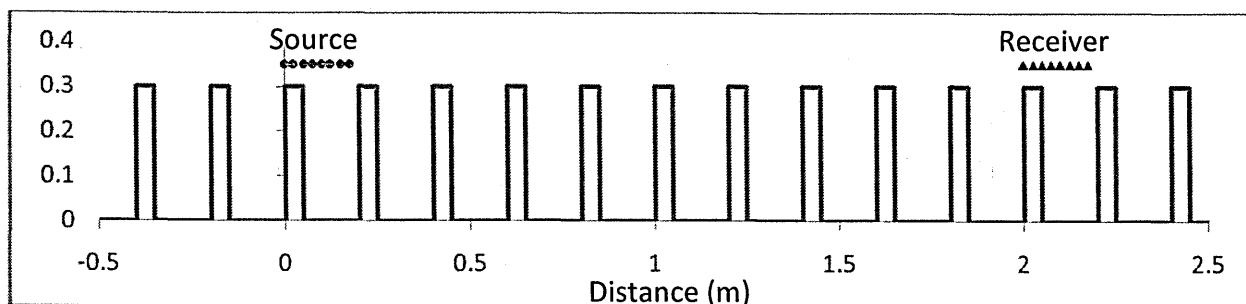
Figure 6.21 A schematic of parallel walls used in BEM with different source and receiver positions.
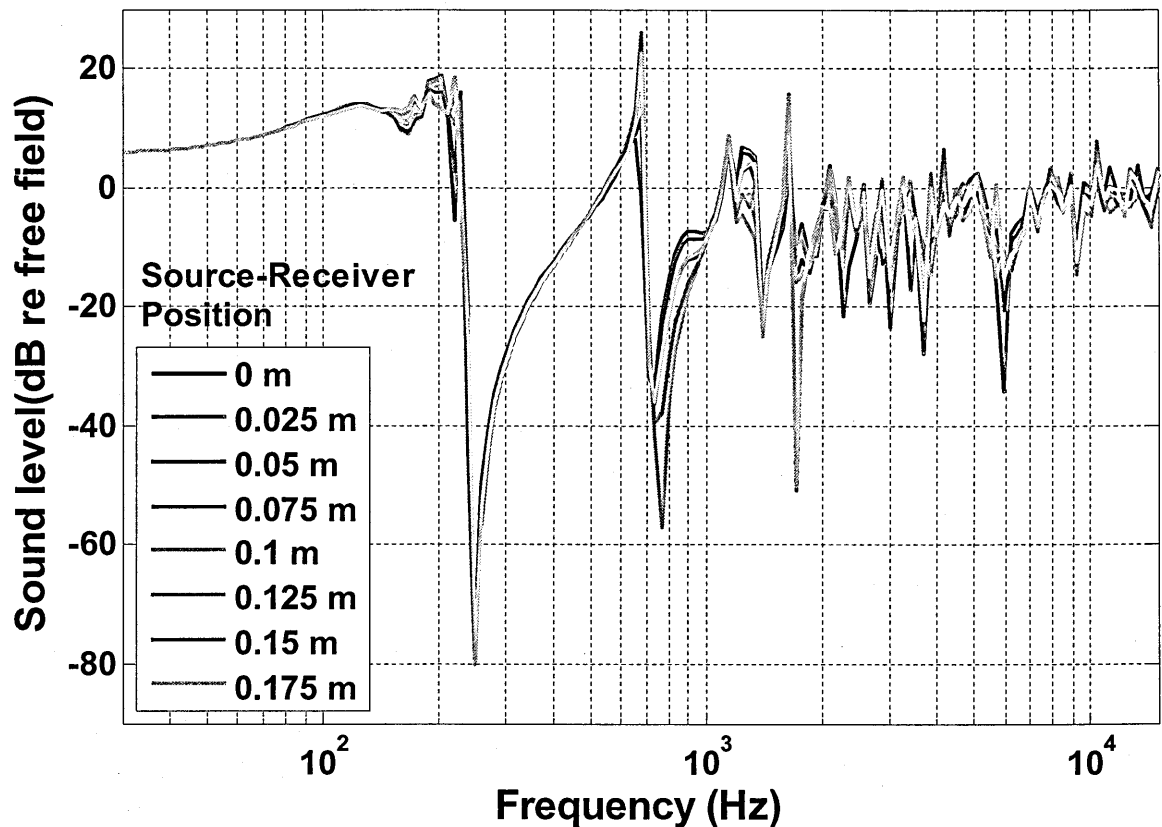
Figure 6.22 Predicted excess attenuation spectra using BEM over 0.05 m thick and 0.3 m high parallel walls with centre-to-centre spacing of 0.2 m. The source and receiver are placed at height of 0.05 m above parallel walls but at different positions (see Figure 6.21) while maintaining a horizontal separation of 2.0 m.

The source and receiver are assumed to be placed at a height of 0.05 m above parallel walls with horizontal separation of 2.0 m. The purpose of these predictions is to check the influence of the source and receiver positions on the BEM predictions. The first prediction is carried out by placing source at the location '0 m' immediately above the edge of a wall (see Figure 6.21). The source and receiver were moved horizontally along the axis perpendicular to parallel walls axis while preserving their horizontal separation. Each time the source-receiver positions were moved by 0.025m. BEM (fully discretised) calculations have been made for each of the locations shown in Figure 6.21 and Figure 6.22 compares the resulting excess attenuation spectra predictions. There are very small differences

between the different EA spectra predictions at different source-receiver positions which may be due to numerical errors. The BEM predictions show that the positions of source and receiver with respect to the parallel walls are not very important.

6.5.3 Slit pore layer

Figure 6.23 compares predicted excess attenuation spectra over a 0.3 m high parallel wall array using BEM with full discretisation of the array and calculations for a point source over an impedance plane in which the top surface of the array is modelled as having a slit pore layer impedance. The walls are 0.05 m thick and placed with the centre-to-centre spacing of 0.2 m. The assumed geometry is such that the source and receiver are at a height of 0.05 m above the parallel walls horizontally separated by 4.0 m. In Figure 6.23 (a) the predictions including the slit pore layer impedance are carried out using the parameters deduced from the array geometry and Eq. 6.3 (flow resistivity = 0.0129, porosity = 0.75 and layer depth = 0.3 m). The agreement between the predictions is very good as shown in Figure 6.23. Although use of the slit pore layer impedance representation for the top array surface does not predict as high surface wave amplitudes as predicted by the fully-discretised BEM, overall the agreement between slit pore layer model predictions and BEM predictions is very good.
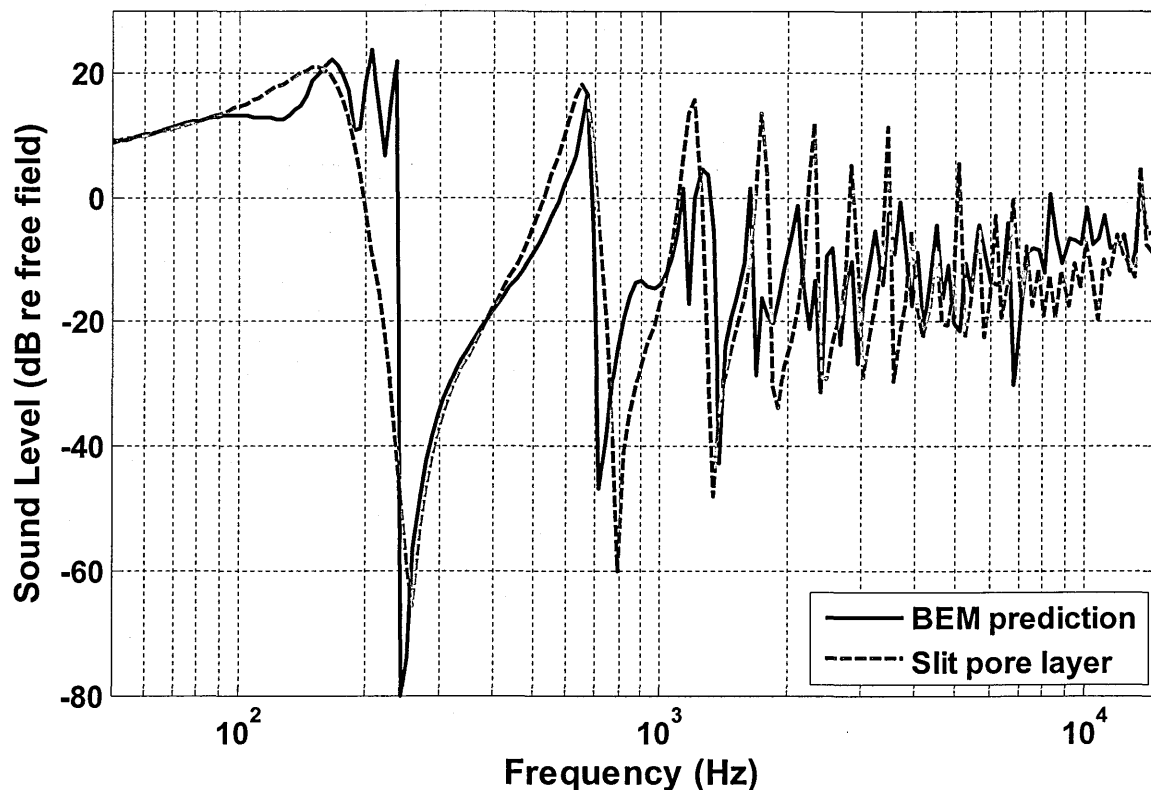
Figure 6.23 Comparison between predicted excess attenuation spectra using BEM and slit pore layer model over 0.05 m thick and 0.3 m high parallel walls with centre-to-centre spacing of 0.2 m by placing the source and receiver at height of 0.05 m above parallel walls with the horizontal separation of 4.0 m. The slit pore layer predictions are carried out using measured parameters with flow resistivity of 0.0129 Pa s m^{-2}, porosity of 0.75 and physical layer depth of 0.3 m. The EA predicted for a point source over an impedance plane in which the top surface of the array is modelled as having a slit pore layer impedance.

6.5.4 Kelders-Allard model

Figure 6.24 gives the comparison between excess attenuation spectra predicted using a fully-discretised BEM and a point source over impedance plane propagation theory using a Kelders-Allard impedance model to represent the surface of a 0.3 m high parallel wall array. The walls are assumed to be 0.05 m thick and to have a centre-to-centre spacing of 0.2 m. The Kelders-Allard model based predictions given in Figure 6.24, where they are denoted by 'Allard'in the key, (a) are carried out using parameters deduced from the array profile (porosity

= 0.75 and effective layer depth (from Eq. (6.2)) = 0.2669 m. The agreement between the predictions is reasonable. The EA spectra predicted by using the Kelders-Allard model to represent the top of the array are shifted towards higher frequencies and exhibit higher amplitude high frequency peaks compared to the BEM predictions. The agreement between the two predictions can be improved by adjusting the impedance model parameters. But since the Kelders-Allard model has only two parameters the frequency shift can be reduced only by adjusting the effective layer depth. Using the slit pore model for the effective impedance has the advantage that the amplitudes of the peaks in the EA spectra can be adjusted also by adjusting the flow resistivity. Alternatively, the EA peak amplitudes resulting from use of the Kelders-Allard model are reduced by making the propagation constant k_o complex i.e. replacing k_o by $k_o(1+0.008i)$. The best fit parameters using the Kelders-Allard model are porosity = 0.75, layer depth = 0.31 m and with the real propagation constant replaced by a complex propagation constant. However it should be noted that the best fit layer depth in the Kelders-Allard impedance model, is higher than the actual layer depth. Figure 6.24 (b) compares predictions of EA spectra using a fully-discretised BEM and those predicted by using point source over an impedance plane theory and the best-fit Kelders-Allard model to represent the surface of the array.
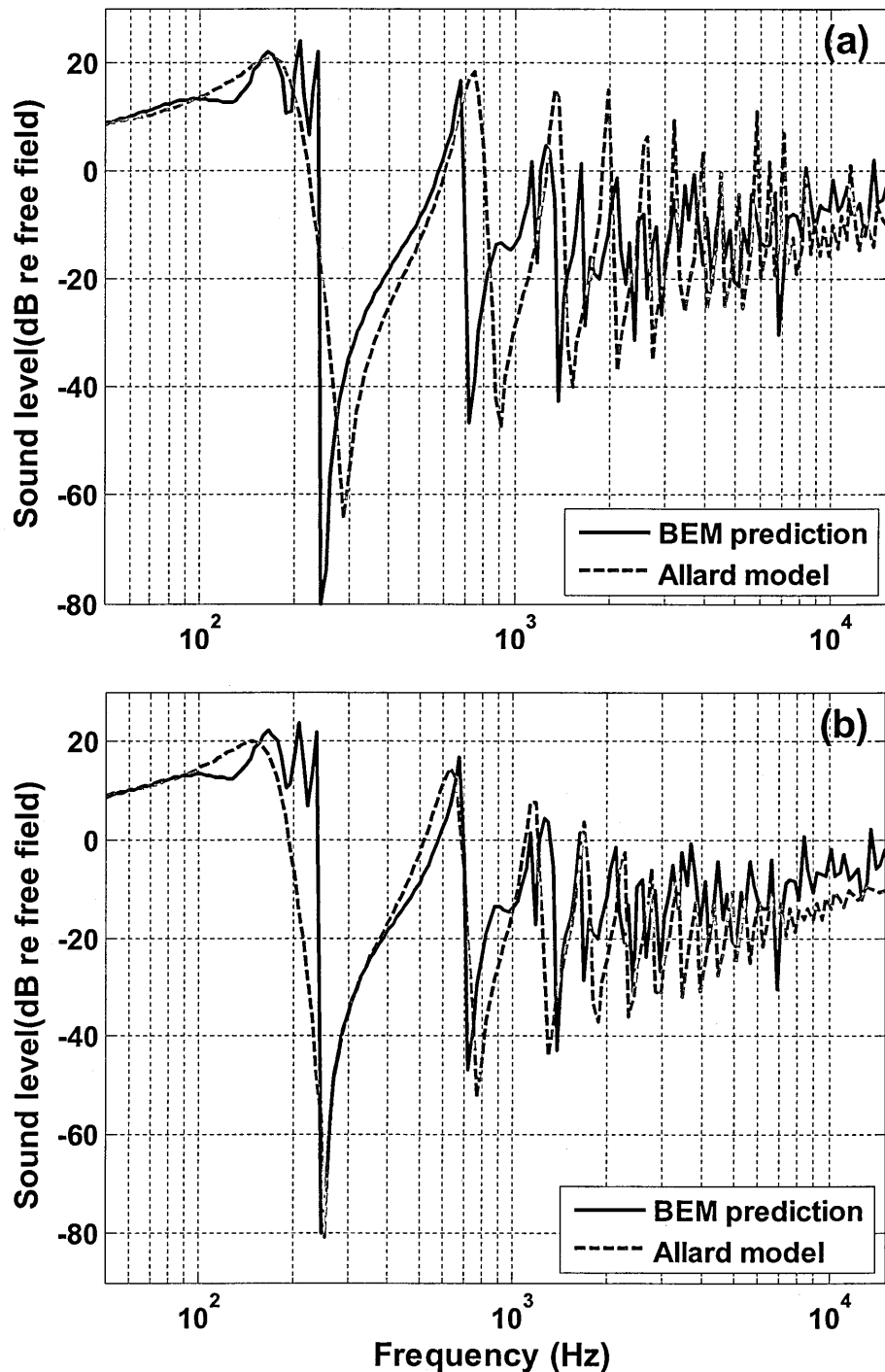
Figure 6.24 Comparison between predicted excess attenuation spectra using BEM and Kelders-Allard model over 0.05 m thick and 0.3 m high parallel walls with centre-to-centre spacing of 0.2 m by placing the source and receiver at height of 0.05 m above parallel walls with the horizontal separation of 4.0 m (a) The Kelders-Allard predictions are carried out using measured parameters with a porosity of 0.75 and effective layer depth of 0.2669 m (b) The Kelders-Allard predictions are carried out using best fitted impedance parameters with a porosity of 0.75 best fitted layer depth of 0.31 m and real propagation constant, k_o replaced by a complex one $k_o(1+0.03i)$.

6.5.5 Influence of centre-to-centre spacing

It has been shown that the EA spectra for the reference parallel wall profile predicted by using the slit pore layer model with parameters deduced from the array geometry are in good agreement with BEM predictions obtained by full discretisation of the wall array. In the following, this work is taken further to test the validity of the impedance surface representation for different edge-to-edge spacings within the array. BEM predictions have been carried out for different spacing with full-discretisation with the slit pore layer and Kelders-Allard models used to represent the top surface of the wall array.

6.5.5.1 Use of Slit pore layer impedance model

Figure 6.24 compares BEM-predicted excess attenuation spectra with source and receiver at height of 0.05 m and a horizontal separation of 4.0 m above 0.05 m thick and 0.3 m high parallel walls with different edge-to-edge spacing (a) 0.05 m (b) 0.10 m (c) 0.15 m (d) 0.20 m (e) 0.25 m (f) 0.30 m (g) 0.35 m (h) 0.40 m (i) 0.45 m (j) 0.50 m (k) 0.55 m (l) 0.60 m (m) 0.65 m (n) 0.70 m (o) 0.75 m. The predictions have been made using either full discretisation or the theory for propagation from a point source over an impedance plane with the slit pore layer model used to represent the impedance of the top surface of the array. The slit pore layer model parameters corresponding to the array geometries with different edge-to-edge spacing between the parallel walls are listed in Table 6.3. As reported in Section 6.2.2, laboratory data have shown that, the slit pore theory become less valid as the gap between strips is increased. Similar conclusions are derived here for larger scale parallel walls. EA spectra are predicted very well by using the slit pore layer model with parameters corresponding to array geometries

with edge-to-edge spacing of between 0.05 m to 0.35 m (see Figures 6.25 (a) – (g)). As the edge-to-edge spacing is increased beyond 0.35 m, the slit pore layer model based predictions are shifted in comparison to predictions using a fully-discretised BEM. The slit pore layer model representation of the top of the array gives reasonable predictions For edge-to-edge spacing of up to 0.5 m. For an edge-to-edge spacing of between 0.55 m to 0.75 m (see Figures 6.24 (k) – (o)) the agreement between the various predictions is not very good.

Comparison between fully-discretised BEM predictions and those using the slit pore layer impedance model to represent the array top suggests that the impedance representation gives reasonably good agreement as long as the wavelength corresponding to the first EA maximum is four times larger than the edge-to-edge spacing between parallel walls. Similar conclusions have been drawn from comparison between laboratory data and EA predictions using the slit pore model (see section 6.21). The slit pore model based predictions and laboratory EA data agree well up to an edge-to-edge spacing of 0.0274 m, which is four times smaller than the wavelength of first EA maxima at 3 kHz (see Figure 6.16 (e)).

An alternative conclusion derived from these predictions is that use of the slit pore model impedance representation of the top of a low parallel wall array is adequate until the edge-to-edge spacing between the walls becomes comparable to their height. The assumed height for the configurations considered in Figure 6.25 is 0.3 m and use of the slit pore layer model impedance representation gives good agreement with fully-discretised BEM predictions up to an edge-to-edge spacing of 0.35 m. Similarly, for the laboratory data, the height of aluminium strips

is 0.0253 m and use of the slit pore model gives good agreement with laboratory

EA data for an edge-to-edge spacing of up to 0.0274 m (see section 6.21).

Table 6.3 The flow resistivity and porosity corresponding to different edge-to-edge spacings in a 0.3 m high parallel wall array.

Figure 6.25 #	Edge-to-edge spacing 'a' (m)	Flow resistivity (Pa s m^{-2}) $R_s = \dfrac{2\mu q^2 s_o}{\Omega r_h^2}$ $\mu = 1.811e^{-5}$, $q^2 = 1.0$, $s_o = 1.5$, $r_h = a/2$	Porosity 'Ω'
(a)	0.05	0.174	0.5
(b)	0.10	0.033	0.6667
(c)	0.15	0.013	0.75
(d)	0.20	0.0068	0.8
(e)	0.25	0.0042	0.8333
(f)	0.30	0.0028	0.8571
(g)	0.35	0.002	0.875
(h)	0.40	0.0015	0.8889
(i)	0.45	0.0012	0.9
(j)	0.50	0.00096	0.9091
(k)	0.55	0.00078	0.9167
(l)	0.60	0.00065	0.9231
(m)	0.65	0.00055	0.9286
(n)	0.70	0.00048	0.9333
(o)	0.75	0.00041	0.9375
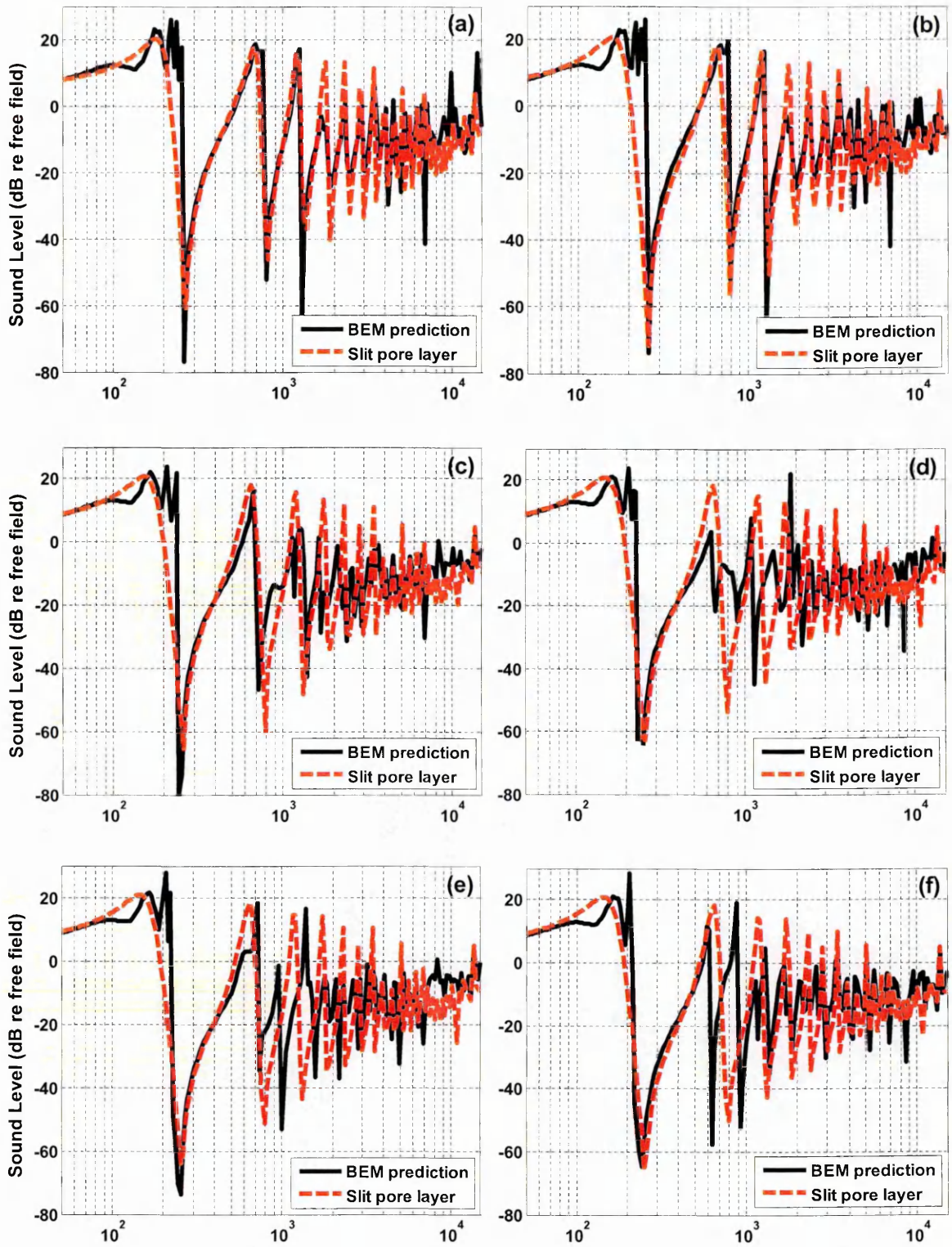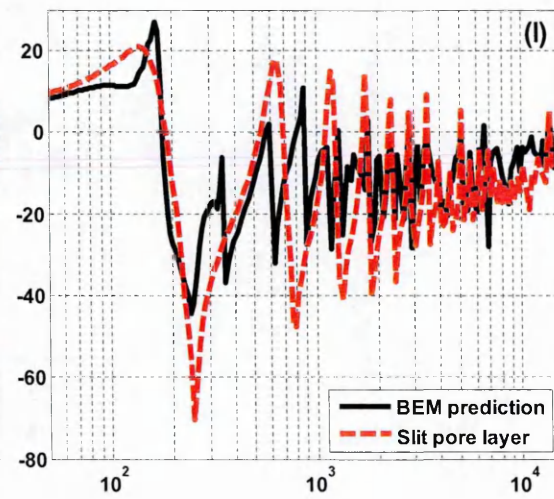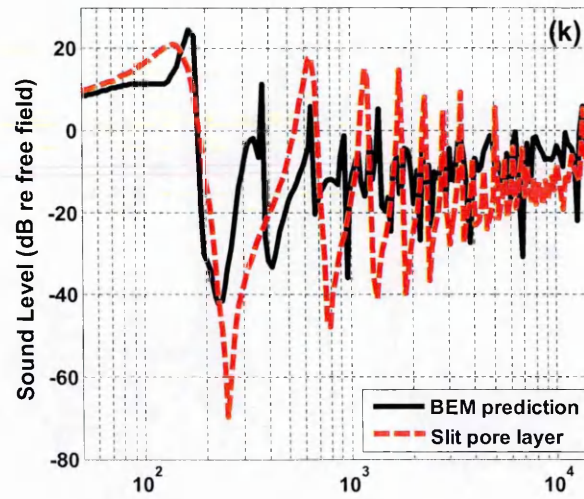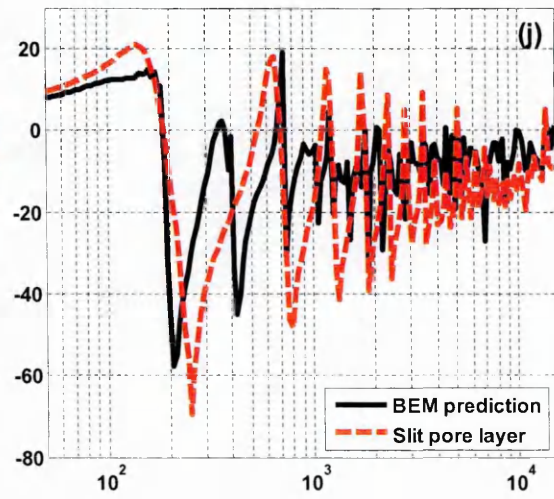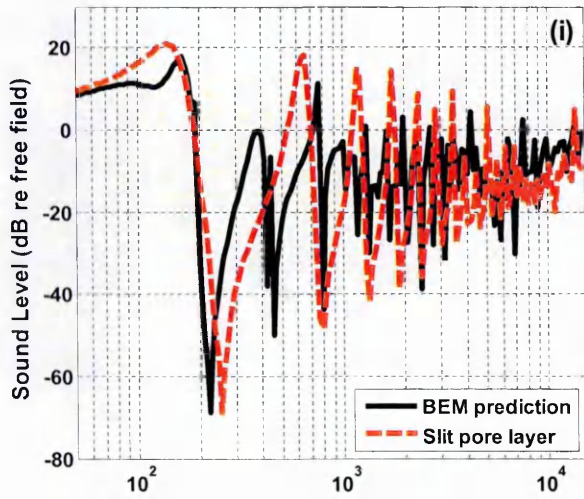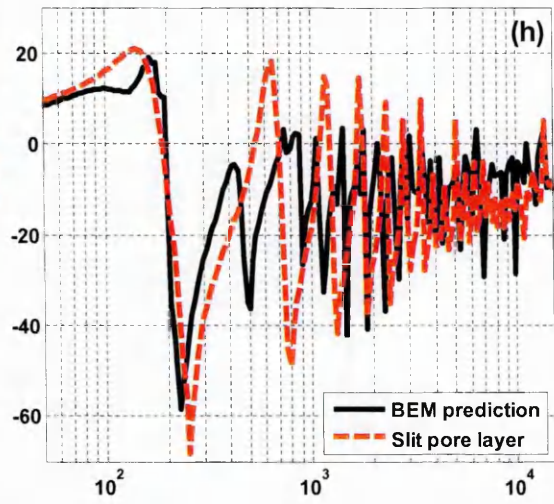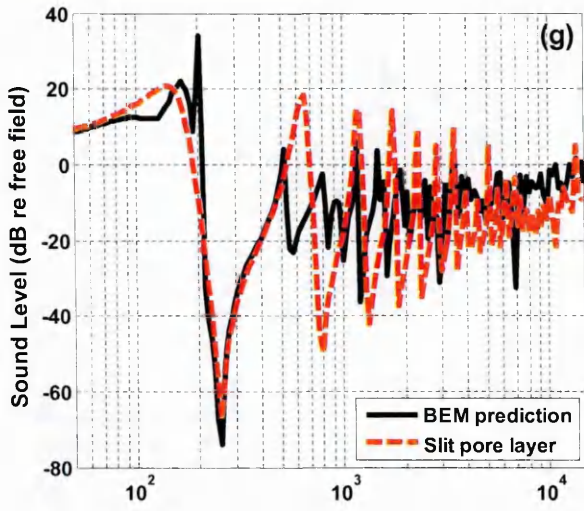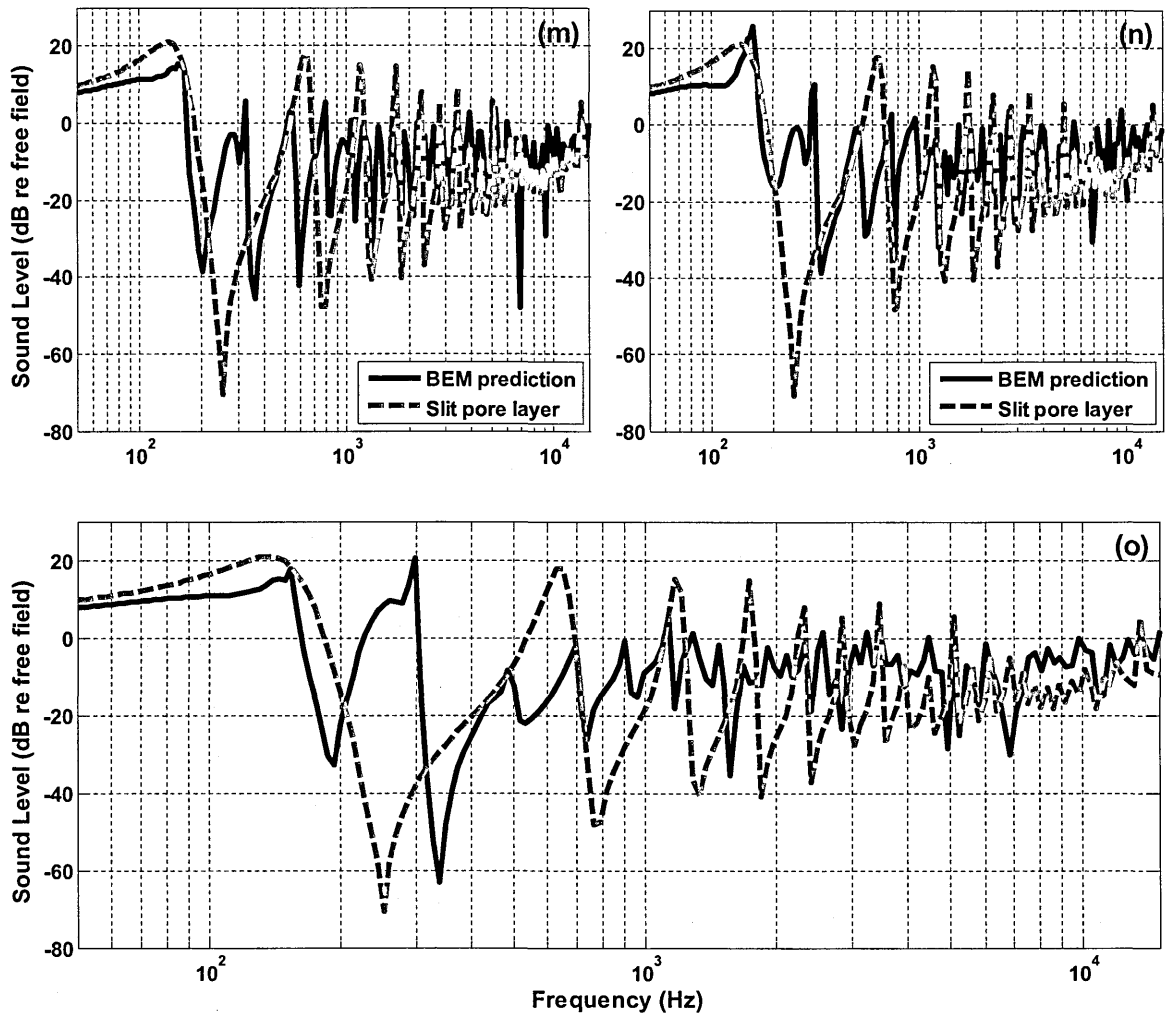
Figure 6.25 Comparison between excess attenuation spectra predicted by using BEM and those obtained by using point source propagation theory with the slit pore layer model to represent the array surface impedance by placing the source and receiver at height of 0.05 m above parallel walls with the horizontal separation of 4.0 m over 0.05 m thick and 0.3 m high parallel walls with different edge-to-edge spacing (a) 0.05 m (b) 0.10 m (c) 0.15 m (d) 0.20 m (e) 0.25 m (f) 0.30 m (g) 0.35 m (h) 0.40 m (i) 0.45 m (j) 0.50 m (k) 0.55 m (l) 0.60 m (m) 0.65 m (n) 0.70 m (o) 0.75 m. The measured impedance parameters using slit pore layer model for different edge-to-edge spacing between parallel walls are given in Table 6.3.

6.5.5.2 Use of the Kelders-Allard impedance model

Figure 6.26 compares predictions using a fully-discretised BEM and predictions using point source theory with the Kelders-Allard impedance model for propagation over parallel walls. As reported earlier (see Section 6.4.2) use of the Kelders-Allard model enables good agreement with measured laboratory data for very narrow spacing between strips. As the gap between the strips is increased, there was a contradiction between the predictions that use the Kelders-Allard theory and BEM predictions. A similar conclusion has been drawn here. The agreement between fully-discretised BEM predictions and those using the Kelders-Allard model is very good for edge-to-edge spacing of 0.05 m. However, as the edge-to-edge spacing between strips increases, EA spectra predicted using the Kelders-Allard model shift towards higher frequencies whereas BEM predicted spectra move to lower frequencies (see Figures 6.26 (b), (c) and (d)).
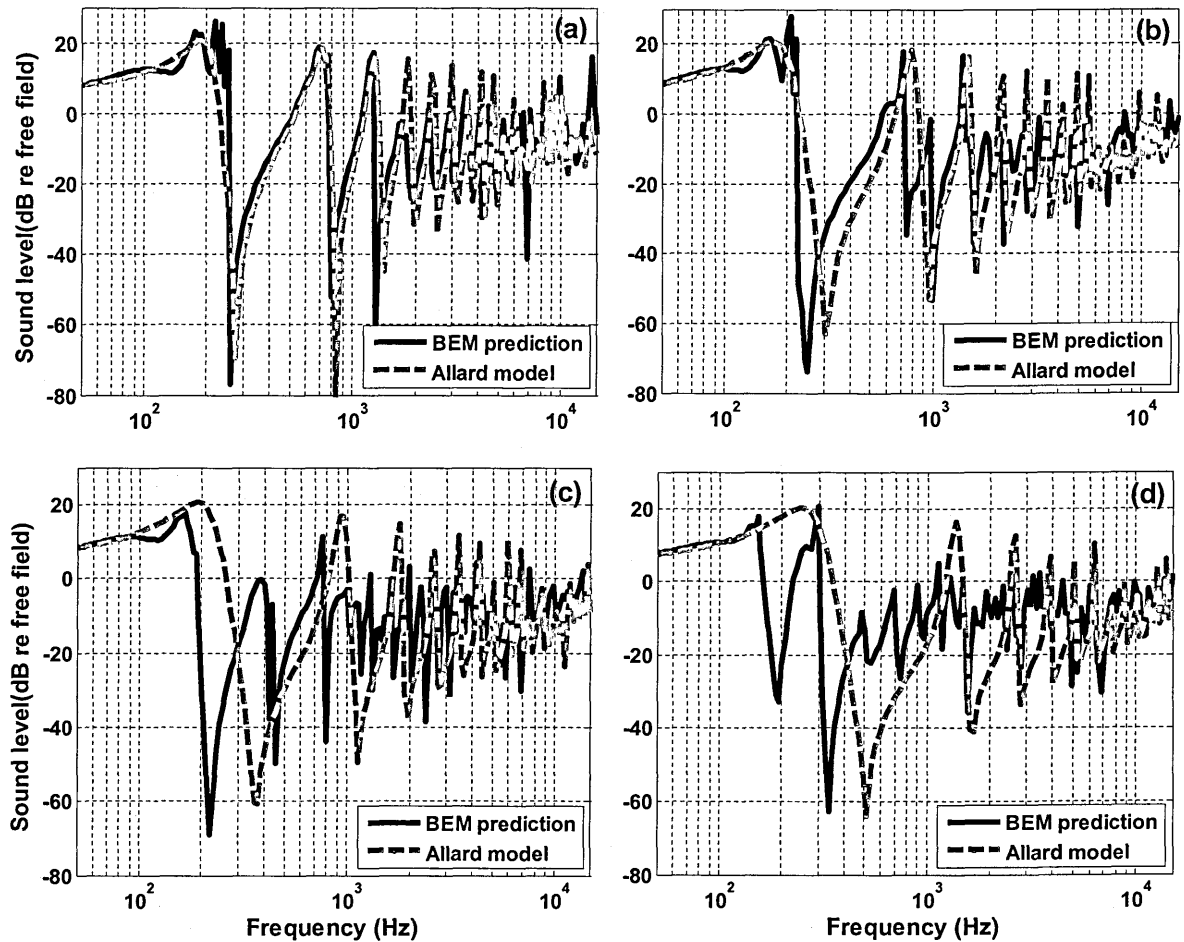
Figure 6.26 Comparison between excess attenuation spectra predicted by using BEM and those obtained by using point source propagation theory with the Kelders-Allard model to represent the array surface impedance by placing the source and receiver at height of 0.05 m above parallel walls with the horizontal separation of 4.0 m over 0.05 m thick and 0.3 m high parallel walls with edge-to-edge spacing as given (a) edge-to-edge spacing = 0.05 m, porosity = 0.5 and effective layer depth = 0.289 m (b) edge-to-edge spacing = 0.25 m, porosity = 0.8333 and effective layer depth = 0.2448 m (c) edge-to-edge spacing = 0.45 m, porosity = 0.9 and effective layer depth = 0.2007 m (d) edge-to-edge spacing = 0.75 m, porosity = 0.9375 and effective layer depth = 0.1345 m.

6.5.6 Comparison between fully-discritized and simplified BEM predictions over parallel walls

It has been shown that the excess attenuation spectra predicted using fully-discritized parallel walls in BEM and a point source over impedance plane propagation theory using a slit pore impedance model to represent the surface of a 0.3 m high parallel wall array gives good agreement (see Sections 6.5.3 and 6.5..5.1). The purpose of representing parallel walls as a simplified raised platform with effective impedance in BEM is to speed up the calculations. As described in Chapter 7 (see Section 7.4.1) a significant amount of time and computing recourses are required to make BEM calculations of insertion loss for all the road types. Using an effective impedance instead of a full discritization for parallel walls speeds up the process of insertion loss calculation. In this Section BEM predictions in which full discretization is carried out for parallel walls are compared with predictions in which the parallel walls are modelled as a raised impedance platform in BEM for a HOSANNA two lane urban road. Once the simplified impedance platform BEM calculation has been validated against a fully-discritized BEM calculation, it can be used with confidence for insertion loss calculations for different road types.

Figure 6.27 shows the schematic for HOSANNA two lane urban road case (see Chapter 11). A single lane road is represented by three sources at heights of 0.01 m, 0.3 m and 0.75 m. The two lanes are represented by 6 sources and separated with a distance of 3.5 m. The receiver is placed at a distance of 50 m from nearest lane and at a height of 1.5 m. The parallel walls start at a distance of 2.5 m from the nearest lane.
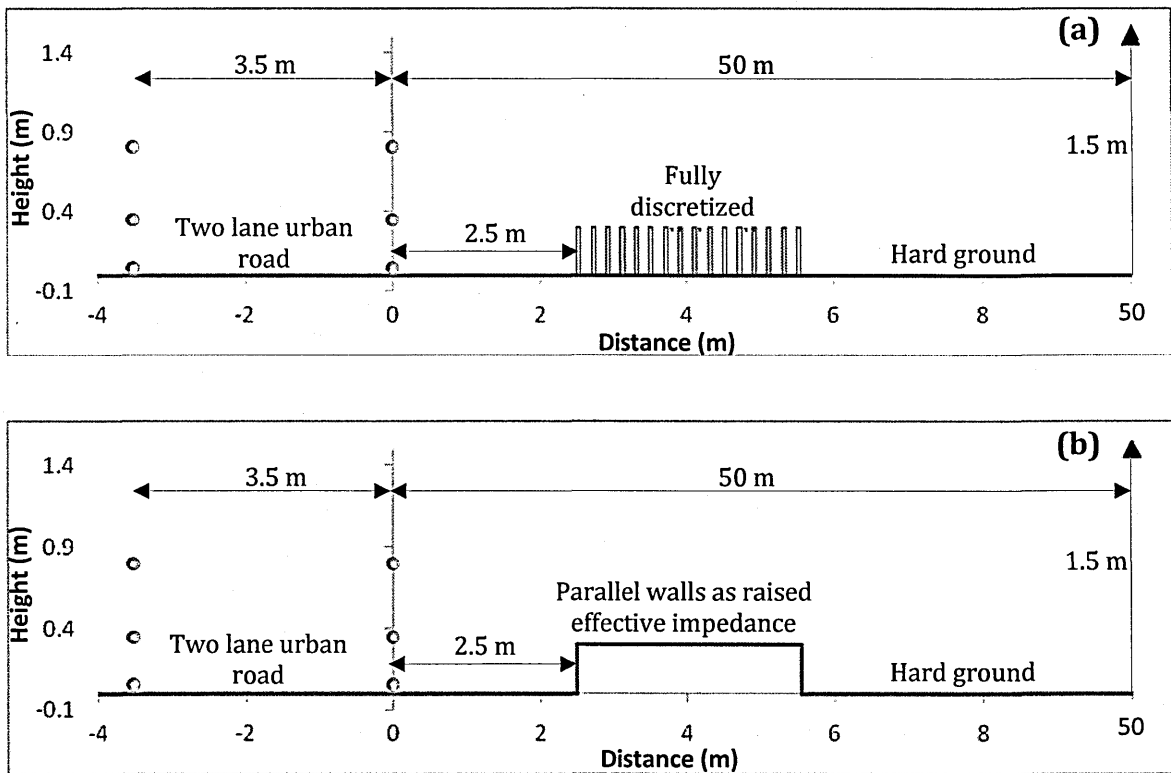
Figure 6.27 Schematic diagrams of a 'HOSANNA' two lane urban road with receiver at a distance of 50 m from nearest lane and at a height of 1.5 m above ground (a) fully discretized parallel walls system for BEM predictions (b) parallel walls modelled as a raised effective impedance surface for simplified BEM calculations.

Figure 6.27 (a) shows schematics of the fully-discritized parallel walls system and of parallel walls modelled as a raised effective impedance surface for simplified BEM calculations. Figure 6.28 compares the excess attenuation spectra predicted using a fully-discretized parallel walls system in BEM and those obtained through the simplified BEM in which the parallel walls are modelled as a raised effective impedance platform using the slit pore layer impedance model with flow-resistivity 0.013 Pa s m^{-2}, porosity 0.75 and layer depth 0.3 m. The EA spectra due to lowest source height of 0.01 m, with receiver at a distance of 50 m and at a height of 1.5 m above ground is plotted in Figure 6.28. The agreement between fully-discritized and simplified BEM predictions is very good. The EA spectra are plotted at narrow band frequencies and at octave band centre frequencies for the

fully discretized and simplified parallel wall raised impedances having different widths of 1.65 m, 3.05, 5.85 and 12.05 m. Table 6.4 summarizes the insertion loss calculated either using a fully-discretized BEM or using a simplified BEM for parallel walls system near to a HOSANNA two lane urban road. There is almost no difference in calculated insertion loss using fully-discretized BEM and simplified BEM for the receiver at a height of 4.0 m. However, the calculated insertion losess using fully-discretized BEM and simplified BEM for a receiver height of 1.5 m differ by between 0.3 dB and 1.0 dB for wall arrays of widths between 1.65 m and 12.05 m. It is concluded that the simplified BEM predictions can be used to calculate insertion losses for parallel wall systems.

Table 6.4 Comparison between calculated insertion loss using either fully-discritized BEM predictions or simplified BEM predictions for parallel wall system.

Parallel walls description	Number of Walls	Parallel walls Array width (m)	Receiver height Hr (m)	Fully-discretized BEM predictions			Simplified BEM predictions		
				IL - Lane1 (dB)	IL- Lane2 (dB)	IL combined (dB)	IL- Lane1 (dB)	IL- Lane2 (dB)	IL combined (dB)
0.3 m high parallel wall array; 0.05 m thick walls, 0.2 m centre-to-centre spacing	9	1.65	1.5	6.0	5.5	5.8	5.7	5.3	5.5
			4.0	6.0	4.7	5.4	5.8	4.8	5.3
	16	3.05	1.5	6.9	6.4	6.6	6.3	6.1	6.2
			4.0	6.3	5.0	5.6	6.0	4.9	5.4
	30	5.85	1.5	7.8	7.5	7.6	7.1	7.1	7.1
			4.0	6.2	4.9	5.6	5.9	4.9	5.4
	61	12.05	1.5	8.5	8.7	8.6	7.4	7.8	7.6
			4.0	5.7	4.5	5.1	5.6	4.6	5.1
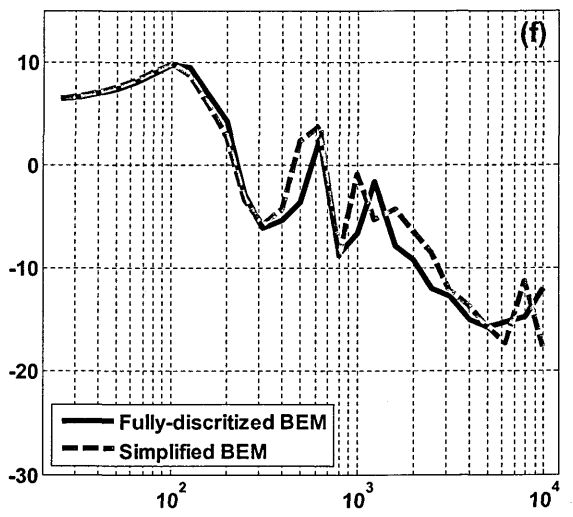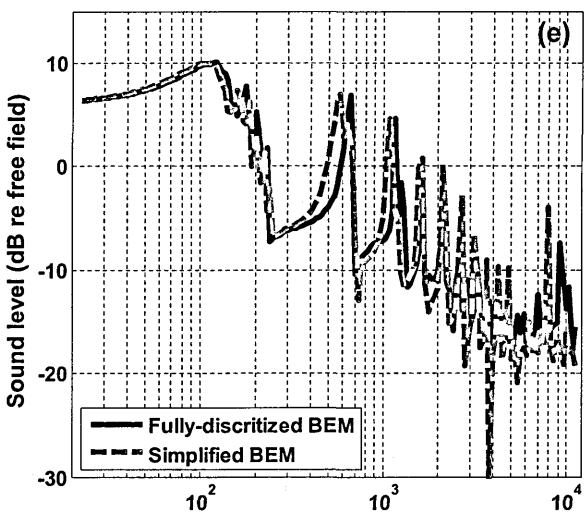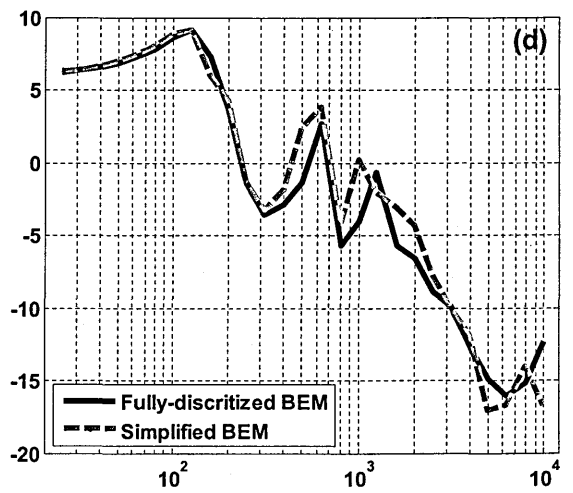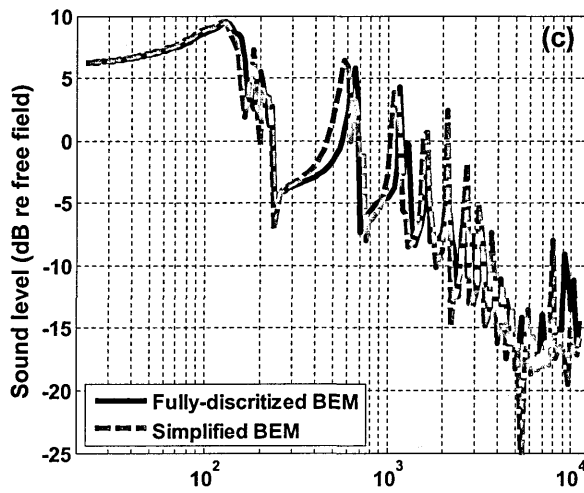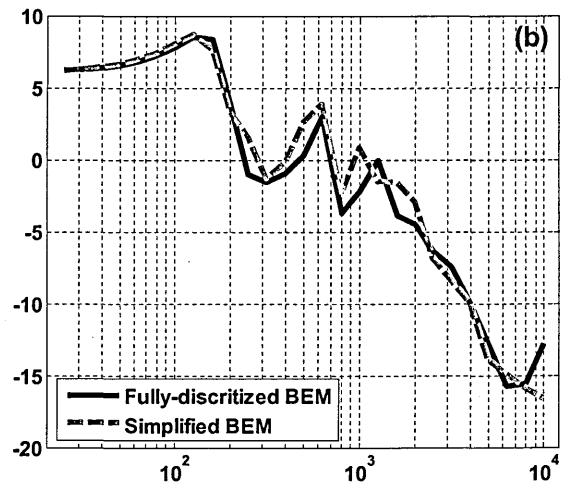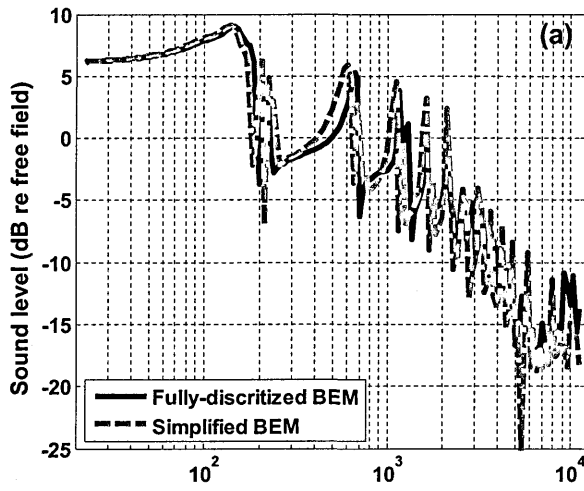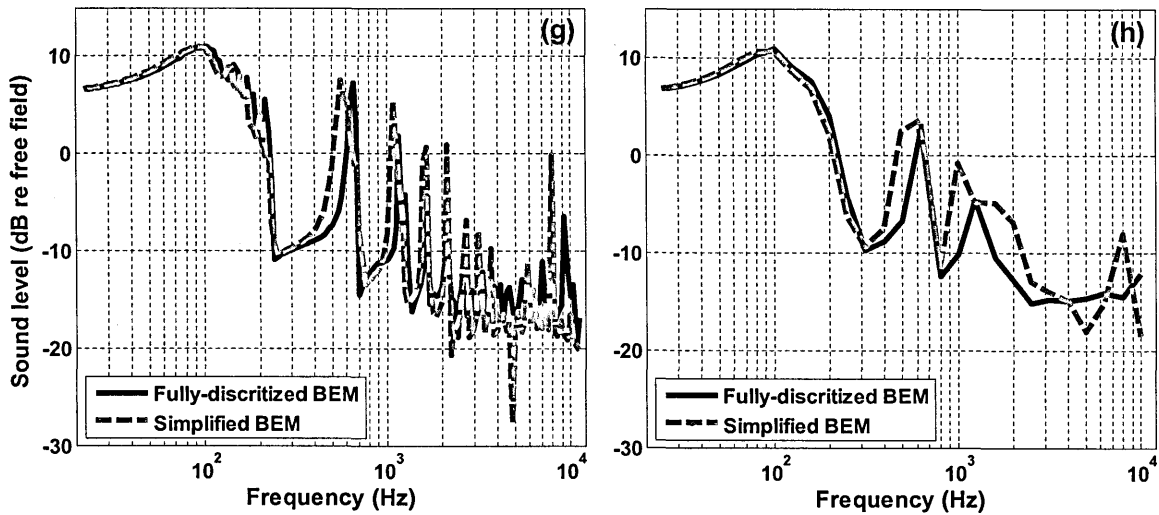
Figure 6.28 Comparison between excess attenuation spectra predicted by fully-discritized parallel walls (walls width = 0.05, height = 0.3 m) using BEM and those obtained simplified BEM by using point source propagation theory to represent the parallel walls as raised effective impedance using slit pore layer model with flow-resistivity 0.013 Pa s m^{-2}, porosity 0.75 and layer depth 0.3 m. The source is placed at height of 0.01 m and receiver is at a distance of 50 m and at height of 1.5 m above ground. The excess attenuation predictions are plotted at narrow frequencies and at octave frequency band for fully discritized and simplified parallel walls having different width of (a) & (b) 1.65 m (c) & (d) 3.05 m (e) & (f) 5.85 m (g) & (h) 12.05 m.

6.6 Conclusions

The slit pore layer and Kelders-Allard impedance models using parameters deduced from the array geometry together with theory for propagation from a point source over an impedance plane enable very good agreement with EA data measured over a laboratory lattice but lead to less good agreement with data obtained at a larger scale with brick lattices outdoors. The agreement between data obtained over outdoor brick lattices and predictions using the slit pore layer model is improved by means of best fit impedance parameters (effective flow resistivity = 400 Pa s m^{-2}, porosity = 0.54 and effective layer depth = 0.16 m) rather than those deduced from the brick lattice geometry (effective flow resistivity = 0.04 Pa s m^{-2}, porosity = 0.54 and effective layer depth = 0.2 m). Predicted spectra using an indirect method in 2D BEM by modelling lattices as raised effective impedance surfaces (characterised by the slit pore layer impedance model with the best fit parameter values) show very good agreement with measured horizontal level difference spectra over a brick lattice.

The effective impedance for parallel walls has been investigated also. The frequencies of the predicted EA maxima obtained using the slit pore layer impedance model with parameters deduced from geometry over narrowly spaced aluminium strips are close to those measured and their depths are predicted with a maximum error of 5 dB. As the spacing between the strips is increased the slit pore model becomes less valid. It was found that the slit model enables good agreement between predictions and data as long as the edge-to-edge spacing between strips is comparable to strips' height. Use of the slit pore layer model also enables good predictions of the first EA maxima as long as the edge-to-edge

spacing between strips is four times smaller than wavelengths corresponding to the first EA maxima. Laboratory investigations over parallel walls have been extended to larger scale parallel walls and have led to similar conclusions to those obtained from laboratory data over aluminium rectangular strips.

The concept of a raised effective impedance for parallel wall systems has been investigated using Kelders-Allard model also. Comparisons between measured data in laboratory over rectangular strips and predictions based on use of the Kelders-Allard model are good only for very small edge-to-edge spacing. As the spacing between the strips increases predictions that use the Kelders-Allard theory contradict the behaviour of EA spectra measured in the laboratory. According to the Kelders-Allard impedance model, the effective layer depth decreases with the increase in spacing which shifts the spectra towards higher frequencies. However, the measured data over rectangular strips and other roughness elements show spectra that shift towards lower frequencies as the centre-to-centre spacing is increased (see chapter 5). A similar contradiction has been found between the Kelders-Allard model predictions and BEM predictions for larger scale parallel walls.

It has been shown that it is possible to use a 2D BEM to calculate the insertion losses due to (3D) lattices near roads by representing the lattices a raised impedance surfaces

Calculated insertion losses over parallel walls near to a two lane urban road using either a fully-discretized BEM or a simplified BEM in which the wall array is represented by a raised impedance plane show good agreement. This suggests

that simplified BEM predictions can be used to calculate insertion losses due to parallel wall systems to speed up the process.

It has been concluded that the slit pore layer model is more appropriate for modelling parallel wall arrays and lattices as raised effective impedance than the Kelders-Allard model. A comprehensive study is already being carried out over different configurations of parallel walls in laboratory and on large scale using BEM predictions. The measured data and BEM predictions over parallel wall have been compared with raised effective impedance model to check its applicability and validity. However, this is not the case for lattice configurations. 2D BEM is not capable of predicting propagation over 3D structure. An attempt was made to use 3D FEM (COMSOL®) for predictions over 3D lattice. However, it was not successful due to limited computational recourses. Moreover, only three lattice configurations (single, double and triple lattice) in laboratory and one configuration in outdoor environment was tested. Nevertheless measured data over lattice in laboratory and outdoor was successfully modelled using raised effective impedance model. Further work over lattice can be extended to carry out measurements over more lattice configurations i.e. to investigate the effect of varying spacing over its traffic noise attenuation performance.

Chapter 7

7. Propagation over Impedance discontinuities

7.1 Introduction

The work presented in this thesis is aimed at exploring natural and artificial ways of exploiting ground effect to reduce traffic noise. The main purpose of the work is to design surfaces along the road side to reduce traffic noise. The basis for some potential designs has been presented and discussed in previous chapters which have described ground effect over porous, hard and rough surfaces and its representation by excess attenuation spectra. Most naturally-occurring outdoor surfaces are porous. As a result of being able to penetrate the porous surface, ground-reflected sound is subject to a change in phase as well as having some of its energy converted into heat. If the hard ground along the road side is replaced with a porous ground surface, it will help to reduce the traffic noise. Short range

measured data for ground characterization over different kinds of acoustically soft ground have been used in Chapter 4. The surface impedances of several grass-lands have been deduced by fitting the data using different impedance models. The excess attenuation at a given receiver may be calculated from knowledge of the ground impedance and the source-receiver geometry (see Chapter 4).

In reality, porous ground starts at some distance from the road and traffic noise sources are over a hard road surface. In the simplest case of a receiver over porous ground there is only one impedance discontinuity between the source and receiver. Nevertheless, because of the discontinuity, the sound propagation model detailed in Chapter 4, which assumes both source and receiver are over the same ground, cannot be used to calculate the sound field at the receiver.

In some cases the receiver can be also over hard ground which means that there are two impedance discontinuities between the source and receiver. In yet more complicated cases, there may be strips of hard ground i.e. walk-ways or cycle-ways in between the road and the receiver and therefore multiple impedance discontinuities. This chapter investigates sound propagation over 2D (strip) and 3D (patch) impedance discontinuities. The main focus in this chapter is the extension of knowledge regarding the applicability of semi-analytical models in the study of propagation over impedance discontinuities. Available theories of sound propagation over impedance discontinuities are reviewed and checked for their validity and applicability. Then ground effect over mixed impedance surfaces is studied using measurements and calculations.

This first section is the introduction for the chapter. The second section discusses the theoretical models for propagation over impedance discontinuities

including the De Jong semi empirical model and the Fresnel zone method. The third section presents data obtained over laboratory scale impedance discontinuities and predictions using theoretical and numerical methods. This section also compares the data over 2D impedance strips and 3D impedance patches. The fourth section investigates a prediction method for larger scale impedance discontinuities in HOSANNA geometries. Conclusions are drawn in section five.

7.2 Models for propagation over impedance discontinuities

When sound propagates over a mixed impedance ground surface, it diffracts at each impedance discontinuity. The problem to be considered here is the propagation of sound from a point source above an infinite plane boundary containing one or more impedance discontinuities. Several authors have studied the sound propagation over a mixed impedance ground surface [07] – [113]. The models developed to predict such sound propagation may be divided into two major categories. The first category of models is based on semi-empirical solutions and the second category is based on numerical methods.

The semi-empirical methods need less computational recourses to obtain a solution. Naglieh and Hayek [106] have presented an analytical solution to predict the sound propagation from a point source over a ground with single impedance discontinuity. Enflo and Enflo [107] have studied the sound propagation over an infinite plane with an impedance discontinuity by considering the Helmholtz equation. Their solution is valid only when the impedance discontinuity is many wavelengths from the source and the receiver. De Jong *et al.* [108] have presented a well known and widely accepted semi-empirical model for sound propagation over single impedance discontinuity with the discontinuity perpendicular to the direction from the source to receiver axis. The De Jong model uses semi-empirical modifications of analytical expressions for diffraction by a rigid half-plane. Daigle *el al.* [109] carried out experimental work over single impedance ground surface and compared the resulting data with the De Jong model [108]. They showed that the agreement between data and De Jong model predictions is very good except when the source and receiver are placed very

close to the ground surface i.e. near grazing. Hothersall and Harriott [110] have shown also that the De Jong method gives very good agreement with the measured data over single impedance discontinuity. Hothersall and Harriott [110] extended the single discontinuity De Jong model to encompass two discontinuities and found some agreement with measured data and calculations using the boundary integral solution. They [110] concluded that the De Jong formulation for two impedance discontinuities gives good agreement with the data only for greater source and receiver heights and the shorter source to receiver distances. This is similar to the limitation previously observed by Daigle *el al.* [109]. Boulanger *et al.* [111] have shown that De Jong model gives good agreement with laboratory data for propagation over a single impedance discontinuity; however it fails if there are multiple impedance discontinuities. Lam and Monazzam [112] have modified the De Jong semi-empirical model and have shown that the modification improves the agreement between data and De Jong predictions. The detailed mathematical formulation for De Jong model and its modification are described in subsection 7.2.1.

Another semi-analytical approach, the Fresnel-zone method, for predicting sound propagation over mixed impedance ground was proposed by Hothersall and Harriott [110]. The Fresnel-zone model is the simplest of available methods and can be applied to a single impedance discontinuity or to multiple impedance discontinuities. It assumes that the reflecting area in a discontinuous plane is related simply to the region around the specular reflection point defined by a Fresnel-zone condition. Later on, Boulanger *et al.* [111] proposed some modifications to the Fresnel-zone method and found that a modified Fresnel-

zone method gives better agreement with data. The detailed mathematical formulation for the Fresnel-zone method is given in subsection 7.2.2.

The second category, based on numerical methods, needs more computational resources and computation time. Robertson *et al.* [113] studied sound propagation over a mixed impedance ground surface using parabolic approximations and found good agreement with measured data. Hothersall and Harriott [110] presented a numerical solution based on a boundary integral equation formulation of the problem. A numerical method based on a boundary integral equation formulation (see Chapter 2) for calculating the sound propagation over a single impedance discontinuities or multi-impedance discontinuities offers high accuracy and very good agreement with measured data [110].

7.2.1 The De Jong model

De Jong *et al.* [108] presented semi-empirical modifications of analytical expressions for diffraction by a rigid half-plane, used to represent an admittance step from a hard surface to air. They introduced a solution by considering the case of an admittance step at a transition between a hard and soft ground. De Jong *et al.* [108] heuristically included the diffraction due to impedance discontinuity. The excess attenuation over a continuous impedance surface is given by (for details see Chapter 4),

$$EA = \frac{P}{P_1} = 1 + Q \frac{R_1 e^{ik(R_2 - R_1)}}{R_2}, \qquad (7.1)$$

where P is the total pressure at the receiver due to a point source above an homogenous impedance plane P_1 is the pressure due to the direct wave from the source, Q is spherical wave reflection coefficient, R_1 is the direct path length from the source to the receiver, R_2 is the path length through the specular reflection point and k is the propagation constant. De Jong modified Eq. (7.1) to obtain the excess attenuation equation above a plane containing a single impedance discontinuity, which is given by,

$$\frac{P}{P_1} = 1 + \frac{R_1}{R_2} Q_G e^{ik(R_2 - R_1)} + (Q_2 - Q_1)e^{-i\pi/4} \frac{1}{\sqrt{\pi}} \frac{R_1}{S_1} X \left[F_2\left(\sqrt{k(S_1 - R_1)}\right) \pm F_2\left(\sqrt{k(S_1 - R_2)}\right) e^{ik(R_2 - R_1)} \right], \qquad (7.2)$$

where S_1 is the path length from source to receiver through the point of impedance discontinuity as shown in Figure 7.1. Q_1 and Q_2 are the spherical wave reflection coefficients calculated from ground impedances Z_1 and Z_2 respectively. Q_G is the spherical wave reflection coefficient calculated from the impedance at the specular reflection point. The third term $(Q_2 - Q_1)/(Q_1 - Q_2)$ in

Eq. (7.2) and the sign inside the square brackets changes with respect to each specific scenario i.e. whether the impedance discontinuity is from hard to soft ground or from soft to hard ground. Suppose that the impedance Z_1 is for an acoustically hard ground surface and impedance Z_2 is for an acoustically soft ground and consider the scenario represented in Figure 7.1 (a) in which the impedance discontinuity occurs from hard to soft ground and the specular reflection point is on the hard ground surface with impedance Z_1, then the third term in Eq. 7.2 will be $(Q_2 - Q_1)$ and the '+' sign is required in the square bracket. For the same scenario (Figure 7.1 (a), if the specular reflection point is on the soft ground with impedance Z_2, then the '−' sign is required inside the square bracket. Similarly consider a second scenario represented in Figure 7.1 (b) in which the impedance discontinuity occurs from soft to hard ground and the specular reflection point is on the hard ground surface with impedance Z_1, then the third term in Eq. 7.2 will be $(Q_1 - Q_2)$ and the '−' sign is required inside the square bracket. For the same scenario given by Figure 7.1 (b), if the specular reflection point is on the soft ground with impedance Z_2, then there will be a '+' sign inside the square bracket.

The $F_2(x)$ function inside the square brackets is the Fresnel integral function defined as [111],

$$F_2(x) = \int_x^\infty e^{(iw^2)} dw,$$

(7.3)

De Jong et al. [108] modified Eq. (7.1) to obtain Eq. (7.2). By comparing Eq. (7.1) and Eq. (7.2) it is clear that the first two terms in both equations are identical. However, the third term determines the sound diffraction by the impedance

discontinuity and depends on the geometry and the difference between the two impedances Z_1 and Z_2. The ± sign inside the square brackets determines the direction of change.
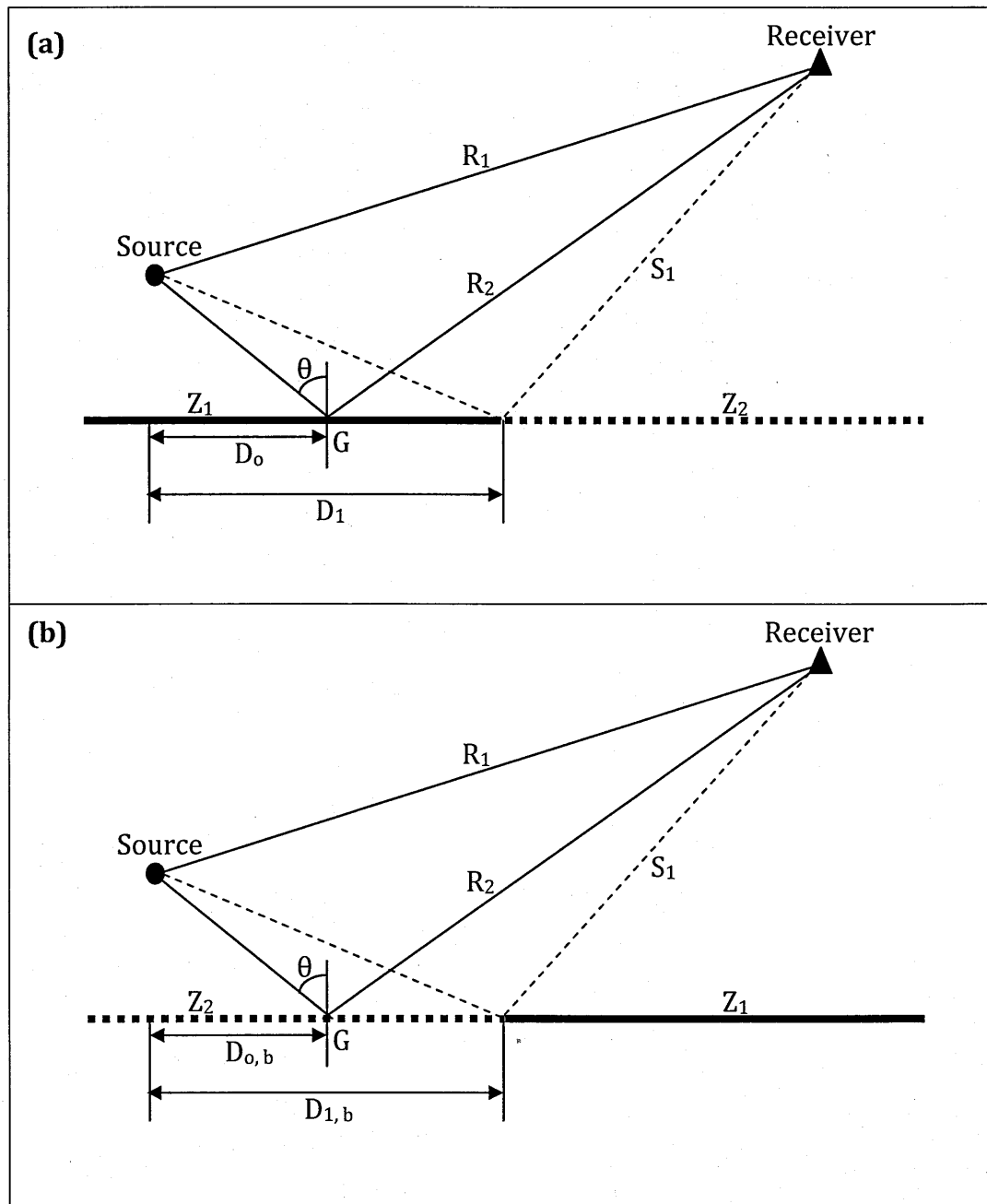
Figure 7.1 A schematic of propagation of sound from a point source to a receiver showing specular reflection and reflection from the point of impedance discontinuity (a) Impedance discontinuity from hard to soft ground (b) Impedance discontinuity from soft to hard ground.

7.2.2 Modified De Jong model

Several authors have compared data from measurements over single impedance discontinuities and compared with predictions of the De Jong semi-empirical formulation [109]–[112]. They have come to the similar conclusion that it gives good give agreement with data as long as the source and receivers are not very close to the ground surface. However, Lam and Monazzam [112] have proposed an important modification to De Jong model. According to Lam and Monazzam [112] the original De Jong model is derived from the case of an impedance step from a hard to soft ground. They proposed that De Jong model theory is correct when impedance discontinuity occurs from a hard ground surface to a soft ground surface i.e. source is on the hard ground and receiver is on the soft ground as shown in Figure 7.1 (a). However, it is theoretically incorrect when the discontinuity occurs from a soft ground surface to a hard ground surface i.e. source is on the soft ground and receiver is on the hard ground as shown in Figure 7.1 (b). They show that De Jong model gives good agreement with data when compared with data for impedance discontinuity from hard to soft ground. However, it fails to give agreement with the data measured over surface having impedance discontinuity from soft to hard ground surface. According to them, the De Jong model violates the reciprocity condition for the case of soft to hard impedance discontinuity. This is due to the inconsistency in changing the ± sign inside the square brackets in Eq. (7.2). According to Lam and Monazzam [112], the modified De Jong model is given by,

$$\frac{P}{P_1} = 1 + \frac{R_1}{R_2} Q_G e^{ik(R_2 - R_1)} + (Q_2 - Q_1) e^{-i\pi/4} \frac{1}{\sqrt{\pi}} \frac{R_1}{S_1} X \left[\mu F_2 \left(\sqrt{k(S_1 - R_1)} \right) + \gamma F_2 \left(\sqrt{k(S_1 - R_2)} \right) e^{ik(R_2 - R_1)} \right]. \quad (7.4)$$

The reciprocity condition is corrected by imposing further condition through the signs of μ and γ. If $D_o < D_I$, then the value of γ is +1 and, if $D_o > D_I$, then the value of γ is -1. The new parameter μ is determined by the admittance value of the mixed impedance ground surface. The admittance is the reciprocal of impedance and for a hard ground its magnitude is equal to zero and for a soft ground its magnitude is greater than zero. If the admittance on the source side is greater than the admittance on the receiver side i.e. soft to hard ground impedance discontinuity then μ is equal to +1. If the admittance on the source side is less than the admittance on the receiver side i.e. hard to soft ground impedance discontinuity then the μ is equal to −1. The modified De Jong model improves the agreement between data and predictions for propagation from soft to hard ground.

7.2.3 Extended multi-impedance De Jong model (nMID)

A schematic of a ground surface with multi-impedance discontinuities is shown in Figure 7.2. The De Jong model proposed for single impedance discontinuity was extended by Hothersall and Harriott [110] to two impedance discontinuities associated with, for example, a soft strip in a hard ground surface. The extended multi-impedance model gives poor agreement with measured data over a ground surface containing two impedance discontinuities. Boulanger *et al.* [111] suggested that there is an error in sign convention for the extended multi-impedance De Jong model proposed by Hothersall and Harriott [110]. Boulanger *et al.* [111] extended and corrected De Jong multi-impedance model for a ground surface composed of periodic strips such as is shown in Figure 7.2. Laboratory measurements of the excess attenuation of the sound from a point source over striped impedance with the source-receiver axis perpendicular to the strips were

compared with predictions of the extended De Jong multi-impedance model which were found to give poor agreement with data. As the original De Jong model was derived for a hard to soft transition, any extended model for multi-impedance De Jong will inherent the incorrect assumptions for soft to hard ground transitions. Lam and Monazzam [112] corrected the De Jong model assumption for soft to hard ground transition. Similarly they proposed the correction for multi-impedance discontinuous ground surface. For a ground with n impedance sections, and hence (n - 1) impedance discontinuities, the new Multi-impedance Discontinuities Model (nMID) is given by,

$$
\frac{P}{P_1} = 1 + \frac{R_1}{R_2} Q_G e^{ik(R_2 - R_1)} + \sum_{j=1}^{n-1} \frac{\left(Q_{j+1} - Q_j\right) e^{-i\pi/4} \frac{1}{\sqrt{\pi}} \frac{R_1}{S_j}}{X\left[\mu_j F_2\left(\sqrt{k(S_j - R_1)}\right) + \gamma_j F_2\left(\sqrt{k(S_j - R_2)}\right) e^{ik(R_2 - R_1)}\right]}.
\tag{7.5}
$$

If $D_o < D_j$, then the value of γ_j is equal to +1 and if $D_o > D_j$, then the value of γ_j is equal to -1. When the admittance $\beta_{j+1} > \beta_j$ then $\mu_j = 1$ and when the admittance $\beta_{j+1} < \beta_j$ then $\mu_j = -1$. The different path lengths used in Eq. (7.5) are shown in Figure 7.2.

Similarly for a mixed impedance ground surface having periodic impedance discontinuities created with strips of impedance Z_1 and Z_2, the excess attenuation term can be written as,

$$
\frac{P}{P_1} = 1 + \frac{R_1}{R_2} Q_G e^{ik(R_2 - R_1)} + \left(Q_2 - Q_1\right) \frac{e^{-i\pi/4}}{\sqrt{\pi}} \sum_{k=1}^{m} \left[\begin{array}{l} \frac{R_1}{S_{2k-1}} \left\{ \begin{array}{l} F_2\left(\sqrt{k(S_{2k-1} - R_1)}\right) + \gamma_{2k-1} \\ F_2\left(\sqrt{k(S_{2k-1} - R_2)}\right) e^{ik(R_2 - R_1)} \end{array} \right\} \\ \frac{R_1}{S_{2k}} \left\{ \begin{array}{l} F_2\left(\sqrt{k(S_{2k} - R_1)}\right) + \gamma_{2k} \\ F_2\left(\sqrt{k(S_{2k} - R_2)}\right) e^{ik(R_2 - R_1)} \end{array} \right\} \end{array} \right].
\tag{7.6}
$$

It was shown that predictions of this nMID model agree well with boundary element method predictions for multiple impedance strips. However, nMID showed some limitations when source and receiver were close to the ground surface. It was found also to give poor agreement with BEM when the widths of the strips were small. Overall, Lam and Monazzam [112] have shown that nMID gives good agreement with BEM for most of the cases.
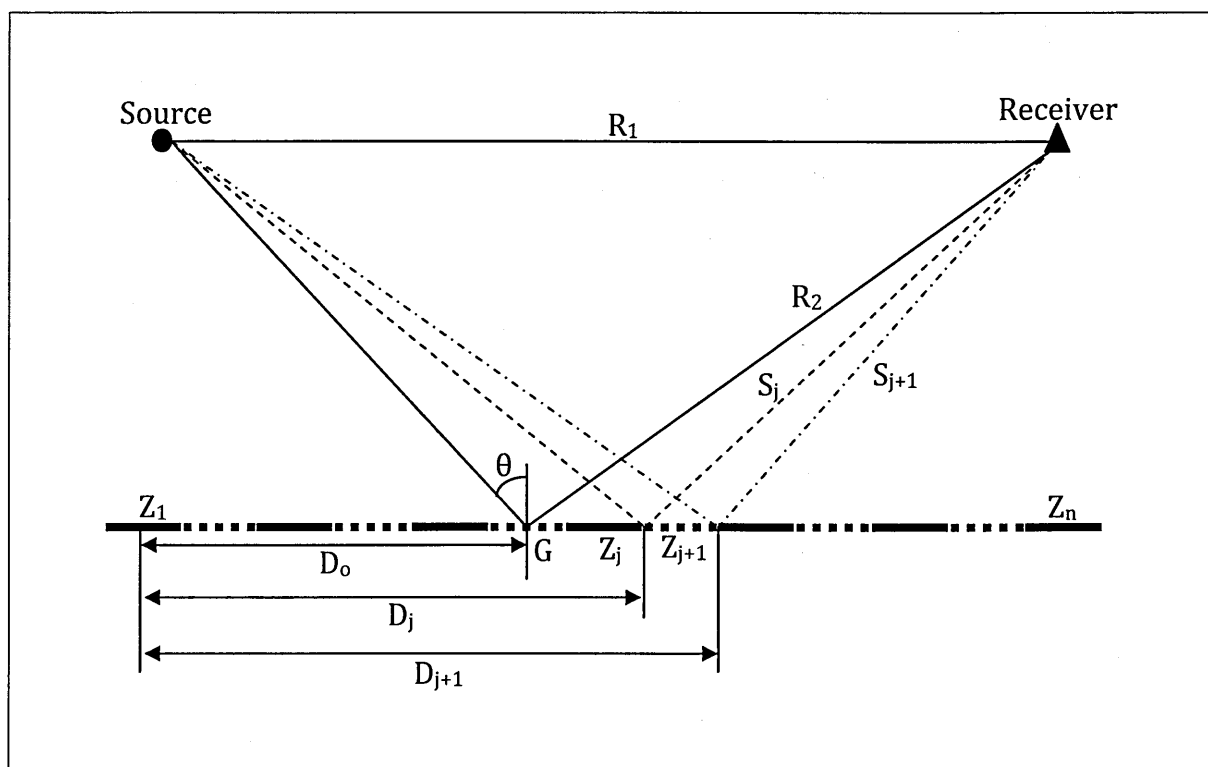
Figure 7.2 A schematic of propagation of sound from a point source to a receiver through specular reflection and through point of impedance discontinuities over a surface composed of multi-impedance discontinuities.

7.2.4 The Fresnel-zone method

Hothersall and Harriott [110] proposed a simple analytical method to predict sound propagation over single and multiple impedance discontinuities. It assumes that the reflecting area in a discontinuous plane is related simply to the region around the specular reflection point defined by Fresnel-zone. When sound propagates over mixed impedance ground surface, it diffracts at the impedance discontinuity which introduces fluctuations into the excess attenuation spectra. The Fresnel-zone method does not take into account diffraction at impedance discontinuities and predicts approximated excess attenuation spectra without diffraction- associated fluctuations. The Fresnel-zone is the elliptical area around the specular reflection point as shown in Figure 7.3. The equation of ellipse in the Cartesian coordinate system is given by [111],

$$\frac{x^2}{b^2} + \frac{(y\cos\theta - c)^2}{a^2} + \frac{y^2 \sin^2\theta}{b^2} = 1, \tag{7.7}$$

where c is calculated from,

$$c = \frac{R_2}{2} - SP, \tag{7.8}$$

and a is the major semi-axis of the ellipsoid along y-axis and b is the minor semi-axis along x-axis given by,

$$a = \frac{R_2 + F\lambda}{2}, \tag{7.9}$$

$$b = \sqrt{\frac{R_2 F\lambda}{2} + \left(\frac{F\lambda}{2}\right)^2}. \tag{7.10}$$

Eq. (7.7) - Eq. (7.10) shows that the size of ellipse depends on the value of constant F, the wavelength considered and the source-receiver geometry. Hothersall and Harriott [110] and Boulanger et al. [111] suggested that the value of F should be equal to $1/3$. The Fresnel-zone area is strongly dependent on the frequency. As frequency increases, wavelength decreases which results in decrease of the Fresnel-zone area. To compute the area of ellipse for a given source-receiver geometry and frequency, it is necessary to determine the location of the boundary of the Fresnel-zone ellipse. The boundary values such as x_1, x_2, y_1 and y_2 for an ellipse such as shown in Figure 7.3 are given by,

$$x_{1,2} = \pm b \sqrt{1 - \frac{(y_m \cos\theta - c)^2}{a^2} + \frac{y_m^2 \sin^2\theta}{b^2}}, \qquad (7.11)$$

$$y_{1,2} = -y_m \pm \sqrt{\frac{1}{A} - \left(\frac{c\sin\theta}{Aab}\right)^2}. \qquad (7.12)$$

where $y_m = \frac{B}{A}$, and A and B are given by,

$$A = (\cos\theta/a)^2 + (\sin\theta/b)^2, \qquad (7.13)$$

$$B = c\cos\theta/a^2, \qquad (7.14)$$

According to the Fresnel zone method, the excess attenuation over a mixed impedance ground surface is linearly dependent on the proportions of the different impedance ground surfaces in the area representing the intersection of the Fresnel zone with the ground plane. The excess attenuation over a mixed impedance ground surface using the Fresnel-zone model proposed by Hothersall and Harriott [110] is given by,

$$\frac{P}{P_1} = \mu 20\log\left|1 + \frac{R_1}{R_2}Q_1 e^{ik(R_2-R_1)}\right| + (1-\mu)20\log\left|1 + \frac{R_1}{R_2}Q_2 e^{ik(R_2-R_1)}\right|, \quad (7.15)$$

where μ is obtained by calculating the proportion of area having surface impedance Z_1 and $(1-\mu)$ is the proportion of the area having surface impedance Z_2 inside the elliptical Fresnel zone.
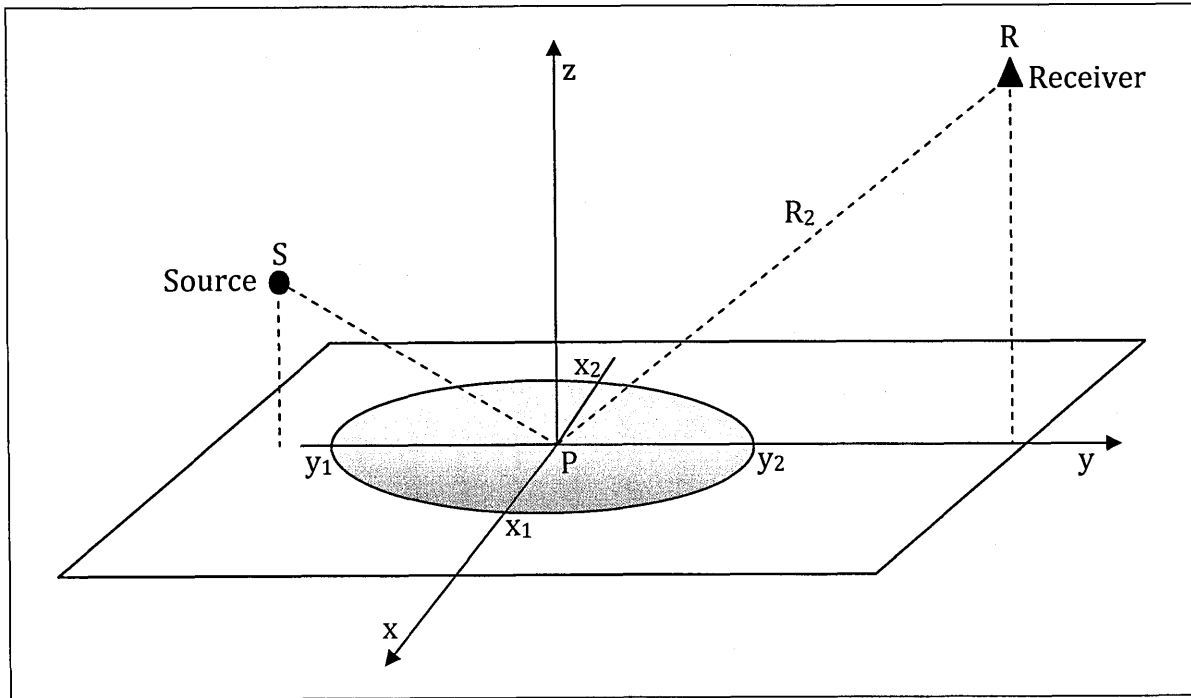
Figure 7.3 A schematic of the propagation of sound from a point source to a receiver showing specular reflection and the intersection between the ground and the elliptical Fresnel zone is shown here.

According to the Fresnel zone method, the excess attenuation over a mixed impedance ground surface is linearly dependent on the proportions of the different impedance ground surfaces in the area representing the intersection of the Fresnel zone with the ground plane. The excess attenuation over a mixed impedance ground surface using the Fresnel-zone model proposed by Hothersall and Harriott [110] is given by,

$$\frac{P}{P_1} = \mu 20\log\left|1 + \frac{R_1}{R_2}Q_1 e^{ik(R_2-R_1)}\right| + (1-\mu)20\log\left|1 + \frac{R_1}{R_2}Q_2 e^{ik(R_2-R_1)}\right|, \quad (7.16)$$

where μ is obtained by calculating the proportion of area having surface impedance Z_1 and $(1-\mu)$ is the proportion of the area having surface impedance Z_2 inside the elliptical Fresnel zone. This method is similar to an averaging of the two excess attenuation spectra according to the percentage of coverage by each ground type. The Fresnel zone method cannot differentiate between single and multiple impedance discontinuities. Consider a situation for a ground surface with single impedance discontinuity of equal proportion of both ground type inside the Fresnel zone. Similarly, consider another situation with multiple impedance discontinuities of equal proportion of both ground type inside the Fresnel zone. For both cases the value of μ is equal to 0.5. Hothersall and Harriott [110] show that the agreement between data and the Fresnel zone model is not very good. The Fresnel-zone model does not produce the oscillations associated with diffraction effects but gives a reasonable estimate of the excess attenuation spectra.

Boulanger *et al.* [111] proposed a modification to the Fresnel zone method given by Eq. (7.16). Instead of the linear interpolation of two excess attenuations as given by Eq. (7.16), Boulanger *et al.* [111] uses a linear interpolation between the two pressure terms. The new modified expressions for excess attenuation over a mixed impedance ground is given by,

$$\frac{P}{P_1} = 20\log\left\{\mu\left|1+\frac{R_1}{R_2}Q_1 e^{ik(R_2-R_1)}\right| + (1-\mu)\left|1+\frac{R_1}{R_2}Q_2 e^{ik(R_2-R_1)}\right|\right\}.$$ (7.17)

Boulanger *et al.* [111] shows that the results of predictions obtained by this modified Fresnel zone model gives better agreement with the measured data to that obtained using the original Fresnel zone model.

7.3 Laboratory scale impedance discontinuities

7.3.1 Single impedance discontinuity

As mentioned previously, several authors have compared the semi-empirical De Jong model with measured data over ground surface containing a single impedance discontinuity. They arrived at a common conclusion that the agreement between data and De Jong model predictions is good for a single impedance discontinuity. Recently, Lam and Monazzam [112] modified the De Jong model and claimed that modified De Jong model gives better agreement to data. In this section initially BEM predictions are compared with the semi-empirical predictions that use the original De Jong model and the modified De Jong model respectively. BEM is selected for testing the empirical models, because it is known to give accurate predictions of excess attenuation over different kind of surfaces. Figure 7.4 compares BEM predictions with predictions of the original De Jong model and the modified De Jong model. A smooth flat surface containing two impedances was selected as a test case. The mixed impedance surface is considered to be made from an MDF board and felt on MDF board. EA predictions over such a mixed impedance surface, require knowledge of the impedance of the surfaces used to make the surface. Measurements have been made of EA spectra over a layer of felt placed on a MDF board and over the MDF board alone without felt. Predictions using a two-parameter variable porosity model have been fitted to these data using a numerical fitting procedure (see chapter 4). The two parameters are effective flow resistivity and rate of change of porosity with depth. The best fit values of flow resistivity and porosity change rate obtained for felt over MDF (see Chapter 4, Section 4.6.1) and for MDF alone (see Chapter 3, Section

3.2.6.2) are 30 kPa s m^{-2} and 15 m^{-1} and 100 MPa s m^{-2} and 15 m^{-1} respectively. The source and receiver were assumed at a height of 0.07 m above ground surface with a horizontal separation of 0.7 m. The impedance discontinuity was assumed to start at different distances with respect to the point source. Two scenarios were considered: first is an impedance discontinuity from hard to soft ground and second one is a discontinuity from soft to hard ground. Figures 7.4 (a), (b) and (c) compare predictions of BEM, the original De Jong model and the modified De Jong model for propagation over a hard to soft impedance discontinuity located at distances of 0.2 m, 0.4 and 0.6 m respectively from the source. The original and modified De Jong model predict identical EA spectra for hard to soft impedance discontinuity as expected. The De Jong model gives good agreement with the numerically predicted EA spectra for an impedance discontinuity at distances of 0.2 m and 0.6 m (see Figures 7.4 (a) and (c) respectively). However, the agreement between De Jong model and BEM degrades if the impedance discontinuity is near the specular reflection point (see Figure 7.4 (b)). Figures 7.4 (d), (e) and (f) compare predictions of BEM, the original De Jong model and the modified De Jong model for a soft to hard impedance discontinuity located at distances of 0.2 m, 0.4 and 0.6 m respectively. As expected the original and modified De Jong models predict different EA spectra for a soft to hard impedance discontinuity. The modified De Jong model gives better agreement with the BEM predictions than the original De Jong model for a soft to hard impedance discontinuity.
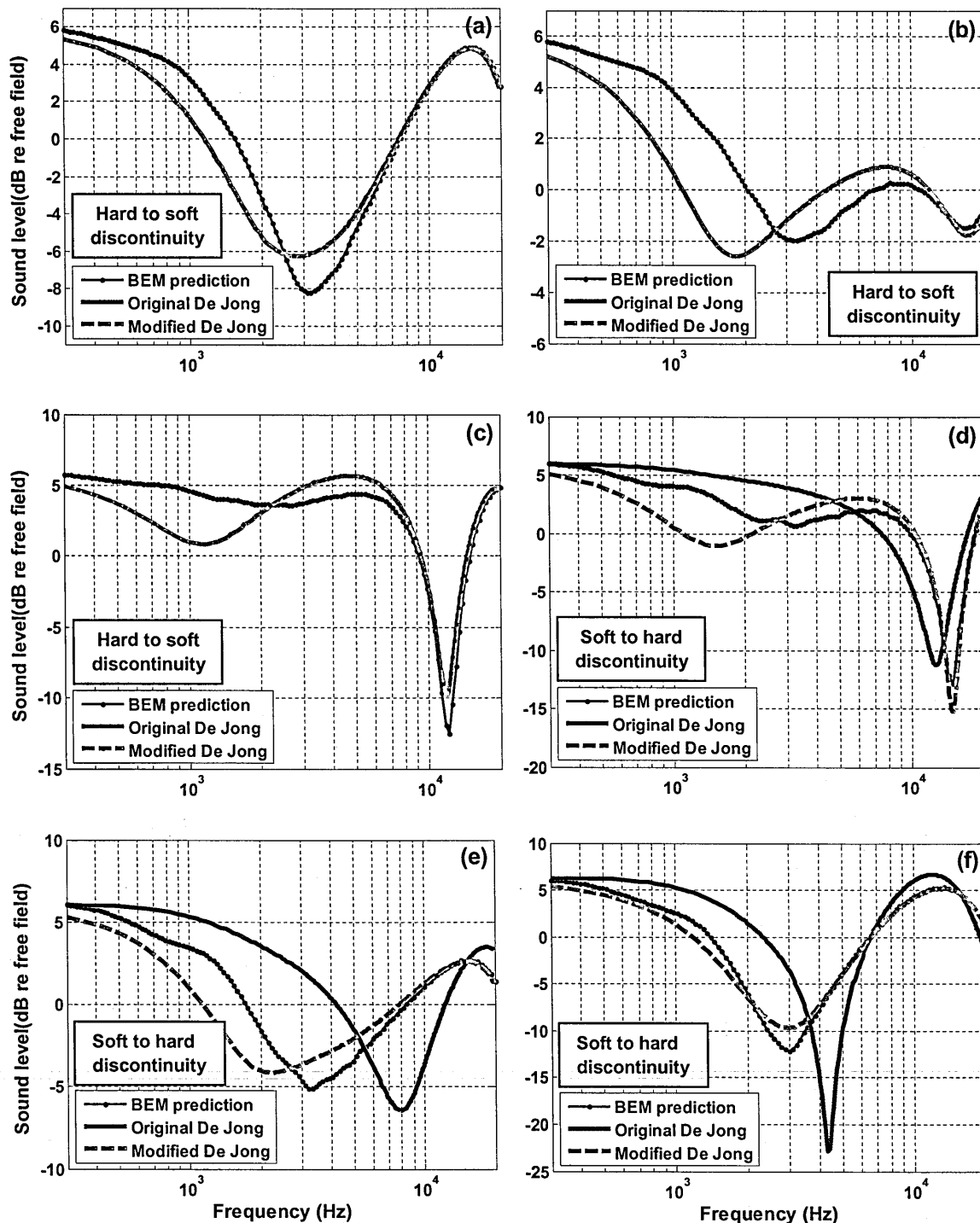
Figure 7.4 Comparison between predictions of BEM, the original De Jong model and the modified De Jong model for EA over a ground surface composed of MDF board and felt on MDF board with single impedance discontinuity by placing source and receiver at height of 0.07 m and source-receiver separation of 0.7 m (a), (b) & (c) MDF on source side and felt on receiver side (hard to soft discontinuity). The discontinuity starts at a distance of (a) 0.2 m (b) 0.4 m (c) 0.6 m from the source. (d), (e) & (f) Felt on source side and MDF on receiver side (soft to hard discontinuity). The discontinuity is located at distances of (a&d) 0.2 m (b&e) 0.4 m (c&f) 0.6 m from the source.

7.3.2 Multiple impedance discontinuities

7.3.2.1 Experimental data

Most of the work presented in the past has focussed on a single impedance discontinuity; much less attention has been given to multiple impedance discontinuities. Here we consider propagation from a point source over periodically spaced impedance discontinuities. Systematic measurements (using the system described in Chapter 3) have been made in an anechoic chamber of excess attenuation spectra due to a point source over surface made with rectangular MDF strips alternating with felt or sand strips respectively. The resulting data have been compared with numerical and Fresnel-zone predictions. Measurements have been made of sound propagation over mixed impedance surfaces formed from rectangular MDF and felt strips of equal widths (2.85cm) and heights (1.2 cm). The felt and MDF used to make strips and patches are of the same thickness so that the resulting composite surfaces were plane. Measurements have been repeated after replacing the felt strips with sand. Either an acoustically hard (MDF) or a soft (felt or sand) strips was placed at the point of specular reflection which was halfway between source and receiver as they are at equal heights. Strips were tightly packed to avoid gaps at the impedance discontinuities. Five measurements were carried out for each surface at different source and receiver heights. Figures 7.5 (a) and 7.5 (b) show the experimental arrangements. The best fit values of flow resistivity and porosity change rate obtained for felt over MDF (see Chapter 4, Section 4.6.1) and for MDF alone (see Chapter 3, Section 3.2.6.2) are 30 kPa s m^{-2} and 15 m^{-1} and 100 MPa s m^{-2} and 15 m^{-1} respectively.
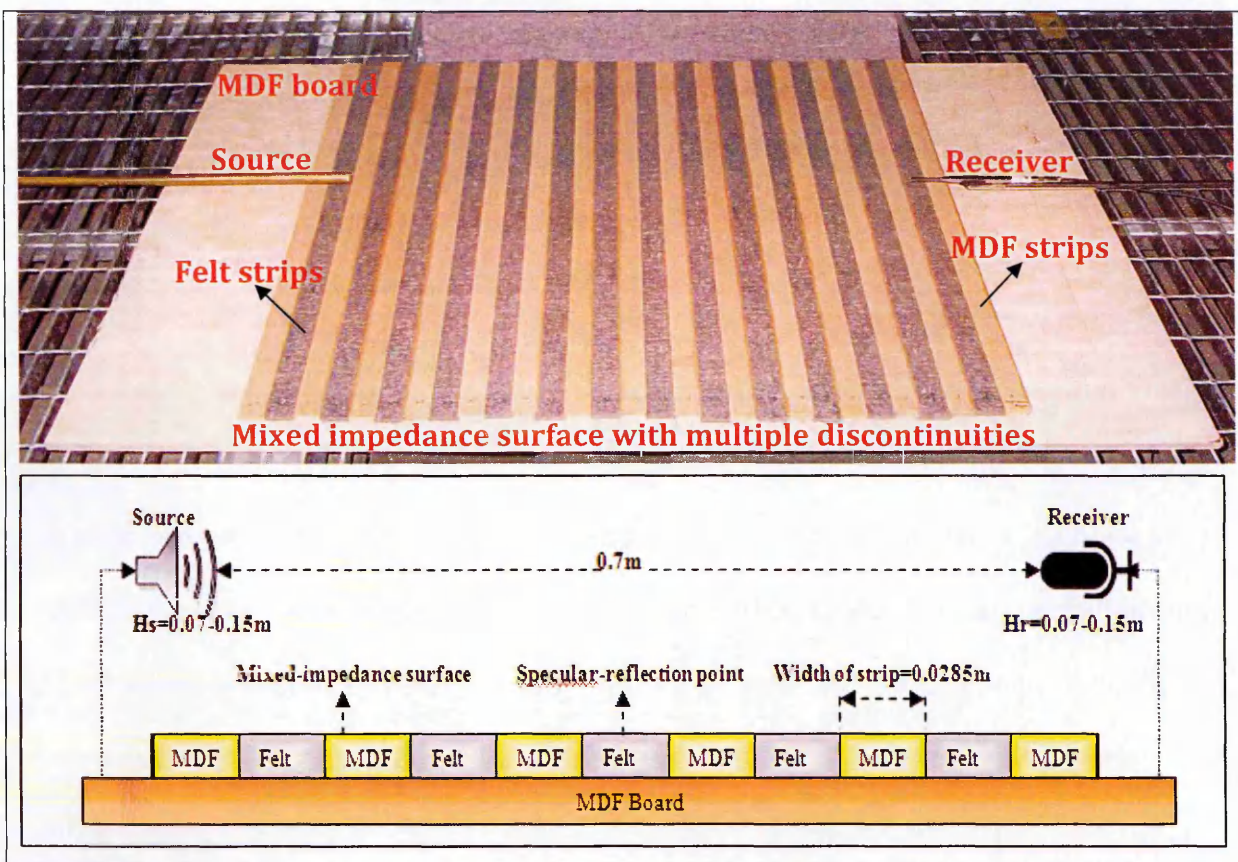
Figure 7.5 Laboratory measurements of sound propagation over mixed impedance surfaces: (a) photograph of a measurement over alternating felt and MDF strips and (b) a schematic of the laboratory geometry.

Figures 7.6 (a) and (b) compare measured excess attenuation (EA) spectra for five different source-receiver heights (0.05 m, 0.07 m, 0.1 m, 0.12 m and 0.15 m) over mixed-impedance grounds (a) a surface composed of felt and MDF strips and (b) a surface composed of sand and MDF strips. For the tested source-receiver geometries, the first destructive interferences between sound travelling directly to the source and sound reflected from a smooth hard surface occur at relatively high frequencies. In comparison the measured EA maxima in presence of mixed impedance ground occur at lower frequencies. Moreover, multiple impedance discontinuities cause greater fluctuations and broaden the ground effect dips. The fluctuations in measured EA spectra are due to sound diffraction at each impedance discontinuity.
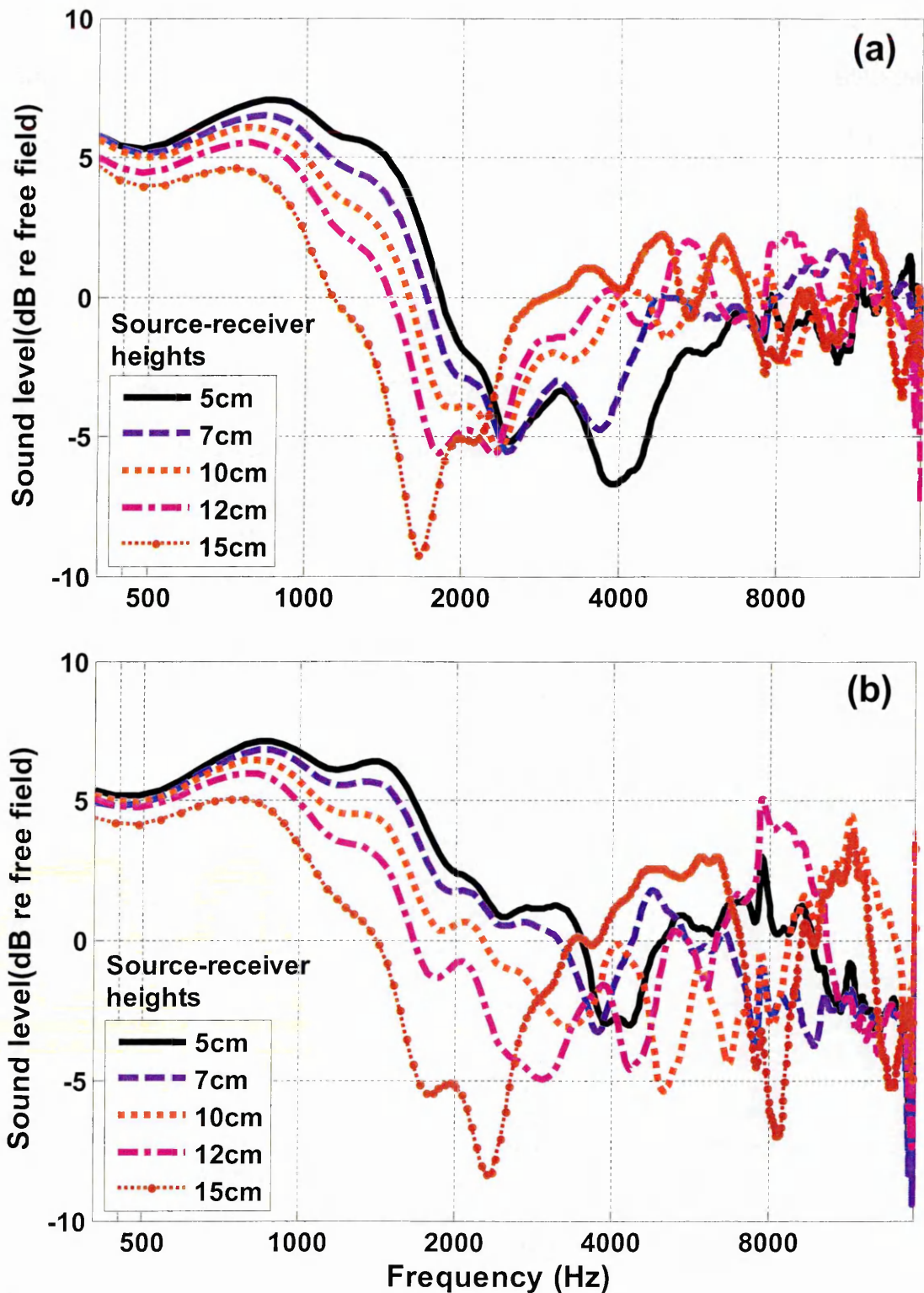
Figure 7.6 Excess attenuation spectra with source and receiver at five different heights (0.05 m – black solid lines, 0.07 m – blue dash lines, 0.1 m - red dotted lines, 0.12 m – magenta dash - dotted lines, 0.15 m – brown solid-dot lines) separated by 0.7 m over surfaces consisting of (a) alternating felt and MDF strips (b) alternating sand and MDF strips.

Figure 7.7 compares measured excess attenuation spectra over mixed impedance surfaces (felt and MDF strips, sand and MDF strips), a rough surface (MDF rectangular strips with centre-centre spacing of 0.057 m) and a smooth hard surface. In comparison to that for the smooth hard surface, the EA maxima are at lower frequencies for both mixed impedance and rough hard surfaces. As reported in chapter 5 rough hard surfaces produce multiple distinct and sharp EA maxima. While these are present to some extent in the EA spectra obtained over mixed impedance surfaces, they are broader and their magnitudes are less. The depth of EA maxima depends on the impedance of the soft material used. EA measurements over felt and sand have shows that felt is 'softer' than sand. Hence, the EA maxima obtained over felt and MDF strips are deeper than the EA maxima observed over sand and MDF strips.
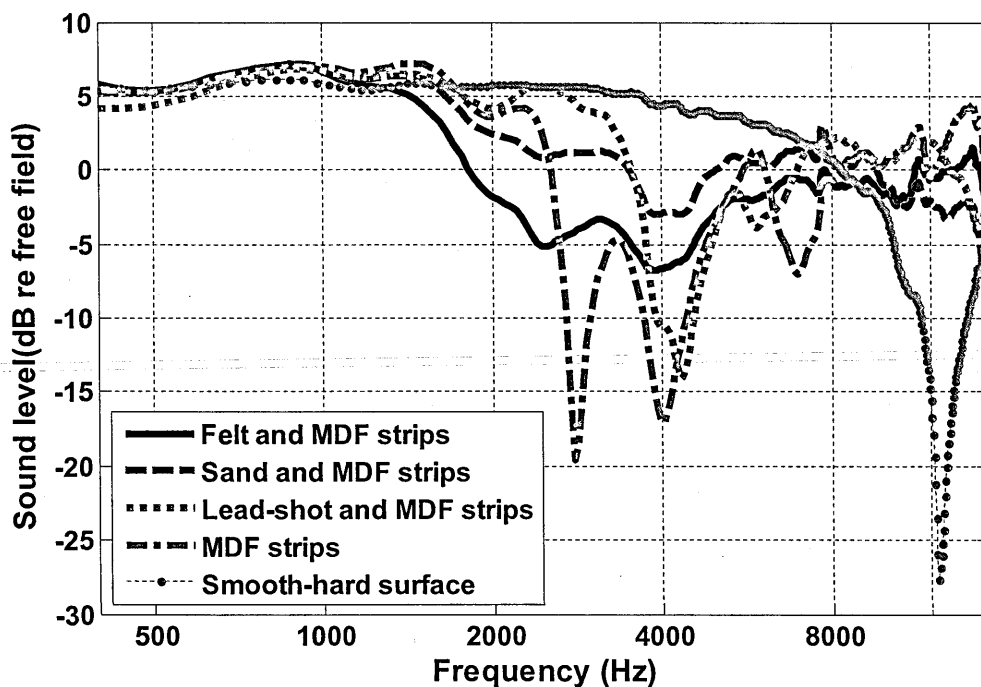
Figure 7.7 Excess attenuation spectra measured with source and receiver at 0.05 m height separated by 0.7 m over surfaces consisting of felt and MDF strips (black solid line), sand and MDF strips (blue dash line), lead-shot and MDF strips (red dotted line) and MDF strips with centre-to-spacing of 0.057 m (magenta dash-dotted line) placed on MDF board. The measured EA spectrum for the smooth hard surface (brown dotted line) is shown also.

Figure 7.8 compares measured excess attenuation spectra obtained over mixed impedance surface (felt and MDF strips), by placing a felt strip or an MDF strip at the specular reflection point. As the source and receiver are placed at equal heights of 0.07 m, so the specular reflection point is at half way between source and receiver. Predictions of the theories of sound propagation over mixed impedance surfaces (except for the Fresnel zone approach) have shown that the location of the specular reflection point is an important factor. Figure 7.8 shows the measured effect of changing the ground type at the specular reflection point. The fluctuations in the EA spectra are altered by changing the acoustical impedance at the specular reflection point.
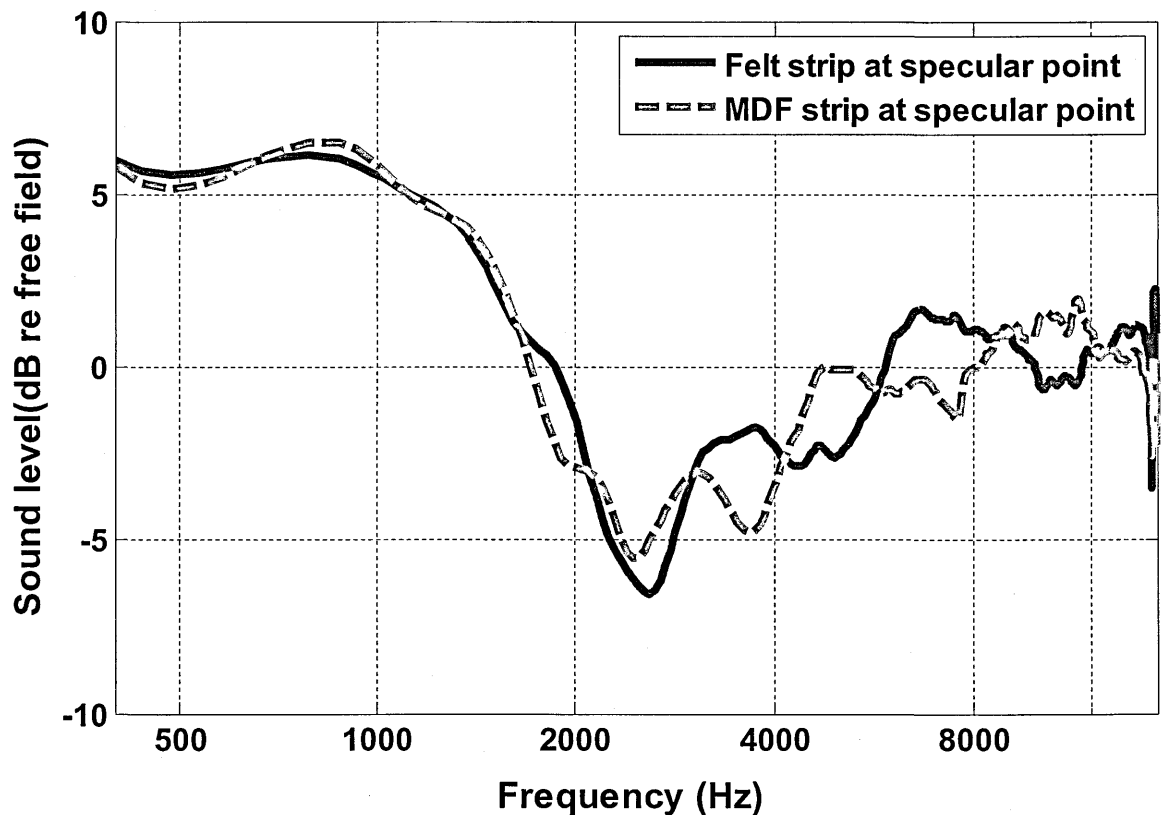
Figure 7.8 Excess attenuation spectra measured with source and receiver at 0.07 m height separated by 0.7 m over surfaces consisting of felt and MDF rectangular strips, by placing felt strips (blue solid line) and MDF rectangles (red dash line) at specular reflection point respectively.

7.3.2.2 Comparison between data and Fresnel zone predictions

Figure 7.9 compares measured EA spectra obtained over surface composed of felt and MDF strips with Fresnel-zone predictions by placing source and receiver at height of 0.07 m with a horizontal separation of 0.7 m. It has been noted previously that the Fresnel-zone method predicts only approximate EA spectra since it ignores diffraction at the impedance discontinuities. So measured EA fluctuations are not shown in the Fresnel-zone predictions. Consequently agreement between data and predictions is not very good. This confirms that the Fresnel-zone approximation while potentially satisfactory for predicting overall broadband levels is not useful for detailed predictions over multiple discontinuities.
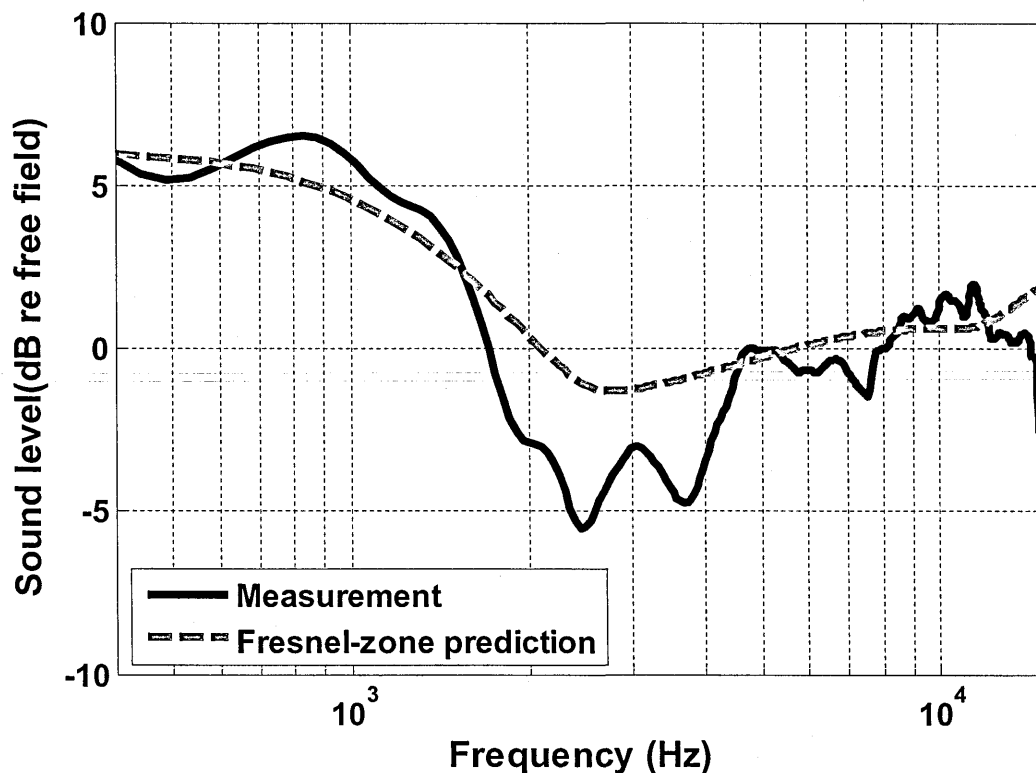
Figure 7.9 Comparison between Fresnel-zone method predictions and measured excess attenuation spectra with source and receiver at 0.07 m height separated by 0.7 m over surface consisting of felt and MDF strips.

7.3.2.3 Comparison between data and BEM predictions

Figure 7.10 compares measured EA spectra obtained over surface composed of felt and MDF strips with BEM predictions by placing source and receiver at height of 0.12 m and source-receiver horizontal separation of 0.7 m. BEM uses the impedance parameters for MDF alone and felt on MDF as given above. The agreement between measured and predicted excess attenuation spectra using BEM is relatively good. BEM predicts fluctuations in excess attenuation spectra obtained over mixed impedance.
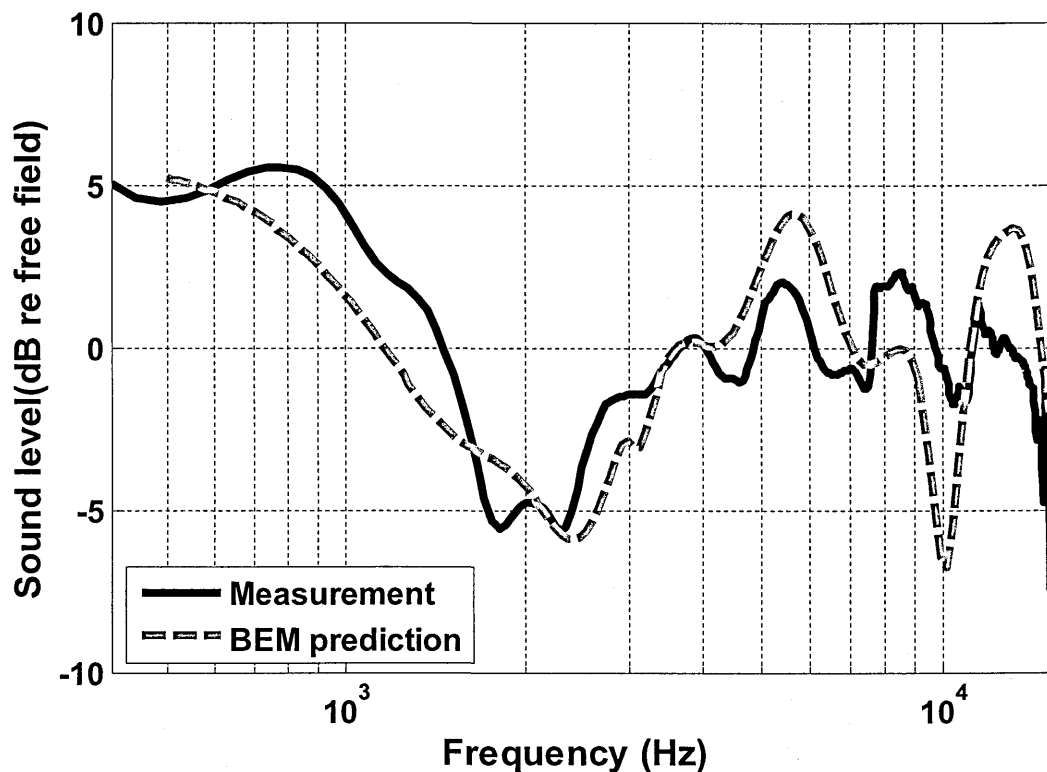
Figure 7.10 Comparison between BEM predictions and measured excess attenuation spectra with source and receiver at heights of 0.12 m and separated by 0.7 m over a surface consisting of alternating felt and MDF strips.

Figure 7.11 compares BEM predictions and measured excess attenuation spectra obtained over a surface composed of felt and MDF strips (a) with an MDF strip at the specular reflection point and (b) with a felt strip at the specular

reflection point. The dip pattern in the excess attenuation spectra is altered by changing acoustical ground impedance at the specular reflection point and this change is predicted reasonably well by BEM. Although the magnitude of the second dip in the EA spectra is over-predicted, the frequency of this dip is well predicted.
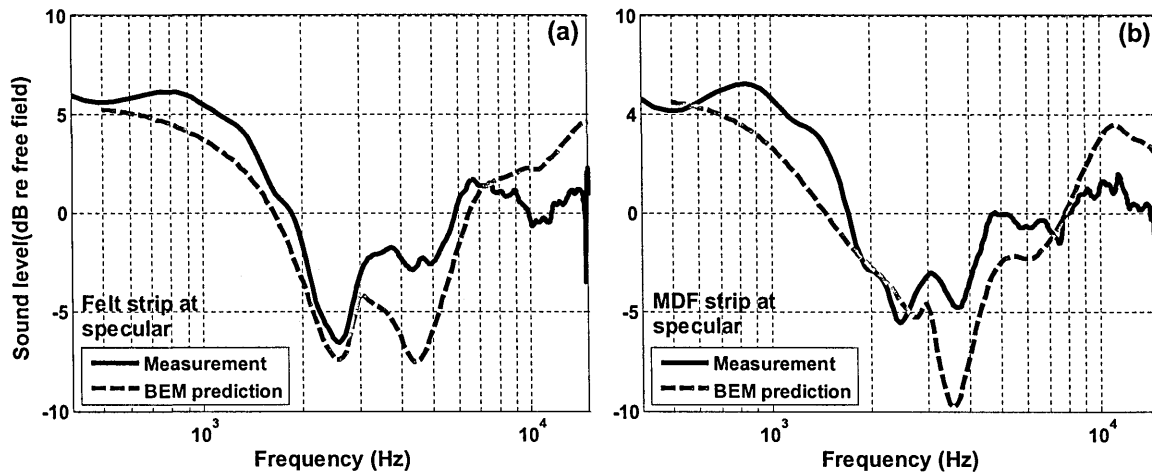
Figure 7.11 Comparison between BEM predictions and measured excess attenuation spectra with source and receiver at 0.07 m height separated by 0.7 m over mixed impedance surface composed of felt and MDF rectangular strips (a) with an MDF strip at the specular reflection point (b) with a felt strip at the specular reflection point.

7.3.2.4 2D vs 3D mixed impedance surfaces

Laboratory experiments have been carried out to investigate the effects of finite impedance strips and patches in an otherwise hard surface. The 2D impedance surface composed of 'soft' strips on a hard surface shown in Figure 7.5 was converted into a 3D impedance patch configuration as shown in Figure 7.12. Figures 7.5 and 7.12 show experimental configurations in which felt was used to provide the finite impedance strips and patches and MDF board was used to provide acoustically-hard surface components. These arrangements represent equal areas of 'hard' and 'soft' ground. Figure 7.13 shows excess attenuation spectra deduced from measurements made with source and receiver separated by

0.7 m and at two different heights (5 and 7 cm). For these data the source-receiver axis was normal to the strip axes. For the configurations shown in Figures 7.5 and 7.12, i.e. with the source receiver axis normal to mixed impedance axes, the EA spectra in Figure 7.13 suggest that there is little advantage in using 3D patches compared with 2D strips. The measured EA spectra over 2D and 3D mixed impedance surface are more or less similar as shown in Figure 7.13.

Figure 7.12 Laboratory configurations used to investigate sound propagation over 3D impedance patches. In these photographs the finite impedance is provided by felt.
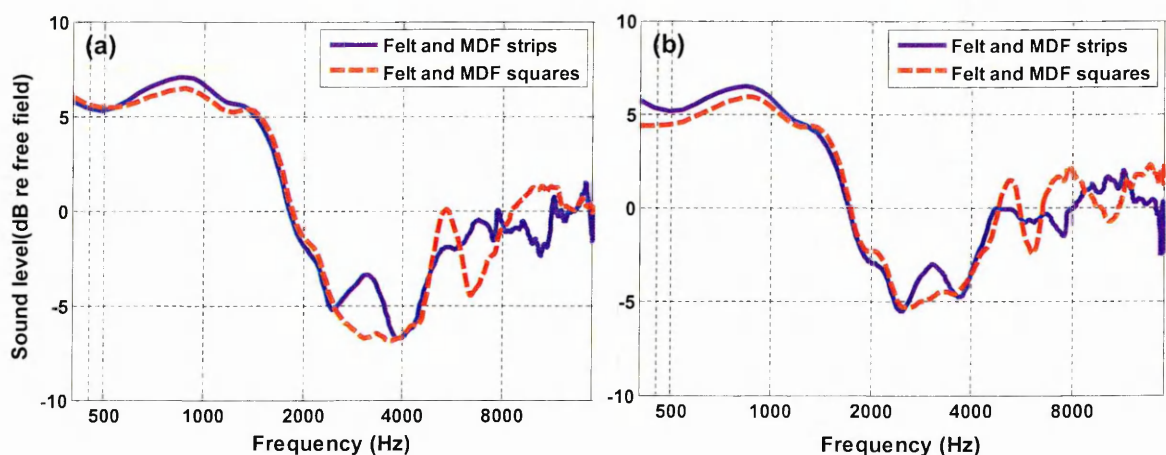
Figure 7.13 Measured excess attenuation spectra for source and receiver separated by 0.7 m over alternating MDF and felt strips and squares and at heights of (a) 5 cm and (b) 7 cm.

Figures 7.14 (a) and (b) show excess attenuation spectra measured over impedance strips and impedance patches with different azimuthal angles i.e. the angle between the source-receiver and the mixed impedance strip axes. The measured EA spectrum over 2D impedance strips changes a little with the change in azimuthal angle. On the other hand the measured EA spectra over 3D impedance patches are more or less azimuthal angle independent.
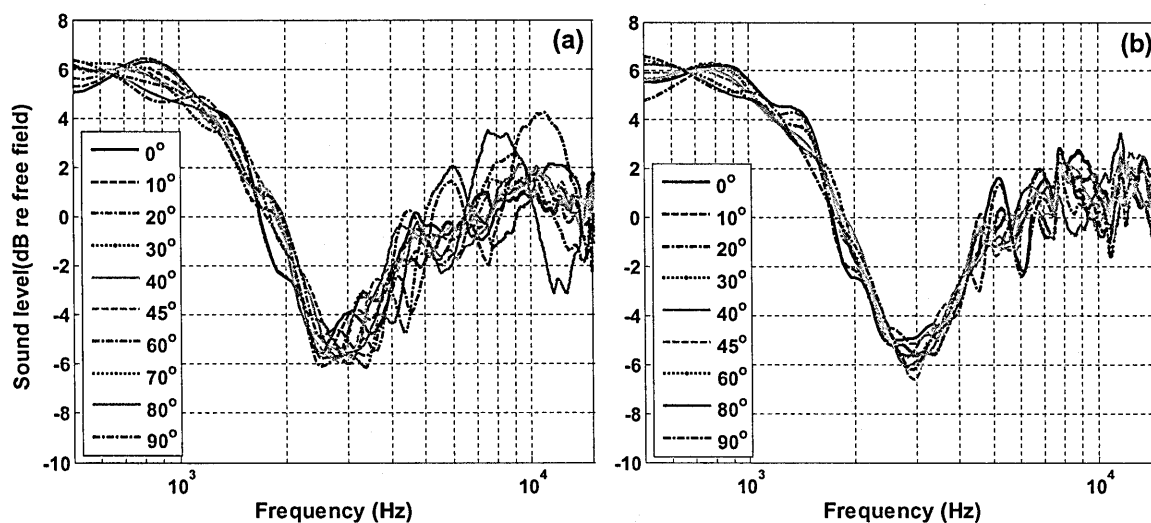
Figure 7.14 EA spectra measured at different azimuthal angles over (a) Felt and MDF impedance strips and (b) Felt and MDF patches.

7.4 Large scale impedance discontinuities

7.4.1 Comparison between BEM and De Jong calculations over single impedance discontinuity

The work presented previously in this Chapter has established the conditions under which semi-empirical methods can be used instead of more time consuming and computationally-intensive numerical methods to predict sound propagation from source to receiver over a mixed impedance ground surfaces at laboratory scales. The aim here is to predict the effect of replacing hard ground by strips or patches of naturally occurring ground surfaces on traffic noise. Chapter 4, reported acoustical characterisation of 47 different naturally occurring ground surfaces. Insertion loss predictions for traffic noise are carried out using standard HOSANNA methods which are described in chapter 11 in more detail. Most of these calculations are carried out for HOSANNA specified cases including a two lane urban road, a four lane urban road, and a 2 x 2 motorway with and without central reservations. Let's consider a four lane urban road. A four lane urban road involves 12 sources at different heights and lanes. Although, BEM gives very good predictions for mixed impedance ground surface, it is numerically very expensive for large scaled geometries. According to the HOSANNA guidelines at least 5 different receiver ranges and two receiver heights of 1.5 m and 4.0 m are considered. So, for a one ground type and the four lane urban road case the number of times excess attenuation has to be calculated is 120 (12 x 5 x 2). For 47 grounds types and the four lane road type, the number of times excess attenuation is calculated over mixed impedance ground is 5640.. A significant

amount of time and computing resources would be required to make BEM calculations of insertion loss for all the road and ground types. To circumvent this problem, an alternative method has been used for many predictions. For cases of a single impedance discontinuity between the source and the receiver, the De Jong semi-empirical model is a potential alternative to BEM. Here predictions of the De Jong model are compared with BEM predictions for a particular ground type and HOSANNA geometry.
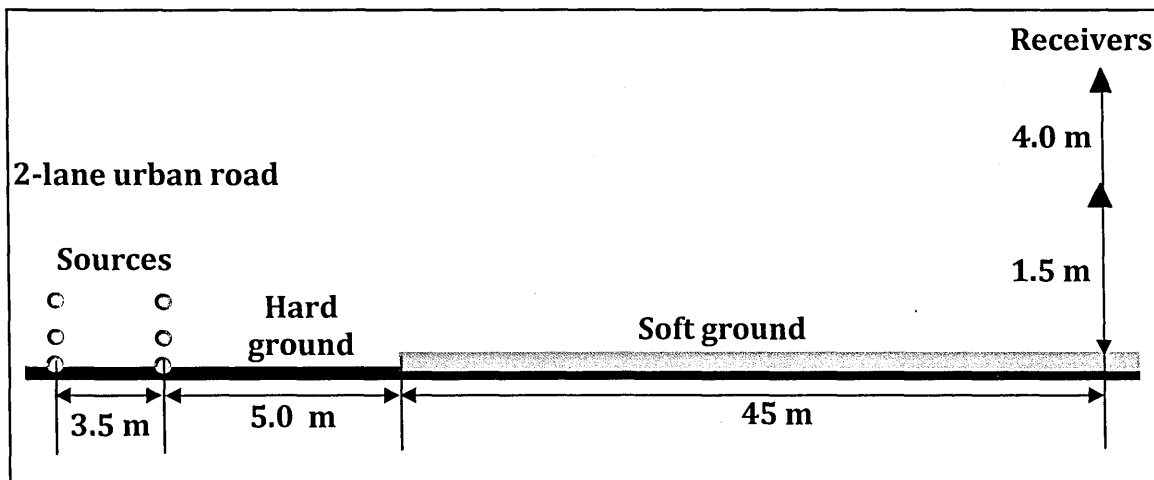
Figure 7.15 A schematic for two lane urban road for single impedance discontinuity by replacing hard ground with soft ground.

Consider the standard HOSANNA two lane urban road case shown in Figure 7.15. The specifications for these calculations are given in more detail in chapter 11. Three source heights of 0.01 m, 0.3 m and 0.75 m are assumed. For two lanes, the total number of sources becomes six. The centres of the two lanes are 3.5 m apart. The receiver is assumed at a distance of 50 m from the centre of the nearest lane and at two different heights of 1.5 m and 4.0 m. The sources are assumed to be over a hard ground and receivers are above a soft ground. There is single hard/soft impedance discontinuity between the source and the receiver. The

soft ground starts at a distance of 5.0 m from the nearest source and extends up to the receiver (see Figure 7.15). Figure 7.16 compares the EA spectra predicted using the De Jong method and BEM for the single impedance discontinuity and all sources and receivers for a two lane urban road. The soft ground was selected to be long grass with relatively low flow resistivity (Nord-test site # 41, see chapter 4 for which the best fit parameters using the slit pore model are a flow resistivity of 104 kPa s m^{-2} and porosity of 0.36). The De Jong model predictions are in good agreement with the BEM predictions with very small differences. The main purpose of making these excess attenuation calculations is to obtain the insertion loss resulting from replacing the hard ground along the road side with long grass. So to check further whether the De Jong model can be used, insertion loss has been calculated over four different ground types using the De Jong model and the resulting values compared with those obtained by using BEM. Table 7.1 summarizes the insertion loss over different ground types for the configurations shown in Figure 7.15. The maximum difference between insertion loss values is 0.5 dB which is considered to be quite acceptable. So it has been concluded that the De Jong model can be used with confidence for single discontinuity cases where hard ground is replaced with soft ground.

Table 7.1 Comparison between De Jong model and BEM predictions for insertion loss near a two lane urban road due to single hard/soft impedance discontinuity.

Surface description	Porosity	Flow resistivity (kPa s m^{-2})	Receiver height Hr (m)	De Jong model predictions			BEM predictions		
				IL - Lane1 (dB)	IL- Lane2 (dB)	IL combined (dB)	IL- Lane1 (dB)	IL- Lane2 (dB)	IL combined (dB)
Lawn	0.50	176	1.5	8.3	7.6	7.9	8.3	7.5	7.9
			4.0	2.8	1.6	2.1	3.0	1.8	2.4
Pasture	0.50	1344	1.5	6.1	5.9	6.0	5.7	5.3	5.5
			4.0	2.2	1.5	1.9	2.3	1.5	1.9
Arable	0.50	2251	1.5	5.3	5.2	5.3	4.8	4.5	4.7
			4.0	2.0	1.4	1.7	2.0	1.3	1.6
Long grass	0.36	104	1.5	8.2	7.4	7.8	8.2	7.4	7.8
			4.0	2.6	1.5	2.0	2.9	1.7	2.3
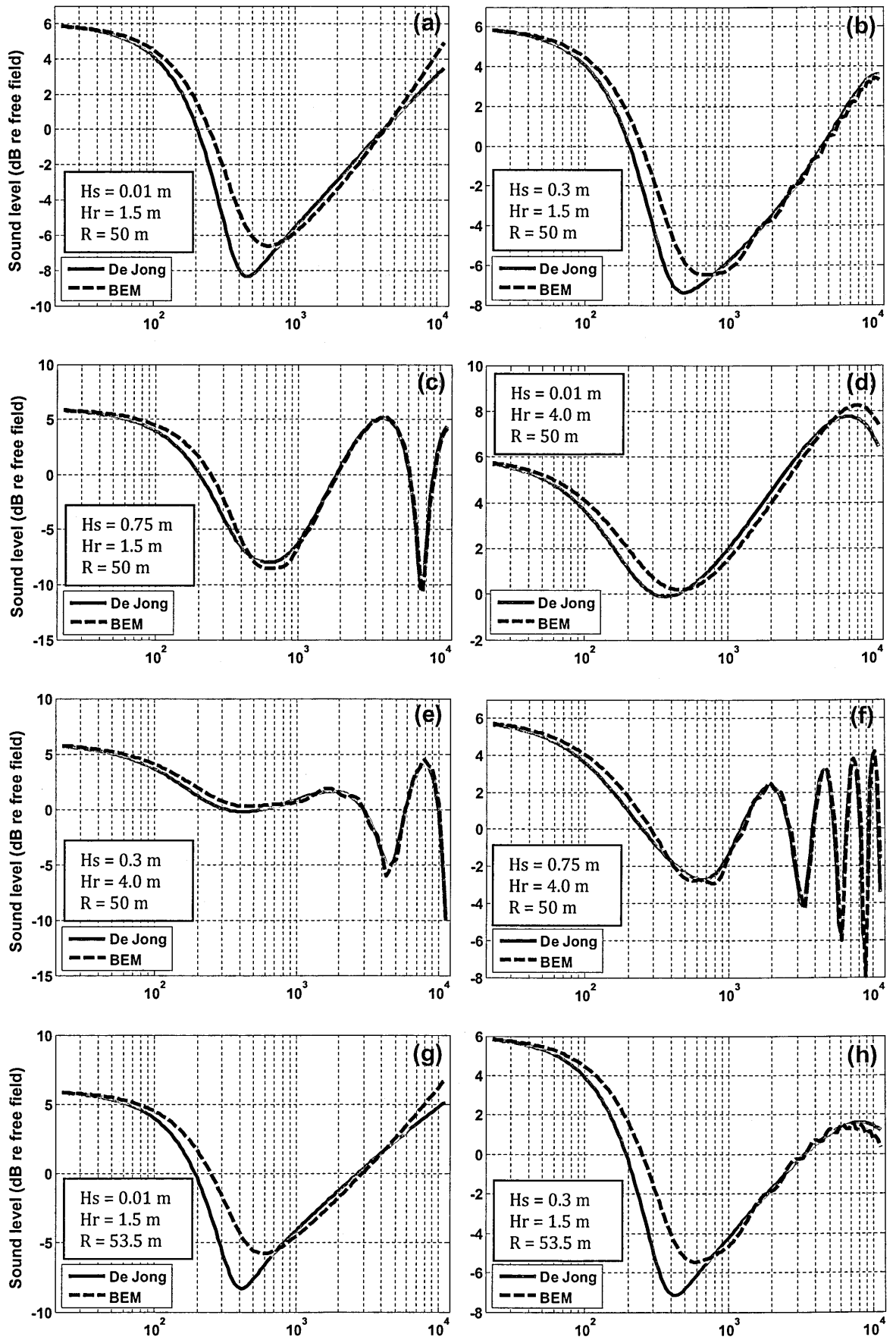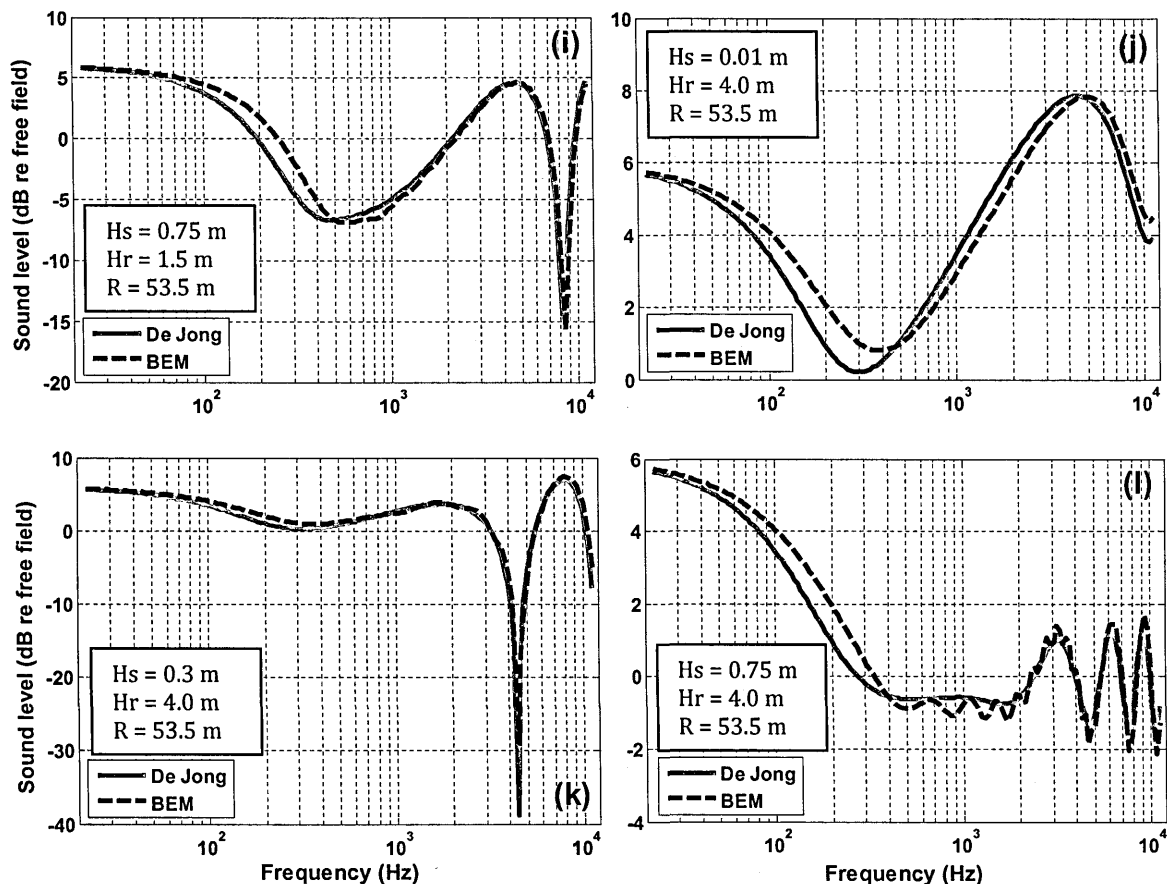
Figure 7.16 Comparison between EA predicted by the De Jong model and BEM for single hard/soft impedance discontinuity at a distance of 5.0 m from the source on hard ground. The soft ground after the discontinuity consists of Long grass (Nord-test site#41, Flow resistivity = 104 kPam^{-2}, Porosity = 0.36). The geometry according to HOSANNA, with source height (Hs) receiver height (Hr) and range (R) as given (a) Hs = 0.01m, Hr = 1.5m, r = 50m (b) Hs = 0.3m, Hr = 1.5m, r = 50m (c) Hs = 0.75m, Hr = 1.5m, r = 50m (d) Hs = 0.01m, Hr = 4.0m, r = 50m (e) Hs = 0.3m, Hr = 4.0m, r = 50m (f) Hs = 0.75m, Hr = 4.0m, r = 50m (g) Hs = 0.01m, Hr = 1.5m, r = 53.5m (h) Hs = 0.3m, Hr = 1.5m, r = 53.5m (i) Hs = 0.75m, Hr = 1.5m, r = 53.5m (j) Hs = 0.01m, Hr = 4.0m, r = 53.5m (k) Hs = 0.3m, Hr = 4.0m, r = 53.5m (l) Hs = 0.75m, Hr = 4.0m, r = 53.5m.

7.4.1 Comparison between BEM and nMID De Jong calculations over multiple impedance discontinuity

Another potentially important scenario for traffic noise reduction is replacing hard ground with multiple impedance strips thereby introducing multiple impedance discontinuities between the source and the receiver. The accuracy of the modified De Jong model (nMID, see Eqs. 7.4 – 7.6) has been tested for multiple impedance discontinuities. Figure 7.17 compares BEM and modified De Jong model predictions of EA spectra at a distance of 50 m from the source due to a single 10 m wide strip starting 2.5 m from the source. The strip impedance is assumed to be that given by a semi-infinite two-parameter slit pore model with a flow resistivity of 10 kPa s m^{-2} and a porosity of 0.4. The calculations have been carried out for a two lane urban road as described above. For this case the modified De Jong model predictions are not in agreement with BEM predictions. To carry out predictions and to calculate insertion loss over strips having multiple discontinuities, it is concluded that the nMID De Jong model is not sufficiently accurate.
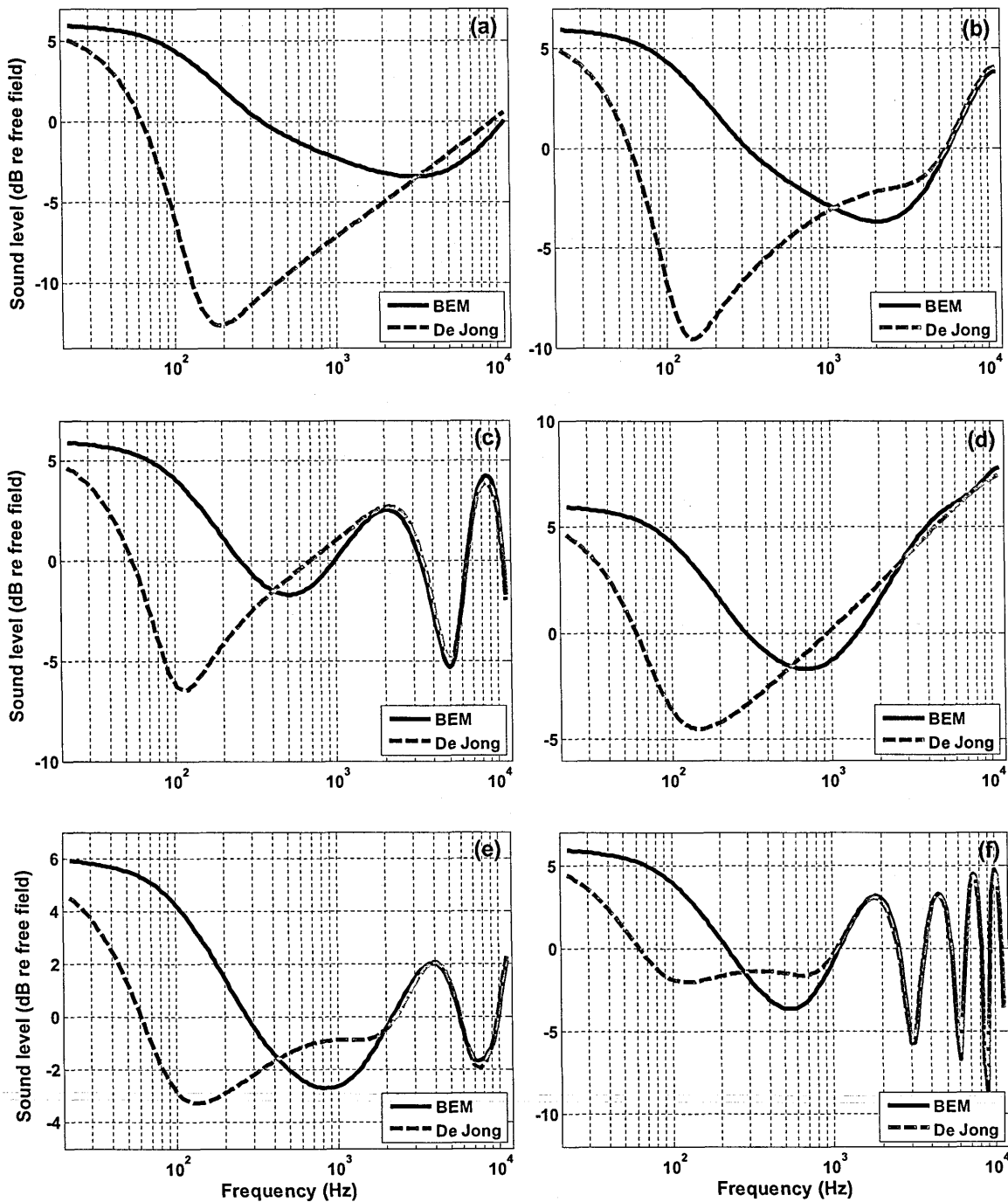
Figure 7.17 Comparison between BEM (continuous black lines) and modified De Jong model (nMID) (broken red lines) predictions of EA spectra at a distance of 50 m from the source due to a single 10 m wide strip starting 2.5 m from the source. The strip impedance is assumed to be that given by a semi-infinite two-parameter slit pore model with a flow resistivity of 10 kPa s m^{-2} and a porosity of 0.4 (a) source height 0.1 m, receiver height 1.5 m (b) source height 0.3 m, receiver height 1.5 m (c) source height 0.75 m, receiver height 1.5 m (d) source height 0.01 m, receiver height 4 m (e) source height 0.3 m, receiver height 4 m (f) source height 0.75 m, receiver height 4 m.

7.4.2 Comparison between BEM and Fresnel zone calculations

The use of the Fresnel zone method for making predictions over large scale impedance strips has also been investigated. Figure 7.18 compares BEM (see Chapter 2, Section 2.3) and Fresnel zone method predictions of EA spectra (see Eq. 7.17) at a distance of 50 m from the source due to a single 10 m wide strip starting 2.5 m from the source. The strip impedance is assumed to be that given by a semi-infinite two-parameter slit pore model with a flow resistivity of 10 kPa s m^{-2} and a porosity of 0.4. The calculations have been carried out for two lane urban road as described above. Predictions using the Fresnel zone method are not in agreement with those obtained using BEM. Table 7.2 summarizes the insertion losses calculated using the Fresnel zone method and BEM for a two lane urban road over two types of mixed impedance ground having single or multiple impedance strips starting at a distance of 2.5 from the nearest lane source. There are large differences between the calculated insertion loss values. It is concluded that the Fresnel zone method is not sufficiently accurate for calculating insertion loss over mixed impedance ground surfaces.

Table 7.2 Comparison between Fresnel zone method and BEM predictions for insertion loss calculation for two lane urban road over two types of mixed impedance ground having single or multiple impedance strips starting at a distance of 2.5 from the nearest lane source.

Surface description	Porosity	Flow resistivity (kPa s m⁻²)	Impedance strips length (m)	Receiver height Hr (m)	Fresnel zone predictions			BEM predictions		
					IL -Lane1 (dB)	IL-Lane2 (dB)	IL combined (dB)	IL-Lane1 (dB)	IL-Lane2 (dB)	IL combined (dB)
Multiple impedance strips of gravel and hard ground by assuming the strips of 1m width	0.40	10	25.0	1.5	3.5	3.1	3.3	8.0	7.1	7.5
				4.0	1.9	0.9	1.3	3.6	2.1	2.8
A continuous single impedance patch of 10 m	0.40	10	10.0	1.5	3.0	3.1	3.2	6.8	5.9	6.3
				4.0	1.2	1.9	2.7	4.4	2.7	3.4
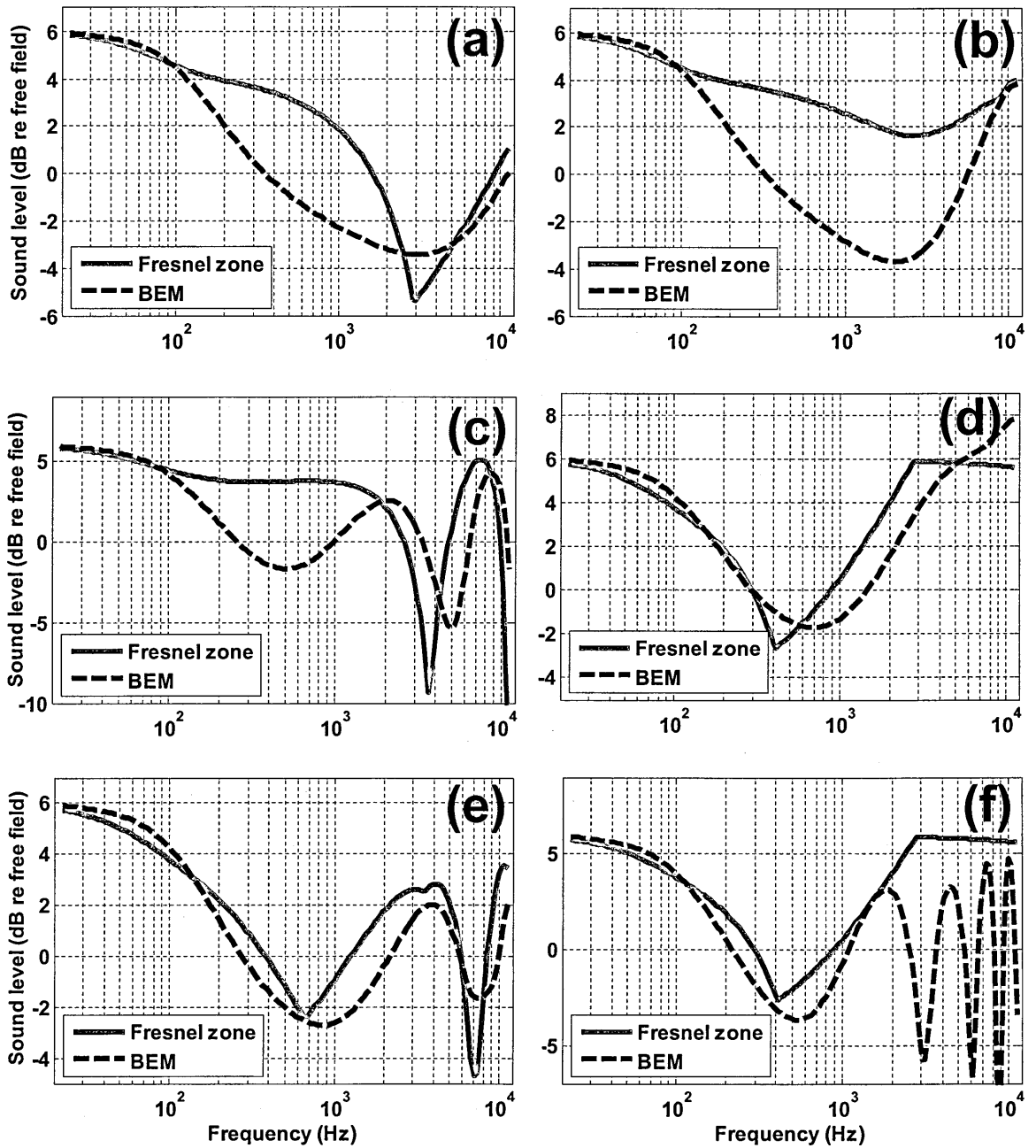
Figure 7.18 Comparison between BEM (broken black lines) and Fresnel zone (continuous red lines) predictions of EA spectra at a distance of 50 m from the source due to a single 10 m wide soft strip starting 2.5 m from the source. The strip impedance is assumed to be that given by a semi-infinite two-parameter slit pore model with a flow resistivity of 10 kPa s m^{-2} and a porosity of 0.4 (a) source height 0.1 m, receiver height 1.5 m (b) source height 0.3 m, receiver height 1.5 m (c) source height 0.75 m, receiver height 1.5 m (d) source height 0.01 m, receiver height 4 m (e) source height 0.3 m, receiver height 4 m (f) source height 0.75 m, receiver height 4 m.

7.5 Conclusions

Sound propagation over ground surfaces containing single or multiple impedance discontinuities has been studied using BEM, De Jong, modified De Jong and Fresnel zone methods.

Predictions using the De Jong model have been found to be in good agreement with BEM predictions over a single impedance discontinuity at laboratory scale. The original De Jong and the modified De Jong models predict identical EA spectra over a single impedance hard/soft discontinuity. However, the modified De Jong model gives much better agreement with BEM predictions for a soft to hard impedance discontinuity as. Predictions using the De Jong model over the larger scale single impedance discontinuities and source-receiver geometries considered for the HOSANNA project also are in very good agreement with BEM predictions. The insertion loss predictions associated with replacing hard ground with soft ground using either BEM or the De Jong model have a maximum difference of 0.5 dB. Computations using the De Jong model are much faster than numerical predictions using BEM. Therefore De Jong model predictions are preferred when hard ground along the road side is replaced with soft ground. On the other hand it has been found that the De Jong model fails to give accurate predictions of sound propagation over mixed impedance ground having multiple impedance discontinuities.

The Fresnel zone method has been used also to predict sound propagation over single and multiple impedance discontinuities. It has been found that the Fresnel zone method predicts only approximate spectra and ignores diffraction effects at the impedance discontinuities. The Fresnel zone method does not give

very good agreement with BEM predictions over single or multiple impedance discontinuities of either EA spectra or insertion loss. It has been concluded that the Fresnel zone method is not a very appropriate choice for predicting insertion loss over mixed impedance ground surfaces consisting of single or multiple impedance discontinuities.

Chapter 8

8. Surface waves over periodically-rough and porous boundaries

8.1 Introduction

In previous chapters sound propagation over different kind of surfaces has been studied extensively (see Chapter 4, 5 and 6). These ground surfaces can be divided into two categories i.e. acoustically soft porous surfaces and rough-hard surfaces. The ability of these surfaces to reduce traffic noise has been studied. Typically the main contribution to traffic noise source is car-tyre noise the source of which is located near to the road surface. According to HARMONOISE [104] guidelines, the car-tyre noise source is at a height of 0.01 m. A typical location for the receiver considered here is at a distance of 50 m and at a height of 1.5 m. When sound waves propagate over a rough hard surface or rough porous surface

at near grazing angles, they are scattered both coherently and incoherently. For a point source the coherently scattered waves combine near grazing to form a reflected wave and a ground wave in addition to the direct wave. Under some circumstances the ground wave includes a surface wave. Above a porous surface the surface wave is essentially a separate contribution propagating close to and parallel to a surface and is associated with elliptical motion of air particles as the result of combining motion parallel to the surface with that normal to the surface in and out of the pores [33]. The surface wave decays principally as the inverse root of horizontal range and exponentially with height above the ground.

While as described in previous chapters that the rough ground surfaces can be exploited for traffic noise attenuation, near grazing angles rough surfaces result in the generation and propagation of surface waves. These roughness-induced surface waves may reduce attenuation performance. The main aim of this study is to investigate different methods for the reduction of surface waves to improve the attenuation performance of the rough surfaces.

The first part of the chapter studies surface wave creation and propagation over different kind of artificial ground surfaces in the laboratory. The second part of the chapter studies surface wave propagation over larger scale parallel walls systems using BEM and investigates the additional insertion loss that can be obtained by attenuating the surface wave.

8.2 Surface waves over parallel wall arrays

The design of parallel wall configurations for traffic noise attenuation has been investigated extensively in Chapter 5 (see Section 5.10). The (2D) BEM has been used to predict excess attenuation spectra over low parallel wall arrays. A consequence of multiple diffraction and scattering by the walls is that, effectively, in the region occupied by the walls, the ground, which is otherwise acoustically hard, has finite impedance. In a limited lower frequency range, the effective impedance due to parallel walls produces an excess attenuation greater than +6 dB (see Figure 8.2) [114]. So the sound field is greater than it would be if the surface were smooth and acoustically-hard. This is associated with sound trapped close to the surface in a surface wave. As a result of the passage of sound near grazing incidence on a parallel wall array, the air particles move forwards and backwards parallel to the wall tops. However the cavities between the walls also allow vertical motion of the air particles into and out of the cavities. The surface wave is associated with the resultant elliptical motion of the air particles at the entrances to the inter-wall cavities. The surface wave requires a minimum number of walls (and cavities) to be generated and it propagates over the walls and after the walls as well.

Figure 8.1 (a) shows that, compared to the regions at a greater height above the walls or on the lee side of the walls, the predicted insertion loss in the region immediately above the parallel wall system is slightly lower. This is the result of acoustic energy being trapped in a surface wave. Figure 8.1 (b) shows the insertion loss for the one third octave frequency band in which the surface wave is strongest. It is clear in this plot that the influence of the surface wave

extends into the region beyond the parallel walls but that the nature of the propagation changes with increasing distance from the end of the wall array.
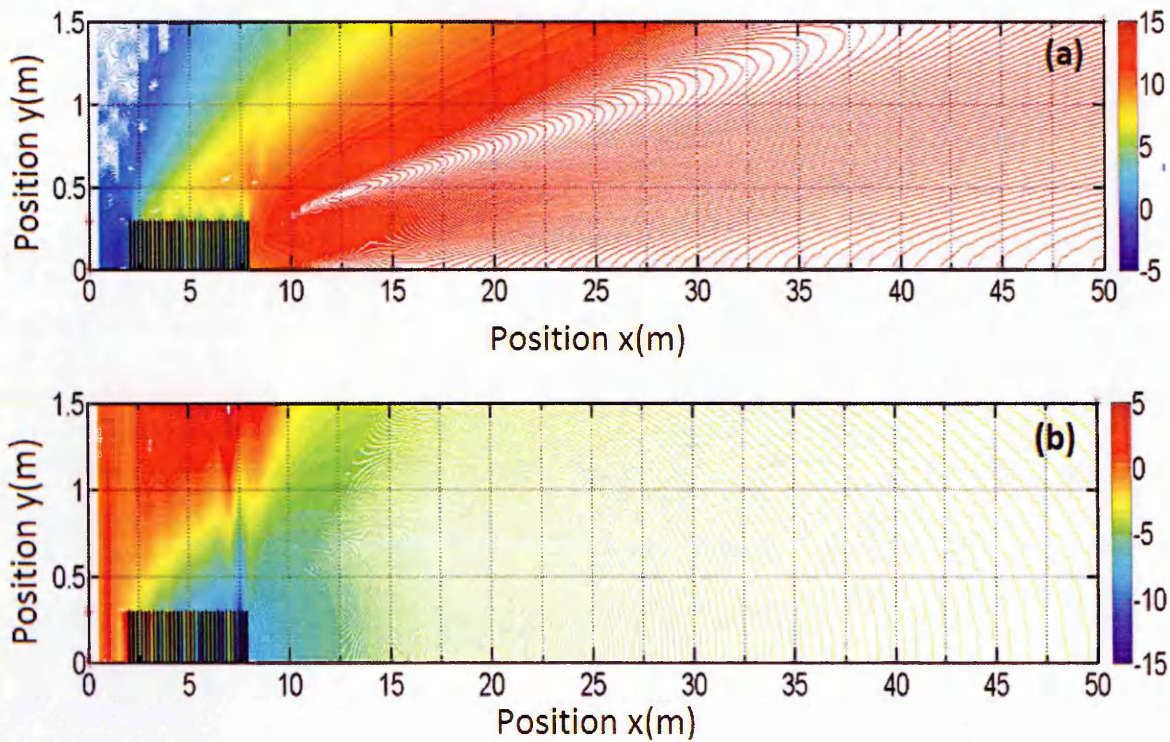
Figure 8.1 BEM predicted insertion loss contours due to an array of 30 low parallel walls (0.30 m height ×0.05 m width ×0.20 m centre-to-centre spacing) on hard ground with the nearest wall 2 m from a single lane of cars moving at 70 km/h (a) broadband (100-10000 Hz) (b) 125 Hz 1/3 octave band (produced by T. J. Hill [114]).

Figure 8.2 shows excess attenuation spectra predicted using BEM over a parallel wall array consisting of 16 identical 0.05 m thick and 0.3 m high walls with centre-to-centre spacing of 0.2 m (total width 3.05 m), the source is placed at distance of 2.5 m from nearest walls array and at three different source heights of 0.01 m, 0.3 m and 0.75 m and receiver is placed at height of 1.5 m and at a distance of 50 m from the source. A very strong surface wave at 150 Hz is predicted for the source heights of 0.01 m and 0.3 m. Some surface wave contribution is predicted also for a source height of 0.75 m.

Surface waves have a negative effect on the insertion loss due to parallel walls. The main purpose of the study presented in this chapter is to investigate the properties of such audio-frequency surface waves and different methods of reducing surface wave propagation which would thereby improve the insertion loss due to parallel wall systems.
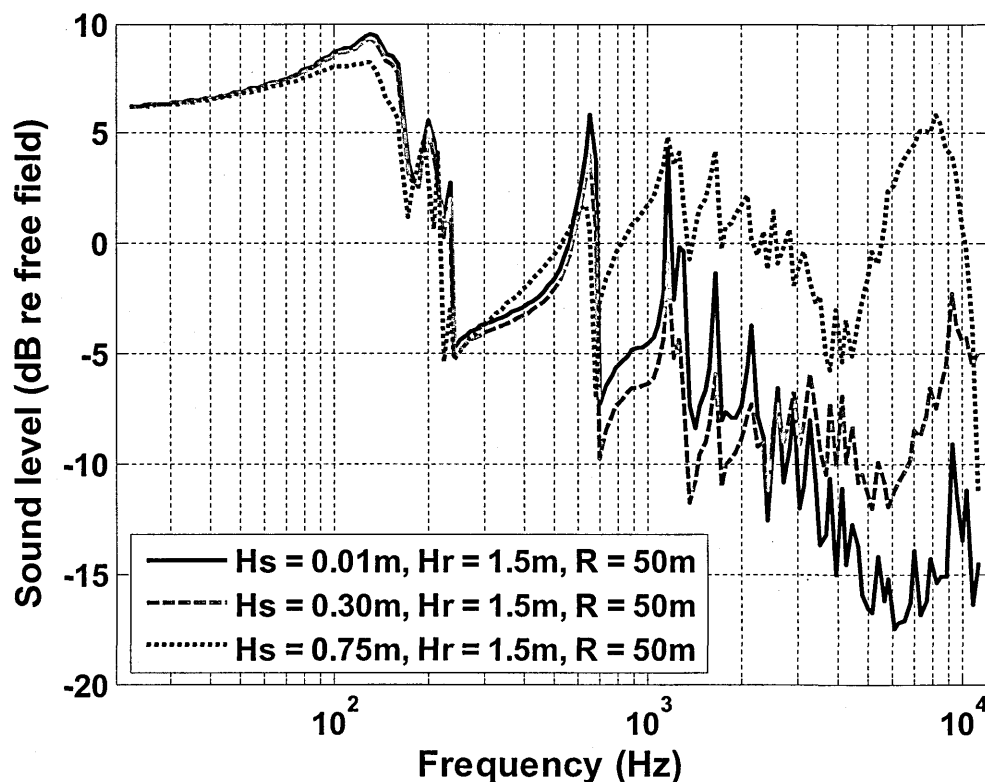
Figure 8.2 Excess attenuation spectra predicted using BEM at height of 1.5 m and at a distance of 50 m from the source due to parallel wall array consisting of 16 identical 0.05 m thick and 0.3 m high walls with centre-to-centre spacing of 0.2 m (total width 3.05 m). The source is placed at distance of 2.5 m from nearest walls array and at three different source heights of 0.01 m, 0.3 m and 0.75 m.

8.3 Literature review

There have been many analytical and experimental studies related to the surface waves that result from a point source located above air-filled porous elastic media [115]–[117]. One of these travels at a little less than the speed of sound in air. It is primarily related to the pore structure and is the dominant type of surface wave observed above a relatively-rigid-framed air-filled porous layer. The other is determined primarily by the elastic properties of the solid frame and is similar to the Rayleigh wave observed at the free boundary of an elastic solid.

This surface wave is an evanescent wave and is associated with an imaginary part (reactance) of the surface impedance that is greater than the real part (resistance). It spreads cylindrically along the surface but decays exponentially with height above the surface. Surface wave propagation has been studied over air-filled porous and rough ground surfaces. Brekhovskikh [118] studied surface wave propagation over a comb-like structure. Donato [119] studied the propagation of surface waves over a rectangular lattice (lighting diffuser) placed on a wooden board and showed that that the measured vertical and horizontal attenuation rates of the acoustically-induced surface waves were consistent with theoretical predictions.

As discussed in Chapter 5, surface waves induced by coherent scattering from rough surfaces have been studied by Tolstoy [89], [90], [92] who described them as 'boundary waves' due to energy trapped between the roughness elements. Tolstoy [89], [90], [92] described a boundary wave as an independent mode of propagation which spreads cylindrically and attenuates exponentially with height. Tolstoy [89], [90], [92] formulated stochastic and boss models which do not

include incoherent scatter and predict that the effective impedance of a rough hard surface is purely imaginary. Medwin *et al.* [93], [94] carried out experimental studies of surface waves and compared the resulting data with predictions of Tolstoy's models. They used microphones that were flush with the base of the rough surface. It was found that although predictions were in reasonable agreement with measurements they over-estimated the amplitude of the surface wave component. According to Tolstoy's theory, the boundary wave continues to grow as it propagates over a rough surface. However, Medwin's experimental work shows that it grows until a certain range and then it stays the same as a consequence of incoherent scattering. Although the theory due to Twersky [85], [86],[87] includes incoherent scatter, it has been found to need modification at low frequency and to allow for periodically-spaced roughness elements [61].

Hutchinson-Howorth and Attenborough [120] carried out measurements using tone bursts above over single and double square cell lattice layers. They managed to separate the surface wave pulse from the main pulse arrival and thereby proved that the surface wave travelled slower than the speed of sound in air. The measured properties of surface waves were found to be in good agreement with theoretical predictions. The measured impedance of the lattice surface shows a reactance that is much larger than the resistance. The measured excess attenuation spectra magnitudes exceed more than +6 dB at certain frequencies thereby indicating the existence and propagation of surface waves [120]. Daigle *et al.* [121] carried out measurements above a model surface consisting of square-cell lattice using pulses generated from a point source. They showed that the surface wave spreads cylindrically, attenuate exponentially with

height and propagates slower than the speed of sound. Zhu *et al.* [122] studied reflection and diffraction and the dispersion and formation of surface waves over a comb-like surface and presented an analytical solution for the plane-wave scattering by a comb-like grating. Subsequently, Zhu *et al.* [123] carried out laboratory measurements on the air coupled surface wave due a point source above a lattice surface and mixed impedance ground surface. They [123] investigated the surface wave generation at each impedance discontinuity and its amplification due to strips of different widths.

Allard, Lauriks and Kelders [124], [125], [126], [127], have studied the formation and propagation of ultrasonic surface waves over triangular grooves [124], rectangular grooves [105], a doubly periodic grating [126] and honeycombs [127]. They presented a modal theory to predict the sound propagation over the periodically-rough surfaces which was found to yield better agreement with their data than Tolstoy's [90], [92] model. Lauriks *et al.* [124] have studied surface wave propagation above a triangular groove grating at ultrasonic frequencies. The measured data over triangular grooves was compared with predictions using the modal model and the Tolstoy model. Predictions obtained using the modal model were found to be in good agreement with measured data whereas the Tolstoy model failed to give as good agreement with the data. Similarly, Kelders *et al.* [105] have studied the surface wave propagation over rectangular groove grating and compared the resulting data with predictions using the modal model, which were found to be in a good agreement. They also presented a simple model which is only valid for prediction of sound propagation over infinitely thin plates. Allard *et al.* [126] investigated the surface wave propagation above doubly periodic grating

and concluded that the modal model gives good agreement with measured data over a plane perforated by square holes. Later on, Tizianel et al. [127] extended their work of surface wave study to more complex structure such as honeycombs. They [127] introduced a modification to modal theory for square pores [126], so that the theory should also be valid for honeycomb structures. The comparison between measured data over honeycombs and predictions showed that the agreement between data and predictions is improved after introducing a correction term. Kelders et al. [117], [118] studied surface waves above thin porous layers of plastic foams having very high porosity values. Through experimental work, they [128] proved the surface wave's existence over thin porous layers of foams and that its phase speed is lower than the speed of sound in air. Most of the experimental work over surface wave propagation described in the literature was carried out in the laboratory. However, Albert [129] has observed an audio-frequency surface wave outdoors over snow covered ground using an impulsive sound source and successfully confirmed the surface wave properties such as exponential decay and a phase speed slower than the speed of sound.

Much previous research on acoustical propagation over periodic surfaces has focused on surface wave creation and on time domain data rather than on frequency domain information such as excess attenuation (EA) or insertion loss (IL) spectra. The latter are important in the context of designing rough surfaces for noise control and for predicting the effective impedance of rough outdoor surfaces for use when predicting outdoor sound propagation.

8.4 Conditions for surface wave propagation

Consider a wave travelling above a ground surface with acoustic impedance Z.

$$P = pe^{i\alpha x} e^{i\gamma y},$$

(8.1)

The solution to the problem is obtained by using the Helmholtz equation (see Chapter 2, Section 2.2) and applying boundary conditions. For wave propagation along the x-axis, the solution for Eq. 8.1 can be written as [130],

$$\tau = \frac{-k\rho c}{Z},$$

(8.2)

$$\alpha = k\sqrt{1 - \left(\frac{pc}{Z}\right)^2},$$

(8.3)

where, $k = \omega/c$ is the propagation constant, ω is the angular frequency, c is the free-space sound speed, ρ is the air density and Z is the specific acoustic impedance of the porous surface.

The solution given by Eq. 8.2 and Eq. 8.3 can be used to establish the criteria for the propagation of the surface wave. The first condition is that the imaginary part of Z must be greater than zero which means that the reactance should be greater than the resistance of the ground surface. Given that this condition is satisfied, τ will have a positive imaginary part and the sound pressure level decreases exponentially with height. This means that the surface wave is present only near the surface and the pressure amplitude decays exponentially with height. The second condition for the existence of surface wave is that the

attenuation of wave along the x-axis should not be too rapid. It states that the surface wave should attenuate with the square-root of the distance from the source. Mathematically the two conditions can be written as,

$$\text{Im}(\tau)\lambda > 1, \quad \text{Im}(\alpha)\lambda < 1,$$

(8.4)

Applying these two conditions, a general conclusion for the surface wave propagation is given as,

$$\text{Im}(Z) > \text{Re}(Z),$$

(8.5)

Thus, for the generation and propagation of surface wave on a ground surface, the imaginary part of the impedance for that ground must be greater than the real part of the impedance.

8.5 Surface wave propagation over lattice layers

8.5.1 Surface wave measurements and characterization

As reported in the review, several authors have studied surface wave propagation over lattice layers in the laboratory [119], [120], [126], [105]. Systematic measurements (using the system described in Chapter 3) have been made in an anechoic chamber of excess attenuation spectra due to a point source over surfaces composed of single, double and triple square-cell lattice layers respectively placed over a MDF board. The measurement arrangement used to study propagation over a single lattice layer is shown in Figure 8.3. The lattice layer is made of small square cells with depth of 12.63 mm, centre-to-centre spacing of 14.04 mm, cell wall thickness of 1.85 mm and a square pore side of 12.19 mm. To form double and triple lattice layers two or three lattice sheets were stacked carefully with the cell walls directly above each other. The measured layer depths of double and triple layer lattices are 25.26 mm and 37.89 mm respectively.
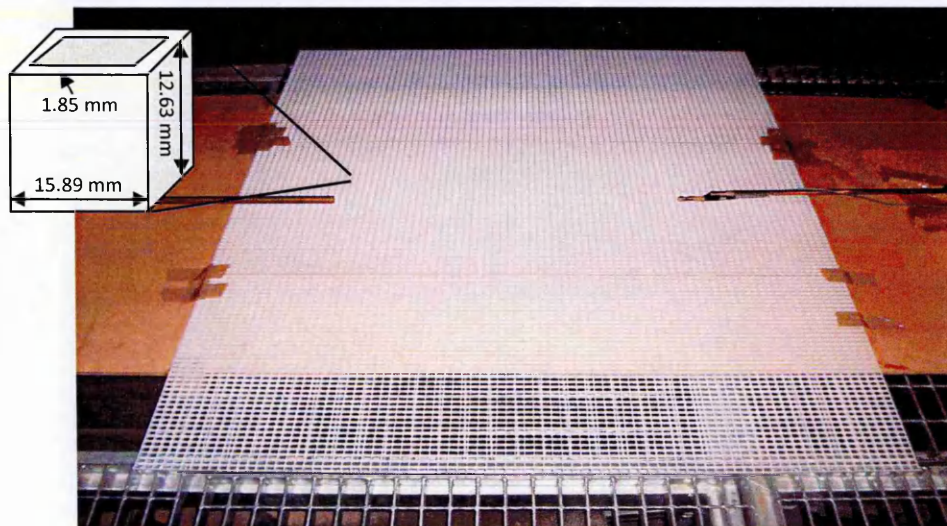
Figure 8.3 Photograph of a laboratory arrangement for measuring surface wave generation and propagation over a single square-cell lattice layer placed on MDF board.

Figure 8.4 (a) compares time domain signals obtained at different receiver heights between 0.03 m and 0.10 m over a surface composed of a single lattice layer placed on an MDF board. The source and receiver were separated by a distance of 0.7 m. For these data and subsequent data the reported source and receiver heights were measured from the MDF board surface. The time domain plots corresponding to the lower receiver heights show a strong surface wave, whereas this feature does not appear when the receiver is in the higher locations. This is consistent with the expected exponential decrease with height required for a surface wave. These characteristics are confirmed by Figure 8.4 (b) which shows measured excess attenuation spectra obtained with source and receiver separated by 0.7 m above a single layer lattice surface with the source height of 0.03 m and receiver heights between 0.03 m and 0.10 m. Below the first destructive interference frequency, the direct and reflected waves reinforce each other and the excess attenuation (EA) is +6 dB. The fact that EA > +6dB between 1.5 kHz and 3 kHz indicates that a surface wave is present. For source and receiver at a height of 0.03 m, the peak EA spectra magnitude is 14 dB. The appearance of extra energy in the spectra is due to surface wave propagation above the lattice surface. Figure 8.4 (b) indicates that the strength of the surface wave depends on the receiver height. There is a strong surface wave when the receiver is at height of 0.03 m but little or no surface wave when the receiver is at a height of 0.10 m. Figure 8.4 compares the measured amplitudes of the surface wave arrivals obtained over single lattice layer placed on MDF board at different receiver heights of 0.03 m, 0.04, 0.05 m, 0.06 m, 0.07 m, 0.08 m, 0.09 m and 0.10 m. The source was at a height of 0.03 m, the source-receiver separation was 0.7 m.
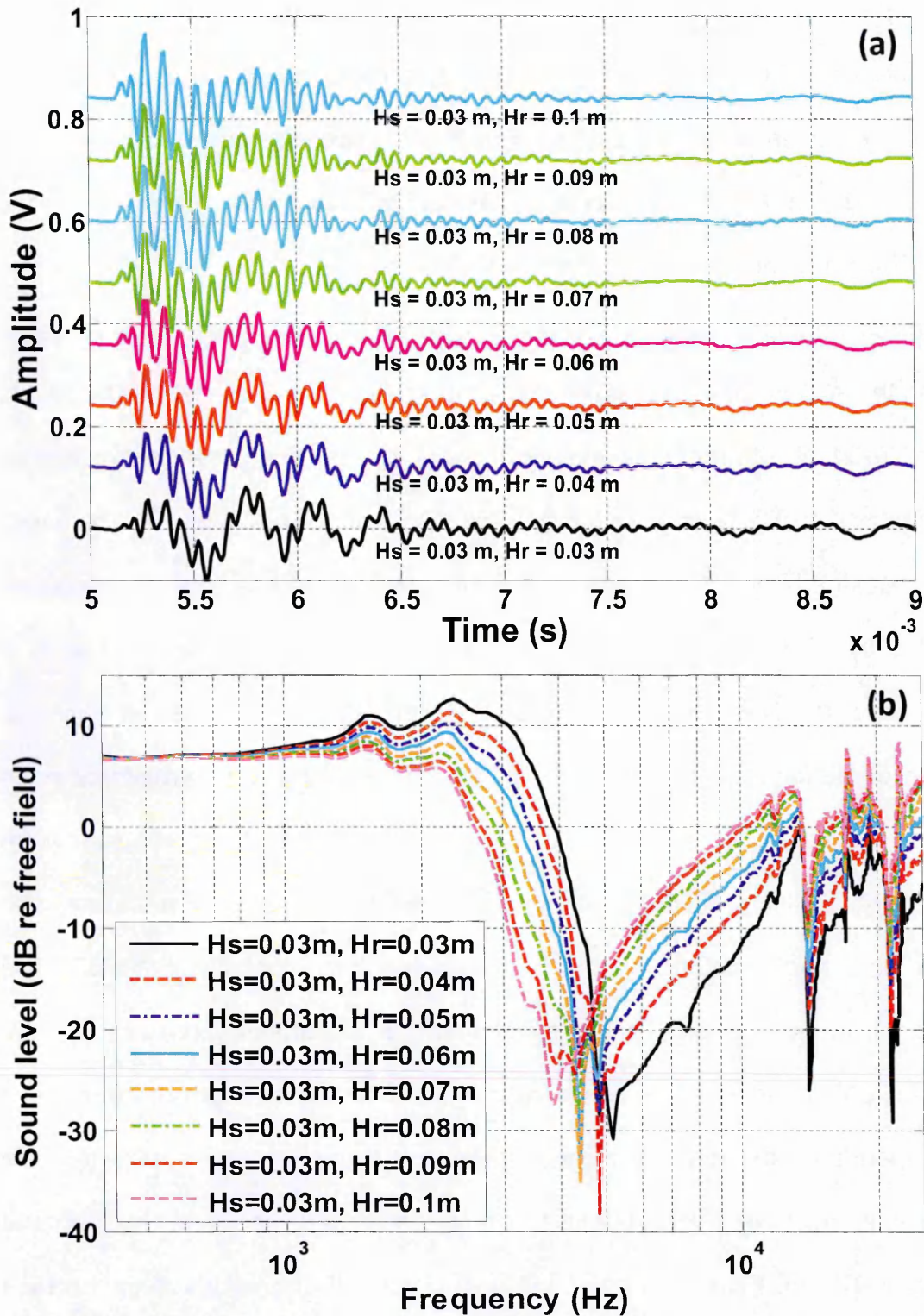
Figure 8.4 (a) Measured time domain signals and (b) corresponding excess attenuation spectra over single lattice layer placed on a MDF board with source at height of 0.03 m and receiver is placed at different heights of 0.03 m, 0.04 m, 0.05 m, 0.06 m, 0.07 m, 0.08 m, 0.09 m and 0.1 m. The source and receiver were separated by a distance of 0.7 m.

As remarked earlier a surface wave should decay exponentially with increasing receiver height. This property has been verified by the laboratory data obtained over the lattice surface. Two time instants have been selected on the measured time domain signals such as shown in Figure 8.5 (a). Figure 8.6 shows an example plot with two time instants selected at 5.75 ms and 6.12 ms respectively. The plot is for source and receiver at height of 0.03 m. The corresponding time instants have been selected on time domain signals for other receiver heights. The measured amplitudes of the time domain signals at the two selected time-instants are plotted against receiver heights in Figure 8.6.
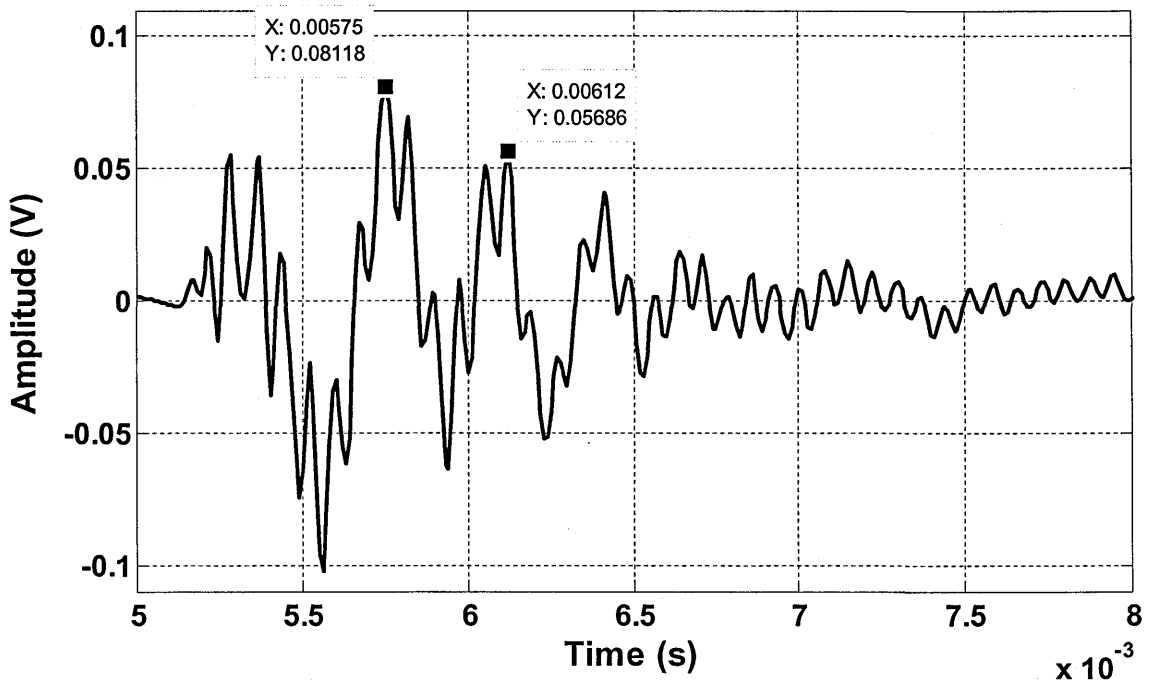
Figure 8.5 Measured time domain signal over single lattice layer placed on a MDF board with source and receiver at height of 0.03 m. The source and receiver were separated by a distance of 0.7 m.

The amplitudes as the receiver height is increased can be fitted by exponential decays of the form,

$$A = \alpha e^{\gamma_{Hr}}, \qquad\qquad (8.6)$$

where A is the amplitude of the surface wave, Hr is the receiver height in meters, α and γ are coefficients. The best fit coefficient values for the exponential curves (continuous red lines) shown in Figure 8.6 (a) and (b) are $\alpha = 0.095$ & 0.065 and $\gamma = -7.76$ & -7.03 respectively. The observed exponential decay with increase in receiver height confirms the existence of surface wave over a lattice surface.
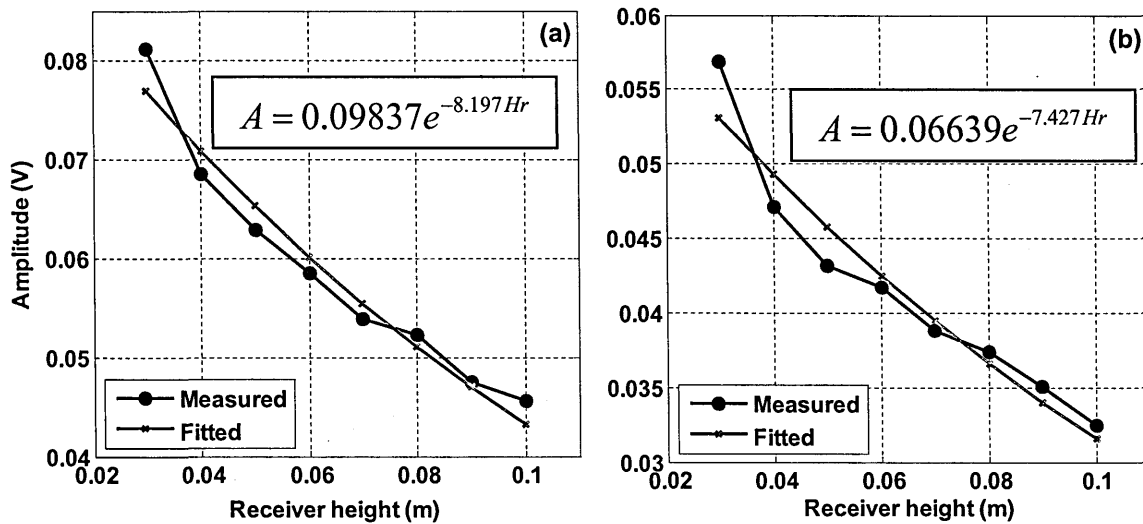
Figure 8.6 Comparison between measured surface wave amplitudes obtained from time domain signals (joined filled circles) and fitted exponential curves (red continuous lines) over a single lattice layer placed on MDF board at different receiver heights of 0.03 m, 0.04 m, 0.05 m, 0.06 m, 0.07 m, 0.08 m, 0.09 m and 0.10 m, source at height of 0.03 m and with source-receiver separation of 0.7 m. (a) First time instant (b) Second time instant.

The fitting to data is obtained using the Matlab Curve Fitting (CF) toolbox (cftool). This uses the nonlinear least-squares formulation to fit the data. The best fit using least-squares method is obtained by minimizing the sum of squared residuals, a residual being the difference between an observed value and fitted value. Exponential fitting is a non-linear problem which does not have a closed form solution. The solution for this kind of problem is obtained by iterative refinement. In Matlab, The CF toolbox provides a choice of three algorithms i.e. Trust-region, Lavenberg-Marguardt and Gauss-Newton to obtain solution for the

problems. According to the Matlab curve fitting toolbox user guide, the Trust-region algorithm is most efficient to solve the non-linear least square problems. However, for the data given in Figure 8.6, all of these algorithms give the same solution to the problem.

Figure 8.7 shows the measured EA magnitude spectra and the impedance spectra deduced from the corresponding complex EA data over single, double and triple lattice layers placed on a MDF board. The measured excess attenuation spectra show a strong surface wave below the first destructive interference i.e. below about 3 kHz. Another important property of surface wave is associated with the imaginary part (reactance) of the surface impedance. For a given impedance of a surface, if the imaginary part of the impedance is greater than the real part then that surface may support the surface wave propagation (see Section 8.4). The deduced impedance spectra shown in Figure 8.7, confirm that the imaginary part of deduced impedance is greater than the real part of impedance for single, double and triple lattice layers placed on a MDF board at the surface wave frequencies. The surface wave frequency decreases as the lattice depth is increased. For a single, double and triple layer lattice, the surface wave exists near 2.5 kHz, 1.5 kHz and 1 kHz respectively as shown by Figure 8.7.
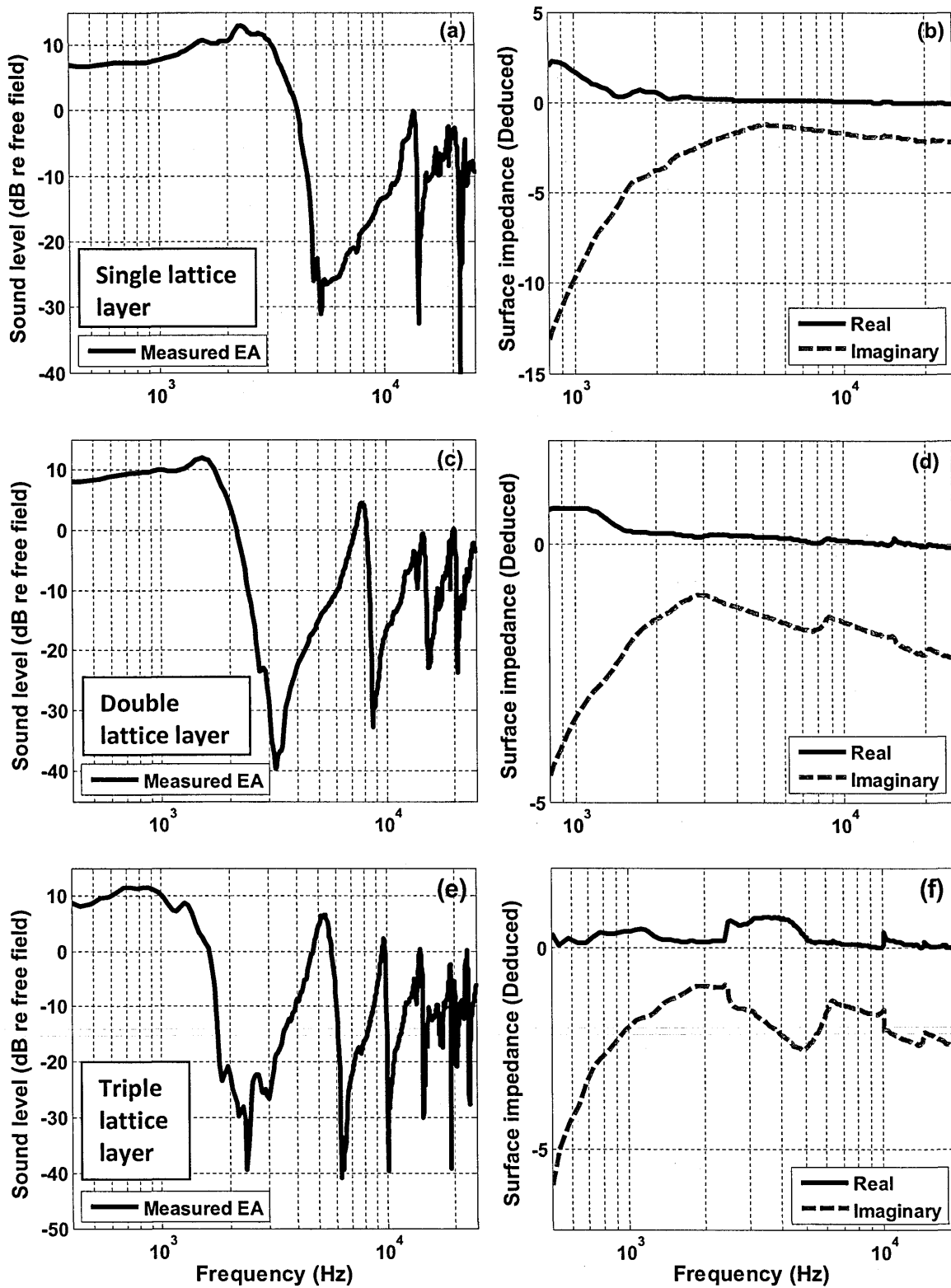
Figure 8.7 EA spectra measured over (a) single (c) double and (e) triple lattice layers placed on a MDF board for source-receiver separation of 0.7 m and source and receiver heights of 0.015 m above the top of lattice surface and (b), (d) and (f) impedance spectra deduced from corresponding complex EA data over (b) single (d) double and (f) triple lattice layers.

8.5.2 Surface wave dispersion

So far the exponential decay of the surface wave with height and its influence of EA spectra have been demonstrated. Another important property of the surface wave above a porous or rough boundary is that it travels slower than speed of sound in air.

8.5.2.1 Dispersion measurement method

Figure 8.9 shows measured surface wave dispersion over single, double

The technique used to measure surface wave dispersion was advised by Dr. od has

Ho-Chul Shin.

been used to measure the surface wave dispersion. A point source was placed very close to the lattice surface and a microphone was moved away from the source in small increments at a fixed height. The distance between source and receiver was measured, and the unwrapped phase angles of received signals were plotted against distance for each frequency point. Figure 8.8 (a) and (b) show the plots for unwrapped phase angles against the source-receiver separation at frequencies of 1.5 kHz and 5.0 kHz respectively. The linear relationship between the phase angle at a specific frequency and distance gives the wave-number, which is used to calculate the phase speed at that frequency. According to Figures 8.8 (a) and (b) respectively, the measured wave-numbers at 1.5 kHz and 5.0 kHz are 27.8 m^{-1} and 123.9 m^{-1}. The speed of sound can be calculated from,

$$c = 2\pi f / k ,$$ (8.7)

where f is the frequency and k is the wave-number. The sound speeds deduced using Eq. 8.7 are 342 m/s and 255 m/s at 1.5 kHz and 5.0 kHz respectively.
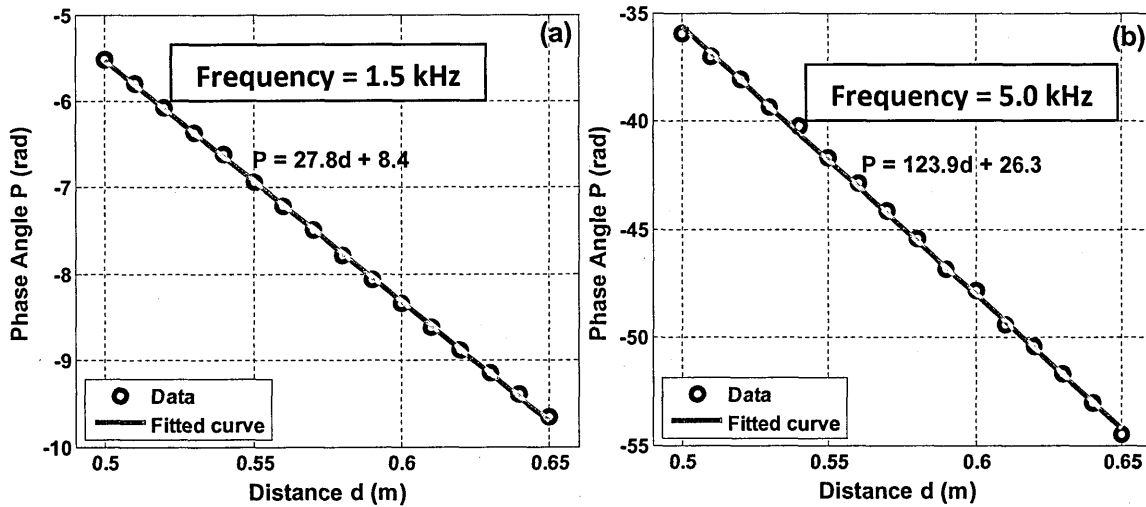
Figure 8.8 Measured phase angles at increasing source-receiver distances between 0.5 m and 0. 65 m with increments of 0.01 m. Also shown are corresponding linear fits.

8.5.2.2 Dispersion predictions

Surface wave dispersion can be predicted from the impedance of the surface on which it is propagating using [121].

$$c_p = \frac{\omega}{k_0\sqrt{1-1/Z^2}},$$ (8.8)

where Z is the impedance of the surface, k_0 is the propagation constant and ω is the angular frequency. Impedance deduced from complex excess attenuation data for single, double and triple lattice layer is shown in Figure 8.7 (b), (d) and (f) respectively. The deduced impedance can be used in Eq. (8.8) to predict the surface wave dispersion. Figure 8.9 shows measured surface wave dispersion over single, double and triple lattice layers placed on a MDF board and predictions using both square pore layer impedance (see Chapter 4, Section 4.2, Table 4.2) and the impedance spectrum deduced from fitting complex excess attenuation

data (see Chapter 4, Section 4.4.3.3). The data indicate that the surface wave travels at a speed less than the unbounded wave speed in air and that its speed decreases with increasing frequency.

The agreement between measured phase speed and that predicted using deduced impedance is better than the agreement using the predicted slit pore layer impedance (see Chapter 6, Section 6.2.2). That the measured phase speeds and those predicted using either the deduced impedance or the slit pore layer impedance significantly deviate from each other above surface wave frequency is consistent with the fact that there was little surface wave energy beyond that frequency so that the received signals were dominated by the direct arrivals. The surface wave frequencies for single, double and triple lattice layers are around 5 kHz, 3 kHz and 2 kHz respectively. Moreover the destructive interference due to roughness is around 6 kHz, 4 kHz and 3 kHz for single, double and triple lattice layers respectively. This means also that there was very little signal available near these frequencies. However, given the good agreement between dispersion data and the predictions using the deduced impedance, the latter method could be used to extrapolate the surface wave speed to higher frequencies.

8.5.2.3 A quick method for estimating surface wave dispersion

To obtain the data presented in Figure 8.9 required slow and precise movement of the receiver away from the source and measurement of excess attenuation spectra at each range. The measured data was analyzed separately at each frequency. This is a very tedious and time consuming method of measuring surface wave dispersion. In contrast, obtaining the dispersion curve from the

deduced impedance is relatively simple, efficient and quick. In this way a measurement of the excess attenuation spectrum in the laboratory can be used to obtain the surface wave dispersion. Figure 8.9 shows good agreement between surface wave dispersion measured by the phase gradient method and the surface wave dispersion obtained through Eq. 8.8 from the deduced impedance. This suggests that a method for estimating surface wave dispersion based on impedance deduced from a complex excess attenuation measurement could be a useful alternative to the phase gradient method. In the following section, the validity of the method is demonstrated further through more laboratory data.
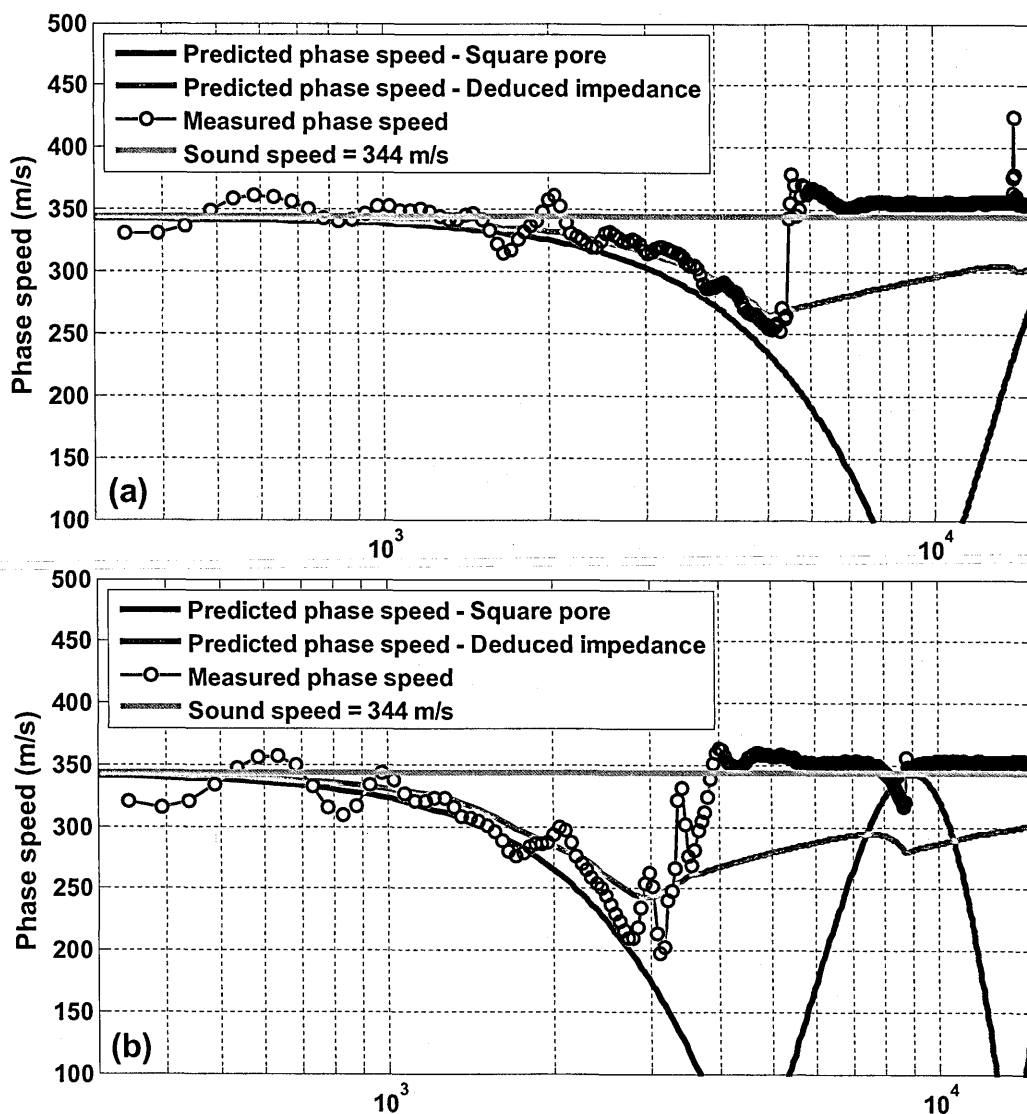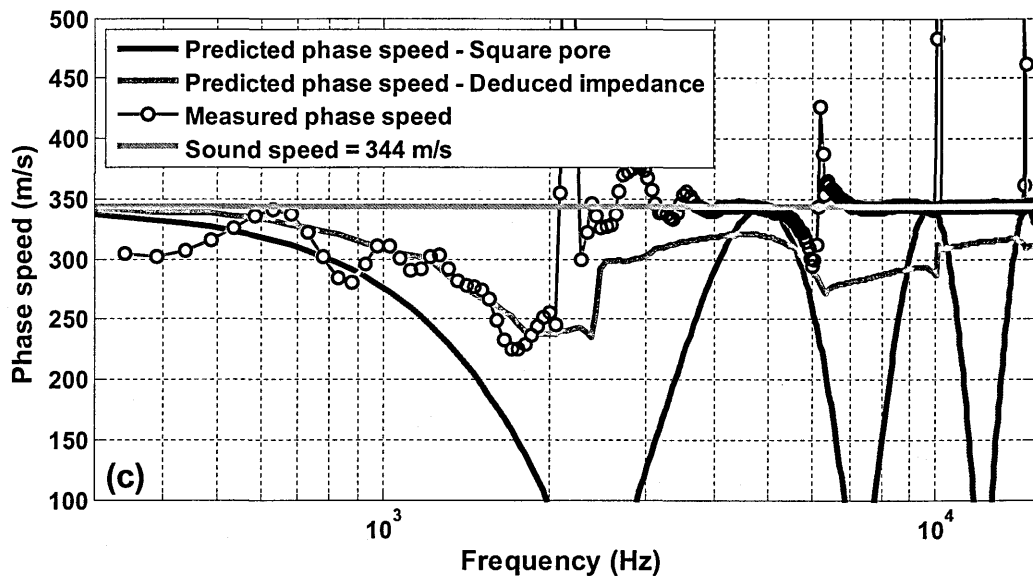
Figure 8.9 Surface wave dispersion measured using the phase gradient method (joined circles), surface dispersion estimated using impedance deduced from complex excess attenuation data (solid line) and dispersion predictions using the slit pore layer impedance and equation (8.3) over (a) single lattice layer (b) double lattice layer (c) triple lattice layer.

8.6 Surface waves over triangular strips

8.6.1 Surface wave characterization

Figure 8.10 compares measured EA spectra obtained with source and receiver at different heights and separated by 0.7 over a surface composed of periodically spaced triangular strips with centre-to-centre spacing of 0.04 m. The presence of a surface wave is indicated by an EA > 6 dB near 3 kHz. The surface wave shows exponential decay in amplitude with the increase of source-receiver heights. Figure 8.10 indicates that the strength of the surface wave depends on the source and receiver heights. There is a strong surface wave when source and receiver are at height of 0.02 m but little or no surface wave when source and receiver are at a height of 0.07 m.
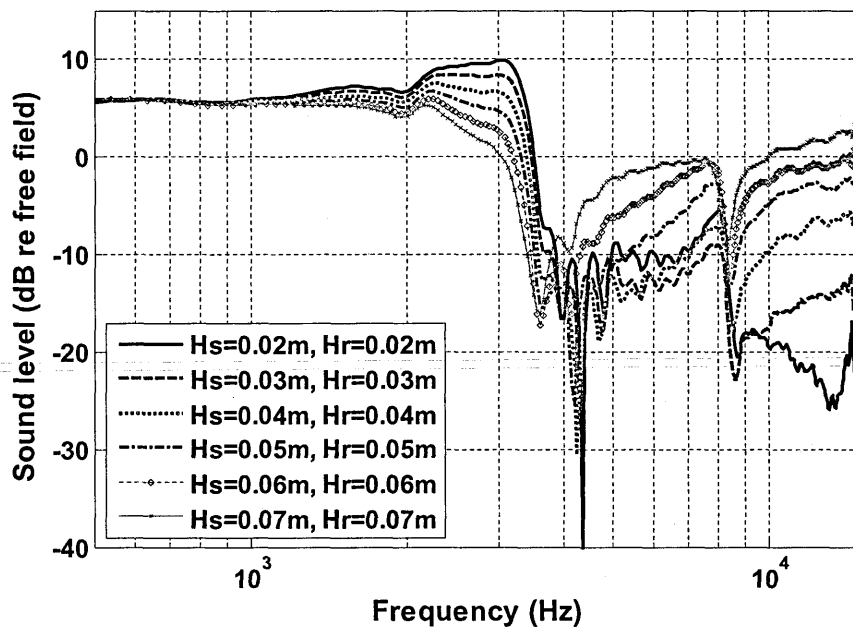
Figure 8.10 Measured EA spectra obtained over 15 triangular strips with centre-to-centre spacing of 0.04 m placed on an MDF board for source-receiver separation of 0.7 m and source-receiver heights of 0.02 m, 0.03 m, 0.04 m, 0.05 m, 0.06 m and 0.07 m.

8.6.2 Surface wave strength and roughness spacing

Figure 8.11 (a) compares the measured EA spectra with source and receiver separated by 0.7 m and at a height of 0.02 m over two different random distributions of 15 triangular strips placed over MDF board with mean centre-to-centre spacing of 0.04 m and over periodically spaced triangular strips having 0.04 m centre-to-centre spacing. Figure 8.11 (b) compares the measured EA spectra for random and periodic distributions with mean centre-to-centre spacing of 0.06 m. The periodically spaced roughness elements cause a stronger surface wave component than observed with randomly spaced elements having the same mean spacing. Figure 8.11 (c) shows the recorded time signal with source and receiver separated by 0.7 m and at a height of 0.02 m over random and periodic distributions of 15 triangular strips placed over MDF board with mean centre-to-centre spacing of 0.04 m. Time domain data shows that the surface wave propagates over both random and periodic spacing. However, the amplitude of surface wave propagating on a periodic rough surface is slightly higher than the amplitude of surface wave propagating on a randomly spaced rough surface having same mean centre-to-centre spacing between roughness elements.
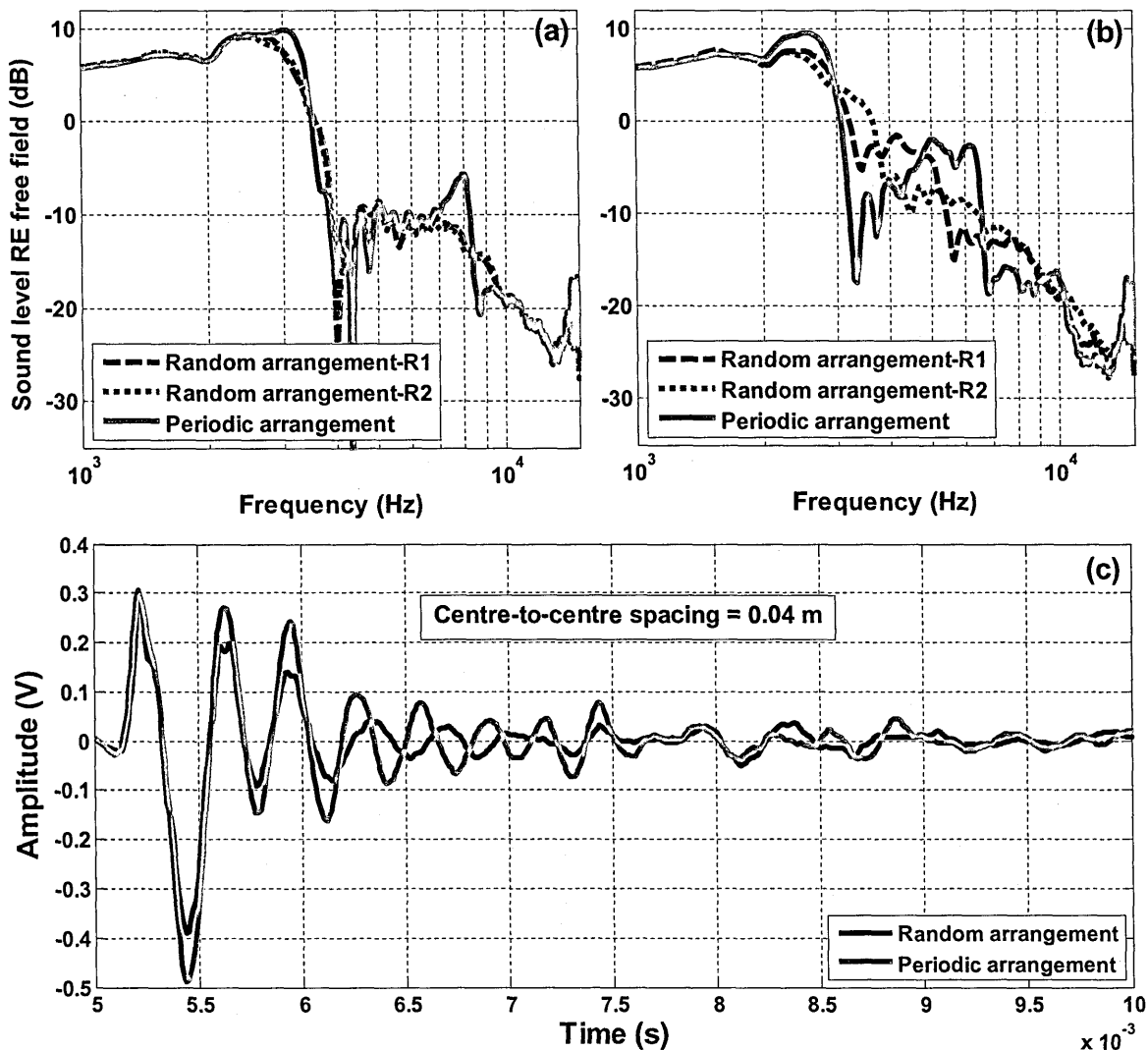
Figure 8.11 Measured EA spectra for source and receiver heights of 0.02 m separated by 0.7 m over 15 triangular strips with either random or periodic distributions (a) with (mean) centre-to-centre spacing of 0.04 m (b) with (mean) centre-to-centre spacing of 0.06 m (c) Time plot with centre-to-centre spacing of 0.04 m.

Figure 8.12 compares the measured EA spectra over triangular strips placed on MDF board with centre-to-centre spacing of 0.04 m and 0.08 m. The example measured EA spectra for triangular strips different spacings (centre-to-centre spacing of 0.04 m & 0.06 m) in Figure 8.12 show also, as might be expected; that a smaller centre-to-centre spacing produces a stronger surface waves.
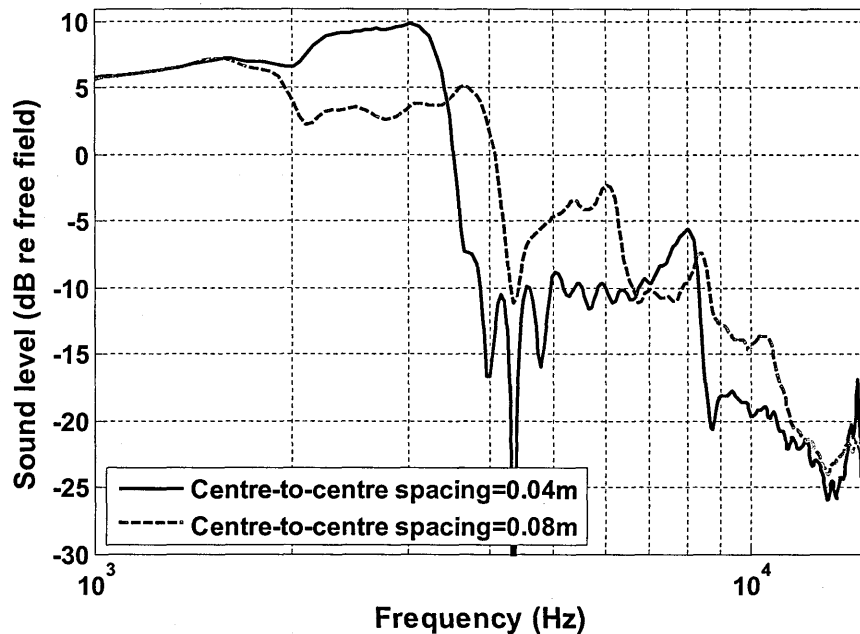
Figure 8.12 Measured EA spectra for source and receiver heights of 0.02 m separated by 0.7 m over 15 regularly-spaced triangular strips with centre-to-centre spacing of 0.04 m (continuous line) or 9 regularly-spaced triangular strips with centre-to-centre spacing of 0.08 m (broken line).

8.6.3 Surface wave dispersion

Figure 8.13 shows measured surface wave dispersion over triangular strips with centre-to-centre spacing of 0.04 m and predictions using either the heuristic surface impedance model (see Chapter 5, Section 5.6.2) or the impedance spectra deduced from complex EA data. The phase gradient method described above has been used to measure the surface wave dispersion. The agreement between measured phase speed and that predicted using the deduced impedance spectrum is better than the agreement with the prediction based on Eq. (8.6) up to 4 kHz. However, after 4 kHz the measured phase speed and phase speed predicted using either the deduced impedance or the heuristic surface impedance model significantly deviate from each other.
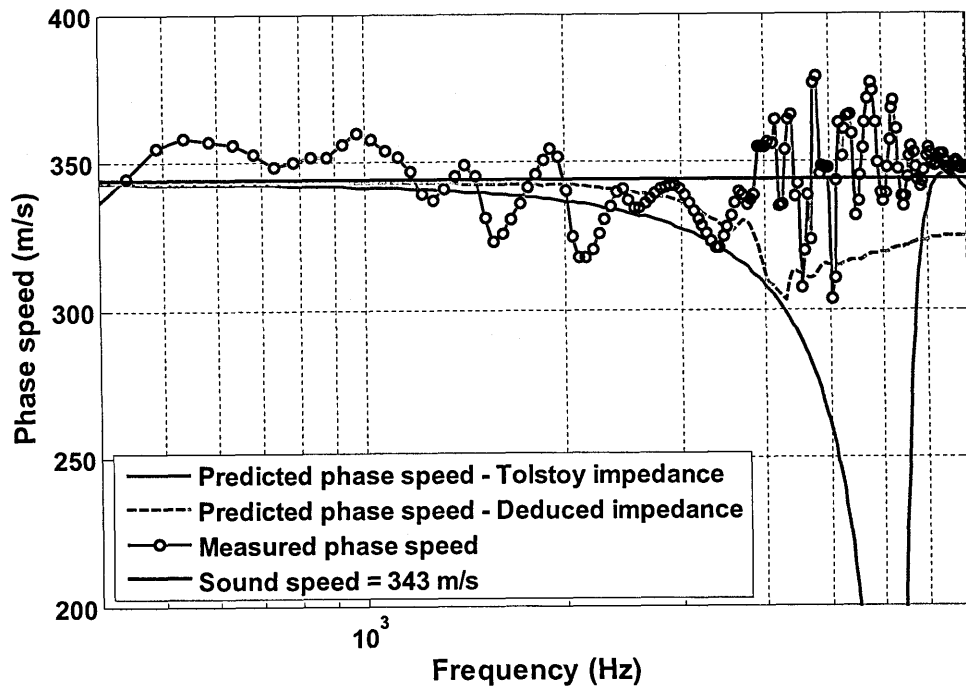
Figure 8.13 Measured surface wave dispersion (joined circles) over a surface composed of 15 triangular strips with centre-to-centre spacing of 0.04 m and predictions using the heuristic surface impedance model (see Chapter 5, Section 5.6.2), (solid line) and impedance deduced from complex EA data (broken line). The source and receiver were placed at a height of 0.015 m and their separation was increased from 0.45 m to 0.55 m in increments of 0.01 m.

8.7 Surface waves over rectangular strips

Figure 8.14 (a) compares time domain signals obtained at different receiver heights between 0.03 m and 0.15 m over a surface composed of 50 aluminum rectangular strips with edge-to-edge spacing of 0.0124 m and with the centre of the source tube located at a height of 0.045 m above the MDF board i.e. 0.02 m above the aluminum strips [125]. The plots corresponding to the lower receiver heights show a strong surface wave, whereas this feature does not appear when the receiver is in the higher location. This is consistent with the exponential decrease with height required for a surface wave. These characteristics are confirmed by Figure 8.14 (b) which shows measured excess attenuation spectra obtained with source and receiver separated by 0.7 m above a surface containing rectangular strips with edge-to-edge spacing of 0.0124 m and receiver heights between 0.03 m and 0.015 m. Below the first destructive interference frequency, the direct and reflected waves reinforce each other and the EA is +6 dB. The fact that EA > 6dB near 2 kHz indicates that a surface wave is present. Figure 8.14 (b) indicates that the strength of the surface wave depends on the receiver height. There is a strong surface wave when the receiver is at a height of 0.03 m but little or no surface wave when the receiver is at a height of 0.15 m.

Figure 8.15 compares the measured amplitudes of the surface wave arrivals obtained over aluminium strips placed on MDF board with edge-to-edge spacing of 0.0124 m at different receiver heights of 0.03 m, 0.05, 0.07 m, 0.09 m, 0.11 m, 0.13 m, 0.15 m, 0.17 m and 0.2 m. The source was at a height of 0.045 m and the source-receiver separation was 0.7 m. Figure 8.15 shows that the

amplitudes as the receiver height is increased can be fitted by an exponential decay curve of the form given by Eq. (8.6). The values for the coefficients, α and γ for exponential curve plotted in Figure 8.15 are with best fit values of 0.032 and -11.9 respectively.
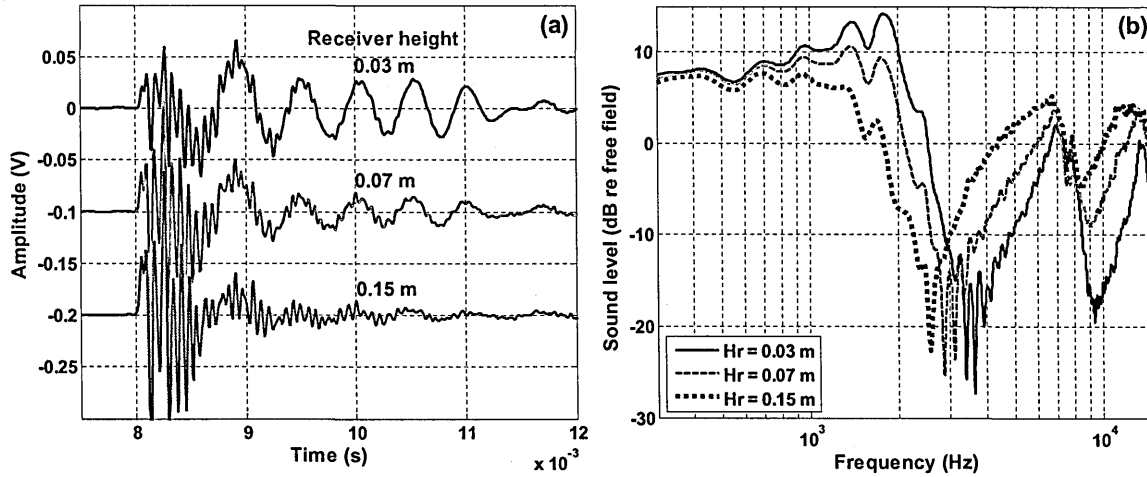
Figure 8.14 Measured data over aluminium strips placed on MDF board with edge-to-edge spacing of 0.0124 m at different receiver heights of 0.03 m, 0.07 m and 0.15 m, source at height of 0.045 m and with source-receiver separation of 0.7 m (a) received time signals (b) excess attenuation spectra. The source and receiver heights are measured with respect to the MDF board base.
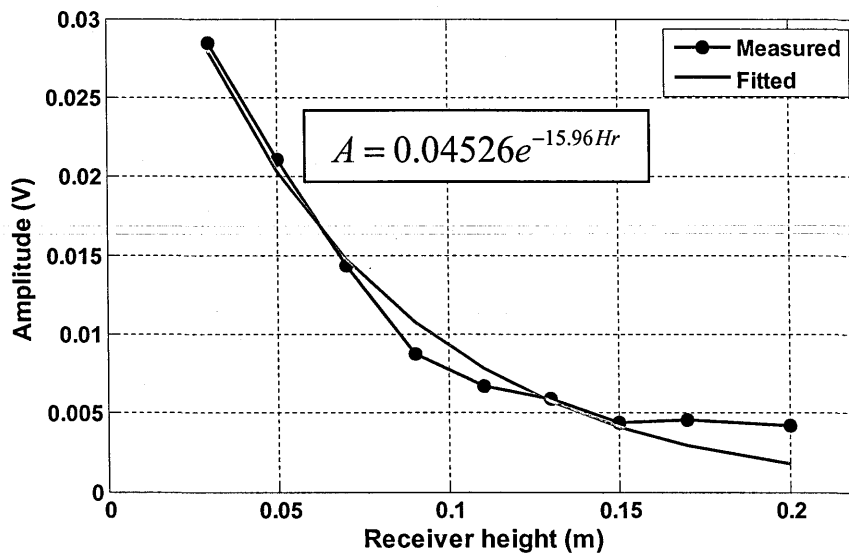
Figure 8.15 Comparison between measured amplitude for time domain surface wave (black-circle line) and fitted exponential curve (red continuous line) aluminum strips placed on MDF board with edge-to-edge spacing of 0.0124 m at different receiver heights of 0.03 m, 0.04 m, 0.05 m, 0.06 m, 0.07 m, 0.08 m, 0.09 m and 0.10 m, source at height of 0.03 m and with source-receiver separation of 0.7 m. The source and receiver heights are measured with respect to the MDF board base.

Figure 8.16 compares the EA spectra measured with source and receiver heights of 0.045 m, separated by 0.7 m over aluminium strips placed on MDF board with edge-to-edge spacings of 0.003 m, 0.0124 m, and 0.0674 m respectively. A surface wave with more or less the same amplitude is evident for all of these configurations but the frequency content of the surface wave moves to lower frequencies as the edge-to-edge spacing is increased. The change in surface wave characteristics is proportionately larger if the spacing is small.
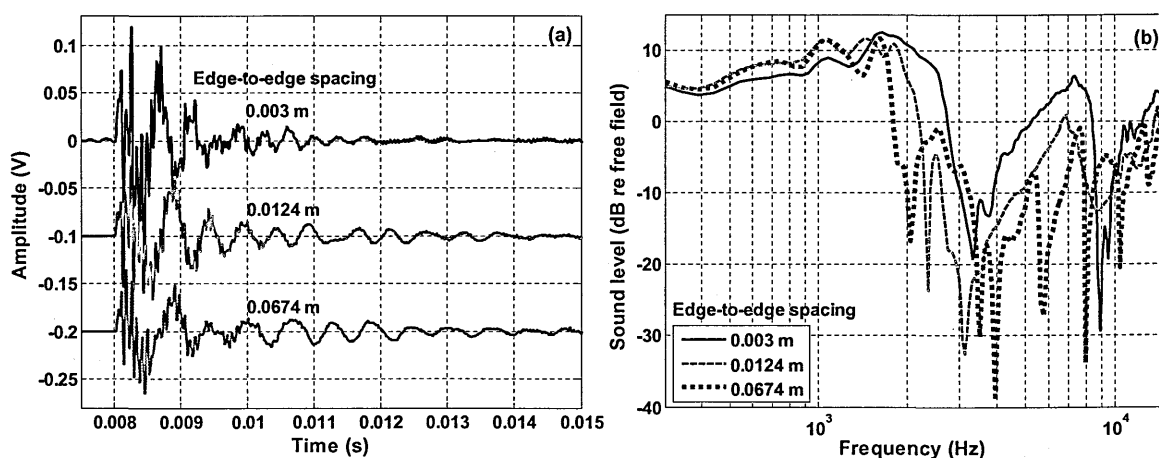
Figure 8.16 Measured amplitude for time domain surface wave over aluminium strips placed on MDF board with edge-to-edge spacing of 0.0124 m at different receiver heights of 0.03 m, 0.05, 0.07 m, 0.09 m, 0.11 m, 0.13 m, 0.15 m, 0.17 m and 0.2 m, source at height of 0.045 m and with source-receiver separation of 0.7 m. The source and receiver heights are measured with respect to the MDF board base.

Figure 8.17 shows measured surface wave dispersion over aluminum rectangular strips with edge-to-edge spacing of 0.0124 m and predictions using both slit pore layer impedance (see Chapter 6, Section 6.2.2) and impedance deduced from complex excess attenuation data see (Chapter 4, Section 4.4.3.3). A phase gradient method described above has been used to measure the surface wave dispersion. Overall the data and predictions are consistent with analysis

given above. Aluminum strips with edge-to-edge spacing of 0.0124 m shows surface waves near 2 kHz with a minimum phase speed of near 280 m/s.
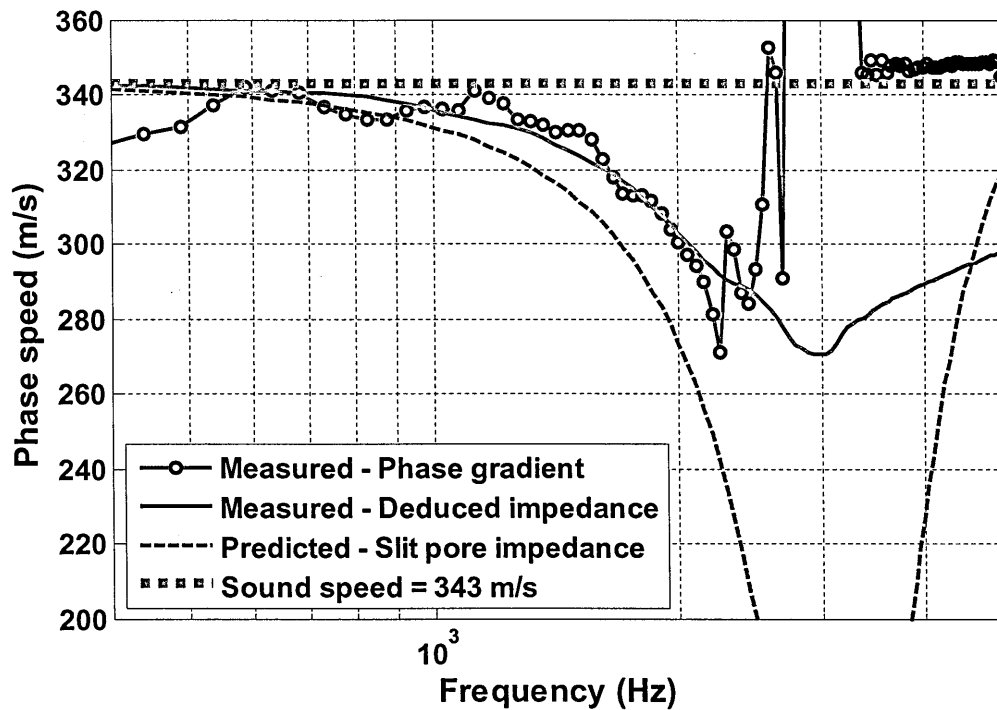
Figure 8.17 Measured surface wave dispersion (joined circles) over aluminum rectangular strips with edge-to-edge spacing of 0.0124 m and impedance deduced from complex excess attenuation data (solid line) and predictions using the slit pore layer impedance model (see Chapter 6, Section 6.2.2).

8.8 Surface waves over porous surfaces

Kelders *et al.* [116], [117] studied surface waves above thin porous layers of plastic foams having very high porosity values. Through experimental work, they [128] proved the surface wave's existence over thin porous layers of foams and that its phase speed is lower than the speed of sound in air. Most of experimental work over surface wave propagation given in literature was carried out in the laboratory. However, Albert [129] has observed an audio-frequency surface wave outdoors over snow covered ground using impulsive sound source and successfully confirmed the surface wave properties such as exponential decay and a phase speed slower than the speed of sound.

So far surface waves over different kinds of rough surfaces have been studied. In this section, the work has been extended to study surface wave propagation over porous layers. Thin layers of porous foams were used in this study. They are more likely to have the imaginary part of the impedance greater than the real part. These kinds of impedance surfaces support the generation and propagation of surface waves (see Section 8.4). Different kinds of polyurethane foams have been used for this study. Five sample foams include two different types of foam with three thicknesses. These foams have different thicknesses such as 0.051 m, 0.027 m, 0.025 m, 0.012 m and 0.012 m and porosity values near to 1. The foam layers having similar thickness have different properties is that one type of foam is slightly stiffer than the other type. Measurements have been carried out by placing the layers of foam on an acoustically hard MDF board (see Figure 8.18).
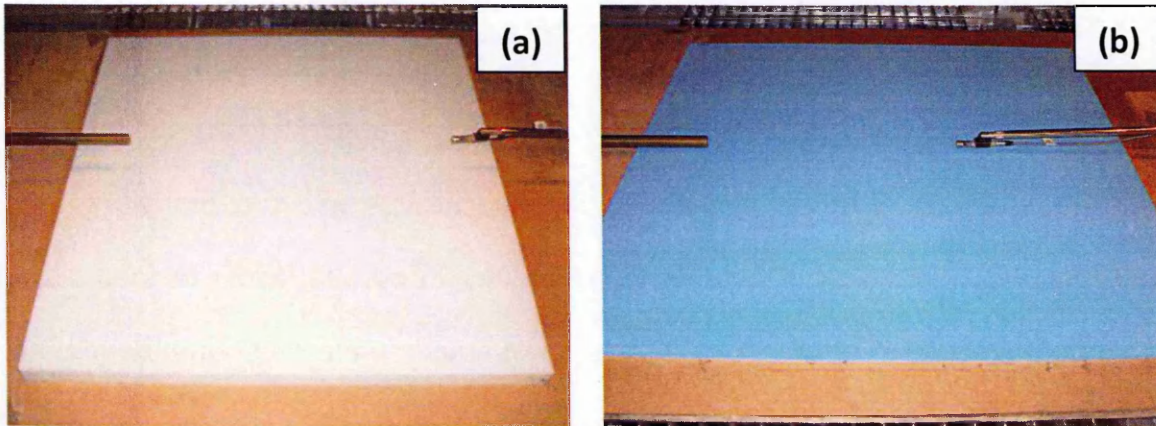
Figure 8.18 Photograph for measurement arrangements over foam placed on MDF board (a) Foam thickness = 0.051 m (b) Foam thickness = 0.012 m.

Figure 8.19 (a) shows the measured time signals and Figure 8.19 (b) shows the measured excess attenuation spectra over five different types of foams having thicknesses of 0.051 m, 0.027 m, 0.025 m, 0.012 m and 0.012 m placed on MDF board. The source and receiver were placed at heights of 0.015 m above foams with source-receiver horizontal separation of 0.7 m. All these foams have a porosity of 98 %. Very little or no surface wave is present over the foam with thickness of 0.051 m. As the foam thickness decreases there is slight increase in surface wave generation and propagation. The porous foam having thickness of 0.012 m gives the strongest surface wave as shown in Figure 8.19. The type of foam appears to have no effect over surface wave propagation. However, the excess attenuation spectra differ a little between the two foam types. The major factor which effects the surface wave propagation is the foam thickness. The surface wave frequency decreases as the foam thickness is increased. For a 0.012 m, 0.025 m and 0.05 m thick foams, the surface wave exists near 1.5 kHz, 700 Hz and 400 Hz respectively. This effect of thickness is similar to that observed over lattice layers.
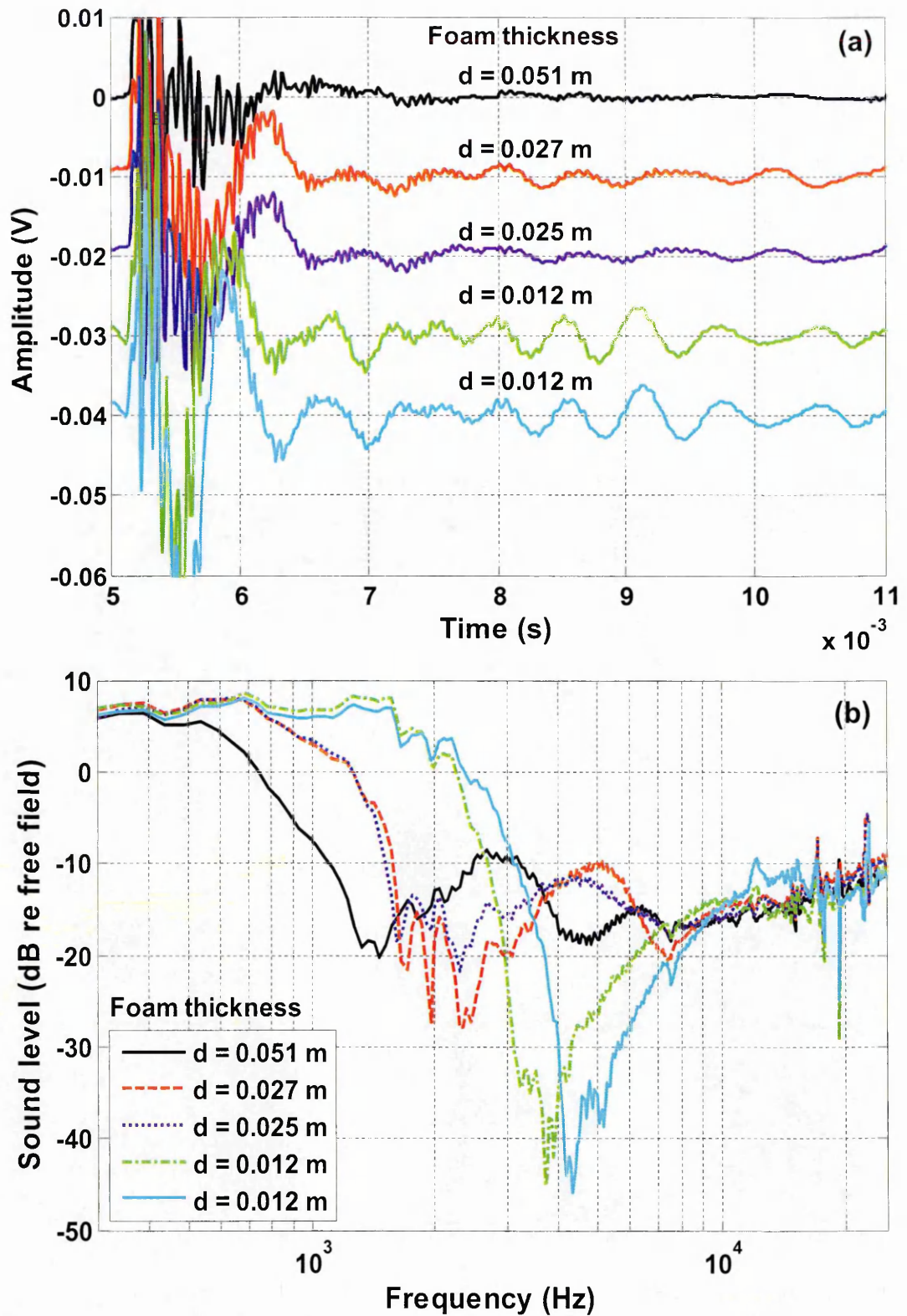
Figure 8.19 Measured data over five different kinds of foam having different thickness placed on a MDF board with source and receiver at height of 0.015 m above foam and source-receiver separation of 0.7 m (a) received time signals (b) excess attenuation spectra.

8.9 Surface wave attenuation in the laboratory

The fact that surface waves attenuate with the square root of the distance from the source may have a negative effect on the insertion loss obtained through parallel wall arrangements (see Section 8.2). Laboratory experiments have been carried out to investigate different ways of reducing surface waves. In this section, the surface wave attenuation due to the addition of sound absorbing materials in between the walls has been investigated.
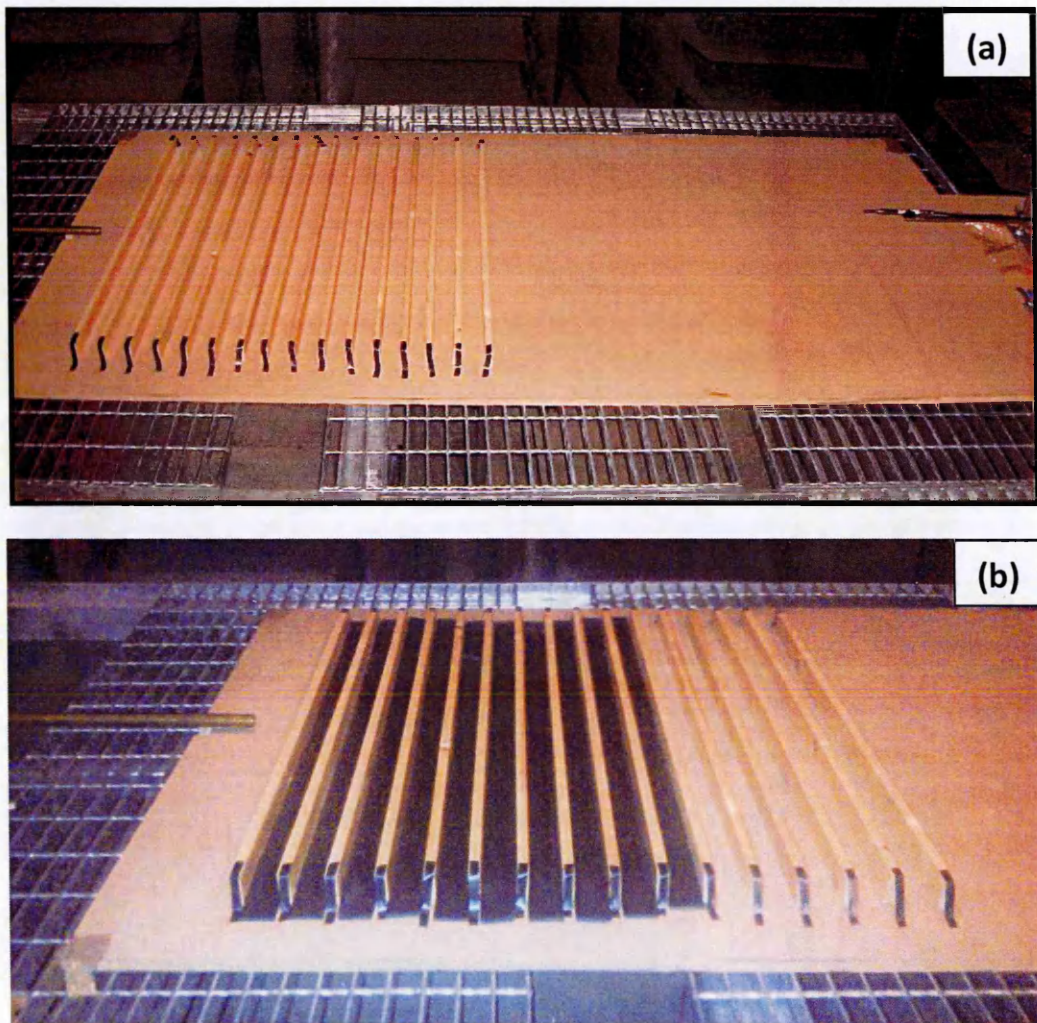
Figure 8.20 Photograph of an array of 16 parallel wooden strips spaced regularly on an MDF board (b) Absorbing material in between the walls.

Figure 8.20 (a) shows laboratory measurement arrangements over parallel wooden strips. The distance between source and first wall is 0.08 m; the receiver is placed at a distance of 2.0 m and at a height of 0.1 m above MDF board. Due to geometrical and finite size restrictions the minimum possible point source height in the laboratory was 0.02 m above MDF sheet (the lower source tube edge was just 3 mm above MDF board). The rectangular wooden strips used in this study are 0.044 m high, 0.015 m wide and 1.0 m long. Sixteen rectangular strips were placed on a MDF board with periodic centre-to-centre spacing of 0.06 m.

Measurements have been made to investigate the effects of adding absorption between parallel wooden strips (see Figure 8.20). Figure 8.21 (a) shows the received time signal and Figure 8.21 (b) shows measured excess attenuation spectra over the parallel wooden strip arrangement shown in Figure 8.20 (a). A very strong surface wave exists between 500 and 2 kHz as shown by time domain signal in Figure 8.21 (a) and the frequency range over which the excess attenuation spectra > +6 dB in Figure 8.21 (b). Figure 8.21 also compares the measured data with and without adding absorption in the form of layers of felt placed between the parallel strips. Different configurations and combinations of felt strips have been used to determine the best possible solution for attenuating the surface waves. Figure 8.21 compares data without (continuous black line) and with a single layer of felt (broken red line) introduced in between the first three wooden strips. Figure 8.21 shows that the surface wave gets attenuated slightly with the introduction of absorbing material. A further increase in the number of spaces between strips into which absorbing material is introduced gives more surface wave attenuation. Figure 8.22 shows data from measurements for which all 15

gaps between the strips were filled with a single layer of felt. The tail of pulse time trace and excess attenuation spectra near 1 kHz is modified by absorbing material in between the walls. Figure 8.23 shows data for which the 14 felt strips are used to create a double layer of absorbing material between the first eight walls i.e. seven spaces filled with a double layer of felt. The strips were used also to create triple layers of absorbing material between the first five strips. The greatest surface wave attenuation was obtained by filling the first eight gaps with double layers of felt. Each felt strip is 0.012 m thick compared with the wooden strip height of 0.044 m. So single, double and triple layers of felt fill the gaps by 27 %, 54 % and 80 % respectively. It is concluded that, the surface wave can be attenuated by introducing absorbing material in between parallel walls without affecting the other 'beneficial' parts of the excess attenuation spectra. The maximum attenuation of surface wave is achieved by filling up to 50 % of the spaces between the walls with absorbing material (see Figure 8.23).
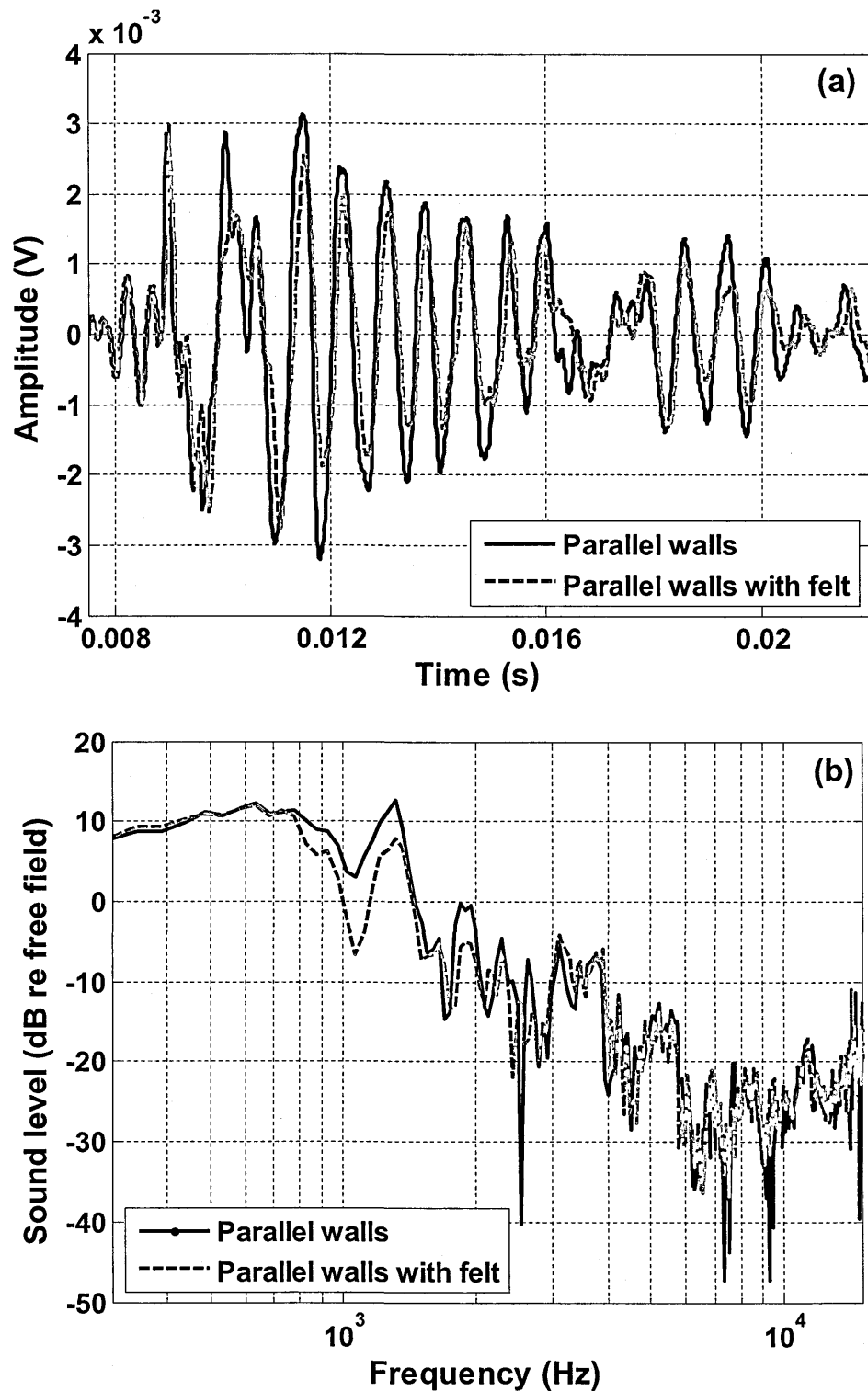
Figure 8.21 Time- and frequency-domain data obtained in the laboratory obtained over 16 parallel wooden strips (0.044 m (H) × 0.012 m (W), 0.06 m centre-to-centre) starting 0.08 m from the source; source height 0.02 m; receiver height 0.1 m and source-receiver separation of 2.0 m without (continuous black line) and with (broken red line) absorbing material in between the walls (a) received time signals (b) excess attenuation spectra. A single layer of absorbing material (felt) was introduced in between first three strips.
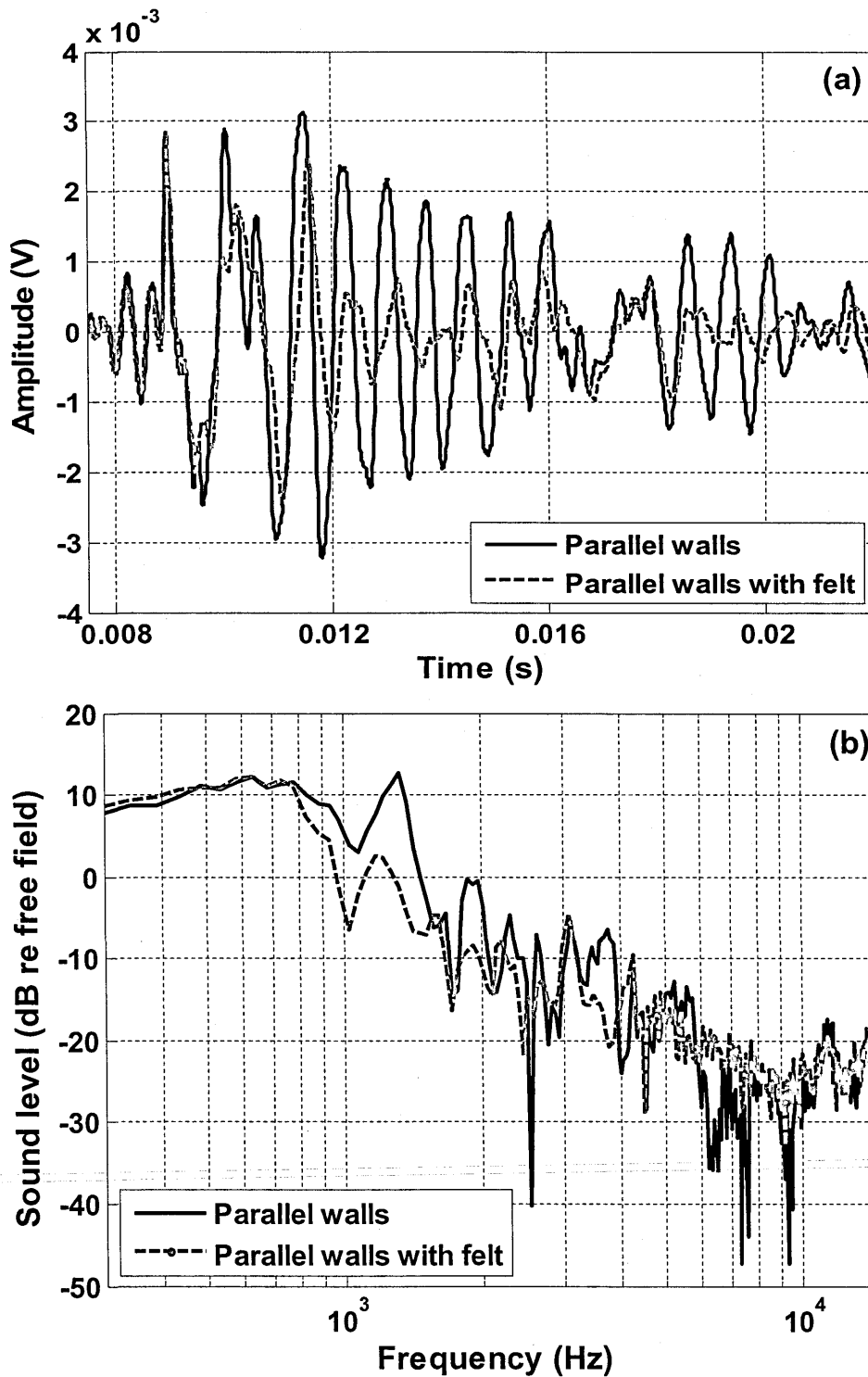
Figure 8.22 Time- and frequency-domain data obtained in the laboratory obtained over 16 parallel wooden strips (0.044 m (H) × 0.012 m (W), 0.06 m centre-to-centre) starting 0.08 m from the source; source height 0.02 m; receiver height 0.1 m and source-receiver separation of 2.0 m without (continuous black line) and with (broken red line) absorbing material in between the walls (a) received time signal (b) excess attenuation spectra. A single layer of absorbing material (felt) was introduced in between all sixteen strips.
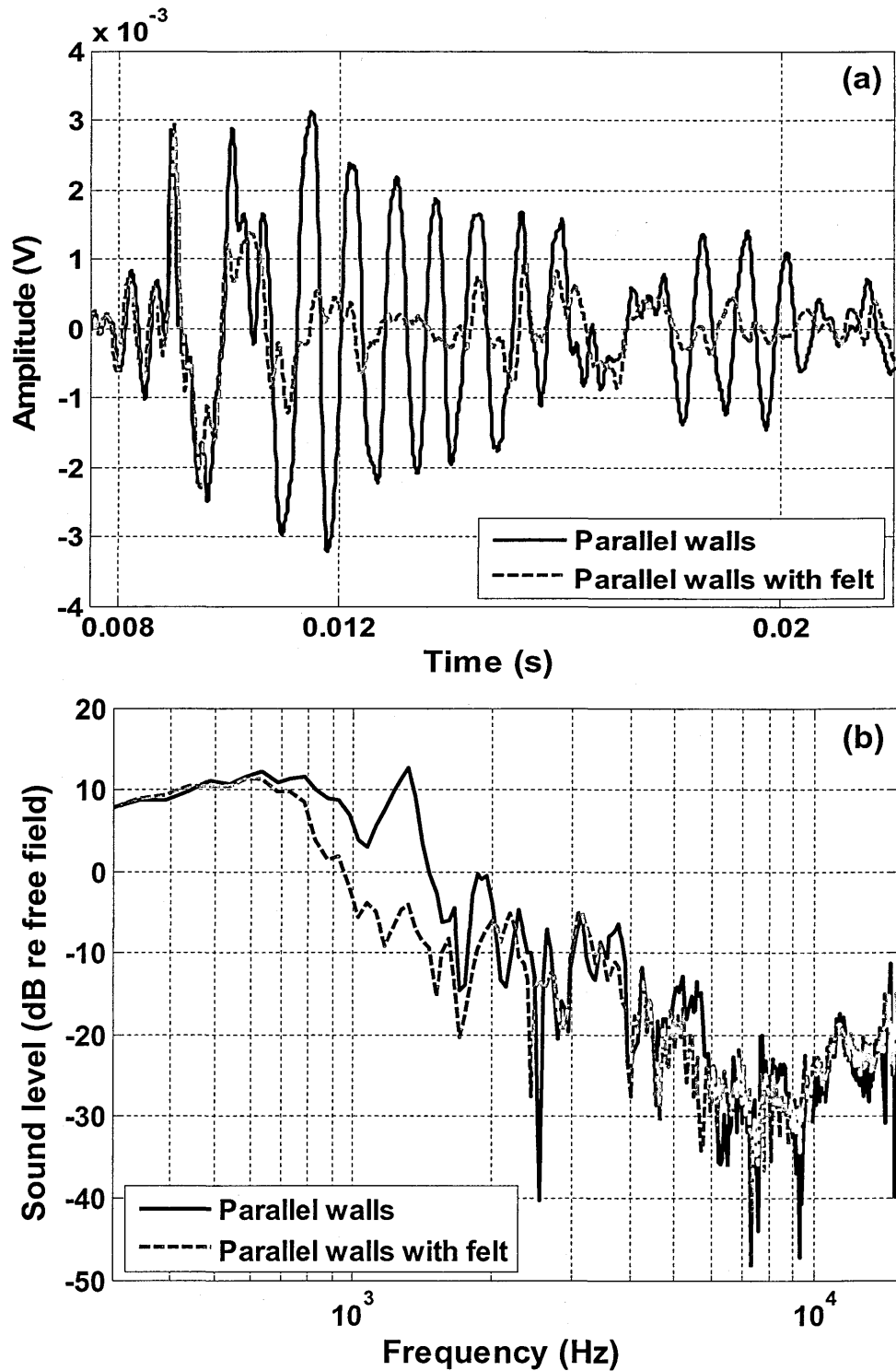
Figure 8.23 Time- and frequency-domain data obtained in the laboratory over 16 parallel wooden strips (0.044 m (H) × 0.012 m (W), 0.06 m centre-to-centre) starting 0.08 m from the source; source height 0.02 m; receiver height 0.1 m and source-receiver separation of 2.0 m without (continuous black line) and with (broken red line) absorbing material in between the walls (a) received time signal (b) excess attenuation spectra. A double layer of absorbing material (felt) was introduced in between eight strips.
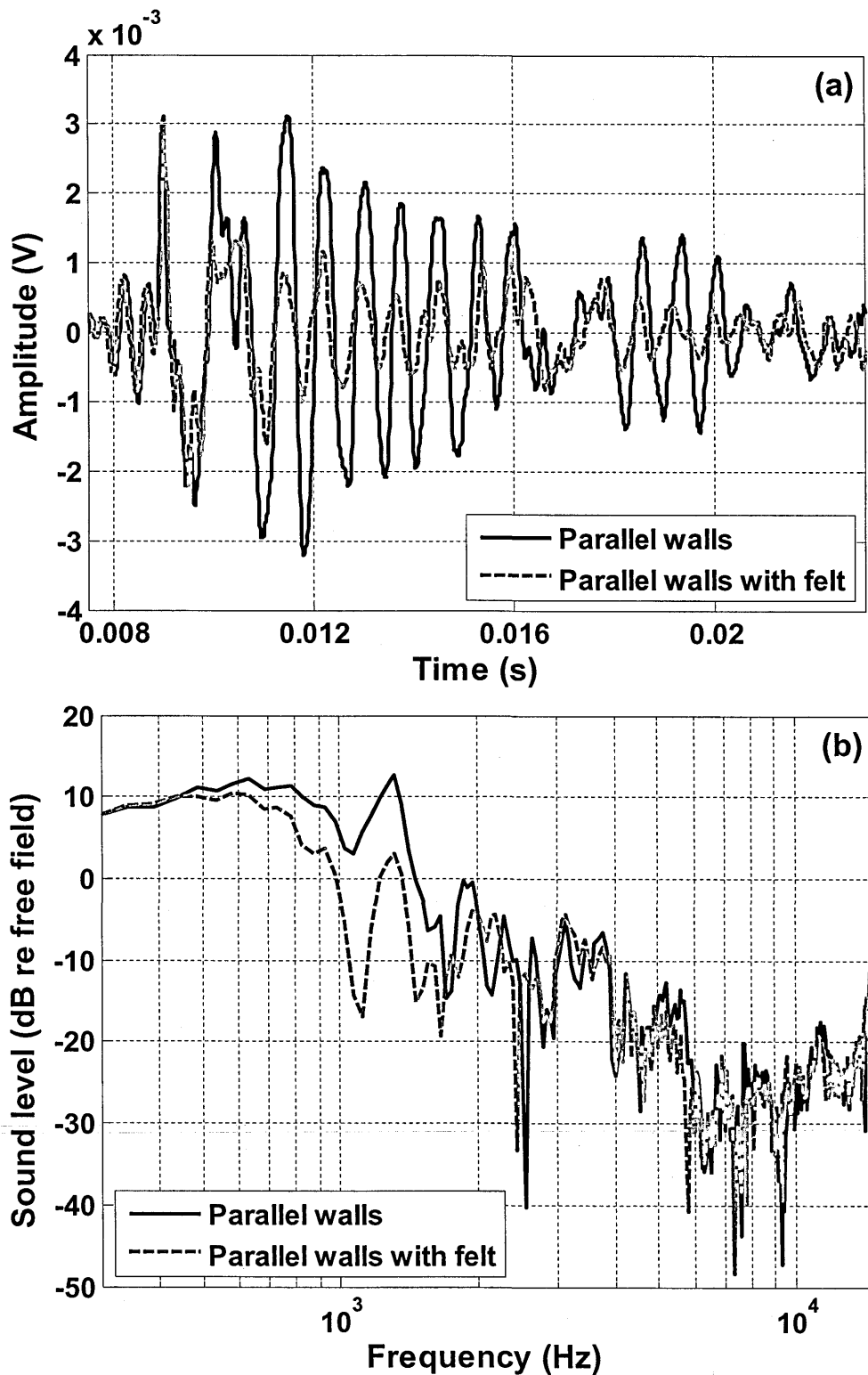
Figure 8.24 Time- and frequency-domain data obtained in the laboratory over 16 parallel wooden strips (0.044 m (H) × 0.012 m (W), 0.06 m centre-to-centre) starting 0.08 m from the source; source height 0.02 m; receiver height 0.1 m and source-receiver separation of 2.0 m without (continuous black line) and with (broken red line) absorbing material in between the walls (a) received time signal (b) excess attenuation spectra. A triple layer of absorbing material (felt) was introduced in between five strips.

8.10 Surface waves attenuation predictions over larger scale parallel walls

Surface waves propagating over parallel walls may reduce the insertion loss. Surface waves can be attenuated by including absorbing surfaces as concluded from laboratory data (see Section 8.9). Figure 8.25 gives the comparison between BEM predicted excess attenuation due to a 3.05 m wide and 0.3 m high parallel wall array, consisting of 16 x 0.05 m thick walls with 0.2 m centre-to-centre spacing with source at height of 0.01 m and receiver at a distance of 50 m and at height of 1.5 m above ground. Figure 8.25 (a) compares the predicted excess attenuation spectra over acoustically hard walls on acoustically hard ground, while the gaps were filled with gravel having different depths. Figure 8.25 (a) also gives the excess attenuation spectra for acoustically hard walls on a semi-infinite gravel ground. Table 8.1 summarizes the predicted insertion losses due to parallel walls along a two lane urban road with gaps filled with gravel of different depths. The gravel impedance is calculated by using slit pore model with a flow resistivity of 10 kPa s m^{-2} and porosity of 0.5 (for details see Chapter 4). The surface waves get attenuated by filling the gaps in between the walls over hard ground with acoustically soft material such as gravel. The insertion loss for a receiver placed at a distance of 50 m from the source and at height of 1.5 m due to a two lane urban road over a 3.05 m wide and 0.3 m high parallel wall array over a hard ground surface is 6.7 dB. However, filling the gap between the walls with 0.05 m deep gravel improves the insertion loss up to half a dB. Further increase in gravel depth up to 0.1 m and 0.15 m gives the insertion losses of 7.2 dB and 7.5 dB respectively. Further increase in filling up the cavity with gravel between the

walls reduces the surface waves. However, it also reduces the depth of first excess attenuation maximum as shown in Figure 8.25 (a). It is concluded that there is not any significant improvement in insertion loss by filling more than 50% of the cavity-gaps between the walls. BEM predictions are repeated by assuming the gravel is semi-infinite. It is found that there is an improvement of nearly a dB for a receiver at a distance of 50 m from the source and at a height of 1.5 m.

Figure 8.25 (b) compares the predicted excess attenuation spectra over acoustically hard walls on acoustically hard ground and acoustically hard walls on different kinds of ground surfaces. Table 8.2 summarizes the predicted insertion losses due to parallel walls along a two lane urban road placed on different ground types such as gravel, porous concrete, long grass, lawn and pasture land. The ground surfaces are modelled as semi-infinite using the slit pore impedance model (for details see Chapter 4). The ground type with lowest flow resistivity value results is the greatest surface wave attenuation.

Figure 8.25 (b) also shows the predicted effects of making the walls from porous concrete rather than a relatively acoustically-hard material. The surface wave is predicted to be much reduced and the first excess attenuation maximum is predicted to be broadened and deepened. Since the surface wave is predicted to occur at relatively low frequencies, after A-weighting the predicted improvement in insertion loss from attenuation of the surface wave is limited to 1 dB.

Table 8.1 Predicted insertion losses due to parallel walls along a two lane urban road (see Chapter 11) with the gaps between the walls filled with gravel of different depths to attenuate surface waves.

Gap in-between Hard-walls filled with Gravel	Range (m)	Receiver height (m)	Insertion for two lane urban road (dB)				
			No Gravel	Gravel depth (Slit pore model parameters for gravel (see chapter 4): Flow resistivity = 10 kPa s m^{-2}, Porosity = 0.5)			
				0.05 m	0.10 m	0.15 m	0.20 m
Hard backed layer	10	0.3	8.6	9.4	9.9	10.4	10.6
Semi-infinite				10.9	10.8	10.7	10.7
Hard backed layer	50	1.5	6.7	7.1	7.2	7.5	7.6
Semi-infinite				7.6	7.5	7.6	7.6
Hard backed layer	50	4.0	5.6	5.9	6.0	6.2	6.3
Semi-infinite				6.3	6.3	6.3	6.3

Table 8.2 Predicted insertion losses for two lane urban road (see Chapter 11) to reduce surface wave propagation.

Range (m)	Receiver height (m)	Insertion for two lane urban road (dB)						
		Hard in-between walls		Gap in between filled with different materials (Slit pore model parameters for different materials are given (see chapter 4))				
		Hard walls	Porous concrete walls (R_s=100 kPa s m^{-2}, Ω=0.5)	Gravel (R_s=10 kPa s m^{-2}, Ω=0.5)	Porous concrete (R_s=100 kPa s m^{-2}, Ω=0.5)	Long grass (R_s=104 kPa s m^{-2}, Ω=0.36)	Lawn (R_s=176 kPa s m^{-2}, Ω=0.5)	Pasture (R_s=1344 kPa s m^{-2}, Ω=0.5)
10	0.3	8.6	11.4	11.0	10.2	10.1	10.0	9.4
50	1.5	6.7	7.9	7.6	7.3	7.3	7.2	7.0
50	4.0	5.6	6,5	6.3	6.1	6.1	6.0	5.8
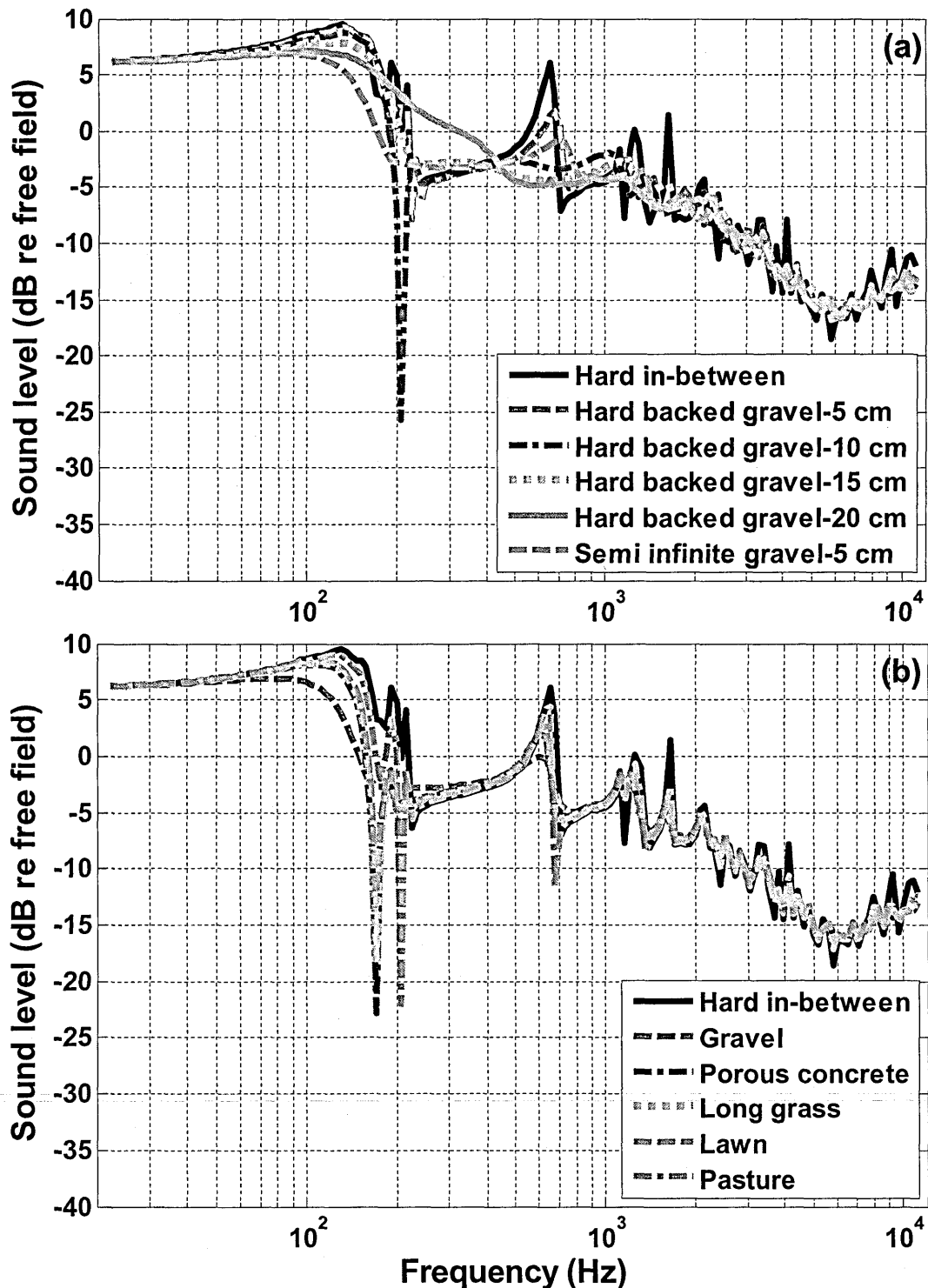
Figure 8.25 Comparison between BEM predicted excess attenuation spectra due to a 3.05 m wide and 0.3 m high parallel wall array, consisting of 16 × 0.05 m thick walls with 0.2 m centre-to-centre spacing with source at height of 0.01 m and receiver at a distance of 50 m and at height of 1.5 m (a) acoustically-hard walls on acoustically-hard ground or with 0.05-0.2 m deep hard-backed layer gravel between the walls and with semi-infinite gravel between the walls (b) acoustically-hard walls on acoustically-hard ground or with semi-infinite different ground types between the walls such as gravel, porous concrete, long grass, lawn and pasture land (see Chapter 4).

8.11 Conclusions

Surface wave propagation over rough and porous surfaces has been studied in this chapter. The rough surfaces include a lattice surface, randomly and periodically spaced triangular strips, rectangular strips in the laboratory and larger-scale parallel walls through numerical predictions. The surface wave frequencies for single, double and triple lattice layers are around 5 kHz, 3 kHz and 2 kHz respectively. The surface wave shows exponential decay with height over a lattice surface and travels slower than speed of sound. The deduced impedance spectra for single, double and triple lattice layers show that the imaginary part of the impedance is larger than the real part. The measured surface wave dispersion shows that the surface wave speed decreases with frequency and can be as low as 300 m/s. Surface waves have been investigated also over rough surfaces created by placing arrays triangular strips and rectangular strips over a MDF board. The frequency content of the surface waves was found to decrease as the spacing was increased. This implies a common mechanism for generating the 'elliptical' particle motion associated with surface waves through the combination of 'vertical' motion of air particles in and out of the spaces between the solid strips and 'horizontal' motion associated with sound incident near grazing. For an edge-to-edge spacing (slit width) of 0.0124 m the surface wave dispersion is predicted better using surface impedance spectra deduced from complex excess attenuation data than by using the equivalent slit-pore layer impedance. This suggests that surface wave dispersion can be measured straightforwardly by using the deduced impedance. Surface waves can also be generated over a randomly spaced rough

surface. However, the strength of surface wave propagation over a periodically spaced rough surface is stronger than randomly spaced rough surface.

The study of surface waves characteristics over foams placed on MDF board shows that the thin porous foam layers support stronger surface wave propagation than a thick porous foam layers and that the surface wave frequency decrease with increasing layer thickness.

The generation of surface waves over rough surfaces has a negative effect on insertion loss. The surface wave over laboratory parallel walls can be attenuated by placing absorbing material such as felt in between the walls. The maximum attenuation of surface wave due to felt is achieved by filling up to 50 % of the spaces between the walls. Investigation of surface wave propagation over larger scale parallel walls has been carried out using BEM. The ground type with lowest flow resistivity value (representing gravel) is predicted to give the greatest surface wave attenuation. Since the surface wave is predicted to occur at relatively low frequencies, after A-weighting the predicted improvement in insertion loss from attenuation of the surface wave is limited to about 1 dB. There is not any significant improvement in insertion loss by filling the spaces between the walls with gravel by more than 50 %.

Chapter 9

9. Sound transmission through low filling fraction arrays of identical rigid cylinders perpendicular to the ground

9.1 Introduction

In recent years, the interest in an alternative to road traffic noise barriers has increased. Lots of research has been carried out to investigate and improve the attenuation performance of sonic crystal arrays to be used as noise barriers. The sonic crystal is a periodic arrangement of, for example, cylindrical tubes. As a result of multiple scattering, sonic crystals exhibit a selective sound attenuation in frequency bands called band gaps or stop bands related to the spacing and size of the cylinders. Most of previous studies have considered sonic crystals alone i.e. in

free space. However, if the sonic crystal meant to be used as a noise barrier, then the effect of ground cannot be ignored. The ground surface plays a significant role in noise attenuation. In this chapter, the combined effect of a sonic crystal array and the ground surface has been investigated. A sonic crystal was constructed in laboratory consisting of cylindrical tubes with their axes perpendicular to the ground surface. The effect of disturbing the periodicity of sonic crystal has also been investigated.

The major aim of this study is to investigate different planting schemes. The extent to which perturbing a periodic arrangement can improve traffic noise attenuation due to tree plantation is investigated. This involves the study of low filling fraction arrays as the trees cannot be planted very close to each other.

This first section gives an introduction and the second section presents a literature review. The third section describes the study of propagation through sonic crystals placed on a ground surface. This section also presents comparisons between data and predictions. Section 4 investigates the effect of aperiodicity on sound transmission through a sonic crystal. Section 5 presents data obtained over a random sonic crystal and section 6 compares results obtained with the various configurations. Conclusions are given in section 7.

9.2 Literature review

9.2.1 Theory and Principles for scattering of sound from array of cylinders

A sonic crystal is a periodic structure that allows sound to pass through in certain frequency bands and prohibits sound transmission in other bands. The structure acts like stop-band and pass-band filters. The sonic crystal is usually made of rigid circular cylinders. The ability of sonic crystal to stop and pass sound at certain frequencies depends on the centre-to-centre spacing between the cylinders and on the filling fraction. In crystallography, a unique arrangement of atoms, which repeats itself in a long-range pattern and symmetry, is called a lattice. A lattice structure which looks exactly the same when viewed from any lattice point is called a 'Bravais Lattice'. Applying the Bravais principle, only five 2D lattice patterns are possible: Square, Oblique, Rectangular, Centred rectangular, and Hexagonal. The five possible Bravais lattice arrangements are shown in Figure 9.1 (a). A lattice is made by repetition of a unit cell, which is the smallest sub-array in a crystal structure containing one or more elements in a specific spatial arrangement as shown in Figure 9.1 (b). The centre-to-centre spacing between two elements placed next to each other is called the lattice constant. The filling fraction is the ratio between the volume occupied by an element to the total volume occupied by a unit cell. In a lattice structure the lattice constant and the size of the elements are used to determine its filling fraction.

$$FillingFraction = \frac{VolumeOfSingleElement}{TotalVolumeOfUnitCell},$$ (9.1)
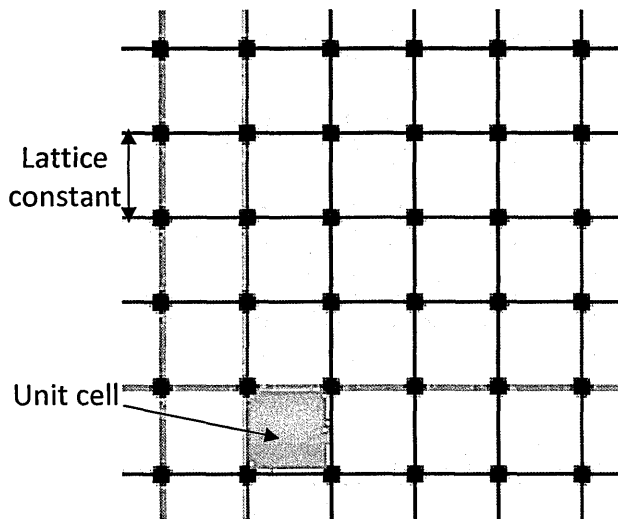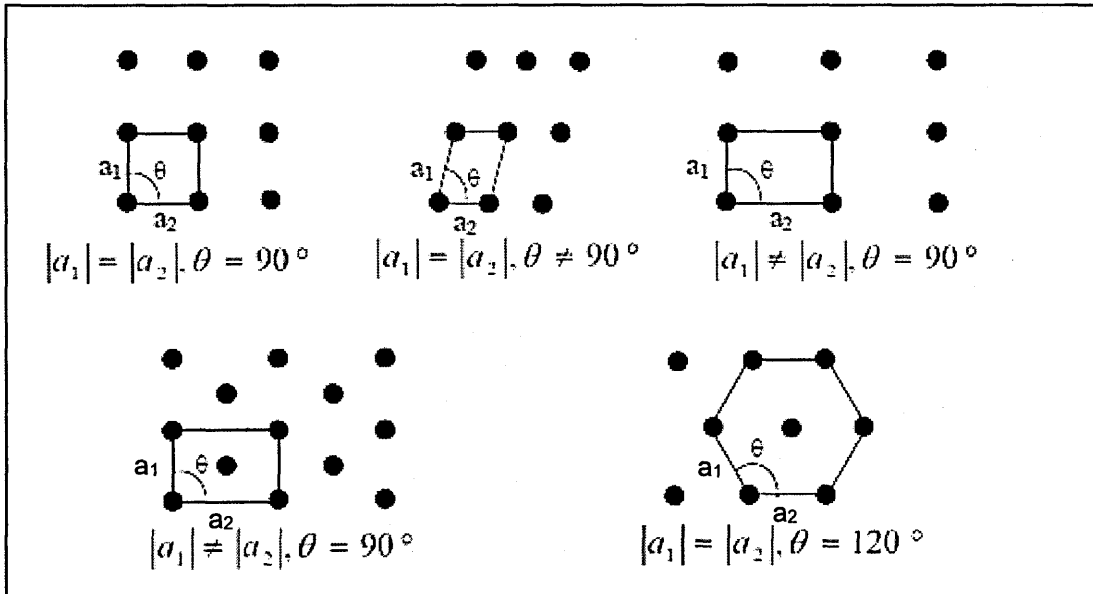
Figure 9.1 (a) The five fundamental 2-Dimensional Bravais lattices: Square, Oblique, Rectangular, Centred rectangular and Hexagonal (Triangular is a special case of Hexagonal) (b) Square lattice arrangement (shaded area shows a unit cell).

W. L. Bragg and W. H. Bragg in 1913 discovered that crystalline solids at certain specific wavelengths and incident angles, produced intense peaks of reflected radiation patterns, in response to incident X-rays. They explained that this type of diffraction from crystalline solids is due to the periodicity, size and arrangements of atoms. The Bragg phenomenon was explained by modelling the crystals as a set of discrete parallel planes separated by a distance d as shown in

Figure 9.2. Bragg diffraction occurs when the incident wavelength is comparable with the spacing, d, between the atoms and the path difference between two waves undergoing constructive interference is $2d\sin\theta$. The Bragg's law is given by,

$$2d \sin \theta = n\lambda ,$$ (9.2)

where, d is the distance between the two planes of the lattice as shown in Figure 9.2, λ is the wavelength, θ is the angle between incident ray and scattering planes and n is an integer. Sonic crystal performance can be described using a similar formulation. Consider a sound wave normally Incident on a sonic crystal with a lattice constant of d, the frequency at which the band gap occurs is given by using Bragg's diffraction theory.

$$f = \frac{nc}{2d} ,$$ (9.3)

where c is the speed of sound in the host medium (i.e. 344 m/s for sound speed in air). The first band gap corresponds to $n = 1$; the frequencies of subsequent higher order band gaps are obtained by substituting higher values of n. The band gap due to sonic crystal can be described by multiple scattering between the cylinders (see Chapter 2).
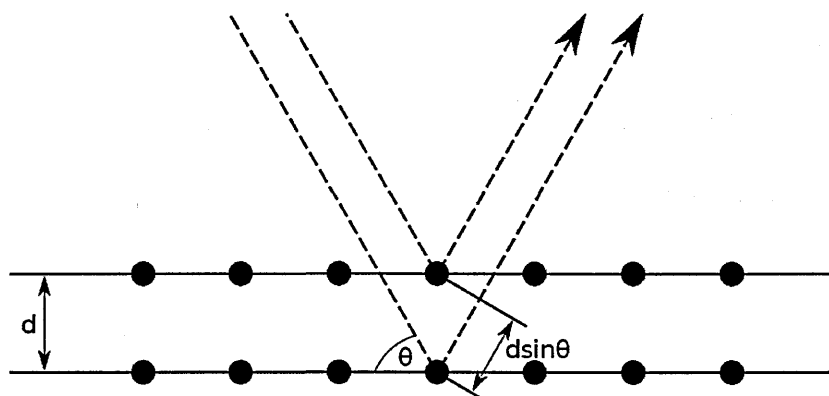
Figure 9.2 A periodic arrangements of atoms in a crystal with a centre-to-centre separation of d.

9.2.2 Sonic crystal as array of Cylinders (Artificial arrangements)

Martinez-Sala *et al.* [131] studied the acoustics of a sculpture with a periodic structure in 1995 in Madrid. The sculpture consists of a periodic distribution of hollow stainless-steel cylinders, with a diameter of 0.029 m and centre-to-centre spacing of 0.1 m. The sculpture [131] produced a band gap around 1.67 kHz, which corresponds to the first Bragg attenuation peak. Sanchez-Perez *et al.* [132] carried out experimental investigations of sonic crystals in laboratory. They considered two types of periodic configurations, i.e. square and triangular (which is a special case of Hexagonal arrangements). They found that the triangular lattice produced the wider attenuation bands for similar filling fractions. Sanchez-Perez *et al.* [133] carried out outdoor experiments on a sonic crystal to check its feasibility as a noise attenuating structure. Based on their laboratory data, a triangular configuration was chosen for the outdoor lattice. The periodic array was constructed using 3 m long PVC pipes with sealed ends and with a diameter of 0.16 m. The lattice was 1.11 m wide and 72 m long, mounted in a triangular pattern with a lattice constant of 0.22 m and filling fraction of 0.47. They [133] concluded that the structures made by arrays of hollow cylinders produce sound attenuation comparable with the attenuation by conventional noise barrier. Chen and Ye [134] presented a theoretical model to predict the sound propagation through a periodic structure based on plane-wave expansion method. The agreement between experimental data and prediction was found to be good. Khelif *et al.* [135], [136] studied the propagation through a square array of hollow steel cylinders using finite-difference-time-domain method. They [135], [136] demonstrated the applicability of periodic structures for filtering and separation of

specific frequencies from a broadband input signal. Goffaux *et al.* [137] concluded that the sound attenuation of a two dimensional sonic crystal increases linearly with the increase in number of rows. However, the diffraction effects due to the finite height of a barrier define a limit to its potential attenuation. Moreover, the noise attenuation due to sonic crystal barriers can be improved at lower frequencies by introducing resonances [138]. Hu *et al.* [139] presented sonic crystals made of cylinders with slits along their lengths, which act as Helmholtz resonators. The resonance effect either introduced an extra peak to insertion loss spectra or widened the band gap of the sonic crystal. Umnova *et al.* [20] improved the attenuation due to a sonic crystal noise barrier by covering the rigid cylinders with porous material. They [20] carried out experimental work on a sonic crystal made of three rows, with a lattice constant of 0.015 m, cylinders with a diameter of 0.635 and porous covering of 0.00175 m. The sonic crystal with a porous covering exhibits a wide band gap which improved its attenuation performance. Sanchez-Dehesa *et al.* [140] also investigated the effect of porous covering of rigid cylinders, following the idea originally proposed by Umnova [20]. The measurements were carried out over a sonic crystal made with rigid-hollow cylinders and perforated metallic cylinders filled with rubber crumb, a porous material that is obtained by recycling used car tyres. They concluded that an array of perforated cylinders filled with rubber crumb shows a better attenuation performance than would be obtained using rigid cylinders. Krynkin *et al.* [141] studied the sound propagation through a periodic array of elastic shells in air. Sonic crystals made of elastic shells gave an additional low frequency band gap which was verified experimentally and analytically. Krynkin *et al.* [142] presented simple analytical solutions to estimate the resonant band gap for a sonic crystal

made of elastic shells. Krynkin *et al.* [143] extended their study to investigate the effect of multiple-slits in cylinders on insertion loss spectra of a sonic crystal. The sonic crystal was made of hollow cylinders with four slits, concentric arrangements with four slit outer cylinders and rigid cylinders inside them and concentric arrangements with four slit outer cylinders and hollow elastic shells inside them. It was found that the concentric arrangements with inner elastic shells and outer four slit cylinders result in additional sound attenuation in the low frequency range below the first Bragg band gap while still preserving the Bragg band gaps.

Most of previous research about the acoustical performance of sonic crystals was concerned with improving the tunablity and noise attenuation over a wide frequency range. Different methods have been proposed such as porous covering and including a resonance phenomenon. Romero-Garcia *et al.* [144] suggested that all of these effects i.e. scattering, resonances and absorption can be combined together to improve the performance of a sonic crystal. They proposed sonic crystals made from a combination of rigid, absorbent and resonant cavities. The rigid cylinders were covered by a porous material and a slit in each cylinder introduced a resonant cavity. Thereby three physical phenomena were exploited successfully in a sonic crystal and its attenuation properties were tuneable in a wide-band of frequencies by changing the parameters of the array, the characteristics of resonant cavity or the thickness and acoustical properties of the absorbent material. Romero-Garcia *et al.* [145] extended their work and presented a theoretical model based on the extended plane wave expansion method to predict the band gaps in a sonic crystal. The detailed mathematical

derivation and explanation of the plane wave expansion method are given elsewhere [146].

Typically conventional noise barriers reduce any pre-existing ground effect by elevating the mean sound path height. If sonic crystals are considered as potential traffic noise attenuation devices, then the ground surface plays an important role in the overall noise attenuation so it is important to study the propagation of sound through a sonic crystal placed on a ground. Krynkin *et al.* [147], [148] have studied the effect of the presence of ground on the noise attenuation performance of a sonic crystal. The sonic crystal is a 2D structure but the problem of a 2D sonic crystal with vertical cylinder axes over a horizontal ground surface is a 3D problem. Although, such 3D arrangements are realistic they require high computational resources for numerical modelling. This 3D problem was converted into 2D problem by arranging the cylinders in the periodic array with their axes parallel to the ground. The attenuation performance of 5 × 3 and 7 × 3 square lattice arrays consisting of either rigid or elastic cylinders with their axes parallel to the ground have been investigated [147], [148]. Semi-analytical and numerical methods have been derived to predict the sound propagation through a periodic array of cylinders with axes parallel to the ground surface. It was concluded that the presence of ground surface has an adverse effect on the sonic crystal band gap peaks. Some experimental data with periodic arrangements of vertical cylinders on an acoustically hard ground also show that the presence of ground surface may have an adverse effect on SC band gap peaks [148].

9.2.3 Modelling tree-belts as sonic crystals

Traffic noise attenuation due to vegetation such as leaves shrubs, bushes and trees near roads has been increasingly given considerable attention for last 40 years (see Chapter 10 for details). Recently, it is discovered that, if the cylinders are arranged in a specific order, then they can act as pass and stop band filters for normally incident sound waves (see Section 9.2.1 and 9.2.2). Various studies have been carried out to use sonic crystal arrangements as alternative to noise barriers (see Section 9.2.2). In this chapter only the attenuation due to periodic arrangements of tree trunks is considered; ignoring the attenuation due to leaves and other phenomena which is the part of the study presented in the Chapter 10. Here, different arrangements of trees have been studied over a ground surface through laboratory experiments. The aim of this study is to enhance the attenuation due to trees by arranging them in a specific order. Individual tree trunks usually don't have considerable effect on traffic noise attenuation. However, the combined effect of tree-trunks regularly arranged as a sonic crystal can improve the attenuation performance of tree belts. One of the major problems in using arrays of tree-trunks as sonic crystals is that they cannot be planted very close to each other. Usually, sonic crystal noise barriers have high filling fractions; in other words small lattice constants. However, the experimental work presented here is with low filling fractions, since the study is in the context of using tree belts as noise barriers where a typical filling fraction would be less than 12 %.

Several authors such as Price *et al.* [149], Huisman and Attenborough [150], Pal *et al.* [151], Fang and Ling [152] and Tarrero *et al.* [153] have studied the sound attenuation due to vegetation, bushes and tree belts (for details see

Chapter 10). However recently, Renterghem *et al.* [154] have studied the attenuation potential of a 15 m deep tree belt. Road noise traffic noise propagation through a tree belt of limited depth containing periodically arranged trees along a road was predicted numerically by means of 3D finite-difference-time-domain (FDTD) calculations. Four different kinds of periodic tree arrangements i.e. cubic, face-centred cubic, rectangular and triangular were investigated. It was found that the insertion loss increased with the increase in the tree-trunk diameter and decrease in spacing between the tree-trunks. The spacing parallel to road was found to be more important than the spacing perpendicular to the road. A significant amount of noise attenuation was predicted with a tree spacing of less than 3 m and tree-trunk diameter of more than 0.11 m. In other words, the tree-trunks show improvement in insertion loss due to the sonic crystal effect at smaller spacing. The effect of omitting some rows of planting was also considered. They found that leaving out some rows does not significantly influence the averaged traffic insertion loss. Renterghem *et al.* [154] also studied the randomness in the stem centre location. They concluded that introducing pseudo-randomness in periodically spaced tree belt does not improve the insertion loss. Later in this chapter it is shown through laboratory experiments that the sonic crystal attenuation can be improved through perturbation.

Other methods such as adding absorption to tree bark was found to broaden the low frequency peak and improve the overall insertion loss. The traffic noise attenuation also increases with the increase in tree heights. It was concluded that in addition to other attenuation mechanisms such as ground effect, 2–3 dB more insertion loss can be obtained by careful arrangements of tree belts.

Taherzadeh *et al.* [155] studied the sound transmission through periodic, perturbed and randomly arranged vertical cylinders placed on an acoustically hard (MDF board) and acoustically soft (Felt-MDF) ground respectively. They found that the ground effects and sonic crystal effects are additive. A quasi-periodic arrangement in which the perturbation has a standard deviation equal to the scatterer diameter was found to give the best overall attenuation performance compared to periodic and random arrangements. The work presented in this chapter is based on this paper [155].

9.3 Low filling fraction sonic crystals

9.3.1 Regular sonic crystals on a hard ground

9.3.1.1 Measurements

Inside the anechoic chamber in the Rheinhold Herman Building at the Open University, a Tannoy driver fitted with a 1.0 m long tube, of 0.03 m internal diameter was used as a point source and an ACO pacific type ¼-inch-diameter condenser microphone fitted with a preamplifier was used as a receiver. A data acquisition system based on Maximum Length Sequence (MLSSA) was used for signal generation and signal processing (For details see Chapter 3). Although most of the laboratory data presented in the thesis is in the form of excess attenuation spectra; in this chapter, for convenience, the sonic crystal transmission loss data will be plotted as Insertion Loss (IL). Mathematically, the insertion loss is the inverse of excess attenuation and is defined as,

$$IL = \frac{FreeField}{TotalField},$$
(9.4)

The free field data needed for calculating insertion loss spectra were obtained by raising source and receiver to a height of 2.0 m above the grid floor of the anechoic chamber so that unwanted reflections were minimized. Measurements have been made of sound propagation through various arrangements of acoustically-hard cylindrical PVC pipes having outer diameter of 0.04 m and length of 0.5 m with their axes vertical to an MDF board as shown in Figure 9.3 (a). The pipes were arranged in 5 X 10 arrays on a MDF board with lattice constants of 0.05 m, 0.07 m and 0.1 m corresponding to filling fractions of 50 %, 26 %, and

13% respectively. The source and receiver were placed at different heights and at a horizontal separation of 1.0 m above a MDF board. The distance between the microphone and nearest row of a sonic crystal array was fixed at 0.05 m and the sonic crystal array extended towards the source to a distance depending on the lattice constant. The dimensions along the source-receiver axis of the sonic crystal arrays were 0.24 m, 0.32 m and 0.44 m and the distance between the source and the nearest-to-source PVC pipe row in a sonic crystal array were 0.71 m, 0.63 m and 0.51 m corresponding to lattice constants of 0.05 m, 0.07 m and 0.1 m respectively. The measurement arrangements are described in schematic 9.3 (b).
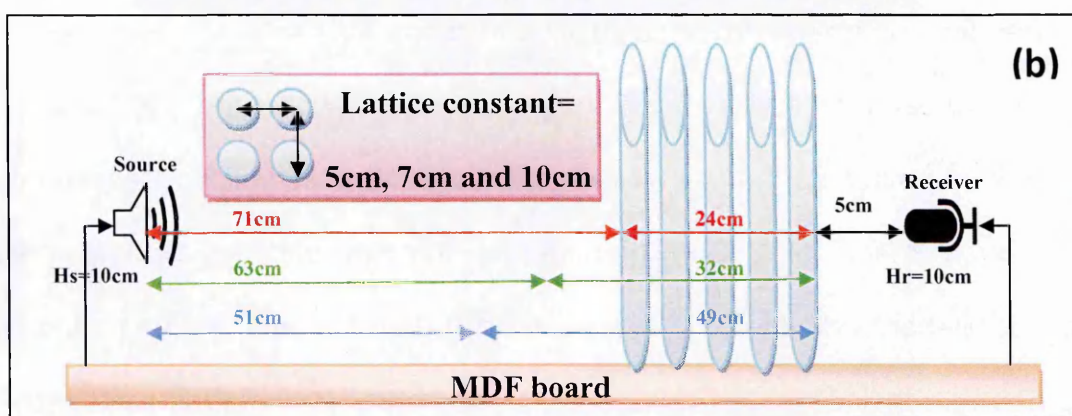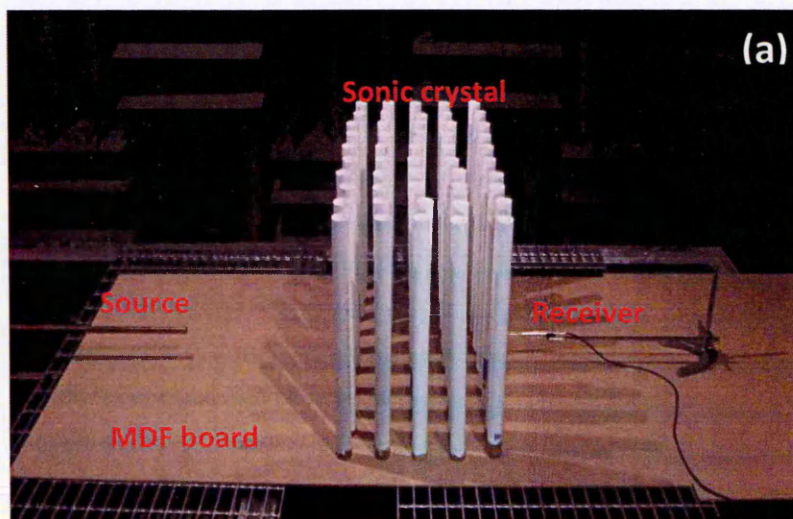
Figure 9.3 Laboratory arrangements of sound propagation through sonic crystal placed over MDF board (a) a photograph and (b) a schematic.

Figures 9.4 (a), (b), (c) and (d) show the measured insertion loss spectra due to regularly spaced 5 × 10 square arrays of rigid PVC pipes over MDF board with lattice constants of 0.05 m, 0.07 m, 0.10 m and 0.10 m respectively. Figures 9.4 (a), (b) and (c) show the measured IL spectra with source and receiver at height of 0.1 m and separation of 1.0 m. However, the data shown by Figure 9.4 (d) was measured by lowering the source height to 0.02 m. Figure 9.4 (a) - (d) also show the corresponding excess attenuation spectra measured for the MDF board alone with same source-receiver geometry as used for the sonic crystal measurements.

The measured insertion loss spectrum due to a sonic crystal with a lattice constant of 0.05 m is shown in Figure 9.4 (a). The lowest band gap centre frequency, calculated using Eq. 9.3 is 3.4 kHz. In Figure 9.4 (a) it spans from 2.3 kHz to 4.5 kHz with centre frequency at 3.4 kHz. The calculated and measured band gap centre frequencies are identical. The second band gap starts at 4.5 kHz and continues to higher frequencies due to the fact that the ground effect destructive interference near 7 kHz comes into play. The calculated 2nd order band gap centre frequency using Eq. 9.3 is 6.8 kHz and is visible also in Figure 9.4 (a). The ground effect (excess attenuation) peak due to destructive interference above hard ground for a source-receiver height of 0.1 m occurs around 8.5 kHz. The second band gap due to the sonic crystal seems to be enhanced by this excess attenuation peak due to hard ground.

Most of the data presented in this chapter shows negative values of insertion loss at lower frequencies i.e. less than 1 kHz (see Figures 9.4 (a) – (d)). Negative IL at lower frequencies is typical of the (constructive interference) hard

ground effect, and is usually +6 dB in excess attenuation spectra (see Chapter 4) corresponding to pressure doubling. This could be represented by a –6 dB line in IL spectra.

An extra low frequency band gap peak appears at 2 kHz in Figure 9.4 (a). The extra peak is not due to the finite size of the MDF board since, if it was, it should also appear in spectra over MDF board alone (see Figure 9.4 (a), black-broken line) obtained using the same geometry as was used for the sonic crystal measurement. The hollow PVC pipes used for measurements were 0.5 m long, with one end closed and other end open. Consequently this extra peak may be a resonance phenomenon caused by standing waves along the finite length PVC pipe cavity. The calculated first order resonance frequency due a closed-open, 0.5 m long tube is 185 Hz. Other possible explanations of this low frequency peak are the finite width and height of the PVC pipes array. The possibility that the peak is caused by the finite width of the array has been investigated using available data. It appears at 1.95 kHz in data obtained for a sonic crystal with a lattice constant of 0.07 m (see Figure 9.4 (b)) but is not present in data obtained for a sonic crystal with a lattice constant of 0.1 m (see Figure 9.4 (c)). The number of PVC pipes arranged periodically to create sonic crystals with different lattice constants during the laboratory experiments was limited to 50. As a result the width and length of sonic crystal array changed with change in lattice constant. The widths of the sonic crystal arrays with lattice constants of 0.05 m, 0.07 m and 0.1 m are 0.49 m, 0.67 m and 0.94 m respectively. Extra low frequency band gap peaks are visible when the sonic crystals are 0.49 m and 0.67 m wide. However, an extra peak below the first band gap is not visible in the data obtained using the sonic crystal

with array width of 0.94 m. This suggests that these extra low frequency peaks could be due to the finite width of the array. As, the width of the array increases this extra low frequency peak disappears. Nevertheless, the appearance of extra low frequency peaks below the first band gap frequencies needs further investigation.

In the insertion loss spectrum shown in Figure 9.4 (b) which was measured for the sonic crystal with a lattice constant of 0.07 m, the first band gap spans from 2.1 kHz to 3.0 kHz with centre frequency of 2.5 kHz. The lowest band gap centre frequency, calculated using Eq. 9.3 is 2.4 kHz, which shows good agreement with the measurement. The 2nd order band gap central frequency calculated using Eq. 9.3 is 4.86 kHz as shown by Figure 9.4 (b). The 2nd band gap spans from 4.0 kHz to 8.5 kHz with centre band gap frequency of 6 kHz. The ground effect interference is around 8.5 kHz as shown by Figure 9.4 (b), which is at the end of 2nd band gap. The ground effect peak is effectively broadened and enhanced by the 2nd band gap due to the sonic crystal.

Figures 9.4 (c) and (d) show measured IL spectra for a sonic crystal with a lattice constant of 0.1 m, but with different source heights. The insertion loss spectra given by Figure 9.4 (c) measured for a sonic crystal with a lattice constant of 0.10 m shows that the first band gap spans from 1.1 kHz to 2.35 kHz with centre frequency at 1.7 kHz. The lowest band gap centre frequency, calculated using Eq. 9.3 is 1.7 kHz. So the measured and calculated first band gap frequencies are identical. The 2nd band gap spans from 2.7 kHz to 5.0 kHz with centre frequency of 3.8 kHz. The 2nd order band gap centre frequency, calculated using Eq. 9.3 is 3.4 kHz. The agreement between the measured and calculated band gap centre

frequencies is good. The ground attenuation (destructive interference) peak near 9 kHz elevates the relatively small higher order band gaps seen in Figure 9.4 (c).

Figure 9.4 (d) shows the measured insertion loss spectra obtained for a sonic crystal with a lattice constant of 0.1 m when the source height was lowered to 0.02 m. Typically, at grazing incidence, if the ground is hard and smooth, then the first destructive interference occurs at too high frequency to have any interaction with sonic crystal induced band gaps.

Figure 9.5 compares the insertion loss spectra due to the sonic crystal with a lattice constant of 0.1 m over MDF board measured with source heights of 0.1 m and 0.02 m respectively. Figure 9.5 also shows the spectra measured over MDF board alone for the same two geometries. The measured IL spectra over MDF board alone show that for a source height of 0.1 m the first ground effect maximum is at 8.5 kHz but with a source height of 0.02 m, the first IL maximum occurs at very much higher frequency. In the measured IL spectra due to the sonic crystal (L.C. = 0.1 m) with source height of 0.1 m the ground effect peak enhances the IL due to the pipe array. On the other hand, the measured IL spectra due to the sonic crystal (L.C. = 0.1 m) with source height of 0.02 m shows that the ground effect maximum is at too high frequency to contribute to the sonic crystal effect. It is concluded from these measurements that the ground effect due to the hard ground adds to the sonic crystal effect.

(a)

- Periodic Sonic Crystal (L.C. = 0.05 m)
- MDF Ground Effect

Extra Low frequency peak

1st band gap (3.4 kHz)

2nd band gap (6.8 kHz)

1st ground effect dip/peak

(b)

- Periodic Sonic Crystal (L.C. = 0.07 m)
- MDF Ground Effect

Extra Low frequency peak

1st band gap (2.4 kHz)

2nd band gap (4.9 kHz)

1st ground effect dip/peak

(c)

- Periodic Sonic Crystal (L.C. = 0.10 m)
- MDF Ground Effect

1st band gap (1.7 kHz)

2nd band gap (3.4 kHz)

1st ground effect dip/peak

Frequency (Hz)

Figure 9.4 Measured insertion loss spectra due to regularly spaced 5 × 10 square array of PVC pipes over MDF board with source and receiver at height of 0.1 m and separation of 1.0 m (a) Lattice constant of 0.05 m (b) Lattice constant of 0.07 m (c) Lattice constant of 0.1 m (d) Lattice constant of 0.1 m, source at 0.02 m and receiver at 0.1 m. Also shown is the attenuation spectrum measured for the MDF board alone.
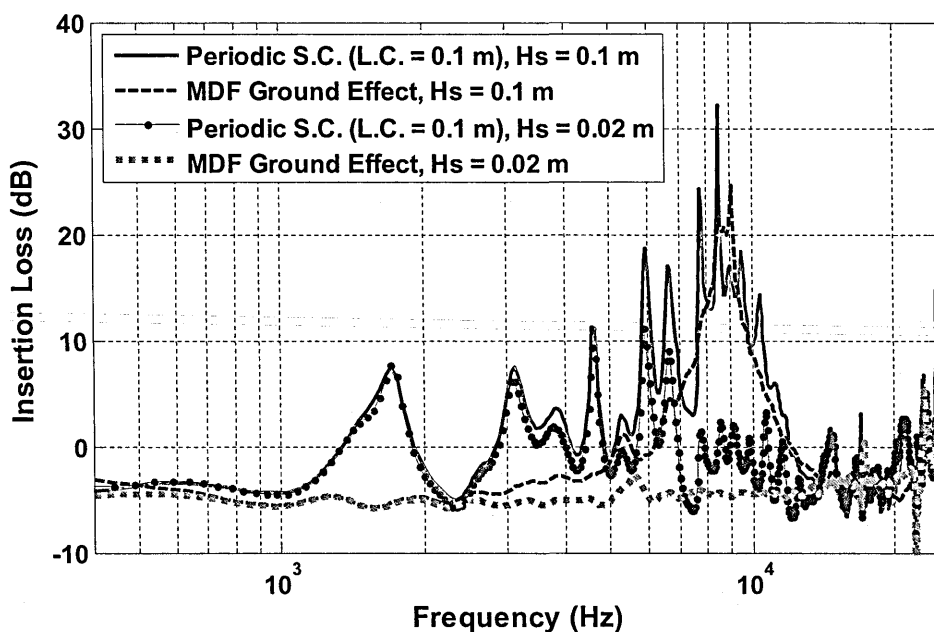
Figure 9.5 Measured insertion loss spectra due to regularly spaced 5 × 10 square array of PVC pipes with a lattice constant of 0.1 m over MDF board with source-receiver separation of 1.0 m, receiver at height of 0.1 m and source at two heights of 0.1 m (red solid lime) and 0.02 m (blue dotted-solid line). Also shown is the attenuation spectrum measured for the MDF board alone for same two geometries.

9.3.1.2 Comparisons between data and predictions

A sonic crystal consisting of vertical cylinders over a horizontal ground surface represents a 3D structure. Predictions of sound propagation through a 3D structure require high computational resources. Krynkin *et al.* [147], [148] converted a potentially 3D problem into 2D problem by placing the cylinders in a periodic array with their axes parallel to the ground. However, since we are interested in vertical cylinders with the tree belt application in mind, a different modelling approach is applied here. In the data from the experiments described previously, excess attenuation peaks due to the ground surface were found to be add to the band gap peaks due to a periodic 2D array of vertical cylinders (see Figures 9.4 and 9.5). So, sound propagation through a 2D periodic structure on the ground may be treated independently from the sound propagation over the ground surface. So the two effects will be added together at each frequency point to predict the overall insertion loss due to vertical cylinder arrangements over a ground surface. The acoustical properties of MDF board and other surfaces have been obtained using a ground characterization method (see Chapter 4). The best fit impedance parameters to data obtained for an MDF board using a variable porosity impedance model (see Chapter 4) are a flow resistivity of about 5×10^5 kPa s m^{-2} and porosity rate of 100 m^{-1}. So the ground effect spectra can be calculated by using the impedance model and parameters in a model for propagation from a point source over an impedance plane for the given source-receiver geometry. Sound propagation through a (free field) 2D array of periodic cylinders is predicted using multiple scattering theory (see Chapter 2). The two effects are added together to obtained the overall effect. Figure 9.6 compares the

measured and predicted insertion loss spectra due to a regularly spaced square array of PVC pipes placed with vertical axes on a MDF board with lattice constant of 0.05 m, 0.07 m and 0.1 m. The predicted insertion loss spectra are in good agreement with those measured.
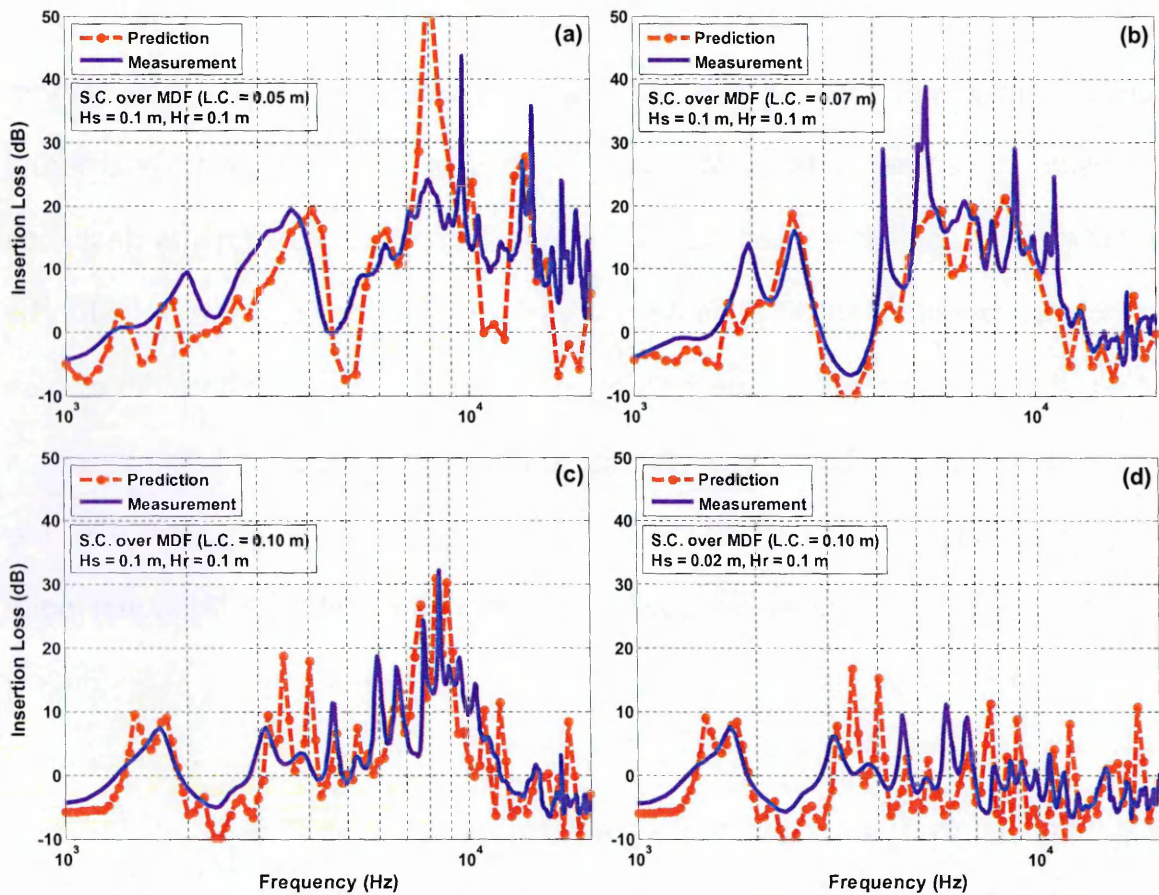
Figure 9.6 Comparison between measured and predicted insertion loss spectra due to regularly spaced 5 × 10 square array of PVC pipes over MDF board with source and receiver at height of 0.1 m and separation of 1.0 m (a) Lattice constant of 0.05 m (b) Lattice constant of 0.07 m (c) Lattice constant of 0.1 m (d) Lattice constant of 0.1 m, source at 0.02 m and receiver at 0.1 m. The predictions are obtained by adding the ground effect predicted for the given geometry and (MDF) surface to multiple scattering predictions of the IL due to the 2D sonic crystal.

9.3.1.3 Discussion

Krynkin *et al.* [147], [148] also studied sound propagation through regular arrays of cylinders placed with their axis parallel to a ground surface. They concluded that the existence of the ground surface has an adverse effect on the band gap peaks. However, the measurements and predictions made using cylinders perpendicular to the ground surface presented in this chapter tell a different story (see Figures 9.4 - 9.6). It has been found that the ground effect enhances the higher order band gap peaks and that two effects are additive. As well as the difference caused by the orientation of the cylinders, other reasons for difference may be due to different measurement geometry and sonic crystal filling fractions. The data presented in this chapter were measured with source-receiver close to the ground surface. However, the data for horizontal cylinders placed on hard ground were obtained with higher source and receiver locations [147], [148]. Most of data presented here was measured over a sonic crystal with a low filling fraction of 13 %. However, Krynkin *et al.* [147], [148] carried out experimental work using sonic crystals with filling fractions of between 26 % and 50 %. This suggests that the interaction between ground effect and sonic crystal effects depends on the cylinder orientation with respect to the supporting plane, source-receiver geometry and sonic crystal filling fraction. These effects need further investigation.

9.3.2 Regular sonic crystals on a soft ground

9.3.2.1 Measurements

Measurements made on periodic vertical cylinders arrays with relatively low filling fractions on a hard ground have shown that the ground attenuation peaks enhance the band gaps. The reason for studying the acoustical performance of periodic arrays of vertical cylinders over a ground surface is to investigate their performance as noise barriers. At higher speeds, the most common traffic noise source is the road-tyre interaction, which is very close to the ground surface. Typically, if the ground is hard and smooth then at grazing incidence the first destructive interference occurs at too high a frequency to be useful in noise control. However, if the ground is acoustically soft, the ground effect maxima move to lower frequencies. Also the lower frequency band gaps due to a sonic crystal can be useful for traffic noise attenuation. If the sonic crystals are to be built on an acoustically soft ground, the ground effect and lower frequency band gaps interfere with each other. So, it is important to study the behaviour of sonic crystal over a soft ground. If the two effects are additive, as has been found to be the case if the ground is hard, then the attenuation performance due to the sonic crystal can be improved significantly by a careful sonic crystal design and adjustment of the acoustical properties of ground surface (Chapter 4 discusses different types of acoustically soft ground).

To study the attenuation performance of a sonic crystal over soft ground, periodic arrays of PVC pipes having outer diameters of 0.04 m were arranged on a surface consisting of a layer of felt over MDF board. Results of measurements are

shown in Figure 9.7 (a). The felt was 0.012 m thick and was glued on the MDF board. The PVC pipes were arranged in square 5 X 10 arrays with a lattice constant of 0.1 m corresponding to a filling fraction of 0.13. Both source and receiver were placed at different but equal heights with a horizontal separation of 1.0 m. The distance between the microphone and nearest row of a sonic crystal array was fixed at 0.05 m and the distance between the source and the nearest PVC pipe row was 0.51 m. The measurement arrangements are described in the schematic in Figure 9.7 (b).
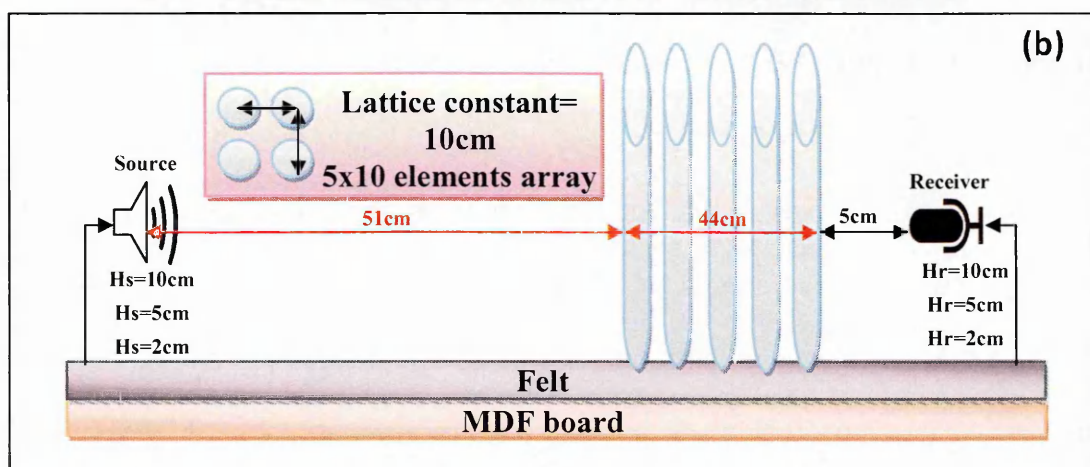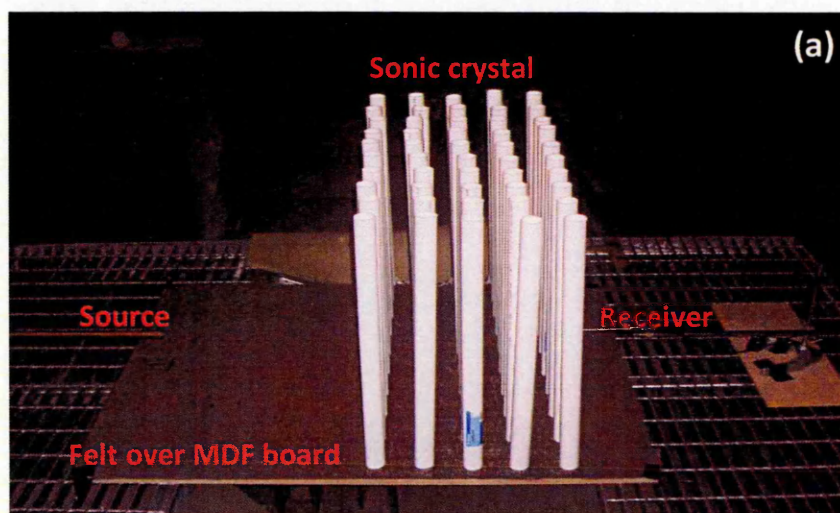
Figure 9.7 Laboratory arrangements of sound propagation through sonic crystal placed over Felt-MDF board (a) a photograph and (b) a schematic.

Figures 9.8 (a), (b) and (c) and show measured insertion loss spectra due to a regularly spaced 5 X 10 square array of rigid PVC pipes with a lattice constant of 0.10 m. Figure 9.8 shows the measured IL spectra with source and receiver at height of 0.1 m, Figure 9.8 (b) with source and receiver at height of 0.05 m and Figure 9.8 (c) with source at height of 0.02 m and receiver at height of 0.1 m. Figures 9.8 (a) - (c) show the corresponding attenuation spectra measured for the Felt-over-MDF board surface alone with same source-receiver geometries as were used for the measurements with PVC pipe arrays present.

The insertion loss spectrum due to a sonic crystal placed on a soft ground with a lattice constant of 0.1 m is shown in Figure 9.8 (a). The first band gap spans from 1.0 kHz and extends up to higher frequencies. The lowest band gap centre frequency calculated using Eq. 9.3 is 1.7 kHz. The broad ground effect due to Felt-over-MDF for a source-receiver height of 0.1 m starts at 1.2 kHz and peaks at 2.1 kHz. The first and second order band gaps due to the periodic array of vertical cylinders and the lowest frequency excess attenuation maximum due to acoustically soft ground overlap over a wider frequency range. According to the data shown in Figure 9.8 the two attenuation effects i.e. the sonic crystal effect and ground attenuation, add constructively to give a larger overall attenuation. The soft ground surface excess attenuation enhances the band gaps due to sonic crystal. Hence, the sonic crystal might be more effective as a traffic noise barrier when constructed over a soft ground surface. Figures 9.8 (b) and (c) show the measured IL spectra for lower source and receiver heights. Nearer grazing incidence, the soft ground is more effective in enhancing band gaps; which is a very useful due to fact that important traffic noise sources are at near the ground.
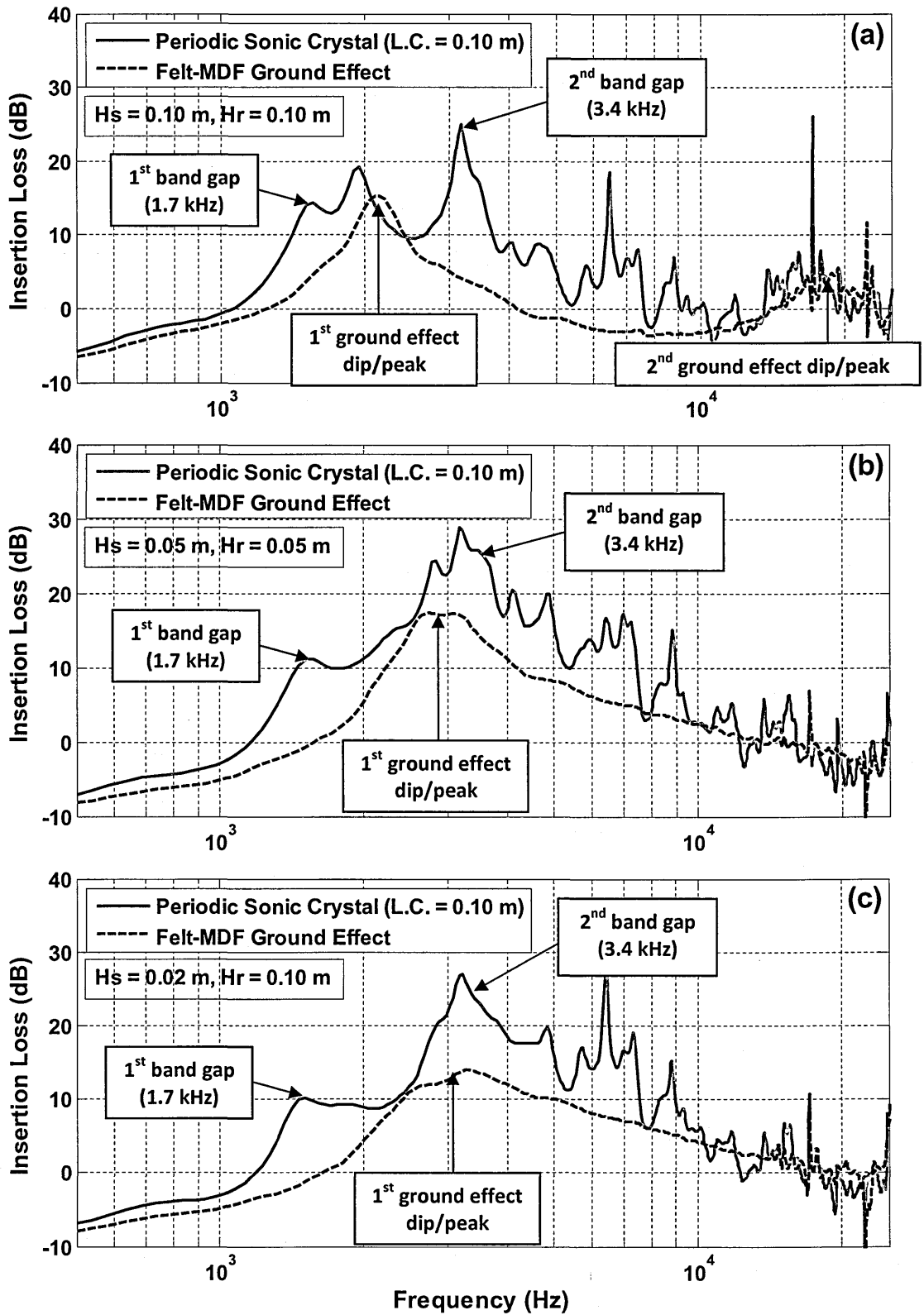
Figure 9.8 Measured insertion loss spectra due to regularly spaced 5 × 10 square array of PVC pipes with lattice constant 0.1 m over Felt-over-MDF board with source-receiver separation of 1.0 m (a) Source height = 0.1 m and Receiver height = 0.1 m (b) Source height = 0.05 m and Receiver height = 0.05 m (c) Source height = 0.02 m and Receiver height = 0.1 m Also shown is the excess attenuation spectrum measured for the Felt-MDF board alone.

Figure 9.9 compares the insertion loss spectra due to a periodic array of vertical cylinders with a lattice constant of 0.1 m over a hard ground (MDF board) and a soft ground (felt-MDF board) measured with source heights of (a) 0.1 m and (b) 0.02 m. Figure 9.9 also show the spectra measured for MDF board and Felt-over-MDF board alone for the two geometries. The first ground effect peak due to destructive interference between the direct and reflected sound field over MDF board and felt-over-MDF board for the source and receiver placed at a height of 0.1 m and separated by 1.0 m occur at 8.5 kHz and 2.1 kHz respectively. The attenuation peak due to felt-over-MDF board is broader than the peak due to MDF board alone. Insertion loss spectra over sonic crystal placed on MDF board and Felt-MDF board show that around the frequency at which ground attenuation peaks occur the ground effect is added to sonic crystal effect. Similarly, Figure 9.9 (b) shows the measured data with a lower source height of 0.02 m. The attenuation peak due to hard ground moves to much higher frequencies and so does not influence the sonic crystal band gap. On the other hand, at a small grazing angle the attenuation due to a soft ground surface becomes more effective.

These measurements suggest that the relatively sparse sonic crystal is more effective as a traffic noise barrier when constructed over a soft ground than on a hard ground. This is consistent with numerical assessments of the effectiveness of tree belts for reducing traffic noise [154].
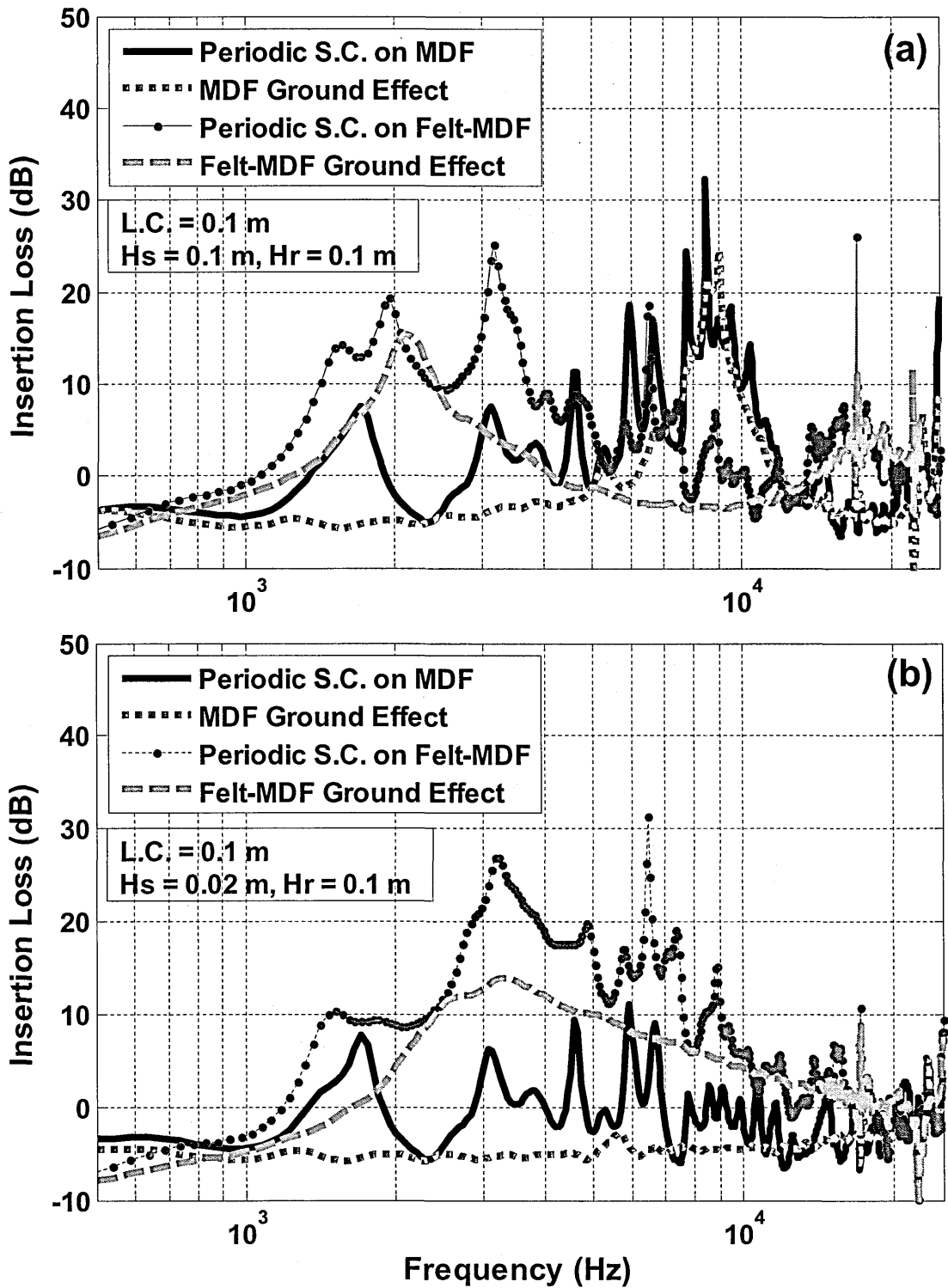
Figure 9.9 Comparison between measured insertion loss spectra due to regularly spaced 5 × 10 square array of PVC pipes with lattice constant 0.1 m over hard ground (MDF board) and soft ground (Felt-over-MDF board) with source-receiver separation of 1.0 m, receiver at height of 0.1 m and source at two heights of (a) 0.1 m and (b) 0.02 m Also shown is the attenuation spectrum measured for the MDF board and Felt-MDF alone for same two geometries.

9.3.2.2 Comparisons between data and predictions

Predictions of sound propagation for a vertical cylinder array on a felt-over-MDF ground were carried out as described in Section 9.3.1.2. The best fit impedance parameters obtained from excess attenuation data for felt-over-MDF board using the variable porosity impedance model are flow resistivity of 20 kPa s m^{-2} and porosity rate of 100 m^{-1}. The ground effect (excess attenuation) spectra are predicted by using the variable porosity impedance model and best fit parameters in a model for propagation from a point source for a given source-receiver geometry. The predicted insertion loss spectra due to periodic arrays of vertical cylinders were obtained using multiple scattering theory (see Chapter 2). The predicted ground effect (excess attenuation) spectra and multiple scattering spectra have been added together to obtained predictions of the overall effect. Figure 9.10 compares the measured and predicted insertion loss spectra due to a regularly spaced square array of PVC pipes placed on a felt-MDF board with lattice constant of 0.1 m for two source-receiver geometries. The predicted insertion loss spectra show very good agreement with the data.
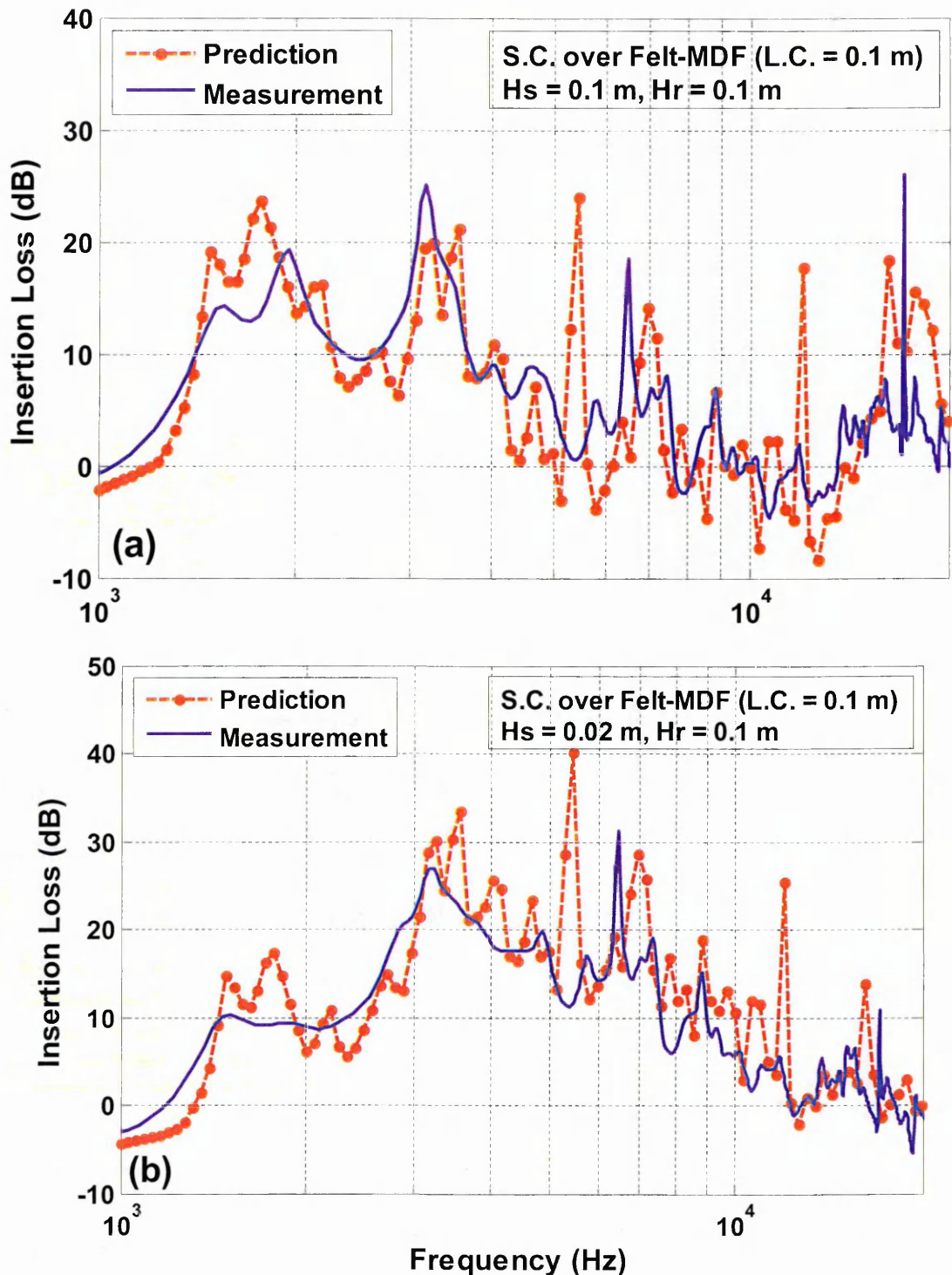
Figure 9.10 Comparison between measured and predicted insertion loss spectra due to a regularly spaced 5 × 10 square array of PVC pipes with a lattice constant of 0.1 m placed on Felt-over-MDF board with the receiver at height of 0.1 m and at a horizontal separation of 1.0 m from the source (a) Source height of 0.1 m (b) Source height of 0.02 m. The predictions are obtained by adding the ground effect predicted due to Felt-over-MDF board for a given geometry to multiple scattering predictions of the IL spectra due to a sonic crystal.

9.4 Aperiodicity effects

9.4.1 Perturbed sonic crystals on a hard ground

Although periodically spaced cylinder arrays produce band gaps at some frequencies, at other frequencies they focus sound energy; i.e. enhance the sound field at some frequencies (See Figure 9.4). The purpose of the studying the effects of array perturbations is to find a way to reduce the focusing effect while preserving the band gap effect.

Two forms of random perturbation of the regular arrangement of PVC pipes with lattice constant 0.1 m have been investigated in the laboratory; one with a standard deviation equal to $0.5r$ where r is the cylinder radius; and one where the standard deviation was $2.0r$. Let $O(x_j, y_j)$ be the coordinates of the position of jth element in the periodic array. Then the position of the perturbed element is given by $O(x_j+\alpha_j, y_j+\beta_j)$ where α_j and β_j are a pair of numbers drawn from a random number set with a normal distribution and a standard deviation equal to $0.5r$ or $2.0r$. Figure 9.11 shows the corresponding measurement arrangements in the laboratory.

Figure 9.12 compares the measured insertion loss spectra due to a regularly spaced 5 × 10 square array of PVC pipes with a lattice constant of 0.1 m and a perturbed version of the array with a standard deviation of 0.5*radius of the cylinders from their original square array positions over hard ground (MDF board). The source and receiver were separated horizontally by 1.0 m and the receiver was placed at height of 0.1 m. Figure 9.12 (a) shows the data measured with source height of 0.1 m and Figure 9.12 (b) presents data obtained with a source height of 0.02 m. The focusing effect due to sonic crystal has been reduced to

some extent while the original band gaps are not much affected. Nevertheless this small perturbation does not offer any significant effects.
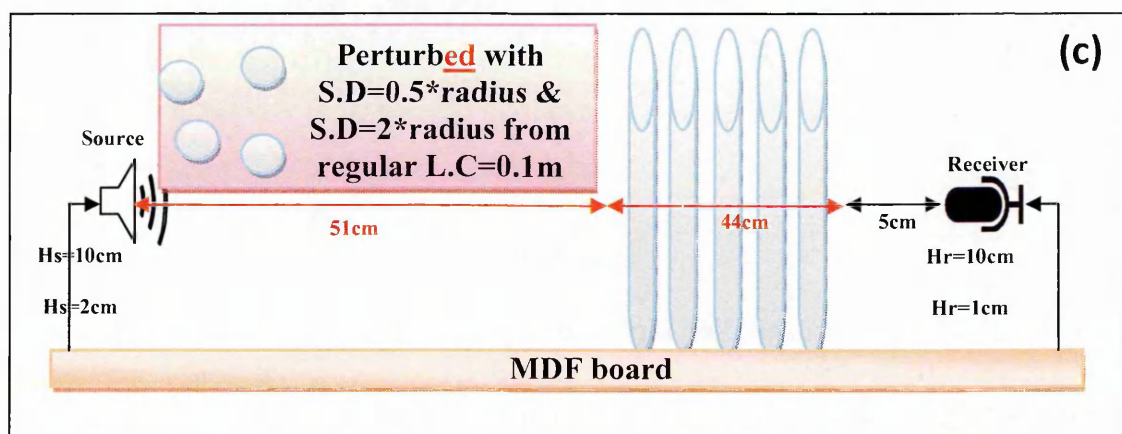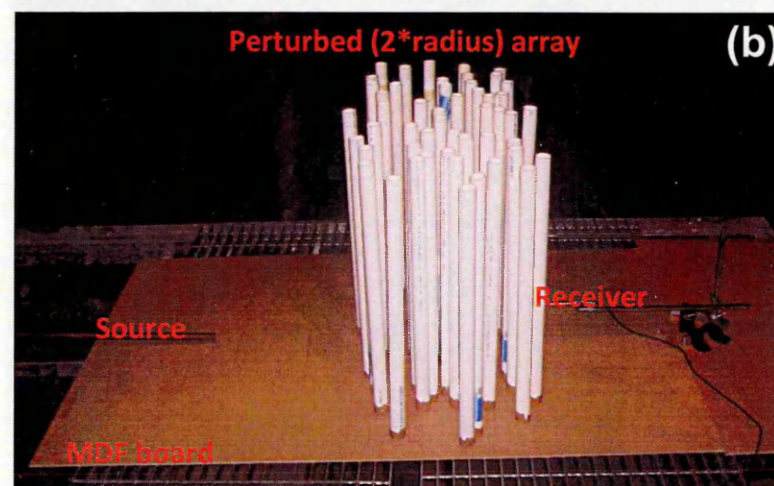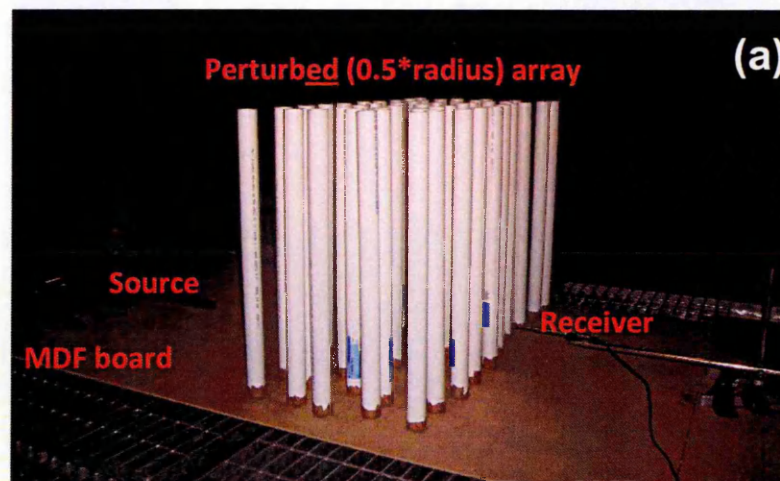
Figure 9.11 Laboratory arrangements of sound propagation through perturbed PVC pipe arrays placed on MDF board (a) a photograph of with perturbation having standard deviation of 0.5*radius (b) a photograph of with perturbation having standard deviation of 2.0*radius (c) a schematic of measurement arrangements.
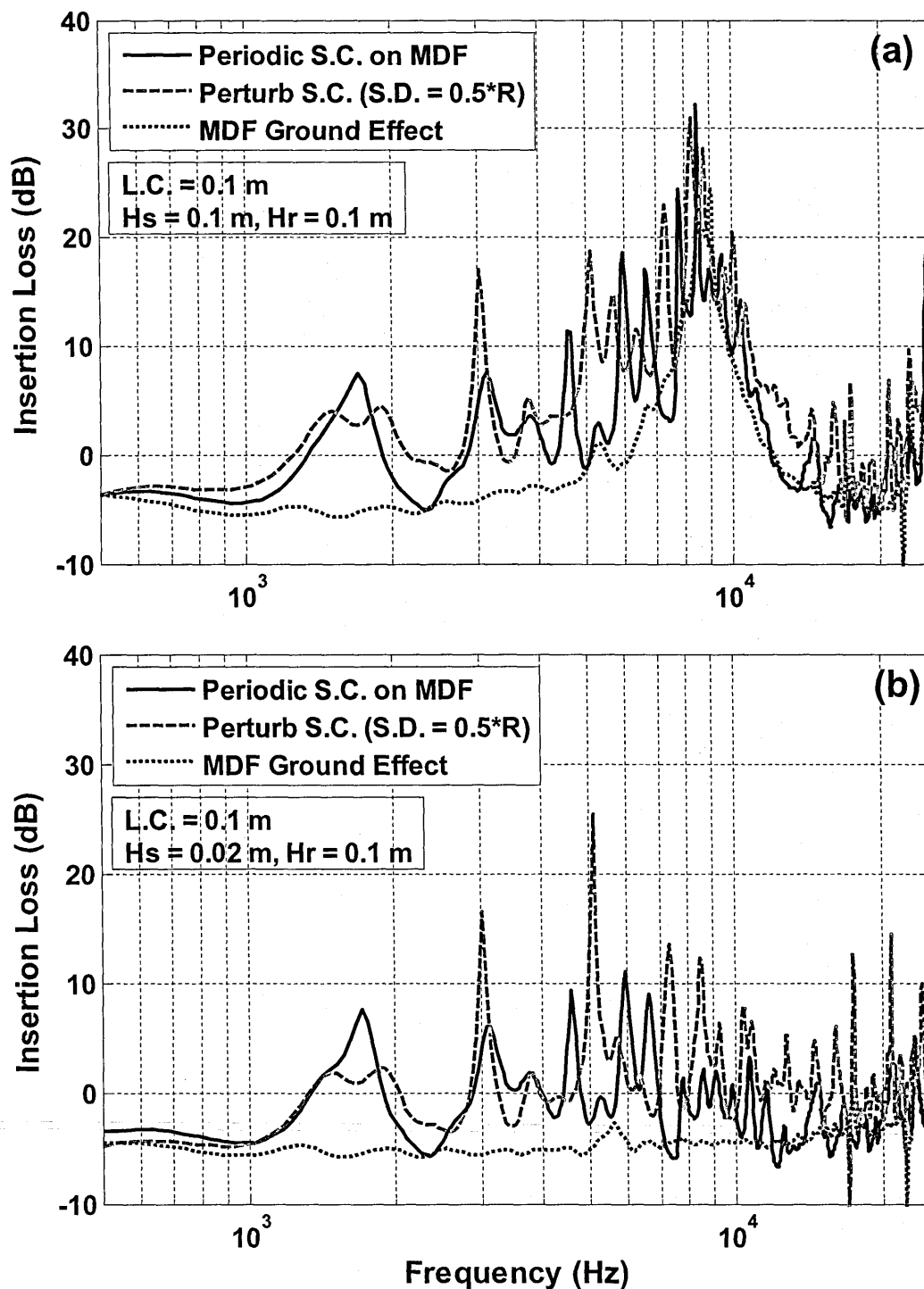
Figure 9.12 Comparison between measured insertion loss spectra due to a regularly spaced 5 × 10 square array of PVC pipes with a lattice constant of 0.1 m and a perturbed array with a SD of perturbation of cylinder locations of 0.5*radius from their original square array positions over hard ground (MDF board) with source-receiver separation of 1.0 m, receiver at height of 0.1 m and source at two heights of (a) 0.1 m and (b) 0.02 m. Also shown is the attenuation spectrum measured for the MDF board alone for same two geometries.

Figure 9.13 compares the measured insertion loss spectra due to the regularly spaced 5 X 10 square array of PVC pipes with a lattice constant of 0.1 m and a perturbed version of this array with a standard deviation of 2.0*radius in cylinders locations from their original square array positions over hard ground (MDF board). The source and receiver were separated horizontally by 1.0 m and the receiver was placed at height of 0.1 m. Figure 9.13 (a) shows data measured with source height of 0.1 m and Figure 9.13 (b) presents data obtained with a source height of 0.02 m. The larger perturbation causes the focusing effect to be reduced significantly, while preserving the original band gaps. The most significant impact is on insertion loss spectra towards higher frequencies. These measurements also confirm that the excess attenuation due to the ground effect enhances the insertion loss spectra.
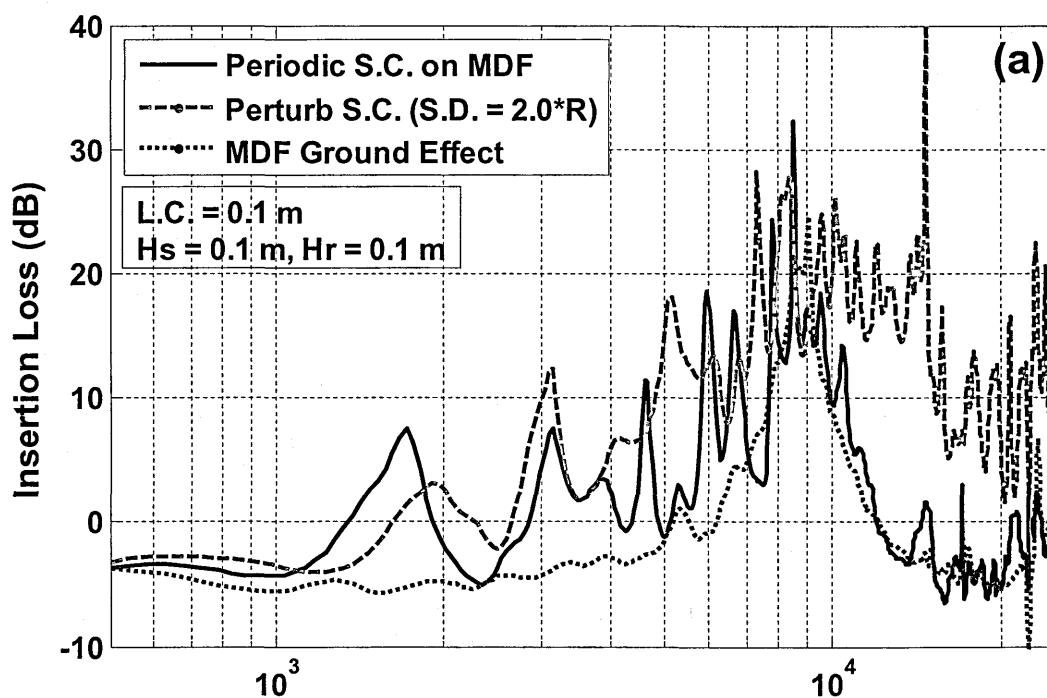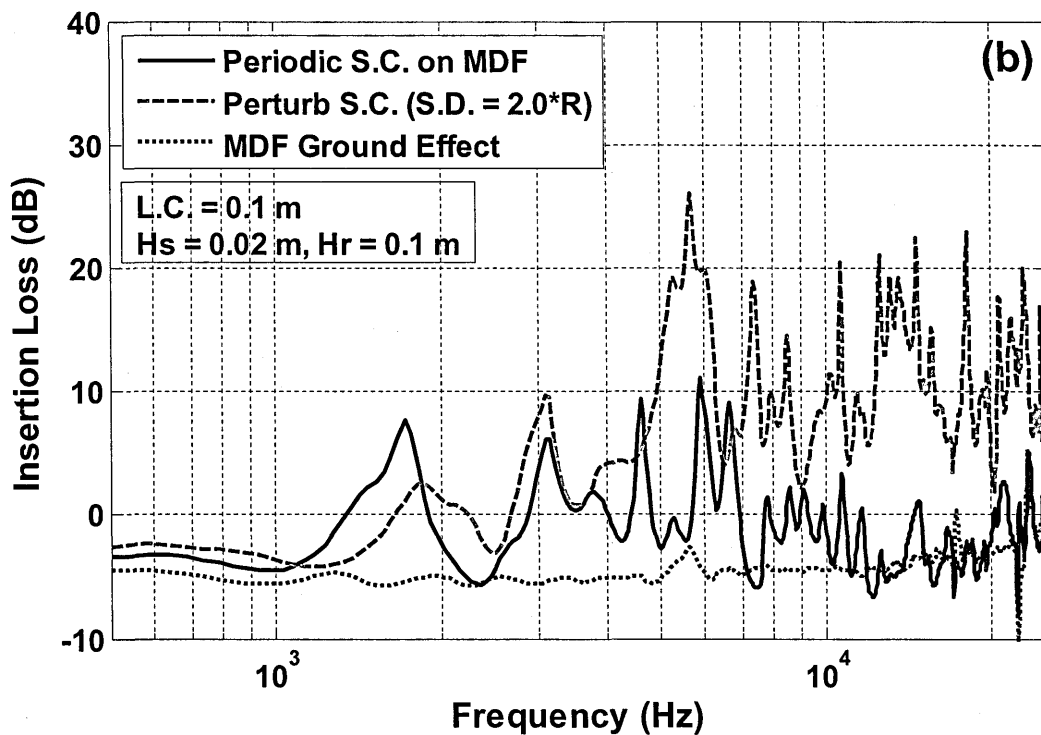
Figure 9.13 Comparison between measured insertion loss spectra due to a regularly spaced 5 × 10 square array of PVC pipes with a lattice constant of 0.1 m and a perturbed array with a SD of perturbation of cylinder locations of 2.0*radius from their original square array positions over hard ground (MDF board) with source-receiver separation of 1.0 m, receiver at height of 0.1 m and source at two heights of (a) 0.1 m and (b) 0.02 m. Also shown are the attenuation spectra measured for the MDF board alone for the same two geometries.

9.4.2 Perturbed arrays over soft ground

Figure 9.14 compares the measured insertion loss spectra due to a regularly spaced 5 × 10 square array of PVC pipes with a lattice constant of 0.1 m and a perturbed version of this array with a standard deviation of 2.0*radius in the cylinder locations from their original square array positions over a soft ground (felt-over-MDF board). The source and receiver were separated horizontally by 1.0 m and the receiver was placed at a height of 0.1 m. Figure 9.14 (a) shows data measured with a source height of 0.1 m and Figure 9.14 (b) presents data obtained with a source height of 0.02 m. The perturbed array with a standard deviation in cylinder locations of 2.0*radius from the original square array positions reduces the focusing effects while also improving the attenuation significantly at higher frequencies.
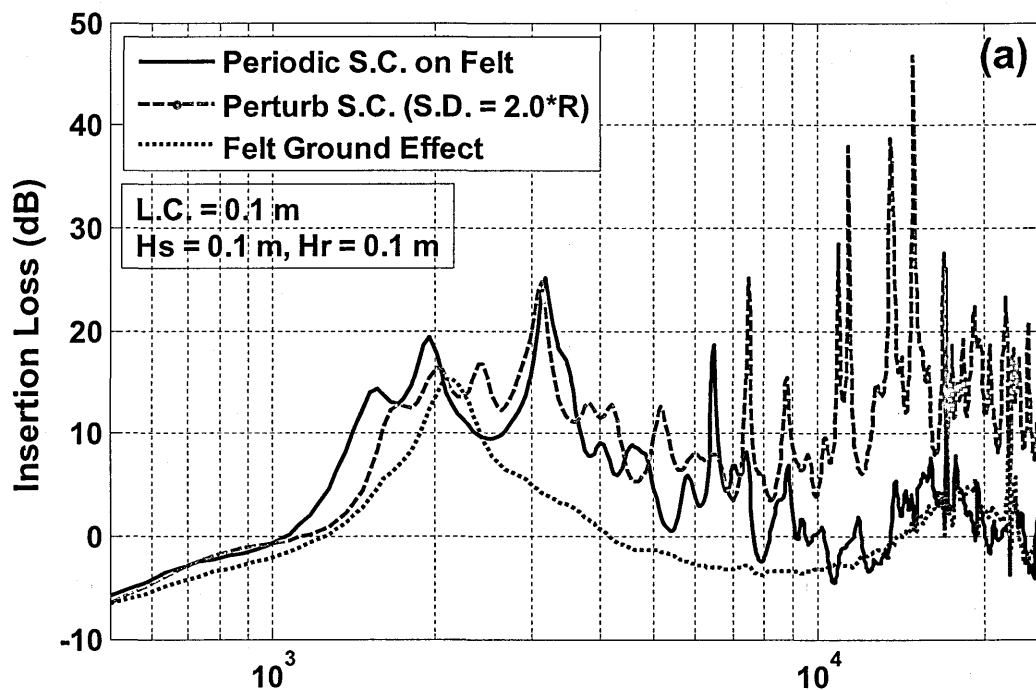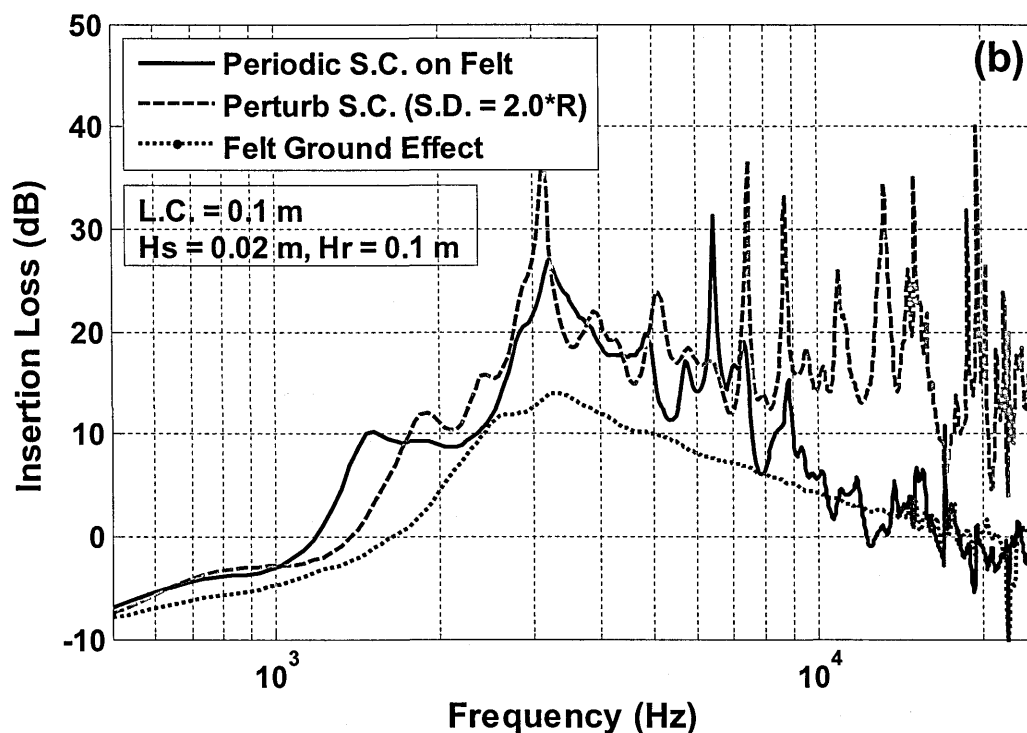
Figure 9.14 Comparison between measured insertion loss spectra due to a regularly spaced 5 × 10 square array of PVC pipes with a lattice constant of 0.1 m and a perturbed array in which the cylinder locations are perturbed with a SD of 2.0*radius from their original square array positions over hard ground (MDF board) with source-receiver separation of 1.0 m, receiver at height of 0.1 m and source at two heights of (a) 0.1 m and (b) 0.02 m. Also shown are the attenuation spectra measured for the MDF board alone for same two geometries.

9.4.3 Comparisons between data and predictions

Predictions of the insertion loss spectra due to perturbed vertical cylinders arrays over ground have been carried out as described in Section 9.3.1.2. The ground attenuation spectra were predicted by using an appropriate impedance model and best fit impedance model parameters in a model for propagation from a point source for a given source-receiver geometry. The insertion loss spectra due to regular and perturbed arrays of cylinders were predicted using multiple scattering theory (see Chapter 2). The centre position of cylinders was given as an input to MST using a Cartesian (x, y) coordinate system. The two effects were

added together to predict the overall effect. Figure 9.15 compares the measured and predicted insertion loss spectra due to an aperiodic array of PVC pipes placed on a MDF board with a perturbation of (a) 0.5*radius and (b) 2.0 *radius. The predicted insertion loss spectra show very good agreement with the measured data. The predictions obtained for a perturbed cylinder array over a layer of felt on MDF board with a perturbation of 2.0* radius also show good agreement with data (see Figure 9.15 (c)).
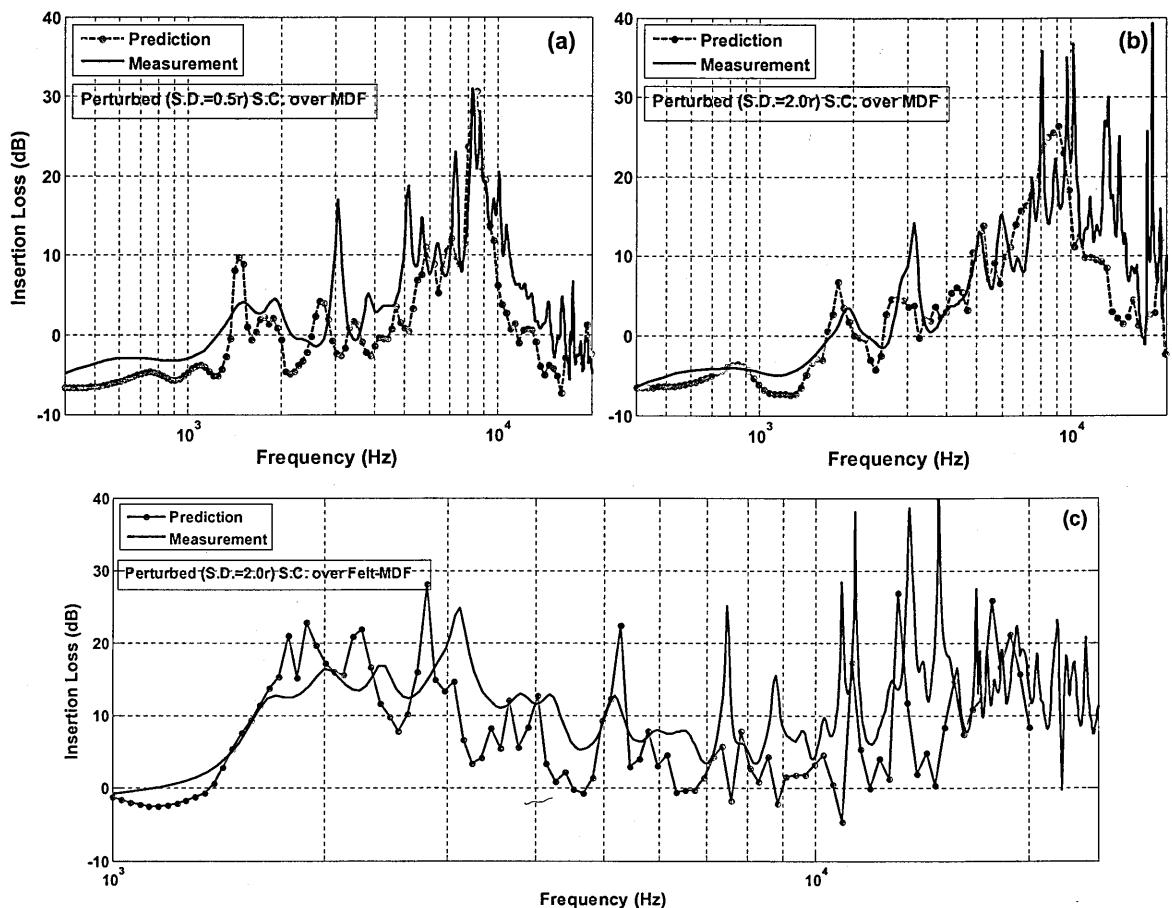
Figure 9.15 Comparison between measured and predicted insertion loss spectra due to perturbed 5 × 10 arrays of PVC pipes with source and receiver at height of 0.1 m and separation of 1.0 m (a) perturbations with an SD of 0.5*radius from original square array positions placed on a MDF board (b) perturbations with an SD of 2.0*radius from original square array positions placed on a MDF board (c) perturbations with an SD of 2.0*radius from original square array positions placed on a layer of felt-on MDF board . The predictions are obtained by adding the ground effect for a given geometry with multiple scattering predictions due to a 2D sonic crystal.

9.5 Random sonic crystal on a hard ground

Measurements and calculations have been made also for a totally random array of 50 PVC pipes placed with their axes perpendicular to MDF board and with a mean centre-to-centre separation of 0.1 m. A periodic array of 5×10 elements with lattice constant a and radius r occupies a rectangular area $(9a + 2r) \times (4a + 2r)$. Locations of cylinders were determined by generating two sets of random numbers within the intervals $[0, (9a + 2r)]$ and $[0, (4a + 2r)]$ for x- and y-coordinates, respectively. Thus, the mean separation of cylinders was the same as the lattice constant of the equivalent periodic array. Figures 9.16 (a) and (b) show the measured insertion loss spectra due to the random PVC pipe array with source-receiver separation of 1.0 m, receiver at height of 0.1 m and source at height of (a) 0.1 m (b) 0.02 m. The lowest band gap central frequency for a periodic sonic crystal with a lattice constant of 0.1 m, calculated using Eq. 9.3, is 1.7 kHz. No band gap is present around that frequency for the random arrangement. However, the measured insertion loss spectra show a frequency shifted narrow peak at 2.35 kHz. The 2nd order band gap for periodic sonic crystal with a lattice constant of 0.1 m spans from 2.7 kHz to 5.0 kHz having a band gap centre frequency of 3.4 kHz. However, Figure 9.16 shows that the corresponding 2nd band gap due to the random sonic crystal arrangement spans from 3.0 kHz to 8.0 kHz with a centre band gap frequency of 5.5 kHz. Moreover, the 2nd order band gap obtained over random sonic crystal shows several peaks.
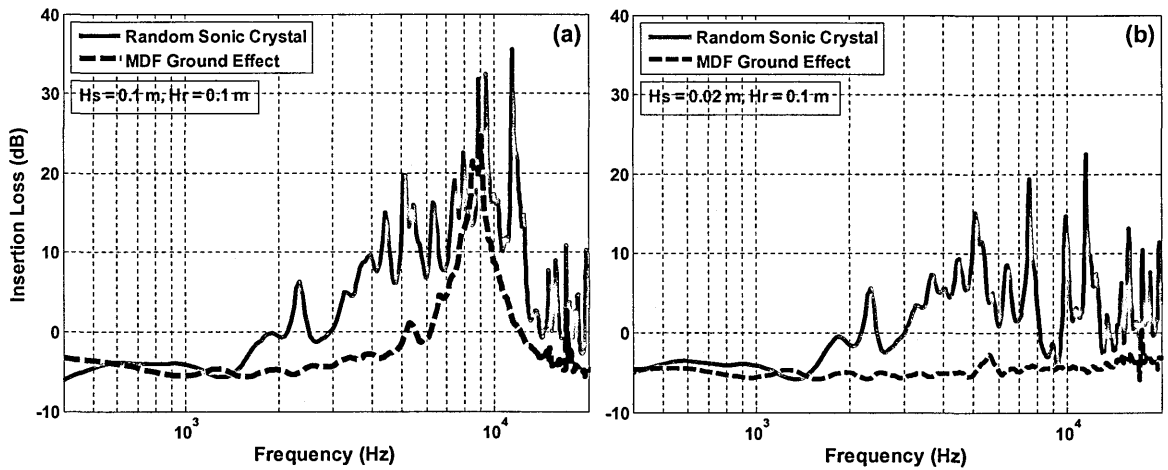
Figure 9.16 Measured insertion loss spectra due to randomly spaced 5 × 10 square array of PVC pipes over MDF board with source-receiver separation of 1.0 m, receiver at height of 0.1 m and source at height of (a) 0.1 m (b) 0.02 m. Also shown is the attenuation spectrum measured for the MDF board alone.

9.6 Comparison between Periodic, Perturbed and Random S.C.

Figure 9.17 compares the measured insertion loss spectra due to (i) a regularly spaced 5 × 10 square array of PVC pipes with a lattice constant of 0.1 m, (ii) perturbed arrays with a standard deviation in cylinder locations of 0.5*radius and 2.0*radius from their square array positions and (iii) randomly spaced cylinders with a mean centre-to-centre spacing of 0.1 m placed over hard ground (MDF board). For a filling fraction of 13%, the small perturbation (S.D. = 0 5.*r) does not produce a significant change in measured or predicted attenuation. Measurements and predictions suggest that a quasi-periodic array with a perturbation in cylinder locations having an S.D. of 2.0r performs better at high frequencies than either periodic or random arrangements while also reducing the negative attenuation associated with the pass bands (focusing). Randomly spaced cylinders with a mean separation equal to the lattice constant of periodic array (L.C. = 0.1 m) give a significantly reduced lower band gap while still giving comparable attenuation at higher frequencies. These measurements confirm the

earlier conclusion that the attenuation due to the ground effect can be added to the attenuation due band gaps corresponding to a low filling fraction of 13 %.
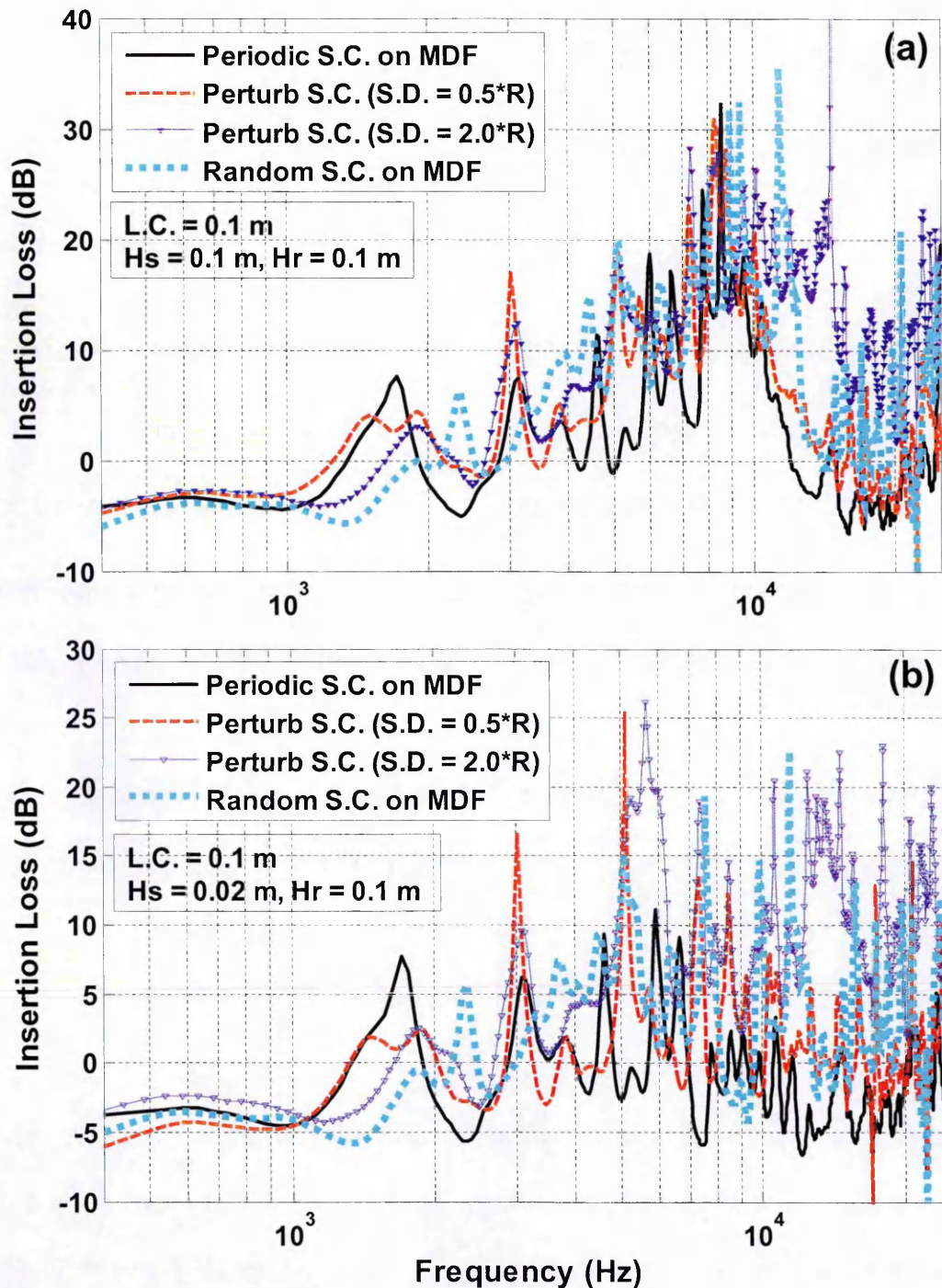
Figure 9.17 Comparison between measured insertion loss spectra due to (i) a regularly spaced 5 × 10 square array of PVC pipes with a lattice constant of 0.1 m (ii) a quasi-periodic sonic crystals with locations perturbed with SDs of 0.5*radius and 2.0*radius from their equivalent square array positions and (iii) randomly spaced cylinders with a mean c-to-c separation of 0.1 m over hard ground (MDF board) with source-receiver separation of 1.0 m, receiver at height of 0.1 m and source at two heights of (a) 0.1 m and (b) 0.02 m.

9.7 Conclusions

Laboratory measurements have been carried out over regular arrangements of 0.5 m long PVC pipes placed on a hard ground and a soft ground respectively. The measured insertion loss spectra obtained over a hard ground show that the ground attenuation peak reinforces the band gaps due to sonic crystal effects. Similarly, the attenuation due to soft ground effect enhances the sonic crystal band gaps significantly. It was concluded that conjunctive use of soft ground effects and sonic crystal effects could be useful to attenuate traffic noise. In fact this can happen 'naturally' with a tree belt.

Measurements have been carried out also to investigate the effects of perturbing the cylinder locations from their original periodic positions. For arrays with a filling fraction of 13%, a small perturbation (S.D. = 0.5*r) does not produce a significant change in measured or predicted attenuation. Measurements and predictions suggest that a quasi-periodic array with a perturbation in cylinder location having an S.D. of 2.0r performs better at high frequencies than either periodic or random arrangements while also reducing the negative attenuation associated with the pass bands (focusing).

It has been shown also that the 3D problem of predicting propagation through vertical cylinders on a (hard or soft) plane can be solved fairly accurately by adding two 2D predictions. The sonic crystal effects in free space have been calculated using MST and propagation over a ground surface for a given source-receiver geometry has been predicted using the classical solution for a point source over an impedance plane. The agreement between data and predictions obtained in this manner was found to be very good.

Chapter 10

10. Sound propagation through crops and hedges

10.1 Introduction

In previous chapters sound propagation over different kinds of artificially created indoor and naturally occurring outdoor ground surfaces has been studied, This chapter considers sound propagation through crops and through hedges. In the past, there was some confusion in discriminating between the effects due to vegetation associated with crops and ground effect. One of the aims of the current study is to separate the effects of crops from the ground effect. As discussed in previous chapters, acoustically soft ground attenuates traffic noise. However, the additional noise attenuation due to vegetation in the form of crops and hedges is investigated here. A series of outdoor measurements through crops have been carried out at short, medium and long ranges. Measurements of sound transmission through hedges have been carried out also. A model for sound

attenuation by vegetation is proposed based on measurements and suggestions made by Aylor [156].

The first section of this chapter presents the introduction, the second section reviews relevant literature and the third explains models for sound attenuation through vegetation. Section 4 presents data for short and medium range sound propagation over crops. This section also compares data and predictions. Section 5 investigates measurements and predictions of sound transmission through hedges. Section 6 presents a summary and conclusions.

10.2 Literature review

There have not been many published studies concerning the propagation of sound through crops. Aylor [156], [157] has studied sound transmission loss through various crops, bushes and trees including dense corn, hemlock, red pine, hardwood brush and dense reeds in water. The field corn was planted with mean plant densities of 27 and 13 plants m^{-2} and total leaf areas per unit volume of 6.3 m^{-1} and 3.0 m^{-1} respectively. The mean stem diameter was 0.015 m and average plant height was 1.8 m. The corn was planted in a fine sandy loam, which has porosity of 0.45 [157]. Hemlock was planted over an area of 37 m × 66 m with a stem density of 0.5 stems m^{-2}. The mean plant height was 1.5 and mean diameter was in between 0.065 m and 0.115 m. Hemlock was planted over sandy loam with a porosity of 0.52.

Sound propagation measurements were also carried out through red pine trees. The trees were 16 m tall with the mean trunk diameter of 0.23 m. The trees were planted with a mean spacing of 3.3 m with a planting density of 0.0865 trees m^{-2}. The trees were planted over mineral soil with a porosity of 0.68. The fallen leaves from the red pine trees created a 0.025 m deep layer of decaying foliage above the soil.

Measurements were carried out also of propagation through dense hardwood brush including trees and shrub species with foliage extending from the ground to a height of 6 m but with the plant density and mean stem diameter varying with height. The plant height was divided into five categories between 0 m and 7.5 m in increments of 1.5 m. The mean stem diameter varied between 0.0065 m and 0.0215 m and plant density was in between 4.5 stems m^{-2} and

6.9 stems m^{-2}. The dense hardwood brush was planted on soil with porosity varying between 0.53 and 0.75. The broadband noise source was placed at a height of 1.5 m except during measurements in corn crops when it was placed at height of 1.0 m. The horizontal level difference was measured by placing a reference microphone at a distance of 3 m from the source and at the same height as the source and a second microphone just outside the vegetation. The distance between the source and the second microphone was 30 m except during the measurements through hardwood bush when it was increased to 65 m.

Aylor [156] suggested that the ground effect can be added to the attenuation due to leaves and stems to obtain the total attenuation for the sound propagation through vegetation. However, he [156] also pointed out that simple addition may not always be accurate due to multiple scattering by stems, leaves and twigs causing some additional interaction with the ground. However, this depends on the type of vegetation. If the vegetation consists of crops like corn, then the attenuation due to corn and ground effect can be added together because they occur at different frequencies i.e. the ground effect occurs at lower frequencies and attenuation due to corn crops occur at higher frequencies. For vegetation with large leaves and shrubs the ground effect and the attenuation due to vegetation are not widely separated in frequencies. Nevertheless, the measurements indicated that adding the two effects was not unreasonable. Aylor [156] considered first whether the sound attenuation due to vegetation is due to viscous and thermal dissipation between the fluid media and plant surfaces. However, the attenuation due to viscous and thermal losses calculated for a given vegetation density is less than the measured attenuation. Aylor [156] argued that

the extra energy loss observed is due to multiple scattering effects within the vegetation. It was concluded that the attenuation is directly proportional to vegetation density and that foliage attenuates the sound at higher frequencies.

Aylor [157] extended his work to study the sound propagation through reeds planted in water since sound reflection due a water surface (assumed to be acoustically-hard) can be determined very accurately thereby enabling ground effect to be separated from the vegetation effect. The reeds were planted with a mean density of 59 ± 10 plants m^{-2}. The average leaf width was 0.032 m with the total leaf area per unit volume of 3.0 m^{-1}. The average plant height was 2.5 m. Aylor [157] concluded that to maximize the sound attenuation due to the vegetation it should be planted densely with high leaf area per unit volume.

Martens [158] investigated sound propagation through vegetation and its effects in laboratory. Marten's [158] data show that the attenuation due to plants are at higher frequencies and that vegetation behaves as a low pass filter. Martens [158] shows that the different kind of vegetation attenuate sound between 2 and 8 kHz. Martens [158] argued that Aylor's empirical prediction method (see section 10.3.1) did not fit his measured data. Subsequently Aylor [159] explained that the excess attenuation measured by Martens [158] was normalized by total plant biomass whereas in his study [156], [157] excess attenuation was normalized using the leaf area per unit volume. When Marten's results were normalized using leaf area per unit volume in the same way the agreement was better. According to Aylor, leaf area per unit volume is more important than the total plant biomass for noise attenuation. However, according to Martens [158] the total biomass of vegetation is more important.

Using a laser-doppler-vibrometer Martens [160] studied the plants' leaf vibration in response to acoustic energy . The sound energy absorbed by each leaf through vibration is very small. However, for a full grown tree the individual leaf attenuations when added together give a significant overall effect [160]. Following on from this, Martens *et al.* [161] carried out model experiments in a laboratory using pulses to study the sound reflection from deciduous plant leaves. They found that the size of the leaf is an important parameter for the reflection of sound i.e. the bigger the leaf size, the larger will be the acoustic reflection. The second important parameter for sound reflection is the mass of the leaf, especially at high frequencies, when the wavelength is less than the leaf size. They reached the same conclusions as Aylor [156], [157], that plants with dense and larger leaf sizes give higher sound attenuation.

Price *et al.* [149] measured sound attenuation due to woodlands and compared the resulting data with the predictions of a model obtained by summing the separate contributions of the ground, the trunks, the branches and the foliage. The simple addition of ground effect predictions to scattering predictions based upon trunk size and density did not give good agreement at high frequencies. However, a semi-theoretical model including a phenomenological adjustment for foliage effects improved the agreement with measured data. Huisman and Attenborough [150] have measured excess attenuation spectra through pine forest at different ranges of between 10 m and 100 m. The excess attenuation was predicted successfully up to 1 kHz using a two parameter impedance model where the ground effect dominated. At higher frequencies the data differed from predictions of ground effect alone and show more attenuation due to scattering by

trunks, branches and viscous losses through the vegetation. The observed high frequency attenuation was modelled as energy loss due to multiple scattering inside the vegetation and it is added to the attenuation due to ground. However, since the agreement between data and prediction remained poor it was concluded that the interaction between the ground effect and multiple scattering is more complicated than a simple addition. Fang and Ling [152] investigated the noise attenuation of 35 different tree belts. A point source was placed in front of the tree belt and sound pressure level inside the tree belt was measured at different positions. The noise attenuation due to different tree belts was found to depend on their width, height, length and density. Large shrubs and densely populated tree belts were found to give more than 6 dBA attenuation, medium size shrubs and tree belts attenuated the sound by between 3 and 6 dBA and sparsely distributed tree belts and shrubs attenuated the sound by less than 3 dBA. The width of vegetation was found to be the most important factor for attenuation of noise, the greater the vegetation width, the greater the pathway of sound through the vegetation resulting in higher sound absorption and diffusion. Also when the tree belt was longer, it was considered that acoustic waves would diffract and scatter more resulting in higher attenuation. In all of the vegetation belts examined, the shrubs were considered to be the most effective in reducing noise due to scattering from dense foliage and branches at lower source-receiver heights. At higher source-receiver height trees were considered to provide good attenuation due to sound diffusion and absorption processes. Thus, it was concluded that tree belts and shrubs should be planted together to provide best attenuation performance [152].

Tarrero *et al.* [153] carried out an experimental investigation of the sound attenuation in different types of forests with different tree densities, different trunk diameters, and both deciduous and evergreen leaves. The measured data at several source-receiver distance ranges showed that the trees have a noticeable effect on sound attenuation at longer distances of more than 40 m. However, if the tree plantation is dense then the attenuation effect due to trees can be seen at shorter ranges. The predictions of the attenuation effect due to vegetation were carried out using a simple scattering model which takes account of the reduced coherence between the direct and reflected sound field.

Attenborough *et al.* [162] studied sound propagation through crops at short (i.e. 1 m) and medium ranges, i.e. 10 m and 20 m. Excess attenuation data over 0.55 m high wheat crops shows that the presence of crops appears to influence the coherence of the ground-reflected sound. Due to the loss of coherence, the excess attenuation maximum gets distorted. Attenborough *et al.* [162] also studied sound propagation through trees and vegetation. Sound propagation through two kinds of pine forests has been studied. Measured data through vegetation and predictions for ground effect alone show good agreement up to 1 kHz. However, at higher frequencies the data have significantly different magnitudes and frequency dependence to those predicted by ground effect alone. It is proposed that sound attenuation was due to scattering of sound by trunks and branches plus the attenuation of sound by viscous loss in the foliage.

Renterghem *et al.* [154] numerically investigated noise propagation through a 15 m deep tree belts using a 3D finite-difference-time-domain calculations. They consider that noise attenuation by tree belts occurs due to three mechanisms. The

first is the scattering of sound by trunks, branches, twigs and leaves, the second is the sound absorption by vegetation due to leaves vibration and viscous-thermal boundary layer effects and the third is sound attenuation due to ground effect. The presence of a forest floor gives significantly more low frequency attenuation than typical grassland. They concluded that the insertion loss due to a tree belt increases with increase in tree stem diameter and decrease in spacing between the trees. Further information and discussion about the findings of Renterghem et al, for example about trunk spacing, is given in Chapter 9.

Fang [163] studied the noise attenuation by five different kinds of hedges. The source was placed in front of the hedges and receivers were placed at different heights and distances behind the hedges. The insertion loss was calculated by subtracting the measured sound pressure level through hedges from the measured sound pressure level (using the same source-receiver geometry) with no hedges. It was concluded that densely populated hedges give better attenuation performance due to increased scattering effect and absorption.

10.3 Models to predict the attenuation through crops

10.3.1 An empirical model

Aylor [157] has suggested that there is a relationship between a normalised excess attenuation, i.e. the attenuation in excess of that due to ground effect divided by the square root of the product of foliage area per unit volume and the scattering parameter (which is the product of wave-number and a characteristic leaf dimension). Attenborough *et al.* [164] fitted Aylor's data using the relationships and parameters suggested in [156], [157]. Figure 10.1 shows that Aylor's data for normalised excess attenuation as a function of scattering parameter, obtained through reeds and corn (with two leaf sizes). By fitting the data given in Figure 10.1, the proposed empirical formula is [164],

$$\frac{EA(dB)}{\sqrt{FL}} = 3[1 - \exp(0.3 - 0.5(ka))], \qquad ka > 0.3 \qquad (10.1)$$

where $EA(dB)$ represents the excess attenuation in dB, F m^{-1} is the foliage area per unit volume, L is the length of the propagation path, k is the wave-number = $2\pi f/c$, c being the adiabatic sound speed in air and a is the mean leaf width. The lower limit on ka is required to avoid negative values of EA. For example, this implies a low frequency limit of around 1 kHz for a mean leaf width of 0.032 m and a low frequency limit of about 100 Hz for a mean leaf width of 0.3 m.
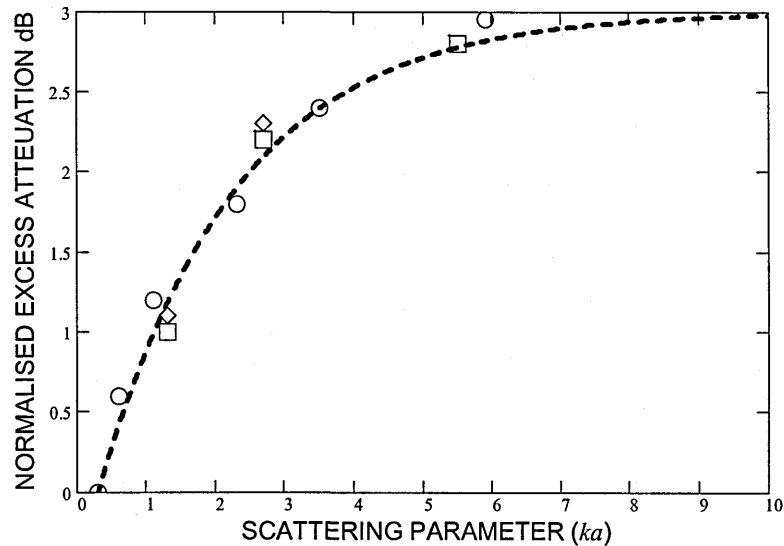
Figure 10.1 Data for normalized excess attenuation [dB/√{(foliage area per unit volume, F)×(propagation path length, L)}] through reeds (open circles) with mean leaf width 0.032 m and corn (boxes F = 3 m⁻¹; diamonds F = 6.3 m⁻¹) with mean leaf width 0.074 m and a fitted curve (Eqn.10.1).

10.3.2 A scattering model

Predictions of the reflection of sound by a hard-backed array of acoustically-hard cylindrical scatterers using a 2D Multiple Scattering Theory (MST) (see Chapter 2) have been used to determine an equivalent wave propagation constant for a specific density and mean size of the scatterers (stems, branches or twigs, with diameters > 0.005 m). The propagation constant is obtained by fitting the reflection predictions with those of a three parameter slit-pore impedance model (see Chapter 4). The required porosity and layer depth are determined respectively from the density or volume fraction (filling fraction) of scatterers and depth of the scattering area used in the simulation. The equivalent flow resistivity is used as an adjustable parameter. This approach defines an equivalent rigid-porous layer in which attenuation due to viscous and thermal

effects is equivalent to that due to (reverberant) scattering in a given region of scatterers [164].

The equivalent complex wave propagation constants for trees and branches simulated by arrays of horizontal cylinders with a log-normal distribution of radii can be calculated from a slit pore layer model (see Chapter 4) for:

- filling fractions in the range 0.001 to 0.1 and

- scatterer diameters in the range 5 to 250 mm.

In this range of filling fractions the porosity may be approximated by the simple linear relationship [164]:

$$Porosity = -0.786 \times FillingFraction + 0.975, \qquad \textbf{(10.2)}$$

Knowing the diameter and volume fraction (filling fraction) of scatterers the ranges of equivalent flow resistivity (R_e) given in Figure 10.2 and Table 10.1 can be used to calculate the propagation constant. Typically flow resistivity (R_e) increases with scatterer density.
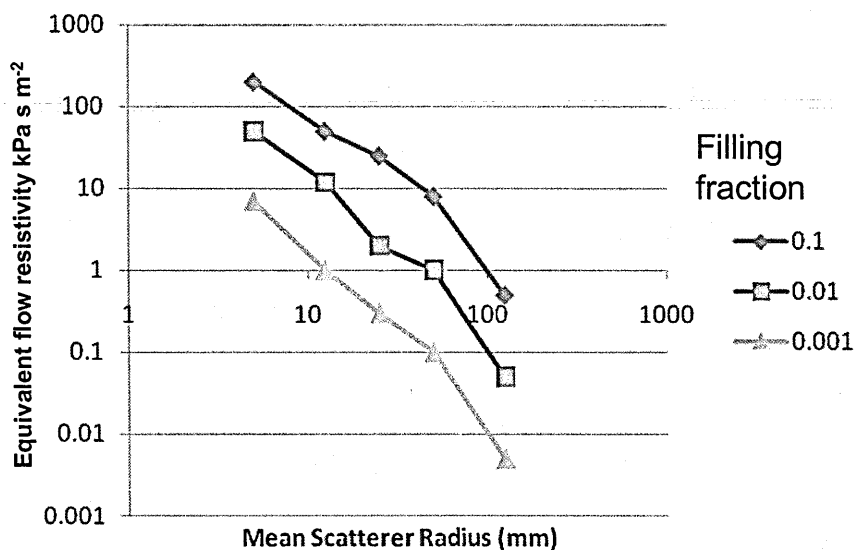
Figure 10.2 Predicted relationships between filling fraction, mean scatterer radius and equivalent flow resistivity [164].

These results have been used to propose a simple empirical formula (See Eq. 10.3) relating mean scatterer radius (r) and filling fraction ($f\!f$) to equivalent flow resistivity (R_e).

$$R_e = 0.11 f\!f^{0.95}/r^2. \tag{10.3}$$

The attenuation constant predictions obtained by using the resulting equivalent flow resistivity and porosity in the slit-pore model can be used to determine the additional attenuation due to (reverberant) scattering by branches and twigs as long as the characteristic scattering element sizes are greater than about 5 mm.

The application of Eq. 3.1 and Eq. 3.2 to predicting multiple scattering by winter wheat stems is considered in a later section.

Table 10.1 Equivalent Flow Resistivities for five average scatterer radii.

Mean Scatterer Radius (mm)	Average Fitted Flow Resistivity kPa s m^{-2}		
	Filling Fraction = 0.1	Filling Fraction = 0.01	Filling Fraction = 0.001
5	197	52	6
12.5	52	6	1
25	25	2	0.3
50	8	0.9	0.075
125	0.5	0.05	0.0053

10.3.3 Modelling for loss of coherence

Another potential effect of scattering by vegetation is to reduce the coherence between direct and ground-reflected sound i.e. to weaken the constructive and destructive interference responsible for the ground effect. This is similar to the effect of turbulence [162]. The influence of turbulence on propagation from a point source near the ground can be calculated from [164],

$$\langle p^2 \rangle = \frac{1}{R_1^2} + \frac{|Q|^2}{R_2^2} + \frac{2|Q|}{R_1 R_2} \cos[k(R_2 - R_1) + \theta]T,$$

(10.4)

where θ is the phase of the spherical wave reflection coefficient, ($Q=|Q|e^{i\theta}$) (a function of source and receiver geometry and ground impedance – see Chapter 4, Section 4.4.1), and T is the coherence factor determined by the turbulence effect given for a Gaussian turbulence spectrum, by

$$T = e^{-\sigma^2(1-\rho)}.$$

(10.5)

In Eq. 10.5, σ^2 is the variance of the phase fluctuation along a path given by,

$$\sigma^2 = A\sqrt{\pi}\langle \mu^2 \rangle k^2 R L_0,$$

(10.6)

where L_0 is the outer scale of turbulence, R is the range, $\langle \mu^2 \rangle$ is the variance of the index of refraction, k is wavenumber and the coefficient A is given by,

$$A = 0.5 , \quad R > kL_0^2 \text{ or } A = 0 , \quad R < kL_0^2 ,$$

(10.7)

ρ is the phase which is a function of L_0 and h the maximum transverse path separation i.e.

$$\rho = \frac{\sqrt{\pi}}{2} \frac{L_0}{h} erf\left(\frac{h}{L_0}\right),$$ (10.8)

where h is the maximum transverse path separation, which in the absence of refraction is given by,

$$\frac{1}{h} = \frac{1}{2}\left(\frac{1}{h_s} + \frac{1}{h_r}\right),$$ (10.9)

where h_s and h_r are the source and receiver heights respectively, and $erf(x)$ is the error function defined by,

$$erf(x) = \frac{2}{\sqrt{\pi}} \int_0^x e^{-t^2} dt .$$ (10.10)

A typical value for L_0 is the source height. Typical values of $\langle \mu^2 \rangle$ are between 2×10^{-6} and 10^{-4}.

In a later section loss of coherence due to scattering is modelled as an 'effective' turbulence using parameter values obtained by best fit with data.

10.4 Winter wheat crops: data and predictions

A series of measurements have been made in a field of 0.45 m – 0.55 m high winter wheat crops at Butt's Close experimental farm in Woburn Sands, Bedfordshire, UK operated by Rothamsted Research. Some data were collected also over other types of crops. Measurements were carried out during summer (June - September) 2011 and in May and June 2012.

10.4.1   Horizontal level difference

The measurement system used for outdoor measurements is described in chapter 3 (see Section 3.3). The characterization for ground growing crops was carried out using vertical level difference (see Chapter 4). The propagation through crops was studied using horizontal level difference method. Schematics of vertical and horizontal level difference measurement arrangements are shown in Figure 10.3.

The history of using the horizontal level difference method for measuring sound propagation goes back to more than 40 years, when Delany and Bazley used this method for the measurement of aircraft noise [165]. Horizontal level difference data have been used to study the effect of crops on sound propagation at several distances. In the measurements of horizontal level difference the microphone nearest to the source is used as a reference to eliminate any effects due to varying source sound power output. Other microphones are placed at a desired horizontal distance from the source. The horizontal level difference is calculated by subtracting the SPL measured at desired location from the SPL measured at reference microphone.
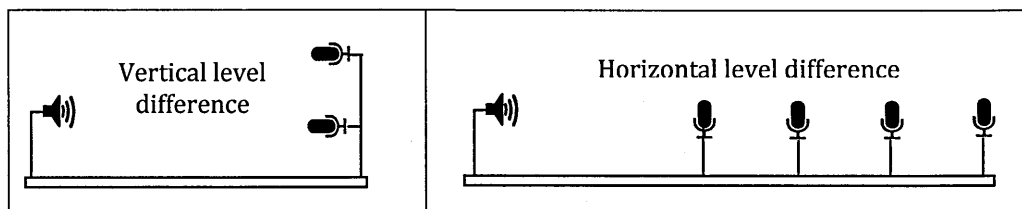
Figure 10.3 Schematics of vertical and horizontal level difference measurement arrangements.

10.4.2 Short range data and predictions

The main aim of this study was to improve understanding of the effect of crops over sound propagation. Initial measurements at the Butt's Close site showed that the acoustical properties of the ground surface growing crops are different from the ground with no crops. The measured spectra over crops using either vertical or horizontal level difference measurement technique consist of two effects, i.e. the ground effect and the effects due to the presence of the crops; henceforth termed the 'crops effect'. It is important to know exactly the acoustical properties of ground to separate ground effects from the crops effect. The purpose for these experiments was to carry out measurements at shorter ranges i.e. 1 m. A small patch of dimensions 1.88 m × 1.84 m was selected for measurements. The selected area was large enough to carry out measurements at a range of 1m. Vertical level difference measurements were carried out inside crops with different geometries and at different positions as shown in Figure 10.4 (a). After that the selected patch was cleared by carefully clipping the stems of the crops without disturbing the ground. The cleared patch is shown in Figure 10.4 (b). Vertical level difference measurements with different geometries and positions were carried out over cleared area on the same day. Consequently two data sets were available i.e. level difference spectra including both ground and crops effects and level

difference spectra due to ground effect only. Figure 10.4 (c) and (d) compares the measured level difference spectra with and without crops using two geometries and it can be concluded that that there are no effects of crops over a range of 1 m. The stems of the wheat crops are very thin with a mean stem diameter of 2.63 mm. Similar measurements have been made at another patch with winter wheat crops and lead to a similar conclusion. Subsequently a 1.9 m × 2.1 m patch of rape seed crops was selected for similar measurements and the resulting data also show that the crops do not influence sound propagation over a range of 1 m.
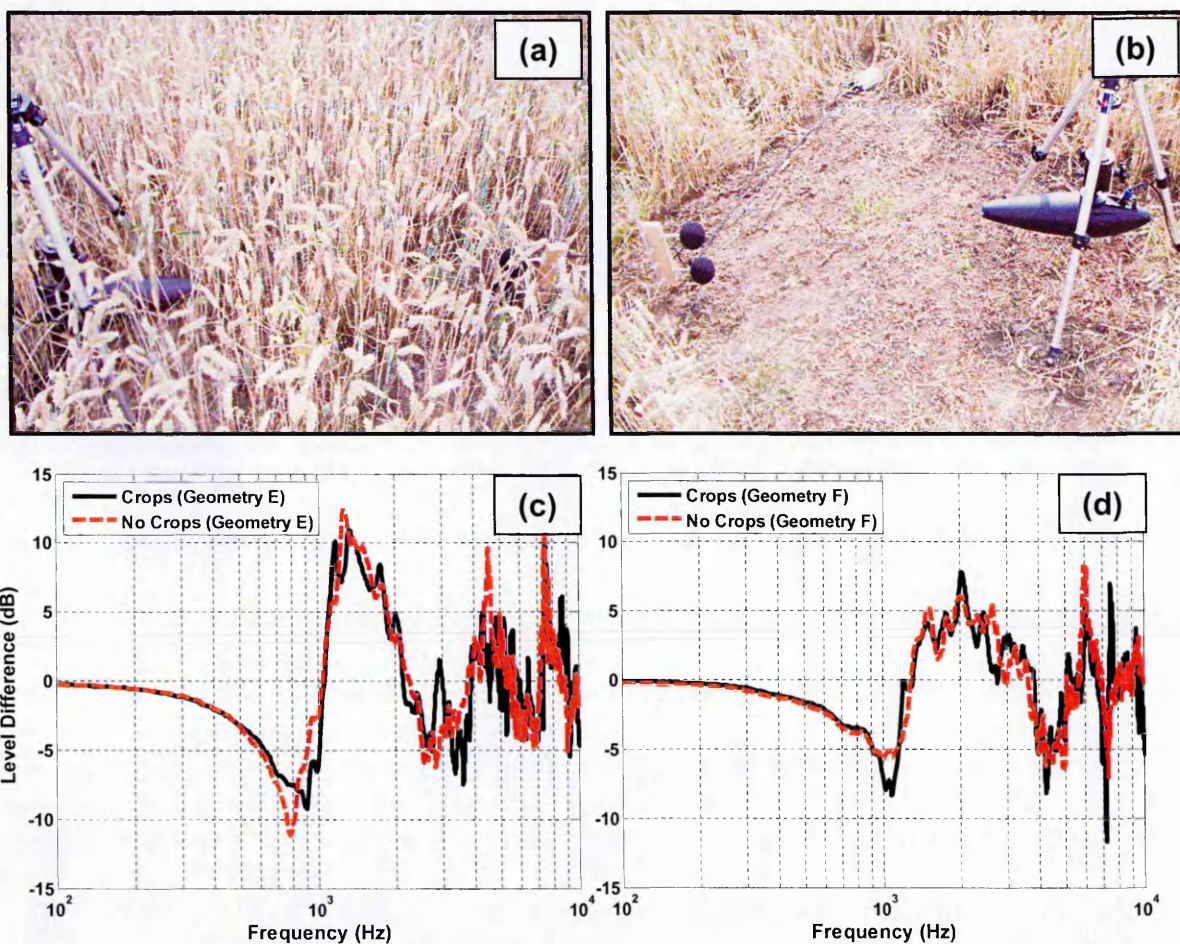
Figure 10.4 Photographs of sites used for short range crops measurements (a) with crops (b) without crops. Level difference spectra measured over ground with 0.5 m high crops (see (a)) and without crops (see (b)) (c) Geometry E: Source height = 0.3 m, Upper microphone height = 0.3 m, Lower microphone height = 0.15 m and source-receiver separation = 1.0 m (d) Geometry F: Source height = 0.21 m, Upper microphone height = 0.3 m, Lower microphone height = 0.15 m and source-receiver separation = 1.0 m.

Although it is not possible to distinguish any effects due to crops at such a short range the short range data is useful for deducing the acoustical properties of the ground beneath the crops. The measured vertical level difference over the area cleared from crops was fitted using slit pore model (see Chapter 4 for fitting details). Figure 10.5 shows an example comparison between measured vertical level difference spectra over ground surface cleared from winter wheat crops and predictions using a two-parameter slit pore model impedance with best fitted flow resistivity of 300 kPa s m^{-2} and porosity of 0.4. These measurements were carried out in July 2011. Data for a second area cleared from wheat crops were fitted with a flow resistivity of 170 kPa s m^{-2} and a porosity of 0.2 again using the slit pore model. Data for a third ground surface growing rape seed plants were fitted with a flow resistivity of 300 kPa s m^{-2} and a porosity of 0.2 using the slit pore model. These measurements were carried out in August 2011.

In May 2012, the outdoor measurements were repeated and extended to longer range. Vertical level difference measurements were carried out over a bare ground with no crops and a close by patch containing growing crops. The best fit flow resistivity and porosity values over the bare ground are 2000 kPa s m^{-2} and 0.2 respectively, and over the ground surface with crops are 200 kPa s m^{-2} and 0.2 respectively. These results suggest that bare ground (no crops) is acoustically-harder than the ground containing growing crops (the best-fit flow resistivity for bare ground is ten times higher than that for the ground with crops). Another set of measurements over ground growing winter wheat crops (which were not cleared) yield flow resistivity and porosity values of 200 kPa s m^{-2} and 0.2 respectively. It is concluded that ground surfaces growing crops have a flow resistivity of between 200 kPa s m^{-2} and 300 kPa s m^{-2} and a porosity of between 0.2 and 0.4. These

impedance model parameters obtained over ground containing growing crops will be useful when studying longer range propagation of sound over ground with crops.
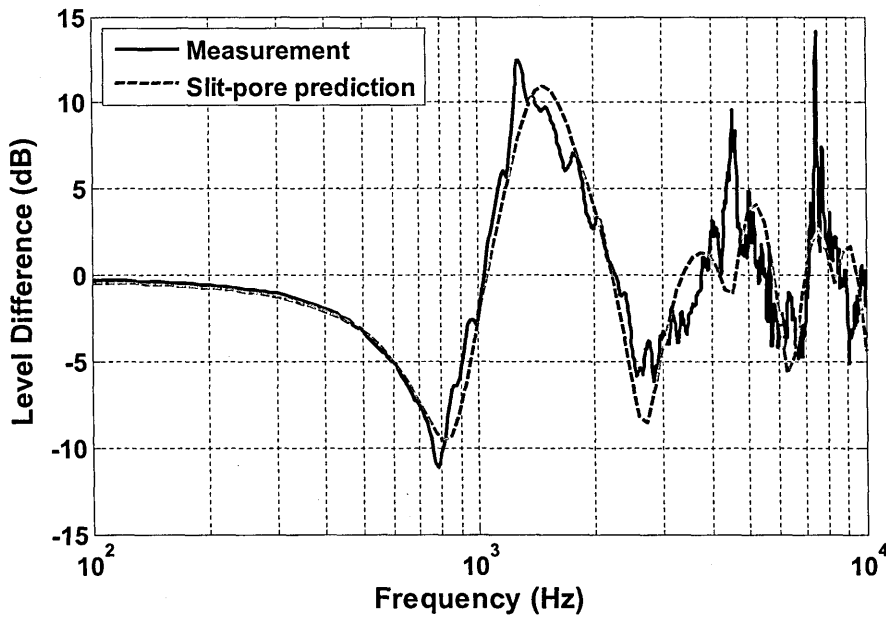
Figure 10.5 Example comparison between measured level difference spectra (black continuous line) over 1.88 m × 1.84 m patch cleared by winter wheat crops with source at height of 0.3 m, upper and lower microphones at heights of 0.3 m and 0.15 m respectively and source-receiver separation of 1.0 m with numerically obtained best fits (red broken line) using slit pore model ground impedance with a flow resistivity of 300.0 kPasm^{-2} and porosity of 0.4.

10.4.2   Medium range data and predictions

10.4.2.1   Data

Level difference spectra have been measured by placing the reference microphone at a distance of 1.0 m from the Tannoy source and further microphones at the same height as the source but at distances of 2.5 m, 5.0 m, 7.5 m and 10.0 m respectively (see Figures 10.6 (b) and (c)). The measured average winter wheat crops height was between 0.45 m and 0.55 m. Measurements were carried out at several source and receiver heights. However, the microphones and source were always inside the crops. Measurements were carried out by placing source and receivers at equal heights of 0.2 m, 0.3 m and 0.4 m. In this chapter only the measured data for a height of 0.3 m are presented since similar results were obtained and similar conclusions were drawn for all three geometries. Measurements were carried out during dry conditions in August 2011, wet conditions May 2012 when the crops were greener and intermediate conditions in June 2012.

Figure 10.6 show photographs of the crops during the different outdoor measurements. Figures 10.7, 10.8, 10.9 and 10.10 show measured level difference spectra between the reference microphone at a distance of 1.0 m and microphones at 2.5 m, 5.0 m, 7.5 m and 10.0 m respectively from the source. Level difference data at a range of 7.5 m are missing for measurement exercise carried out in June 2012 due to time and weather constraints. The source and the receivers were placed at equal heights of 0.3 m above ground. Figures 10.7-10.10 compare the measured spectra over crops during different times of the year. It is

concluded from the longest range data (Figure10.10) that dry crops with fallen leaves (August 2011 – see Figure 10.6 (a) & (b)) give the least sound attenuation at frequencies above 3 kHz. Whereas the green crops with leaves (May 2012 – see Figure 10.6 (c) & (d)) give the most sound attenuation at these frequencies. The crops in an intermediate state (June 2012 – see Figure 10.6 (e) & (f)) produced high frequency attenuation spectra lying between the other two. Similar conclusions can be drawn from data at other ranges i.e. 2.5 m, 5.0 m and 7.5 m. The data measured over greener crops (May 2012) show more scattering at high frequencies than the less green crops (June 2012 and August 2011). Comparisons of Figures 10.8 – 10.10 suggest that, as the propagation path for the sound propagation through the crops is increased the attenuation and scattering due to crops is increased. Level difference data measured over crops at different times of the year also show spectral differences between 1 and 3 kHz, where the main ground effect maximum occurs (See spectra between 1 and 3 kHz in Figures 10.8 – 10.10). These spectral differences may be due to the difference in ground effect since the measurements were carried out at different locations; and at different times of the year, under different weather and temperature conditions. Also the presence of crops influences the coherence between the direct and ground-reflected sound causing the ground effect maxima to become shallower, The loss of coherence may be another reason for the spectral differences between 1 and 3 kHz. This is also evident from the data as the greenest crops (see Figure 10.8-10.10, May 2012) provide maximum scattering and loss of coherence which result in the shallowest ground effect. Other measurements (not reported here) that have been carried out at several source and receivers height give similar results.
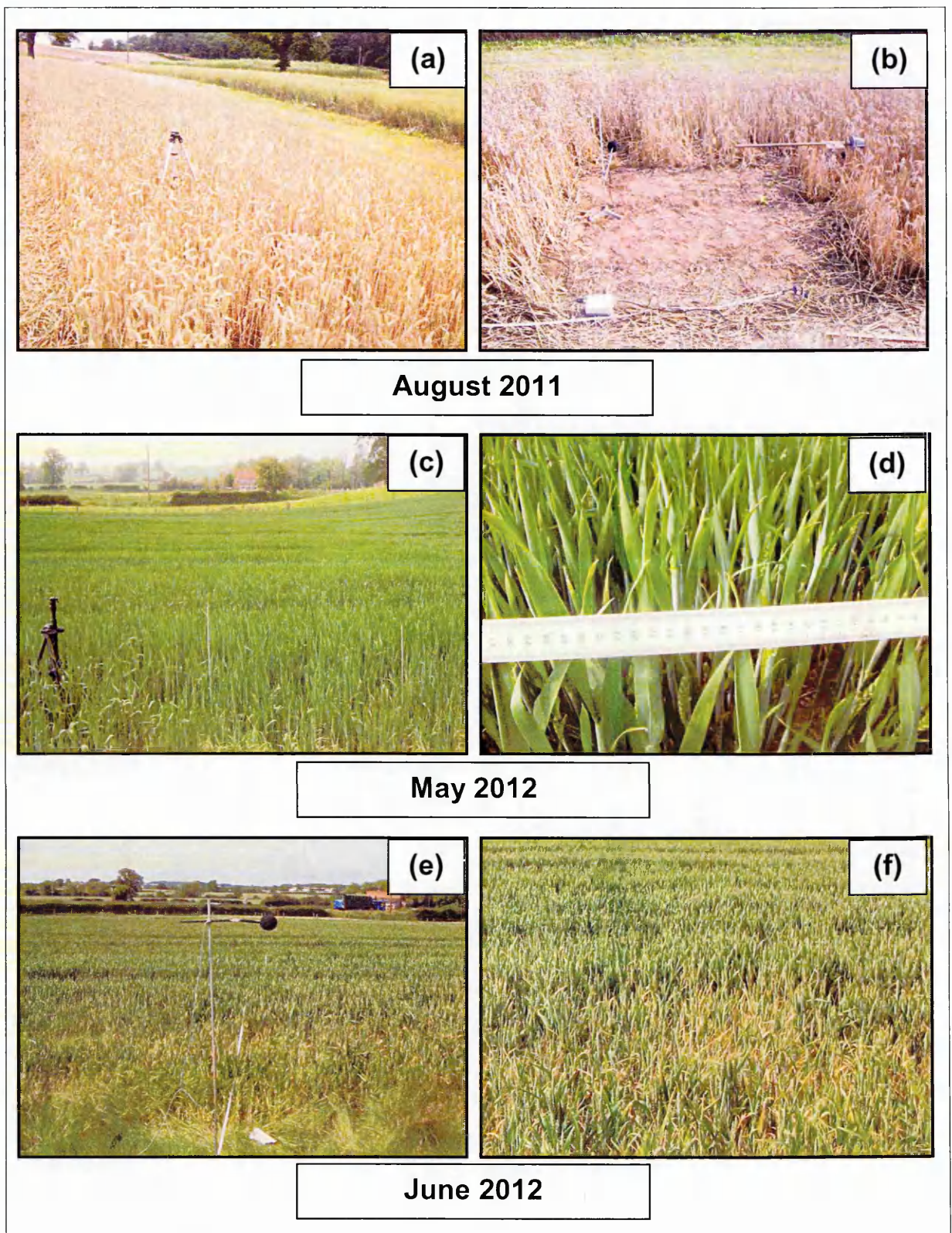
Figure 10.6 Photographs of measurements over crops at Woburn Sands at different times (a) and (b) August 2011; (c) and (d) May 2012; (e) and (f) June 2012.
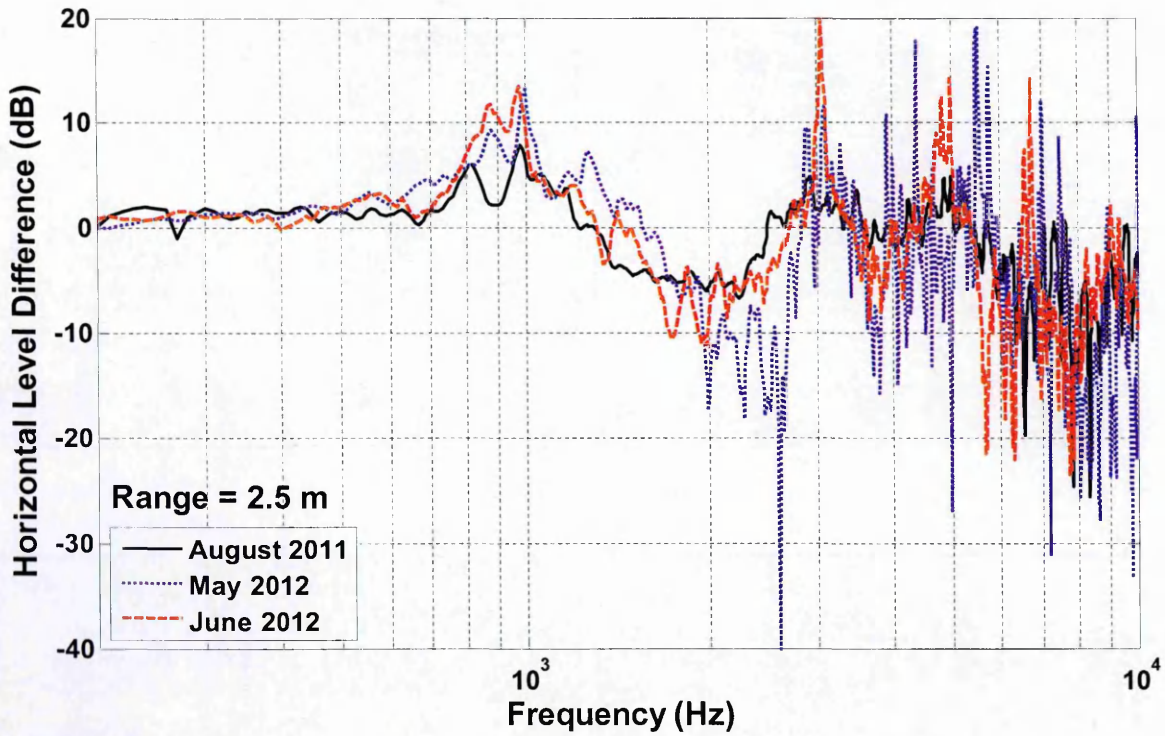
Figure 10.7 Spectra of the difference in levels measured by receivers at 1.0 m and 2.5 m from the source (source and receivers 0.3 m above ground) over winter wheat crops at different times of the year.
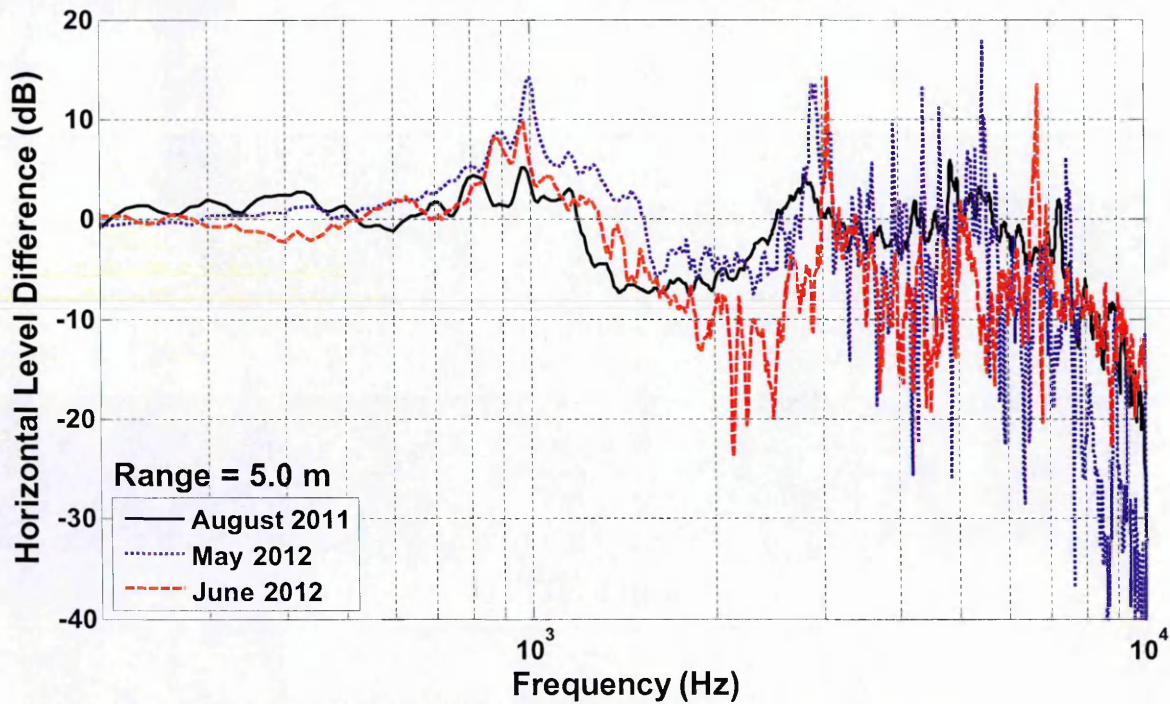
Figure 10.8 Spectra of the difference in levels measured by receivers at 1.0 m and 5 m from the source (source and receivers 0.3 m above ground) over winter wheat crops at different times of the year.
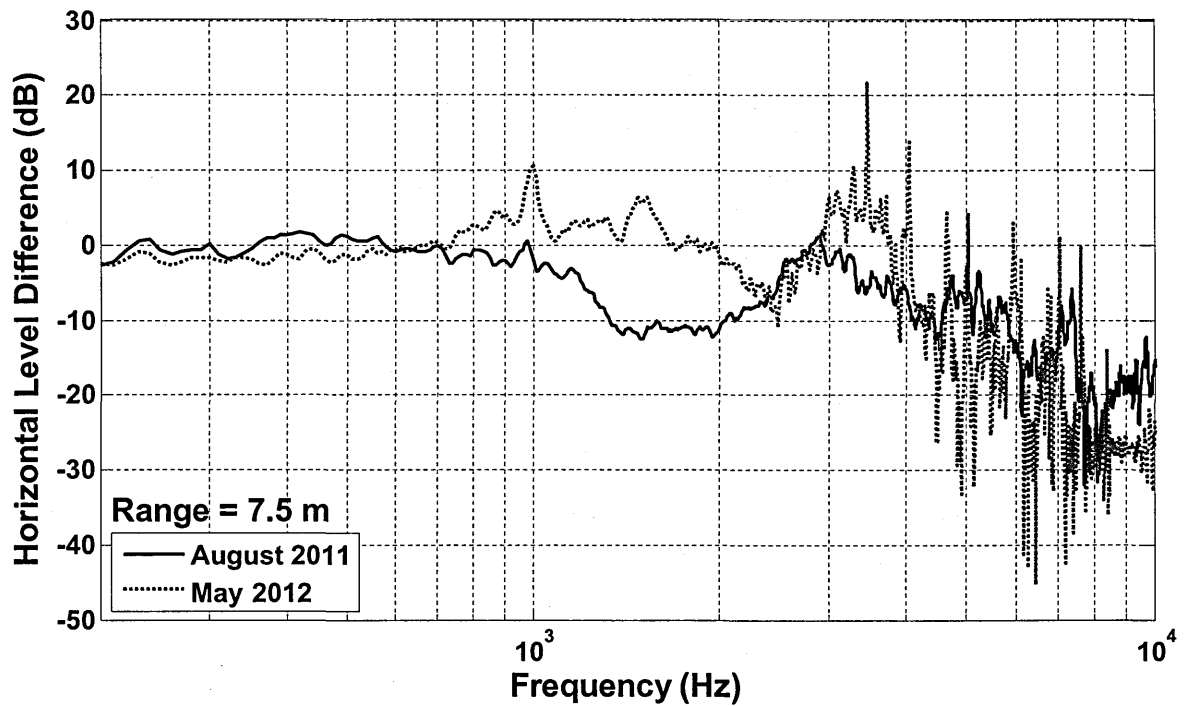
Figure 10.9 Spectra of the difference in levels measured by receivers at 1.0 m and 7.5 m from the source (source and receivers 0.3 m above ground) over winter wheat crops at different times of the year.
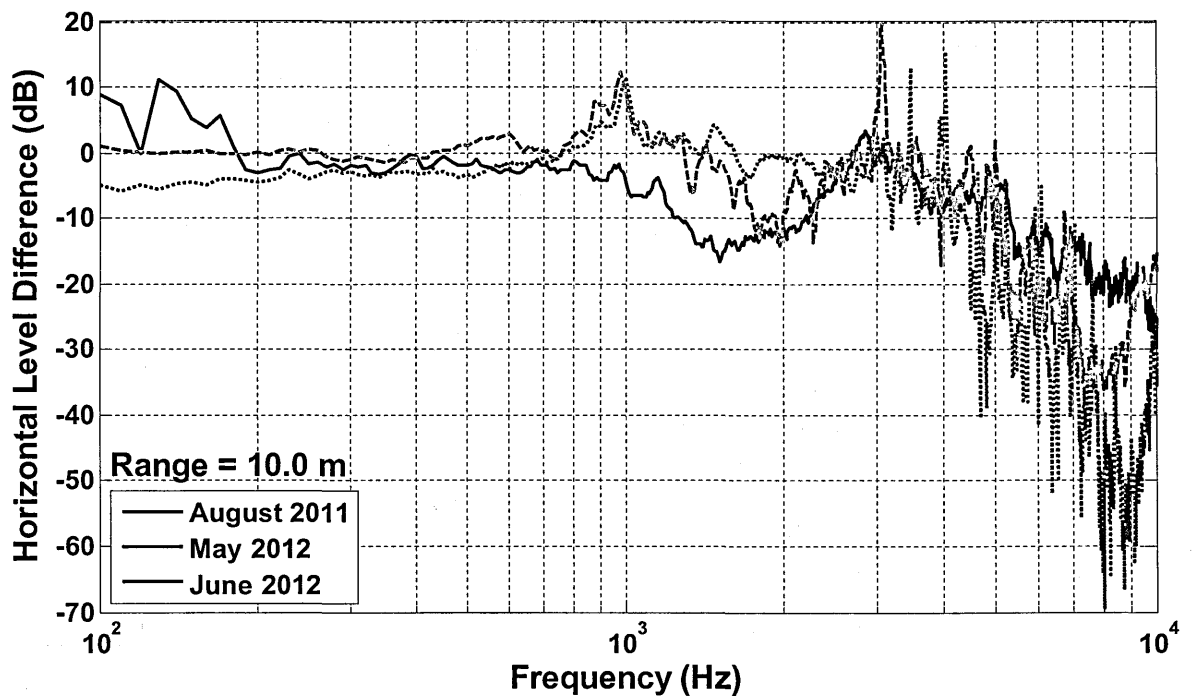
Figure 10.10 Spectra of the difference in levels measured by receivers at 1.0 m and 10 m from the source (source and receivers 0.3 m above ground) over winter wheat crops at different times of the year.

10.4.2.2   Predictions

Predictions of sound propagation through crops have been carried out by adding ground effect and acoustical effects of the crops. The complete calculation includes reverberant multiple scattering between the stems, the loss of coherence between ground-reflected and direct sound due to stem and foliage scattering and sound absorption by vegetation.

10.4.2.3   Multiple scattering by stems

The winter wheat stems have been modelled as randomly located vertical rigid cylinders having a distribution of diameters with the measured mean diameter and standard deviation. The Insertion Loss spectrum at a receiver 1 m away from a source has been calculated using multiple scattering theory (see Chapter 2). A polynomial curve has been fitted through the predicted attenuation spectrum (see Figure 10.11) [157]. Multiple scattering theory was used to model randomly distributed crops. An area of 1.88 m x 1.84 m was cleared with winter wheat crops. A total number of 1414 crops stems were planted randomly in this area. The mean diameter of stems was 0.00263 m with a standard deviation of 0.00078 m. Figure 10.11 shows MST predictions for a random distribution of 1414 vertical cylinders with a mean diameter of 0.00263 m. The low amplitude oscillations at high frequencies are due to randomness and small mean diameter of the scatterers. The oscillations shown in Figure 10.11 are for a particular random realization. To obtain an average effect due to random scatterers, a smooth exponential curve was fitted. However, even with including the oscillations, the overall effect is small.
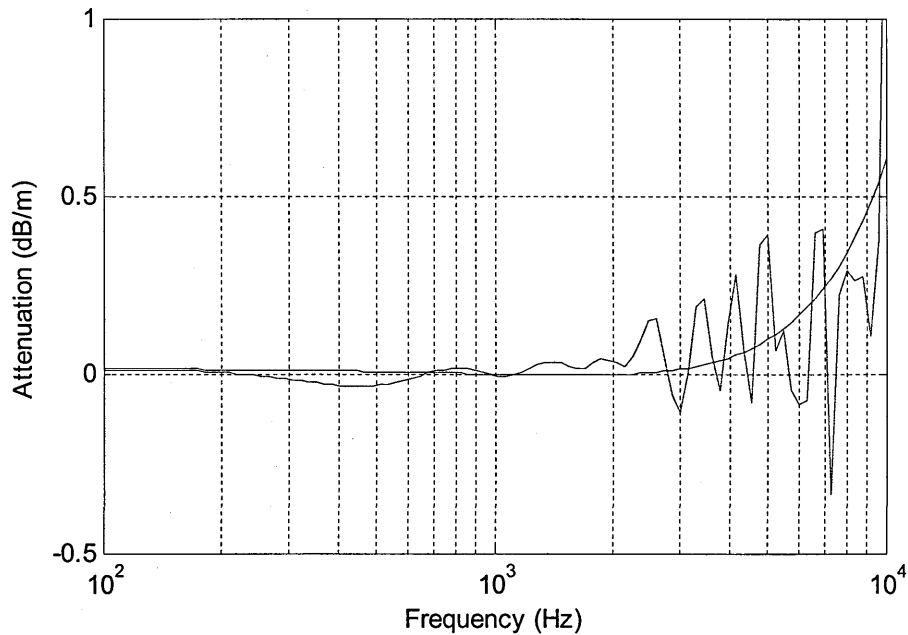
Figure 10.11 Attenuation as a function of frequency predicted through 414 randomly located parallel rigid cylinders with mean diameter 0.263 mm and a smooth polynomial curve fit.

The fitted polynomial curve is given by,

$$IL = a_2 f^2 + a_1 f + a_0 ,$$

(10.11)

where $a_2 = 8.45 \times 10^{-9}$, $a_1 = -2.60 \times 10^{-5}$ and $a_0 = 0.0193$.

The resulting predictions of attenuation due to scattering in dB m^{-1} have been added to the predicted normalized level difference due to ground effect. The comparisons between predictions and data indicate that, although (reverberant) multiple scattering by the stems can account for part of the extra attenuation in the wheat crop, it does not account for all of it.

Eq. 10.3 can be used also to predict attenuation due to multiple scattering by winter wheat stems. The calculated value for filling fraction was 0.0025. The derived values for equivalent flow resistivity and effective porosity (Eq. 10.2) are 194 Pa s m^{-2} and 0.975 respectively. However, a better fit at lower frequencies can

be obtained by taking a value of 29 Pa s m^{-2} for the equivalent flow resistivity. This value has been used for subsequent predictions. However the predicted attenuation due to multiple scattering alone is not sufficient to account for measured levels, in particular those at frequencies above 3 kHz.

10.4.2.4 Loss of Coherence

The scattering of sound due to vegetation reduces the coherence. The incoherence induced by stem scattering has been modelled by an effective turbulence. Predictions for turbulence-affected ground effect (see Eqs. 10.4 – 10.10) due a point source near the ground have been compared with the winter wheat data at 10 m range. Allowance for the influence of scattering on ground effect has been made by using effective values of variance of index of refraction and outer scale of turbulence of 5.0 × 10^{-4} and 0.3 m respectively as well as the multiple scattering by stems.

10.4.2.5 Viscous and thermal loss due to foliage

The major sound attenuation factor at high frequencies is due to viscous and thermal losses at foliage surfaces. The magnitude of the attenuation due to viscous and thermal losses and its frequency range depends on leaf size, vegetation density, stem diameter and the length of the propagation path through the crops. The attenuation due to viscous and thermal losses can be predicted using an empirical formula (see Eq. (10.1)) based on Aylor's data [157]. The viscous and thermal losses can be added to attenuation due to multiple scattering and effects due to loss of coherence to obtain the overall effect. The multiple scattering and loss of coherence contribute little to overall attenuation.

10.4.2.6   Comparison between data and predictions

The contributions to attenuation are ground effect, thermal and viscous losses at leaf surfaces, multiple scattering by stems and leaves and loss of coherence effects. These effects can be summed to obtain the over-all attenuation due to crops and ground. The ground effect for a particular ground surface growing crops was obtained by a ground characterization method (see Chapter 4). A short range vertical level difference measurement is carried out inside crops and the resulting data is fitted using an impedance model to obtain best fit impedance model parameters. The attenuation due to crops is obtained by putting estimated foliage area per unit volume (F m^{-1}), measured leaf size (a) and measured propagation path through crops (L) into Eq. (10.1). Multiple scattering effects are calculated using Eq. (10.4). Loss of coherence is calculated using the specified effective turbulence parameters in Eqs. (10.4) to (10.10). All effects are added together to obtain the total attenuation.

Figure 10.12 (a) shows the measured and predicted level difference (LD) spectra between microphones at 1 m and 2.5 m from the source. The source and receivers were at height of 0.3 m. Measurements were carried out in August 2011 over approximately 0.5 m high winter wheat crops. The impedance parameters obtained from ground characterization using the slit pore model are flow resistivity of 100 kPa s m^{-2} and porosity of 0.27. The solid blue line represents the data. The dashed red line represents the predicted ground effect; the dashed black line shows the predicted result of a combination of loss of coherence and attenuation caused by multiple scattering by the stems and the (thicker) black line is the sum attenuation due to scattering-affected ground effect and foliage using Eq. 10.1 with

F = 20 m^{-1} and a = 0.008 m. Figures 10.12 (b) and (c) compare measured LD between microphones at 1 m and 5 m and 1 m and 10 m with the corresponding predictions. The data for these larger ranges are fitted consistently with F = 20 m^{-1} and a = 0.008 m.
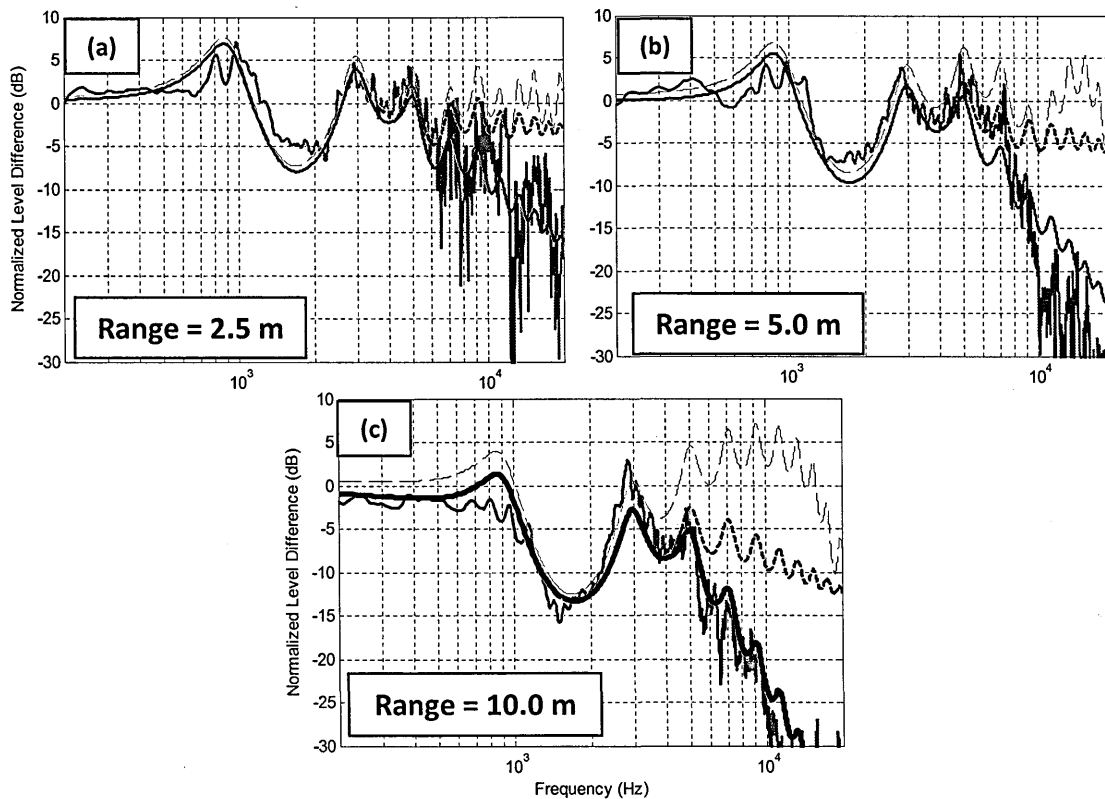
Figure 10.12 (Data collected in August 2011) Measured spectrum of the level difference between receivers at 1 m and (a) 2.5 m (b) 5.0 m (c) 10.0 m from the source (solid blue line); predicted ground effect alone - broken red line; ground effect plus incoherence plus multiple scattering by stems - broken black line; ground effect plus incoherence plus multiple scattering by stems plus viscous and thermal attenuation (Eq. 10.1 with F = 20 m^{-1} and a = 0.008 m) – black solid line.

The major contributions to attenuation are ground effect and thermal and viscous losses due to vegetation. Indeed it is possible to avoid calculating the multiple scattering and loss of coherence effects and to compensate for these effects by using larger values for foliage per unit area and mean leaf size in Eq. 10.1 [164]. Thereby it is possible to obtain reasonable predictions by only adding

ground effect to attenuation due viscous and thermal losses as predicted by Eq.10.1. The ground effect for a particular ground surface growing crops was obtained by a ground characterization method (see Chapter 4). The attenuation due to crops is obtained by putting estimated foliage area per unit volume (F m^{-1}), measured leaf size (a) and measured propagation path through crops (L) into Eq. (10.1). The effects are added together to obtain the total attenuation.

Figure 10.13 shows spectra of the difference in levels measured by the reference microphone at a distance of 1.0 m and microphones at distances of 2.5 m, 5.0 m, 7.5 m and 10.0 m from the source respectively. The source and receivers were at height of 0.3 m. Measurements were carried out in August 2011 over approximately 0.5 m high winter wheat crops. Also shown are predictions of ground effect and of ground plus crop effects. The impedance parameters obtained from ground characterization using the slit pore model are flow resistivity of 100 kPa s m^{-2} and porosity of 0.27. The crops were dry with reduced foliage (see Figure 10. 6 (a) and (b)). The estimated foliage area per unit volume was 20 m^{-1} and mean leaf size was 0.012 m. The propagation path length depends on the further microphone position. The agreement between the measured spectra and those predicted by adding ground effect to foliage/stem attenuation using parameters given above is good. At lower frequencies the ground effect is dominant and there is no crops effect as expected given the thinner stem sizes. At higher frequencies i.e. above 3-4 kHz the crops effect is dominant. Lower frequency attenuation is due to ground effect and high frequency attenuation is due to crops.
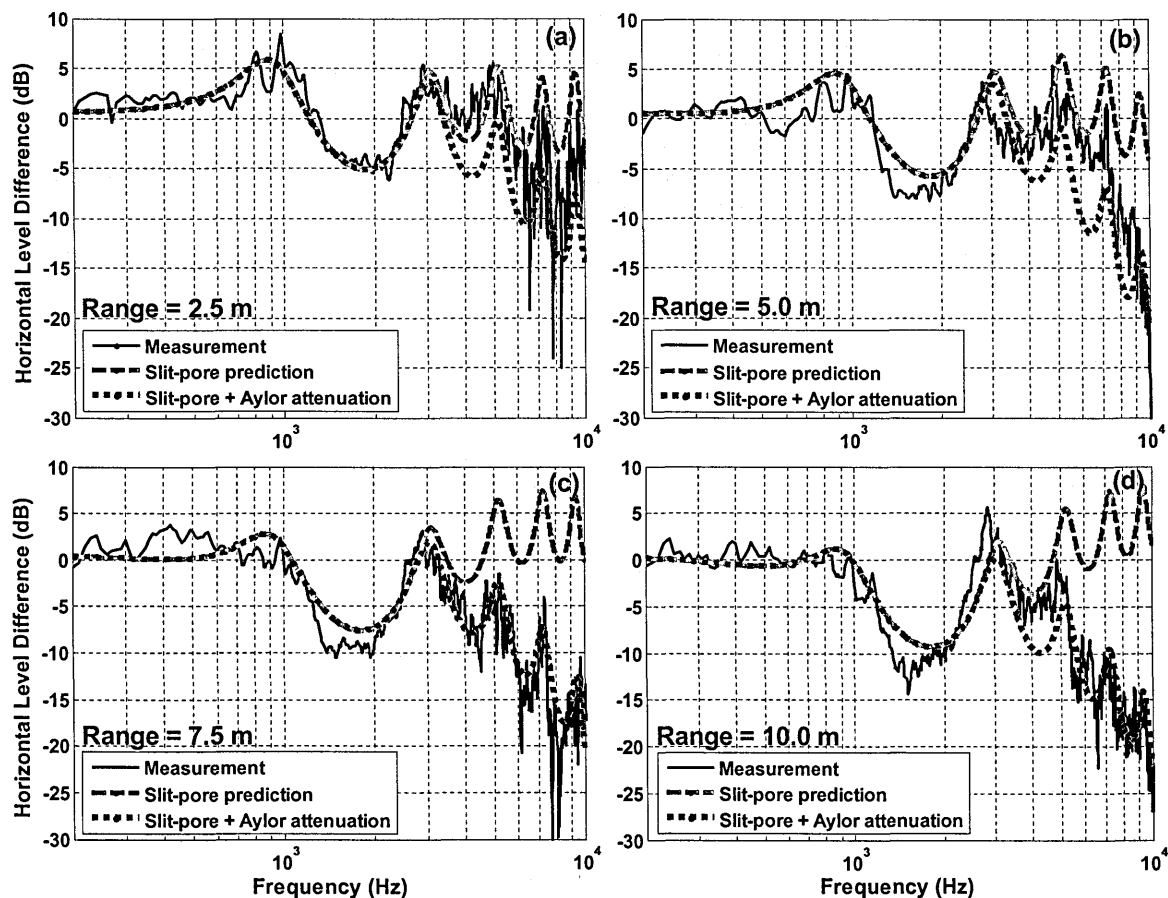
Figure 10.13 (Data collected in August 2011) Comparison between measured level difference spectra (source and receivers at height of 0.3 m above ground) over 0.5 m high winter wheat crops and predictions using ground effect alone (ground impedance given by the slit pore model with Flow resistivity = 100 kPa s m^{-2}, Porosity = 0.27) and ground effect plus the attenuation predicted by Eq.10.1 (Foliage area per unit volume = 30 m^{-1}, Mean leaf width = 0.012 m) (a) receivers at 1.0 m and 2.5 m (b) receivers at 1.0 m and 5.0 m (c) receivers at 1.0 m and 7.5 m and (d) receivers at 1.0 m and 10.0 m from the source.

Figure 10.14 shows spectra of the difference in levels measured over winter wheat crops in May 2012 when the crops were very green and leafy (see Figures 10.6 (c) and (d)). The reference microphone placed at a distance of 1.0 m and other microphones placed at distances of 2.5 m, 5.0 m, 7.5 m and 10.0 m from the source respectively. Also shown are ground effect predictions obtained by using two-parameter slit pore impedance for the ground with a flow resistivity of 200 kPa s m^{-2} and porosity of 0.2 with the addition of a crops effect attenuation

based on Eq. 10.1 using an estimated foliage area per unit volume of 50 m^{-1} and mean leaf size of 0.012 m. The agreement between the data and predictions is good except between 1 and 3 kHz at longer ranges where incoherence due to scattering reduces the ground effect. Both data and predictions in Fig.10.14 corresponding to wetter greener leafier conditions show higher attenuation above 3 kHz than shown in Figure 10.13 corresponding to dry crop conditions.
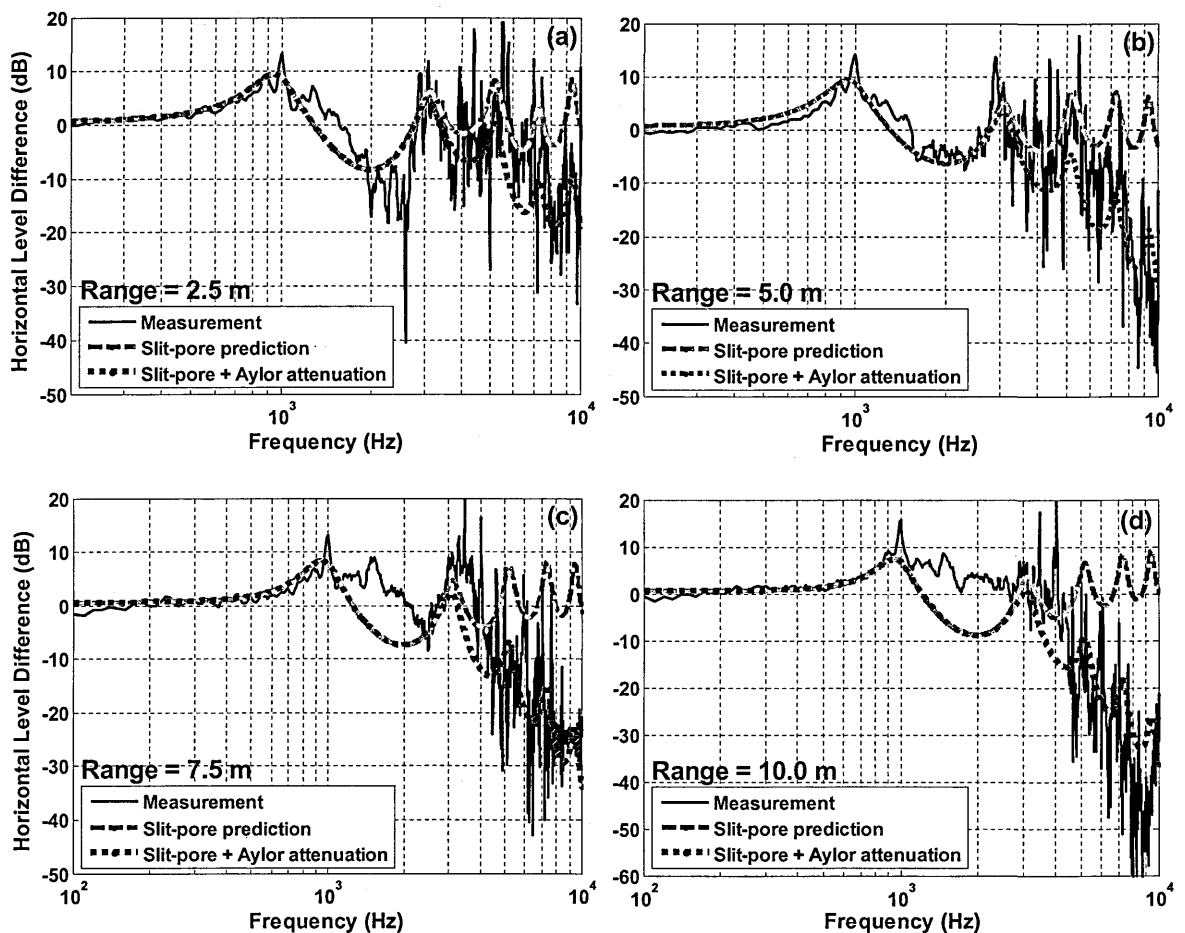
Figure 10.14 (Data collected in May 2012) Comparison between measured level difference spectra (source and receivers 0.3 m above ground) over winter wheat crops and predictions of ground effect alone (slit pore impedance with flow resistivity = 200 kPa s m^{-2}, Porosity = 0.2) and predictions obtained by adding ground effect to the attenuation predicted by Eq. 10.1 (Foliage area per unit volume = 50 m^{-1}, Mean leaf width = 0.012 m) (a) receivers at 1.0 m and 2.5 m (b) receivers at 1.0 m and 5.0 m (c) receivers at 1.0 m and 7.5 m and (d) receivers at 1.0 m and 10.0 m from the source.

Measurements over winter wheat were again carried out in June 2012, when the crops were neither very green nor very dry (see Figure 10.6 (c) and (d)). Figure 10.15 compares the spectra of the difference in levels measured by the reference microphone at a distance of 1.0 m and microphones placed at distances of 2.5 m, 5.0 m, 10.0 m and 10.0 m from the source respectively with predictions of ground effect alone and ground effect plus crops attenuation. The ground effect is predicted using the slit pore model with flow resistivity of 200 kPa s m^{-2} and porosity of 0.2. The crops effect is predicted from Eq. 10.1 with estimated foliage area per unit volume of 40 m^{-1} and mean leaf size of 0.012 m. There is good agreement between the measured horizontal level difference spectra and the predictions of ground effect plus crops effect.
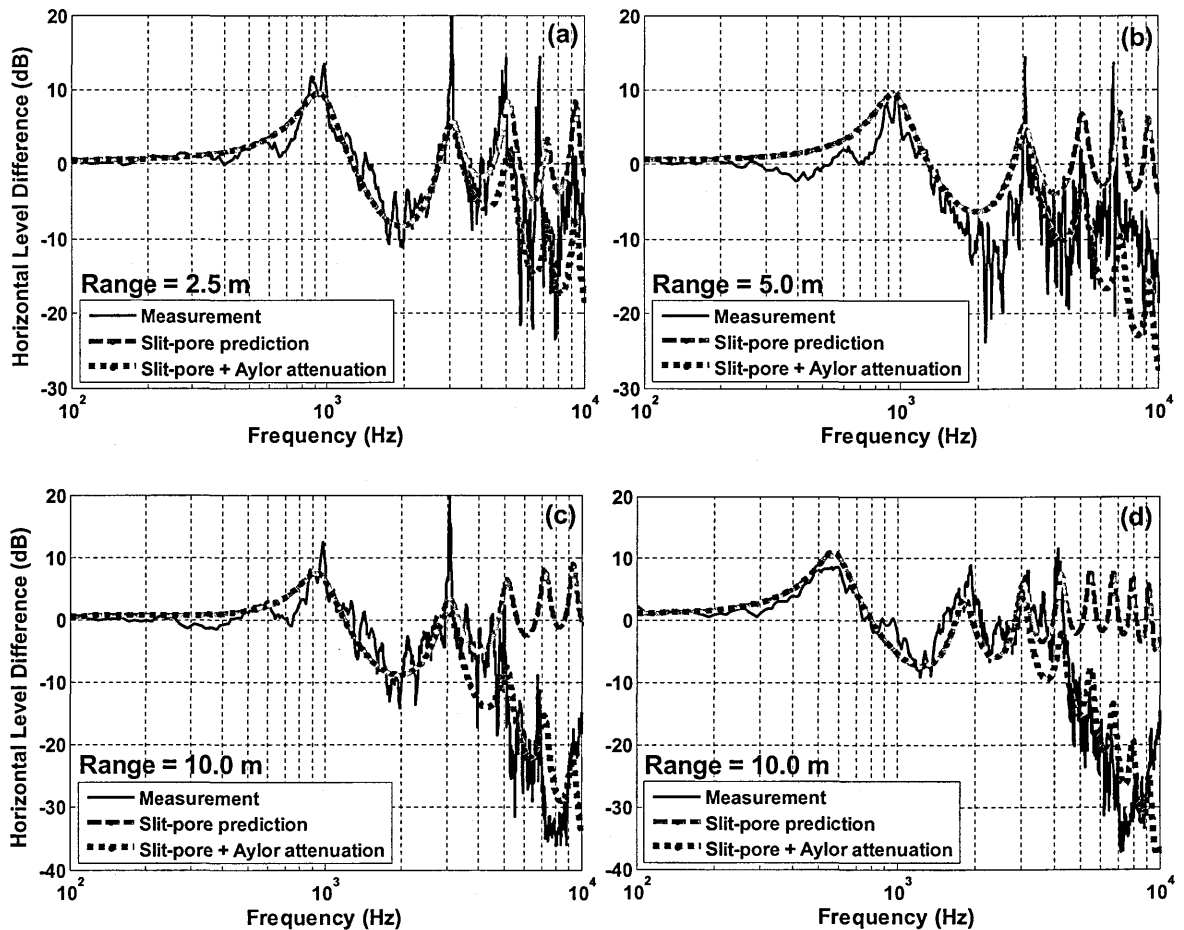
Figure 10.15 (Data collected in June 2012) Comparison between measured level difference spectra (with source and receivers at 0.3 m height except for 10 m range) over winter wheat crops and predictions using ground effect alone (slit pore impedance given by flow resistivity = 200 kPa s m⁻², Porosity = 0.2) and predictions obtained by adding ground effect and the attenuation predicted by Eq. 10.1 (Foliage area per unit volume = 40 m⁻¹, Mean leaf width = 0.012 m) (a) receivers at 1.0 m and 2.5 m (b) receivers at 1.0 m and 5.0 m (c) receivers at 1.0 m and 10.0 m from the source and (d) receivers at 1.0 m and 10.0 m from the source but source and receivers at a height of 0.4 m.

10.4.2.7   Willow crops

Level difference spectra have been measured over willow crops by placing the reference microphone at a distance of 1.0 m from the source and further microphones at the same height as the source but at distances of 2.5 m, 5.0 m, 7.5 m and 10.0 m respectively. Willow crops had 0.07 m long stems and 0.01 m wide leaves. The crops were not densely populated and there were empty areas inside the crops. The average willow crop height was between 2.0 m and 2.2 m. Measurements were carried out at several source and receiver heights. However, the microphones and source were always inside the crops. Photographs of Willow crops are shown in Figure 10.16.

Figure 10.16 Photographs of measurements through Willow crops at Woburn Sands.

Figure 10.17 shows spectra of the difference in levels measured over Willow crops in June 2012 when the crops were very green and leafy (see Figures 10.16). Figure 10.17 compares the spectra of the difference in levels measured by the by the reference microphone placed at a distance of 1.0 m and other microphones placed at distances of 2.5 m, 5.0 m, 7.5 m and 10.0 m from the source respectively. Also shown are ground effect predictions obtained by calculating ground effect using the two-parameter slit pore impedance model for

the ground with a flow resistivity of 100 kPa s m^{-2} and porosity of 0.2 and adding a crops effect attenuation based on Eq. 10.1 using an estimated foliage area per unit volume of 10 m^{-1} and mean leaf size of 0.01 m. The agreement between the data and predictions is good. Willow crops were not planted very densely and had small leaf size. The resulting data show relatively little attenuation at higher frequencies.
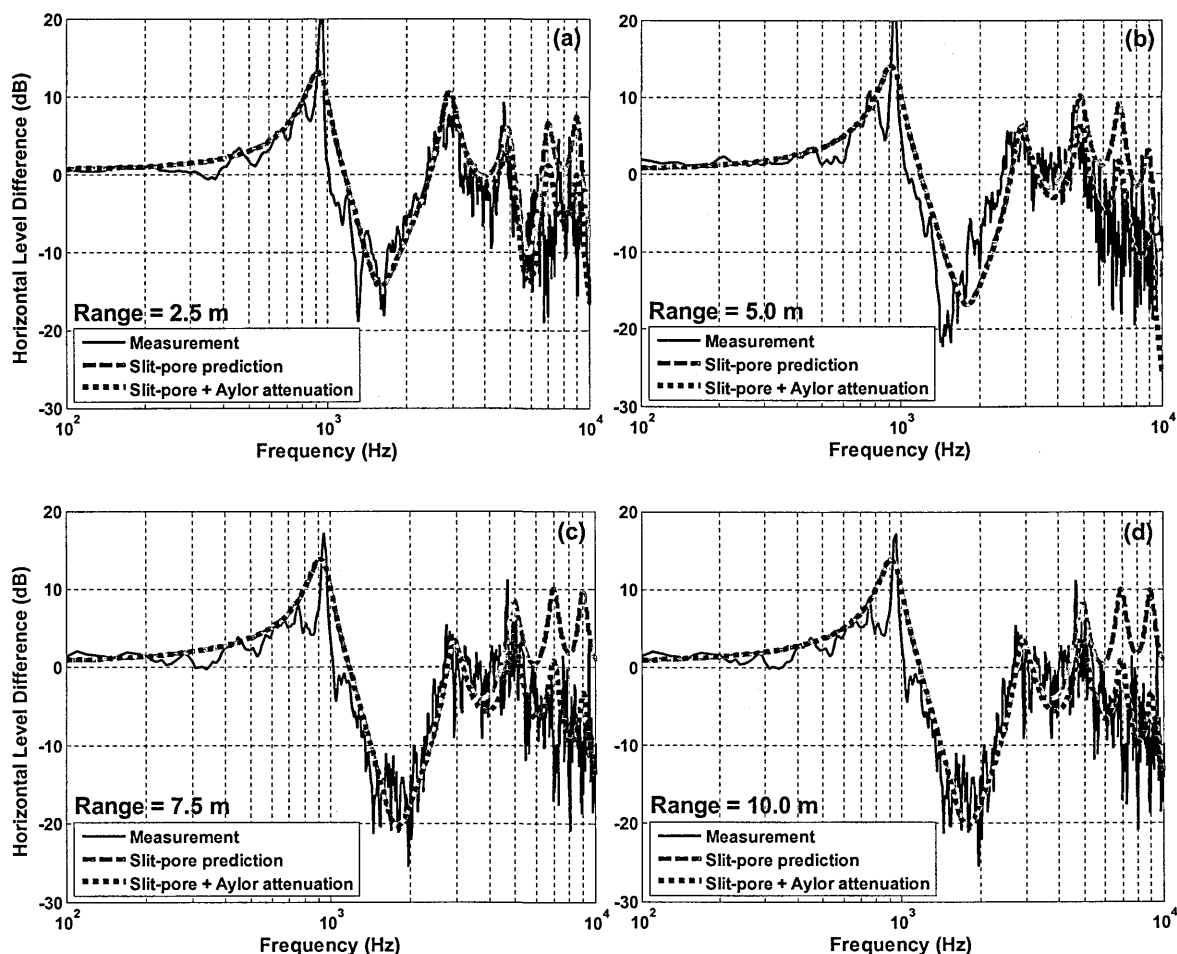
Figure 10.17 (Data collected in June 2012) Comparison between measured level difference spectra (with source and receivers at 0.3 m height) over Willow crops and predictions using ground effect alone (slit pore impedance given by flow resistivity = 100 kPa s m^{-2}, Porosity = 0.2) and predictions obtained by adding ground effect and the attenuation predicted by Eq. 10.1 (Foliage area per unit volume = 10 m^{-1}, Mean leaf width = 0.01 m) (a) receivers at 1.0 m and 2.5 m (b) receivers at 1.0 m and 5.0 m (c) receivers at 1.0 m and 7.5 m and (d) receivers at 1.0 m and 10.0 m from the source.

10.4.3 Longer range data and predictions

10.4.3.1 Winter wheat crops (Propane cannon as a source)

Longer range measurements of up to 50 m have been carried out through 0.45 m – 0.55 m high winter wheat crops at Woburn Sands (see Figure 10.18). One reason for carrying out measurements at 50 m range is that the HOSANNA project guide lines, for the two lane urban road case require that the insertion loss due to designed abatements should be calculated at a 50 m range from the nearest lane source (see Chapter 11). Secondly, the measurements reported in this thesis are differentiated from each other by defining three range categories: short range (r < 2 m), medium range (2 m < r < 15 m) and longer range (r = 50 m). In these longer range measurements a powerful impulse source (propane cannon) has been used. A modified version of the measurement system described in Chapter 3 has been used. The propane cannon is connected to a gas cylinder and has a manual switch. The microphones were set to record and then propane cannon switched on manually. The timing was adjusted; so that the propane cannon bang occurred in the middle of a 20 second recording (see Figure 10.19 (a)). Each time the propane cannon banged twice after being switched on manually. Both bangs were recorded and each measurement was repeated three times. So the resulting data is an average of 6 impulse measurements. The averaging and signal processing of the recorded impulses were similar to those described in Chapter 3. Each impulse was windowed using a Blackman-Harris (see Chapter 3) window (see Figure 10.19 (b)). Level difference measurements were carried out with the reference microphone and further microphones at distances of 10.0 m and 50.0 m respectively from the source. The reference

microphone was placed at a distance of 10.0 m from the source instead of 1.0 m, as in previously reported level difference measurements using a loudspeaker source, to avoid damage to the microphone from the high amplitude output of the propane cannon. The data acquisition system range was adjusted to make sure that the recorded impulse was not clipped as a result of its high amplitude. The propane cannon was fitted with a 1.0 m long tube having a diameter of 0.11 m. The centre of the propane cannon tube was located at a height of 0.3 m above ground surface in all of the measurements. Measurements were carried out with the reference and further microphones at two different heights of 0.3 m and 1.5 m.

Figure 10.18 Photographs of measurements a using a Propane cannon over winter 0.45 m – 0.55 m high winter wheat crops.
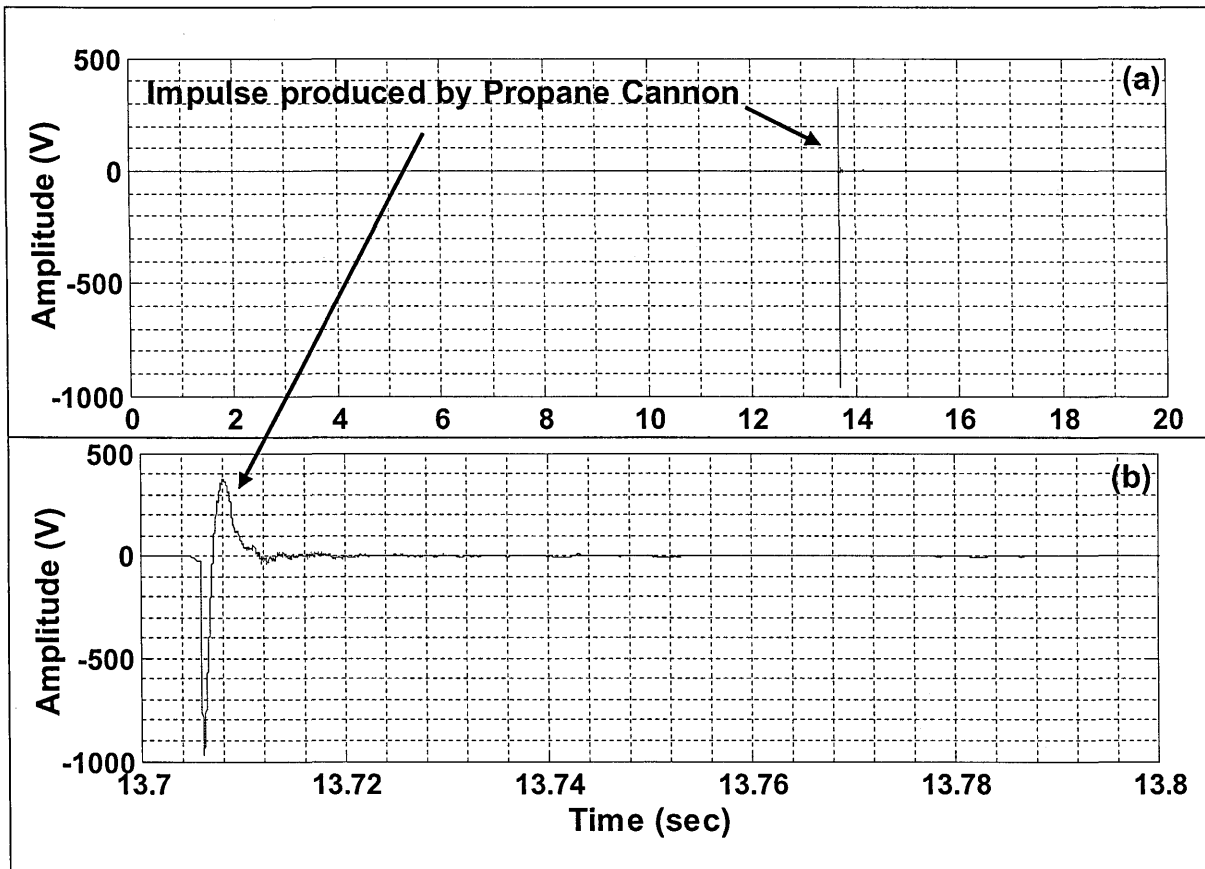
Figure 10.19 An example time domain signal (impulse) generated by the Propane cannon (a) total recorded signal (b) Magnified view of impulse shown in (a).

Figure 10.20 compares the measured level difference spectra over winter wheat crops with predictions of ground effect obtained by using a variable porosity impedance model with best fit flow resistivity and porosity rate of 10 kPa s m^{-2} and 100 m^{-1} respectively. The source and receivers were placed at a height of 0.3 m above ground and the horizontal distances between source and reference microphone and 2nd microphone were 10.0 m and 50.0 m respectively. The agreement between data and predictions is reasonable up to 1 kHz. However, at higher frequencies there is greater attenuation than predicted by ground effect alone.
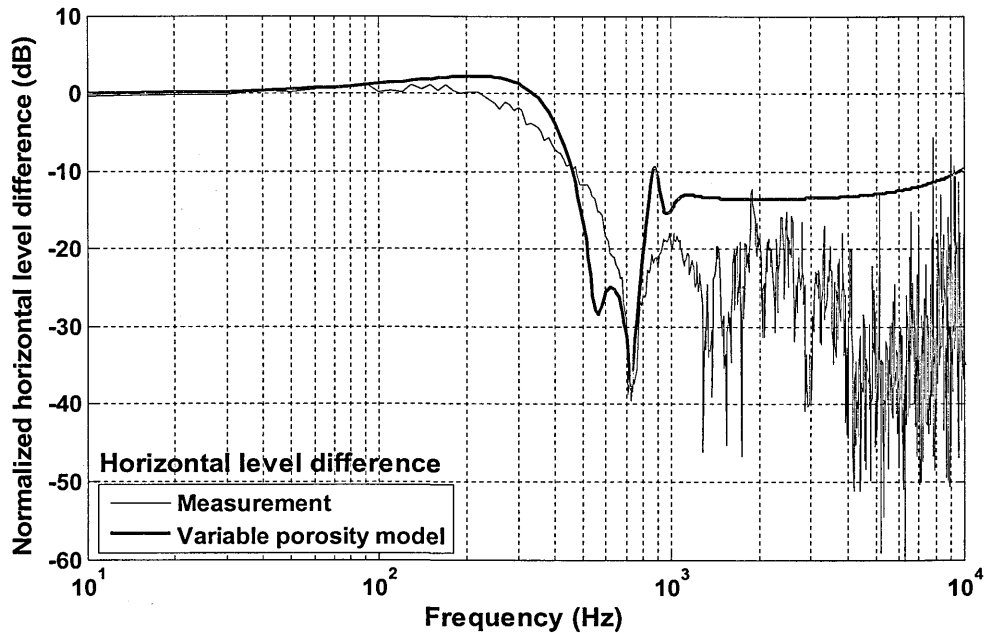
Figure 10.20 A horizontal level difference spectrum measured over winter wheat crops with source and receivers at a height of 0.3 m above ground and horizontal distances between source and microphones of 10.0 m and 50.0 m respectively. Also shown is a prediction including ground effect only obtained by using variable porosity impedance model (Flow resistivity = 10 kPa s m^{-2}, Porosity rate = 100 m^{-1})
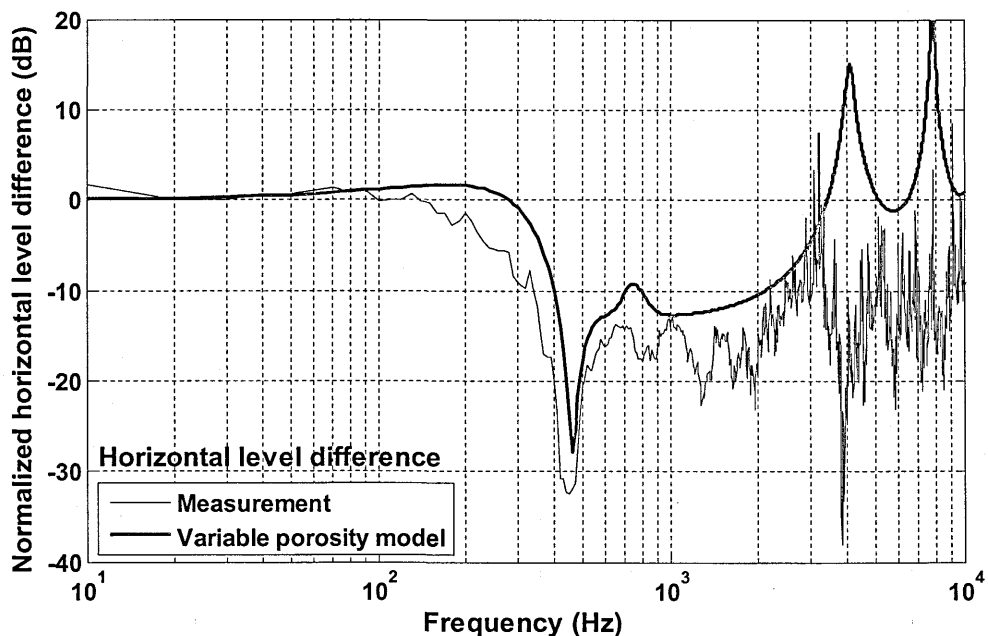
Figure 10.21 A horizontal level difference spectrum measured over winter wheat crops with propane cannon source at a height of 0.3 m above ground, receivers at 1.5 m height and horizontal distances between source and microphones of 10.0 m and 50.0 m respectively. Also shown is a prediction including ground effect only obtained by using variable porosity impedance model (Flow resistivity = 10 kPa s m^{-2}, Porosity rate = 100 m^{-1})

Figure 10.21 compares the measured and predicted horizontal level different spectra over winter wheat crops with propane cannon at a height of 0.3 m, reference and further microphones above crops at a height of 1.5 m. The agreement between data and predictions is good up to 3 kHz, in contrast to the comparison between data and predictions in Figure 10.20. The fact that the data presented in Figure 10.20 is with microphones inside crops and that given in Figure 10.21 is for outside crops is not the reason. Similar measurements carried out over grass at the Open University Noise barrier site where source and receivers were placed at a height of 0.8 m above ground and the horizontal distances between source and reference microphone and 2nd microphone were 10.0 m and 50.0 m respectively. Figure 10.22 compares the measured horizontal level difference spectra over grass with predictions using variable porosity model (see Chapter 4). In this case the both microphones were above grass. However, the agreement between data and predictions is good only up to 1 kHz and at higher frequencies the data and predictions deviate from each other. Moreover, the vertical level difference spectra over winter wheat crops and predictions of ground effect obtained by using variable porosity model with best fit flow resistivity and porosity rate of 10 kPa s m^{-2} and 100 m^{-1} respectively only show good agreement up to 1 kHz as shown by Figure 10.23. Similarly, the horizontal level difference data for receiver heights of 0.5 m reached to same conclusion. Only the data and predictions with receivers at height of 1.5 m contradict with other data. This difference may be caused by the characteristics of the propane cannon, The next section investigates these characteristics.
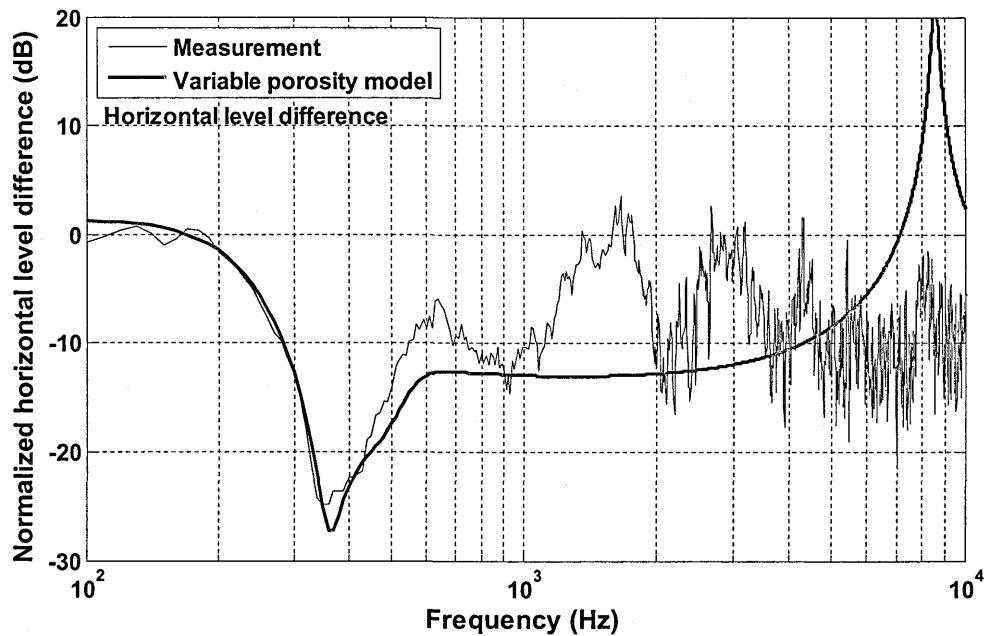
Figure 10.22 A horizontal level difference spectrum measured over grass at Open University Noise Barrier site with propane cannon source at a height of 0.255 m above ground, receivers at 0.8 m height and horizontal distances between source and microphones of 10.0 m and 50.0 m respectively. Also shown is a prediction including ground effect only obtained by using variable porosity impedance model (Flow resistivity = 10 kPa s m^{-2}, Porosity rate = 40 m^{-1})
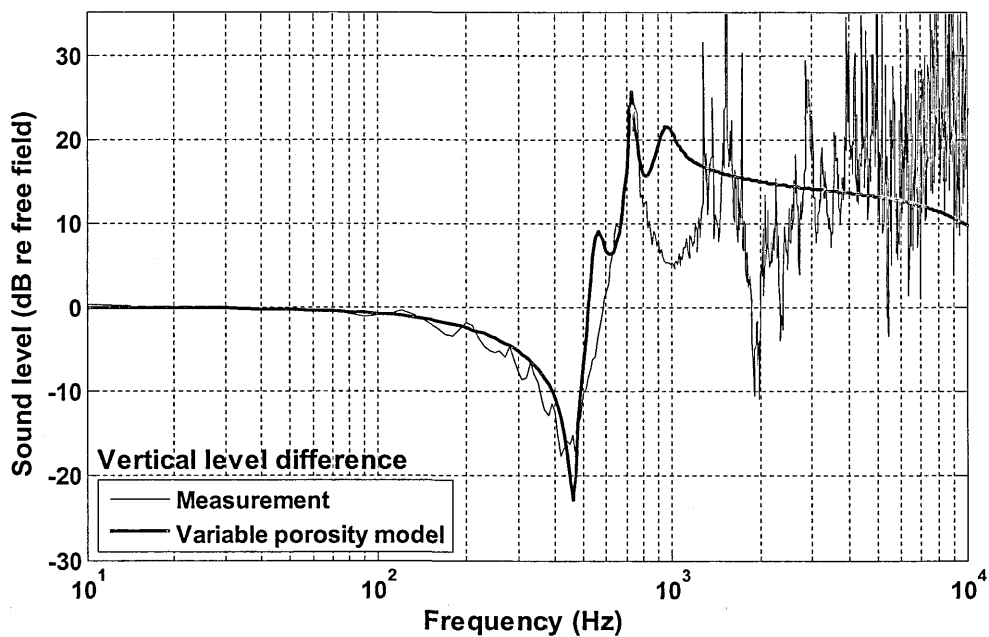
Figure 10.23 Comparison between a measured vertical level difference spectrum over winter wheat crops and that predicted including only ground effect and obtained using the variable porosity impedance model (Flow resistivity = 10 kPa s m^{-2}, Porosity rate = 100) with source at a height of 0.3 m above ground and 50.0 m from vertically separated microphones at heights of 1.5 m and 0.3 m.

10.4.3.2 Propane cannon as a noise source

The data obtained over winter wheat crops using propane cannon as a source shows that the measured and predicted spectra deviate from each other above 1 kHz. The absolute measured spectrum was analyzed to check that whether this difference is not caused by poor signal to noise ratio. Figure 10.24 shows an example for absolute spectra measured using propane cannon at a height of 0.3 m and at a distance of 50.0 m. The spectra show a peak between 30 Hz – 400 Hz and drop off at height frequencies. However, the most important thing in the spectra that propane canon is capable of producing a signal up to 2.5 kHz with reasonable signal to noise ratio. At higher frequencies, the spectra descend to the microphone noise floor.
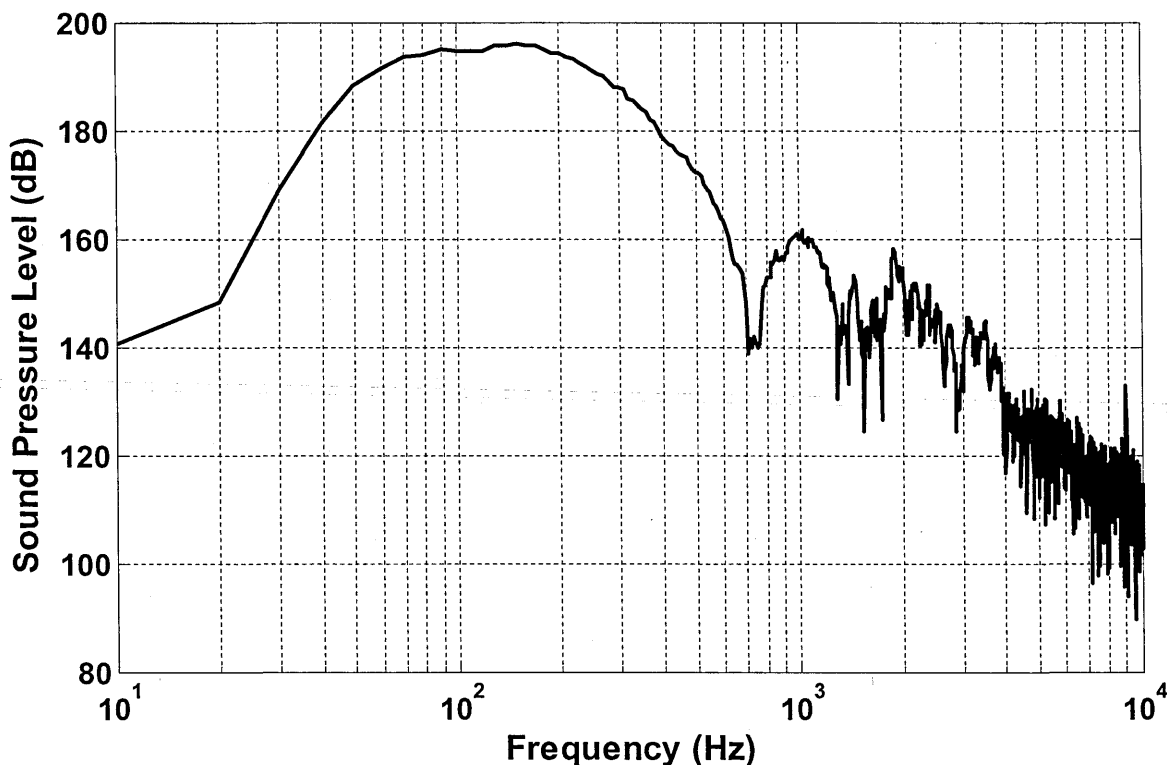
Figure 10.24 Absolute Sound Pressure Level (dB) measured over winter wheat crops with propane cannon source at a height of 0.3 m above ground, receiver at 0.3 m height and horizontal distance between source and microphone of 50.0 m.

Another set of outdoor measurements were carried out to compare the propane canon data with a large loudspeaker noise source. The large loudspeaker was placed horizontally during measurements and height was taken from centre of the source to the ground as shown in Figure 10.25

Figure 10.25 A photograph of large loudspeaker used for outdoor measurements.

Unfortunately, by that time the winter wheat crops had been harvested, so the test was carried out over willow (more details of these measurements are given in section 10.4.3.2). Figure 10.25 compares the measured horizontal level difference spectra over Willow crops using the propane cannon and a large loudspeaker. Source and receivers were placed at a height of 0.3 m above ground and the horizontal distances between source and reference microphones were 10.0 m and 50.0 m. The horizontal level difference spectra measured using the propane cannon and the large loudspeaker agree up to 1 kHz. However, the two spectra deviate from each other above 1 kHz. The spectra measured using the large loudspeaker is less noisy than those measured using propane cannon as a

source particularly at the higher frequencies. It is concluded that the propane cannon is a relatively low frequency noise source. However, it is capable of producing noise with good signal to noise ratio up to 2.5 kHz (see Figure 10.24). The deviation of measured data from predicted spectra at higher frequencies may be due to larger tube diameter of the propane cannon (diameter = 0.11 m). The predictions assume a point source and the propane cannon may not act as a point source at higher frequencies. Moreover, the good agreement between data and predictions up to 3 kHz (see Figure 10.21) may be coincidental as other all other data disagree with it. This work would need to be extended for more, longer range measurements to reach a final conclusion.
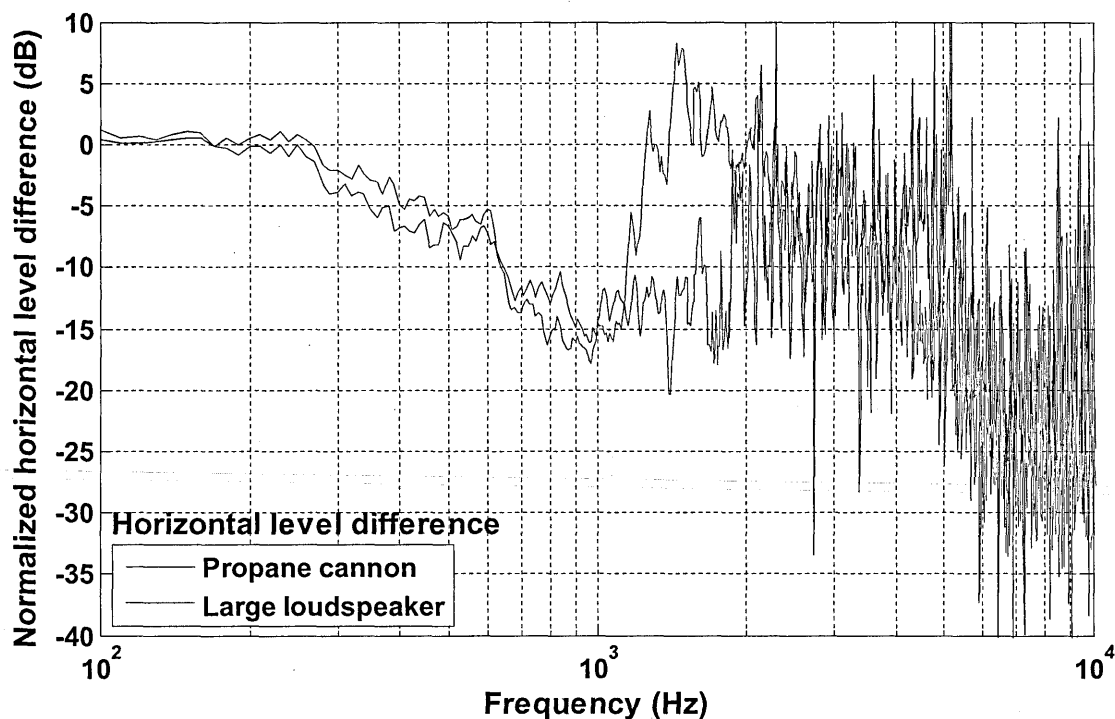
Figure 10.26 Comparison between horizontal level difference spectra over measured over willow using a propane cannon and a large loudspeaker as noise sources. Both sources and receivers were at a height of 0.3 m above ground with horizontal distances between sources and microphones of 10.0 m and 50.0 m respectively.

10.4.3.3 Impedance parameters obtained through short range and long range data

Figure 10.27 compares the a horizontal level difference spectrum measured over 0.45 m – 0.55 m high winter wheat using propane cannon with those for predicted for ground effect alone using variable porosity impedance model with best fit impedance parameters for longer ranges [flow resistivity and porosity rate of 10 kPa s m^{-2} and 100 m^{-1} respectively] and with best fit impedance parameters obtained through short range ground characterization (flow resistivity = 150 kPa s m^{-2} and porosity rate of 100 m^{-1}). The source and receivers were at a height of 0.3 m above ground and the horizontal distances between source and microphones were 10.0 m and 50.0 m respectively. Ideally the parameters obtained for shorter ranges should be similar to those obtained for longer ranges. The flow resistivity obtained by fitting the data for longer range is lower than the one obtained for shorter range. There are two reasons for an apparently lower flow resistivity at longer range. The ground surface was not homogenous over 50 m. The ground was cultivated and contained growing crops and therefore, was rough and uneven. As discussed in Chapter 5, roughness has an impact on the effective impedance of the ground surface. Indeed the impedance of a rough hard surface is lower than the impedance of smooth hard surface. Nevertheless the measurements display a high frequency attenuation that cannot be explained by ground effect alone.
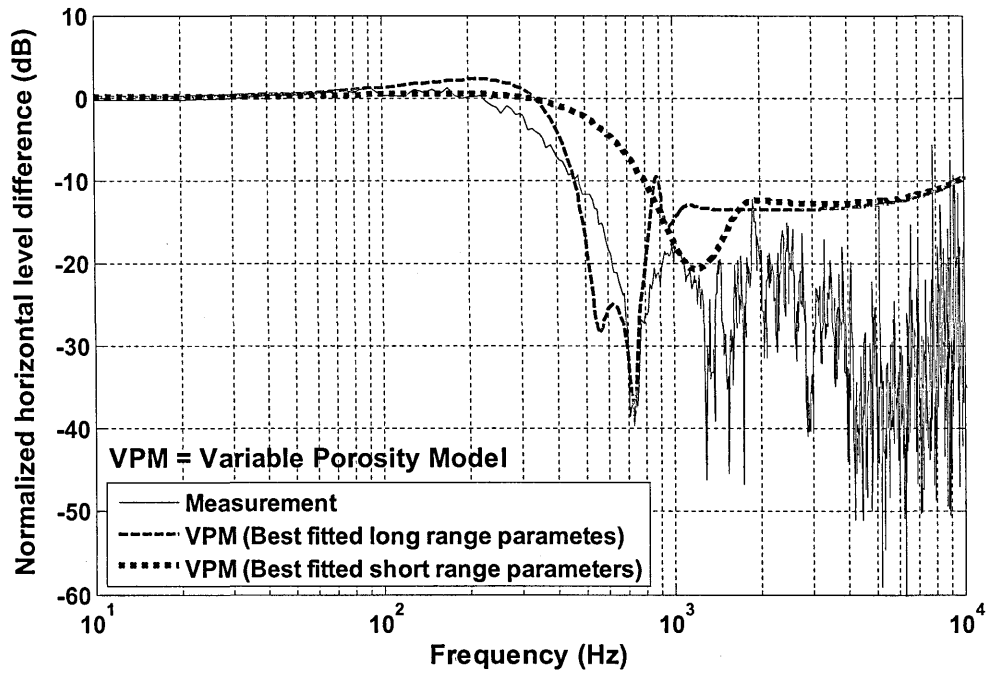
Figure 10.27 Comparison between a measured horizontal level difference spectrum over 0.45 m – 0.55 m high winter wheat crops and predictions of ground effect alone using the variable porosity impedance model with best fit parameters for longer range – Red broken line (Flow resistivity = 10 kPa s m^{-2}, Porosity rate = 100); and best fit parameters obtained from short range ground characterization– Blue dotted line (Flow resistivity = 150 kPa s m^{-2}, Porosity rate = 100). Source and receivers were at a height of 0.3 m above ground and the horizontal distances between source and microphones were 10.0 m and 50.0 m.

10.4.3.4 Measurements over Willow Crops

Figure 10.28 compares a measured horizontal level difference spectrum over Willow crops using the large loudspeaker with predictions of ground effect alone using the variable porosity impedance model with best fit parameters for longer ranges (flow resistivity and porosity rate of 45 kPa s m^{-2} and 200 m^{-1} respectively); and of this ground effect plus the crop effect predicted by Eq. 10.1 (Foliage area per unit volume = 10 m^{-1}, Mean leaf width = 0.01 m) and with ground effect alone predicted using the best fit impedance parameters obtained through short range ground characterization (flow resistivity = 200 kPa s m^{-2} and porosity rate of 200 m^{-1}). The source and receivers were placed at a height of 0.3 m above ground and horizontal distances between source and microphones were 10.0 m and 50.0 m. The agreement between the measured spectrum obtained using a large loudspeaker and the predicted ground effect obtained using the impedance model parameters giving best fit for longer ranges is reasonable up to 1.5 kHz. The agreement between measured data and predictions of ground effect plus the attenuation predicted by Eq. 10.1 is good up to 9 kHz. Again the presence of crops seems to be the reason for the additional high frequency attenuation. The Willow crops were 2 m tall, without thick stems or broad leaves and were planted sparsely. Consequently, the fitted foliage area per unit volume is only 10 m^{-1}.

The differences between the fitted flow resistivity values for long and short ranges (200 kPa s m^{-2} and 45 kPa s m^{-2} respectively) can be attributed to the reasons discussed in connection with the similar difference observed in Fig. 10.24.
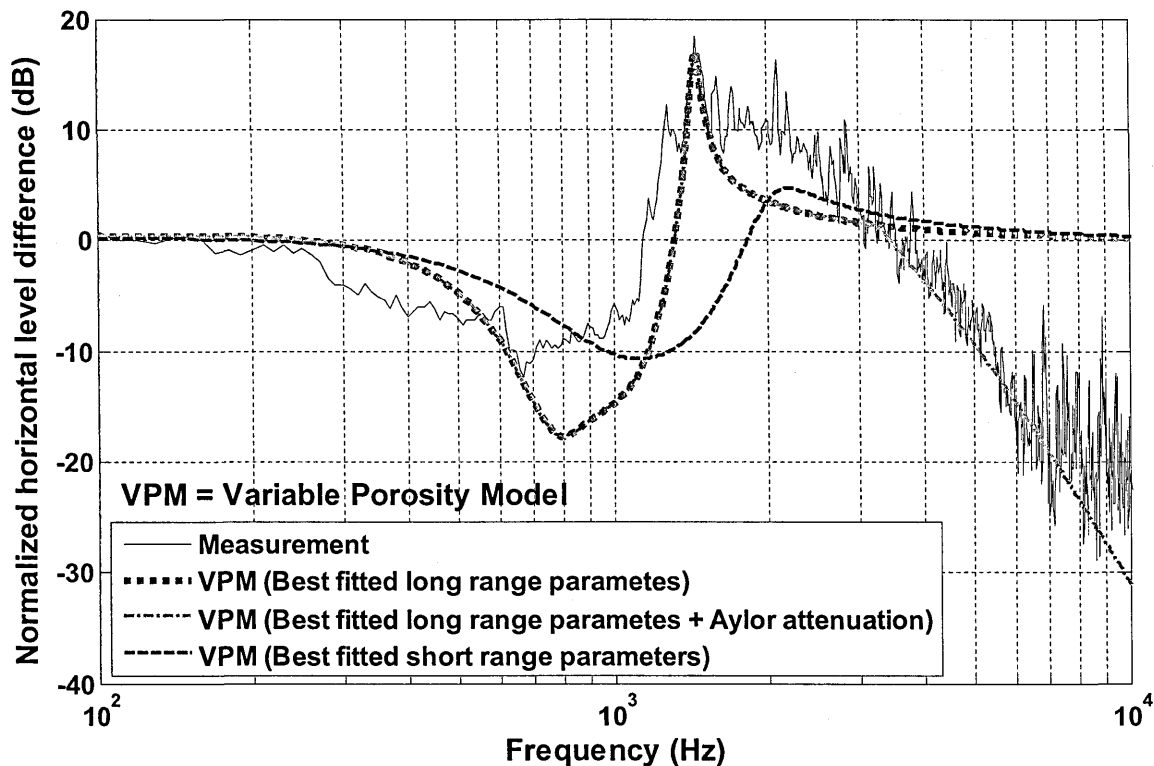
Figure 10.28 A measured horizontal level difference spectrum obtained using a large loudspeaker with source height 0.3 m and receivers at the same height 10 and 50 m from the source over Willow crops. Also shown are predictions of ground effect alone using the variable porosity impedance model with best fit parameters for longer range– Red dotted line (Flow resistivity = 45 kPa s m^{-2}, Porosity rate = 200) and best fit parameters obtained from short range ground characterization– Blue dash line (Flow resistivity = 200 kPa s m^{-2}, Porosity rate = 200); and of ground effect with best fit parameters for longer range plus plus attenuation predicted by Eq. 10.1– Green dash dotted line (Flow resistivity = 45 kPa s m^{-2}, Porosity rate = 200, Foliage area per unit volume = 40 m^{-1}, Mean leaf width = 0.012 m); ;

10.5 Sound propagation through Hedges: Data and predictions

Sound propagation through two hedges has been studied. The overall insertion loss due to hedges has been calculated. The hedges are at the Open University Milton Keynes campus. One hedge borders a car park and the other hedge is between the perimeter road and the tennis court. Drive-by tests have been carried out and the resulting data compared with predictions.

10.5.1　Hedge bordering car park

The deciduous Hawthorn hedge grown alongside a car park is shown in Figure 10.29. The hedge which was 1.9 m wide, 1.6 m tall and has 0.02 m wide leaves grows red haws. Figure 10.31 shows a top view plan of the drive-by test measurements. A reference microphone was placed near the car park entrance (i.e. corresponding to a gap in the hedge) at two distances from the road corresponding to the positions shown as 'A', and 'B' and 'C' in Figure 10.31. Behind the hedge another microphone was placed at each of the same two distances from the road denoted by positions 'A', and 'B' and 'C' in Figure 10.31. The reference microphones were at a height of 1 m above the (acoustically-hard) car park surface. A single mini-cooper (model year 1991) was driven along the straight line shown in Figure 10.31. There is 1.6 m wide footpath beside the road and a 3.1 m wide patch of grass next to the footpath. The hedge was grown on a 2.0 m wide strip of soft ground. Microphone positions 'B' and 'C' were at a distance of 0.5 m behind the hedge and positions 'A' were 5.5 m behind the hedge. The distance between the car drive-by line and the microphone position 'A' was 16.1 m and the distance between the car drive-by line and the microphone positions 'B' and 'C' was 11.1 m.

The car was driven long enough along the road to achieve a fairly constant speed while passing by the hedge. The microphone behind the hedges and the reference microphone were set to record during the car pass by. To identify the exact time interval of the car pass by, two microphones were placed next to two cables which were laid down on the ground at either end of desired passage length. Whenever a car-tyre ran over each cable the microphones on the ground recorded a high amplitude peak. Figure 10.30 shows four such peaks due to front and back tyres crossing each cable. The time between two of the peaks that corresponded to front and back tyres and the distance between the tyres enable determination of the pass by period and the speed of the car. An example time domain recording is shown in Figure 10.30. The time difference between two peaks (T1 and T2) is 0.22 s and distance between front and back tyres of the car was 2.0 m which gives the car speed of 34.7 km/h. Similarly, the time interval between T2 and T3 is when the car was passing the gap in the hedge. Using this technique the time interval at which car was passing by the hedges and the gap between the hedges was detected accurately. The time domain signals were windowed accordingly before taking an FFT of these sections of time domain signals. The resulting pressure spectra represent energy averages over the passage times (typically less than a second).
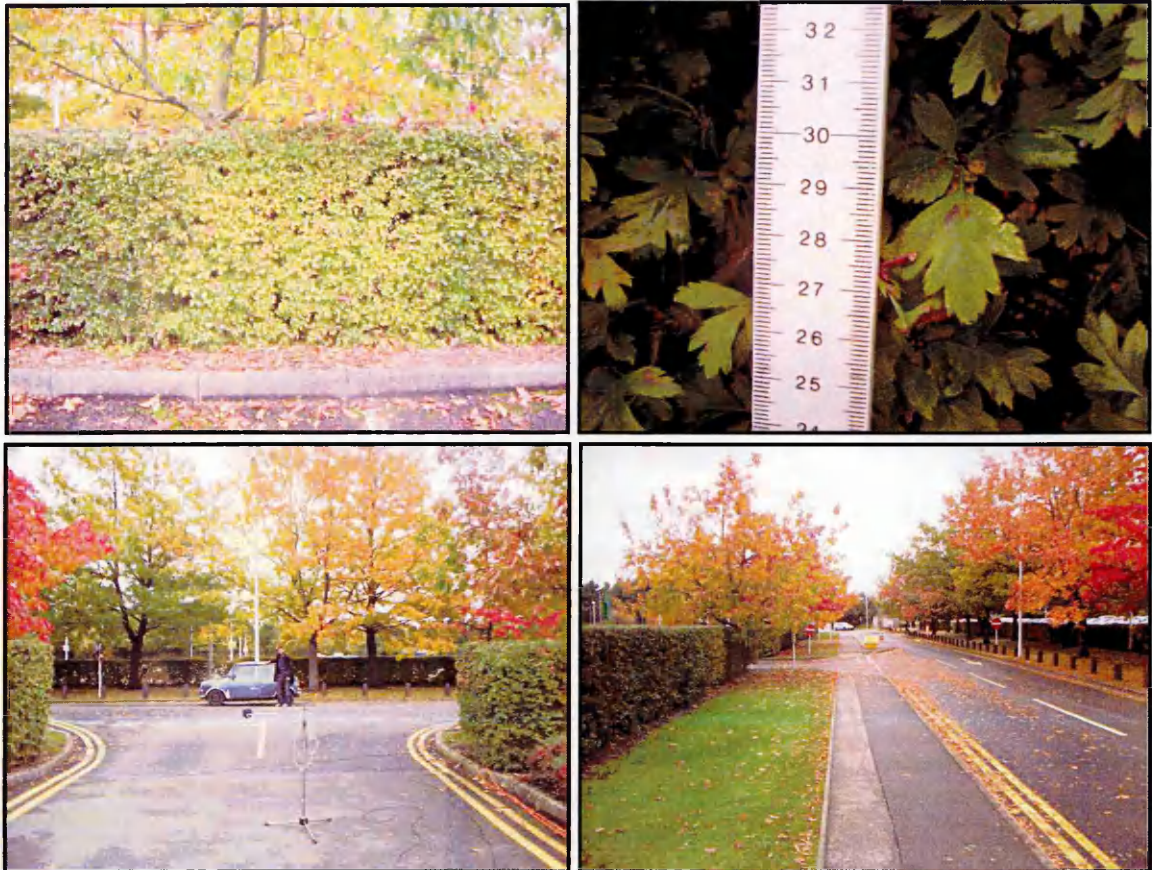
Figure 10.29 Photographs of the hedge at the car park border and a drive-by test.
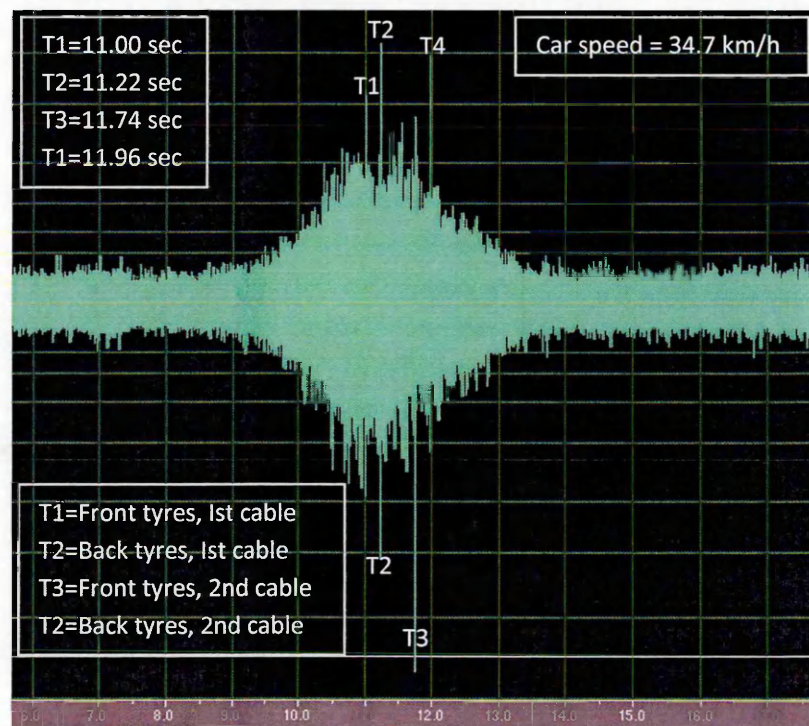
Figure 10.30 Recorded time domain signal by microphone on ground at Venebles car park
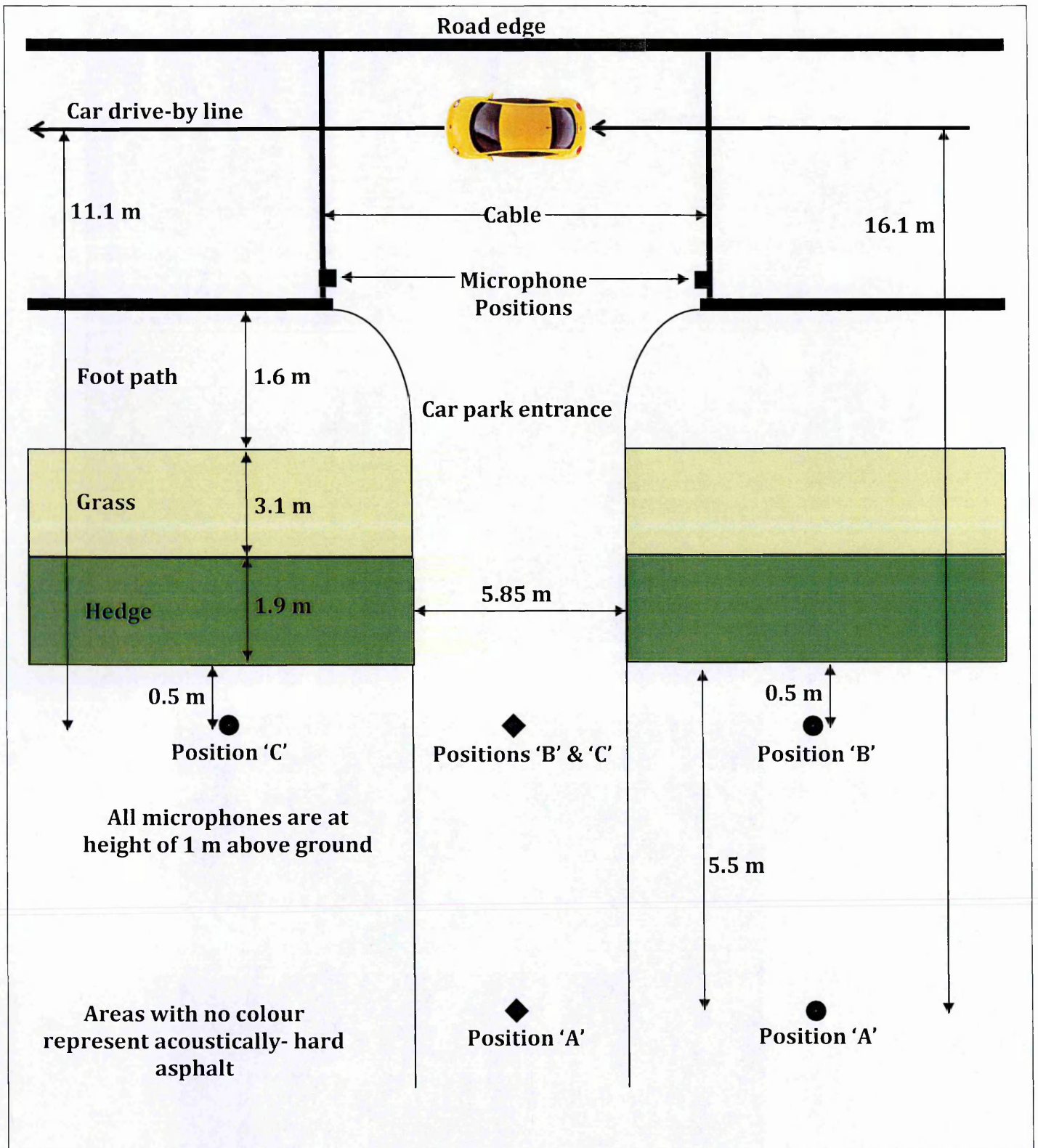
Figure 10.31 Plan view of or drive-by tests at the car park border hedge. The microphones are placed at height of 1 m above ground at positions 'A', 'B' and 'C' behind the edge or opposite the car park entrance. The white areas in the figure represent acoustically-hard asphalt and shaded areas represent acoustically-soft areas. The locations of the cables used for timings are shown also.

The main purpose of drive by test is to calculate sound attenuation due to hedges. The sound pressure level due to a car passing-by was measured with and without (i.e. in the gap) hedges simultaneously using two microphones. The two microphones must be calibrated and should capable of producing similar sound pressure level spectra for all frequencies, when expose to identical environment. The two B&K microphones used for measurements were calibrated and tested before actual recordings. Figure 10.32 shows the measured A-weighted SPL spectra during a car pass-by when the two microphones were placed very close to each other and at a height of 1.0 m above ground. The two microphones produced identical SPL spectra. Later on, the microphones were moved at positions A, B or C behind the hedge and in the car park entrance for the measurements such as shown in Figure 10.30. The background noise measured by two microphones also had identical spectra.
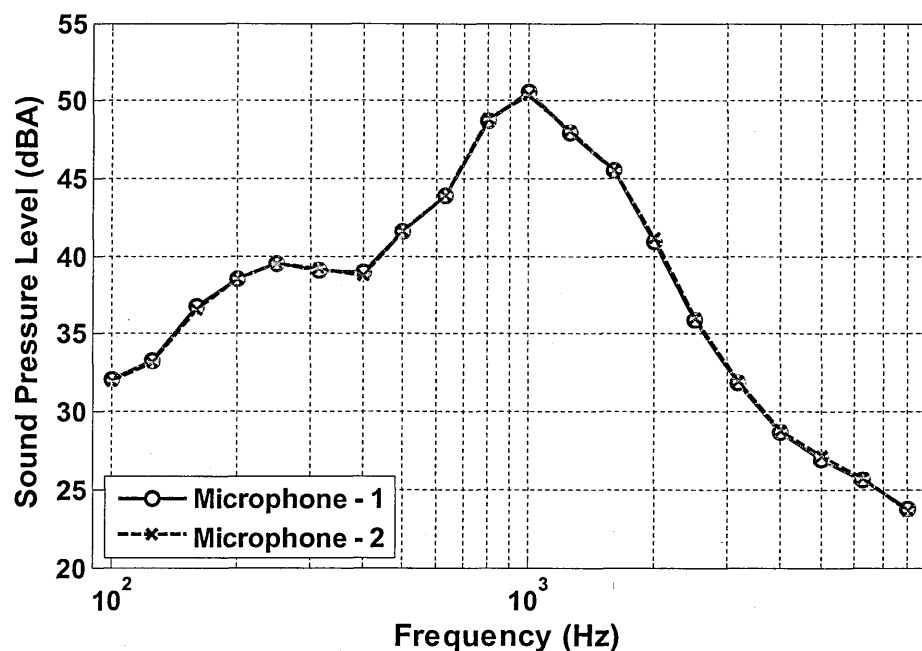
Figure 10.32 Measured A-weighted Sound Pressure Level (SPL) for a car passing by using microphone – 1 (reference microphone in car park entrance) and microphone – 2 (at the same distance from the road and behind the hedge); placed at height of 1 m above ground surface.

Figures 10.33, 10.34 and 10.35 show the sound pressure levels measured at microphones at positions 'A', 'B' and 'C' in the car park entrance and corresponding positions behind the hedge. Table 10.1 summarizes the insertion losses due to hedges at positions 'A', 'B' and 'C'. Several drive-by tests with the same vehicle have been carried out to measure the attenuation due to this hawthorn hedge. The average insertion losses due to the hedge between positions 'A', 'B' and 'C' are 2.79 dB, 2.12 dB and 2.10 dB respectively. The average car speeds during the pass-bys were 35.1 km/h, 33.5 km/h and 32.6 km/h respectively. The average insertion loss at position 'A' is greater than those at positions 'B' and 'C'. The insertion losses are a combination of the attenuation due to ground effect and the attenuation due to hedge itself. No soft ground was present between the car drive by line and the reference microphone in the car park entrance. However, the measured insertion losses include not only the attenuation due to the ground underneath the hedge but also that due to the 3.1 m wide grass land between the road and the hedge. Position 'A' was 5.5 m behind the hedge whereas positions 'B' and 'C' were 0.5 m behind the hedge. The higher insertion obtained for position 'A' may be due to the increase in ground attenuation with the reduced grazing angle at the further distance.

Table 10.2 Insertion losses measured due to the car park border hedge during six pass-bys.

Measurement	Insertion Loss (dB)	Measured Car Speed (km/h)	Insertion Loss (dB)	Measured Car Speed (km/h)	Insertion Loss (dB)	Measured Car Speed (km/h)
	Position - 'A'		Position - 'B'		Position - 'C'	
# 1	1.96	30.2	3.2	32.9	2.0	22.2
# 2	2.92	29.0	2.5	34.7	1.7	34.7
# 3	2.62	31.4	2.4	34.7	1.6	33.3
# 4	3.15	35.5	1.8	32.0	2.0	35.0
# 5	2.45	35.4	2.1	34.7	1.8	34.0
# 6	3.62	49.0	2.7	32.0	2.1	33.4
# 7	-	-	-	-	3.1	36.0
# 8	-	-	-	-	2.3	32.0
Average	2.79	35.1	2.12	33.5	2.1	32.6
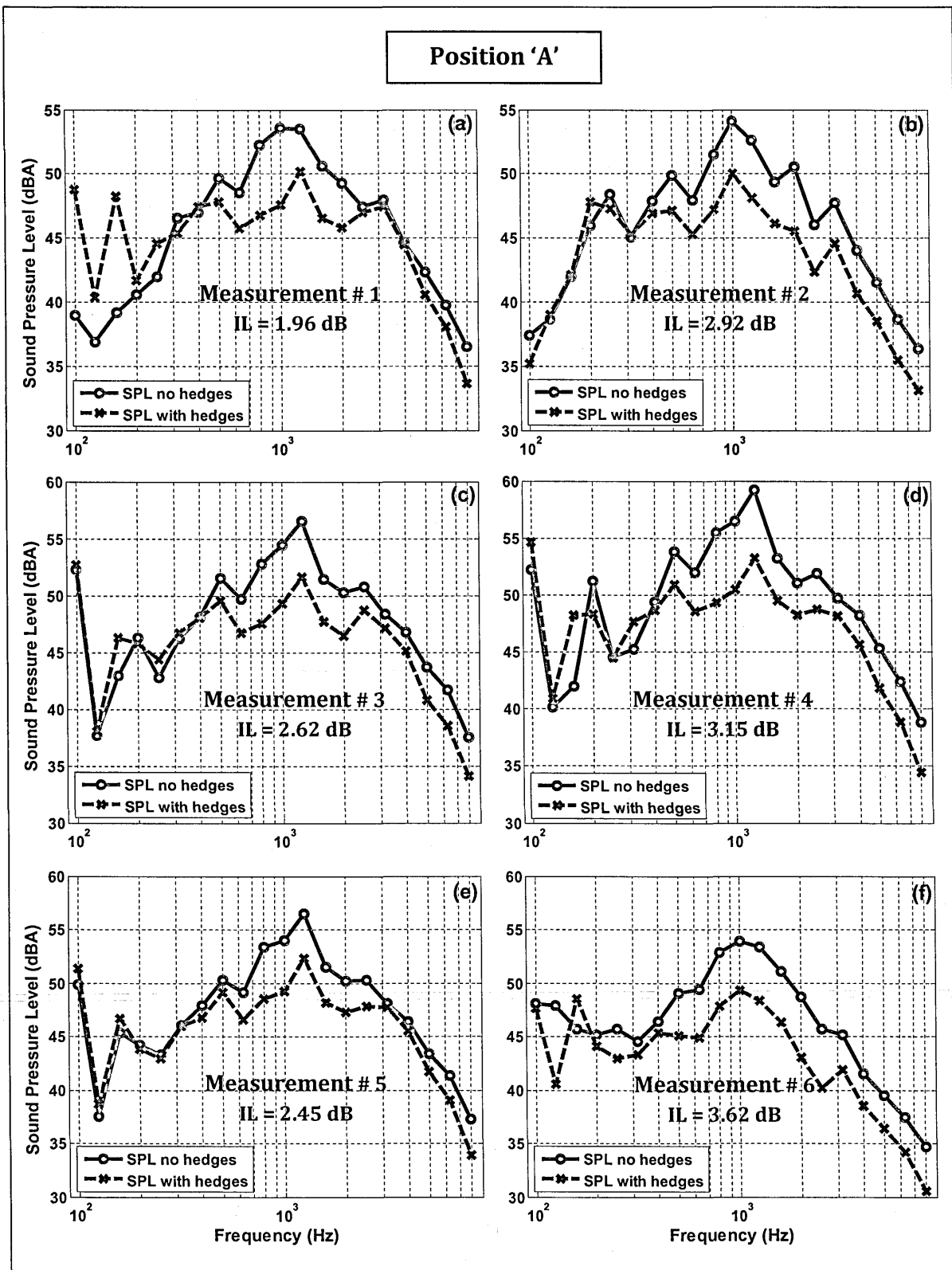
Figure 10.33 Measured 1/3 octave band A-weighted Sound Pressure Levels (SPL) during six car pass-bys at positions 'A' in the car park entrance i.e. 'without hedge' and behind the hedge i.e. 'with hedge' (See Figure 10.28).
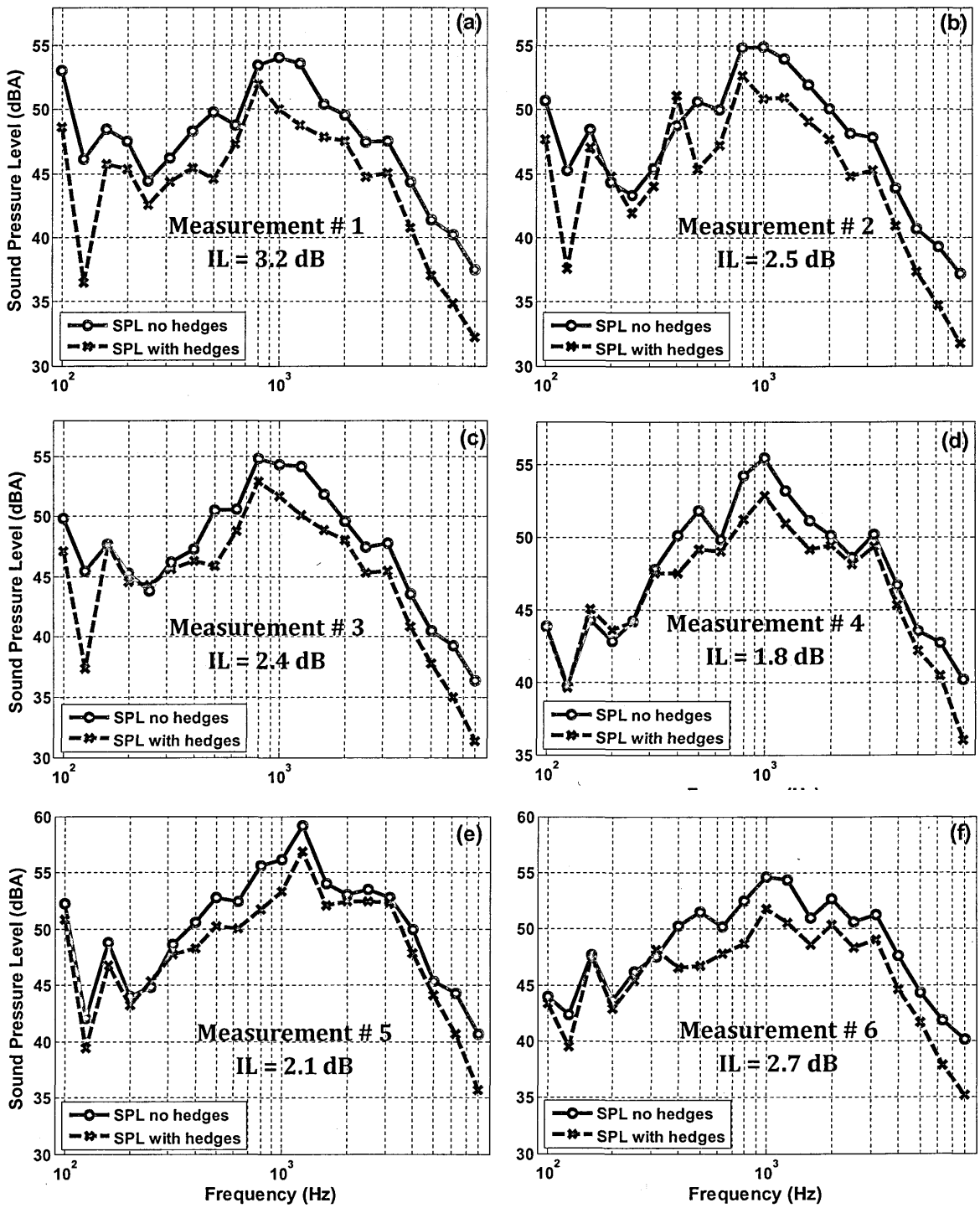
Figure 10.34 Measured 1/3 octave band A-weighted Sound Pressure Levels (SPL) during six car pass-bys at positions 'B' in the car park entrance i.e. 'without hedge' and behind the hedge i.e. 'with hedge' (See Figure 10.28).
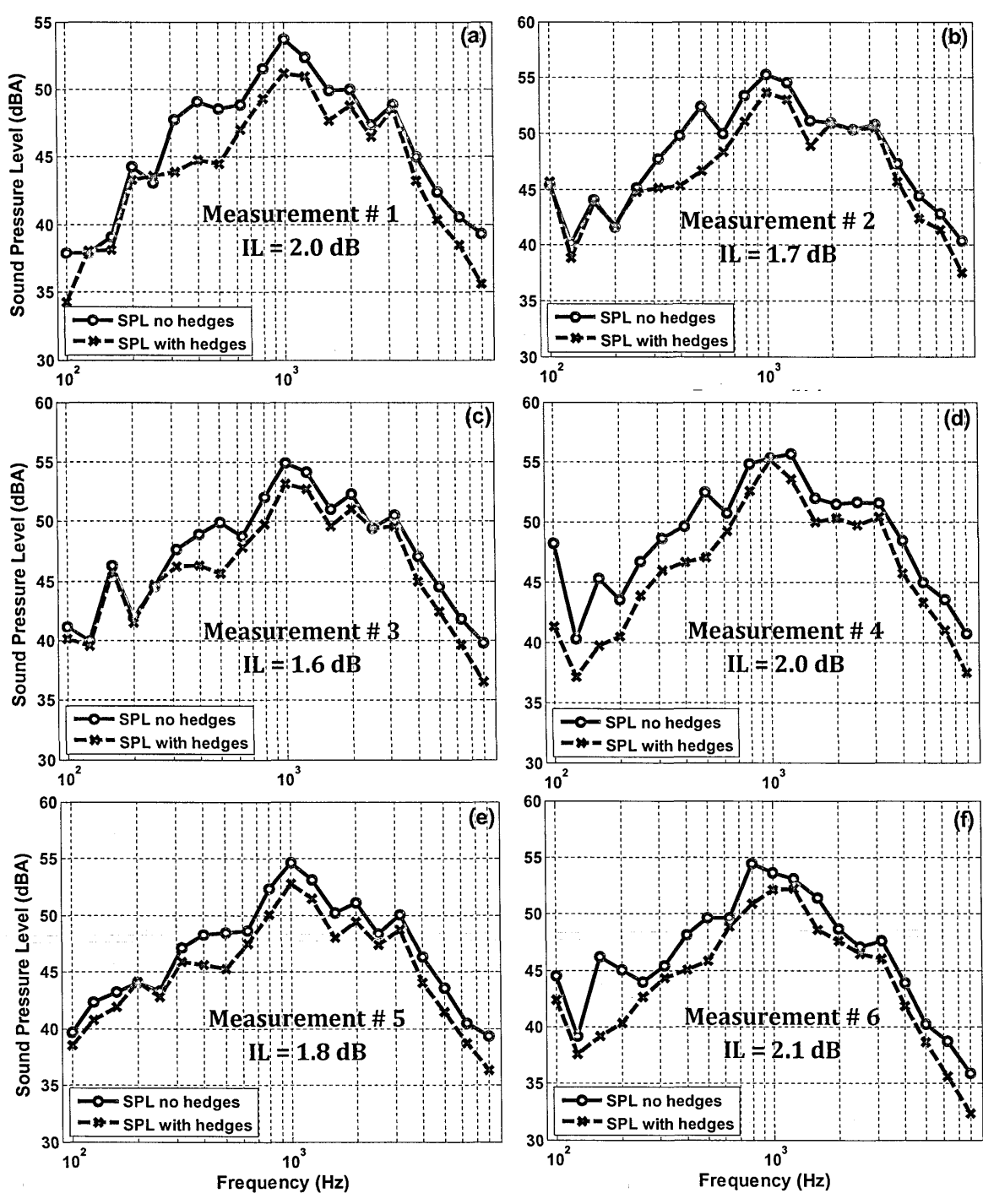
Figure 10.35 Measured 1/3 octave band A-weighted Sound Pressure Levels (SPL) during six car pass-bys at positions 'C' in the car park entrance i.e. 'without hedge' and behind the hedge i.e. 'with hedge' (See Figure 10.28).

10.5.2 Hedge near Tennis court

10.5.2.1 Pass-by Data

The sound propagation through a 'Hornbeam' hedge near the tennis court at the Open University. The hedge was 2.0 m wide and 1.9 m tall and has an average leaf size of 0.03 m. The hedge was parallel to the campus perimeter road (see Figure 10.36). There was 0.11 m high kerb present at the road edge. Recordings have been carried out behind the hedge and at the same distance from the road opposite a gap in the hedge during pass-bys of several vehicles belonging to Open University staff. (see the plan view in Figure 10.37 and the photographs in Figure 10.36). The recording microphones were placed at height of 1 m above the ground surface. Two additional microphones were placed on the ground and used to determine the car pass-by times. No cables were placed on the ground for these tests since the measurements used OU staff vehicle pass-bys and were made during normal working hours.

Nine drive-bys have been used to determine the attenuation due to the 'hornbeam' hedge. Figure 10.38 shows the measured sound pressure levels Table 10.2 summarizes the corresponding insertion losses. The average insertion loss due to hedge was 2.01 dB. No soft ground was present between the car drive by line and the reference microphone opposite a gap in the hedge. However, since the overall insertion loss due to hedge is that due to foliage plus the attenuation due to the presence of acoustically soft ground, the 3.1 m wide area of soft ground near the car park hedge causes the overall attenuation due to the hedge near the tennis court to be less than that due to the car park border hedge.

Figure 10.36 Photographs of the measurement location for the 'hornbeam' hedge near the tennis court.
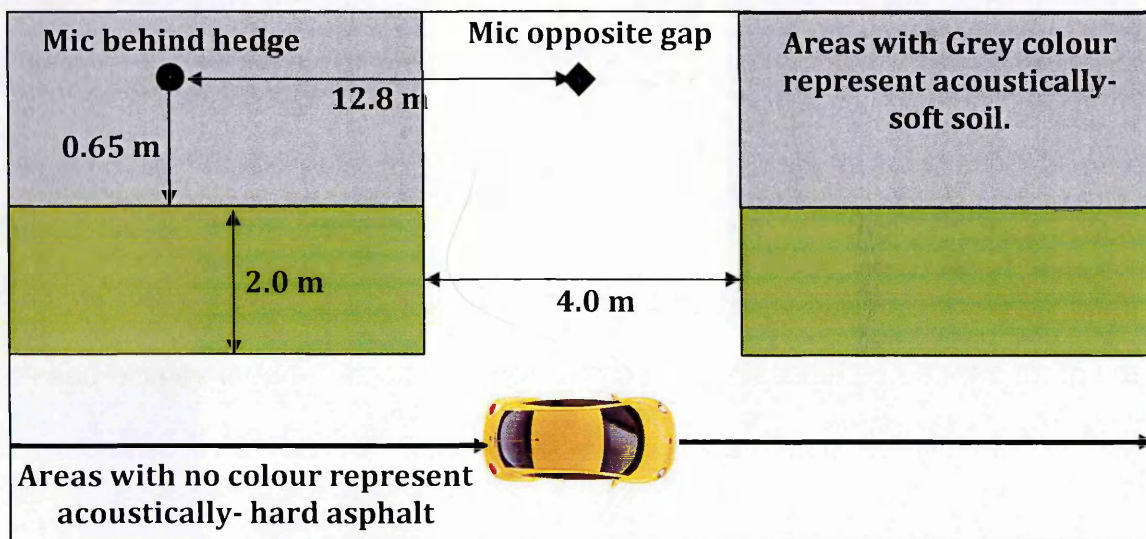
Figure 10.37 Plan view of measurement arrangement near the 'hornbeam' tennis court hedge during pass-bys by staff vehicles.

Table 10.3 Insertion losses due to the hedge near the tennis court during drive-bys of Open University staff vehicles.

OU staff-vehicles pass-by recordings	# 1	# 2	# 3	# 4	# 5	# 6	# 7	# 8	# 9	Average
Insertion loss (dB)	1.7	1.91	2.35	1.83	1.8	2.44	2.5	2.02	1.6	**2.01**
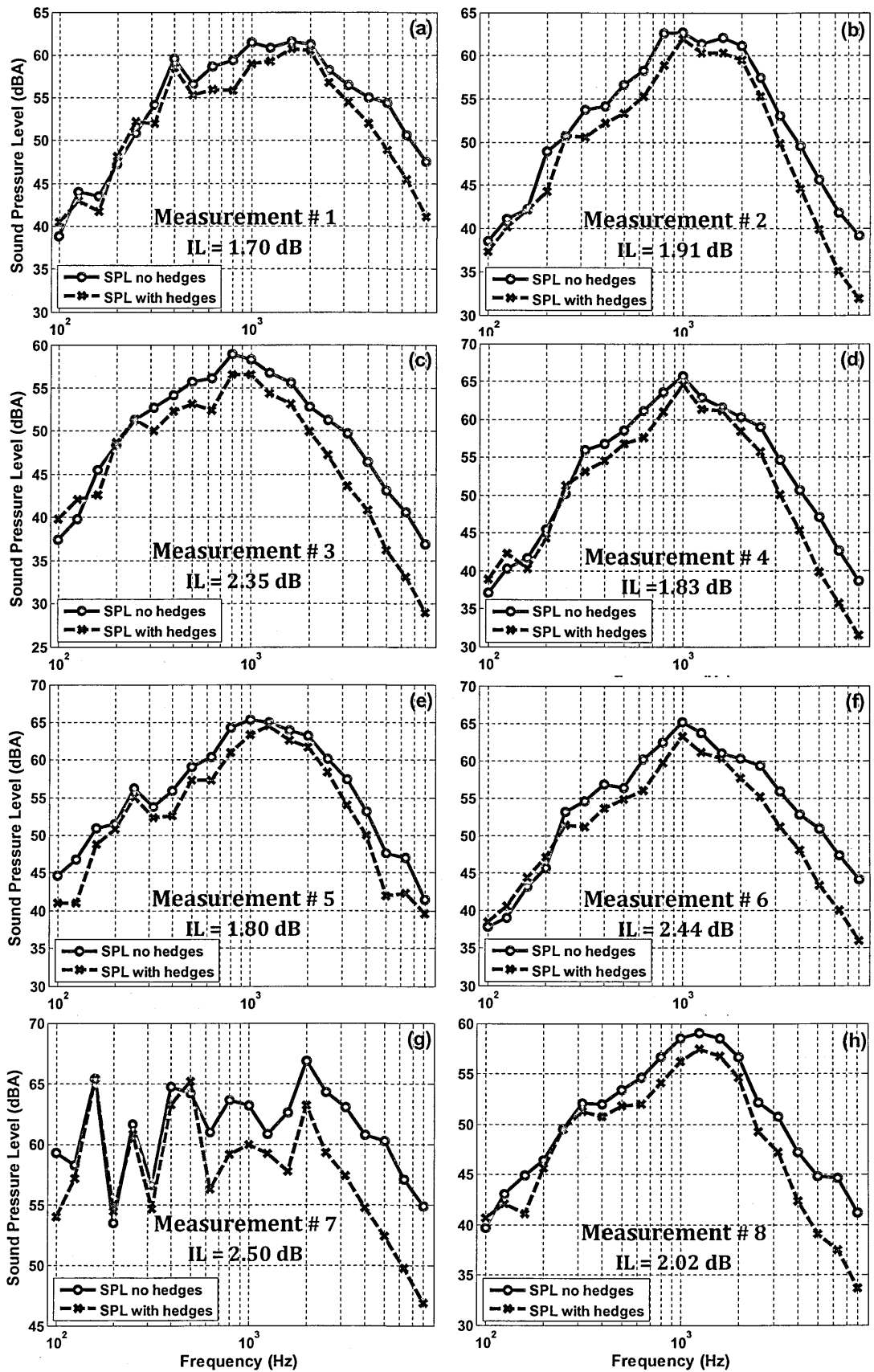
Figure 10.38 Measured 1/3 octave band A-weighted Sound Pressure Levels (SPL) during nine car pass-bys at positions opposite a gap in the hedge i.e. 'without hedge' and behind the hedge i.e. 'with hedge' (See Figure 10.30).

10.5.2.2   Predictions

The ground effect due to the discontinuous profile at the hedge near the tennis court has been modelled using a 2D BEM. Excess attenuation has been predicted for a car tyre/road source at height of 0.01 m (a) for a receiver at a height of 1 m above hard ground and (b) for a receiver at a height of 1 m over soft ground i.e. in the presence of an impedance discontinuity. The hedges were planted on a 0.1 m high kerb and gap in between the hedges had a 0.1 m high slope. BEM was used to model 0.1 high kerb and slope to create a model as close as possible to the real scenario. Figure 10.39 shows the predicted hard ground effect, the hard to soft ground effect with an impedance discontinuity and the difference between the two ground effects. The soft ground was modelled using the slit pore impedance model with flow resistivity of 50 k Pa s m^{-2} and porosity of 0.5 (see Chapter 4). These ground parameters could not be validated by independent ground characterization due to the unfavourable environment. However, these parameters were 'guesstimates' based on previous ground characterization experience for similar ground types (see Chapter 4).

Figures 10.40 (a) – (r) compare sound level spectra measured during different vehicle pass-bys with predictions obtained by subtracting the excess attenuation difference due to the discontinuous ground and including foliage attenuation based on Eq. 10.1 (foliage area per unit volume 4.5 m^{-1}, length of propagation path 2.2 m and mean leaf width 0.03 m) to represent the extra attenuation due to the hedge from the source spectrum measured at the reference microphone location for each passing vehicle . The parameter values used in Equation 10.1 have been adjusted to fit the data but represent reasonable values.

Eq. 10.1 predicts attenuation only at higher frequencies. The measured and predicted attenuation at lower frequencies (400 Hz to 1 kHz) is due to the discontinuous ground including soft ground underneath the hedge. The agreement between data and predictions suggests an explanation for the overall attenuation yielded by hedges over a soft ground. These results show that although shielding provided by above-ground biomass alone might be limited for road traffic at low vehicle speeds, hedges provide the opportunity to benefit also from soft ground effects.
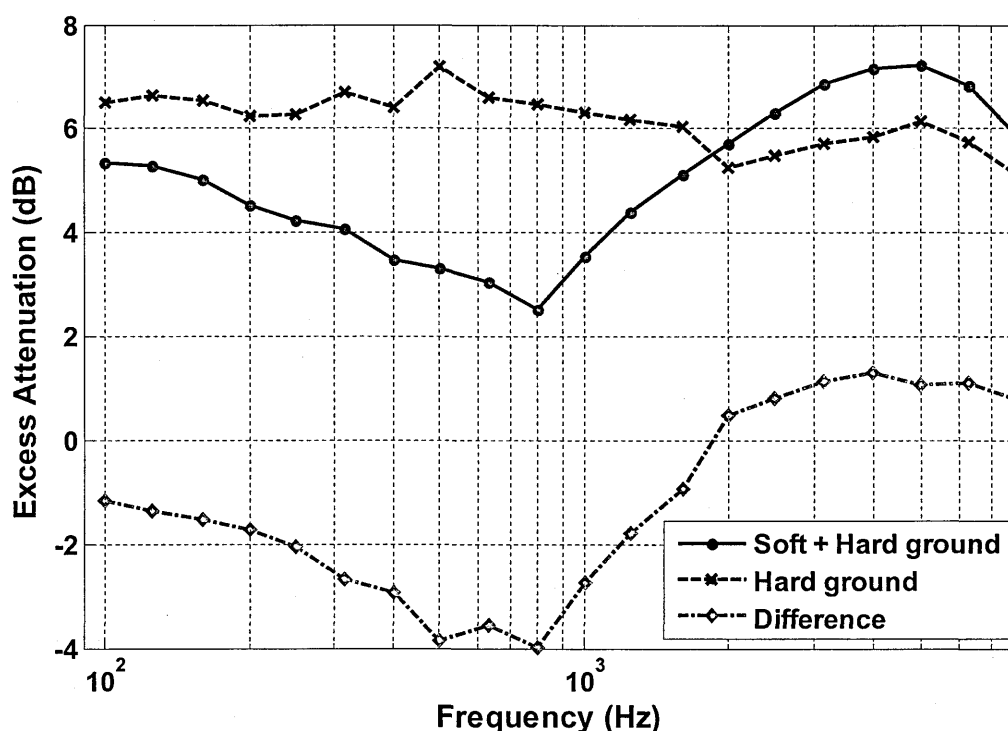
Figure 10.39 BEM excess attenuation predictions for a source height of 0.01 m, receiver height of 1.0 m and source-receiver separation of 4.35 m over hard ground (black dash-cross line); hard ground with a single hard/soft discontinuity (blue continuous dotted line) and the difference between them (red dash-diamond line).
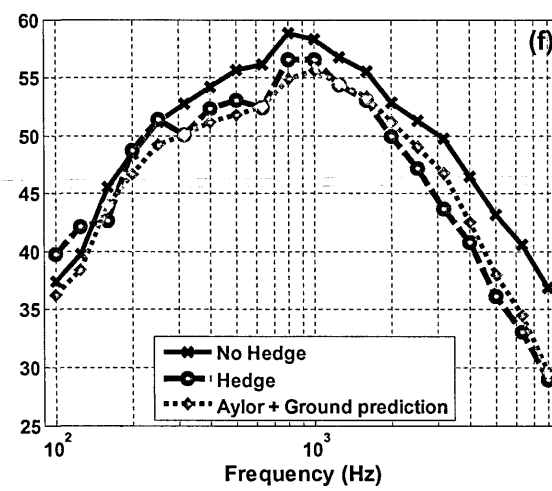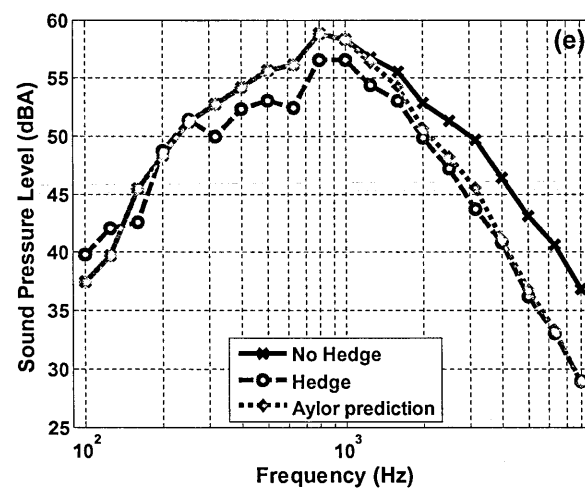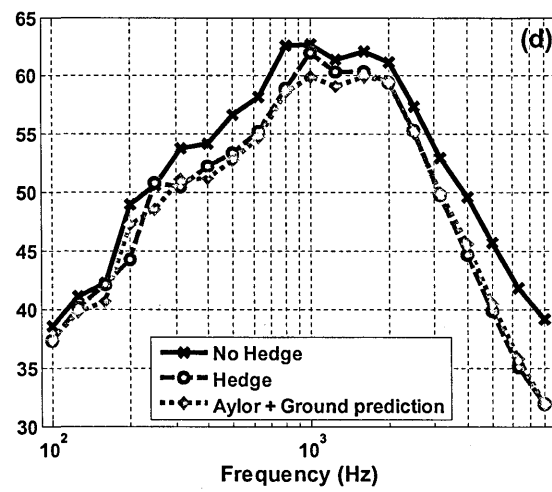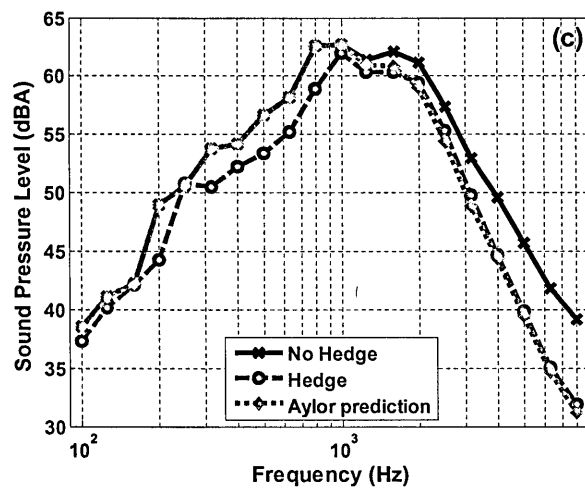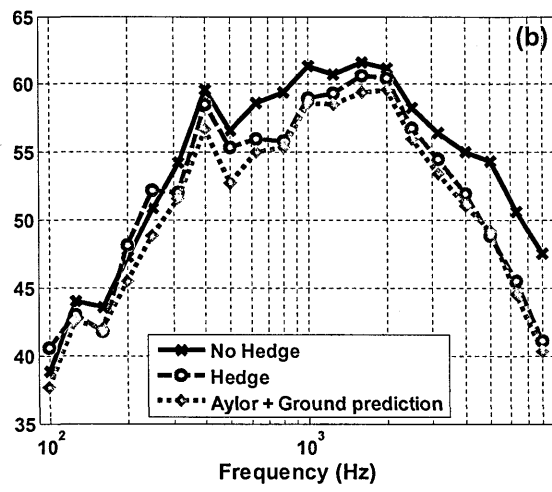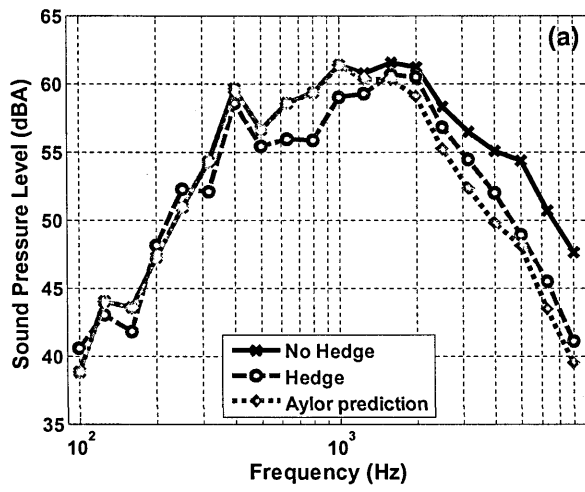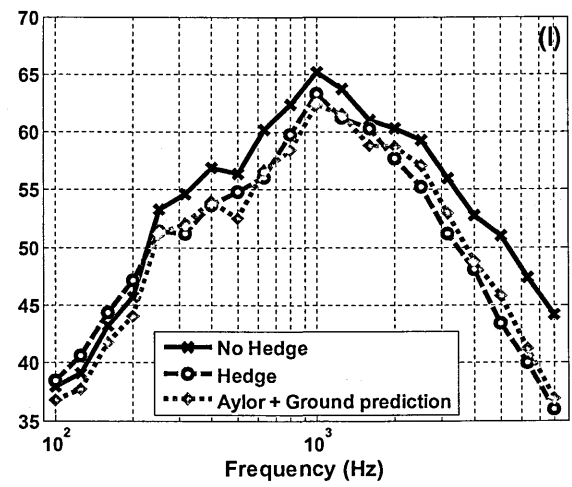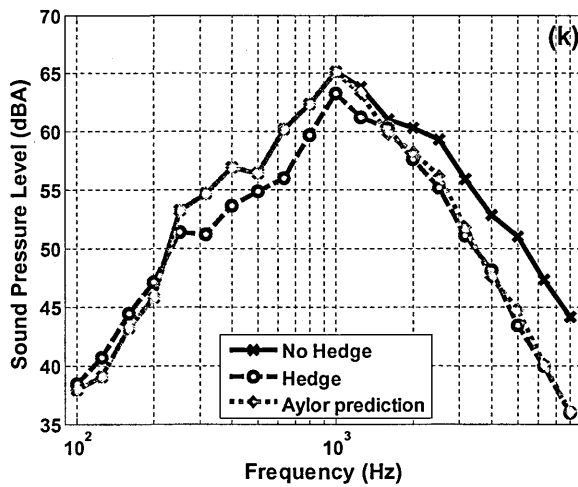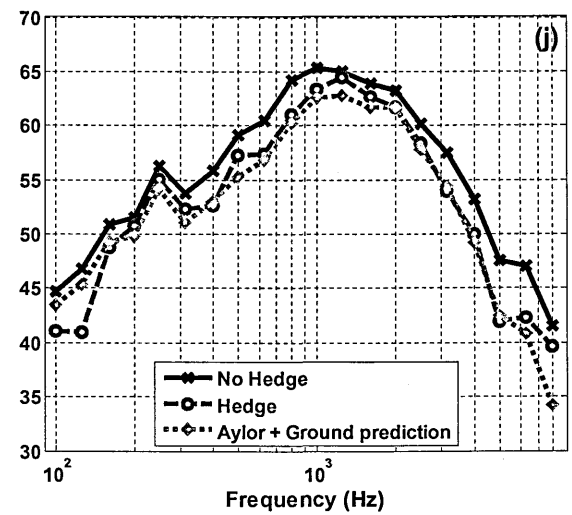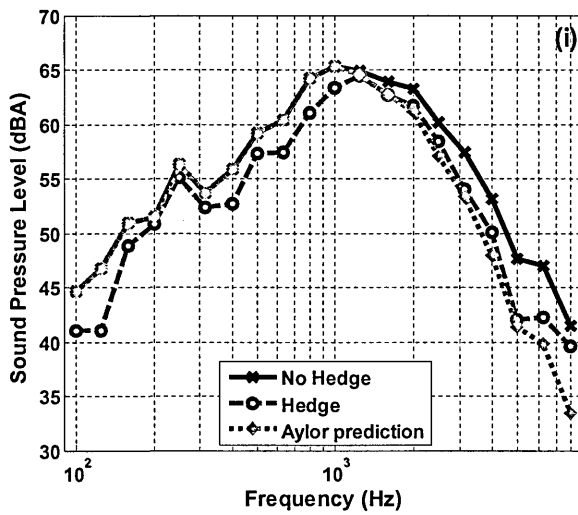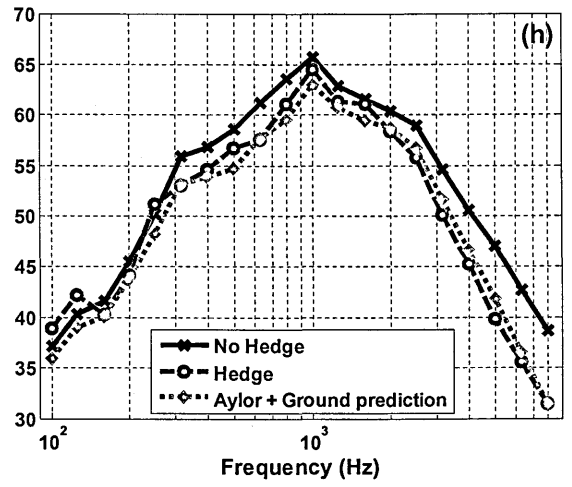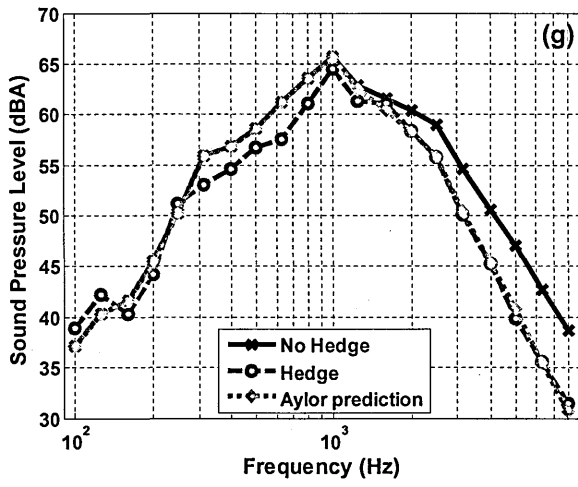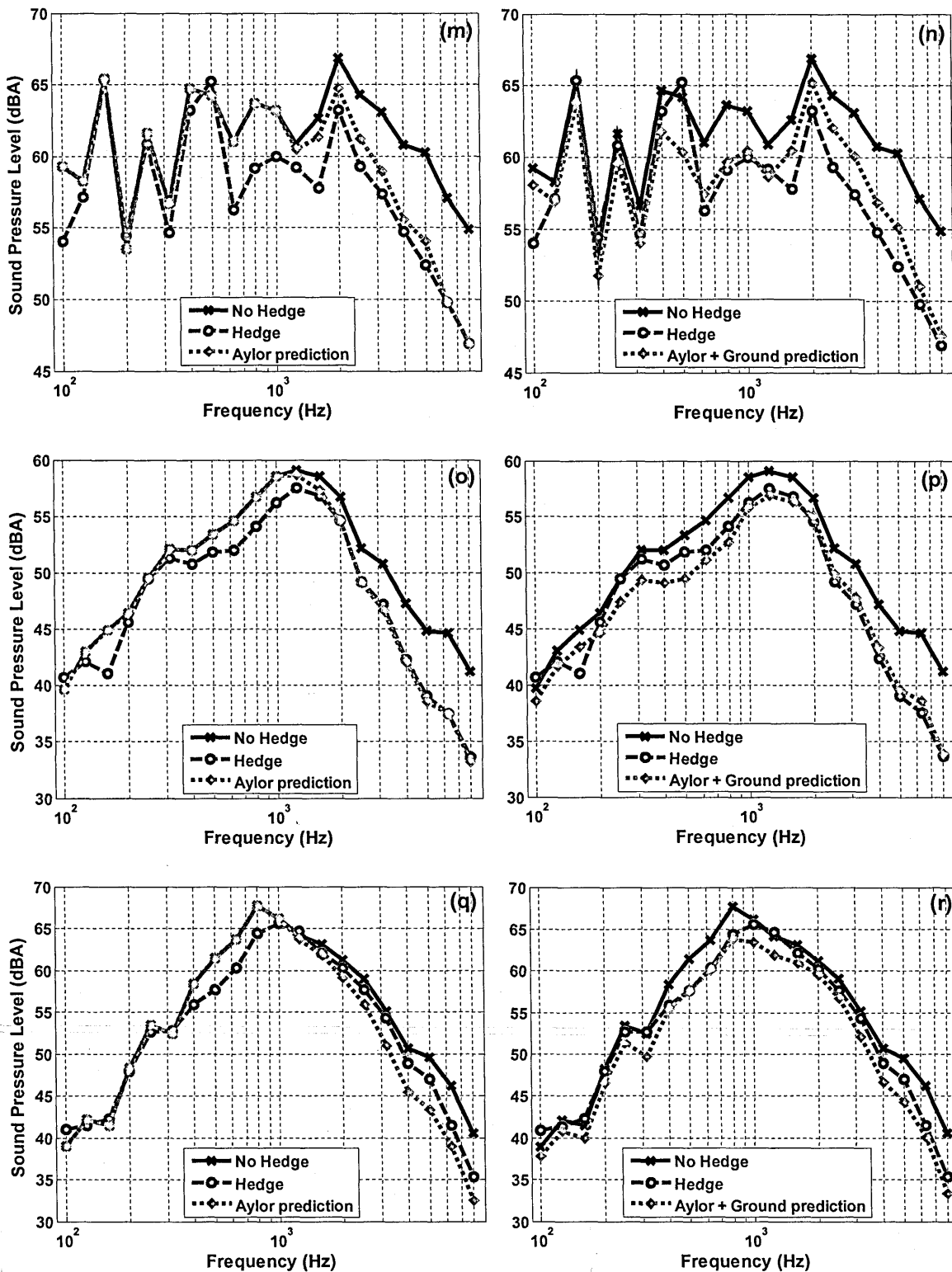
Figure 10.40 Comparison between measured A-weighted SPLs behind the tennis court hedge ('Hedge') and opposite a gap in the hedge ('No hedge) during nine vehicle pass-bys with predictions using only attenuation predicted by Eq.10.1 (foliage area per unit volume 4.5 m^{-1}, length of propagation path 2.2 m and mean leaf width 0.03 m) and this foliage attenuation plus discontinuous soft ground effect underneath hedge.

10.6 Conclusions

A series of measurements have been carried over winter wheat and willow crops. Vertical level difference was measured by clearing crops to characterize the ground surface on which crops were growing. However, later it was found that vertical level difference measurements can be carried out inside crops without clearing the area. Horizontal level difference data was used to study the sound propagation through crops. It is concluded that the sound attenuation occurs due to multiple scattering between the stems and leaves, loss of coherence and viscous and thermal losses due to foliage. However, the major contribution to attenuation due to crops is due to viscous and thermal losses, which can be predicted by using an empirical formula (see Eq. 10.1). This may be termed the 'crops effect'. At lower frequencies ground effect is dominant and there is little or no crops effect. At higher frequencies above 3-4 kHz the crops effect is dominant. It was also found that the ground and crops effects can be treated independently and can be added to obtain the total effect. Green leaf crops result in more attenuation than dry crops with fallen leaves.

Longer range measurements over winter wheat were carried out using propane cannon as a source. The agreement between data and ground effect predictions was not good above 1 kHz as a result of relatively poor signal to noise ratios.

For ideal homogeneous ground, the parameters obtained through short range ground characterization method should also fit data obtained over longer ranges. However, it was found that the parameters obtained through short range characterization method do not fit the data over longer ranges. This is due to

ground in-homogeneity, roughness and unevenness of cultivated ground surface at longer ranges.

It is concluded that the noise attenuation due to crops is dependent on the length of the sound propagation path through the crops. If, crops are not very tall and receivers are usually at some height above ground i.e. 1.5 and 4.0 m then less sound passes through crops which make them not very effective for traffic noise attenuation. Moreover, the crops effect usually at higher frequencies and traffic noise is a low frequency source peaks at 1 kHz.

Vehicle pass-by measurements have been made near two hedges along the perimeter road at The Open University campus in Milton Keynes. A single car moving at average speeds of between 32 and 35 km/h was used for the measurements near *hedge 1* (approx. 1.9 m wide hawthorn hedge on a raised kerb at the edge of a s car park). Pass-bys by nine vehicles (used by Open University staff) were involved with the measurements near *hedge 2* (approx. 2 m wide on soft ground near a tennis court). The average difference in levels between three locations behind *hedge 1* and reference locations at the same distances from the pass-by path but opposite a gap in the hedge was between 2 and 3.5 dBA. The average difference in levels between a location behind *hedge 2* and a reference location, i.e. at the same distance from the pass-by path, was between 1.5 and 2.5 dBA. It has been found possible to fit the data obtained near hedge 2 using a combination of predicted discontinuous ground effect and foliage attenuation predicted by Eq. 10.1 with reasonable parameter values.

Chapter 11

11. Insertion loss calculations for

surface transport noise

11.1 Introduction

Growing demand on transportation, road and railway networks has resulted in increased levels of annoyance from road traffic and railway noise. Research in more efficient and effective methods of mitigating the effects of traffic noise is ongoing. The traditional way of reducing noise is to erect a noise barrier which divides the communities and is ineffective for long source-barrier-receiver distances. The main idea being investigated in this thesis is to optimize the use of green areas, green surfaces and other natural elements in combination with artificial elements in urban and rural environments for reducing the noise impact of road and rail traffic. The work has been carried out as part of a project "Holistic and Sustainable Abatement of Noise by optimized combinations of Natural and Artificial means" (HOSANNA). The project studied a studied a number of green abatement strategies that might achieve cost-effective improvements using new

barrier designs, planting of trees, shrubs, ground and road surface treatments. The research project involved 13 universities from seven countries and has been funded from European Union Seventh Framework Programme.

The aim of this chapter is to investigate (numerically) the efficacy of different proposed ways of achieving noise attenuation i.e. replacing hard ground with porous ground, growing vegetation and low height roughness to real scenarios. Different traffic noise sources have been considered such as 2-lane urban road or 4-lane motorway. The work has also been extended to railway noise and tramway noise. The insertion loss for various noise sources due to different ground treatments have been calculated using Boundary Element Method and Matlab

This chapter presents work on exploiting the ground surfaces near roads and railways for noise mitigation purposes. The chapter is divided into three major parts concerned respectively with road, railway and tramway noise. The last section presents corresponding conclusions. This chapter is based on HOSANNA deliverable 4.5 [166].

11.2 Road traffic noise

11.2.1 HARMONOISE source spectrum

The A-weighted sound pressure level due to road traffic has been calculated using an engineering method [HARMONOISE, [104]]. The method was developed to give a detailed description of noise sources. The source spectra calculated using HARMONOISE take into account of the height of source, road type, speed of vehicle, vehicle type and traffic flow. The sound power output of individual, moving vehicles is combined into an equivalent sound power output for the total traffic flow [104]. An individual vehicle is defined as having multiple source heights depending on its type i.e. a car is defined with source heights of 0.01 m and 0.3 m above ground. The source spectrum due to each source height is calculated using HARMONOISE. The source spectrum due to different source heights are added together to obtained the total source spectrum due to a vehicle. The traffic flow of each vehicle type is weighted according to its flow on a given road type e.g. on a two lane urban road, the traffic flow of cars and trucks are 95 % and 5 % respectively. The average vehicle speed and number of vehicles per day for a given road type are also used as an input to determine the source spectrum. Table 11.1 summarizes the source type and source height for different vehicle types. According to HARMONOISE the source power output for a source height of 0.01 m is given by,

$$L_{W1,i} = L_{WRN1,i} \oplus L_{WTN1,i},$$

(11.1)

$$L_{WRN1,i} = \alpha_{RN,i} + \beta_{RN,i} \log\left(\frac{v}{v_{ref}}\right) + 10\log(0.8),$$ (11.2)

$$L_{WTN1,i} = \alpha_{T,i} + \beta_{T,i} \log\left(\frac{v - v_{ref}}{v_{ref}}\right) + 10\log(0.2).$$ (11.3)

The source power output for a source height of 0.3 m is given by,

$$L_{W2,i} = L_{WRN2,i} \oplus L_{WTN2,i},$$ (11.4)

$$L_{WRN2,i} = \alpha_{RN,i} + \beta_{RN,i} \log\left(\frac{v}{v_{ref}}\right) + 10\log(0.2),$$ (11.5)

$$L_{WTN2,i} = \alpha_{T,i} + \beta_{T,i} \log\left(\frac{v - v_{ref}}{v_{ref}}\right) + 10\log(0.8).$$ (11.6)

The source power output for a source height of 0.75 m is given by,

$$L_{W3,i} = L_{WRN3,i} \oplus L_{WTN3,i},$$ (11.7)

$$L_{WRN3,i} = \alpha_{RN,i} + \beta_{RN,i} \log\left(\frac{v}{v_{ref}}\right) + 10\log(0.2),$$ (11.8)

$$L_{WTN3,i} = \alpha_{T,i} + \beta_{T,i} \log\left(\frac{v - v_{ref}}{v_{ref}}\right) + 10\log(0.8).$$ (11.9)

where L_{WRN} is the rolling noise sound power, L_{WTN} is the traction noise sound power, α_{RN} and β_{RN} are the rolling coefficients, α_T and β_T are the traction noise coefficients, v is the vehicle speed in *km/h* and v_{ref} is the reference vehicle speed in *km/h*. The reference vehicle speed v_{ref} is 70 km/h, for all vehicle categories. The detailed coefficients are given in HARMONOISE [104].

Figure 11.1 shows an example source spectrum calculated using the HARMONOISE method for a source height of 0.01 m travelling at a speed of 70 km/h. To calculate the insertion loss due to a specific ground treatment, the (A-weighted) sound pressure level spectrum due to a given road type is calculated over a hard ground for the receiver location of interest, then the corresponding (A-weighted) sound pressure level after ground treatment is predicted. The difference between the two spectra gives the insertion loss spectrum due to that treatment.

Table 11.1 Traffic noise source types and heights [104].

Vehicle type	Source type	Source height (m)
Light vehicles	Road-Tyre noise: Applicable to every vehicle	0.01
Medium heavy vehicles	Engine noise	0.30
Heavy vehicles	Engine noise	0.75
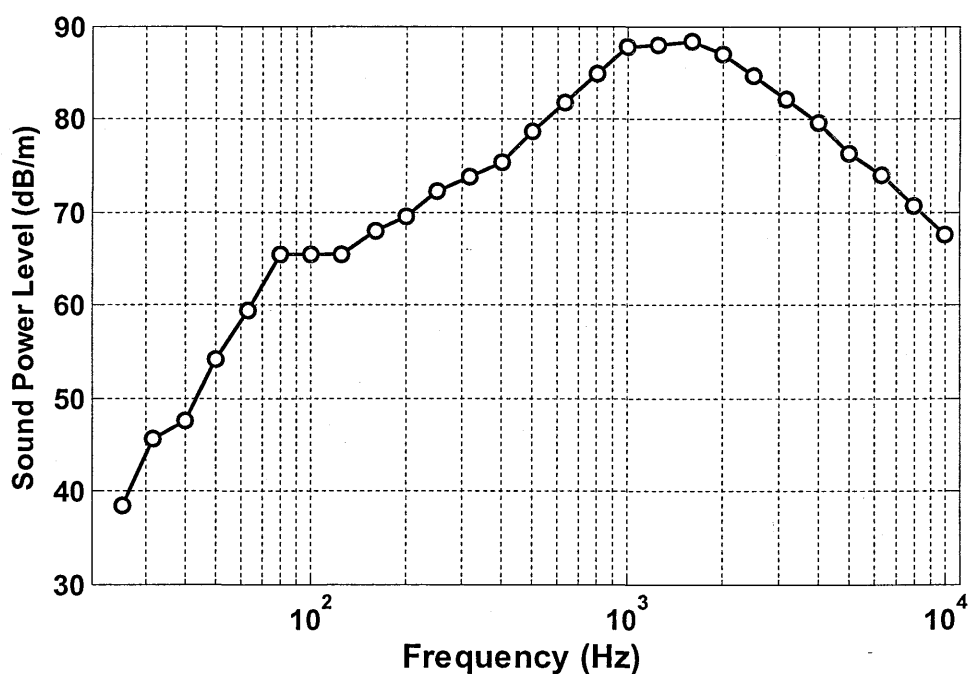
Figure 11.1 Source spectrum for a road-tyre noise with a height of 0.01 m, vehicle travelling at speed of 70 km/h calculated using the HARMONOISE method.

11.2.2   HOSANNA road scenarios

According to HOSANNA project guidelines, the insertion loss calculations have been carried for different road types. The vehicle distributions and their speed vary with every road type. All noise sources are assumed to be acoustically incoherent. Each source is assumed to be an omni-directional point source in 3D. The level of sound power per unit length, L_w, can be written as [167],

$$L'_W = L_W + 10\log\left(\frac{Q}{1000v}\right),$$ **(11.10)**

where L_w is the output power of each vehicle, Q is the number of vehicles per hour and v is the speed in *km/h*. For multiple lanes road Q is the flow per lane.

11.2.2.1   2-lane urban road

According to HOSANNA WP 2.3 [167], [168] the standard two lane urban road case is shown by Figure 11.2. Each lane is 3.5 m wide with a distance of 3.5 m in between the two lanes. The source heights are 0.01 m, 0.3 m and 0.75 m depending of vehicle type. In city centres, it is assumed that the traffic distributions consist of 95 % of light vehicles and 5 % of heavy vehicles. The average speed of the vehicles is assumed to be 50 km/h. The traffic flow is assumed to be 833 vehicles per hour which corresponds to 20,000 vehicles per day. This information is used in HARMONOISE engineering method (see Eq. 11.1 – 11.10) to obtain the source spectrum due to a HOSANNA 2-lane urban road.
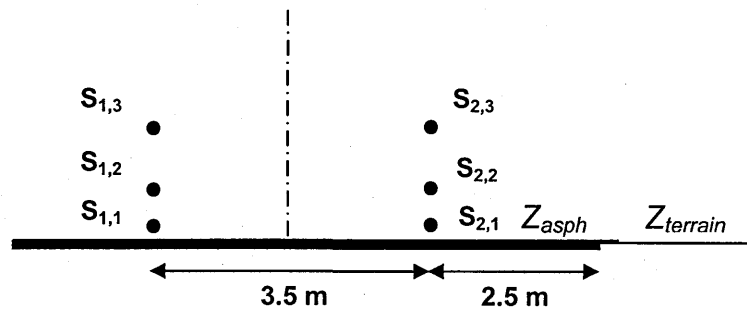
Figure 11.2 Configuration of the 2-lane urban road: 3.5 m between lanes; source height 0.01 m for $S_{x,1}$, 0.3 m for $S_{x,2}$ and 0.75 m for $S_{x,3}$ where x is 1 or 2.

11.2.2.2   4-lane urban road

According to HOSANNA WP 2.3 [168], [169], the standard four lane urban road case is shown in Figure 11.3. Each lane is 3.5 m wide with a distance of 3.5 m in between the lanes. In city centres, the traffic distributions consist of 95 % light vehicles and 5 % heavy vehicles. The average speed of the vehicles is assumed to be 50 km/h. The traffic flow is assumed to be the 833 vehicles per hour which corresponds to 20,000 vehicles per day. The traffic flow assumed here is same as for 2-lane urban road. In this chapter, the traffic noise attenuation due to ground treatments is given as insertion loss. The insertion loss calculation is not affected by traffic flow. It becomes important only when traffic noise is presented as sound pressure level.
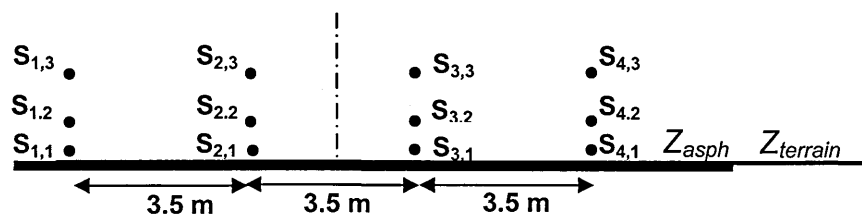
Figure 11.3 Configuration of the 4-lane urban road: 3.5 m between lanes; source height 0.01 m for $S_{x,1}$, 0.3 m for $S_{x,2}$ and 0.75 m for $S_{x,3}$.

11.2.2.3   2x2 lane motorway

According to HOSANNA WP 2.3 [168], the standard 2x2 lane motorway is shown by Figure 11.4. Each lane is 3.5 m wide with a distance of 3.5 m in between the lanes. Unlike the urban road, the motorway is assumed to have a 2.0 m wide central reservation. The traffic distributions on a motorway consist of 85 % light vehicles and 15 % heavy vehicles. The average speed of the vehicles is assumed to be 120 km/h. The height of sources over the asphalt plane is 0.01 m for $S_{x,1}$, 0.3 m for $S_{x,2}$ and 0.75 m for $S_{x,3}$ where x is the lane number.
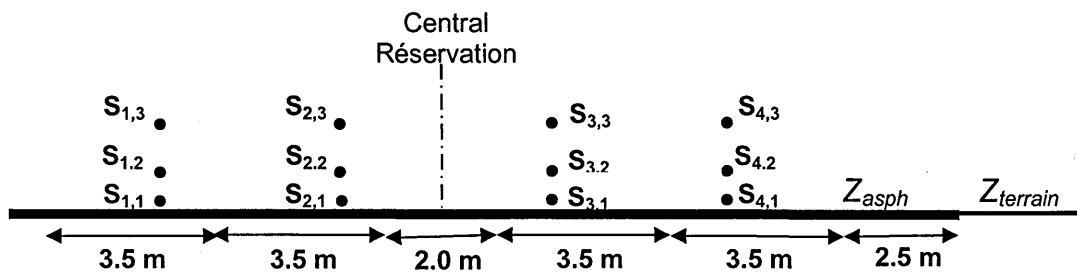
Figure 11.4 Configuration of the 2x2 lane motorway: 3.5 m wide lanes and 2.0 m wide central reservation; source height 0.01 m for $S_{x,1}$, 0.3 m for $S_{x,2}$ and 0.75 m for $S_{x,3}$.

11.3 Traffic noise mitigation by ground treatments, roughness and vegetation

If the listeners are at some distance from the road, alternatives to noise barriers for reducing noise levels can utilize the ground surfaces near the road. Noise reduction by exploiting the acoustical properties of the ground surfaces between the road and listeners can be more cost-effective and visually less intrusive than, for example, erecting noise barriers. To understand ground effect on traffic noise, consider a reference listener point at a height of 1.5 m and at a distance of 50 m from the road. Sound from a vehicle that is reflected from the ground interferes with the sound traveling directly to the reference point. At some frequencies these two sound levels interfere constructively to reinforce each other and thereby increase the total sound level compared to the sound level if the ground were not present. At some frequencies these two sound levels interfere destructively to partly cancel each other and thereby reduce the total sound level compared to that if the ground were not present. These constructive and destructive interferences depend on the source-receiver geometry and the acoustical properties of the ground surface. For a traffic noise source which is close to ground and receiver at a height of 1.5 m, the destructive interference over hard ground having infinite impedance occurs at relatively high frequencies which are not useful for traffic noise attenuation. However, if the ground is modified to have finite impedance, the destructive interference occurs at relatively low frequencies and can be useful for traffic noise attenuation. There are several ways to modify the ground impedance. These include replacing the hard ground with

soft ground, introducing low height roughness and creating impedance discontinuities which may be in the form of strips or patches.

Ground treatments along the road side have been studied using a Boundary Element Method (BEM) (see Chapter 2) and a semi-empirical method i.e De Jong model (see Chapter 7). For the purposes of HOSANNA many different configurations and geometries have been used for insertion loss calculations. Predictions have been carried out for 2-lane urban road, 4-lane urban road and 2x2 lane motorways with and without central reservation treatments. The receiver was placed at several locations i.e. at distances of 5 m, 10 m, 22 m, 49 m and 100 m from the urban road and at distances of 25 m, 50 m, 110 m, 245 m and 500 m from the motorway. The receiver height was assumed to be either 1.5 m or 4.0 m. However, in this section, predictions are presented and discussed only for the 2-lane urban road and the receiver at a distance of 50 m from the road. Predictions of the insertion losses due to various ground treatments for a 4-lane motorway, a railway and a tramway are presented later in the chapter. Results of all calculations are available through the HOSANNA website. The ground treatments considered are,

- Replacing hard ground with soft ground.
- Introducing low height roughness.
- Single or multiple impedance discontinuity.
- Dense crops.

11.3.1 Replacing hard ground with soft ground

Most naturally-occurring outdoor surfaces are porous. As a result of being able to penetrate the porous surface, ground-reflected sound is subject to a change in phase as well as having some of its energy converted into heat [166]. As a result, if the ground is acoustically soft, the destructive interference occurs at relatively low frequencies and can be useful for traffic noise attenuation. According to HARMONOISE engineering methods [104], the traffic noise source spectrum has a peak at 1 kHz as shown in Figure 11.1. So, acoustically soft ground which has a broad ground effect centered at 1 kHz could give useful traffic noise attenuation. The sound attenuation due to different soft ground types are explored here.

11.3.1.1 Influence of ground type on ground effect

Short range ground characterization along with an appropriate impedance model and geometry information enables prediction of sound propagation over a ground surface (see Chapter 4). An extensive amount of ground characterization for different types of ground surfaces has been carried out and reported in Chapter 4. The impedance parameters obtained for different ground types with acoustical properties modeled by slit pore or slit pore layer impedance are used to predict the excess attenuation spectra for various traffic sources and receiver locations. The source spectrum for 2-lane urban road is given by HARMONOISE [104]. The insertion loss for a given ground surface is calculated by using source spectrum along with predicted excess attenuation.
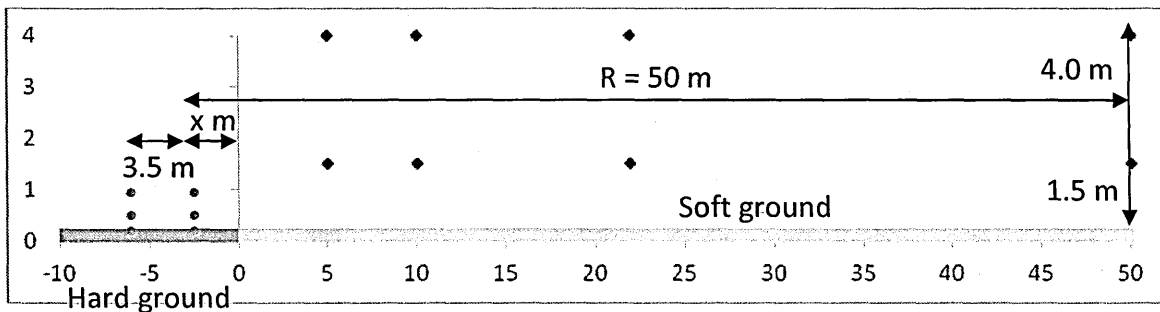
Figure 11.5 A schematic of the standard HOSANNA two lane urban road.

The source-receiver-ground geometry considered is shown in Figure 11.5. This involves a single hard-soft impedance discontinuity and receivers at a horizontal distance of 50 m from the nearest traffic. Three values of the distance x between the nearside traffic and the start of the soft ground or other ground treatment have been considered; 0, 2.5 m and 5 m.

The insertion loss calculation has been carried out for all 44 Nordtest ACOU NT 104 [69], [70] sites, ANSI. S1. 18 - 2010 [71] sites and for surfaces composed of the granular materials measured in laboratory (see Chapter 4). Nine examples of grass-covered ground surfaces have been selected here. The best fit parameters for these nine surfaces resulting from use of the slit pore impedance model are listed in Table 11.2. The excess attenuation for these sites for a given geometry is predicted using slit pore model either with the De Jong single discontinuity method (see Chapter 7) or a 2D Boundary Element Method (BEM) (see Chapter 2). Although the BEM gives more accurate predictions, the De Jong [108] method gives similar output with overall discrepancies of only 0.5 dB in insertion loss. The De Jong [108] single discontinuity method is relatively efficient in terms of computational demands. The De Jong [108] single discontinuity method has been used for the results given in Tables 11.3 and 11.4

Table 11.2 Parameter values for the nine ground types used to calculate the results listed in Table 11.3 – 11.5.

Surface description	porosity	Flow resistivity kPa s m^{-2}	Layer depth m
# 22 pasture	0.50	1344.0	∞
# 24 arable	0.50	2251.0	∞
# 28 sports field	0.22	664.0	∞
# 16 Lawn	0.50	176.0	∞
# 18 Arable	0.70	397.0	∞
# 41 long grass	0.36	104.0	∞
# 7 arable	0.56	85.0	0.034
# 9 urban	0.52	59.0	0.050
# 27 long grass	0.65	51.0	0.046

Tables 11.3 and 11.4 show the predicted effects of these types of ground on the noise levels at a distance of 50 m from the closest point of approach on a two lane urban road (95% type 1 cars and 5% HGV) travelling at a mean speed of 50 km/h for three values of the distance x m from the road edge to the start of the soft ground (see Figure 11.5). According to these calculations the introduction of a 45 m wide area of any soft ground to replace hard ground will decrease levels by at least 5 dB at a 1.5 m high receiver and by between 1 dB and 3.5 dB at a 4 m high receiver. The difference between the types of soft ground illustrated in Table 11.2 is predicted to result in up to 3 dB difference in the sound levels at a 1.5 m high receiver 50 m from the road as long as the soft ground extends from 2.5 m from the road edge to the receiver. The noise reductions predicted for the soft ground types are more similar if the width of hard ground before the start of the soft ground is increased to 5 m and if the receiver height is increased to 4 m.

Table 11.3 Calculated reductions of noise from a two lane urban road for the source and receiver locations shown in Figure 11.5 after replacing hard ground by the three ground types: Pasture land, Arable land and Sports field.

Surface description	x m	Reduction (dB) compared with smooth hard ground					
		$H_r = 1.5$ m			$H_r = 4$ m		
		Lane 1	Lane 2	**Combined**	Lane 1	Lane 2	**combined**
#22 pasture	0	6.4	6.6	**6.5**	3.7	3.0	**3.3**
	2.5	6.4	6.3	**6.3**	3.0	2.2	**2.6**
	5	6.1	5.9	**6.0**	2.2	1.5	**1.9**
#24 arable	0	5.5	5.7	**5.6**	5.5	5.7	**2.9**
	2.5	1.5	5.5	**5.5**	5.5	5.5	**1.7**
	5	1.5	5.3	**5.3**	2.0	1.4	**1.3**
#28 sports field	0	6.2	6.2	**6.2**	3.6	2.8	**3.2**
	2.5	6.1	5.9	**6.0**	2.8	2.1	**2.4**
	5	5.8	5.6	**5.7**	2.1	1.4	**1.7**

Table 11.4 Calculated noise reductions from a two-lane urban road for the source and receiver locations shown in Figure 11.5 after replacing hard ground by the three ground types: Lawn, Arable and Long grass.

Surface description	x m	Reduction (dB) compared with smooth hard ground					
		$H_r = 1.5$ m			$H_r = 4$ m		
		Lane 1	Lane 2	**combined**	Lane 1	Lane 2	**Combined**
#16 Lawn	0	9.4	9.1	**9.3**	5.5	3.9	**4.6**
	2.5	9.0	8.4	**8.7**	4.1	2.6	**3.3**
	5	8.3	7.6	**7.9**	2.8	1.6	**2.1**

#18 Arable	0	9.0	8.8	**8.9**	5.2	3.8	**4.4**
	2.5	8.7	8.2	**8.4**	4.0	2.7	**3.3**
	5	8.1	7.5	**7.8**	2.8	1.7	**2.2**
#41 long grass	0	9.5	9.0	**9.3**	5.6	3.8	**4.6**
	2.5	8.9	8.3	**8.6**	4.0	2.5	**3.2**
	5	8.2	7.4	**7.8**	2.6	1.5	**2.0**

An important difference between these types of grassland is revealed by the (fitted) flow resistivity values listed in Table 11.2. Higher traffic noise reductions are predicted if the ground has relatively low flow resistivity such as Pasture (# 22), Arable (# 24) and Sports field (# 28). Flow resistivity increases with compaction. Ground surfaces that have been compacted, for example by frequent mowing, rolling, or heavy wheeling are likely to have higher flow resistivity. This seems to be the case for the grassland types such as Lawn (# 16), Arable (# 18) and Long grass (# 41). Figure 11.6 compares the SPL spectra due to a 2-lane urban road at a 1.5 m high receiver 50 m from the road (see Figure 11.5) predicted for hard ground, an example low flow resistivity ground and an example high flow resistivity ground. The lower resistivity ground provides extra reduction in levels up to 2 kHz.
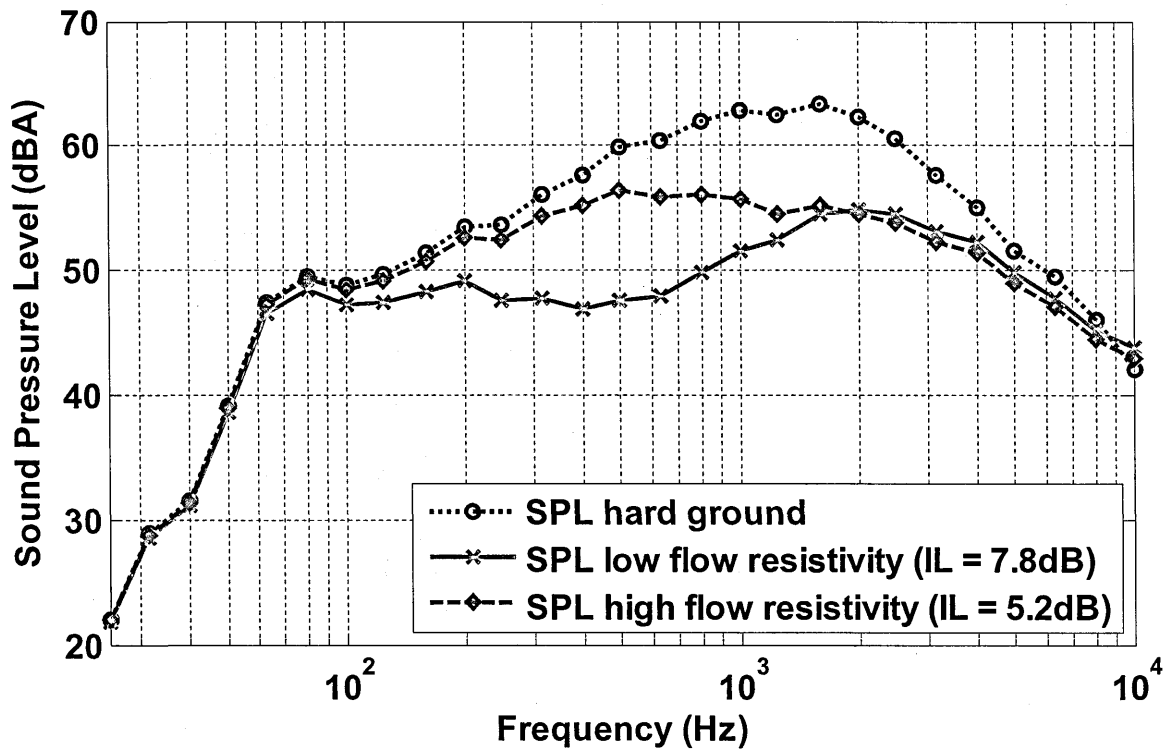
Figure 11.6 Comparison between predicted Aweighted sound pressure levels over a hard ground – black dotted-circle line, low flow resistivity Nordtest long grass site # 41 (R_s = 104.0 kPasm^{-2}, Ω = 0.36) – red continuous-cross line and high flow resistivity Nordtest sports field site # 28 (R_s = 664.0 kPasm^{-2}, Ω = 0.22) – blue broken-diamond line, the soft ground starts at a distance of 2.5 m from nearest lane; for two lane urban road at 1.5 m high receiver and at 50 m distance from the nearest lane.

The predicted reductions in Table 11.5 indicate that, even if the ground has a low flow resistivity, the presence of an acoustically-hard layer at a shallow depth, as implied by the short range data fitting for the ground types, will result in a slightly lower overall noise reduction than will non-layered grounds with comparably low flow resistivity.

The insertion loss due to soft ground compared with hard ground is between 2 and 3 dB if the width of hard ground before the start of the soft ground is increased to 5 m and if the receiver height is increased to 4 m. However the difference between the noise reducing effects of the considered range of soft ground types at a 4 m high receiver is predicted to be less than 1 dB.

These calculations have been carried out in context of HOSANNA project guidelines in which only two receiver heights i.e. 1.5 m and 4.0 m have been considered. Table 11.3 – 11.5 show that the insertion loss due to porous ground surfaces is less for higher receiver height of 4.0 m This is a consequence of the fact that the ground treatments are more effective at near grazing angles and are less effective for higher receivers. The insertion loss will decrease as the receiver height is increased. However, here the insertion is given only for a single receiver location, at a distance of 50 m from the nearest lane source. Insertion loss calculations for receivers at longer ranges show that the attenuation performance of porous ground improves as the distance between the source and receiver increases since this decreases the grazing angle. This implies that the porous ground is less effective for noise attenuation at shorter ranges and higher receiver heights and more effective at longer ranges and lower receiver heights. Also the HOSANNA study constrained the nearest location of ground treatments to 2.5 m from the source. The effectiveness for higher receiver heights can be improved if the treatment is moved closer to the source.

Table 11.5 Noise reductions from a two lane urban road calculated for the configuration shown in Figure 11.5 after replacing hard ground by the three ground types using the hard-backed layer parameter values.

Surface description	x m	Reduction (dB) compared with smooth hard ground					
		$H_r = 1.5$ m			$H_r = 4$ m		
		Lane 1	Lane 2	Combined	Lane 1	Lane 2	Combined
#7 arable	0	8.2	8.0	**8.1**	5.2	3.7	**4.4**
	2.5	7.9	7.5	**7.7**	3.9	2.5	**3.1**
	5	7.4	6.8	**7.1**	2.6	1.4	**2.0**
#9 urban	0	8.6	8.4	**8.5**	5.4	3.7	**4.4**
	2.5	8.3	7.7	**8.0**	3.9	2.4	**3.1**
	5	7.7	7.0	**7.3**	2.6	1.3	**1.9**
#27 long grass	0	8.6	8.4	**8.5**	5.2	3.7	**4.4**
	2.5	8.3	7.7	**8.0**	3.9	2.4	**3.1**
	5	7.7	7.0	**7.3**	2.5	1.3	**1.9**

11.3.1.2   Effects of cultivation

The potential effects of cultivation on noise from standard HOSANNA 2-lane urban road have been investigated by using published data [156], [170] for ground effect before and after disking or ploughing. Figure 11.7 shows the measured and predicted ground effect before and after disking. The fitted impedance model parameters have been used to predict the insertion loss compared with hard ground for a 45 m wide soft ground area assuming the configuration shown in Figure 11.5. Table 11.6 lists the results.

On the basis of these calculations it seems that ploughing and disking ground up to 45 m from an urban road will achieve relatively little in terms of traffic noise reduction. However, in both cases, the published data are for soils that have relatively low flow resistivity before they were disked or ploughed so that the further reductions in 'effective' flow resistivity caused by disking or ploughing are not significant.
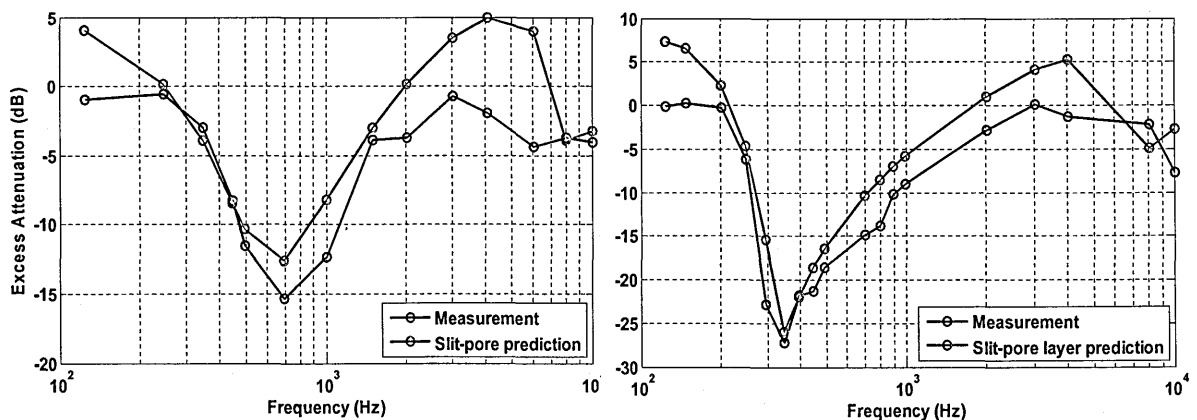
Figure 11.7 Comparisons between measured excess attenuation data for source height = 1.0m, Receiver height = 1.0m, Separation = 52.0m (Figure 3 of [156]) and predictions using a slit pore impedance model: Left –weather-slaked fine sandy loam before disking (Flow resistivity = 270 k Pa s m^{-2}, Porosity = 0.6); Right – after disking (Flow resistivity = 100 kPa sm^{-2}, Porosity = 0.7, layer depth = 0.035m).

Table 11.6 Noise reductions from a two lane urban road calculated for the configuration shown in Figure 11.5 after replacing hard ground by various ground types based on the listed parameter values.

Fitted data	Surface descript-ion	Poro-sity	Flow resist-ivity kPa s m⁻²	Layer depth (m)	x m	Hr m	IL-Lane 1 (dB)	IL-Lane 2 (dB)	IL combined (dB)
Data from Aylor [156]	weather-slaked fine sandy loam	0.60	270	∞	0.0	1.5	9.2	9.0	9.1
						4.0	5.3	3.9	4.5
					2.5	1.5	8.9	8.3	8.6
						4.0	4.1	2.7	3.3
					5.0	1.5	8.2	7.5	7.9
						4.0	2.8	1.7	2.2
Data from Aylor [156]	Sandy loam after disking	0.70	100	0.035	0.0	1.5	8.7	8.5	8.6
						4.0	5.3	3.8	4.5
					2.5	1.5	8.4	7.9	8.1
						4.0	4.0	2.5	3.2
					5.0	1.5	7.8	7.2	7.5
						4.0	2.7	1.4	2.0
Data from Chambers and Sabatier [170]	Undist-urbed soil surface	0.46	159	∞	0.0	1.5	9.4	9.1	9.2
						4.0	5.5	3.8	4.6
					2.5	1.5	8.9	8.3	8.6
						4.0	4.0	2.6	3.3
					5.0	1.5	8.2	7.5	7.9
						4.0	2.7	1.6	2.1
Data from Chambers and Sabatier [170]	Ploughed surface	0.60	5	∞	0.0	1.5	10.2	9.4	9.8
						4.0	5.7	3.5	4.5
					2.5	1.5	9.3	8.4	8.8
						4.0	3.8	2.2	2.9
					5.0	1.5	8.4	7.5	7.9
						4.0	2.3	1.1	1.7

11.3.1.3 Cultivating crops over soft ground

Sound propagation through crops has been studied in Chapter 10. The measured data over crops has been fitted using an empirical attenuation formula (See Chapter 10, Eq. 10.1) based on Aylor's data [156], [157] including data for dense large leaf corn crops. Also analysis of data for sound transmission loss through smaller leaf winter wheat crops makes it possible to predict the extra attenuation (i.e. in addition to that due to soft ground effect) due to winter wheat foliage using the formula.

The reductions in noise in dB m^{-1} calculated for four combinations of two types of 1 m high crops with two types of soft ground assuming the configuration depicted in Figure 11.8 with x = 5 m are listed in Table 11.7. The dense corn crop is characterized by a leaf area per unit volume of 6.3 m^{-1} and a mean leaf size of 0.0784 m. For winter wheat the corresponding values are 30 m^{-1} and 0.012 m i.e. the winter wheat is assumed to have a higher foliage area per unit volume but much smaller leaves than corn.

The overall attenuation is calculated as the sum of that due to ground effect and the attenuation along those parts of the direct paths from the vehicle sources to the receivers that pass through the crop (see Figure 11.8). The combination of high flow resistivity ground and small leaf crop is predicted to have little acoustical merit. On the other hand combinations of low flow resistivity ground and dense large leaf crops are predicted to give a *total attenuation of between 9 and 13 dB* at the 1.5 m high receiver of which *between 1 and 5 dB is contributed by the crops*. The corresponding predicted total attenuations at the 4 m high receiver are between 2.5 and 7 dB of which between 0.3 and 4.5 dB are contributed by crops.

The 1 m high corn crop is predicted to offer nearly 3 dB additional attenuation at the 4 m high receiver.
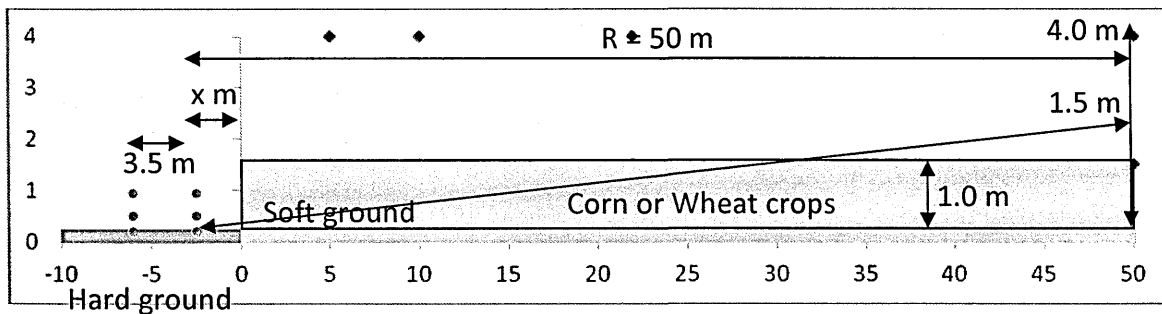
Figure 11.8 A schematic of the standard HOSANNA two lane urban road with 1.0 m high crops.

Table 11.7 Attenuation (dB) of noise from a 2-lane urban road predicted for four combinations of soft ground and 1 m high crops assuming the configuration shown in Figure 11.5.

Ground	Crop	Reduction (dB) compared with smooth hard ground			
		1.5 m high receiver		4 m high receiver	
		Ground alone	Ground + crop	Ground alone	Ground + crop
#18 arable	Dense corn	7.8	13.1	2.2	6.7
	Winter wheat		8.6		2.5
#24 arable	Dense corn	5.3	9.0	1.7	5.4
	Winter wheat		5.6		1.9

The attenuation due to crops depends on the propagation path through crops. As the height of the receiver increases, the propagation path through crops decreases as shown in Figure 11.8. It means that as the height of the receiver increases the attenuation effect due to crops decreases.

11.3.2 Traffic noise attenuation by roughness

The introduction of relatively small objects, i.e. 0.3 m or less in height (0.3 m is approximately the wavelength of sound in air at 1 kHz), on a hard smooth surface causes a change in the reflection of sound and thereby a reduction in the frequencies at which there is destructive interference. The acoustical effects of an array of roughness elements depend on their mean height, mean spacing, cross-sectional shape and whether the array configuration is random or periodic. If the roughness elements are distributed randomly the ground effect spectrum shows a single destructive interference resulting in excess attenuation over a broad range of frequencies. If the spacing is regular then there can be additional destructive interferences but these reduce narrower ranges of frequencies than does random roughness of the same height and mean spacing.

A series of indoor and outdoor measurements have been carried over artificially created rough surface. Ground roughness effects have been investigated theoretically and numerically. The predictions techniques such as Multiple Scattering theory (only valid semi-cylindrical roughness), Boundary Element Method, Finite Element Method (COMSOL) and using effective impedance models have been found to give good agreement with measured data (see Chapter 5 and 6). These methods have been used to predict the excess attenuation spectra over rough surfaces for a given traffic noise source and receiver geometry. In this section, the calculated insertion losses due to various rough surfaces near to a HOSANNA 2-lane urban road are presented. The maximum roughness height was restricted to 0.3 m in accordance with an agreed HOSANNA guideline [167], [169], [168].

11.3.2.1   Roughness effect Vs Receiver height

It is concluded earlier that the ground treatments are more effective at near grazing angle, i.e. at lower receiver heights. Table 11.8 – 11.12 summarizes the calculated insertion loss due to either parallel walls or lattice structure at two receiver heights i.e. 1.5 m and 4.0 m. The insertion loss for a receiver placed at a height of 1.5 m is always greater than the receiver at a height of 4.0 m. This implies that the insertion loss will reduced further with the increase in receiver height. The insertion loss due to rough surfaces depends on the angle of incidence between the source and the receiver and specular reflection point. Tables 11.8 and 11.11 show that, for a receiver placed at height of 1.5 m and at a distance of 50 m from nearest lane source; the attenuation due to rough ground increases with the increase in the width of the array. However, for a receiver placed at height of 4.0 m and at a distance of 50 m from the nearest lane source, the insertion loss doesn't increase with the increase in the width of the array (see Table 11.8 & 11.11). Moreover, for a receiver placed at a height of 4.0 m and at a distance of 100 m from the nearest lane source the insertion loss increases with the increase in the lattice width (see Table 11.12). The effect of rough dependent on the angle of incidence, the lower the angle is, the more the rough surfaces will be effective.

11.3.2.2   Parallel walls

The insertion losses due to periodically spaced parallel walls placed on a hard ground near a 2-lane urban road (example configuration shown in Figure 11.9) have been calculated and are listed in Table 11.8.
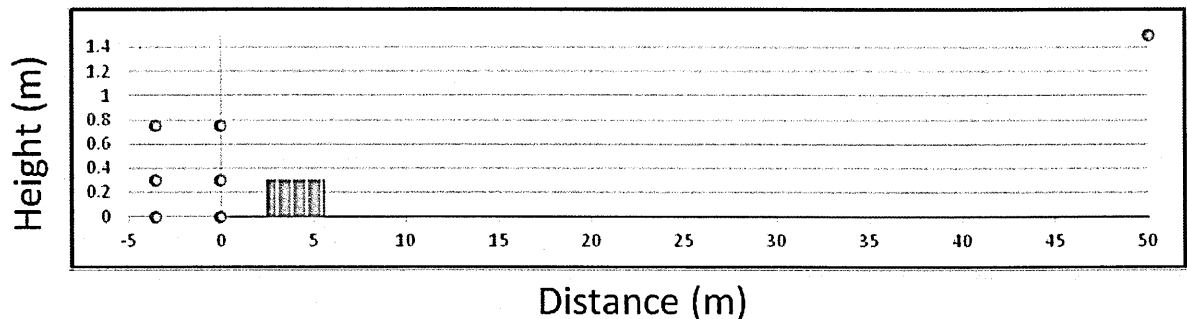
Figure 11.9 Schematic of a two lane road and an example 3 m wide parallel low wall configuration starting 2.5 m from nearest traffic lane. A 1.5 m high receiver is 50 m from road.

The reduction is caused by the modification of the ground effect due to the presence of the roughness array. Calculations have been carried out to investigate the effect on insertion loss values due to parallel walls by altering its configurations such as width of wall array, its height and receiver location. The insertion loss due to a parallel wall array increases with the increase in width of the array. The predicted insertion loss due to a 0.3 m high and 1.65 m wide wall array is 5.8 dB for a receiver placed at a height of 1.5 m and at a distance of 50 m from the nearest lane source. The insertion loss is increased by 3 dB if the width of the array is increased up to 12.05 m. The predicted effects due to the parallel wall array are reduced if the receiver is closer to the road or higher. The predicted insertion loss due to a 0.3 m high and 3.05 m wide wall array is 6.6 dB for a receiver placed at a height of 1.5 m and at a distance of 50 m from the nearest lane source. The predicted insertion loss is reduced to 3.6 dB, when the receiver is only 10 m from the source. Similarly, the predicted insertion loss at a height of 4.0

m and at a distance of 50 m from the source is 5.6 dB, and is reduced to -0.3 dB when the receiver is placed at a distance of 10 m. In other words the wall array has no effect for a receiver at height of 4.0 m and at a distance of 10.0 m. It is concluded that the parallel wall array is more effective for near grazing angles.

Another important factor that affects insertion loss is the height of the roughness. The predicted insertion is reduced by between 1.0 and 1.5 dB, when the parallel wall array height is reduced from 0.3 m to 0.2 m. The centre-to-centre spacing and wall width was fixed at 0.2 m and 0.05 m respectively. As long as the centre-to-centre spacing and wall width are between 0.1 m – 0.5 m and 0.05 m – 0.15 m respectively, there is not much change in overall insertion loss value as described and concluded in Chapter 5.
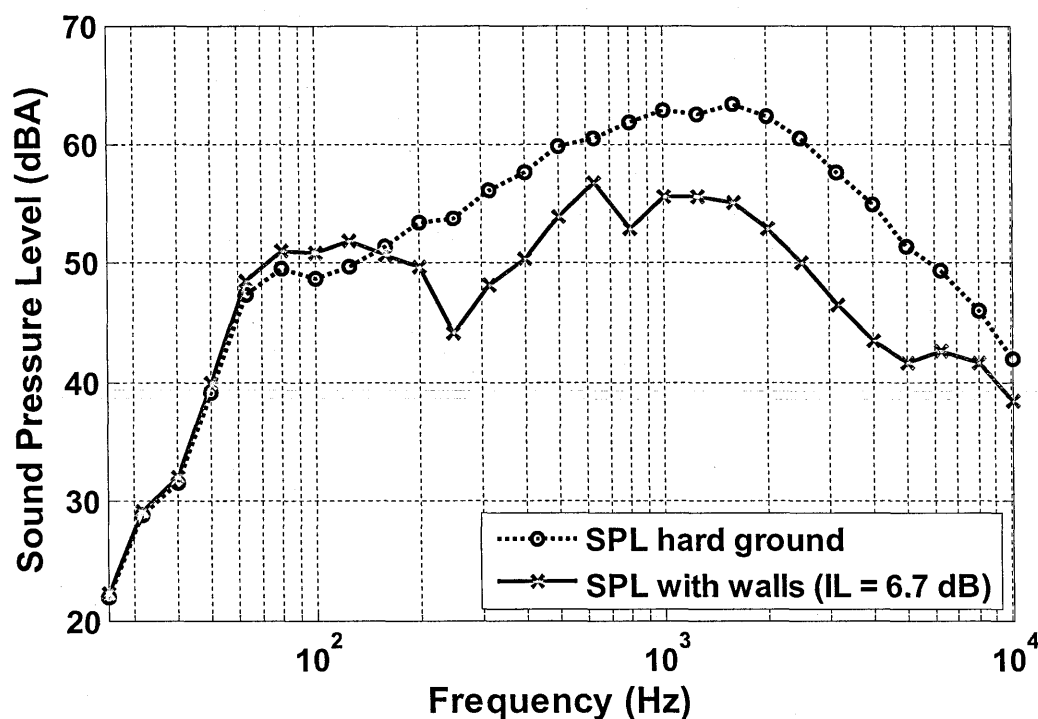
Figure 11.10 Sound level spectra due to a two lane urban road (95% cars, 5% lorries travelling at 50 km/h) predicted at a 1.5 m high receiver at a distance of 50 m along the centre line of the array, without and with a low parallel wall array consisting of 16 identical 0.05 m thick acoustically-hard walls with centre-to-centre spacing of 0.2 m (total width 3.05 m). The arrays are assumed to start 2.5 m from the nearest traffic lane (see Figure 11.9).

Figure 11.10 compares the Sound level spectra due to a two lane urban road (95% cars, 5% lorries travelling at 50 km/h) predicted at a 1.5 m high receiver at a distance of 50 m along the centre line of the array, without and with a 0.3 m high and 3.05 wide parallel wall array. The wall array attenuates sound over all frequencies except at lower frequencies (50 Hz – 150 Hz), where the SPL over parallel walls is higher than hard ground. This is due to surface wave generation by the wall array (see Chapter 8).

Table 11.8 Insertion losses predicted for parallel wall configurations (see Figure 11.9) with two receiver heights of 1.5 m and 4.0 m and at two distances from the road having different wall array width and height.

Profile	Range 'R' (m)	Receiver height (dB)	Insertion loss (dB)		
			Lane-1	Lane-2	IL Combined
Parallel walls					
1.65 m wide and **0.3** m high parallel wall array; 9 × 0.05 m thick walls, 0.2 m centre-to-centre spacing	50	1.5	6.0	5.5	5.8
		4.0	6.0	4.7	5.4
3.05 m wide and **0.3** m high parallel wall array; 16 × 0.05 m thick walls, 0.2 m centre-to-centre spacing	50	1.5	6.9	6.4	6.6
		4.0	6.3	5.0	5.6
5.85 m wide and **0.3** m high parallel wall array; 30 × 0.05 m thick walls, 0.2 m centre-to-centre spacing	50	1.5	7.8	7.5	7.6
		4.0	6.2	4.9	5.6
12.05 m wide and **0.3** m high parallel wall array; 61 × 0.05 m thick walls, 0.2 m centre-to-centre spacing	50	1.5	8.5	8.7	8.6
		4.0	5.7	4.5	5.1
3.05 m wide and **0.2** m high parallel wall array; 16 × 0.05 m thick walls, 0.2 m centre-to-centre spacing	50	1.5	5.6	5.2	5.4
		4.0	4.9	3.7	4.3
3.05 m wide and **0.3** m high parallel wall array; 16 × 0.05 m thick walls, 0.2 m centre-to-centre spacing	10	1.5	4.4	2.8	3.6
		4.0	-0.1	-0.5	-0.3

11.3.2.3　Azimuthal angle dependence of parallel wall insertion loss

The insertion loss due to parallel walls is azimuthal angle dependent. The maximum attenuation obtained through parallel walls is when the source –receiver axis is perpendicular to the parallel wall array axis. The azimuthal angle dependence of parallel wall insertion loss has been tested in the laboratory (see Chapter 5). However, since this is a 3D problem and the available Boundary Element code is only capable of predicting sound propagation in two dimensions, calculations of sound propagation over a given parallel walls configurations at different azimuthal angles between the array and the source have been made using a 3D Pseudo-Spectral Time Domain (PSTD) code [171], [114], [172]. A vertical cross section of the parallel wall roughness configuration used in the PSTD calculation is shown in Figure 11.11.
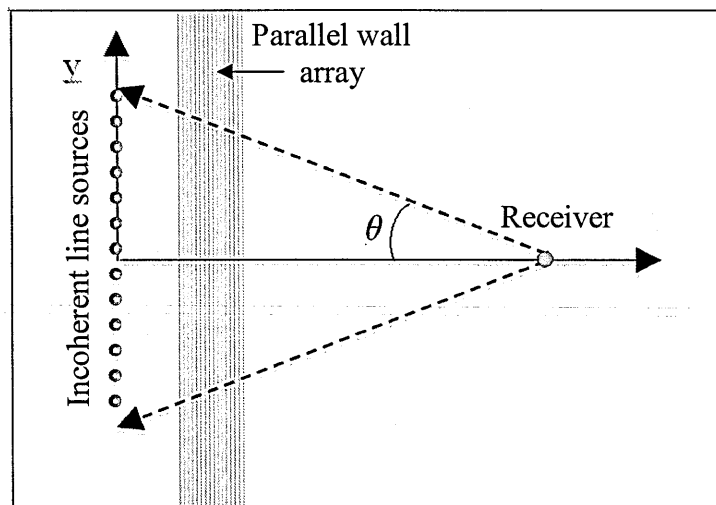
Figure 11.11 Plan view of a finite incoherent line source (FILS) and the receiver location in the presence of an infinitely long low parallel wall array.

Using the PSTD numerical method, the acoustical performance of the configuration has been computed in the presence of incoherent line sources, at each of three source heights 0.01 m, 0.30 m and 0.75 m. The receiver was placed

at two heights of 1.5 m and 4.0 m. The separation between the source and receiver was assumed to be 50 m. The parallel wall array was 6.05 m high and 0.3 high; 16 x 0.05 m thick walls with centre-to-centre spacing of 0.4 m. Figure 11.12 compares the predicted excess attenuation spectra over parallel walls with a 0.01 m high source and receiver is at a height of 1.5 m and at 50 m distance. The angle between the source - receiver axis and the normal to the parallel wall array is varied between 0° and 70° (see Figure 11.11).
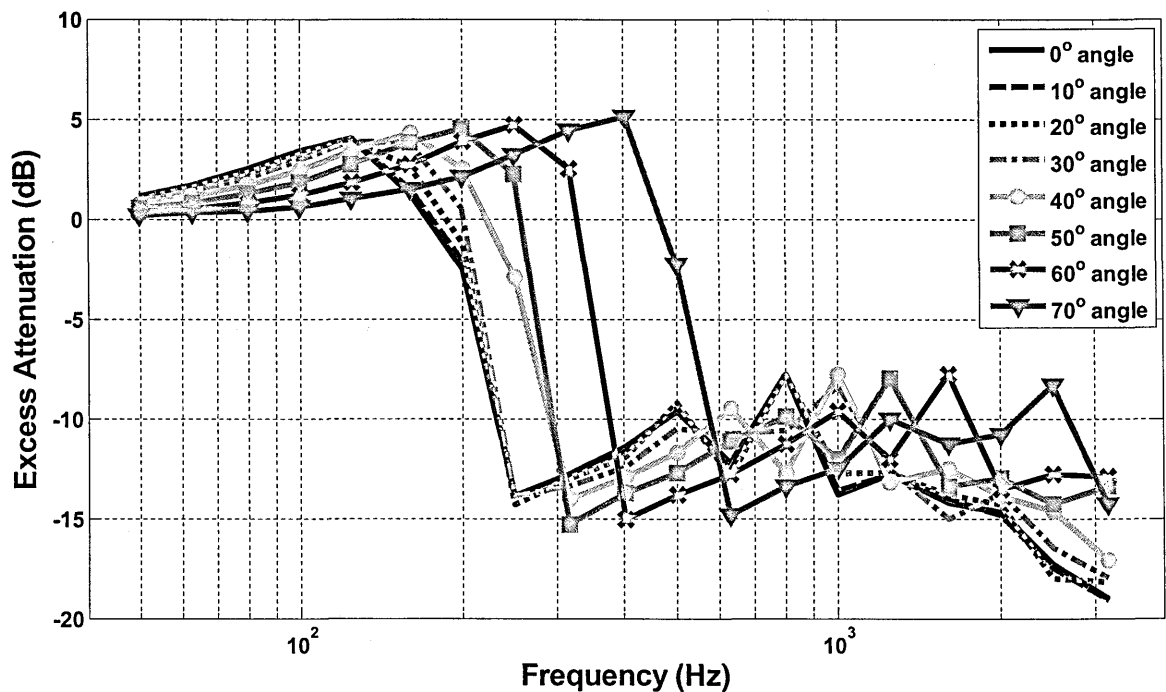
Figure 11.12 Comparison of predicted excess attenuation spectra using PSTD [171], [114], [172] over sixteen 0.05 m thick, 0.3 m high parallel walls with centre-to-centre spacing of 0.4 m with the first wall at a distance of 2.0 m from a 0.01 m high source and receiver is at a height of 1.5 m and at 50 m distance. The angle between source and receiver to parallel walls normal axis is varied from 0° to 70° (see Figure 11.11 for θ).

These predictions show that, up to 30° the insertion loss due to parallel walls is not dependent on angle. A similar conclusion has been drawn from laboratory data (see Chapter 5). However, for angles greater than 30° the excess

attenuation spectrum is shifted to higher frequencies. For every ten degrees increase in angle, the excess attenuation is shifted approximately by one third octave frequency. A formula has been deduced to predict the shift in excess attenuation spectrum for a given angle.

$$f_{out} = 10^{\wedge}[\log 10(f_{input}) + 0.010033(\alpha - 30)],$$ (11.1)

where α is the angle in degrees and f_{out} gives the shifted output frequencies for given input frequencies f_{input}. This can be exploited to enable calculations of the azimuthal angle dependence for other source, receiver and array configurations using the 2D BEM.

Figure 11.13 compares the predicted excess attenuation spectra over parallel walls using either PSTD or BEM modified by Equation (11.1) at different angles between the source receiver axis and the normal to the parallel wall array. The 2D BEM predicted spectra were shifted using Eq. 11.1 to obtain the spectra at various angles. The source was assumed at height of 0.01 m and receiver at height of 1.5 m and at a distance of 50 m from the source. The agreement between the predicted excess attenuation spectra is very good. Similar agreement has been found between the two prediction methods for other traffic noise source and receiver heights i.e. engine noise source at 0.3 m and 0.75 m height and receiver at a height of 4.0 m.
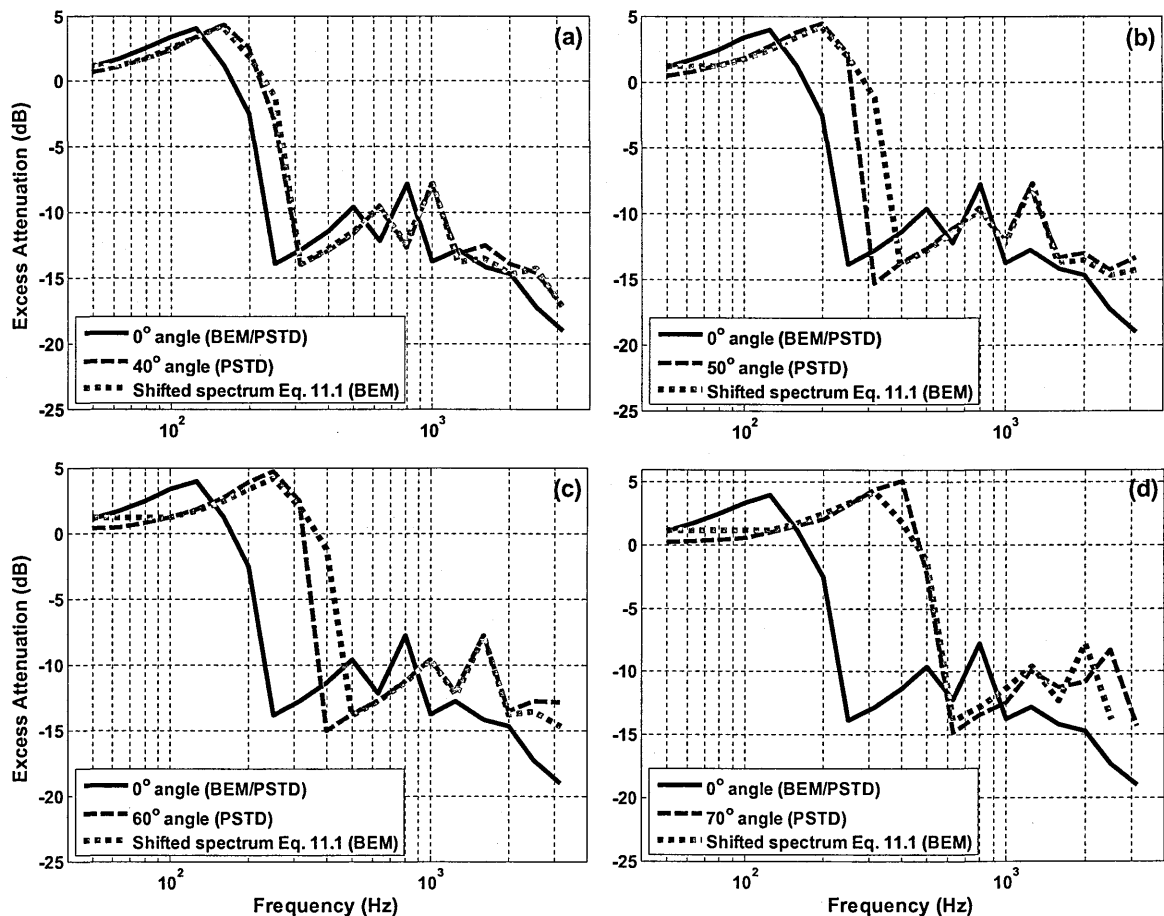
Figure 11.13 Comparison between excess attenuation spectra at a 1.5 m receiver 50 m from 0.01 m high source due to sixteen, 0.05 m thick, 0.3 m high parallel walls predicted using PSTD [171], [114], [172] and by BEM modified by Eq. 11.1 to obtain shifted spectra at several angles (a) α = 40° (b) α = 50° (c) α = 60° (d) α = 70°.

The assumed source and receiver positions and parallel wall array location near a two lane urban road are shown in Figure 11.14. The insertion loss due to the parallel wall array was predicted at multiple receiver locations and two heights i.e. 1.5 m and 4.0 m. The two lane urban road is represented by line of incoherent point sources along the x-axis. As the source is moved along x -axis, there is an increase in the azimuthal angle between source and receiver. The effect of parallel walls deteriorates with the increase in angle. This effect is predicted using BEM and Eq. 11.1. The insertion losses due parallel walls with source and receiver at several locations are summarized in Table 11.9. The maximum value of θ

corresponds to the source at 100 m distance along x-axis from central axis line and receiver at a distance of 22.0 m from the nearest lane. For the maximum value of θ, the insertion loss predicted due to a 0.3 m high and 3.05 m wide wall array is reduced from 6.8 dB to 3.5 dB. Similarly for 5.85 m wide array, it is reduced from 7.1 dB to 3.7 dB.
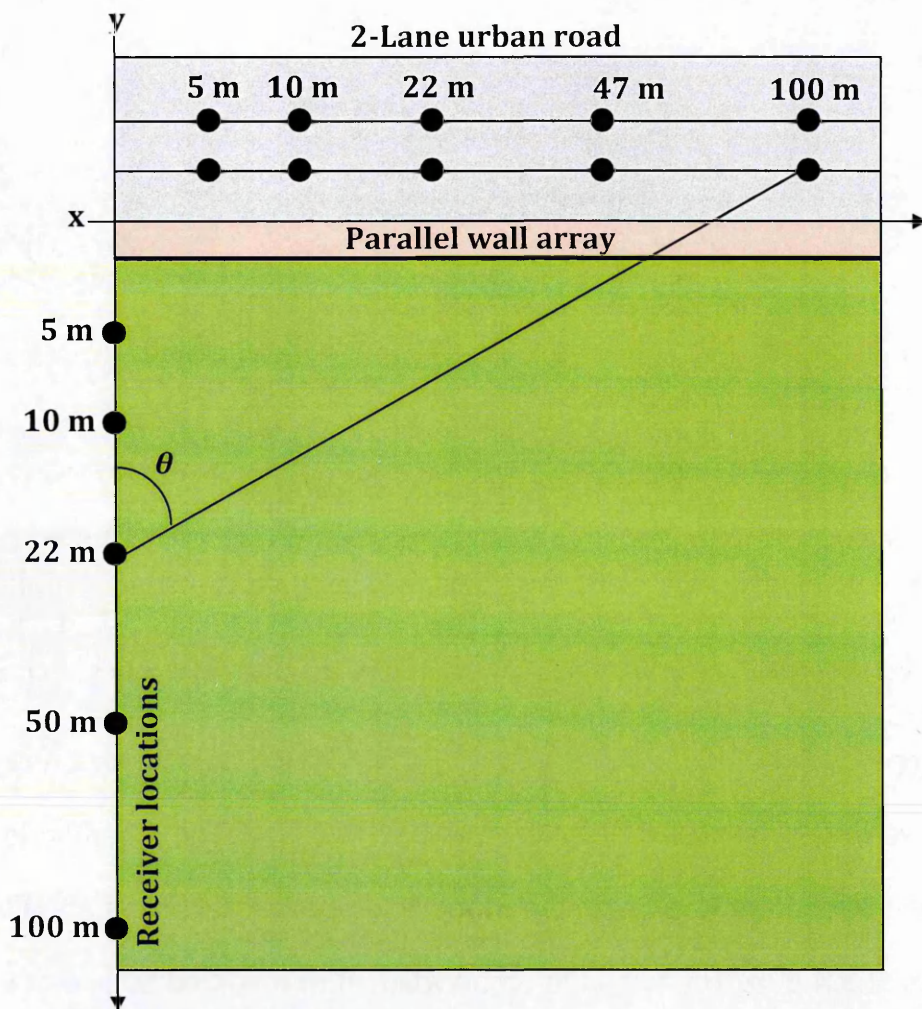
Figure 11.14 Top view for source-receiver and abatement configurations.

Table 11.9 Insertion losses predicted for parallel wall configurations (see Figure 11.14) using BEM and the angle dependence given by Eq. 11.1.

Detailed configuration	Range 'R' (m) Receiver position along Y	Receiver height 'Hr' (m)	Combined Insertion loss for two lane urban road (dB)					
		Source position along X	0 m	5 m	10 m	22 m	49 m	100 m
3.05 m wide and 0.3 m high parallel wall array; 16 × 0.05 m thick walls, 0.2 m centre-to-centre spacing	22.0	1.5	6.8	6.8	6.8	6.1	4.8	3.5
		4.0	1.8	1.8	1.8	2.1	2.6	2.3
		Angle	0.0°	11.5°	22.2°	41.9°	63.4°	76.2°
	47.0	1.5	6.6	6.6	6.6	6.6	5.7	4.5
		4.0	5.6	5.6	5.6	5.6	5.3	4.2
		Angle	0.0°	5.8°	11.4°	24.0°	43.5°	63.7°
	100.0	1.5	6.1	6.1	6.1	6.1	6.1	5.3
		4.0	6.5	6.5	6.5	6.5	6.5	5.4
		Angle	0.0°	2.8°	5.6°	12.1°	25.6°	44.3°
5.85 m wide and 0.3 m high parallel wall array; 30 × 0.05 m thick walls, 0.2 m centre-to-centre spacing	22.0	1.5	7.1	7.1	7.1	6.5	5.2	3.7
		4.0	1.6	1.6	1.6	1.9	2.1	1.9
		Angle	0.0°	11.5°	22.2°	41.9°	63.4°	76.2°
	47.0	1.5	7.6	7.6	7.6	7.6	6.6	5.1
		4.0	5.6	5.6	5.6	5.6	5.4	4.5
		Angle	0.0°	5.8°	11.4°	24.0°	43.5°	63.7°
	100.0	1.5	7.1	7.1	7.1	7.1	7.1	6.1
		4.0	7.4	7.4	7.4	7.4	7.4	6.2
		Angle	0.0°	2.8°	5.6°	12.1°	25.6°	44.3°

11.3.2.4   Other cross-sectional shapes

A series of laboratory measurements and BEM simulations have been carried over different cross-sectional shapes roughness (semi-cylinder, triangular, square, tall and short rectangular strips). It was concluded from laboratory data that the triangular strips give the best attenuation performance (see Chapter 5). BEM predictions have led to similar conclusions. For a road-tyre source at height of 0.01 m and receiver at a distance of 50 m and at height of 1.5 m it was concluded in HOSANNA report 4.3 [101], that for a given roughness height the triangular strip gives best attenuation performance. However, this conclusion has been changed as a result of more recent BEM predictions for a 2-lane urban road. The insertion losses due to 0.3 high parallel walls and 0.3 m high triangular strips with two base-widths (0.05 m & 0.1 m) for 2-lane urban road are listed in Table 11.10. The insertion losses due to these three configurations are almost identical with a maximum difference of 0.1 dB. It is concluded that the roughness shape effect averages out and that the roughness height and array width are more important factors in determining broadband insertion loss.

Table 11.10 Insertion loss due to parallel walls and triangular strips for 2-lane road.

Profile Parallel walls Vs Triangular strips	Range 'R' (m)	Receive r height (dB)	Insertion loss (dB)		
			Lane-1	Lane-2	IL Combined
3.05 m wide and 0.3 m high **parallel wall array**; 16 × **0.05 m thick walls**, 0.2 m centre-to-centre spacing	50	1.5	6.9	6.4	6.6
		4.0	6.3	5.0	5.6
3.05 m wide and 0.3 m high **triangular strips** array; 16 × **0.05 wide base**, 0.2 m centre-to-centre spacing	50	1.5	6.8	6.4	6.6
		4.0	6.2	4.9	5.5
3.05 m wide and 0.3 m high **triangular array**; 16 × **0.1 m wide base**, 0.2 m centre-to-centre spacing	50	1.5	6.6	6.3	6.5
		4.0	6.1	4.9	5.5

11.3.2.5   Lattice configurations

The insertion losses due to square lattices placed on a hard ground for 2-lane urban road (example configuration shown in Figure 11.15) have been calculated and are listed in Table 11.11.
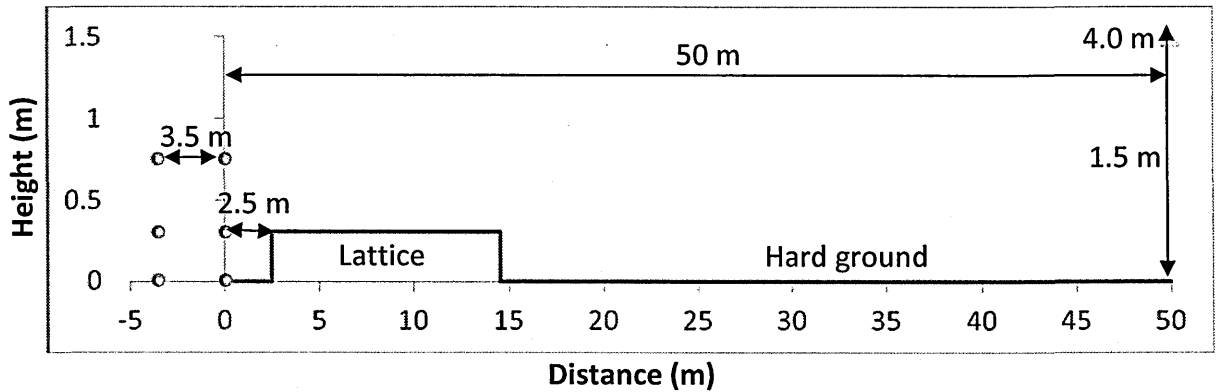
Figure 11.15 Schematic of a two lane road and an example 12.05 m wide lattice configuration starting 2.5 m from nearest traffic lane.
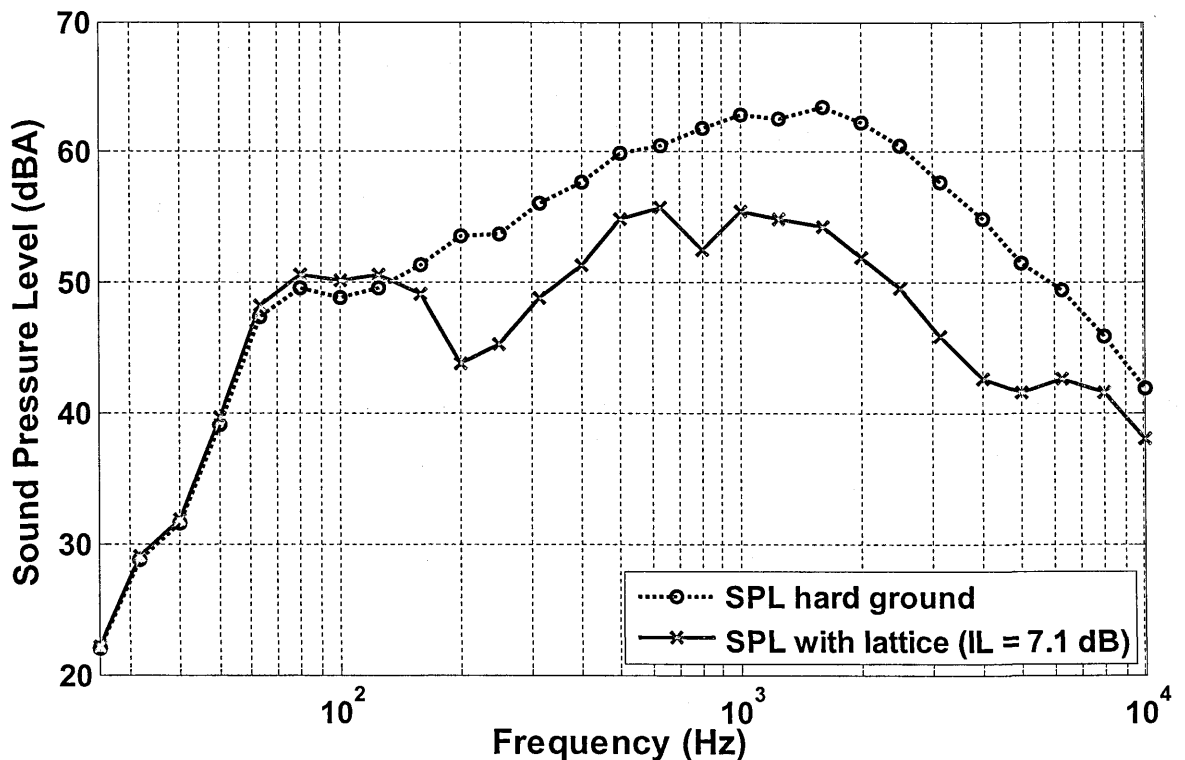
Figure 11.16 Sound level spectra due to a two lane urban road (95% cars, 5% lorries travelling at 50 km/h) predicted at a 1.5 m high receiver at a distance of 50 m along the centre line of the array, without and with a 0.3 m high and 3.05 wide lattice array. The arrays are assumed to start 2.5 m from the nearest traffic lane (see Figure 11.15).

Calculations have been carried out to investigate the effect on the insertion loss values due to a lattice structure near to a 2-lane urban road by altering its width and height and changing the receiver location. The details of the lattice design and the raised impedance prediction method are given in Chapters 5 and 6. A lattice is a 3D structure and its insertion loss is predicted to increase with increase in its width. The predicted insertion loss due to a 0.3 m high and 1.53 m wide lattice array is 5.9 dB for a receiver placed at a height of 1.5 m and at a distance of 50 m from the nearest lane source. The insertion loss due to lattice is predicted to be doubled by increasing the width of lattice array to 24.05 m. The predicted effects due to a lattice are reduced if the receiver is closer to the road or higher. The predicted insertion loss due to a 0.3 m high and 3.05 m wide wall array is 7.2 dB for a receiver placed at a height of 1.5 m and at a distance of 50 m from the nearest lane source. The insertion loss is predicted to reduce to 4.0 dB if the receiver is only 10 m from the source. Similarly, the insertion loss predicted at a height of 4.0 m and at a distance of 50 m from the source is 6.1 dB and is reduced to 0.2 dB when the receiver is only 10 m from the source. It is concluded that the lattice array is more effective at near grazing angles.

Figure 11.16 compares the Sound level spectra due to a two lane urban road (95% cars, 5% lorries travelling at 50 km/h) predicted at a 1.5 m high receiver at a distance of 50 m along the centre line of the array, without and with a 0.3 m high and 3.05 wide lattice array. The lattice array attenuates sound except at lower frequencies (50 Hz – 150 Hz), where the SPL over lattice is higher than over hard ground. This is due to the surface wave generation by the lattice array (see Chapter 8).

Table 11.11 Insertion losses predicted for Lattice configurations (see Figure 11.15) with two receiver heights of 1.5 m and 4.0 m and at two distances from the road having different lattice array width and height.

Profile	Range 'R' (m)	Receiver height (dB)	Insertion loss (dB)		
			Lane-1	Lane-2	IL Combined
Lattice configurations					
1.53 m wide and **0.3** m high square lattice	50	1.5	6.2	5.5	5.9
		4.0	6.4	4.9	5.6
3.05 m wide and **0.3** m high square lattice	50	1.5	7.6	6.7	7.2
		4.0	7.0	5.3	6.1
5.85 m wide and **0.3** m high square lattice	50	1.5	9.1	8.2	8.7
		4.0	7.2	5.4	6.3
12.05 m wide and **0.3** m high square lattice	50	1.5	10.9	10.2	10.5
		4.0	7.1	5.3	6.1
24.05 m wide and **0.3** m high square lattice	50	1.5	12.0	11.6	11.8
		4.0	6.8	5.0	5.9
3.05 m wide and **0.2** m high square lattice	50	1.5	5.9	5.4	5.7
		4.0	5.5	4.2	4.8
3.05 m wide and **0.3** m high square lattice	10	1.5	4.1	3.8	4.0
		4.0	0.3	0.1	0.2

11.3.2.6   Comparison between parallel walls and lattices

Unlike parallel wall arrays, lattice structures are 3D structures and their predicted insertion loss is not angle dependent. Figure 11.17 shows predictions carried out using PSTD [171], [114], [172].The predicted excess attenuation spectra due to a square lattice are not predicted to be changed much by changing the azimuthal angle between the source - receiver axis and the normal to the lattice between 20° and 70°.
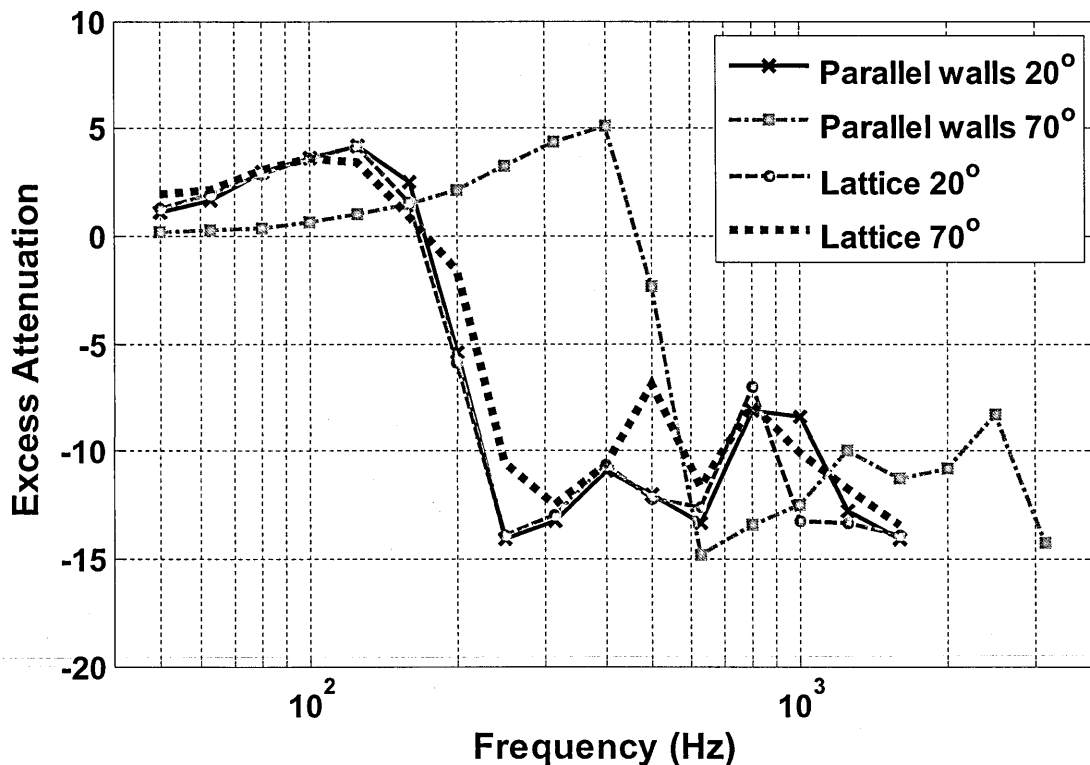
Figure 11.17 Comparison of predicted excess attenuation spectra using PSTD [171], [114], [172] over sixteen 0.05 m thick, 0.3 m high parallel walls with centre-to-centre spacing of 0.4 m and 0.3 high square lattice, 16 squares having sides 0.4 m long and 0.05 thick walls . The source was placed at height of 0.01 m and receiver is at a height of 1.5 m and at 50 m distance. The angle between source and receiver to parallel walls/lattice normal axis is varied between 20° and 70° (see Figure 11.11 for θ).

Tables 11.8 (predicted insertion losses due to parallel walls) and 11.11 (predicted insertion losses due to lattices) show that, for a given height and width

of the roughness array, the lattice structure performs better than parallel walls. Similar conclusions were drawn from drive by tests near lattices and parallel walls (see Chapter 5). For a 3.05 m and 12.05 m wide arrays the parallel walls and lattice give predicted insertion losses of 6.6 dB & 8.6 dB and 7.2 dB & 10.5 dB respectively.

Although, the attenuation performance of lattice is found superior to that of parallel walls it is important to note that the prediction for parallel walls were carried out using a fully discritized BEM whereas for the lattice they were obtained using the raised effective impedance model (see Chapter 6). Predictions carried out using a raised effective impedance indicate less surface waves than predicted using the fully discretized BEM (see Chapter 8 on surface wave propagation). This is also evident in Figure 11.18 which compares the predicted SPL spectra over 0.3 high and 3.05 wide parallel walls and lattice array. The predicted spectra over lattice show less surface wave generation than those for parallel walls around 50 – 250 Hz. Nevertheless, a given height and width of lattice is still to be preferred to parallel wall array of the same height and width because its attenuation performance is relatively azimuthal angle independent.

At the time of writing HOSANNA report 4.3 [101], it was concluded that beyond a certain width there is not any extra attenuation obtained due to parallel walls by increasing the width of the array. However, more recent insertion loss calculations suggest a different conclusion. Tables 11.8 and 11.11 indicate that there is a continuous increase in predicted insertion loss at a receiver height of 1.5 m and 50 m distance from the nearest lane source with increase in the array width. On the other hand the insertion loss predicted at a 4.0 m high receiver 50 m

from the nearest lane does not show much improvement due to increase in array width. This may be due to the receiver being in the shadow zone in respect of surface wave propagation [101] and that ground roughness is less effective at higher source-receiver grazing angles. Table 11.12 shows that the predicted insertion loss for receiver at 4.0 m height, increases with the increase in width of the array at longer ranges.
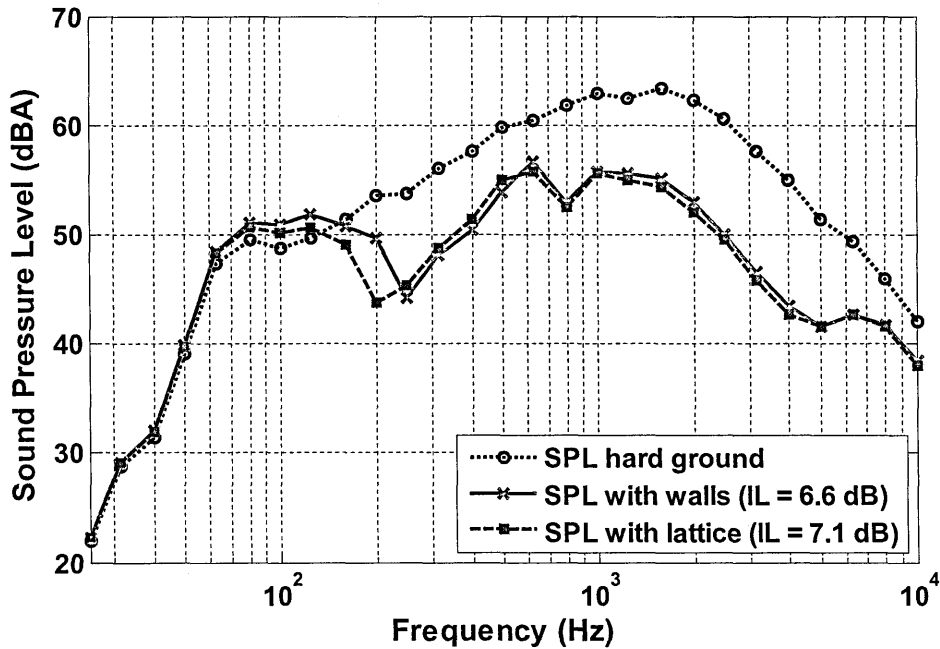
Figure 11.18 Comparison between predicted SPL over 0.3 m high and 3.05 m wide lattice and parallel walls (see Tables 11.8 and 11.11) for 2-lane urban road.

Table 11.12 Insertion losses predicted for different Lattice width configurations (see Figure 11.15) with receiver at 4.0 m high and 50 m distance from 2-lane urban road.

Profile (Lattice configurations)	Receiver height (dB)	Range 'R' (m)	Insertion loss (dB)		
			Lane-1	Lane-2	IL Combined
1.53 m wide and 0.3 m high square lattice	4.0	100	6.3	5.4	5.8
3.05 m wide and 0.3 m high square lattice	4.0	100	7.5	6.5	7.0
5.85 m wide and 0.3 m high square lattice	4.0	100	8.8	7.7	8.3
12.05 m wide and 0.3 m high square lattice	4.0	100	10.2	9.2	9.6
24.05 m wide and 0.3 m high square lattice	4.0	100	10.9	10.0	10.4

11.3.2.7 Raised Vs Recessed Lattice (Roughness Vs Grooves)

There may be some circumstances when it is not possible to build a raised roughness along the road side. Consequently BEM predictions have been carried out to investigate the effectiveness of recessed roughness (grooves) for reducing traffic noise. As a raised roughness, it is concluded that lattice structure is the best choice due to its predicted attenuation performance and azimuthal angle independence. Bearing this in mind, BEM predictions have been carried out of insertion loss near to a 2-lane urban road due to a recessed lattice. Table 11.13 compares the insertion loss due to a 2-lane road for recessed and raised lattices with receivers at heights of 1.5 m and 4.0 m and at distances of 50 m and 100 m from nearest lane source. Figure 11.19 compares the insertion loss due to raised and recessed lattice with different array widths. The receiver was placed at a height of 1.5 m and at a distance of 50 m from the source. It is concluded that, compared with that due to a 0.3 m high lattice, the insertion loss for a recessed lattice is reduced by 3 dB to 4 dB at two receiver locations, two receiver heights and various lattice widths.

Figure 11.19 compares the predicted excess attenuation spectra over 3.05 m wide and 0.3 m raised and recessed lattice for a source height of 0.01 m and receiver at a height of 1.5 m and a distance of 50 m from the source. The arrays are assumed to start 2.5 m from the source. There is a significant difference between predicted excess attenuation spectra for raised and recessed lattice. The difference increases with increasing frequency.
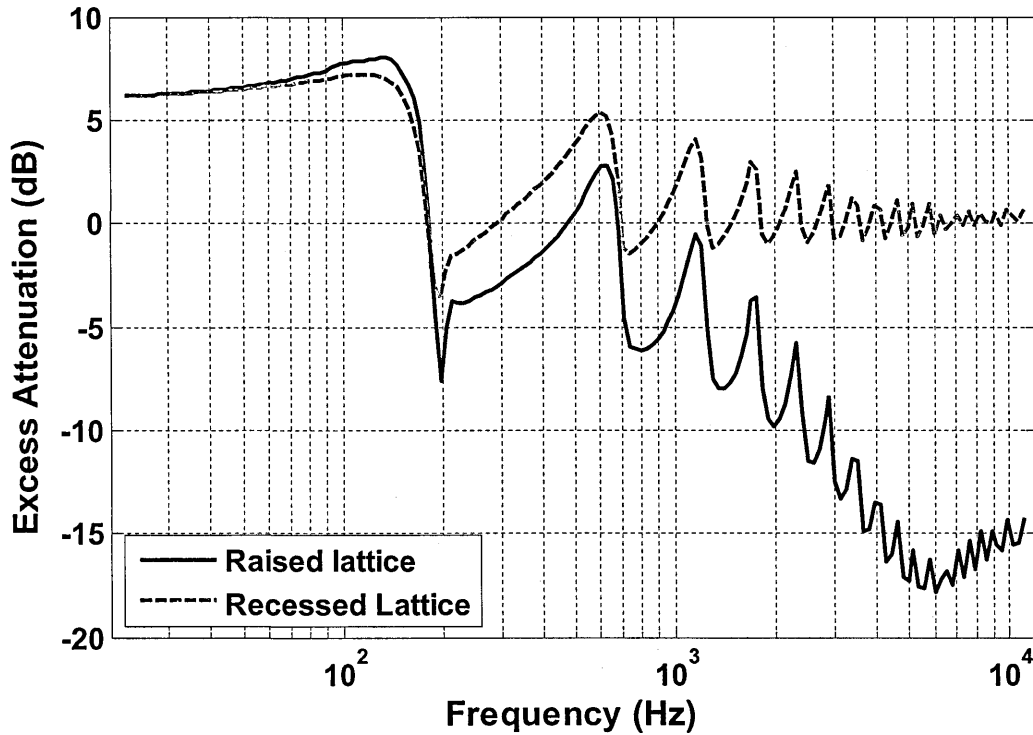
Figure 11.19 Comparison between predicted excess attenuation spectra over 3.05 m wide and 0.3 m high raised lattice and recessed lattice for a source height of 0.01 m and receiver at a height of 1.5 m and a distance of 50 m from the source. The arrays are assumed to start 2.5 m from the source.
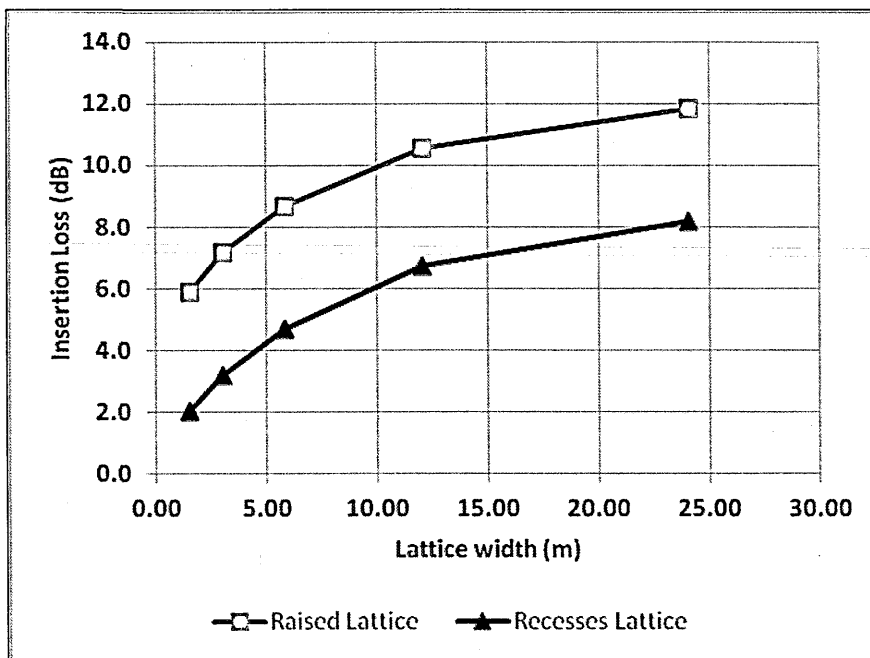
Figure 11.20 Comparison between insertion loss over raised lattice (h = 0.3 m) and recessed lattice (h = 0.0 m) with different lattice width for two lane urban road at distance of 50.0 m from nearest source and at height of 1.5 m.

Detailed configuration	Range 'R' (m)	Receiver height 'Hr' (m)	Insertion Loss (dB) Frequency range: 25 - 10 kHz			Insertion Loss (dB) Frequency range: 25 - 10 kHz		
Raised Vs Recessed Lattice configurations								
			Lane-1	Lane-2	Combined	Lane-1	Lane-2	Combined
			Lattice height = 0.3 m			Lattice height = 0.0 m		
1.53 m wide and 0.3 m/0.0 m high square lattice	50	1.5	6.2	5.5	5.9	2.2	1.9	2.0
		4.0	6.4	4.9	5.6	2.4	1.7	2.0
	100	1.5	5.6	5.0	5.3	2.0	1.8	1.9
		4.0	6.3	5.4	5.8	2.2	1.9	2.0
3.05 m wide and 0.3 m/0.0 m high square lattice	50	1.5	7.6	6.7	7.2	3.3	3.0	3.2
		4.0	7.0	5.3	6.1	3.3	2.3	2.8
	100	1.5	6.9	6.2	6.5	3.0	2.8	2.9
		4.0	7.5	6.5	7.0	3.3	2.9	3.1
5.85 m wide and 0.3 m/0.0 m high square lattice	50	1.5	9.1	8.2	8.7	4.9	4.4	4.7
		4.0	7.2	5.4	6.3	3.9	2.6	3.2
	100	1.5	8.4	7.6	8.0	4.4	4.1	4.2
		4.0	8.8	7.7	8.3	4.8	4.2	4.5
12.05 m wide and 0.3 m/0.0m high square lattice	50	1.5	10.9	10.2	10.5	7.0	6.4	6.7
		4.0	7.1	5.3	6.1	3.6	2.2	2.9
	100	1.5	10.4	9.6	10.0	6.5	6.0	6.3
		4.0	10.2	9.2	9.6	6.5	5.7	6.1
24.05 m wide and 0.3 m/0.0m high square lattice	50	1.5	12.0	11.6	11.8	8.4	7.9	8.2
		4.0	6.8	5.0	5.9	3.2	1.9	2.5
	100	1.5	12.5	11.8	12.1	9.0	8.4	8.7
		4.0	10.9	10.0	10.4	7.4	6.6	7.0

While recessed systems are predicted to be acoustically less effective and, potentially, they are more expensive to construct, they might be preferred where there are restrictions on above ground constructions close to roads or where they might be combined usefully with drainage arrangements. It is possible to recover some of the reduced insertion loss by starting them closer to the noise source or by making the recessed configurations deeper than 0.3 m. Being closer to the source also makes roughness-based noise reduction less susceptible to meteorological effects. Figure 11.21 summarizes the increase in insertion loss due to recessed lattice with the increase in depth. There is no great advantage in making a recessed lattice deeper in terms of insertion loss. However, increasing the width of a recessed lattice is another possibility where there are restrictions on inserting a raised platform.
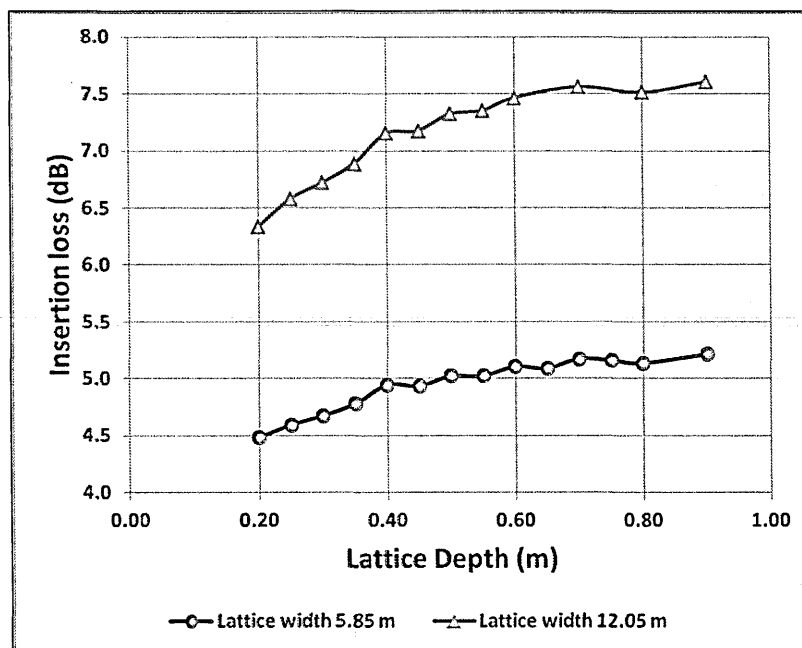
Figure 11.21 Comparison between predicted insertion loss over recessed lattice (h = 0.0 m) with different lattice depth and two selected lattice width (5.85 m and 12.05 m) for two lane urban road at distance of 50 m from the source and at height of 1.5 m.

11.3.3 Traffic noise attenuation by impedance strips

11.3.3.1 Single/Multiple impedance strips

The insertion losses due to single and multiple impedance strips of acoustically soft and hard ground at a 1.5 m or 4.0 m high receiver 50 m from a 2-lane urban road (see Figure 11.22) have been calculated and are listed in Table 11.14.
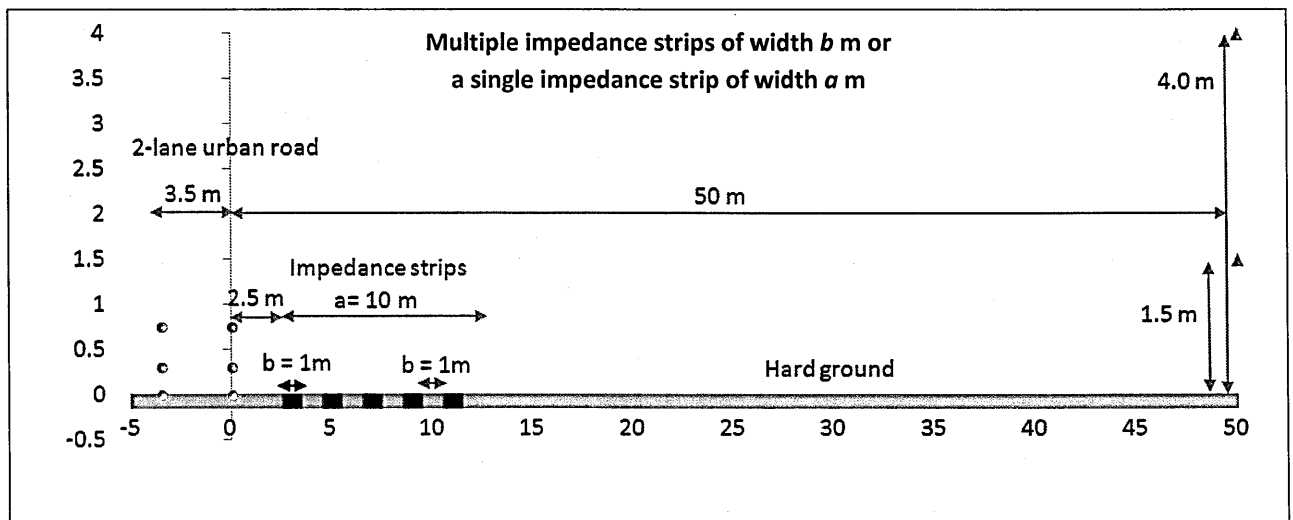
Figure 11.22 Configuration used to predict attenuation due to impedance strips.

Two types of acoustically soft grounds, gravel and 'best' grass have been selected to investigate the effect of single or multiple impedance discontinuities over noise. The impedance parameters for gravel using slit pore model are given with a flow resistivity of 10 kPa s m^{-2} and porosity of 0.4 (see Chapter 4). Similarly the 'best' grass has been selected as that likely to give the highest attenuation from 26 grassland sites (see Chapter 4) and is defined using slit pore model with a flow resistivity of 150 kPa s m^{-2} and porosity of 0.5. It is concluded that the inserting multiple impedance strips does not offer greater attenuation than a single patch of soft ground with the same overall width. A single 25 m wide soft ground

leads to a higher predicted attenuation than a 25 m wide array of strips including multiple impedance discontinuities.

Table 11.14 Compares predictions for a single wide strip of 'gravel' or 'grass' (i.e. b = 0 m) with x = 2.5 m and nine soft/hard strips of varying widths.

Strip widths and configuration		Receiver Height (m)	Insertion Loss (dB)					
			Semi-infinite 'gravel' (Flow resistivity = 10 kPa s m⁻², Porosity = 0.4)			Semi-infinite 'grass' (Flow resistivity = 150 kPa s m⁻², Porosity = 0.5)		
a (m)	b (m)		Lane 1	Lane 2	Combined	Lane 1	Lane 2	Combined
5.0	0	1.5	4.5	3.9	**4.2**	3.6	3.1	**3.4**
		4.0	4.1	2.7	**3.4**	3.4	2.4	**2.9**
10.0	1.0	1.5	4.8	4.2	**4.5**	3.6	3.1	**3.4**
		4.0	3.8	2.5	**3.1**	3.1	2.2	**2.7**
9.0	0	1.5	6.4	5.6	**6.0**	5.1	4.6	**4.9**
		4.0	4.4	2.8	**3.5**	3.9	2.7	**3.3**
15.0	0	1.5	8.2	7.3	**7.7**	6.8	6.1	**6.5**
		4.0	4.0	2.5	**3.2**	3.9	2.6	**3.2**
25.0	0	1.5	9.5	8.6	**9.1**	8.1	7.5	**7.8**
		4.0	3.8	2.3	**3.0**	4.0	2.6	**3.3**
25.0	0.1	1.5	7.8	6.9	**7.4**	-	-	-
		4.0	3.5	2.2	**2.8**	-	-	-
25.0	1.0	1.5	8.0	7.1	**7.5**	3.6	3.1	**3.4**
		4.0	3.6	2.2	**2.8**	3.1	2.2	**2.7**
25.0	2.0	1.5	7.9	7.0	**7.5**	-	-	-
		4.0	3.7	2.2	**2.9**	-	-	-
25.0	5.0	1.5	7.7	6.8	**7.3**	-	-	-
		4.0	3.9	2.4	**3.1**	-	-	-

11.3.3.2 Predicted effects of flat/raised/triangular soft strip configurations

Calculations have been made also for the insertion loss due to various forms of 5 metre wide and 0.3 m high 'raised', acoustically-soft strips (see Figure 11.23) in otherwise hard ground and with a 2-lane urban road source. The surface impedance of 'grass' is calculated from the two-parameter slit-pore model with flow resistivity 104 kPa s m^{-2}, and Porosity 0.36 (Nordtest site #41 long grass – representative of 'low flow resistivity' grassland – see Chapter 4). Four scenarios have been considered: (i) an in plane strip as in Figure 11.22 (ii) an elevated i.e. a 0.3 m high platform of grass (iii) a strip with right-angle triangular section, slope facing the source and (iv) right-angle triangular section strip with the slope facing the receiver (see Figure 11.23). The soft ground starts either 5 m or 2.5 m from the road and receivers are 50 m from the road at a height of either 1.5 m or 4 m.
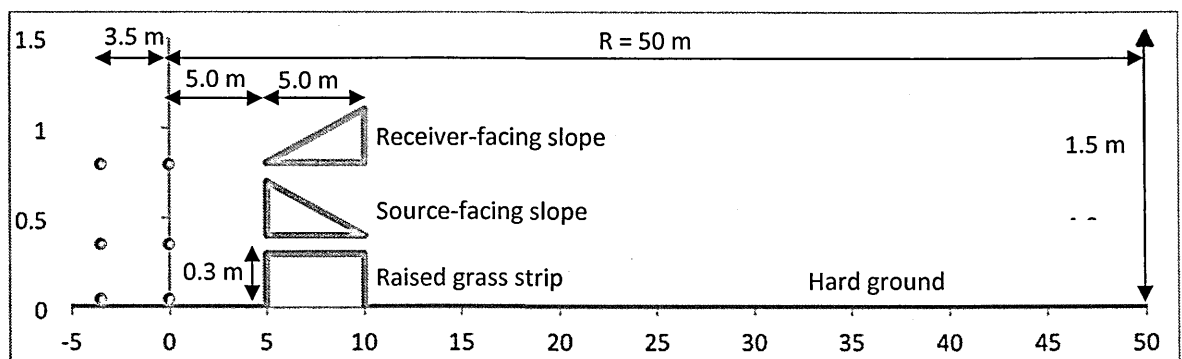
Figure 11.23 5m wide grass strip configurations used to predict attenuation: , 0.3 m high raised grass strip, 0.3 high source-facing sloped grass strip and receiver-facing grass strip for 2-lane urban road.

The results of the calculations are shown in Table 11.15. The raised rectangular 'grass' platform is predicted to result in more than 3 dB higher insertion loss than the in-plane case. While the insertion loss predicted for the triangular 'soft' section with source-facing slope is less than that predicted for the raised

platform, it offers a marginally greater insertion loss than the receiver-facing slope. Figure 11.25 compares the insertion loss due to various strips configurations.

Figure 11.24 compares the predicted sound pressure level spectra due to a 2-lane urban road at a 1.5 m high receiver 50 m from the road for continuous hard ground, an in-plane grass strip starting at 5.0 m from nearest source, a 0.3 m high grass platform, 0.3 m high right-angle triangle section slope facing source and 0.3 m high right-angle triangle section slope facing receiver. The SPL spectra show that the raised rectangular profile gives attenuation over a wide frequency range whereas the flat in-plane profile gives attenuation only up to 2.5 kHz. The source-facing slope grass and receiver-facing slope grass gives similar attenuation up to 2 kHz. Above this frequency the source-facing slope grass gives an the attenuation similar to that predicted as due to raised rectangular profile and the predicted attenuation due to the receiver-facing grass slope is similar to the predicted attenuation due to flat ground.
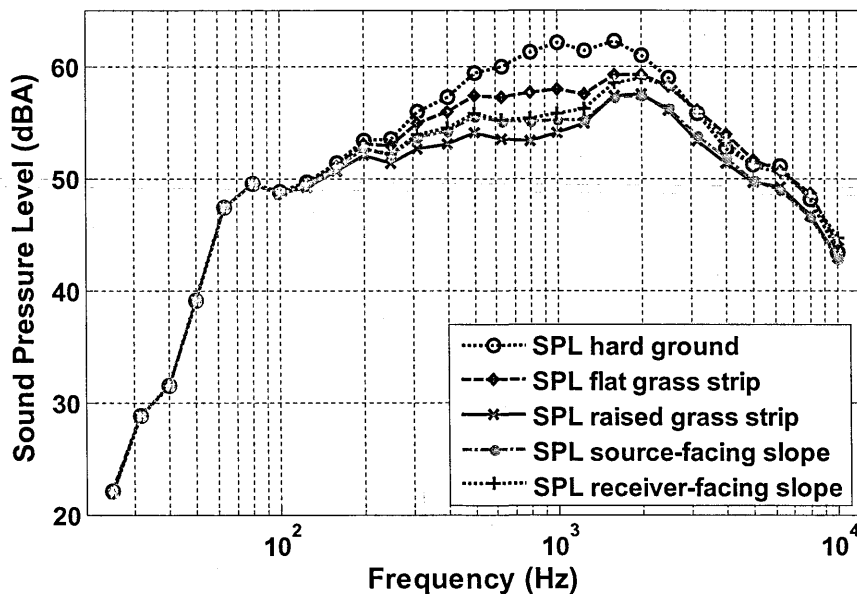
Figure 11.24 Predicted SPL spectra due to a 2-lane urban road (95% cars type 1 and 5% HGV, mean speed of 50 km/h) at a 1.5 m high receiver 50 m from the road for continuous hard ground (black dotted-circle line), an in-plane grass strip starting at 5.0 m from nearest source (blue broken-diamond line), a 0.3 m high grass platform starting at 5.0 m from nearest source (red joined crosses), 0.3 m high right-angle triangle section slope facing source and 0.3 m high right-angle triangle section slope facing receiver.

Table 11.15 Insertion loss predicted for various forms of 5 m wide grass strip starting at 2.5 m or 5 m from a 2-lane urban road (95% cars type 1 and 5% HGV, mean speed of 50 km/h) at 1.5 m and 4 m high receivers 50 m from the road.

Distance between nearest source and start of soft ground x (m)	Form of 5 m wide 'soft' strip	Receiver height 'Hr' (m)	Insertion Loss (dB) Frequency range: 25 - 10 kHz		
			Lane-1	Lane-2	Combined
5.0	In plane	1.5	3.2	2.8	3.0
		4.0	2.5	1.7	2.1
	0.3 m high platform	1.5	6.5	5.8	6.1
		4.0	5.2	3.8	4.5
	Right-angle triangle of 0.3 m height with slope facing source	1.5	5.2	4.6	4.9
		4.0	4.5	3.4	3.9
	Right-angle triangle of 0.3 m height with slope facing receiver	1.5	4.9	4.4	4.7
		4.0	3.6	2.5	3.0
2.5	In plane	1.5	3.5	3.0	3.3
		4.0	3.4	2.4	2.9
	0.3 m high platform	1.5	7.2	6.2	6.7
		4.0	6.6	5.0	5.8
	Right-angle triangle of 0.3 m height with slope facing source	1.5	5.7	5.0	5.3
		4.0	5.7	4.3	5.0
	Right-angle triangle of 0.3 m height with slope facing receiver	1.5	5.4	4.7	5.1
		4.0	4.8	3.5	4.1
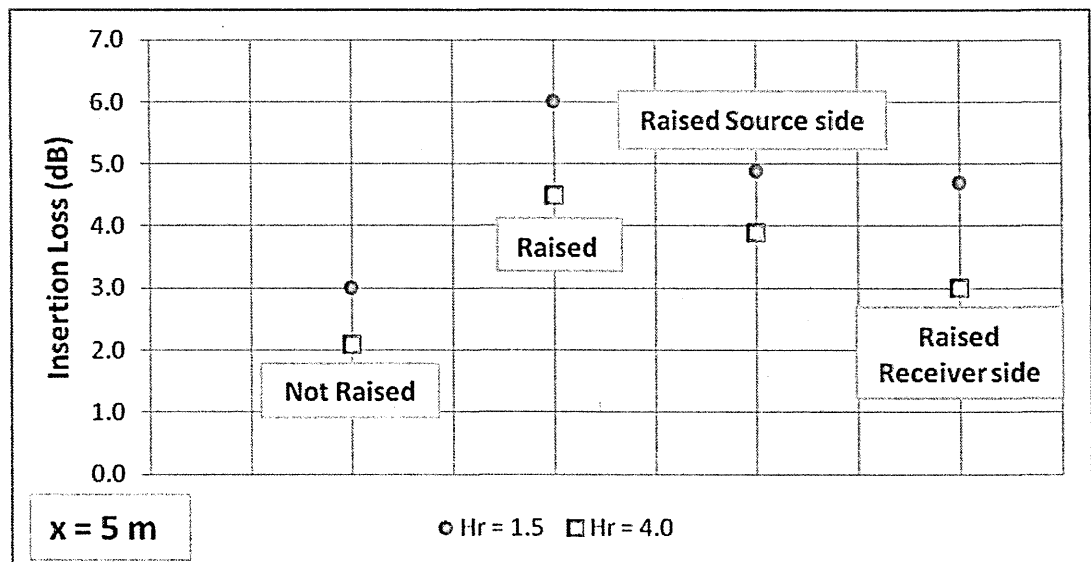
Figure 11.25 Comparison between insertion loss calculated for 5 m wide not raised soft strip, raised, raised source side and raised receiver side (See Table 11.15).

11.4 Predicted insertion loss due to ground treatments for other road types

11.4.1 Four Lane road

The four lane configurations are specified in the same way as the two lane configurations except that the two extra lanes are present. The insertion loss due to a four lane road has been calculated for all previously-reported cases. The major conclusion is that the effect of mitigation is less for the furthest lanes i.e. lane 3 and lane 4. This suggests that the improvement due to a nearer grazing angle is less than the reduction in insertion loss due to the treatment being further away.

11.4.2 2x2 lane motorway with central reservation

The 2x2 lane motorway configuration (see Section 11.2.2.3) consists of 4 lanes with a 2 m central reservation in between the pair of lanes. The mean assumed speed of vehicles on a motorway is 120 km/h and traffic flow is also higher, which results in higher noise levels. Since motorways are usually further away from residential areas, the insertion loss for a motorway is calculated at longer distances such as 25m, 50 m, 110 m, 235 m and 500 m. The insertion loss for a motorway has been calculated for all of the mitigation methods considered previously. However, in this section only example attenuation due to parallel walls for 2 x 2 motorway (an example configuration is shown in Figure 11.26) with and without central reservation treatments are presented.
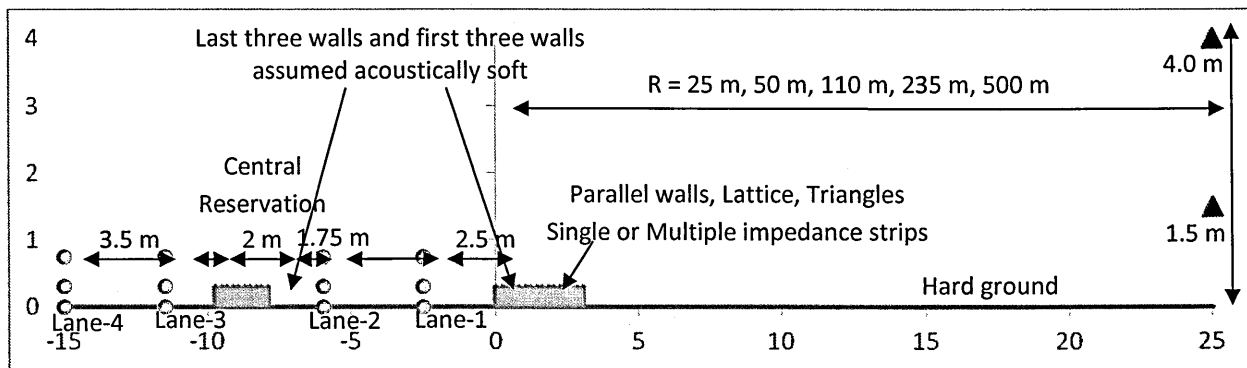
Figure 11.26 Schematic of a 2x2 motorway lane and an example 3 m wide parallel low wall configuration starting 2.5 m from nearest traffic lane and 2 m wide central reservations treated with 0.3 high parallel walls array.

The insertion losses due to parallel walls near a 2 x 2 motorway with and without central reservation treatments have been calculated and are listed in Table 11.15. Figure 11.27 compares the insertion losses corresponding to source lanes # 1, 2, 3 & 4 due to 0.3 m high and 3.05 wide parallel walls array with and without central reservation treatments for a receiver at height of 1.5 and at a distance of 50 m from nearest lane source. The attenuation due to the parallel walls decreases as the distance between the walls and noise source increases, so is lower for the further lanes as shown in Figure 11.27 (red circles). The predicted insertion losses due to 0.3 m high and 3.05 m wide parallel walls for lanes # 3 and # 4 are less than those for lanes # 1 and # 2 by between 1 and 1.5 dB. The insertion losses for lanes # 3 and # 4 can be improved by introducing ground treatments in the 2 m wide central reservation (see Figure 11.27 (blue squares)). The introduction of 0.3 m high and 2 m wide wall arrays on the central reservation improves the predicted insertion loss by between 3 and 4 dB for lanes # 3 and # 4. However, these treatments reduce the insertion losses predicted for lanes # 1 and lane # 2. This is due to reverberation between the parallel wall arrays. The Lane # 1 and # 2 noise sources are between the wall arrays and so reverberation

increases the noise level. This reverberation can be mitigated by introducing some soft covering on the facing walls (see Figure 11.26). The introduction of soft walls is predicted to increase the insertion losses for all four lanes. The soft material not only removes the reverberation between the walls but also reduced the surface wave propagation over the parallel walls.

The predicted insertion losses due to lattices show similar effects in that reverberation is removed by the covering the lattice sides with soft materials.
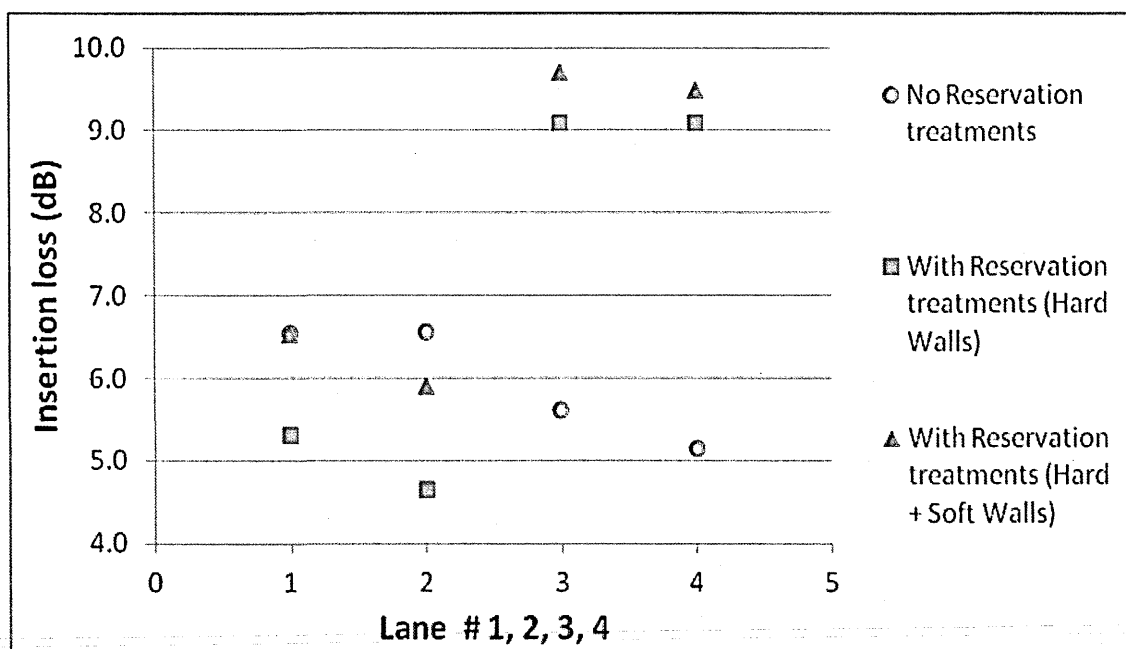
Figure 11.27 Comparison between insertion loss calculated due a 2 x 2 motorway for a 0.3 m high and 3.05 m wide wall array; without and with central reservation treatments of 0.3 high and 2 m wide wall array (see Figure 11.26); for a receiver at height of 1.5 and at a distance of 50 m from the source (See Table 11.16).

Table 11.16 Insertion losses predicted for parallel wall configurations (see Figure 11.26) with two receiver heights of 1.5 m and 4.0 m and at 50 m distance.

Detailed configuration (0.3 m high parallel wall array; 0.2 m centre-to-centre spacing)	Receiver height 'Hr' (m)	Insertion Loss (dB) Frequency range: 25 - 10 kHz				
		Lane-1	Lane-2	Lane-3	Lane-4	Combined
2 x 2 lane motor way with no central reservation treatments						
3.05 m wide and 16 × 0.05 m thick walls	1.5	6.5	6.6	5.6	5.2	6.0
	4.0	6.5	5.2	3.5	2.8	4.4
5.85 m wide and 30 × 0.05 m thick walls	1.5	7.9	7.8	6.8	6.3	7.2
	4.0	6.4	5.1	3.5	2.7	4.3
2 x 2 lane motor way with central reservation treatments (Hard walls)						
3.05 m wide and 16 × 0.05 m thick walls	1.5	5.3	4.6	9.1	9.1	6.3
	4.0	4.6	2.9	7.0	6.1	4.8
5.85 m wide and 30 × 0.05 m thick walls	1.5	6.5	5.9	9.9	9.9	7.5
	4.0	4.4	2.9	6.8	6.0	4.7
2 x 2 lane motor way with central reservation treatments (Hard + soft wall – See Figure 11.26)						
3.05 m wide and 16 × 0.05 m thick walls	1.5	6.5	5.9	9.7	9.5	7.4
	4.0	6.1	4.4	7.4	6.3	5.9
5.85 m wide and 30 × 0.05 m thick walls	1.5	8.1	7.3	10.6	10.4	8.7
	4.0	6.2	4.4	7.2	6.2	5.8

11.5 Railway noise

11.5.1 Track profile and ballast representations

BEM predictions of insertion losses for railway noise abatements have carried out using a British (Network Rail) railway track profile [173] and for two source spectra (see Figure 11.28 [173], [168]). One spectrum was measured at distance of 1 m for a train running at a speed of 145 km/h on a British railway track and other was that assumed in HOSANNA 2.3 [168].
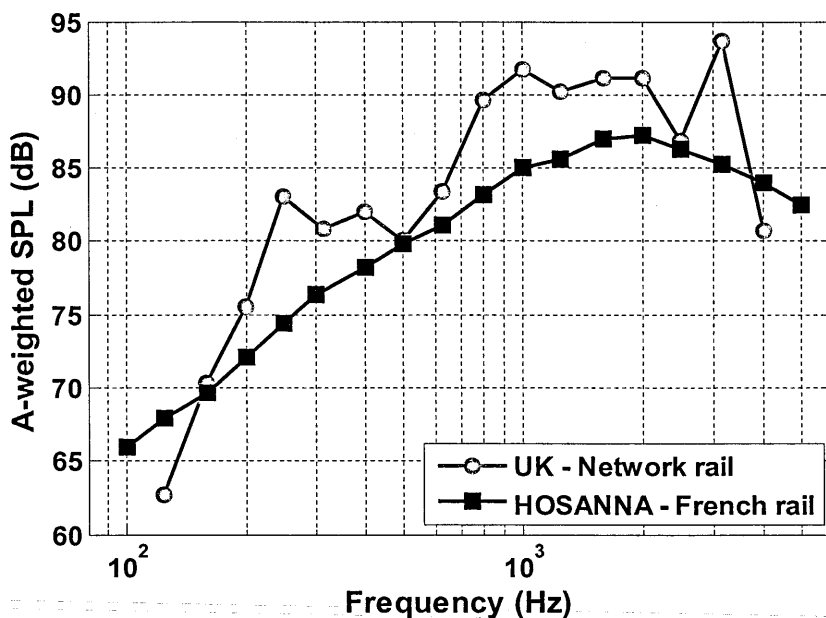
Figure 11.28 Source spectrum at 1 m corresponding to a (UK) train running at 145 km/h [144] (red line); Source spectrum for French railway given in HOSANNA deliverable 2.3 [138]

Figures 11.29 shows the network rail profile used for calculations [173]. The assumed railway profile includes two tracks. Each track has two wheel sources. The source is at height of 0.05 m above the top of 0.171 m high rails. S1 and S2 are sources on track 1 and S3 and S4 are sources on track 2. The two railway tracks are treated independently to calculate the insertion loss because at any

given time only one train might be passing by. Two trains are only present together only for a short period of time when they are crossing over.
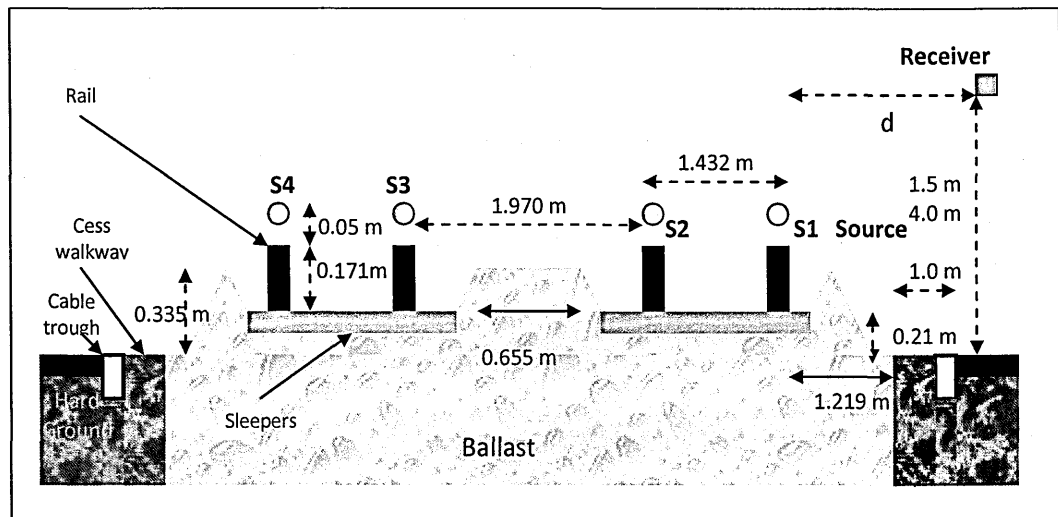
Figure 11.29 Detailed Network rail track profile [173].

In the UK track profile, ballast is heaped to a height of 0.335 m above the surrounding ground plane on both sides of the track and in the centre. The acoustical properties of the ballast (assumed 30 cm deep) have been calculated using the Johnson-Allard-Umnova model [60], [173] and the parameter values listed in Table 11.17.

Table 11.17 Parameter values used for calculating the acoustical properties of railway ballast, porous concrete and grass as given in ref. [173].

Material	Flow resistivity (kPa s m^{-2})	Porosity	Tortuosity	Viscous Characteristic length (m)
Railway Ballast	0.2	0.491	1.3	0.01
Porous concrete	3.619	0.3	1.8	2.2 x 10^{-4}
Grass	125	0.5	1.85	0.001

For convenience in the repeated 2D BEM calculations, despite its rather low flow resistivity, the ballast has been assumed to be locally-reacting. Figure 11.30 shows an example of the differences between the local and non-local reaction assumptions on the predicted spectra at a 1.5 m high receiver approximately 21 m from nearest edge of the ballast due to a train on the nearest track. Predictions given by Figure 11.30 has been taken from the work reported by Boulanger [174]. Although the differences in predictions are up to 7 dB they occur at frequencies below 400 Hz. Since the source spectrum (Figure 11.28) has low energy content below 400 Hz, the errors in insertion loss calculations stemming from the local reaction assumption for ballast are considered to be acceptable being no more than 0.5 – 1 dB.
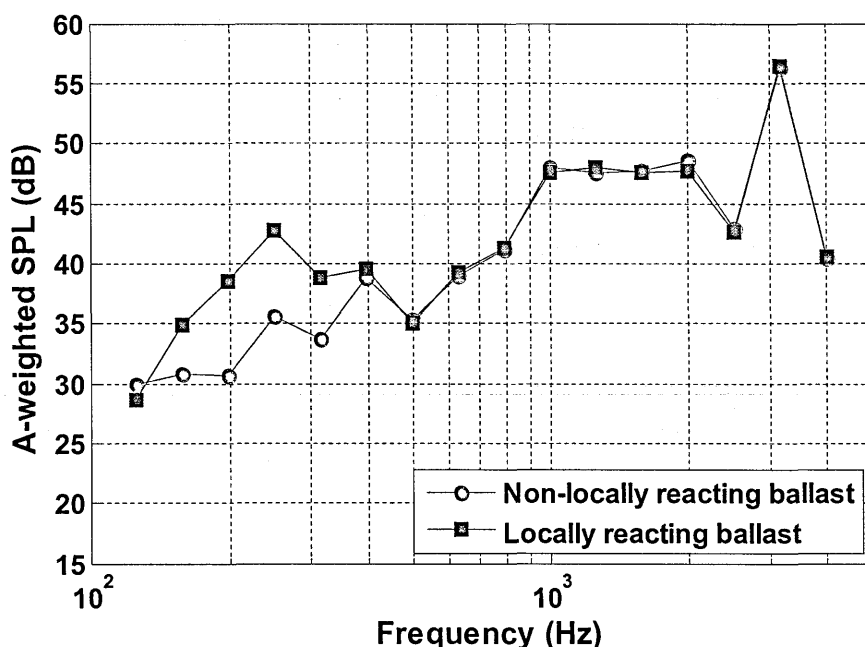
Figure 11.30 comparison between predicted spectra at a receiver about 21 m from the track above 'grass' (see Figure 11.29) assuming either local or extended reaction for the ballast.

The 2D BEM has been used to calculate the excess attenuation over reference railway track profile (see Figure 11.29) with no abatements treatments.

Similarly, another BEM prediction is carried out for railway track with abatement treatments. The predicted excess attenuation spectra have been combined with the source spectra (Figure 11.28) to predict sound pressure levels. The insertion losses have been calculated by subtracting the predicted SPL over reference track profile with no abatements from the SPL predicted over reference track profile with different abatements. Although insertion loss calculations have been carried out using both source spectra i.e. UK Network railway source spectra and French-HOSANNA WP 2.3 source spectra only to the calculations corresponding to the UK Network railway source are give here. This is due to fact that both spectra more or less gives similar conclusion, so to avoid repetition predictions for only one source spectra given here. The insertion losses have been calculated at various receiver locations such as 5 m, 10 m, 22 m, 50 m and 100 m and two receiver heights of 1.5 m and 4.0 m. However, only predictions for the receiver placed at a distance of 50 m from the railway track are presented. According to HOSANNA project [174] guidelines, a standard distance of 50 m was chosen for comparison purposes and to avoid repetition. The ground treatments that have been considered are:

- Parallel walls

- Lattice structure

- Replacing hard ground with soft ground.

- Single or multiple impedance discontinuity.

- Growing dense crops.

- Modifying the railway track profile.

11.5.2 Parallel walls

The insertion loss due to periodically spaced parallel walls placed on a hard ground for railway noise (example configuration shown in Figure 11.31) has been calculated and the results are listed in Table 11.18. The receiver was placed at heights of 1.5 m or 4.0 m and at a distance of 50 m from nearest railway track source. Figure 11.31 (a) show the railway track profile with no mitigation treatments. Figure 11.31 (b) shows the parallel walls treatments placed at a distance of 2.5 m from the railway track. The predicted insertion loss due to a 0.3 m high and 1.65 m wide wall array at 1.5 m high receiver is 5.6 dB and 3.3 for track-1 and track-2 respectively. The insertion loss is increased by between 2 and 2.5 dB by increasing the width of wall array up to 5.85 m. Instead of placing the parallel walls at some distance, these were placed on the railway track as shown in Figures 11.31 (c) and (d). The insertion losses predicted by placing a 0.65 m wide and 0.3 m high parallel wall array at the edge of the railway track (see Figure 11.31 (c)) are 7.7 dB and 3.5 dB for track 1 and 2 respectively, at a distance of 50 m and at a height of 1.5 m. The insertion for track 2 can be improved by introducing a 0.65 m wide array of parallel walls between the two tracks (see Figure 11.31 (d)). This improves the insertion loss for track 2 by 3 dB, but it also reduces the insertion loss for track 1 by 1.5 dB due to reverberation. The reverberation can be reduced by covering the last wall at the centre of track and first wall at edge of the track with soft materials. The insertion losses due to placing walls between the tracks and at the receiver-side edge of the track with soft material is 7.3 dB and 6.9 dB for track 1 and 2 respectively for a receiver

placed at height of 1.5 and at a distance of 50 m from the nearest source of track-1.
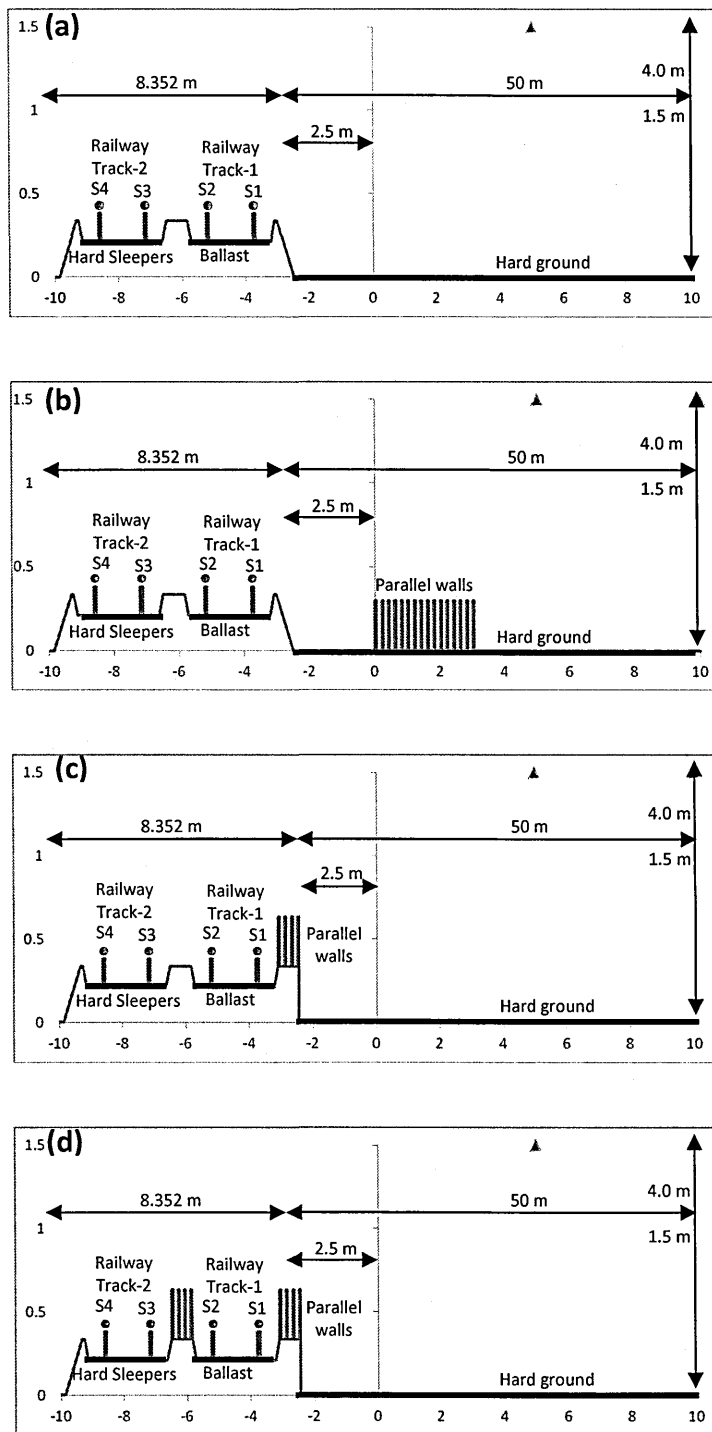
Figure 11.31 A schematic for railway track (a) no treatments (b-d) parallel walls treatments.

Table 11.18 Predicted insertion loss due to different walls configurations for railway.

Detailed configuration (0.3 m high parallel wall array; 0.2 m centre-to-centre spacing)	Range 'R' (m)	Receiver height 'Hr' (m)	Insertion Loss (dB) Frequency range: 25 - 10 kHz					
			Source-1	Source-2	Combined 1&2	Source-3	Source-4	Combined 3&4
1.65 m wide and 9 × 0.05 m thick walls at a distance of 2.5 m from railway track (see Figure 11.31 (b))	50	1.5	6.1	4.8	5.6	3.4	3.2	3.3
		4.0	2.0	2.2	2.1	0.6	0.8	0.7
3.05 m wide and 16 × 0.05 m thick walls at a distance of 2.5 m from railway track (see Figure 11.31 (b))	50	1.5	7.3	5.8	6.7	4.2	3.9	4.1
		4.0	1.9	2.3	2.1	0.5	0.8	0.6
5.85 m wide and 30 × 0.05 m thick walls at a distance of 2.5 m from railway track (see Figure 11.31 (b))	50	1.5	8.9	7.2	8.2	5.4	5.0	5.2
		4.0	1.8	2.1	1.9	0.4	0.6	0.5
0.65 m wide and 4 × 0.05 m thick parallel walls placed at edge of railway ballast (see Figure 11.31 (c))	50	1.5	9.0	6.0	7.7	3.7	3.3	3.5
		4.0	8.5	5.2	6.9	2.6	2.4	2.5
0.65 m wide and 4 × 0.05 m thick parallel walls placed at centre and edge of railway ballast (see Figure 11.31 (d))	50	1.5	8.1	4.3	6.4	7.3	6.0	6.6
		4.0	7.5	1.8	4.3	7.1	5.1	6.1
4 × 0.05 m thick parallel walls placed at centre & edge of railway ballast (see Figure 11.31 (d))-last wall of centre and first wall of edge is assumed soft	50	1.5	9.0	5.3	7.3	7.7	6.2	6.9
		4.0	8.8	3.8	6.1	7.4	5.4	6.3

11.5.3 Lattice configurations

The insertion losses at a 1.5 m or 4 m high receiver 50 or 100 m from the nearest track of a 2-track railway due to periodically spaced square lattice placed on a hard ground (example configuration shown in Figure 11.32) have been calculated and are listed in Table 11.19.
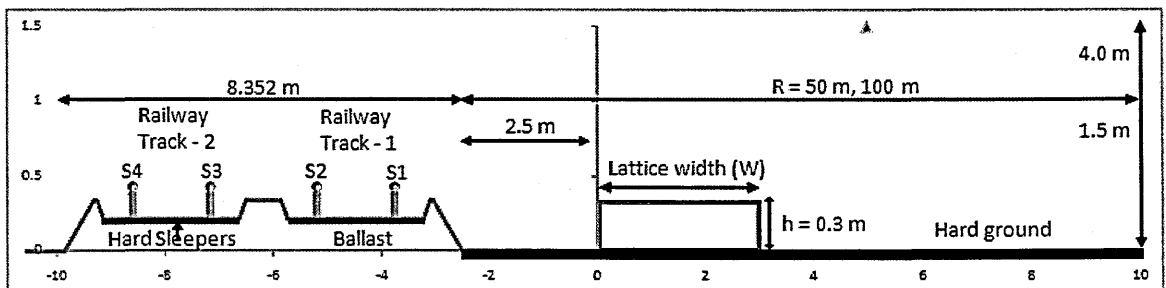
Figure 11.32 Schematic of a two track railway and an example 3.05 m wide lattice configuration starting 2.5 m from edge of railway track.

The predicted insertion loss increases with the increase in width of the array. The predicted insertion loss due to a 0.3 m high and 1.53 m wide lattice array is 5.5 dB for railway track-1 with a receiver placed at a height of 1.5 m and at a distance of 50 m from the edge of the railway track. The insertion loss due to lattice is doubled by increasing the width of lattice array up to 24.05 m. Similar values for predicted insertion loss have been obtained for railway track-1 with a receiver at 1.5 m height and 100 m distance. The predicted effects due to lattice are reduced if the receiver is closer to the road or higher.

It should be noted that compared with road traffic noise where the lowest sources are assumed to be 0.01 m high, the railway noise sources above track are elevated at height of 0.431 m above ground. The insertion loss due different lattice widths (1.53 m – 24.05 m) for railway track-1 and with receiver at height of 4.0 and 50 m distance from edge of railway track is only 2.0 dB. However, at longer

ranges, the lattice structure is predicted to give a useful insertion loss even at a receiver height of 4.0 m. The insertion loss at a distance of 100 m from the nearest edge of the railway track and at height of 4.0 m due to a 1.53 m wide lattice is predicted to be 5.2 dB for the railway track-1 source. The predicted insertion loss due to the lattice is increased by 2.5 dB if its width is increased up to 24.05 dB. Similar insertion loss predictions have been obtained for the railway track-2 source, but with relatively lower insertion loss values due to its larger distance from the lattice.

Table 11.19 Predicted insertion loss due to different lattice widths for railway track 1 and 2; two receiver heights of 1.5 m and 4.0 and two distances of 50 m and 100 m.

Lattice configuration	Range 'R' (m)	Receiver height 'Hr' (m)	Insertion Loss (dB) Frequency range: 25 - 10 kHz					
			Source-1	Source-2	Combined 1&2	Source-3	Source-4	Combined 3&4
1.53 m wide and 0.3 m high lattice	50	1.5	6.0	4.7	5.5	3.3	3.0	3.2
		4.0	2.1	2.2	2.1	0.5	0.7	0.6
	100	1.5	5.5	4.3	5.0	2.9	2.7	2.8
		4.0	5.7	4.4	5.2	2.8	2.6	2.7
3.05 m wide and 0.3 m high lattice	50	1.5	7.1	5.7	6.6	4.3	4.0	4.2
		4.0	2.1	2.4	2.3	0.6	0.8	0.7
	100	1.5	6.5	5.2	6.0	3.8	3.5	3.7
		4.0	6.7	5.3	6.2	3.6	3.4	3.5
5.85 m wide and 0.3 m high lattice	50	1.5	8.5	7.0	7.9	5.4	5.1	5.3
		4.0	2.1	2.4	2.2	0.5	0.7	0.6
	100	1.5	7.9	6.4	7.3	4.9	4.5	4.7
		4.0	7.7	6.4	7.2	4.3	4.2	4.3
12.05 m wide and 0.3 m high lattice	50	1.5	10.2	8.7	9.6	7.0	6.8	6.9
		4.0	1.8	1.9	1.8	0.2	0.4	0.3
	100	1.5	9.7	8.0	9.0	6.7	6.1	6.4
		4.0	8.7	7.6	8.3	5.1	5.2	5.1
24.05 m wide and 0.3 m high lattice	50	1.5	11.1	10.2	10.7	8.0	8.2	8.1
		4.0	1.6	1.7	1.7	0.0	0.3	0.2
	100	1.5	11.5	9.6	10.7	8.6	7.9	8.3
		4.0	8.9	8.3	8.7	5.3	5.7	5.5

11.5.4   Continuous grassland

The insertion losses at the reference receiver locations (specified previously) due to continuous grassland starting at 5 m from edge of railway track (configuration shown in Figure 11.33) have been calculated and are listed in Table 11.20.
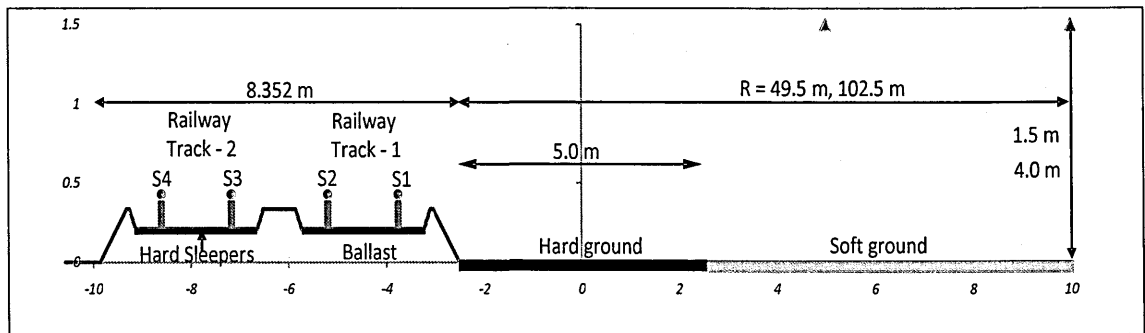
Figure 11.33 A railway track profile showing four rail/wheel sources, profiled ballast and soft ground extending from 5 m up to 50 m/100 m from the foot of the ballast.

The acoustically-soft ground is assumed to start 5.0 m from the nearest edge of the ballast (see Figure 11.33), instead of at 2.5 m as for other abatement types. However as with the previous considerations it is assumed to extend to the receiver. Four soft ground types have been chosen for calculation with the 2-parameter slit pore impedance model parameters specified in Tables 11.20. The insertion loss calculations listed in Table 11.20 are with source spectrum given by UK-Network rail [173]. At a 1.5 m high receiver the predicted insertion losses vary between about 3 dB at 50 m from the nearest track and 11 dB at 100 m from the furthest track. The corresponding IL predictions at a 4 m high receiver lie between less than a dB and a little over 3 dB. The ground surfaces with low flow resistivity give best attenuation performance.

Table 11.20 Predicted insertion loss due to different soft near railway track 1 and 2; two receiver heights of 1.5 m and 4.0 and two distances of 50 m and 100 m.

Detailed configuration	Ground parameters		Range 'R' (m)	Receiver height 'Hr' (m)	Insertion Loss (dB) Frequency range: 25 - 10 kHz					
	Flow resistivity (kPa s m⁻²)	Porosity			Source-1	Source-2	Combined 1&2	Source-3	Source-4	Combined 3&4
Long grass (NT site # 41)	104	0.36	49.5	1.5	7.1	7.2	**7.1**	5.0	5.4	**5.2**
				4.0	1.1	1.0	**1.0**	0.4	0.4	**0.4**
			102.5	1.5	12.9	12.7	**12.8**	10.4	10.7	**10.6**
				4.0	5.1	5.4	**5.2**	3.0	3.6	**3.3**
Lawn (NT site # 16)	176	0.5	49.5	1.5	7.2	7.2	**7.2**	5.0	5.4	**5.2**
				4.0	1.1	1.1	**1.1**	0.4	0.3	**0.4**
			102.5	1.5	13.0	12.7	**12.9**	10.3	10.5	**10.4**
				4.0	5.3	5.6	**5.4**	3.1	3.6	**3.3**
Pasture (NT site # 22)	1344	0.5	49.5	1.5	5.8	5.1	**5.5**	3.7	3.7	**3.7**
				4.0	1.1	1.1	**1.1**	0.3	0.3	**0.3**
			102.5	1.5	9.5	8.0	**8.9**	6.8	6.3	**6.6**
				4.0	4.9	4.6	**4.8**	2.7	2.9	**2.8**
Arable (NT site # 24)	2251	0.5	49.5	1.5	5.1	4.3	**4.8**	3.3	3.2	**3.2**
				4.0	1.0	1.0	**1.0**	0.3	0.3	**0.3**
			102.5	1.5	8.3	6.9	**7.8**	6.0	5.5	**5.8**
				4.0	4.5	4.1	**4.4**	2.5	2.7	**2.6**

11.5.5 Impedance strips

Similar predictions have been made for the insertion losses due to introducing either continuous gravel or alternating strips of gravel and acoustically-hard material in place of a continuous hard surface next to a railway (see Figure 11.34). The results are listed in Table 11.21. The insertion loss calculations given by Table 13 are with source spectrum given by UK-Network rail [173]. The predicted IL values are between 2 and 5 dB.
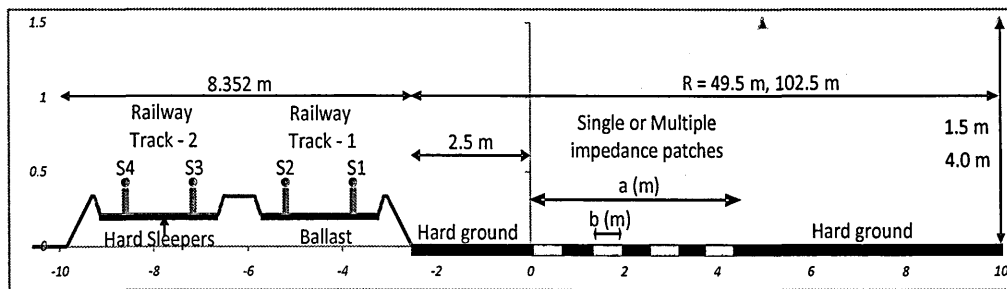
Figure 11.34 Railway track and multiple alternating gravel/hard strips.

Table 11.21 Predicted IL due to for single or multiple strips of gravel near railway tracks (gravel impedance represented by slit-pore model with flow resistivity = 10 kPa s m^{-2}, and porosity = 0.4).

Detailed configuration (Gravel : Flow resistivity = 10 kPa s m^{-2}, Porosity=0.4)	Strips widths and configurations		Range 'R' (m)	Receiver height 'Hr' (m)	Insertion Loss (dB) Frequency range: 25 - 10 kHz					
	a (m) Total width	b (m) Strips width			Source-1	Source-2	Combined 1&2	Source-3	Source-4	Combined 3&4
Single 5 m wide gravel strip	5.0	0	50	1.5	3.7	3.1	3.5	2.1	2.1	2.1
				4.0	0.9	1.3	1.1	0.2	0.4	0.3
Single 10 m wide gravel strip	10.0	0	50	1.5	5.8	5.1	5.5	3.6	3.6	3.6
				4.0	0.6	1.1	0.8	0.3	0.5	0.4
Single 25 m wide gravel strip	25.0	0	50	1.5	8.1	8.1	8.1	5.6	6.0	5.8
				4.0	0.4	0.7	0.5	0.1	0.1	0.1
25 m wide area of multiple 1 m wide gravel/ hard strips	25.0	1.0	50	1.5	6.9	6.5	6.8	4.8	5.0	4.9
				4.0	0.9	1.0	0.9	0.3	0.4	0.3
25 m wide area of multiple 2 m wide gravel/ hard strips	25.0	2.0	50	1.5	6.8	6.4	6.6	4.7	4.9	4.8
				4.0	0.8	1.0	0.9	0.3	0.4	0.3
25 m wide area of multiple 5 m wide gravel/ hard strips	25.0	5.0	50	1.5	6.6	6.1	6.4	4.5	4.6	4.5
				4.0	0.9	1.1	1.0	0.3	0.4	0.3

11.6 Modifying the railway track profile

11.6.1 Replacing hard slab track with porous concrete slab track

Figure 11.35 shows the track profile and source-receiver geometry assumed for predicting the effect of replacing an acoustically hard slab track by a porous concrete track for a high speed train. The assumed railway profile includes two tracks. Each track has two wheel sources. The source is at height of 0.1 m above the top of 0.21 m high slab track. The receiver is placed at height of 1.5 m above grass surface. The distance between sources 1, 2, 3, 4 (see Figure 11.35) and the receiver is 28.34 m, 26.9 m, 24.9 m and 23.5 m. 2D BEM is used for calculate excess attenuation which is combined with UK-Network rail source spectrum [173] to predict sound pressure level. The insertion loss is calculated by subtracting SPL over reference profile from SPL over modified profile.
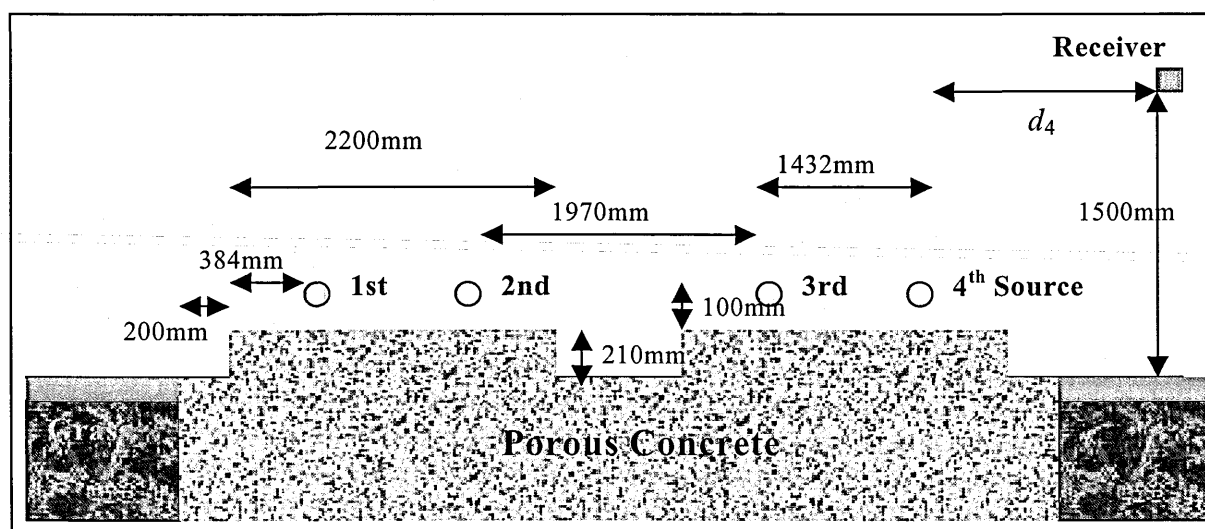
Figure 11.35 Slab track profile and assumed source/receiver geometry.

The impedance parameters used for porous concrete and grass using Johnson-Allard-Umnova model are listed in table 11.17. These parameters are taken from the paper to modeled [173] railway track. Again for convenience

despite low flow resistivity, the porous concrete has been assumed to be locally-reacting. However, as the result of the higher flow resistivity of porous concrete, the error from the local reaction assumption is less than that for the ballast. The hard slab track profile was modified by replacing it with porous concrete using impedance parameters given in Table 11.17. IL has been calculated by using both UK – Network rail source spectrum [173] and French railway source spectrum given in HOSANNA deliverable 2.3 [168]. The overall IL using both source spectra predicted for a train on the nearest track (combined source 3 & 4) is 5.5 dB and that for a train on the furthest track (combined source 1 & 2) is nearly 3.0 dB. Figure 11.36 gives the SPL plot for BEM prediction over slab track profile.
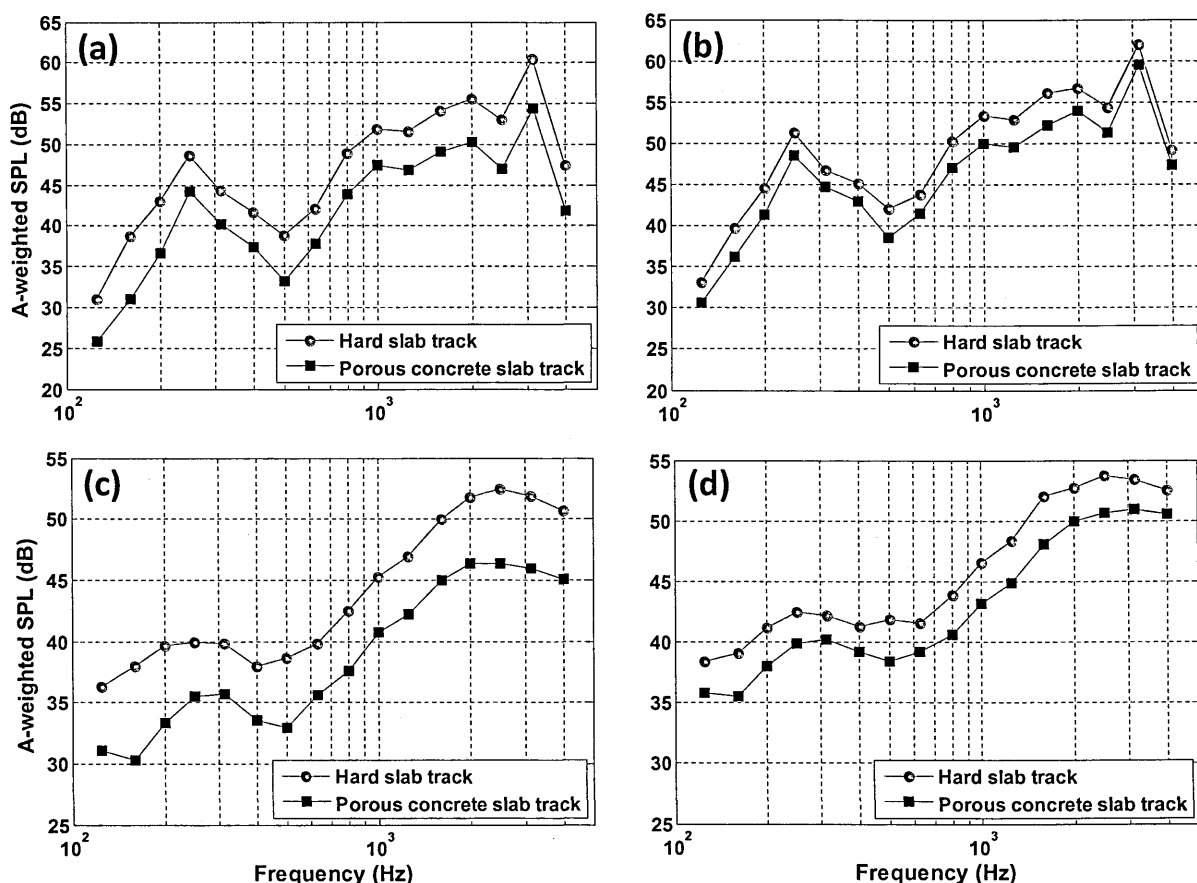
Figure 11.36 Comparison between BEM-predicted A-weighted SPL spectra at 25 m from the nearest source over acoustically-hard and porous concrete slab tracks using the profile shown in Figure 11.35 and porous concrete properties listed in Table 11.17 (a, b) Using UK – Network rail source spectrum [173] (c, d) Using French railway source spectrum given in HOSANNA deliverable 2.3 [168] (a, c) combined effects of sources at positions 1 and 2 (b, d) combined effects of sources at positions 3 and 4 .

11.6.2 Replacing hard sleepers with porous concrete sleepers

Figure 11.29 shows the profiled railway track and source-receiver geometry assumed for predicting the effect of replacing acoustically hard sleepers with porous concrete sleepers for a high speed train. The hard sleepers were replaced with porous concrete sleepers using the impedance parameters given in Table 11.17. SPL has been calculated by using UK – Network rail source spectrum [173]. The predicted SPL spectra shown in Figure 11.37 over railway track with porous concrete sleepers are smaller at lower frequencies than those predicted for hard sleepers. However, the overall effect of replacing hard sleepers by porous concrete sleepers averages out and no extra attenuation is obtained by modifying the sleepers.
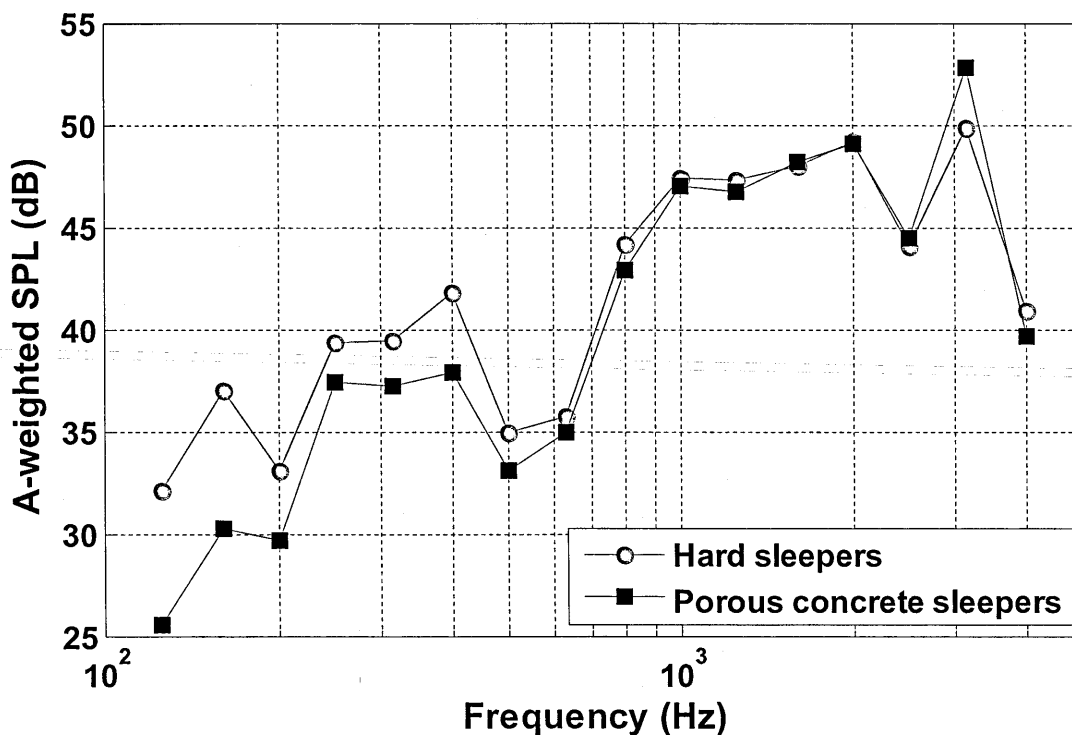
Figure 11.37 Comparison between BEM-predicted A-weighted SPL spectra at 25 m from the nearest source over acoustically-hard sleepers and replacing them by porous concrete using the profile shown in Figure 11.29 and porous concrete properties listed in Table 11.17, using UK – Network rail source spectrum [173] with combined effects of sources at positions 1 and 2.

11.7 Tramways

11.7.1 Noise attenuation by ground treatments near tramways

Figure 11.39 shows the schematic of a 2-track tramway infrastructure with four sources, two wheel sources for each tram at height of 0.05 m [168]. S1 and S2 are sources for tram-1; S3 and S4 are sources for tram-2. The insertion losses due to various ground treatments have been calculated using the A-weighted source spectrum plotted in Figure 11.38 [168].
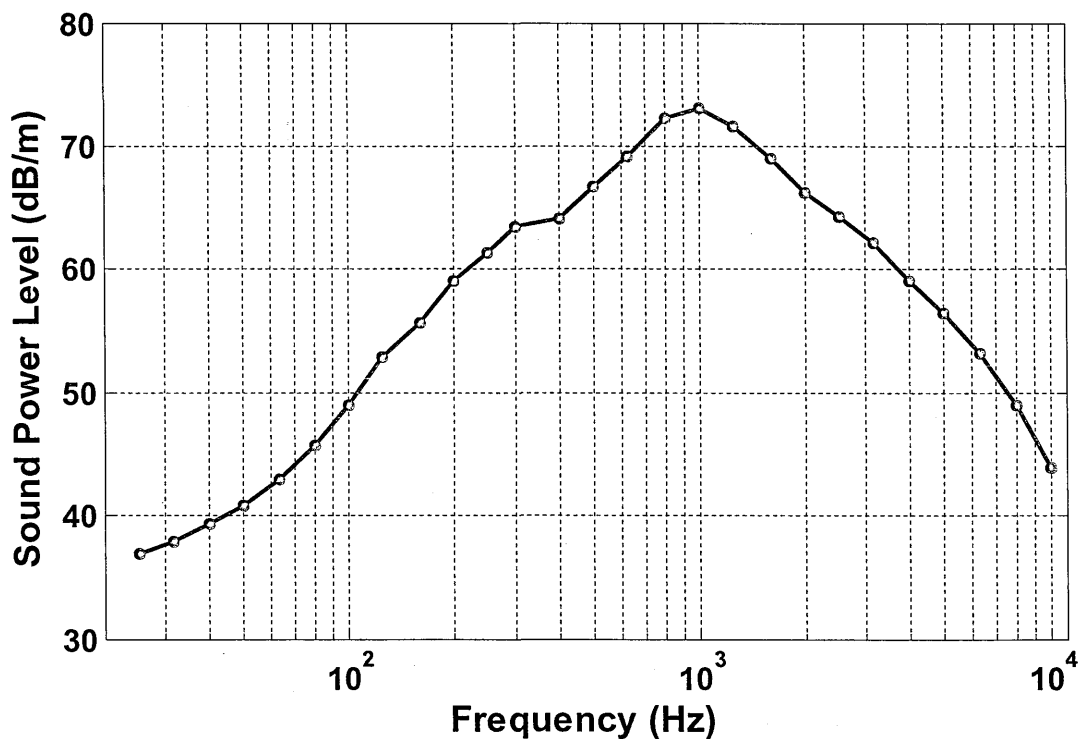
Figure 11.38 Source spectrum for tram noise given in HOSANNA report 2.3 [168].

The two tracks are treated independently to calculate the insertion loss because at any given time only one tram might be passing by. Two trams are only present together for short periods of time when they are crossing over. The distance between two tram-wheel sources is 1.45 m. The tramways are separated

by 1.6 m. The receivers are placed at heights of 1.5 m and 4.0 m and distances of 5 m, 10 m, 22 m, 47 m and 100 m from where the abatement starts as shown in Figure 11.39. The distance between the abatement and the nearest tram source is 2.5 m so the distance between nearest tram source and a receiver is 2.5 m more than the receiver distances stated above. Figure 11.39 shows example configurations of parallel walls. However, the insertion loss have been calculated for different types of ground treatments as given below,

- Replacing hard ground with soft ground.

- Introducing low height roughness (Parallel walls, Lattices and Triangles).

- Single or multiple impedance discontinuity.

- Growing dense crops.
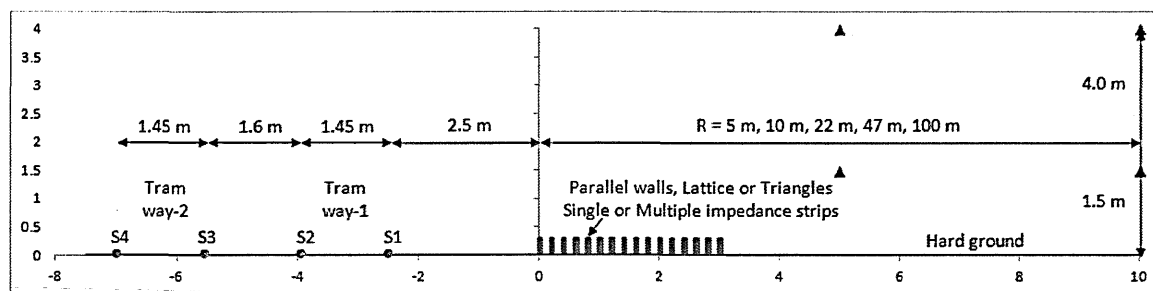
Figure 11.39 A 2 tramway infrastructure with two 0.05 m high wheel sources for each tram track and a low parallel walls abatement.

Figure 11.38 shows the source spectrum due to tram noise [168]. The source spectrum shows a peak at 1 kHz, which is similar to that in the A-weighted traffic noise spectrum. The traffic noise and tram noise source spectra plotted in Figures 11.1 and 11.38 respectively, exhibit similar characteristics. Also, the tramway noise source height of 0.05 m above ground is similar to that of the major source of traffic noise (road-tyre noise) at a height of 0.01 m. The ground

treatments start at a distance of 2.5 m from nearest noise source for both cases. The receiver heights and locations for tramway noise calculations are identical to those used for the traffic noise calculations. The tramway noise sources S1, S2, S3 and S4 corresponds to traffic noise source lane1, lane2, lane3 and lane4 respectively. Tramway noise source S1 and S2 are combined to give noise due to tramway track-1, which corresponds to combined source spectrum due lane1 and lane2 (HOSANNA 2-lane urban road). Insertion losses have been calculated for tramways due to different ground treatments and the conclusions drawn for tramways noise attenuation due to ground treatments are more or less similar to those obtained for traffic noise.

11.7.2   Modifying tram track

The tram ways are usually built on an acoustically hard ground surface as shown by schematic Figure 11.40 (a). The tram track can be modified to reduce the noise due to trams. Figure 11.40 (b) shows a situation in which the hard tram track is replaced by soft ground surface i.e. gravel. The gravel impedance is calculated using the 2-parameter slit pore model with a flow resistivity of 10 kPa s m^{-2} and porosity of 0.4. The insertion losses calculated by replacing hard tram track by gravel are listed in Table 11.22. As the noise source due to tram is very close to the tram track i.e. at a height of 0.05 m, replacing hard ground by gravel appears to be very effective in reducing the noise levels. The insertion loss of 5 dB and 10 dB obtained for track 1 and track 2 respectively with different receiver positions and heights.

Table 11.22 Predicted insertion loss due to different soft near railway track 1 and 2; two receiver heights of 1.5 m and 4.0 and two distances of 50 m and 100 m.

Detailed configuration	Ground parameters		Range 'R' (m)	Receiver height 'Hr' (m)	Insertion Loss (dB) Frequency range: 25 - 10 kHz					
	Flow resistivity (kPa s m^{-2})	Porosity			Source-1	Source-2	Combined 1&2	Source-3	Source-4	Combined 3&4
Track underneath the tram is assumed to be made of gravel	10	0.4	50	1.5	3.7	7.0	5.0	9.0	10.3	9.6
				4.0	3.7	7.2	5.1	9.3	10.6	9.9
			100	1.5	3.7	7.0	5.0	8.9	10.2	9.5
				4.0	3.7	7.0	5.0	9.0	10.3	9.6
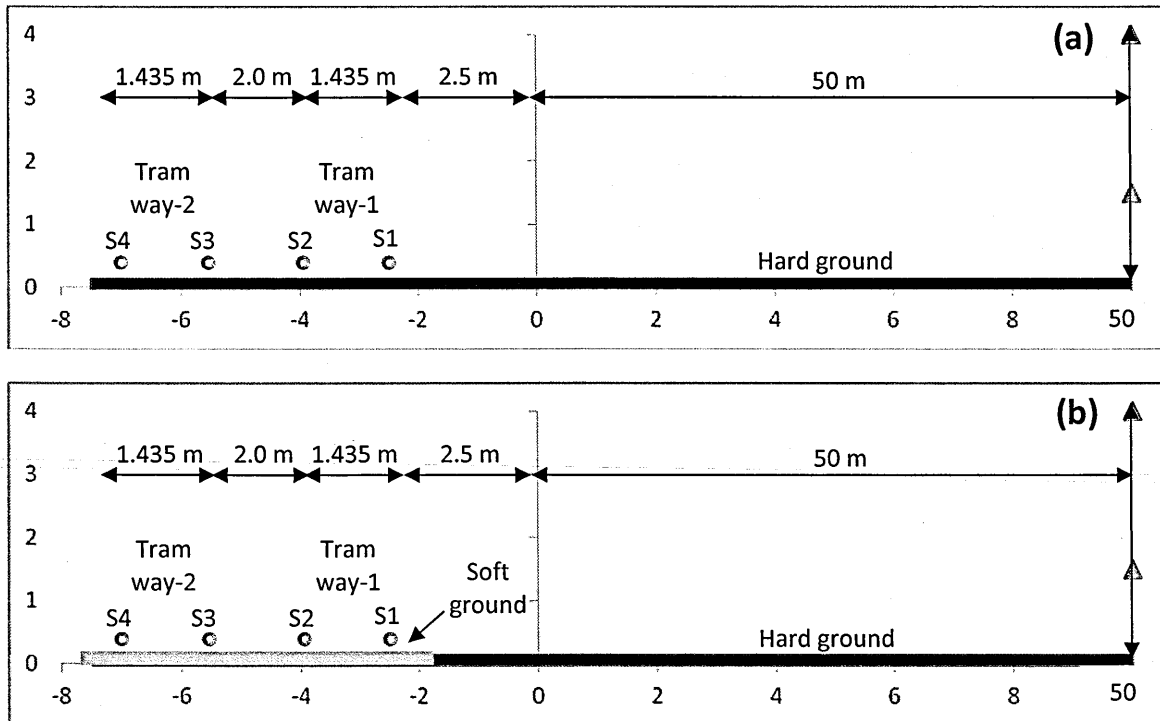
Figure 11.40 A 2 tramway infrastructure with two 0.05 m high wheel sources for each tram track 1 and 2 (a) Hard tram track (b) Hard tram track replaced with gravel (Flow resistivity = 10 kPa s m^{-2} and porosity of 0.5).

11.7.3 Predictions and measurements for a tramway

A measurement campaign in Grenoble has compared tramway noise levels in the situations shown in Figure 11.41 [175]. In the left hand photograph there is grass between and alongside the tracks in place of the acoustically-hard surfaces shown in the right hand photograph. Results of comparative noise level measurements in these situations are shown in Figure 11.42. These show that the introduction of grass between and alongside the tracks reduces tram noise levels at a 1.5 m high receiver about 4 m from the nearest track by between 1 and 10 dBA with an average of about 3 dBA.

Figure 11.41 Contrasting ground surfaces around a tramway in Grenoble (Image 11 [175]).
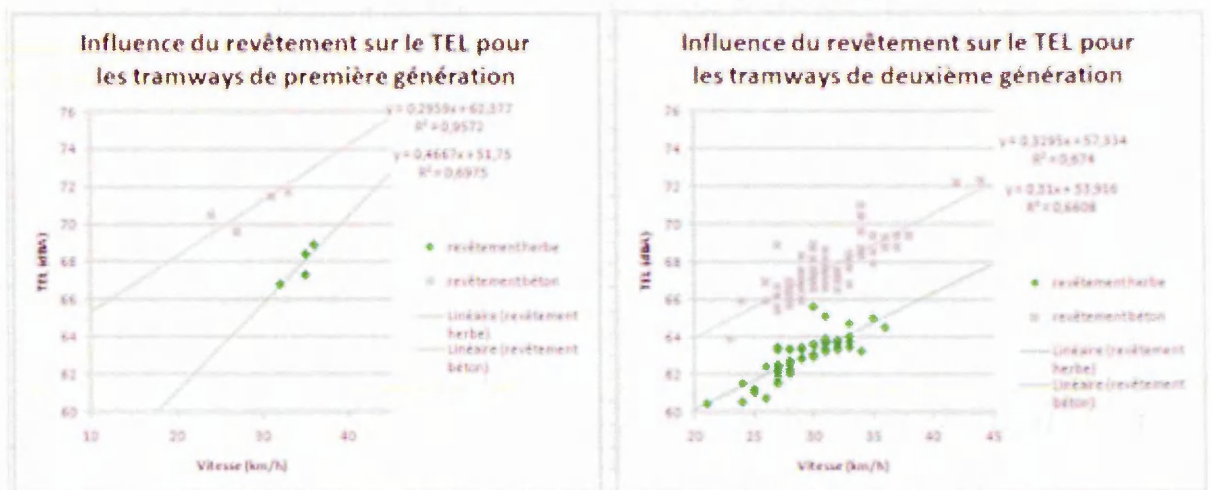
Figure 11.42 Results of noise measurements for two kinds of tram vehicles at 'hard' and 'soft' ground situations (Image 27 [175]). TEL is SEL corrected for length of tramway and speed of vehicles.

The noise from a tramway is radiated primarily by the tram wheels (see Figure 11.43). In making BEM calculations to compare with data each wheel has been modelled by an array of three point sources at heights of 0.05 m, 0.3 m and 0.5 m (see Figure 11.44). The tram noise spectrum given in HOSANNA deliverable 2.3 [168] has been assumed. In the absence of impedance information for the grass shown in Figure 11.41, six 'grass' type impedance spectra, corresponding to six values of the effective flow resistivity in the 2-parameter slit pore model have been used in the calculations. The results in Table 11.23 indicate that reductions of between 1 and 6 dBA are predicted for trams on the further track and of between 0.5 and 4.5 dBA for trams on the nearer track. The predictions for the lowest source height (0.05 m) and a 'grass' flow resistivity of 200 kPa s m^{-2} are closest to results of the Grenoble tramway measurements.
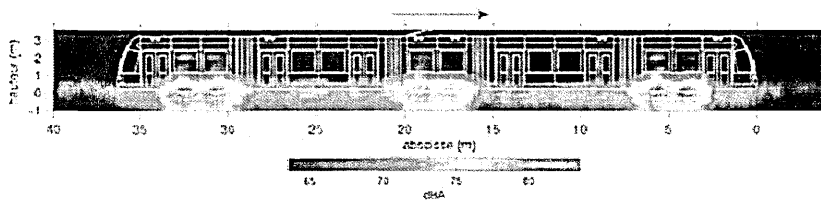
Figure 11.43 Sound intensity map of a tram vehicle (Image 6 [175])
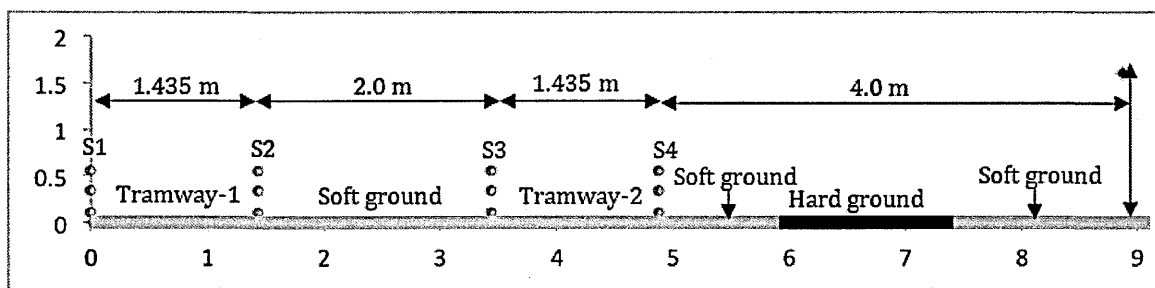
Figure 11.44 Side elevation of geometry assumed for predicting Grenoble tram track noise levels [175].

Table 11.23 Predicted insertion losses due to the introduction of grass near a tramway at Grenoble [175].

Ground parameters		Source height 'Hs' (m)	Insertion Loss (dB) Frequency range: 25 - 10 kHz					
Flow resistivity (kPa s m^{-2})	Porosity		Source-S1	Source-S2	Combined S1&S2	Source-S3	Source-S4	Combined S3&S4
100	0.5	0.05	6.6	5.9	**6.3**	5.0	4.1	**4.5**
		0.3	3.0	2.1	**2.6**	0.8	0.6	**0.7**
		0.5	0.5	0.8	**0.7**	1.3	1.1	**1.2**
200	0.5	0.05	5.1	4.6	**4.9**	3.9	3.1	**3.5**
		0.3	3.2	2.3	**2.8**	1.0	0.4	**0.7**
		0.5	0.8	0.9	**0.9**	1.1	0.8	**0.9**
300	0.5	0.05	4.3	3.9	**4.1**	3.3	2.5	**2.9**
		0.3	3.2	2.4	**2.8**	1.0	0.3	**0.6**
		0.5	1.0	0.9	**0.9**	0.9	0.6	**0.8**
500	0.5	0.05	3.5	3.1	**3.3**	2.6	2.0	**2.3**
		0.3	2.9	2.2	**2.6**	1.0	0.3	**0.6**
		0.5	1.0	0.9	**1.0**	0.8	0.5	**0.6**
1000	0.5	0.05	2.5	2.2	**2.4**	1.9	1.4	**1.7**
		0.3	2.4	1.9	**2.2**	0.9	0.2	**0.5**
		0.5	1.0	0.8	**0.9**	0.6	0.3	**0.5**
2000	0.5	0.05	1.8	1.6	**1.7**	1.4	1.0	**1.2**
		0.3	1.9	1.5	**1.7**	0.7	0.1	**0.4**
		0.5	0.9	0.7	**0.8**	0.4	0.2	**0.3**

11.8 Comparisons of surface transport noise attenuation predictions

Figure 11.45 compares example source spectra due to road traffic noise, railway noise and tramway noise. Table 11.24 compares the insertion loss for road traffic noise, railway noise and tramway noise due to identical ground treatment and receiver heights and locations being considered. The ground treatments start at a distance of 2.5 m from nearest noise source for three cases. The receiver heights and locations for road traffic noise, railway noise and tramway noise calculations are identical. The magnitude of source spectrum has not much effect on insertion loss as it is applied before and after the ground treatments (see Section 11.2).
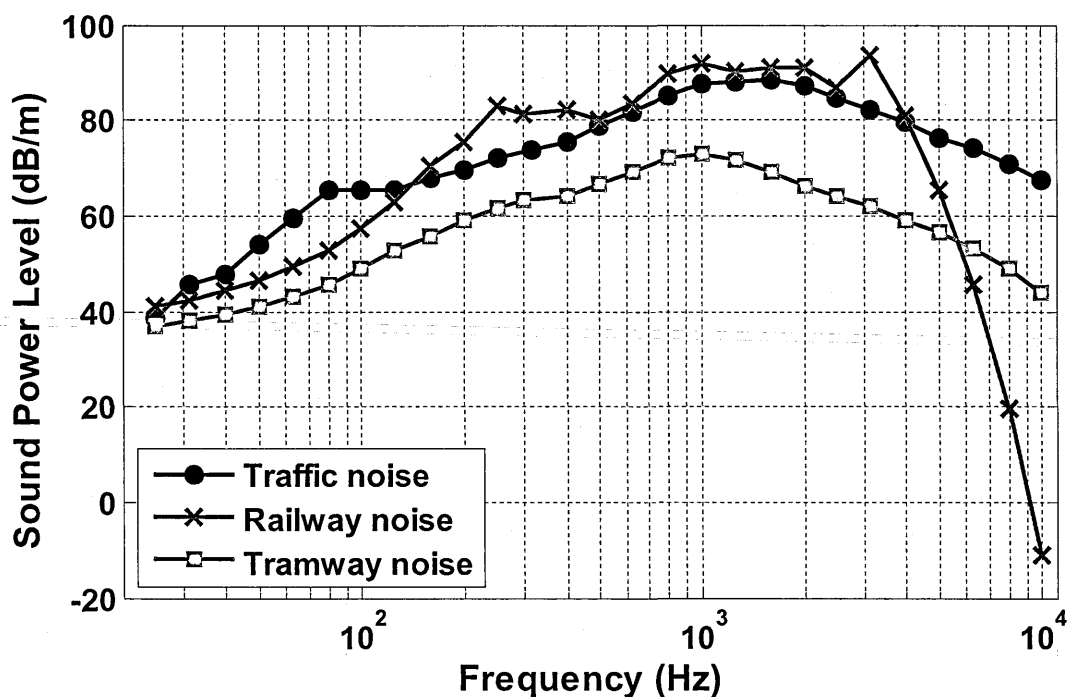
Figure 11.45 Source spectra for (i) a road-tyre noise (black-circles) with a height of 0.01 m, vehicle travelling at speed of 70 km/h calculated using the HARMONOISE method [104]; (ii) at 1 m corresponding to a (UK) train (blue-crosses) running at 145 km/h [173] ; (iii) tram noise (red-squares) given in HOSANNA report 2.3 [168].

The major differences between road traffic, railway and tram noise are the shape of the source spectrum, the locations of the sources and the number of sources. All three source spectra peak at 1 kHz. However, the railway noise spectrum differs from the other two. The road traffic noise sources in lanes 1 and 2 (see Figure 11.2) correspond to railway noise sources S1 and S2 (see Figure 11.29) and to tramway noise sources S1 and S2 (see Figure 11.39) respectively. The distance between two lanes is assumed to be 3.5 m, between two railway sources on a track is 1.43 m and two tramway sources on a track is 1.45 m. Road traffic noise sources are assumed to be at 0.01 m, 0.3 m and 0.75 m, with the major contributions being those from the sources heights of 0.01 m and 0.3 m. However, the railway and tramway noise are assumed to be due to a single source at heights of 0.431 m and 0.05 m respectively. Traffic noise and tramway noise sources are assumed to be above a flat ground. However, the railway noise source is above a profiled track (see Figure 11.29).

Ground treatments are more effective to attenuate noise at near grazing angles. Consequently the more elevated source i.e. railway (h = 0.431 m), different ground treatments result in less insertion loss than if the sources are closer to the ground i.e. tramway noise (h = 0.05 m) and tyre/road noise (h = 0.01 m). Similarly, a source height in the middle of above two i.e. engine noise source (h = 0.3 m) gives insertion loss values in between the two. These conclusions are summarizes in Table 11.24. It is concluded that the different ground treatments are most effective for tramway noise, least effective to railway noise and that the effectiveness on traffic noise is in between these two.

Table 11.24 Comparison between road traffic noise, railway noise and tramway noise attenuation due to different ground treatments.

Noise source type (Road traffic noise, Railway noise, Tramway noise)	x m	Reduction (dB) compared with smooth hard ground					
		$H_r = 1.5$ m, r = 50 m			$H_r = 4.0$ m, r = 50 m		
		Lane 1/ Source 1	Lane 2/ Source 2	**Combi ned**	Lane 1/ Source 1	Lane 2/ Source 2	**Combi ned**
Replacing hard ground with soft ground (#41 long grass, see Table 11.2)							
2 lane urban road	2.5	8.9	8.3	**8.6**	4.0	2.5	**3.2**
2 track railway	2.5	7.1	7.2	7.1	1.1	1.0	1.0
2 track tramway	2.5	10.0	9.4	9.7	3.4	2.8	3.1
5.85 m wide and 0.3 m high parallel wall array; 30 × 0.05 m thick walls, 0.2 m centre-to-centre spacing							
2 lane urban road	2.5	7.8	7.5	**7.6**	6.2	4.9	5.6
2 track railway	2.5	6.9	6.0	6.5	1.8	2.1	1.9
2 track tramway	2.5	9.4	8.7	9.0	9.7	8.3	8.9
5.85 m wide and 0.3 m high square lattice							
2 lane urban road	2.5	9.1	8.2	8.7	7.2	5.4	6.3
2 track railway	2.5	8.5	7.0	7.9	2.1	2.4	2.2
2 track tramway	2.5	10.9	9.6	10.2	11.3	9.4	10.2
25.0 m wide mixed impedance ground with 1.0 m wide strips of alternative hard and gravel strip							
2 lane urban road	2.5	8.0	7.1	**7.5**	3.6	2.2	**2.8**
2 track railway	2.5	6.9	6.5	6.8	0.9	1.0	0.9
2 track tramway	2.5	9.3	8.6	8.9	4.4	3.4	3.9

11.9 Conclusions

In this chapter the attenuations due to various ground treatments have been studied. The ground treatments that have been considered include,

- Replacing hard ground with soft ground.

- Introducing low height roughness (Parallel walls, Lattice and Triangles).

- Single or multiple impedance discontinuity.

- Growing dense crops.

Insertion losses near to various road traffic noise sources, railway noise and tramway noise have been calculated by subtracting the predicted SPL with ground treatments from those predicted without any treatments. The insertion losses have been calculated for several receiver locations and heights for the appropriate source spectrum.

Insertion losses have been calculated that result from replacing hard ground with different types of acoustically soft ground along the road sides. It is predicted that replacing 45 m of hard ground by any kind of soft ground gives at least 5 dB insertion loss at a 1.5 m high receiver 50 m from the road. A low flow resistivity ground surface can give up to 3 dB more traffic noise attenuation than a high flow resistivity ground. Grassland left untouched and allowed to grow wild improves traffic noise attenuation performance. Investigations based on published information about the acoustical properties of ploughed ground suggest that ploughing helps relatively little to improve the traffic noise attenuation. Cultivating the intervening ground (between the road and receivers) and adding crops such

that they block direct line of sight between the noise source and the receiver (at least partially) can result in an additional IL of between 3 and 5 dB. On the other hand, thinner crops like winter wheat are predicted to increase the reduction due to soft ground effect by less than 1 dB.

The insertion losses due to parallel wall arrays increase with increase in the width of the array. The predicted insertion loss due to a 0.3 m high and 1.65 m wide wall array is 5.8 dB for a receiver placed at a height of 1.5 m and at a distance of 50 m from the nearest lane source. The insertion loss is increased by 3 dB if the width of wall array is increased to 12.05 m. The predicted effects due to a parallel wall array are reduced if the receiver is closer to the road or higher. The ILs due to parallel walls are angle dependent and the effect of parallel walls deteriorates with the increase in angle (> 30°) between source - receiver axis and the normal to the parallel wall array. Calculations for different cross-sectional shape roughness show that the shape has negligible effect on the overall insertion loss near to a road.

The attenuation performance of a lattice roughness structure is not azimuthal angle dependent. The predicted insertion loss due to a 0.3 m high and 1.53 m wide lattice array is 5.9 dB for a receiver placed at a height of 1.5 m and at a distance of 50 m from the nearest lane source. The insertion loss due to a lattice is doubled, by increasing the width of lattice array to 24.05 m. For a given height and width of the array, the lattice structure gives the best attenuation performance of the considered roughness configurations. Recessed lattices can be used where there are restrictions on above ground constructions close to roads. It is concluded from BEM predictions, that the insertion loss for a recessed lattice is between 3 dB

and 4 dB lower than that predicted for a 0.3 m high lattice. It is possible to recover some of the reduced insertion loss by starting them closer to the noise source or by making the recessed configurations deeper than 0.3 m or by increasing the width of the lattice array. Roughness array width and height are the most important factors in determining the insertion loss.

Dividing a single width of soft ground into alternating strips of hard and soft surfaces does not improve the IL. The overall width of the soft surface is the main factor. If the strip of soft ground is raised (up to 30 cm) above ground, the IL can be enhanced by up to 3 dB. A strip raised at one side only (i.e. with a triangular cross section) is more effective if the slope is facing the receiver rather than the source.

The attenuation of noise from the two further lanes in a 2 x 2 motorway can be improved significantly by introducing 2 m wide ground treatments on a central reservation.

Railway noise can also be mitigated by introducing ground treatments. Insertion losses at a receiver placed at height of 1.5 m and at a distance of 50 m / 100 m from the edge of the nearest track of between 5 dB and 10 dB for the nearest railway track and between 3 dB and 6 dB for furthest railway track can be obtained by placing a 0.3 m high x 5.85 m wide parallel wall or lattice array 2.5 m m from the nearest track. Predictions were made also of the effect of inserting acoustically softer strips on otherwise hard ground near railway tracks. It was predicted that replacing a hard ground between the tracks and a 1.5 m high receiver 50 m away by grass covered ground can lead to an insertion loss of up to

7 dB. Replacing hard slab tractor sleepers by porous concrete gives an additional IL of between 3.0 and 5.5 dB.

Predictions of tramway noise above different ground surfaces indicate that covering the ground under and alongside the tracks will give an insertion loss of up to 6 dB for grass with a flow resistivity of about 100 kPa s m^{-2} at a receiver situated 4 m from the edge of the nearest track and a height of 1.5 m. However, as flow resistivity is increased the insertion loss becomes progressively smaller. Replacing hard ground between and alongside tram tracks with soft ground has been measured and predicted to give significant noise attenuation. An insertion loss of between 5 dB and 10 dB can be obtained by replacing hard ground between tracks with gravel.

Chapter 12

12. Summary of conclusions and suggestions for further work

12.1　Conclusions

Growing demand on transportation, road and railway networks has resulted in increased levels of annoyance from road traffic and railway noise. The traditional way of reducing noise is to erect a noise barrier which divides the communities and is ineffective for long source-barrier-receiver distances. The main aim of the HOSANNA project that has supported the development of the thesis is to develop new, efficient and cost-effective ways of reducing traffic noise by optimizing the use of green areas, green surfaces and other natural elements in combination with artificial elements in urban and rural environments for reducing

the noise impact of road and rail traffic. This thesis has studied the possibilities for exploiting ground effects.

Significant insertion losses near to road traffic, railways and tramways are predicted due to ground treatments such as, replacing hard ground with soft ground, introducing low height roughness, single or multiple impedance discontinuity and growing dense crops.

12.1.1   *Porous and mixed impedance surfaces*

A comparative study of seven impedance models (Delany and Bazley, Miki, Taraldsen, Zwikker and Kosten (phenomenological), Attenborough four parameter, Identical pores (Cylindrical, Slit, Triangular and Rectangular), variable porosity and Johnson Allard Umnova) has been carried out by studying the sound propagation over 47 outdoor surfaces. It is concluded that the two parameters variable porosity model is the best to characterize grassland. The slit pore and phenomenological models gives equally good fits to data over most of ground sites specially, where other models failed to give good fits such as forest floors and *'gravel in a pit'* sites. The slit pore layer model gives good agreement to data obtained over low flow resistivity gravel using measured impedance parameters. However, the phenomenological model fails to give good agreement to low flow resistivity data over gravel. Finally the slit pore model was selected to carry out research work as its use resulted in minimum error for most of ground sites. The impedance parameters obtained through ground characterization over 47 different outdoor surface have been used to calculate the insertion loss for replacing the hard ground along the road side with porous ground. It is concluded that replacing 45 m of hard ground by any kind of soft ground gives at least 5 dB insertion loss at a 1.5

m high receiver 50 m from the road. Grassland left untouched and allowed to grow wild gives up to 3 dB higher traffic noise attenuation at a 1.5 m high receiver than ground which is compacted for example as a result of frequent maintenance such as a lawn. Dividing a single width of soft ground into alternating strips of hard and soft surfaces does not improve the IL. The overall width of the soft surface is the main factor. If the strip of soft ground is raised (up to 30 cm) above ground, the IL can be enhanced by up to 3 dB. A strip raised at one side only (i.e. with a triangular cross section) is more effective if the slope is facing the receiver rather than the source.

Laboratory experiments have been carried out to investigate the effects of finite impedance strips and patches in an otherwise hard surface. The measured EA spectra suggest that there is little advantage in using 3D patches compared with 2D strips. Study of sound propagation over mixed impedance ground concludes that the De Jong model can be used for the larger scale single impedance discontinuities and source-receiver geometries considered for the HOSANNA project. The insertion loss predictions associated with replacing hard ground with soft ground using either BEM or the De Jong model have a maximum difference of 0.5 dB. Computations using the De Jong model are much faster than numerical predictions using BEM. On the other hand it has been found that the De Jong model fails to give accurate predictions of sound propagation over mixed impedance ground having multiple impedance discontinuities. The Fresnel zone method has been used also to predict sound propagation over single and multiple impedance discontinuities. The Fresnel zone method does not give very good agreement with BEM predictions over single or multiple impedance discontinuities

of either EA spectra or insertion loss. It is concluded that the Fresnel zone method is not a very appropriate choice for predicting insertion loss over mixed impedance ground surfaces consisting of single or multiple impedance discontinuities.

12.1.2   Vegetation

Laboratory measurements carried out over regular arrangements of 0.5 m long PVC pipes placed on a hard ground and a soft ground respectively show that conjunctive use of soft ground effects and sonic crystal effects could be useful to attenuate traffic noise. In fact this can happen 'naturally' with a tree belt. Measurements and predictions suggest that a quasi-periodic array with a perturbation in cylinder location having an S.D. of $2.0r$ performs better at high frequencies than either periodic or random arrangements while also reducing the negative attenuation associated with the pass bands (focusing). It has been shown also that the 3D problem of predicting propagation through sparse arrays of vertical cylinders on a (hard or soft) plane can be solved fairly accurately by adding two 2D predictions i.e of mulitple scattering by cylinders and of propagation from a point or line source over an impedance plane for a given source-receiver geometry. The agreement between data and predictions obtained in this manner is found to be very good.

The work has been extended to study the sound propagation through crops outdoors. Horizontal level difference data used to study the sound propagation through crops show that sound attenuation occurs due to multiple scattering between the stems and leaves, loss of coherence and viscous and thermal losses due to foliage. However, the major contribution to attenuation due to crops is due to viscous and thermal losses, which can be predicted by using an empirical

formula. At lower frequencies the ground effect is dominant and there is little or no crop effect. At higher frequencies above 3-4 kHz the crop effect is dominant. It was also found that the ground and crop effects can be treated independently and can be added to obtain the total effect. Green leaf crops result in more attenuation than dry crops with fallen leaves. Cultivating the intervening ground (between the road and receivers), adding crops such that they block direct line of sight between the noise source and the receiver (at least partially) is predicted to result in up to 5 dB additional IL at a 1.5 m high receiver. Vehicle pass-by measurements made near two hedges along the perimeter road at The Open University campus in Milton Keynes, show that a 2 m wide hedge can attenuate traffic noise between 2 and 3 dBA. However, half of this attenuation comes from ground effect due to the soft ground on which the hedge is planted.

12.1.3   Rough surfaces

A comprehensive study of sound propagation over rough surfaces created in the laboratory concludes that, in comparison to that over a smooth hard surface, the ground effect dips, corresponding to the first destructive interference, observed in EA spectra measured over surfaces supporting randomly and periodic spaced roughness elements, which are small compared to the incident wavelengths, are at significantly lower frequencies. This is a useful phenomenon to be exploited for traffic noise attenuation. Outdoor measurements over low brick arrays confirm that a careful design of rough surfaces along the road can be used to attenuate traffic noise. A 3D lattice structure design is found to be very effective and useful for traffic noise attenuation. Moreover, a square lattice structure is azimuthal angle independent. An indirect method was developed to predict the sound propagation

over 3D lattice using a 2D BEM. Measured level difference data over 3D lattice structures outdoors show very good agreement with BEM predictions obtained using a raised platform, the top of which is defined using an effective impedance model. Parallel walls can also be modelled in BEM using a raised impedance platform with an effective surface impedance to speed up the predictions. The effective impedance model for parallel walls was obtained using either slit-pore or Kelders-Allard models. However the Kelders-Allard model is found to contradict the observed data behaviour as the spacing between elements is increased. It is concluded that the slit pore layer model is the more appropriate to model parallel walls and lattices as effective impedances.

The generation and propagation of surface waves over rough surfaces reduces the insertion loss. It was found that the surface wave over laboratory parallel walls can be attenuated by placing absorbing material such as felt in between the walls. Investigation of surface wave propagation over larger scale parallel walls has been carried out using BEM. The ground type with lowest flow resistivity value (representing gravel) is predicted to give the greatest surface wave attenuation. Since the surface wave is predicted to occur at relatively low frequencies, after A-weighting the predicted improvement in insertion loss from attenuation of the surface wave is limited to about 1 dB. There is not any significant improvement in insertion loss by filling the spaces between the walls with gravel by more than 50 %.

Roughness array width and height are the most important factors in determining the insertion loss. The attenuation performance of a square lattice roughness structure is not angle dependent. For a given height and width of the

array, the lattice structure gives the best attenuation performance of the considered roughness configurations. Recessed lattices can be used where there are restrictions on above ground constructions close to roads but lead to about 3 dB less insertion loss than the equivalent raised structure located in the same place.

12.2 Future work

12.2.1   Meteorological influences on ground effects.

In reality the performance of the ground treatments proposed predicted and measured in this thesis will be influenced by meteorological effects as is the case with conventional noise barrier performance. Investigations are necessary therefore on the influence of meteorological effects over attenuation performance due to artificially created and naturally occurring ground surfaces. Of particular interest might be the effects of turbulence and downward refraction which tend to reduce the destructive interference component of ground effects. Laboratory experiments on the effects of refraction can be carried out by using curved surfaces [176], [177]. Numerical studies will need the use of 3D codes such as PSTD [171].

12.2.2   Back-scattered sound from rough ground

Most of the BEM calculations carried out have assumed that the traffic noise source on the road, the ground treatments to attenuate noise start at a distance of 2.5 m from the road and a receiver is placed at some greater distance from the road. Roughness is 0.3 m high, therefore some sound will be back-

scattered towards the road. Indeed some effects of back scattering were observed in the results of calculations for a 2 x 2 lane motorway when 0.3 high roughness was also placed at central reservation (see Chapter 11, Section 11.4.2). This results in reverberation between the rough surface alongside the road and the rough surface at the central reservation. This reverberation was predicted to reduced considerably by covering the last wall of central reservation and first wall of ground treatment with porous material. In other words, the back scattering of sound can be attenuation by making the first wall of the ground treatment sound absorbing. Absorbent on or between the first few walls has another advantage of reducing the surface wave propagation (see Chapter 8).

Although, the backscattering can be reduced by sound absorbing material, some further work is needed to investigate the effect of backscattered sound on a receiver on the opposite side of the road.

12.2.3   Resonant roughness.

The initial studies carried out so far on the additional low frequency ground effect maximum introduced by resonant roughness are sufficiently encouraging to warrant further studies of the effects of incorporating resonance behaviour in roughness elements. Forms of resonant structures similar to those investigated already for sonic crystals including split ring and elastic shells [141], [147] could be investigated.

12.2.4   Mystery LF effects with SCs.

The appearances of extra low frequency peaks below the first band gap in insertion loss spectra measured due to vertical cylinder arrays on a ground plane

remain unexplained and need further investigation. The possibility that they are

due to the finite width of the array needs to be tested further. Recently there has

been interest also in potential effects due to the finite height of the cylinders [178].

References

[1]   K. Attenborough, K. M. Li, and K. Horoshenkov, *Predicting Outdoor Sound*. London (UK): Taylor and Francis, 2007.

[2]   P. M. Morse and K. U. Ingard, *Theoretical acoustics*. Princeton university press, Reprinted edition, 1986.

[3]   I. Fredholm, "Sur une classe d'équations fonctionnelles," *Acta Math.*, vol. 27, no. 1, pp. 365–390, Dec. 1903.

[4]   A. Daumas, "Study of diffraction by a thin screen set-up on ground," *J. Acoust.*, vol. 40, pp. 213–222, 1978.

[5]   R. Seznec, "Diffraction of sound around barriers: Use of the boundary elements technique," *J. Sound Vib.*, vol. 73, no. 2, pp. 195–209, Nov. 1980.

[6]   S. N. Chandler-Wilde and D. C. Hothersall, "Sound propagation above an inhomogeneous impedance plane," *J. Sound Vib.*, vol. 98, no. 4, pp. 475–491, Feb. 1985.

[7]   D. C. Hothersall, S. N. Chandler-Wilde, and M. N. Hajmirzae, "Efficiency of single noise barriers," *J. Sound Vib.*, vol. 146, no. 2, pp. 303–322, Apr. 1991.

[8]   S. N. Chandler-Wilde and D. C. Hothersall, "Efficient calculation of the green function for acoustic propagation above a homogeneous impedance plane," *J. Sound Vib.*, vol. 180, no. 5, pp. 705–724, Mar. 1995.

[9]   S. N. Chandler-Wilde and D. C. Hothersall, "A uniformly valid far field asymptotic expansion of the green function for two-dimensional propagation above a homogeneous impedance plane," *J. Sound Vib.*, vol. 182, no. 5, pp. 665–675, May 1995.

[10] S. Taherzadeh, K. M. Li, and K. Attenborough, "A hybrid BIE/FFP scheme for predicting barrier efficiency outdoors," *J. Acoust. Soc. Am.*, vol. 110, no. 2, p. 918, Aug. 2001.

[11] P. M. Laughlin, "Outdoor sound propagation and the Boundary Element Method," 2005.

[12] S. N. Chandler-Wilde and S. Langdon, "Boundary element methods for acoustics."

[13] HOSANNA Deliverable 2.1 Technical Report HSNNA_21_TRP_2010_06_08, "Innovative barriers exploiting natural materials," 2010.

[14] V. Twersky, "Multiple Scattering of Radiation by an Arbitrary Configuration of Parallel Cylinders," *J. Acoust. Soc. Am.*, vol. 24, no. 1, p. 42, Jan. 1952.

[15] L. Rayleigh, "On the influnce of obstacles arranged in rectangular order upon the properties of a medium," *Phil. Mag.*, vol. 34, no. 5, pp. 481–502, 1892.

[16] C. M. Linton and D. V. Evans, "The interaction of waves with arrays of vertical circular cylinders," *J. Fluid Mech.*, vol. 215, no. -1, p. 549, Apr. 2006.

[17] F. Zaviska, "Uber die beugung elektromagnetischer wellen an parallelen, unendlich langen kreisylindern," *Ann. Phys.*, vol. 40, p. 1023, 1913.

[18] C. M. Linton and P. A. Martin, "Multiple scattering by random configurations of circular cylinders: Second-order corrections for the effective wavenumber," *J. Acoust. Soc. Am.*, vol. 117, no. 6, p. 3413, Jun. 2005.

[19] P. Boulanger, K. Attenborough, Q. Qin, and C. M. Linton, "Reflection of sound from random distributions of semi-cylinders on a hard plane: models and data," *J. Phys. D. Appl. Phys.*, vol. 38, no. 18, pp. 3480–3490, Sep. 2005.

[20] O. Umnova, K. Attenborough, and C. M. Linton, "Effects of porous covering on sound attenuation by periodic arrays of cylinders," *J. Acoust. Soc. Am.*, vol. 119, no. 1, p. 278, Jan. 2006.

[21] I. S. Gradshteyn and I. M. Ryzhik, *Table of integrals, series and products*. Academic Press, 1980.

[22]   R. W. Clough, *The Finite Element Method in Plane Stress Analysis*. American Society of Civil Engineers, 1960, p. 35.

[23]   O. C. Zienkiewicz and K. Cheung, "Finite elements in the solution of field problems," *Engineer*, vol. 200, pp. 507–510, 1965.

[24]   Y. J. Kang, "Sound transmission through elastic porous wedges and foam layers having spatially graded properties," *J. Acoust. Soc. Am.*, vol. 102, no. 6, p. 3319, Dec. 1997.

[25]   Y. J. Kang, "A finite element model for sound transmission through foam-lined double-panel structures," *J. Acoust. Soc. Am.*, vol. 99, no. 5, p. 2755, May 1996.

[26]   T. Johansen, J.-F. Allard, and B. Brouard, "Finite element method for predicting the acoustical properties of porous samples," *Acta Acust.*, vol. 3, pp. 487–491, 1995.

[27]   R. Panneton, "Numerical prediction of sound transmission through finite multilayer systems with poroelastic materials," *J. Acoust. Soc. Am.*, vol. 100, no. 1, p. 346, Jul. 1996.

[28]   R. Panneton, "An efficient finite element scheme for solving the three-dimensional poroelasticity problem in acoustics," *J. Acoust. Soc. Am.*, vol. 101, no. 6, p. 3287, Jun. 1997.

[29]   M. S. Ressl and P. E. Wundes, "Design of an Acoustic Anechoic Chamber for Application in Hearing Aid Research," *Recent Adv. Acoust. Music*, pp. 18–23, 2003.

[30]   M. R. Schroeder, "Integrated-impulse method measuring sound decay without using impulses," *J. Acoust. Soc. Am.*, vol. 66, no. 2, p. 497, Aug. 1979.

[31]   A. V. Oppenheim, R. W. Schafer, and J. R. Buck, "Design of FIR filters by windowing," in in *Discrete – time signal processing*, Second edi., Pearson, New York, 1998, pp. 465–471.

[32]   K. Attenborough, I. Bashir, and S. Taherzadeh, "Outdoor ground impedance models.," *J. Acoust. Soc. Am.*, vol. 129, no. 5, pp. 2806–19, May 2011.

[33]   K. Attenborough, K. M. Li, and K. Horoshenkov, "Predicting the acoustical properties of outdoor ground surfaces," in in *Predicting Outdoor Sound*, 2007, pp. 25–100.

[34] L. E. Kinsler, A. R. Frey, and A. B. Coppens, *Fundamentals of acoustics*, Fourth edi. Wiley, 2000.

[35] U. Ingard, "On the Reflection of a Spherical Sound Wave from an Infinite Plane," *J. Acoust. Soc. Am.*, vol. 23, no. 3, p. 329, May 1951.

[36] B. Van Der Pol, "Theory of the reflection of the light from a point source by a finitely conducting flat mirror, with an application to radiotelegraphy," *Physica*, vol. 2, no. 1–12, pp. 843–853, Jan. 1935.

[37] J. W. L. S. Rayleigh, *Theory of Sound (Volumes I & II)*. Dover publications, New York (USA), 1877.

[38] K. Attenborough, "Acoustical characteristics of porous materials," *Phys. Rep.*, vol. 82, no. 3, pp. 179–227, Feb. 1982.

[39] C. Zwikker and C. W. Kosten, *Sound absorbing materials*. Elsevier publishing company, New York (USA), 1949.

[40] M. C. Bérengier, M. R. Stinson, G. A. Daigle, and J.-F. Hamet, "Porous road pavements: Acoustical characterization and propagation effects," *J. Acoust. Soc. Am.*, vol. 101, no. 1, p. 155, Jan. 1997.

[41] M. E. Delany and E. N. Bazley, "Acoustical properties of fibrous absorbent materials," *Appl. Acoust.*, vol. 3, no. 2, pp. 105–116, Apr. 1970.

[42] P. Dunn and W. A. Davern, "Calculation of acoustic impedance of multilayer absorbers," *Appl. Acoust.*, vol. 19, pp. 321–334, 1986.

[43] Y. Miki, "Acoustical properties of porous materials - Modifications of Delany and Bazley models," *J. Acoust. Soc. Japan*, vol. 11, no. 1, pp. 19–24, 1990.

[44] Y. Miki, "Acoustical properties of porous materials – Generaliztions of empirical models," *J. Acoust. Soc. Japan*, vol. 11, no. 1, pp. 25–28, 1990.

[45] G. Taraldsen and H. Jonasson, "Aspects of ground effect modeling.," *J. Acoust. Soc. Am.*, vol. 129, no. 1, pp. 47–53, Jan. 2011.

[46] G. Taraldsen, "The Delany-Bazley Impedance Model and Darcy's Law," *Acta Acust. united with Acust.*, vol. 91, no. 1, p. 10, 2005.

[47] K. Attenborough, "Acoustical impedance models for outdoor ground surfaces," *J. Sound Vib.*, vol. 99, no. 4, pp. 521–544, Apr. 1985.

[48] K. Attenborough, "Acoustical characteristics of rigid fibrous absorbents and granular materials," *J. Acoust. Soc. Am.*, vol. 73, no. 3, p. 785, Mar. 1983.

[49] M. A. Biot, "Theory of Propagation of Elastic Waves in a Fluid-Saturated Porous Solid. II. Higher Frequency Range," *J. Acoust. Soc. Am.*, vol. 28, no. 2, p. 179, Mar. 1956.

[50] P. C. Carman, *Flow of gasses through porous media*. Academic Press, London (UK), 1956.

[51] K. Attenborough, "On the acoustic slow wave in air-filled granular media," *J. Acoust. Soc. Am.*, vol. 81, no. 1, p. 93, Jan. 1987.

[52] M. R. Stinson, "The propagation of plane sound waves in narrow and wide circular tubes, and generalization to uniform tubes of arbitrary cross-sectional shape," *J. Acoust. Soc. Am.*, vol. 89, no. 2, p. 550, Feb. 1991.

[53] M. R. Stinson and Y. Champoux, "Propagation of sound and the assignment of shape factors in model porous materials having simple pore geometries," *J. Acoust. Soc. Am.*, vol. 91, no. 2, p. 685, Feb. 1992.

[54] Y. Champoux and M. R. Stinson, "On acoustical models for sound propagation in rigid frame porous materials and the influence of shape factors," *J. Acoust. Soc. Am.*, vol. 92, no. 2, p. 1120, Aug. 1992.

[55] K. Attenborough, "Models for the acoustical properties of air-saturated granular media," *Acta Acust.*, vol. 1, pp. 213–226, 1993.

[56] D. K. Wilson, "Relaxation-matched modeling of propagation through porous media, including fractal pore structure," *J. Acoust. Soc. Am.*, vol. 94, no. 2, p. 1136, Aug. 1993.

[57] D. K. Wilson, "Relaxation models for the acoustical properties of sound-absorbing porous materials," *Proc. Noise Conf., Pennsylvania State Univ.*, pp. 85–90, 1997.

[58] R. J. Donato, "Impedance models for grass-covered ground," *J. Acoust. Soc. Am.*, vol. 61, no. 6, p. 1449, Jun. 1977.

[59] R. Raspet and J. M. Sabatier, "The surface impedance of grounds with exponential porosity profiles," *J. Acoust. Soc. Am.*, vol. 99, no. 1, p. 147, Jan. 1996.

[60] O. Umnova, K. Attenborough, and K. M. Li, "A cell model for the acoustical properties of pickings of spheres," *Acta Acust.*, vol. 87, pp. 226–235, 2001.

[61] P. Boulanger, K. Attenborough, S. Taherzadeh, T. Waters-Fuller, and K. M. Li, "Ground effect over hard rough surfaces," *J. Acoust. Soc. Am.*, vol. 104, no. 3, p. 1474, Sep. 1998.

[62] A. Sommerfeld, "On propagation of waves in wireless telegrpahy," *Ann. Phys.*, vol. 28, pp. 665–737, 1909.

[63] H. Weyl, "Ausbreitung elektromagnetisher wellen uber einen eben-leiter" ("Propagation of electromagnetic waves over a conducting plane)," *Ann. Phys.*, vol. 60, pp. 481–500, 1919.

[64] B. Van der Pol, "Theory of the reflection of the light from a [oint source by a finitely conducting flat mirror with an application to radiotelegraphy," *Physica*, 1935.

[65] C. F. Chein and W. W. Soroka, "Sound propagation along an impedance plan," *J. Sound Vib.*, vol. 43, no. 1, pp. 9–20, 1975.

[66] R. J. Donato, "Propagation of a spherical wave near a plane boundary with a complex impedance," *J. Acoust. Soc. Am.*, vol. 60, no. 1, p. 34, Jul. 1976.

[67] K. Attenborough, S. I. Hayek, and J. M. Lawther, "Propagation of sound above a porous half-space," *J. Acoust. Soc. Am.*, vol. 68, no. 5, pp. 1493–1501, Nov. 1980.

[68] S. Taherzadeh and K. Attenborough, "Deduction of ground impedance from measurements of excess attenuation spectra," *J. Acoust. Soc. Am.*, vol. 105, no. 3, p. 2039, Mar. 1999.

[69] NORDTEST ACOU 104, "Ground Surfaces: Determination of acoustic impedance, Nordic innovation centre," 1999.

[70] NORDTEST ACOU 104, "Revision of NT ACOU 104: Measurement of the acoustic impedance of ground, Nordic innovation centre," 2006.

[71] ANSI/ASA S1.18, "Method for Determining the Acoustic Impedance of Ground Surfaces, American National Standard, revision of S1.18-1998," 2010.

[72] C. Nocke, V. Mellert, T. Waters-Fuller, K. Attenborough, and K. M. Li, "Impedance deduction from broad-band, point-source measurements at grazing incidence," *Acta Acust. united with Acust.*, vol. 83, no. 6, p. 6, 1997.

[73] M. Abramowitz and I. A. Stegun, "Eq. 7.1.20," in in *Handbook of mathematical functions with formulas, graphs and mathematical tables*, U.S. Department of Commerce, USA, 1972.

[74] C. Hutchinson-Howorth, K. Attenborough, and N. W. Heap, "Indirect in situ and free-field measurement of impedance model parameters or surface impedance of porous layers," *Appl. Acoust.*, vol. 39, no. 1–2, pp. 77–117, Jan. 1993.

[75] K. Heutschi, "Sound Propagation over Ballast Surfaces," *Acta Acust. united with Acust.*, vol. 95, no. 6, pp. 1006–1012, Nov. 2009.

[76] M. A. Biot, "Reflection on a Rough Surface from an Acoustic Point Source," *J. Acoust. Soc. Am.*, vol. 29, no. 11, p. 1193, Nov. 1957.

[77] M. A. Biot, "Generalized Boundary Condition for Multiple Scatter in Acoustic Reflection," *J. Acoust. Soc. Am.*, vol. 44, no. 6, p. 1616, Dec. 1968.

[78] V. Twersky, "On the Non-Specular Reflection of Plane Waves of Sound," *J. Acoust. Soc. Am.*, vol. 22, no. 5, p. 539, Sep. 1950.

[79] V. Twersky, "On the Nonspecular Reflection of Sound from Planes with Absorbent Bosses," *J. Acoust. Soc. Am.*, vol. 23, no. 3, p. 336, May 1951.

[80] V. Twersky, "On Scattering and Reflection of Sound by Rough Surfaces," *J. Acoust. Soc. Am.*, vol. 29, no. 2, p. 209, Feb. 1957.

[81] V. Twersky, "Acoustic Bulk Parameters of Random Volume Distributions of Small Scatterers," *J. Acoust. Soc. Am.*, vol. 36, no. 7, p. 1314, Jul. 1964.

[82] J. E. Burke and V. Twersky, "Elementary Results for Scattering by Large Ellipsoids," *J. Acoust. Soc. Am.*, vol. 38, no. 4, p. 589, Oct. 1965.

[83] V. Twersky, "Multiple scattering of sound by a periodic line of obstacles," *J. Acoust. Soc. Am.*, vol. 53, no. 1, p. 96, Jan. 1973.

[84] V. Twersky, "Multiple scattering of sound by correlated monolayers," *J. Acoust. Soc. Am.*, vol. 73, no. 1, p. 68, Jan. 1983.

[85] V. Twersky, "Reflection and scattering of sound by correlated rough surfaces," *J. Acoust. Soc. Am.*, vol. 73, no. 1, p. 85, Jan. 1983.

[86] V. Twersky, "Wavelength-dependent bulk parameters for coherent sound in correlated distributions of small-spaced scatterers," *J. Acoust. Soc. Am.*, vol. 77, no. 1, p. 29, Jan. 1985.

[87] R. J. Lucas, "Coherent response to a point source irradiating a rough plane," *J. Acoust. Soc. Am.*, vol. 74, no. S1, p. S122, Nov. 1983.

[88] I. Tolstoy, "The scattering of spherical pulses by slightly rough surfaces," *J. Acoust. Soc. Am.*, vol. 66, no. 4, p. 1135, Oct. 1979.

[89] I. Tolstoy, "Coherent sound scatter from a rough interface between arbitrary fluids with particular reference to roughness element shapes and corrugated surfaces," *J. Acoust. Soc. Am.*, vol. 72, no. 3, p. 960, Sep. 1982.

[90] I. Tolstoy, "Smoothed boundary conditions, coherent low-frequency scatter, and boundary modes," *J. Acoust. Soc. Am.*, vol. 75, no. 1, p. 1, Jan. 1984.

[91] H. Medwin, J. Bailie, J. Bremhorst, J. Savage, and I. Tolstoy, "The scattered acoustic boundary wave generated by grazing incidence at a slightly rough rigid surface," *J. Acoust. Soc. Am.*, vol. 66, no. 4, p. 1131, Oct. 1979.

[92] I. Tolstoy, "Rough surface boundary wave attenuation due to incoherent scatter," *J. Acoust. Soc. Am.*, vol. 77, no. 2, p. 482, Feb. 1985.

[93] H. Medwin, G. L. D'Spain, E. Childs, and S. J. Hollis, "Low-frequency grazing propagation over periodic steep-sloped rigid roughness elements," *J. Acoust. Soc. Am.*, vol. 76, no. 6, p. 1774, Dec. 1984.

[94] H. Medwin and G. L. D'Spain, "Near-grazing, low-frequency propagation over randomly rough, rigid surfaces," *J. Acoust. Soc. Am.*, vol. 79, no. 3, p. 657, Mar. 1986.

[95] M. S. Howe, "On the long range propagation of sound over irregular terrain," *J. Sound Vib.*, vol. 98, no. 1, pp. 83–94, Jan. 1985.

[96] K. Attenborough and S. Taherzadeh, "Propagation from a point source over a rough finite impedance boundary," *J. Acoust. Soc. Am.*, vol. 98, no. 3, p. 1717, Sep. 1995.

[97] J. P. Chambers, J. M. Sabatier, and R. Raspet, "Grazing incidence propagation over a soft rough surface," *J. Acoust. Soc. Am.*, vol. 102, no. 1, p. 55, Jul. 1997.

[98] K. Attenborough and T. Waters-Fuller, "Effective impedance of rough porous ground surfaces," *J. Acoust. Soc. Am.*, vol. 108, no. 3, p. 949, Sep. 2000.

[99] P. Boulanger, K. Attenborough, and Q. Qin, "Effective impedance of surfaces with porous roughness: Models and data," *J. Acoust. Soc. Am.*, vol. 117, no. 3, p. 1146, Mar. 2005.

[100] HOSANNA Deliverable 4.2 Technical Report HSNNA_42_TRP_2010_10_11, "Acoustical effects of hard rough surface," 2010.

[101] HOSANNA Deliverable 4.3 Technical Report HSNNA_43_TRP_2011_10_15, "Acoustical performance of parallel wall systems," 2011.

[102] L. A. M. van der Heijden and M. J. M. Martens, "Traffic noise reduction by means of surface wave exclusion above parallel grooves in the roadside," *Appl. Acoust.*, vol. 15, no. 5, pp. 329–339, Sep. 1982.

[103] H. Bougdah, I. Ekici, and J. Kang, "A laboratory investigation of noise reduction by riblike structures on the ground," *J. Acoust. Soc. Am.*, vol. 120, no. 6, p. 3714, Dec. 2006.

[104] HARMONOISE WP3 Technical Report, "Engineering method for road traffic and railway noise after validation and fine tuning," 2005.

[105] L. Kelders, J. F. Allard, and W. Lauriks, "Ultrasonic surface waves above rectangular-groove gratings," *J. Acoust. Soc. Am.*, vol. 103, no. 5, p. 2730, May 1998.

[106] M. Naghieh and S. I. Havek, "Diffraction of a point source by two impedance covered half-planes," *J. Acoust. Soc. Am.*, vol. 69, no. 3, p. 629, Mar. 1981.

[107] B. O. Enflo and P. H. Enflo, "Sound wave propagation from a point source over a homogeneous surface and over a surface with an impedance discontinuity," *J. Acoust. Soc. Am.*, vol. 82, no. 6, p. 2123, Dec. 1987.

[108] B. A. de Jong, A. Moerkerken, and J. D. van der Toorn, "Propagation of sound over grassland and over an earth barrier," *J. Sound Vib.*, vol. 86, no. 1, pp. 23–46, Jan. 1983.

[109] G. A. Daigle, J. Nicolas, and J. L. Berry, "Propagation of noise above ground having an impedance discontinuity," *J. Acoust. Soc. Am.*, vol. 77, no. 1, p. 127, Jan. 1985.

[110] D. C. Hothersall and J. N. B. Harriott, "Approximate models for sound propagation above multi-impedance plane boundaries," *J. Acoust. Soc. Am.*, vol. 97, no. 2, p. 918, Feb. 1995.

[111] P. Boulanger, T. Waters-Fuller, K. Attenborough, and K. M. Li, "Models and measurements of sound propagation from a point source over mixed impedance ground," *J. Acoust. Soc. Am.*, vol. 102, no. 3, p. 1432, Sep. 1997.

[112] Y. W. Lam and M. R. Monazzam, "On the modeling of sound propagation over multi-impedance discontinuities using a semiempirical diffraction formulation," *J. Acoust. Soc. Am.*, vol. 120, no. 2, p. 686, Aug. 2006.

[113] J. S. Robertson, P. J. Schlatter, and W. L. Siegmann, "Sound propagation over impedance discontinuities with the parabolic approximation," *J. Acoust. Soc. Am.*, vol. 99, no. 2, p. 761, Feb. 1996.

[114] I. Bashir, T. J. Hill, S. Taherzadeh, K. Attenborough, and M. Hornikx, "Reduction of surface transport noise by ground roughness," *Appl. Acoust.*, 2013.

[115] T. L. Richards and K. Attenborough, "Solid particle motion induced by a point source above a poroelastic half-space," *J. Acoust. Soc. Am.*, vol. 86, no. 3, pp. 1085–1092, Sep. 1989.

[116] W. Lauriks, L. Kelders, and J. F. Allard, "Poles and zeros of the reflection coefficient of a porous layer having a motionless frame in contact with air," *Wave motion*, vol. 28, pp. 59 – 67, 1998.

[117] J. F. Allard, G. Jansens, G. Vermeir, and W. Lauriks, "Frame-borne surface waves in air-saturated porous media," *J. Acoust. Soc. Am.*, vol. 111, no. 2, p. 690, Feb. 2002.

[118] L. M. Brekhovskikh, *Waves in layered media Translated by D. Liberman and R. T. Beyer.* Academic press, London and New York, 1960, pp. 44 – 61.

[119] R. J. Donato, "Model experiments on surface waves," *J. Acoust. Soc. Am.*, vol. 63, no. 3, p. 700, Mar. 1978.

[120] C. Hutchinson-Howorth and K. Attenborough, "Model experiments on air-coupled surface waves," *J. Acoust. Soc. Am.*, vol. 92, no. 4, p. 2431, Oct. 1992.

[121] G. A. Daigle, M. R. Stinson, and D. I. Havelock, "Experiments on surface waves over a model impedance plane using acoustical pulses," *J. Acoust. Soc. Am.*, vol. 99, no. 4, p. 1993, Apr. 1996.

[122] W. Zhu, M. R. Stinson, and G. A. Daigle, "Scattering from impedance gratings and surface wave formation," *J. Acoust. Soc. Am.*, vol. 111, no. 5, p. 1996, May 2002.

[123] W. Zhu, G. A. Daigle, and M. R. Stinson, "Experimental and numerical study of air-coupled surface waves generated above strips of finite impedance," *J. Acoust. Soc. Am.*, vol. 114, no. 3, p. 1243, Sep. 2003.

[124] W. Lauriks, L. Kelders, and J. F. Allard, "Surface waves above gratings having a triangular profile," *Ultrasonics*, vol. 36, no. 8, pp. 865–871, Jul. 1998.

[125] I. Bashir, T. J. Hill, S. Taherzadeh, and K. Attenborough, "Surface waves over periodically-spaced rectangular strips," *J. Acoust. Soc. Am.*, 2013.

[126] J. F. Allard, L. Kelders, and W. Lauriks, "Ultrasonic surface waves above a doubly periodic grating," *J. Acoust. Soc. Am.*, vol. 105, no. 4, p. 2528, Apr. 1999.

[127] J. Tizianel, J. F. Allard, and B. BROUARD, "Surface waves above honeycombs," *J. Acoust. Soc. Am.*, vol. 104, no. 4, p. 2525, Oct. 1998.

[128] L. Kelders, W. Lauriks, and J. F. Allard, "Surface waves above thin porous layers saturated by air at ultrasonic frequencies," *J. Acoust. Soc. Am.*, vol. 104, no. 2, p. 882, Aug. 1998.

[129] D. G. Albert, "Observations of acoustic surface waves in outdoor sound propagation," *J. Acoust. Soc. Am.*, vol. 113, no. 5, p. 2495, May 2003.

[130] M. R. Stinson, "Surface wave formation at an impedance discontinuity," *J. Acoust. Soc. Am.*, vol. 102, no. 6, p. 3269, Dec. 1997.

[131] R. Martínez-Sala, J. Sancho, J. V. Sánchez, V. Gómez, J. Llinares, and F. Meseguer, "Sound attenuation by sculpture," *Nature*, vol. 378, no. 6554, pp. 241–241, Nov. 1995.

[132] J. Sánchez-Pérez, D. Caballero, R. Mártinez-Sala, C. Rubio, J. Sánchez-Dehesa, F. Meseguer, J. Llinares, and F. Gálvez, "Sound Attenuation by a Two-Dimensional Array of Rigid Cylinders," *Phys. Rev. Lett.*, vol. 80, no. 24, pp. 5325–5328, Jun. 1998.

[133] J. V. Sanchez-Perez, C. Rubio, R. Martinez-Sala, R. Sanchez-Grandia, and V. Gomez, "Acoustic barriers based on periodic arrays of scatterers," *Appl. Phys. Lett.*, vol. 81, no. 27, p. 5240, Dec. 2002.

[134] Y.-Y. Chen and Z. Ye, "Acoustic Attenuation by Two-Dimensional Arrays of Rigid Cylinders," *Phys. Rev. Lett.*, vol. 87, no. 18, p. 184301, Oct. 2001.

[135] A. Khelif, P. A. Deymier, B. Djafari-Rouhani, J. O. Vasseur, and L. Dobrzynski, "Two-dimensional phononic crystal with tunable narrow pass band: Application to a wavelength with selective frequency," *Appl. Physcis*, vol. 94, 2003.

[136] Y. Pennec, B. Djafari-Rouhani, J. O. Vasseur, A. Khelif, and P. A. Deymier, "Tunable filtering and demultiplexing in phononic crystals with hollow cylinders.," *Phys. Rev. E. Stat. Nonlin. Soft Matter Phys.*, vol. 69, no. 4 Pt 2, p. 046608, Apr. 2004.

[137] C. Goffaux, F. Maseri, J. O. Vasseur, B. Djafari-Rouhani, and P. Lambin, "Measurements and calculations of the sound attenuation by a phononic band gap structure suitable for an insulating partition application," *Appl. Phys. Lett.*, vol. 83, no. 2, p. 281, Jul. 2003.

[138] K. M. Ho, C. K. Cheng, Z. Yang, X. X. Zhang, and P. Sheng, "Broadband locally resonant sonic shields," *Appl. Phys. Lett.*, vol. 83, no. 26, p. 5566, Dec. 2003.

[139] X. Hu, C. Chan, and J. Zi, "Two-dimensional sonic crystals with Helmholtz resonators," *Phys. Rev. E*, vol. 71, no. 5, p. 055601, May 2005.

[140] J. Sánchez-Dehesa, V. M. Garcia-Chocano, D. Torrent, F. Cervera, S. Cabrera, and F. Simon, "Noise control by sonic crystal barriers made of recycled materials.," *J. Acoust. Soc. Am.*, vol. 129, no. 3, pp. 1173–83, Mar. 2011.

[141] A. Krynkin, O. Umnova, A. Yung Boon Chong, S. Taherzadeh, and K. Attenborough, "Predictions and measurements of sound transmission through a periodic array of elastic shells in air.," *J. Acoust. Soc. Am.*, vol. 128, no. 6, pp. 3496–506, Dec. 2010.

[142] A. Krynkin, O. Umnova, S. Taherzadeh, and K. Attenborough, "Analytical approximations for low frequency band gaps in periodic arrays of elastic shells.," *J. Acoust. Soc. Am.*, vol. 133, no. 2, pp. 781–91, Feb. 2013.

[143] A. Krynkin, O. Umnova, A. Y. B. Chong, S. Taherzadeh, and K. Attenborough, "Scattering by coupled resonating elements in air," *J. Phys. D. Appl. Phys.*, vol. 44, no. 12, p. 125501, Mar. 2011.

[144] V. Romero-García, J. V. Sánchez-Pérez, and L. M. Garcia-Raffi, "Tunable wideband bandstop acoustic filter based on two-dimensional multiphysical phenomena periodic systems," *J. Appl. Phys.*, vol. 110, no. 1, p. 014904, Jul. 2011.

[145] V. Romero-García, L. M. Garcia-Raffi, and J. V. Sánchez-Pérez, "Evanescent waves and deaf bands in sonic crystals," *AIP Adv.*, vol. 1, no. 4, p. 041601, Dec. 2011.

[146] A. Y. B. Chong, "Sonic crystal noise barriers, Phd thesis, Chapter 2: The Plane Wave Expansion (PWE) Method," The Open University, UK, 2012.

[147] A. Krynkin, O. Umnova, J. V. Sánchez-Pérez, A. Y. B. Chong, S. Taherzadeh, and K. Attenborough, "Acoustic insertion loss due to two dimensional periodic arrays of circular cylinders parallel to a nearby surface.," *J. Acoust. Soc. Am.*, vol. 130, no. 6, pp. 3736–45, Dec. 2011.

[148] A. Yung Boon Chong, "Sonic crystal noise barriers, PhD thesis, Chapter 8: Performance of sonic crystal noise barriers above a ground surface," The Open University, UK, 2012.

[149] M. A. Price, K. Attenborough, and N. W. Heap, "Sound attenuation through trees: Measurements and models," *J. Acoust. Soc. Am.*, vol. 84, no. 5, p. 1836, Nov. 1988.

[150] W. H. T. Huisman and K. Attenborough, "Reverberation and attenuation in a pine forest," *J. Acoust. Soc. Am.*, vol. 90, no. 5, p. 2664, Nov. 1991.

[151] A. K. Pal, V. Kumar, and N. C. Saxena, "NOISE ATTENUATION BY GREEN BELTS," *J. Sound Vib.*, vol. 234, no. 1, pp. 149–165, Jun. 2000.

[152] C.-F. Fang and D.-L. Ling, "Investigation of the noise reduction provided by tree belts," *Landsc. Urban Plan.*, vol. 63, no. 4, pp. 187–195, May 2003.

[153] A. I. Tarrero, M. A. Martín, J. González, M. Machimbarrena, and F. Jacobsen, "Sound propagation in forests: A comparison of experimental

results and values predicted by the Nord 2000 model," *Appl. Acoust.*, vol. 69, no. 7, pp. 662–671, Jul. 2008.

[154] T. Van Renterghem, D. Botteldooren, and K. Verheyen, "Road traffic noise shielding by vegetation belts of limited depth," *J. Sound Vib.*, vol. 331, no. 10, pp. 2404–2425, May 2012.

[155] S. Taherzadeh, I. Bashir, and K. Attenborough, "Aperiodicity effects on sound transmission through arrays of identical cylinders perpendicular to the ground.," *J. Acoust. Soc. Am.*, vol. 132, no. 4, pp. EL323–8, Oct. 2012.

[156] D. Aylor, "Noise Reduction by Vegetation and Ground," *J. Acoust. Soc. Am.*, vol. 51, no. 1B, p. 197, Jan. 1972.

[157] D. Aylor, "Sound Transmission through Vegetation in Relation to Leaf Area Density, Leaf Width, and Breadth of Canopy," *J. Acoust. Soc. Am.*, vol. 51, no. 1B, p. 411, Jan. 1972.

[158] M. J. M. Martens, "Foliage as a low-pass filter: Experiments with model forests in an anechoic chamber.," *J. Acoust. Soc. Am.*, vol. 67, no. 1, p. 66, Jan. 1980.

[159] D. E. Aylor, "Comments on "Foliage as a low-pass filter: Experiments with model forests in an anechoic chamber" [J. Acoust. Soc. Am. 67, 66–72 (1980)]," *J. Acoust. Soc. Am.*, vol. 70, no. 3, p. 891, Sep. 1981.

[160] M. J. M. Martens, "Absorption of acoustic energy by plant leaves," *J. Acoust. Soc. Am.*, vol. 69, no. 1, p. 303, Jan. 1981.

[161] M. J. M. Martens, P. P. J. Severens, H. A. W. M. Van Wissen, and L. A. M. Van Der Heijden, "Acoustic reflection characteristics of deciduous plant leaves," *Environ. Exp. Bot.*, vol. 25, no. 3, pp. 285–292, Aug. 1985.

[162] K. Attenborough, K. M. Li, and K. Horoshenkov, "Chapter 10: Predicting effects of vegetation, trees and turbulence," in in *Predicting Outdoor Sound*, Taylor and Francis, 2007, pp. 311–341.

[163] C.-F. Fang, "The criterion of noise attenuation by hedges," *Des. Nat. II*, 2004.

[164] HOSANNA Deliverable 4.4 Technical Report HSNNA_44_TRP_2011_10_15, "Model for effects of vegetation, crops and shrubs," 2011.

[165] M. E. Delany and E. N. Bazley, "A note on the effect of ground absorption in the measurement of aircraft noise," *J. Sound Vib.*, vol. 16, no. 3, pp. 315–322, 1971.

[166] HOSANNA Deliverable 4.5 Technical Report HSNNA_45_TRP_2012_11_22, "Acoustical effects of porous surfaces," 2012.

[167] HOSANNA Deliverable 8.2 Technical Report HSNNA_MEMO_2011_11_29_CTH01, "Production of the handbook and the summary brochure," 2011.

[168] HOSANNA Deliverable 2.3 Technical Report HSNNA_23_TRP_2011_11_29_CTH01, "Innovative barriers exploiting natural materials," 2011.

[169] HOSANNA Deliverable 6.2 Technical Report HSNNA_MEMO_2012_07_03_CTH02, "Holistic design and perceptual evaluation," 2012.

[170] J. P. Chambers and J. M. Sabatier, "Recent advances in utilizing acoustics to study surface roughness in agricultural surfaces," *Appl. Acoust.*, vol. 63, no. 7, pp. 795–812, 2002.

[171] M. Hornikx and J. Forssén, "Modelling of sound propagation to three-dimensional urban courtyards using the extended fourier PSTD method," *Appl. Acoust.*, vol. 72, no. 9, pp. 665–676, 2011.

[172] M. Hornikx, "PSTD results for configurations of parallel walls staggered, walls and a lattice," *Priv. Commun.*

[173] K. Attenborough, P. Boulanger, Q. Qin, and R. Jones, "Predicted influence of ballast and porous concrete on rail noise," *inter-noise, Brazil*, 2005.

[174] P. Boulanger, "Locally reacting compared to non-locally reacting ballast, Unpublished technical report, The Open University," 2005.

[175] B. Torino, J. Maillard, and C. Viardot, "Enregistrements de bruit de tramway, unpublished report, CSTB, Grenoble, France," 2012.

[176] K. M. Li, "Sound propagation over convex impedance surfaces," *J. Acoust. Soc. Am.*, vol. 104, no. 5, p. 2683, Nov. 1998.

[177] Q. Wang and K. M. Li, "Sound propagation over concave surfaces," *J. Acoust. Soc. Am.*, vol. 106, no. 5, p. 2358, Nov. 1999.

[178] C. Segio, R. Constanza, S. Pérez, and J. Vicente, "Analysis of the diffraction on the upper edge of an acoustic barrier formed by arrays of rigid scatterers," in *Inter-noise, Innsbruck, Austria*, 2013.